

# **The Last Interglacial in the Labrador Sea**

**LEILA DAWN HUME**

**PHD THESIS**

University of East Anglia  
School of Environmental Sciences

March, 2018

© This copy of the thesis has been supplied on condition that anyone who consults it is understood to recognise that its copyright rests with the author and that use of any information derived therefrom must be in accordance with current UK Copyright Law. In addition, any quotation or extract must include full attribution.



# ABSTRACT

A multi-proxy age model protocol was established using Labrador Sea sediment cores U1305 (57°N,48°W) and U1302 (50°N,45°W). These cores provided centennial-scale surface and deep-water records spanning the last interglacial (153-100ka). Ice rafted debris (IRD) counts and meltwater-runoff proxy Ba/Ca were used to investigate ice sheet instabilities; planktonic foraminiferal assemblages, planktonic  $\delta^{18}\text{O}$  and multi-species Mg/Ca records were used to reconstruct temperature and salinity; and fluctuations in Atlantic meridional overturning circulation (AMOC) were inferred from benthic  $\delta^{13}\text{C}$ .

Intense cold and ice rafting accompanied Heinrich events H11 (135–130ka) and H12 (140ka), as well as a previously unrecognised Heinrich event (H13; 150–148ka), during which benthic and planktonic  $\delta^{13}\text{C}$  values indicate reduced AMOC and nutrient-rich Antarctic bottom-water (AABW) incursions. During H11, three warm phases preceded cooling and massive IRD pulses. Strongly depleted U1302 planktonic  $\delta^{18}\text{O}$  accompanied all IRD-rich cold periods, particularly H11, attributed to sea-ice formation and enhanced meltwater input. No Younger Dryas-like event was observed.

Last interglacial temperatures were 2–5°C warmer in U1305, but similar to modern values at U1302, suggesting differing latitudinal responses to increased insolation (129–126ka). A diatom mat deposited ~128.7–128.6ka in U1305 indicates a proximal subarctic convergence front. Palaeotemperature reconstructions reveal two last interglacial warm maxima. The first (128.5–126.5ka) had the most diverse foraminiferal assemblages and was coeval with continued Greenland ice-sheet melt. A previously reported red layer, linked to a Laurentide outburst flood, has been dated to ~126.5ka and marks the culmination of localised intra-interglacial cooling. Subsequent AABW incursion events suggest rapid AMOC weakening and instability. Mg/Ca results reveal a second warming (123–117ka) associated with a vigorous AMOC, and was attributed to a stronger Irminger Current. IRD, SST and isotopic evidence indicate a prominent cold event ~117ka, followed by surface cooling and ice rafting linked to the North Atlantic cold events C26–C23.

# CONTENTS

Abstract .....	i
Contents .....	ii
List of Figures .....	vi
List of Tables .....	xii
Acknowledgements .....	xiv
<b>1   Introduction</b> .....	<b>1</b>
1.1   Aims and Objectives .....	2
1.2   Thesis Outline .....	4
<b>2   North Atlantic Oceanography</b> .....	<b>6</b>
2.1   Wind Stress .....	7
2.2   Thermohaline Circulation .....	9
2.2.1   Convection in the Nordic Seas .....	11
2.2.2   Open Ocean Convection.....	11
2.3   Bathymetry .....	14
2.4   Major Water Masses of the North Atlantic.....	17
2.4.1   Seawater Oxygen Isotope Database .....	17
2.4.2   Subpolar Mode Water .....	19
2.4.3   Labrador Sea Water.....	20
2.4.4   Denmark Strait Overflow Water .....	21
2.4.5   Iceland-Scotland Overflow Water.....	21
2.4.6   North East Atlantic Deep Water.....	22
2.4.7   North Atlantic Deep Water .....	23
2.4.8   Antarctic Bottom Water .....	24
2.5   Major Ocean Currents of the North Atlantic.....	24
2.5.1   North Atlantic Current .....	26
2.5.2   Irminger Current.....	27
2.5.3   East Greenland Current .....	28
2.5.4   West Greenland Current.....	29
2.5.5   Labrador Current .....	30

2.5.6   Deep Western Boundary Current .....	30
2.6   Oceanography Summary .....	31
<b>3   Palaeoceanography</b> .....	<b>32</b>
3.1   Pleistocene Glacial Cycles .....	32
3.2   Marine Isotope Stages .....	34
3.3   Ice Rafted Debris.....	35
3.3.1   Heinrich Events .....	36
3.3.2   Terminations.....	43
3.4   The Penultimate Deglaciation .....	46
3.5   The Last Interglacial.....	48
3.6   The Last Glacial Inception .....	52
3.7   Changes in Ocean Circulation.....	53
3.8   Palaeoceanography Summary .....	56
<b>4   Sedimentology</b> .....	<b>57</b>
4.1   Expedition 303 .....	57
4.1.1   Eirik Ridge .....	59
4.1.2   Orphan Knoll.....	63
4.1.3   Sediment Core Processing.....	66
4.2   Ice Rafted Debris.....	66
4.2.1   Method .....	66
4.2.2   A Question of Carbonate.....	68
4.2.3   Ice Rafted Debris Count U1305 Results .....	70
4.2.4   Ice Rafted Debris Count U1302 Results .....	77
4.3   Red Layer in the Labrador Sea.....	82
4.3.1   U1305 Depth Measurements .....	85
4.3.2   U1302 Depth Measurements .....	88
4.4   Diatom Mats .....	90
4.4.1   Mechanisms of Diatom Mat Deposition .....	93
4.4.2   Diatom Mat in U1305 .....	94
4.5   Sedimentology Summary .....	97

<b>5   Planktonic Foraminifera</b> .....	99
5.1   Planktonic Foraminifera .....	99
5.2   Major Subpolar Planktonic Foraminiferal Species .....	100
5.2.1   Neogloboquadrina pachyderma (sinistral) .....	103
5.2.2   Neogloboquadrina incompta .....	104
5.2.3   Globigerina bulloides .....	105
5.2.4   Globigerinita glutinata .....	106
5.2.5   Globigerinita uvula.....	106
5.2.6   Turborotalita quinqueloba .....	107
5.2.7   Globorotalia inflata .....	108
5.2.8   Complications with Foraminifera.....	109
5.3   Transfer Functions.....	110
5.4   Assemblage Counts .....	113
5.4.1   Methods .....	113
5.4.2   U1305 Faunal Assemblage Results.....	115
5.4.3   U1302 Faunal Assemblage Results.....	119
5.5   Foraminifera Summary .....	125
<b>6   Geochemistry</b> .....	127
6.1   Mg/Ca Ratios.....	127
6.1.1   Picking.....	128
6.1.2   Cleaning .....	129
6.1.3   ICP-OES Analysis.....	130
6.1.4   Temperature Calibration .....	132
6.1.5   Vial Blanks.....	135
6.1.6   U1305 Size Fraction Tests .....	137
6.1.7   Mg/Ca Ratio Results .....	146
6.2   Ba/Ca as a Proxy for Meltwater Runoff.....	149
6.3   Stable Isotopes.....	151
6.3.1   Oxygen .....	151
6.3.2   Carbon .....	153
6.3.3   Stable Isotope Methods .....	155
6.3.4   Stable Isotope Results .....	157
6.4   Geochemistry Summary .....	162

<b>7   Age Model</b> .....	164
7.1   Benthic Foraminiferal Oxygen Isotopes .....	164
7.2   Radiometric Dating .....	167
7.3   Ice Core Chronologies.....	168
7.4   Age Models for U1305 and U1302 .....	169
7.4.1   Previously Published Chronologies .....	170
7.4.2   Age Model Construction .....	177
7.4.3   Tie Points.....	178
7.4.4   Age Models for Reference Records .....	186
7.5   Age Model Summary .....	189
<b>8   Discussion</b> .....	192
8.1   Cause for Controversy.....	192
8.1.1   Heinrich Events .....	193
8.1.2   North Atlantic Cold Events .....	193
8.1.3   Cores for Comparison .....	196
8.2   Penultimate Glacial Period.....	197
8.2.1   Heinrich Event 13.....	201
8.2.2   The Penultimate Glacial Maximum .....	208
8.2.3   Termination II .....	210
8.2.4   Diatom Mat .....	215
8.3   The Last Interglacial.....	216
8.3.1   The Early Last Interglacial .....	222
8.3.2   The Red Layer .....	224
8.3.3   The C27 Last Interglacial Climate Events .....	228
8.3.4   The 117 ka Cold Event.....	229
8.3.5   Normalised Last Interglacial Temperature Estimates .....	2300
8.4   The Last Glacial Inception .....	232
8.5   Summary and Conclusions .....	235
8.6   Suggestions for Future Improvements .....	239
<b>References</b> .....	242

# LIST OF FIGURES

Figure 2.1	Modern North Atlantic surface circulation	6
Figure 2.2	Average mean wintertime (Dec – Mar) atmospheric conditions above the North Atlantic (1968 – 1997)	7
Figure 2.3	Deep water circulation in the North Atlantic	10
Figure 2.4	Open ocean convection in the Labrador Sea	11
Figure 2.5	Winter mixed layer depths (1996 – 1998) obtained using profiling floats	12
Figure 2.6	Bathymetric map of the subpolar North Atlantic	15
Figure 2.7	Vertical section showing the effect of the Greenland-Scotland Ridge on potential temperature and salinity	16
Figure 2.8	Global gridded surface seawater $\delta^{18}\text{O}$ including the locations of U1305 and U1302	18
Figure 2.9	Characteristics of major North Atlantic water masses.	20
Figure 2.10	Subpolar North Atlantic schematic circulation diagram	22
Figure 2.11	Deep and intermediate water masses of the North Atlantic	19
Figure 2.12	North Atlantic surface circulation deduced from surface drifters	25
Figure 2.13	Flow of the North Atlantic Current around the “north west corner”	27
Figure 2.14	Map of the Labrador Sea showing Eddy Kinetic Energy overlain by individual trajectories of drifters	28
Figure 2.15	Eddy activity within the Labrador Sea	29
Figure 3.1	Interglacials of the last 800 ka	32
Figure 3.2	Distribution of insolation by latitude	33
Figure 3.3	The LR04 benthic foraminiferal $\delta^{18}\text{O}$ stack	34
Figure 3.4	Recently updated lettering scheme for marine isotope substages	34
Figure 3.5	Location of North Atlantic cores containing Heinrich deposits	37
Figure 3.6	Comparison of the last four Terminations	39

Figure 3.7	Distribution of types and thickness of Heinrich Layer 1 in the Labrador Sea	40
Figure 3.8	Planktonic ( <i>N. pachyderma</i> ( <i>s</i> )) $\delta^{18}\text{O}$ and coarse fraction from HU90-013-013 on the Eirik Ridge	42
Figure 3.9	Sequence of events during the last deglaciation	44
Figure 3.10	Estimates of global mean sea level from the Red Sea	45
Figure 3.11	Comparison between the Termination II and Termination I illustrated using proxy data from MD99-2227	47
Figure 3.12	Reconstructed temperature and elevation history of the NEEM ice core	48
Figure 3.13	A probabilistic study of last interglacial global sea level	49
Figure 3.14	Selection of palaeoclimate records covering the last interglacial	50
Figure 3.15	Schematic suggesting changes to the subpolar gyre	52
Figure 3.16	Section along the North Atlantic including the topographic high of the Greenland-Scotland Ridge	54
Figure 3.17	Circulation and ventilation changes during the Holocene, Last Glacial Maximum and Heinrich Stadial 1	54
Figure 4.1	Site locations for Expedition 303/306 within the North Atlantic	57
Figure 4.2	Core locations of U1302 and U1305	59
Figure 4.3	Magnetic susceptibility, bulk density, carbonate content and planktonic oxygen isotopes within Core MD99-2227	61
Figure 4.4	Schematic showing surface current flow of the North Atlantic Current near to Orphan Knoll	63
Figure 4.5	Map showing potential bedrock sources of ice rafted debris	67
Figure 4.6	U1305 IRD percentage abundance and concentration including spurious carbonate	69
Figure 4.7	U1302 IRD percentage abundance (red) and concentration (blue) including spurious carbonate	69
Figure 4.8	U1305 IRD percentage composition by lithology	71
Figure 4.9	U1305 IRD percentage abundance for individual lithologies	72
Figure 4.10	U1305 IRD composition by lithology as a concentration	73
Figure 4.11	U1305 IRD concentration of individual lithologies on a log scale	74

Figure 4.12	U1305 non-IRD categories as a concentration	76
Figure 4.13	U1302 IRD percentage composition by lithology	77
Figure 4.14	U1302 IRD percentage abundance for individual lithologies	78
Figure 4.15	U1302 IRD composition by lithology as a concentration	79
Figure 4.16	U1302 IRD concentration of individual lithologies	80
Figure 4.17	U1302 non-IRD categories as a concentration	81
Figure 4.18	Digital line-scan images showing a red layer in sediment cores U1302A and U1305C	83
Figure 4.19	Map showing glacial lake Agassiz trapped behind the melting Laurentide ice sheet	84
Figure 4.20	Close-up digital photographs of sediment core U1305	87
Figure 4.21	Close-up digital photographs of sediment core U1302	89
Figure 4.22	Location of site U1304 and EW9303-17 which contained thick laminated diatom ooze deposits	91
Figure 4.23	Climate proxy evidence within core EW9303-2JPC from the Flemish Cap showing the position of a diatom layer	92
Figure 4.24	Schematic of a proposed mechanism which concentrates mat-forming diatoms on the warm side of ocean frontal systems	93
Figure 4.25	Selected proxy evidence relating to the red layer and diatom mat found in U1305	95
Figure 5.1	Biogeographical abundance of three dominant modern polar-subpolar-transitional planktonic foraminifera	101
Figure 5.2	Summary of species distribution, assemblage and abundance across the five major latitudinal provinces	102
Figure 5.3	Scanning electron microscope image of <i>N. pachyderma</i> ( <i>s</i> )	103
Figure 5.4	Scanning electron microscope image of <i>N. incompta</i>	104
Figure 5.5	Scanning electron microscope image of <i>G. bulloides</i>	105
Figure 5.6	Scanning electron microscope image of <i>G. glutinata</i>	106
Figure 5.7	Scanning electron microscope image of <i>G. uvula</i>	106
Figure 5.8	Scanning electron microscope image of <i>T. quinqueloba</i>	107
Figure 5.9	Scanning electron microscope image of <i>G. inflata</i>	108
Figure 5.10	Monthly modern seawater temperature profiles at the locations of U1302 and U1305	109

Figure 5.11	Annually stacked and biweekly averages from a sediment trap time-series of <i>N. pachyderma</i> ( <i>s</i> ) and <i>G. bulloides</i> (bottom) shell flux	110
Figure 5.12	U1305 planktonic foraminiferal percentage abundance results	116
Figure 5.13	U1302 planktonic foraminiferal percentage abundance results	120
Figure 5.14	Proportion of major foraminifera species percentage abundance in sediment cores U1305 and U1302	123
Figure 6.1	Illustration of Mg/Ca calibrations	132
Figure 6.2	Comparison between Mg/Ca ratios in <i>N. pachyderma</i> ( <i>s</i> ) and estimates of calcification temperature	134
Figure 6.3	The effect of drying location upon the drying time of 10 acid cleaned vials	136
Figure 6.4	Size fraction tests for typical interglacial and glacial conditions using <i>N. pachyderma</i> ( <i>s</i> ) from sediment core U1305	138
Figure 6.5	Replicate analyses for four <i>G. bulloides</i> size fractions from U1305 coretop samples	139
Figure 6.6	Replicate analyses for three different size fractions using <i>N. pachyderma</i> ( <i>s</i> ) from the coretop of sediment core U1305	141
Figure 6.7	Size fractions used to produce Mg/Ca ratios from U1305 <i>G. bulloides</i>	144
Figure 6.8	Size fractions used to produce Mg/Ca ratios from U1305 <i>N. incompta</i>	144
Figure 6.9	Size fractions used to produce Mg/Ca ratios from U1305 <i>N. pachyderma</i> ( <i>s</i> )	145
Figure 6.10	Temperature proxies from sediment core U1305	147
Figure 6.11	Temperature proxies and abundance data from sediment Core U1302	148
Figure 6.12	U1305 Ba/Ca ratios in <i>N. pachyderma</i> ( <i>s</i> )	149
Figure 6.13	U1302 Ba/Ca ratios in <i>N. pachyderma</i> ( <i>s</i> )	151
Figure 6.14	Comparison between new and previously published U1305 stable oxygen and carbon data	156
Figure 6.15	U1305 multi-species $\delta^{18}\text{O}$ data	157
Figure 6.16	U1305 multi-species $\delta^{13}\text{C}$ data	159
Figure 6.17	Comparison between U1302 oxygen and carbon isotopes	161

Figure 7.1	Last interglacial records from sediment core MD95-2042 dated using radiometric dating of fossil corals	168
Figure 7.2	The relationship between percentage of <i>N. pachyderma</i> ( <i>s</i> ) and summer SST in the North Atlantic	170
Figure 7.3	Sedimentation rates from the age model of Hillaire-Marcel et al. (2011)	171
Figure 7.4	U1305 and U1302 data plotted on the timescale of Hillaire-Marcel et al. (2011).	172
Figure 7.5	Sedimentation rates for the latest working age models of U1305 (Hillaire-Marcel, personal communication), and U1302 on the timescale of Channell et al. (2012)	173
Figure 7.6	u1305 on the latest working age model of Hillaire-Marcel (personal communication) and U1302 data on the timescale of Channell et al. (2012)	175
Figure 7.7	Multi-species oxygen and carbon isotopes from U1302 and Eirik Ridge core HU90-013-013	176
Figure 7.8	Age control points used to tie U1305 to LS15	179
Figure 7.9	Age control points used to tie U1302 to LS15	179
Figure 7.11	Multi-proxy U1305 and U1302 data illustrating tie points used in the construction of the age model for this study	181
Figure 7.12	Tie points for the age model constructed for this study showing sedimentation rates for U1305 and U1302	186
Figure 7.13	Age model adjusting MD03-2664 to LS15	187
Figure 7.14	Age model adjusting MD95-2042 to LS15	188
Figure 7.15	Age model adjusting ODP-980 to LS15	188
Figure 8.1	IRD, abundance of <i>N. pachyderma</i> ( <i>s</i> ) and MAT summer SSTs from sediment core ODP-980, illustrating the series of North Atlantic cold (“C”) events.	194
Figure 8.2	Map showing location of sediment cores MD03-2664, ODP-980 and MD95-2042	197
Figure 8.3	U1305 multi-proxy results and planktonic isotopes from U1302 through 128 – 154 ka	198
Figure 8.4	U1302 multi-proxy results and benthic isotopes from U1305 through 128 – 142 ka	199
Figure 8.5	Expanded section showing Heinrich Event 11 in more detail	200
Figure 8.6	U1302 multi-proxy data (Channel et al. 2012)	203

Figure 8.7	Proxy data from U1308 comparing TI with TII	204
Figure 8.8	Evidence for a period of cold surface waters related to European ice sheet collapse at ~150 ka	205
Figure 8.9	Detrended seawater $\delta^{18}\text{O}$ from Pacific core TR163-19	206
Figure 8.10	The timing of Mg/Ca SST, $\delta^{18}\text{O}$ of calcite from eastern equatorial Pacific sediment core TR163-19 over the last interglacial	207
Figure 8.11	Speleothem $\delta^{18}\text{O}$ from Sanbao Cave, China	208
Figure 8.12	Sea ice cover in the Labrador Sea	213
Figure 8.13	Last interglacial palaeotemperature estimates	218
Figure 8.14	Last interglacial IRD and Ba/Ca results	219
Figure 8.15	Last interglacial ice core, planktonic and benthic $\delta^{18}\text{O}$	220
Figure 8.16	Last interglacial planktonic and benthic $\delta^{13}\text{C}$	221
Figure 8.17	Data concerning the red layer from U1302 by Nicholl et al. (2012)	226
Figure 8.18	Normalised temperature reconstructions using MAT and Mg/Ca from <i>G. bulloides</i> , <i>N. incompta</i> and <i>N. pachyderma (s)</i> for U1305 and U1302	231
Figure 8.19	Proxy records from NEAP18K in the North Atlantic	233

# LIST OF TABLES

Table 2.1	North Atlantic water mass characteristics	19
Table 2.2	Observed mean and maximum speeds for major North Atlantic currents obtained from surface drifters	24
Table 3.1	Comparison of labels and ages for Heinrich events within the literature	41
Table 4.1	Summary of Expedition 303 operations for cores relevant to this study	62
Table 4.2	Detailed identification information about samples containing the red layer in U1305A	86
Table 4.3	Detailed identification information about samples containing the red layer in U1302C	88
Table 4.4	IRD data from the three samples containing a diatom mat in U1305	95
Table 4.5	Individual foraminifera species percentages from the three samples containing a diatom mat in U1305	96
Table 5.1	Summary statistics for faunal assemblage data from U1305 and U1302 used in generating a MAT SST estimate	113
Table 5.2	Depths and ages of stratigraphic zonation of the planktonic assemblage identified by cluster analysis	115
Table 5.3	Maximum relative abundance of low abundance species in sediment cores U1305 and U1302	118
Table 6.1	Preferred size fraction and number of each foraminifera species picked for Mg/Ca analysis	128
Table 6.2	Criteria used to screen samples for contaminant phases of clay or silicate which could compromise Mg/Ca ratios	131
Table 6.3	Results from the vial blank cleaning test	136
Table 6.4	Summary statistics for size fraction tests representing typical interglacial and glacial samples using <i>N. pachyderma</i> ( <i>s</i> ) from sediment core U1305	138
Table 6.5	Summary statistics for size fraction tests using <i>G. bulloides</i> from U1305 coretop samples	140
Table 6.6	Summary statistics for surface replicate Mg/Ca analyses using different size fractions of <i>N. pachyderma</i> ( <i>s</i> ) from the coretop of sediment core U1305	141

Table 6.7	Summary statistics for surface replicate Mg/Ca analyses of “dirty” specimens of <i>N. pachyderma</i> ( <i>s</i> ) subject to the usual cleaning protocol from the coretop of sediment core U1305	142
Table 7.1	Age control points pertinent to the present study from Hillaire-Marcel et al. (2011)	171
Table 7.2	Estimated tie points derived from sedimentation rate changes from the latest working age model for U1305 (Claude Hillaire-Marcel, personal communication), the published age model of Channell et al. (2012) for U1302	174
Table 7.3	Isotopic range of mean $\delta^{18}\text{O}$ values for the penultimate glacial (132 – 142 ka) and last interglacial (128 – 116 ka) periods	176
Table 7.4	Tie points used to construct age models for U1302 and U1305 in this study	179
Table 7.5	Tie points used to construct age models for MD03-2664, MD95-2042 and ODP-980 based on LS15	189
Table 7.6	Protocol for age model construction in the Labrador Sea, based on the methods outlined in this study	191
Table 8.1	Sequence of climate events including dates, proxies used and references	195
Table 8.2	Details of North Atlantic sediment cores discussed in the text	196

# ACKNOWLEDGEMENTS

This thesis would never have been written if my friends and family had not believed that I could do it, even (and especially) when I did not. Firstly, particular thanks to my husband Matt, for endless patience and cups of tea, also to his parents Jacky and John for endless babysitting, and to my son Mortimer, for endless amusement and distraction, and for understanding that Mummy had to work. Many thanks to my Mum Carol, for constant love and encouragement.

Enormous gratitude to my incredibly patient supervisor Mark Chapman, whose support and advice over 7 years helped me understand the incomprehensible, as well as to Karen Heywood and Nikolai Pedentchouk for their patience and guidance. Grateful thanks to Stefanie Kaboth, for allowing me to display her U1302 benthic isotopes, and for kind and generous helpful emails from Claude Hillaire-Marcel and Antje Volker.

Thanks in advance to my examiners (and apologies for the length!).

My thanks also to Liz Farmer and Katie Miller, for teaching me that forams can be friends. Thanks also to Graham Chilvers, for reassembling the ICP on many occasions.

I would like to thank the University of East Anglia for funding this study.

# 1 | INTRODUCTION

Human society is dependent upon the climate, which is a constantly changing product of complex interactions between the land, oceans, atmosphere, cryosphere and biosphere. One way to help understand and prepare for possible rapid and global changes in an uncertain future (IPCC 2013) is to understand how the climate has operated in the past. The most complete surviving evidence exists for the last interglacial period, which occurred between 129 – 116 thousand years ago (ka) (Dutton and Lambeck 2012). Also referred to as marine isotope substage (MIS) 5e, it is generally correlated with the Eemian *sensu stricto* in terrestrial pollen records (e.g. Govin et al. 2015). The last interglacial was one of the warmest periods of the last 800,000 years (PAGES 2016). Although orbital configuration and therefore insolation were not the same as during the Holocene (Berger et al. 2007), MIS 5e provides a good test bed to analyse climate response to increased global temperatures.

To call this planet Earth is to ignore the fact that over 70 % of its surface is ocean. The high heat capacity of water means the constant flow through all major ocean basins (Broecker 1991) redistributes vast amounts of heat globally. Heat is released to the atmosphere from surface waters, which can then become dense enough to sink, and which further affects the strength of surface water circulation. Changes in ocean circulation, therefore, play a pivotal role in abrupt climate change (e.g. Clark et al. 2002). In the northern hemisphere, deep water formation occurs only in the Nordic and Labrador Seas. Open ocean convection within the Labrador Sea is highly variable (Yashayaev 2007) and depends upon winter conditions within the cyclonic subpolar gyre (Lazier et al. 2002). Located within the Irminger and Labrador Seas, the subpolar gyre is periodically subject to vast quantities meltwater from the surrounding Greenland and Laurentide ice sheets, particularly during glacial and interglacial transitions (Clark et al. 2002a). Global ocean circulation is therefore sensitive to relatively small changes in the temperature and freshwater balance of the North Atlantic (Keigwin et al. 1994; Rahmstorf 2000), which makes the Labrador Sea the ideal location to study palaeoceanography.

## 1.1 | AIMS AND OBJECTIVES

The overall aims of this study were to investigate both long-term and rapid climate fluctuations across the last interglacial period using two high resolution sediment cores from the north (U1305) and south (U1302) of the Labrador Sea. These cores provide material capable of answering questions about the rate, character and magnitude of oceanographic change as the climate cycled from glacial to interglacial and back to glacial conditions between ~153 and ~100 ka. Previously, a planktonic isotopic stratigraphy was published for both cores (Hillaire-Marcel et al. 2011), along with several palaeomagnetic and detrital layer stratigraphies based upon core scanning techniques (Mazaud et al. 2009, 2012; Channell et al. 2012; Channell and Hodell 2013; Stoner et al. 2013; Channell 2017a, b, c), as well as studies of diagenesis (Kawamura 2010, 2012) and chemical weathering (Crocket 2012). In this study, detailed palaeoclimatic and palaeoceanographic investigations have been undertaken using ice rafted debris counts, planktonic foraminiferal assemblages, planktonic and benthic isotopes and multi-species magnesium-to-calcium ratios. Three main climate states are considered in this study, the penultimate glacial period (MIS 6b-a), the last interglacial itself (MIS 5e) and the last glacial inception (MIS 5d-c), and results reveal how oceanographic conditions changed in the Labrador Sea as the climate shifted between these states.

The following series of objectives and specific research questions are considered:

1. The extent and stability of large ice sheets on surrounding land masses.
  - Were rates and sources of marine calving glaciers steady or episodic during the three climate states identified above?
  - Can any Heinrich-type events be identified at the end of the penultimate glacial period?
  - What is the relationship between periods of enhanced or reduced ice rafting and other climate proxies?
  - Was the Greenland ice sheet smaller than today during the last interglacial period?
  - Does glacial build-up during the last glacial inception appear to be regionally synchronous?

2. The timing of climate events.
  - How can new age models be constructed for these cores with the aid of additional proxy information?
  - Are these age models consistent with each other?
  - How do these new age models compare with previously published chronologies?
  
3. The nature of the penultimate deglacial period (Termination II) in the Labrador Sea.
  - Was Termination II a single event, or a series of events?
  - How rapidly did the climate change?
  - Is there evidence of a Younger Dryas-type event during Termination II?
  - How can the start of the last interglacial period be defined?
  
4. The character of the last interglacial period (MIS 5e) in the Labrador Sea.
  - How warm was the Labrador Sea during the last interglacial period?
  - Is there an identifiable period of optimum climate (i.e. the warmest temperatures)?
  - If so, when did that occur and how does it compare to insolation and global ice volumes?
  - Was there a glacial lake outburst event analogous to the 8.2 ka event which occurred during the Holocene?
  - If so, what was its relationship with the wider climate (i.e. a cause or a consequence of climate change)?
  - Is there evidence of climate instability within the last interglacial (i.e. the C27 series of intra-interglacial climate events of Oppo et al. 2006, the 117 ka event of Irvalı et al. 2016)?
  
5. The expression of the last glacial inception (MIS 5d-c) in the Labrador Sea.
  - What was the extent and rapidity of climate deterioration during the last glacial build-up?

- Are the North Atlantic series of cold (“C”) events (e.g. Chapman and Shackleton 1999, Bond et al. 1999, Bond and Lotti 1995, McManus et al. 1994) represented in climate proxies of the Labrador Sea?

Several different and complimentary methods which have not previously been applied to either sediment core U1305 or U1302 were selected in order to provide detailed information about surface, sub-surface and deep water masses in the Labrador Sea across the last interglacial period. This study presents the first series of ice rafted debris counts and temperature reconstructions from both planktonic foraminiferal faunal assemblage data and multi-species magnesium-to-calcium ratios reflecting both surface and sub-surface conditions, together with barium-to-calcium ratios reflecting terrestrial meltwater runoff, a new benthic isotope record for U1305, and supplementary stable isotope data which infill gaps in previously published planktonic isotope records for both U1305 and U1302 (Hillaire-Marcel et al. 2011).

## 1.2 | THESIS OUTLINE

Chapter 2 outlines the current oceanography of the region, defining major water masses and currents of importance to this study. Chapter 3 presents a brief introduction to palaeoceanography in general: what is known, how it is known (and what is unknown) about the last interglacial in the Labrador Sea. Sedimentology is covered in Chapter 4, and which includes detailed information about both marine sediment cores used in this study, discussion of an unusual red layer found within both cores, a diatom mat in sediment core U1305, and results from ice rafted debris counts. The major relevant foraminiferal species are introduced in Chapter 5, together with planktonic foraminiferal assemblage results and temperature reconstructions using the modern analogue technique (MAT). Chapter 6, the final results chapter, concerns geochemical methods and results for magnesium to calcium ratios (Mg/Ca) and barium to calcium ratios (Ba/Ca) from planktonic foraminifera, and stable isotopes (oxygen and carbon) from both planktonic and benthic foraminifera. Chapter 7 contains a short review of methods used to date sediment cores generally, and previously published age models for both cores, followed by the approach and precise methods used to produce age models for both cores in this study. Discussion (Chapter 8) is split into three chronological sections covering the penultimate deglacial period, the last interglacial itself, and the last glacial

inception. After this, the conclusion synthesises these results into a cohesive picture, summarising the major findings and their implications for the wider region, and therefore the contribution this study makes to the state of knowledge about the last interglacial in the Labrador Sea. Chapter 8 concludes with areas that may be improved upon in the future.

*“The mind seemed to grow giddy by looking so far into the abyss of time; and while we listened with earnestness and admiration to the philosopher who was now unfolding to us the order and series of these wonderful events, we became sensible how much farther reason may sometimes go than imagination can venture to follow.”*

John Playfair, *Biographical Account of the Late Dr James Hutton, F.R.S. Edin.* (read 10<sup>th</sup> January 1803)

## 2 | NORTH ATLANTIC OCEANOGRAPHY

Before considering the last interglacial, it is necessary to examine what is known about North Atlantic circulation and water masses in the present, which can be observed and measured in far greater detail. The oceans and atmosphere form an intrinsically linked climate system. This system is driven by the sun, which influences both the major drivers of ocean circulation – wind stress (section 2.1), which principally affects horizontal currents within the upper ocean, and thermohaline forcing (section 2.2), which ventilates the deep oceans. Bathymetry is of particular influence on circulation in the Labrador Sea (section 2.3). The major water masses (section 2.4) and surface currents (section 2.5) have been known to mariners for centuries (Figure 2.1), but the details and driving mechanisms of global meridional overturning circulation are still areas of active research. Note that throughout this thesis salinity is measured on the practical salinity scale, which is a conductivity ratio and as such has no units.

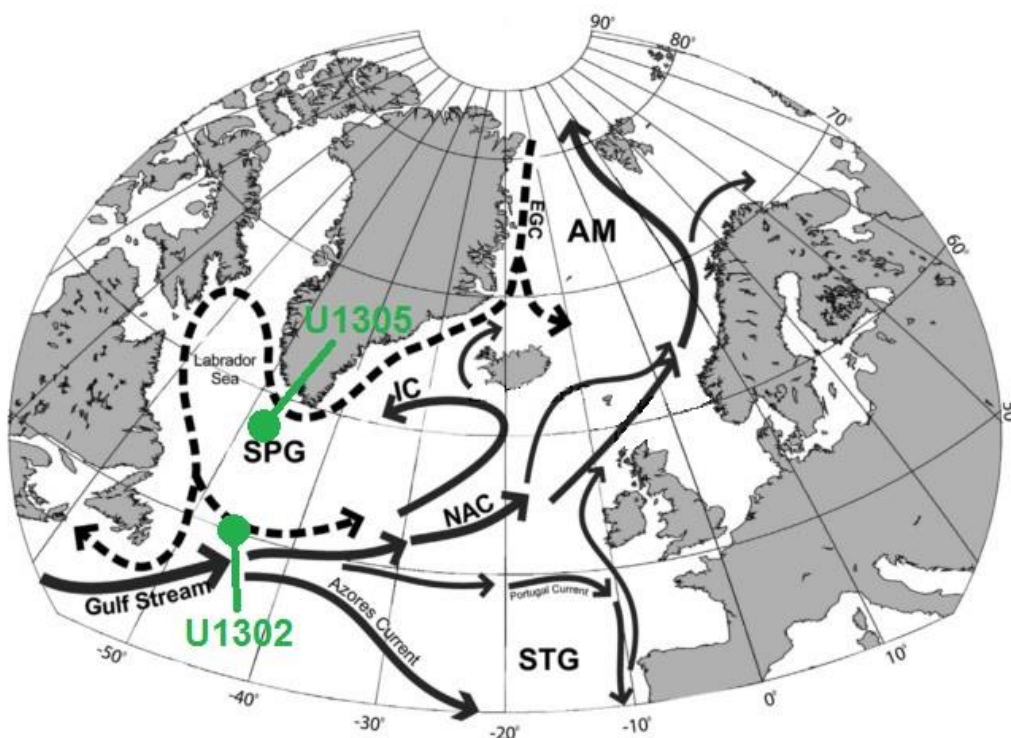


**Figure 2.1** | Modern North Atlantic surface circulation. Sediment core locations U1305 and U1302 are shown in green. Solid (dashed) arrows indicate warm (cold) currents. The polar East Greenland Current (EGC) and warm saline Irminger Current (IC) carry surface waters into the Labrador Sea, forming the northern limb of the subpolar gyre (SPG). The subtropical gyre (STG) circulates anti-cyclonically south of the North Atlantic current (NAC), which also advects water into the Arctic Mediterranean (AM) (Adapted from Staines-Urías et al. 2013).

## 2.1 | WIND STRESS

The varying angle of incidence upon the spherical Earth means the poles receive a net deficit of solar radiation, whilst the equator receives a net surplus. As natural systems tend towards equilibrium, excess heat is redistributed from low to high latitudes by the atmosphere and by ocean currents. The influence of Coriolis force (caused by motion upon a rotating sphere)

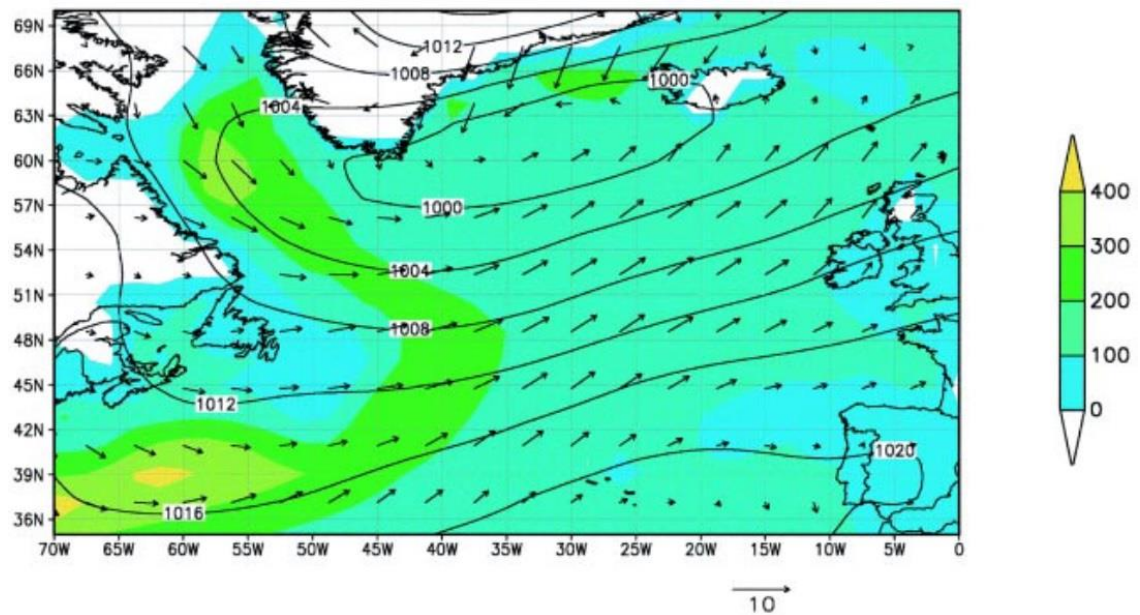


**Figure 2.2** | Average mean wintertime (Dec – Mar) atmospheric conditions above the North Atlantic (1968 – 1997). Cyclonic circulation and high heat loss from the Labrador and Irminger Seas are evident. Sea level pressure (mb, contour), 10 m wind velocity ( $\text{m s}^{-1}$ , vector), and total heat flux ( $\text{W m}^{-2}$ , colour scale) (The Lab Sea Group 1998).

upon atmospheric circulation results in the global pattern of prevailing winds, which drive surface ocean circulation through frictional coupling at the air-sea interface. This has been validated by drifter studies which reveal actual circulation that is very similar to “expected” circulation calculated from the wind stress curl (Fratantoni 2001). During winter, the North Atlantic is dominated by westerly winds, sandwiched between the Azores high and the Iceland low, which produces cyclonic (anticlockwise) subpolar low pressure systems (Figure 2.2). The North Atlantic Oscillation (NAO) is a manifestation of the northern annular mode, which is a hemispheric-scale pattern of climate variability due to mid-latitude internal atmospheric dynamics affecting the storm-track and associated moisture transport (Hurrell 1995), best visualised as a meridional “wobble” in the position of the subtropical jet stream. The NAO index is defined as the normalised sea level pressure difference between the Iceland low and the Azores high.

A positive NAO index indicates a stronger pressure gradient, causing a northward shift in the jet stream and stronger Westerlies. This is associated with stronger a North Atlantic Current which produces more intense cyclonic circulation in the Irminger Basin, an eastward shift of the subpolar front (Flatau et al. 2003), more intense convection (due to stronger atmospheric forcing) in the Labrador Sea, and milder winters across Europe (Hurrell 1995; Dickson et al. 1996). The situation is reversed during a negative NAO phase, as the subpolar front shifts westward in the Irminger and Iceland Basins where cyclonic circulation reduces, and the subpolar gyre contracts (Bersch 2002). Although wind stress only directly drives currents within the upper few hundred metres, known as the Ekman layer (Wunsch 2002), wind stress can indirectly induce deeper flow in the form of rotating water masses known as gyres.

Gyres are induced by wind-stress curl, which causes Ekman divergence or convergence of surface waters. Water “piles up” around the edge (centre) of cyclonic low (anticyclonic high) pressure centres, creating a pressure gradient which generates geostrophic flow. When modified by Coriolis force, currents circulate along isobars of equal pressure. Because it is only indirectly wind-driven, such geostrophic flow can extend to the full depth of the ocean, although deep currents are typically very slow. The subtropical gyre circulates anticyclonically at mid-latitudes with the Gulf Stream at its western edge. The subpolar gyre circulates cyclonically within the Irminger Basin and Labrador Sea (Figure 2.1). It is bounded by the Irminger current to the east, the east and west Greenland currents to the north, the Labrador Current to the west and the North Atlantic Current to the south (Schmitz and McCartney 1993). Gyres are important because they recirculate water masses within their interior, which allows mixing and preconditioning for open ocean convection in the Labrador Sea (Marshall and Schott 1999). The vigour of the subpolar gyre has also been linked with the strength of thermohaline circulation across the region (Häkkinen and Rhines 2004; Hatun 2005).

Investigating variations in subpolar gyre circulation between 1992 – 2002 observed from satellite altimetry (sea surface height) supported by direct current-meter measurements from the Labrador Sea boundary current, Häkkinen and Rhines (2004) proposed that a gyre strength index (defined as the principal component from an empirical orthogonal function analysis of sea surface height) echoes salinity anomalies in the northeast Atlantic. When buoyancy forcing is weak, the doming up of isopycnals within the subpolar gyre is suppressed and circulation reduces (Häkkinen and Rhines

2004). This correlation was extended back to the 1960s through modelling by Hátún et al. (2005), who concluded that it is the shape of the subpolar gyre, as well as the intensity of circulation, which affects the salinity of Atlantic inflow across the Greenland-Scotland Ridge, by changing the relative contribution from the (fresher) subpolar and (more saline) subtropical gyres to the North Atlantic Current. The change in distribution of water masses of different density are picked up as changes in sea surface height, which is what the gyre index measures. In high-index periods, when subpolar gyre circulation is more intense, the gyre extends eastwards, and freshens Atlantic inflow across the Greenland-Scotland Ridge, possibly inhibiting deep convection in the Nordic Seas (Häkkinen and Rhines 2004). In low-index periods the subpolar gyre followed a more north-south axis west of the Mid Atlantic Ridge, and Atlantic inflow salinity increased. Although Häkkinen and Rhines (2004) concluded that gyre strength is not attributed to NAO wind stress, Böning et al. (2006), using hindcast simulations using ocean circulation models to show a link between changes in sea surface height and Labrador Sea boundary current volume transport, suggested trends are driven by changes in the NAO due to heat flux and wind stress. Whatever the cause, circulation within the subpolar gyre is intimately linked to the Atlantic meridional overturning circulation.

## 2.2 | THERMOHALINE CIRCULATION

Water has a much higher heat capacity than air, and this heat is carried to high latitudes by surface currents before being released to the atmosphere. The effect can be vast. For example, heat flux into the North Atlantic is estimated at 1.3 PW (1 PW =  $10^{15}$ W) (Ganachaud and Wunsch 2000), sufficient to warm mean annual air temperatures of northwest Europe by over 10°C compared to the zonal average (Rahmstorf and Ganopolski 1999). The effect is even stronger in winter, and as a result, mean January temperature at Goose Bay, Newfoundland is around 30°C colder than that of Galway, Ireland, even though the two are at a similar latitude (53°N) (Marshall and Plumb 2008). This atmospheric cooling increases seawater density, as does increased salinity. If surface waters become sufficiently dense they can sink. In the charming words of Stommel (1958), in a few key regions the thermocline “springs a leak”. The intermediate and deep water masses created by this process slowly return towards the equator, via deep western boundary currents (Stramma et al. 2004) or interior pathways

(Bower et al. 2009). Water flows between all ocean basins continuously driven by these changes in density due to temperature and salinity differences, colloquially known as the thermohaline “conveyor belt” (Broecker 1987). The energy supply behind the Atlantic meridional overturning circulation (AMOC) is still poorly understood (Kuhlbrodt et al. 2007), and some workers conclude that the AMOC is not driven by deep water production, but must also be affected by prevailing winds and the ocean’s eddy field (Lozier 2010; Lozier 2012). To what extent the strength of the overturning circulation is determined by the “push” of high-latitude deep water formation or the “pull” of diapycnal mixing determines unclear

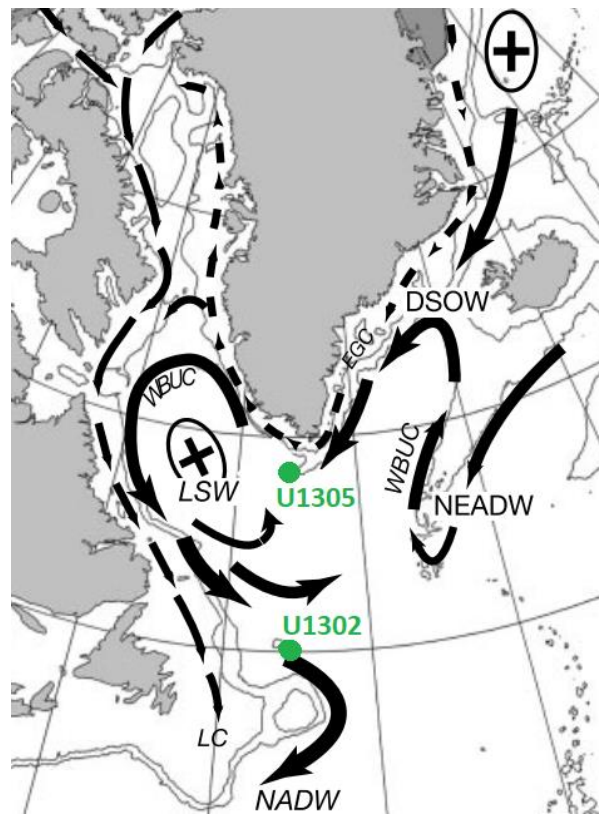


**Figure 2.3** | Deep water circulation in the North Atlantic. Sediment core locations U1305 and U1302 are shown in green. Crosses indicate locations of deep water formation. Deep water masses are indicated by thick arrows: Denmark Strait Overflow Water (DSOW), Northeast Atlantic Deep Water (NEADW), North Atlantic Deep Water (NADW), Labrador Sea Water (LSW), Western Boundary Under Current (WBUC). Dashed arrows indicate surface currents, the East Greenland Current (EGC), and Labrador Current (LC). Adapted from Hillaire-Marcel et al. (2001).

(Visbeck 2007), and it has been argued that the physical force required to maintain the AMOC is actually provided by mechanical stirring by tides or winds, with the movement of heat and salt a consequence, rather than a driver, of these processes (see Wunsch 2002; Kuhlbrodt et al. 2007). Nonetheless, this “conveyor belt” is a useful conceptual model (Broecker 1991), accounting for the ventilation of the abyss and connecting all ocean basins by transporting mass, heat, salt, dissolved gasses and nutrients between them (Marshall and Plumb 2008). Therefore, in this study, the term (thermohaline) convection refers to the circulation of heat and salt, whilst AMOC refers to the mass flux that carries these properties. Convection is inhibited in the northern Pacific by low salinity. Consequently, deep water is only formed in the Nordic and Labrador Seas in the northern hemisphere (Figure 2.3).

## 2.2.1 | Convection in the Nordic Seas

The fate of warm surface Atlantic Inflow to the Nordic Seas is to cool and sink behind the Greenland-Scotland Ridge during episodes of deep winter convection (Marshall and Schott 1999), where sea ice preconditions surface waters by enhancing salinity due to brine rejection, after which deep convection typically occurs in an ice-free embayment (Roach et al. 1993; Wadhams et al. 1996). Winter observations suggest vertical convection in the Nordic Seas is also highly variable (Schott et al. 1993). There are also some observations that the centre of deepest convection alternates between the Nordic and Labrador Seas (Dickson et al. 1996), possibly due to changes in the subpolar gyre index (Hakkinen and Rhines 2004; Hatun 2005).

## 2.2.2 | Open Ocean Convection

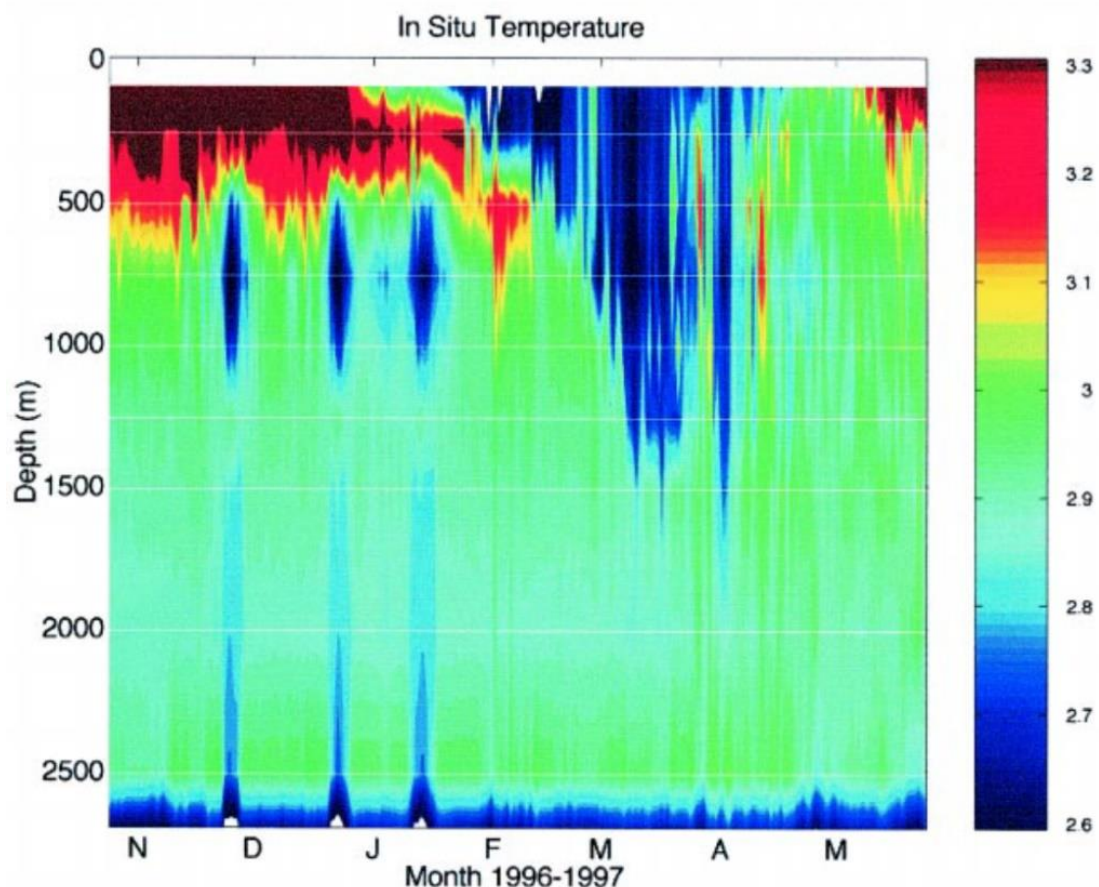


**Figure 2.4** | Open ocean convection in the Labrador Sea. Colours show the potential temperature ( $^{\circ}\text{C}$ ) at the Bravo mooring in the central Labrador Sea during October 1996 – May 1997. Red colours at the surface illustrate the warm saline surface mixed layer, which persists from the summer until January, when surface cooling initiates vertical convection down to 1500 m, after which surface waters stratify again during May (The Lab Sea Group 1998).

In the Labrador Sea, and to a certain extent the Irminger Sea (de Jong et al. 2012), intermediate Labrador Sea Water (LSW) is sporadically formed by open ocean convection (Marshall and Schott 1999; Lazier et al. 2002). During most of the year, surface waters are stratified, whereby a relatively thin warm and saline surface layer floats atop the cold,

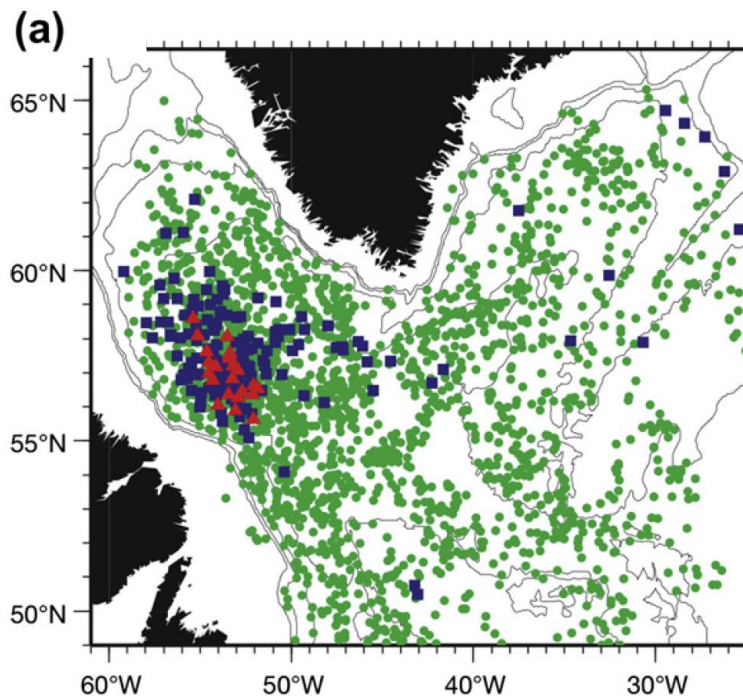


**Figure 2.5** | Winter mixed layer depths (1996 – 1998) obtained using profiling floats, showing >800 m (red), 400 – 800 m (blue), <400 m (green) (Adapted from Lavender et al. 2000).

fresh abyssal waters. This “mixed layer” of relatively homogeneous properties is maintained by convection and wind-induced turbulence. Below the mixed layer lies the thermocline where there is a strong temperature and density gradient between the warm surface layer and the cold dense water below. Stratification suppresses turbulent mixing across the thermocline. During winter, storms break down the shallow seasonal thermocline through cooling and convection (Figure 2.4). The mixed layer can then become very deep (up to 2500 m) depending on the severity of the winter, which allows turbulent mixing to overturn deeper into the water column (Lazier et al. 2002). Three factors precondition the Labrador Sea for deep convection: strong atmospheric heat loss, due to cold dry air passing over from the Canadian Arctic (insulating sea ice does not usually extend across the interior of the Labrador Sea); weak stratification beneath the surface mixed layer, possibly due to convection during previous winters; and the drawing up of dense deeper waters, as favoured by Ekman divergence due to cyclonic circulation within the subpolar gyre, which causes isopycnals to “dome up” towards the surface within the centre of the gyre (Marshall and Schott 1999). This theory was supported by direct velocity measurements from over 200 subsurface floats released as part of the WOCE Labrador Sea Deep Convection Experiment (The Lab Sea Group 1998). Using this data, Lavender et al. (2000) observed the deepest mixed layers

associated with cyclonic recirculation between the Labrador Sea interior and the Labrador Current (Figure 2.5). Heat loss and consequent deepening of convection was exacerbated by “sluggish flow”, which retained floats within the region for up to 110 days (Lavender et al. 2000).

Production rates, properties and depth of convection are highly variable (Yashayaev et al. 2007) for reasons that are not fully understood (Avsic et al. 2006). LSW is not formed in every winter if surface water does not become sufficiently dense to sink (Dickson et al. 1996), but in some years convection has been observed down to 2,300 m in a layer 1,800 m thick (Lazier et al. 2002). It is unclear whether this variability is due to changes in meridional heat transport or LSW transport rates out of the SPG (Rhein et al. 2002), or it may be linked to atmospheric variability, particularly over decadal timescales (Dickson et al. 1996; Sarafanov 2009). It is not clear how LSW leaves the area either, with the traditional assumption that the major conduit was via the Deep Western Boundary Current (Schott et al. 2004; Schott et al. 2006) not observed by data from subsurface floats, which instead detected an anticyclonic countercurrent within the Labrador Sea interior flowing into the Irminger Sea (Lavender et al. 2000),

The observation that LSW could spread surprisingly rapidly into the Irminger Sea (Sy et al. 1997) has led to the suggestion by Pickart et al. (2003), using both hydrographic data and modelling, that Labrador Sea Water can instead form in the southwest Irminger Sea to a depth of 1500 – 2000 m, argued using tracer observations of distribution and spreading rate, and similar preconditioning east of Greenland. This argument is ongoing, but data from more recent hydrographic transects and volumetric water mass analysis support the suggestion of intermittent LSW formation within the Irminger Sea (Våge et al. 2011).

Sea water density at temperatures approaching 0°C depends predominantly on salinity. The North Atlantic Current is not only warm but salty. This salinity can be modified by lateral mixing with fresher water masses, the balance between precipitation and evaporation, brine rejection during sea ice formation, and meltwater runoff from the continents. Because of its density dependence, both computer models and data suggest the AMOC is highly sensitive to freshwater perturbations in the northern North Atlantic (Clark et al. 2002b; Stouffer et al. 2006). The Labrador Sea is subject to massive influxes of freshwater from the Laurentide, Inuitian and Greenland ice sheets over glacial/interglacial cycles. Studies suggest rates of overturning at present are sporadic

and variable (Lazier et al. 2002), and may have ceased entirely during the last glacial cycle (Duplessy et al. 1988; Manabe and Stouffer 1988), and potentially during the last interglacial period as well (Hillaire-Marcel et al. 2001). Enhanced freshwater input to the Labrador Sea may therefore suppress deep convection (Koenigk et al. 2007), which models suggest could destabilise the AMOC with even relatively small changes to the freshwater balance (Rahmstorf 1995). Therefore, the Labrador Sea forms a lynch pin of the AMOC where LSW is formed and deep water masses are modified (Stramma et al. 2004).

## 2.3 | BATHYMETRY

Bathymetry, the shape of the ocean basins, is an important influence on circulation due to topographic steering, whereby currents follow sea-floor topography in order to conserve their potential vorticity. The North Atlantic Ocean basin is bounded by the continental shelves of North America, Greenland and Europe, between which stretch the deep abyssal plains to a depth of 4 km (Figure 2.6). The most substantial feature of the North Atlantic basin is the Mid Atlantic Ridge. The Mid Atlantic Ridge is a divergent plate boundary separating the Eurasian and North American plates, effectively a long underwater mountain chain rising around 2 km from the ocean floor. The most prominent interruption of the Mid Atlantic Ridge is the Charlie Gibbs Fracture Zone (CGFZ), two parallel transverse faults which provide a deep passage across the Mid Atlantic Ridge at around 53°N. Flow in either direction crosses the Mid Atlantic Ridge preferentially at the CGFZ, even surface waters far above the sea floor, therefore the Mid Atlantic Ridge acts to keep ocean basins separate (Bower et al. 2002). The Mid Atlantic Ridge continues on as the Reykjanes Ridge, which separates the Irminger and Iceland Basins, and on above sea level through Iceland.

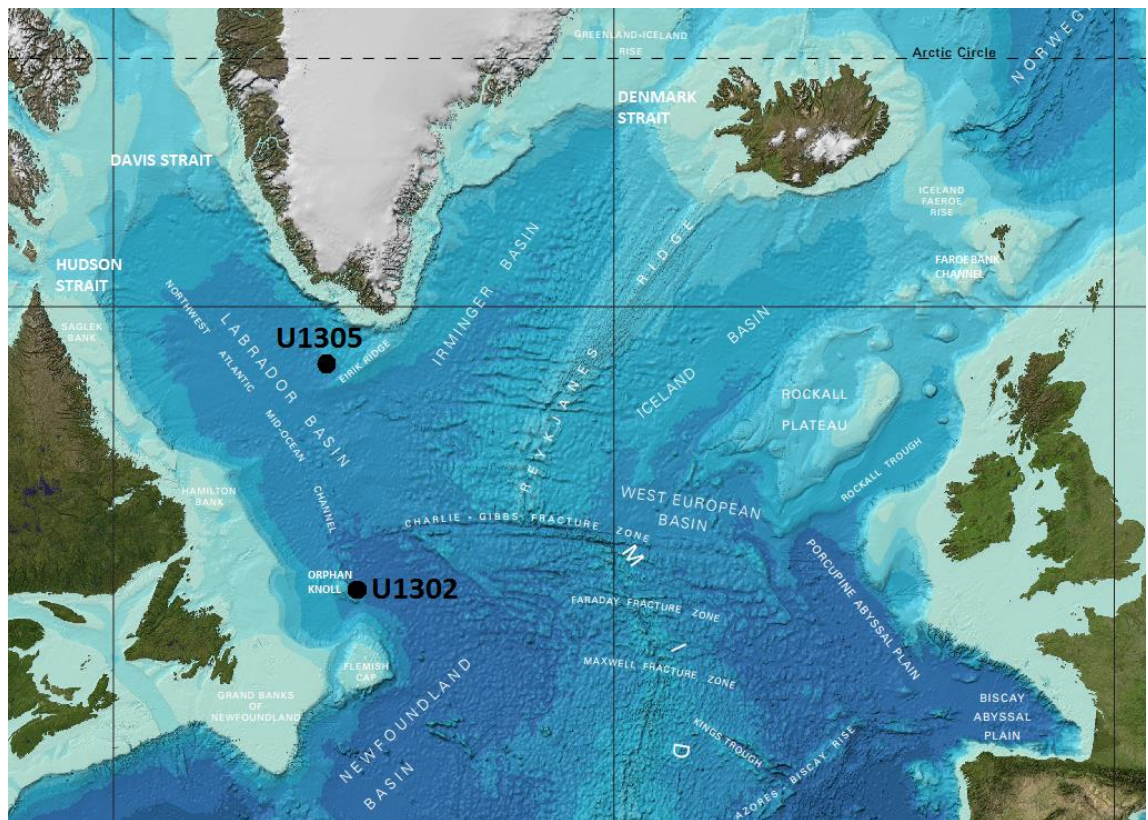


**Figure 2.6** | Bathymetric map of the subpolar North Atlantic. Black circles indicate the locations of U1302 and U1305 marine sediment cores Adapted from Weatherall et al. (2015).

Another prominent bathymetric feature is the 4000 km long Greenland–Scotland Ridge, which forms a shallow barrier between the North Atlantic and the Nordic Seas (Hansen and Østerhus 2000) (Figure 2.6). South west of the Greenland-Scotland Ridge lie three basins with ridges between – the Irminger Basin, Iceland Basin and Rockall Trough, separated by the Reykjanes Ridge and the Rockall Plateau respectively. Warm saline North Atlantic water flows across into the Nordic Seas near the surface, some west of Iceland and some over the Rockall Plateau, with a further contribution from the Continental Slope Current. Mixing with fresher water masses, cooling and convection during winter storms forms cold dense deep water which pools behind the ridge, only overflowing it at particular points – through Denmark Strait (110 km wide, 620 m deep), the Iceland-Faroe Ridge (300 – 500 m deep), and the Faroe Bank Channel (840 m deep) (Hansen and Østerhus 2000). Figure 2.7 shows warmer ( $>5^{\circ}\text{C}$ ) more saline ( $S>35.0$ ) waters in upper 1000 m of the Atlantic, with cold ( $<0^{\circ}\text{C}$ ) fresh ( $S\sim 34.9$ ) waters pooled below the sill within the Norwegian Sea. The Iceland-Faroe Front is the boundary where these two water masses meet. Thus both surface water conditions and bathymetry help to determine the properties of deep water masses. Pressure gradients

initiated by deep convection drive deep overflows across the ridge. These dense water masses circulate through the Iceland and Irminger basins, entraining surrounding waters and eventually becoming components of North Atlantic Deep Water (NADW).

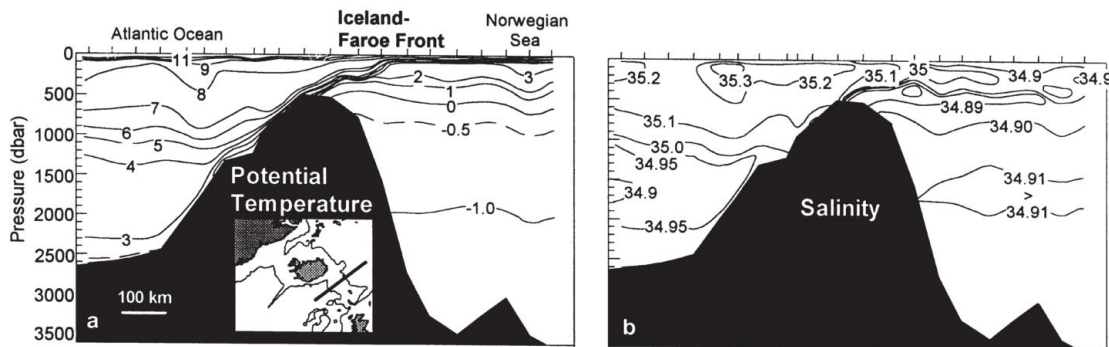


**Figure 2.7** | Vertical section showing the effect of the Greenland-Scotland Ridge on (a) potential temperature, and (b) salinity. The Iceland-Faroe Front is where Atlantic water meets cold, low-salinity water of the Nordic Seas, and is topographically locked to the ridge (Hansen and Østerhus 2000).

Oceanography of the Labrador Sea is particularly influenced by the shape of the surrounding continents, with strong surface and deep water boundary currents forced to detour, curving around the southern tip of Greenland (Figure 2.6). Turbulence associated with this feature creates eddies, which spin off into the interior of the Labrador Sea, and can influence the suitability of surface waters for deep convection (Lazier et al. 2002, Yashayaev et al. 2007, Marshall and Schott 1999). The deep embayment to the north of the Flemish Cap also drives the North Atlantic Current to turn around the “northwest corner”, close to the Orphan Knoll, before it flows across the North Atlantic. A final important bathymetric feature of the Labrador Sea is the Northwest Atlantic Mid Ocean Channel (NAMOC), a system of channels and levees 3800 km long, up to 16 km wide and up to 200 m deep, known to provide a conduit for deep ocean turbidites (described in section 4.1.1) (Hiscott et al. 1989; Hillaire-Marcel and Bilodeau 2000). Turbidite deposits extend for 100 km either side of the channel, and may extend to the locations of Orphan Knoll and Eirik Ridge (e.g. Nicholl et al. 2012).

## 2.4 | MAJOR WATER MASSES OF THE NORTH ATLANTIC

A water mass is a body of water possessing distinct physical and chemical properties, determined at its surface formation region, which are largely conservative at depth (i.e. only change at the water mass boundaries). Therefore, the boundaries between water masses are subject to mixing, where properties will be exchanged or modified. These properties are typically specific combinations of temperature and salinity, which together determine density, though dissolved gases (such as oxygen), nutrients (such as silicate), or seawater oxygen-18 content ( $\delta^{18}\text{O}$ ) are also sometimes useful. Each water mass has a “core depth” which exhibits its typical characteristics. Water masses are usually classified as upper, intermediate, deep or abyssal water. Table 2.1 contains a summary of North Atlantic water mass properties. Figure 2.9 shows potential temperature-salinity diagram of major water masses discussed below. The well-oxygenated mode waters, discussed in the next section, show up clearly in Figure 2.9 (b), as groups of points around 18°C (Eighteen Degree Water or Subtropical Mode Water), 11 – 14°C (NAC Subpolar Mode Water), and 8 – 11°C (northeastern and northwestern Atlantic Subpolar Mode Waters).

### 2.4.1 | Seawater Oxygen Isotope Database

One useful conservative water mass tracer is  $\delta^{18}\text{O}$ , which is described in detail in section 6.3. In a massive collaborative effort based on Schmidt (1999a) and Bigg and Rohling (2000), a database of modern seawater oxygen-18 measurements since 1950 has been compiled (Schmidt 1999b). Data from various sources were calibrated to the GEOSECS database (Ostlund et al. 1987) to produce consistent deep water properties (which are assumed to be stable cross this time period). The  $\delta^{18}\text{O}$  of seawater has been used to trace glacial meltwater and deep water mass origin, as well as tracing how deep water masses are formed (LeGrande and Schmidt 2006). Figure 2.8 shows the 1° x 1° gridded data set for annual mean surface water (0 – 50 m), and indicates the location of U1305 and U1302. Surface seawater  $\delta^{18}\text{O}$  values in the Labrador Sea are typically ~0 ‰, though seasonal variations due to sea ice formation may influence results. These Holocene interglacial data can be compared to the last interglacial seawater  $\delta^{18}\text{O}$  values calculated using proxy data produced in this study.

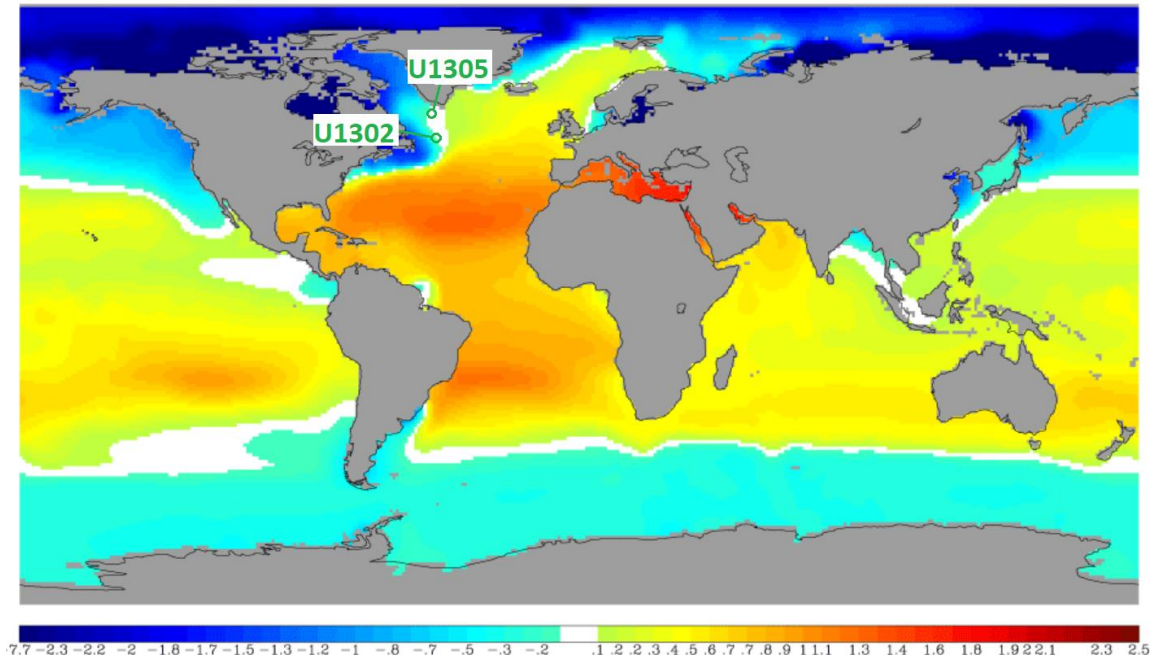


**Figure 2.8** | Global gridded surface seawater  $\delta^{18}\text{O}$  including the locations of U1305 and U1302. Adapted from LeGrande and Schmidt (2006).

Within palaeoclimatology, the  $\delta^{18}\text{O}$  of planktonic foraminifera found within marine sediment core samples is the product of calcification temperature, global ice volume, local seawater  $\delta^{18}\text{O}$ , vital effects, ecology and dissolution (Berger and Gardner 1975). Schmidt (1999a) used forward modelling to determine that modelled seawater  $\delta^{18}\text{O}$  covaried with temperature, though the salinity relationship was more complex, and ecological differences were not found to strongly influence predicted calcite  $\delta^{18}\text{O}$ . Potentially, using proxy data from the Labrador Sea, which is particularly subject to the influence of deglacial meltwater, variations in planktonic foraminiferal  $\delta^{18}\text{O}$  during meltwater pulses may help to clarify the degree to which isotopically depleted meltwater  $\delta^{18}\text{O}$ , or enhanced sea ice production (Hillaire-Marcel and De Vernal 2008), may mask the impact of local temperature changes (Schmidt 1999a).

**Table 2.1** | North Atlantic water mass characteristics.

Water Mass	Potential Temperature (°C)	Salinity	Other	References
North Atlantic Water	9.5 – 10.5	35.35 – 35.45		(Hansen and Østerhus 2000)
Denmark Strait Overflow Water	–0.18 – 0.17	34.88 – 34.66	High O <sub>2</sub>	(Tanhua et al. 2005)
Iceland-Scotland Overflow Water (Near overflows)	~ –0.5	~34.92	High O <sub>2</sub>	(Hunter et al. 2007)
Iceland-Scotland Overflow Water (Irminger Basin)	1.8 – 3.5	~34.96 – 35.05	Low O <sub>2</sub>	(Hunter et al. 2007)
North East Atlantic Deep Water	2 – 3	35.1	Low O <sub>2</sub>	(Dickson and Brown 1994; Stramma et al. 2004)
Subpolar Mode Water (Nordic Seas Inflow)	8	35.23	Low potential vorticity	(van Aken & deBoer 1995).
Labrador Sea Water	~3 – 4	34.85	Low potential vorticity	(Hunter et al. 2007)
North Atlantic Deep Water	2 – 3.5	34.88 – 34.98	High salinity	(Hunter et al. 2007)
Antarctic Intermediate Water	~3	34.1	Low salinity	(Talley et al. 2011 p. 286)
Antarctic Bottom Water	~2		Low O <sub>2</sub> High Si	(Hunter et al. 2007)

## 2.4.2 | Subpolar Mode Water

Voluminous water masses of largely homogenous salinity and temperature are known as mode waters. The Subpolar Mode Water (SPMW) is an upper (0 – 700 m) water mass of low potential vorticity found throughout the subpolar North Atlantic, formed from a mixture of subtropical and subpolar waters transported by the North Atlantic Current (NAC) as they form a thick surface mixed layer in the Iceland Basin during winter (McCartney and Talley 1982; de Boisséson et al. 2012). SPMW is important for deep water formation both in the Labrador and Nordic Seas as it is carried by the branches of the NAC (Marshall and Schott 1999; Lazier et al. 2002). From south of the NAC where SPMW is warmest (14°C), it cools towards the British Isles (11°C) where some contributes to the subtropical gyre, and some spreads north east, cooling to 8°C as it crosses the Iceland-Faroe Ridge into the Nordic Seas, where during winter cooling, it contributes to NADW constituents as deep overflows (Talley et al. 2011). Some SPMW crosses the Reykjanes Ridge and circulates cyclonically around the SPG within the

Irminger Current, and East and West Greenland Currents, becoming colder and denser until it forms a constituent of LSW.

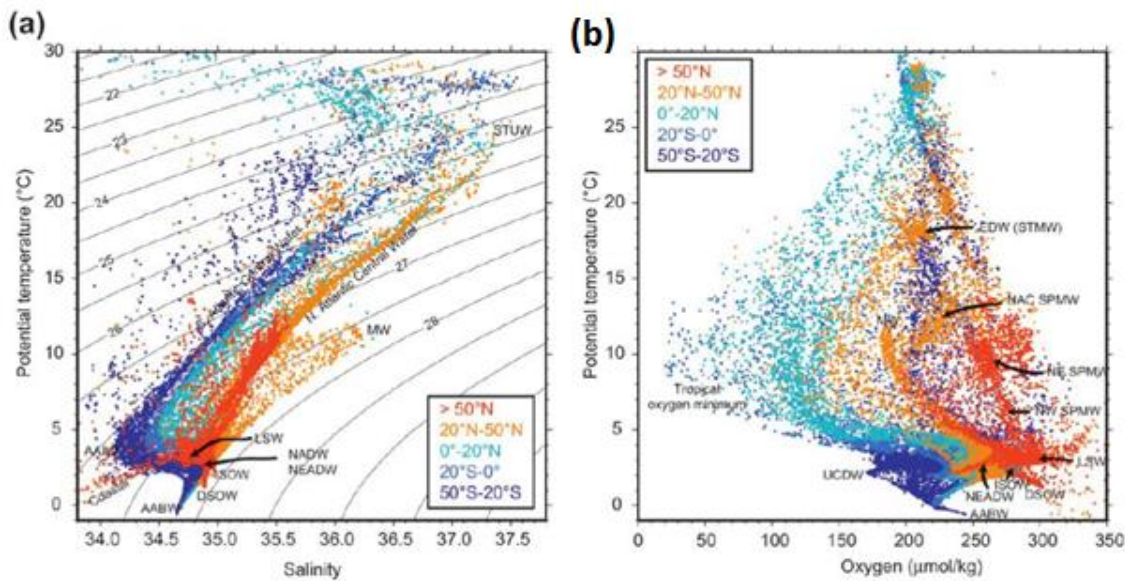


**Figure 2.9** | Characteristics of major North Atlantic water masses, (a) potential temperature-salinity diagram, contours indicate potential density referenced to 0 dbar, and (b) potential temperature-oxygen diagrams, both for full water column. Data from the World Ocean Circulation Experiment 1988 – 1997. Water masses from the T-S diagram (a) north of 50°N (red) are pertinent to the present study. Note that this figure also includes tropical, subtropical and South Atlantic water masses not discussed in this study (Talley et al. 2011 p. 285).

### 2.4.3 | Labrador Sea Water

Labrador Sea Water (LSW) is the major intermediate water mass of the subpolar North Atlantic. Lying between the surface layer and the pycnocline (500 – 2000 m), LSW is characteristically cold and fresh (Lazier 1973; Talley and McCartney 1982). Its high oxygen content apparent in Figure 2.9 (b) is the result of recent ventilation. LSW is formed largely from SPMW and fresh surface waters brought through the Davis Strait during winter convection in the south west Labrador Sea (Figure 2.5) (The Lab Sea Group 1998), and possibly also within the Irminger Sea when conditions are favourable (Pickart et al. 2003; Kieke et al. 2006; De Jong et al. 2012). LSW can remain within the region for several years, contributing to precondition waters for further convection in subsequent winters. Data from floats and CFC budgets has shown that the majority of LSW spreads at intermediate depths (between 700 m and 2,000 m) into the North Atlantic interior (Bower et al. 2009), across the MAR into the eastern North Atlantic, and south as the upper part of the Deep Western Boundary Current (Sy et al. 1997; Marshall and Schott 1999). The formation of Upper Labrador Sea Water, a fresher and

less dense intermediate water mass of variable properties, has been observed within submesoscale eddies within the DWBC between Grand Banks and the Flemish Cap of the Labrador Current (Pickart et al. 1996). LSW is entrained into deeper water masses as they circulate around the SPG, and forms a major portion of NADW.

#### 2.4.4 | Denmark Strait Overflow Water

The two densest deep water masses formed in the North Atlantic are the overflow waters formed in the Nordic Seas. The densest, Denmark Strait Overflow Water (DSOW) is the coldest and freshest water mass that contributes to NADW (LeBel et al. 2008). DSOW sinks to the bottom of the Irminger Basin (600 – 4500 m) after passing through the Denmark Strait, and entrains overlying LSW as it flows along the continental slope of Greenland. Eddy-resolving simulations paired with passive tracers indicate the narrow deep western boundary current (DWBC) transports DSOW south into the Irminger Basin, beyond which some continues around the edges of the Labrador Sea within tight boundary currents, whilst the deepest layers spread west to the Labrador coast across the basin floor (Figure 2.10) (Xu et al. 2015). DSOW is distinct from the second Nordic Seas overflow water, ISOW, by its high oxygen content and low salinity (Figure 2.9).

#### 2.4.5 | Iceland-Scotland Overflow Water

Iceland-Scotland Overflow Water (ISOW) is a deep water mass (2500 – 3500 m) which overflows the Iceland-Scotland Ridge, and is strongly modified by mixing and turbulent entrainment with overlying SPMW within the Iceland Basin (from which it acquires its characteristic high salinity and low oxygen seen in Figure 2.9) (Dickson and Brown 1994). ISOW crosses the Mid-Atlantic Ridge through the CGFZ, turns north and mixes with DSOW and LSW within the Irminger Basin, increasing in volume and forming North East Atlantic Deep Water (Figure 2.10) (Hansen and Østerhus 2000).

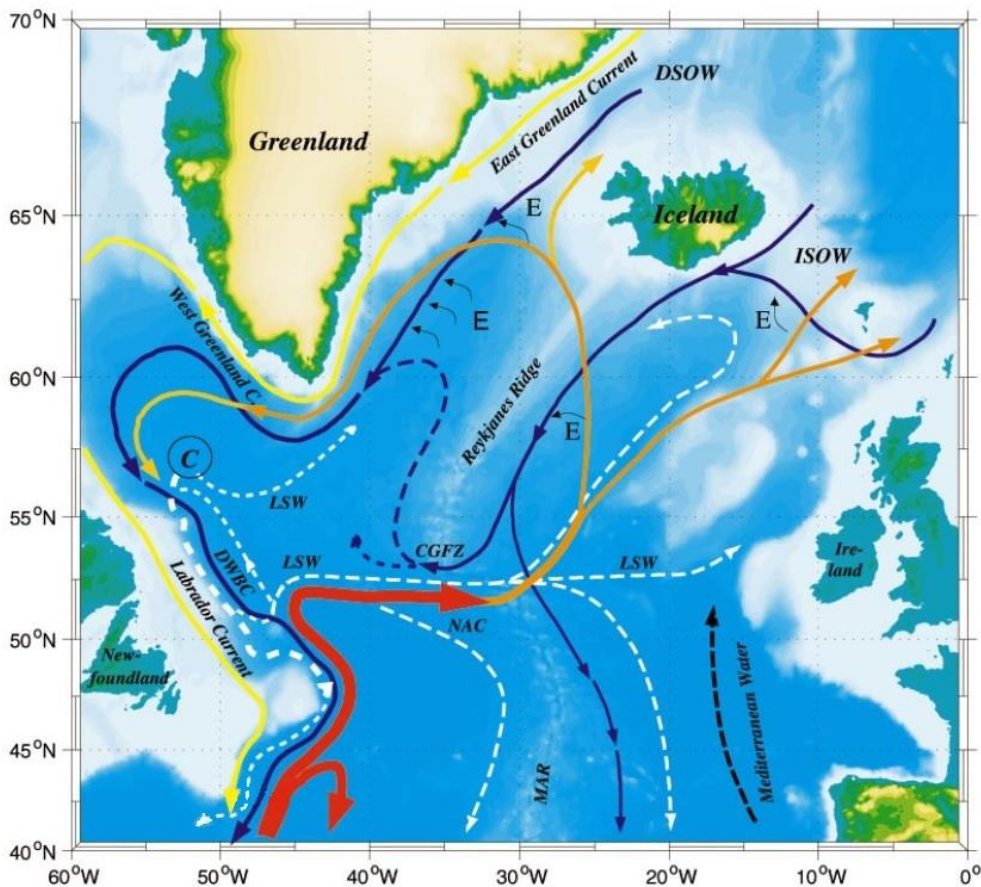


**Figure 2.10** | Subpolar North Atlantic schematic circulation diagram. The North Atlantic Current (NAC) brings warm saline surface waters from the south across the Charlie Gibbs Fracture Zone (CGFZ) before spreading across the Greenland-Scotland Ridge into the Nordic Seas, and across the Reykjanes Ridge into the Irminger Basin where it forms the Irminger Current. Convection forms Labrador Sea Water (LSW) in the Labrador Sea, which spreads at intermediate depths throughout the North Atlantic, whilst some is exported south within the Deep Western Boundary Current (DWBC) along with denser Denmark Strait Overflow Water (DSOW) and Iceland-Scotland Overflow Water (ISOW), which combine to form North Atlantic Deep Water. E = Entrainment, C = Convection. (Adapted from Schott et al. 2004).

## 2.4.6 | North East Atlantic Deep Water

Also referred to as Gibbs Fracture Zone Water, north east Atlantic deep water (NEADW) is a low oxygen, high salinity water mass (Figure 2.9) formed from ISOW which crosses through the Charlie Gibbs Fracture Zone, and is greatly modified through mixing with Mediterranean water in the eastern basin, as well as LSW in the Irminger Basin (Stramma et al. 2004) (Figure 2.11). One estimate of NEADW composition is ~30% ISOW, ~45% LSW and ~23% AABW (van Aken 2000). This water mass is apparent as an intermediate depth salinity maximum, typically 2300 – 3300 m (Marshall and Schott 1999; Lazier et al. 2002). NEADW is then transported north along the western flank of the Reykjanes Ridge and around the Irminger Basin within the

SPG, between DSOW beneath and LSW above, and freshens as it mixes with both during transit around the Labrador Sea (Smethie Jr. et al. 2000). There are indications that some NEADW may also be advected directly across the western basin outside of the boundary current system (Stramma et al. 2004; Yashayaev 2007).

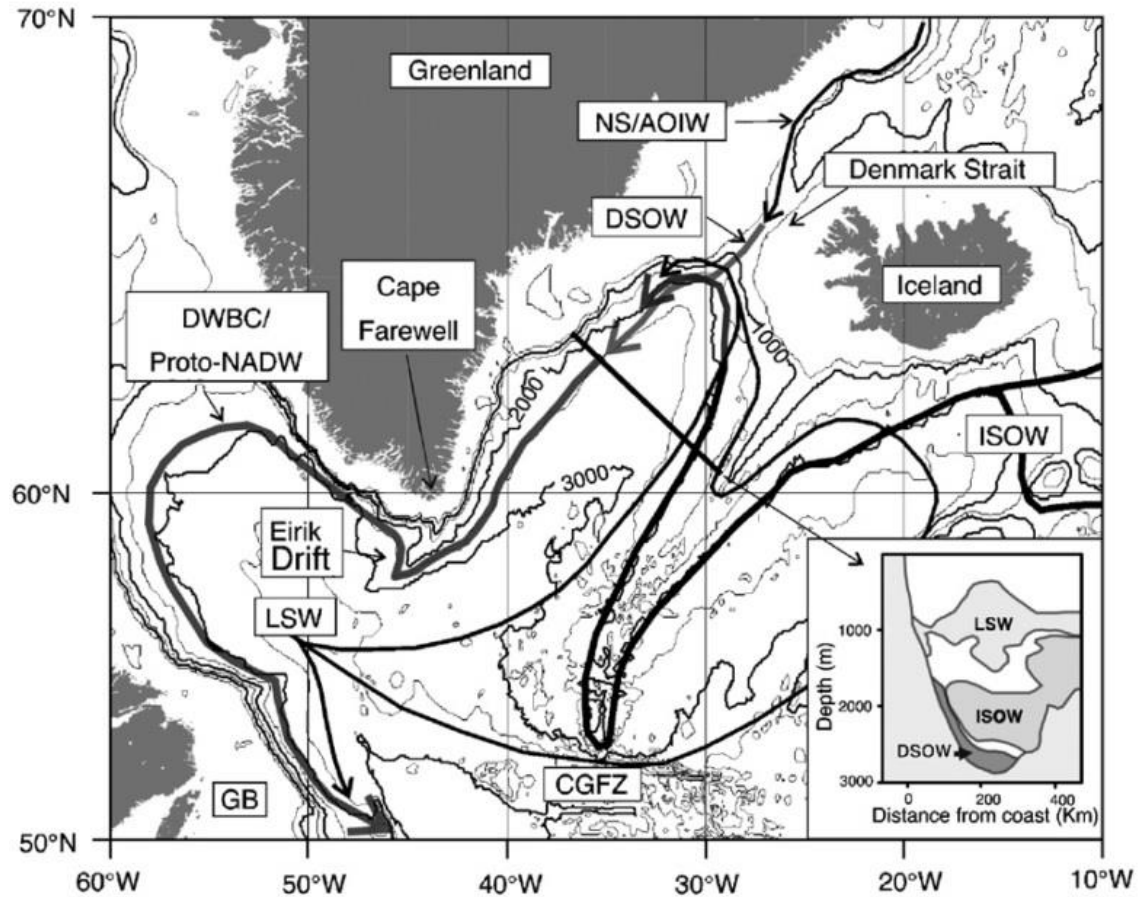


**Figure 2.11** | Deep and intermediate water masses of the North Atlantic. Abbreviations: Denmark Strait Overflow Water (DSOW), Iceland-Scotland Overflow Water (ISOW), Labrador Sea Water (LSW), Deep Western Boundary Current (DWBC), North Atlantic Deep Water (NADW), Norwegian Sea/Arctic Ocean Intermediate Water (NS/AOIW), Grand Banks (GB), Charlie Gibbs Fracture Zone (CGFZ) (Hunter et al. 2007).

### 2.4.7 | North Atlantic Deep Water

North Atlantic deep water (NADW) is newly formed deep water from the Nordic and Labrador Seas that flows south between 1500 – 3500 m along the North American continental rise as part of the DWBC, forming the lower limb of the AMOC (Figure 2.11). NADW is high in oxygen and salinity, but low in nutrients, being mostly composed of DSOW and ISOW (or NEADW) which entrain overlying LSW and denser Antarctic Bottom Water (AABW) as they flow (Dickson & Brown 1994, Smethie Jr. et

al. 2000). NADW is recognised by its high  $\delta^{13}\text{C}$  content (Curry and Oppo 2005). CFC budgets have revealed that a large portion of newly formed NADW recirculates from the DWBC into the interior regions of the North Atlantic (LeBel et al. 2008) before transiting south via complex pathways (Smethie Jr. et al. 2000). This may also contribute towards preconditioning for deep convection. Ganachaud and Wunsch (2000) estimated NADW is formed at the rate of  $15 \pm 2$  Sv (1 sverdrup =  $1 \times 10^6 \text{ m}^3 \text{ s}^{-1}$ ) using data from the World Ocean Circulation Experiment, which is in line with more recent calculations using in situ floats and satellite altimetry of  $15.5 \pm 2.4$  Sv, but with lots of high frequency variability (Willis 2010).

## 2.4.8 | Antarctic Bottom Water

AABW is an extremely cold and dense water mass formed from brine rejection in the Southern Ocean. AABW is a low-nutrient, saline and high oxygen water mass found below 3000 m that spreads into the North Atlantic basin at the lowest levels, mixing with overlying NADW, where it is also referred to as Lower Deep Water (LDW) (Hunter et al. 2007). In sharp contrast to NADW, AABW is recognised by its low  $\delta^{13}\text{C}$  content (Curry and Oppo 2005).

## 2.5 | MAJOR OCEAN CURRENTS OF THE NORTH ATLANTIC

The swiftest currents in the North Atlantic are the western boundary currents (east and west Greenland

Currents and the Labrador Current) and the North Atlantic Current (Fratantoni 2001; Reverdin 2003), which form the rim currents of the SPG (Figure 2.12). Combined surface to sea floor transport at

**Table 2.2** | Observed mean and maximum speeds for major North Atlantic currents obtained from surface drifters (Fratantoni 2001).

Current	Maximum Speed ( $\text{cm s}^{-1}$ ) <sup>a</sup>	Mean Speed ( $\text{cm s}^{-1}$ ) <sup>b</sup>
North Atlantic Current	209	38
East Greenland Current	188	27
West Greenland Current	179	27
Labrador Current	107	21

Cape Farewell north into the Labrador Sea is  $53.8 \pm 10.8$  Sv (Holliday et al. 2009). Illustrative current speeds deduced from surface drifters are found in Table 2.2. Inherent instabilities in fast currents such as these can create eddies, swirling vortices that peel away into basin interiors and can last for several months, carrying parcels of water as they travel. They can transport heat, salt or freshwater far from their source regions. The full effect of eddies are not fully understood and difficult to represent in models, but may play a pivotal role in preconditioning surface waters within the Labrador Sea for deep convection (Lazier et al. 2002; Yashayaev et al. 2007). In the northern hemisphere, cold-core eddies are always cyclonic (anticlockwise), whilst warm-core eddies are anticyclonic.

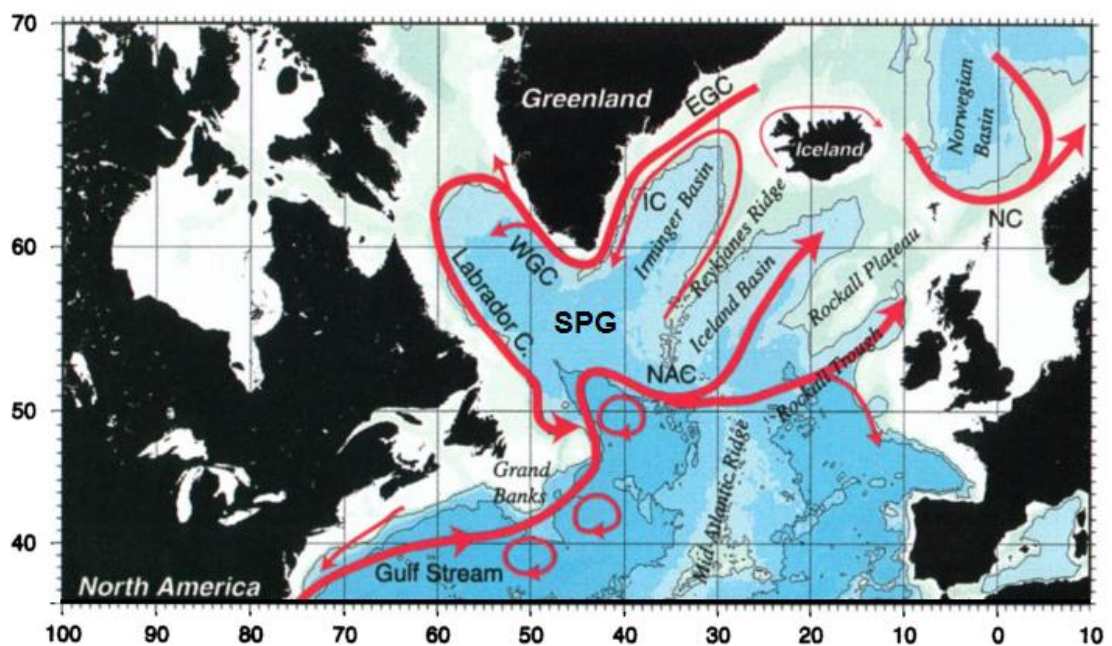


**Figure 2.12** | North Atlantic surface circulation deduced from surface drifters, superimposed over bathymetry. This data shows how even surface currents tend to follow bathymetry. Abbreviations: North Atlantic Current (NAC), Norwegian Current (NC), East Greenland Current (EGC), Irminger Current (IC), West Greenland Current (WGC) (Adapted from Fratantoni, 2001).

Flow within the interior of the Labrador Sea is slow and dominated by eddies (Cuny et al. 2002). Prater (2002) described eddies 20 – 50 km wide peeling away from the West Greenland Current (WGC) with varying mixtures of Irminger Sea Water entrained, being injected into the interior of the Labrador Sea. Eddies such as these could homogenise intermediate waters, and help restratify surface waters after deep convection, though the author thought it more likely they were associated with the strength of the WGC, rather than with dissipating mixed patches following deep

convection (Marshall and Schott 1999). Much smaller submesoscale (~5 km diameter) eddies were observed by Gascard et al. (2002) in the Greenland Sea, which lasted ~1 year, also composed of a mixture of cold Arctic surface water and more saline modified Atlantic water, which extended down to ~2 km and may therefore release the homogenous waters of their core at depth upon decay. The existence of similar sized eddies (~5 – 15 km) within the Labrador Sea has been inferred by Lilly and Rhines (2002) using data from a mooring near Ocean Weather Station Bravo combined with numerical modelling. Four anticyclonic eddies with cold fresh cores were produced by open ocean convection with the Labrador Sea interior, whilst two larger warm cyclonic eddies were attributed to an origin from within the Irminger Current. The role of eddies in transporting LSW into the subtropical North Atlantic (Bower et al. 2013) complements observations from mid-depth floaters that the DWBC may not be the dominant export pathway for LSW (Lavender et al. 2000).

### 2.5.1 | North Atlantic Current

The North Atlantic Current (NAC) is an extension of the Gulf Stream, an intense wind-driven belt of fast moving waters known as a western boundary current, originating in the Gulf of Mexico which transports tropical saline waters into the North Atlantic (Figure 2.12). It lies between the anticyclonic subtropical gyre to the south, and the cyclonic subpolar gyre to the north, from which it also entrains and recirculates fresher subpolar waters. This meeting zone is called the subarctic front. The NAC flows northward along the Grand Banks of Newfoundland to 51°N, where it follows bathymetry and turns abruptly around the “north west corner” (Figure 2.13) past the Flemish Cap (Rossby 1996; Rossby 1999) in a region of high eddy kinetic energy, where eddies spin off into the North Atlantic interior, breaking up the southward flowing deep western boundary current (DWBC). The NAC then broadens and meanders around topographic features, preferentially crossing the Mid-Atlantic Ridge through the CGFZ, beyond which it splits into three topographically-influenced branches which transport SPMW. One core flows along the eastern boundary of the Rockall Trough and on into the Nordic Seas, one along the subpolar front within the Iceland Basin and the third flows along the western side of the Reykjanes Ridge into the Irminger Basin, forming the Irminger Current (Bower et al. 2002; Flatau et al. 2003). Although the NAC is a major source of salinity in the North Atlantic, salt is also

advected into the region via Mediterranean Water, which forms through winter convection and overflows the Strait of Gibraltar, and contributes to the subtropical gyre at intermediate depths (700 – 1700 m).

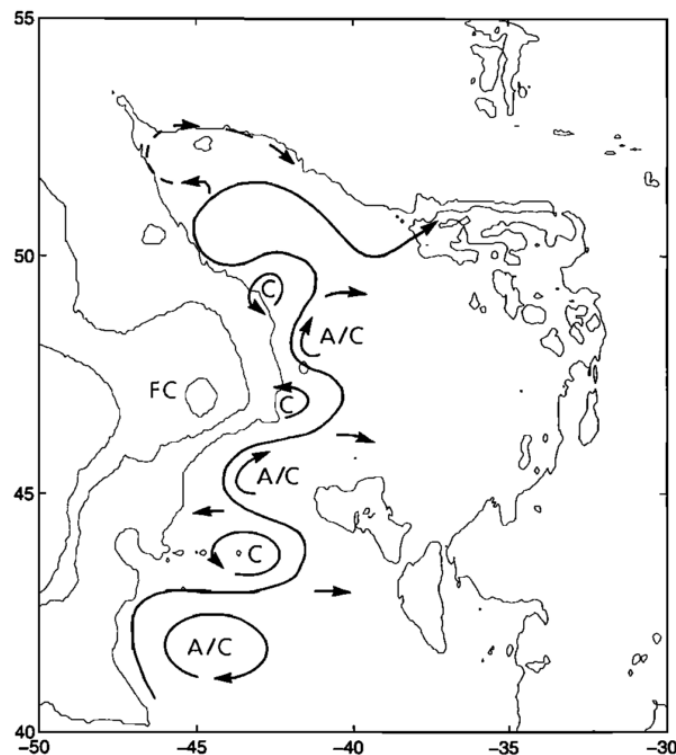


**Figure 2.13** | Flow of the North Atlantic Current around the “north west corner” with associated cyclonic (C) and anticyclonic (A/C) recirculation cells past the Flemish Cap (FC). Arrows indicate NAC lost to surrounding waters. Isobaths at 200, 2000 and 4000 m are shown (Rossby 1996).

## 2.5.2 | Irminger Current

The Irminger Current is formed by the northern branch of the NAC which flows north along the western flank of Reykjanes Ridge. It then flows cyclonically around the Irminger Basin offshore from and below the colder East Greenland Current (EGC) at 200 – 700 m depth along the continental slope, forming the northeastern section of the SPG (Reverdin 2003; Straneo 2006). Both the EGC and the Irminger Current then round the tip of southern Greenland and combine to form the West Greenland Current (WGC). The Irminger Current carries ~11 Sv (Clarke 1984) of warm saline ( $\theta \sim 4.5^\circ\text{C}$ ,  $S \sim 34.95$ ) SPMW, sometimes called Irminger Sea Water, which is transported into the central Labrador Sea within eddies whose salt and heat help to restratify the SPG after winter convection and reduce sea ice cover (Figure 2.14) (Lazier 1973; Lazier et al. 2002; Yashayaev et al. 2007).

### 2.5.3 | East Greenland Current

The East Greenland Current (EGC), together with the smaller east Greenland coastal current (EGCC), is a narrow subpolar western boundary current which carries cold, fresh water from the Arctic along the eastern shelf of Greenland from the Fram Strait (79°N) to Cape Farewell (60°N). The EGC also transports sea ice, much of which melts through turbulent mixing with the warm Irminger current around the southern tip of Greenland, transporting up to 15.5 Sv south of Cape Farewell (Holliday et al. 2007). The reduction in transport (to 11.7 Sv) north west into the Labrador Sea via the West Greenland Current (see below) is in part due to significant loss (up to 5.1 Sv) of fresh waters to the centre of the Irminger Basin (Figure 2.14) (Holliday et al. 2007).

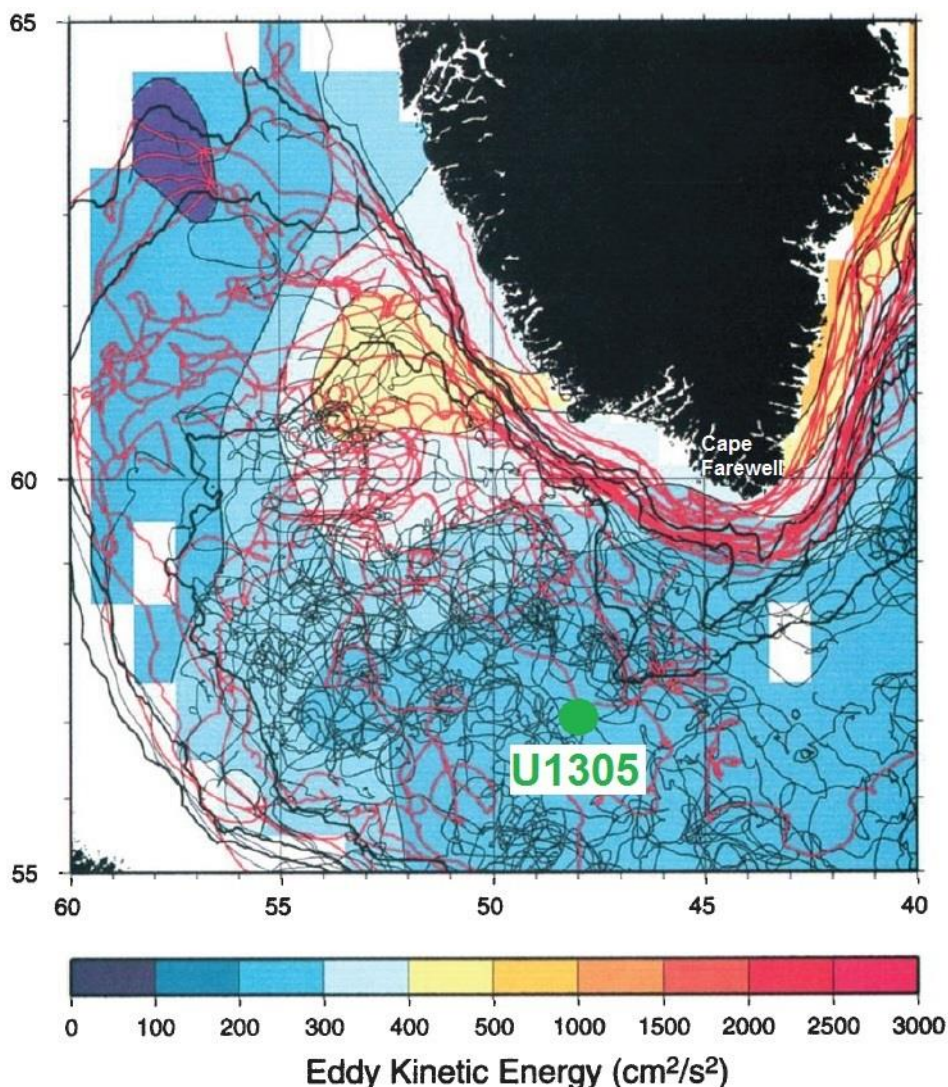


**Figure 2.14** | Map of the Labrador Sea showing Eddy Kinetic Energy overlain by individual trajectories of drifters. Shown in red are the paths taken by drifters in the East Greenland Current passing within 100 km of Cape Farewell. It can be seen that many drifters became caught within eddies which covered much of the SPG interior. Core location U1305 is also shown (Adapted from Fratantoni 2001).

## 2.5.4 | West Greenland Current

The West Greenland Current (WGC) is a subpolar eastern boundary current ( $\Theta \sim 1.8^\circ\text{C}$ ,  $S \geq 34.5$ ) that flows north west along the Greenland shelf break (Cuny et al. 2002). It is formed from two distinct components: inshore near surface ( $< 150$  m) cold fresh waters from the EGC (and EGCC), overlying the warm saline Irminger Water flowing along the continental slope ( $> 200$  m depth), as they round Cape Farewell (Fratantoni and Pickart 2007) (Figure 2.12). The relative proportion of each water mass can vary significantly (Myers et al. 2007; Myers et al. 2009). The WGC then leaves the Greenland coast, following isobaths to turn west and then south to join the Labrador Current. Turbulent mixing is evident in drifter studies which reveal an area of high eddy kinetic energy along the west coast of Greenland from which eddies spin off, meandering across the entire Labrador Sea (Figure 2.14) (Fratantoni 2001). These eddies dominate flow within the centre of the SPG (Figure 2.15) (Cuny et al. 2002) and influence the preconditioning of the SPG for deep convection (Stramma et al. 2004) by

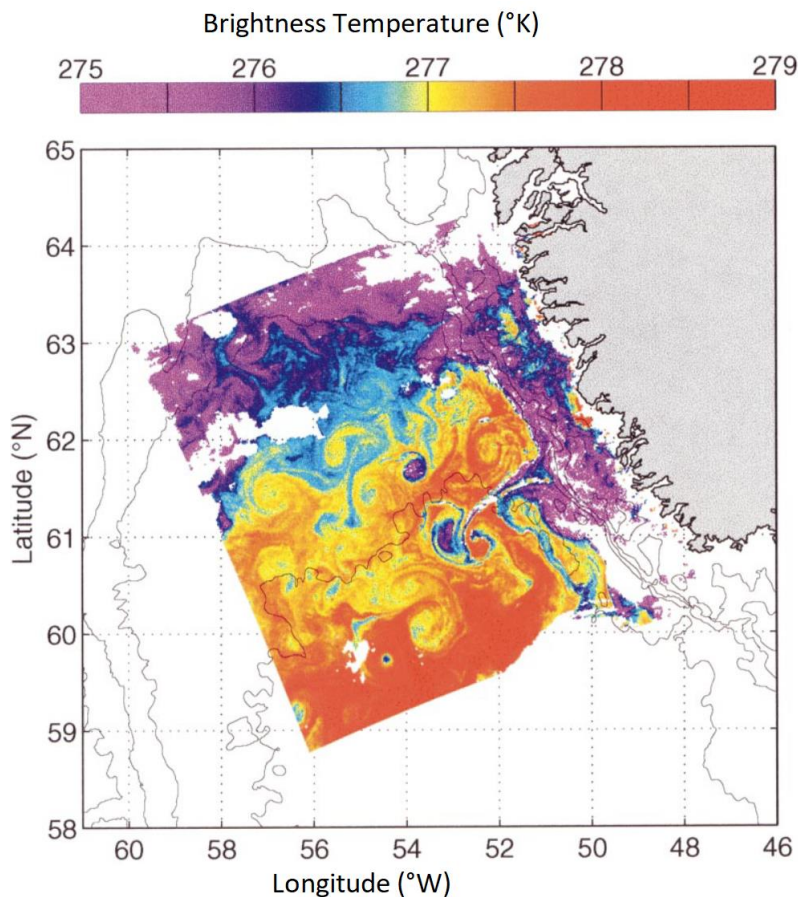


**Figure 2.15** | Eddy activity within the Labrador Sea originating where the 3000 m isobath leaves the shelf, visible in a temperature sea surface brightness satellite image from infrared ( $11 \mu\text{m}$ ) wavelengths (Prater 2002).

injecting varying quantities of fresh (EGC) or saline (Irminger Current) water and changing surface buoyancy across the northern and central Labrador Sea (Yashayaev 2007). This may be why transport of more saline Irminger Water transport at Cape Farewell has been found to be correlated with LSW formation with a lag of one year (Myers et al. 2007).

## 2.5.5 | Labrador Current

The Labrador Current is a subpolar western boundary current whose main axis flows south along the North American shelf break to a depth of ~1800 m, below which modified SPMW transported into the boundary current system by the Irminger Current can be found along the upper slope, with the Western Boundary Undercurrent between 2000 – 3000 m (Cuny et al. 2002). It transports cold, fresh ( $\theta \sim -1.5$  °C,  $S \leq 34$ ) (Cuny et al. 2002) Arctic water from the EGC and the Davis Strait south, along with fresh water from continental runoff, melting sea ice and LSW (The Lab Sea Group 1998), although a study using Lagrangian floats in the region by Bower et al. (2009) did not observe transport of LSW directly, highlighting the complexity of circulation in this region. The Labrador Current then flows south beneath the NAC beyond the “north west corner”, interacting with and entraining Gulf Stream waters (Pickart and Smethie 1993). Summer transport is ~11 Sv, with a large annual range of ~4 Sv (Lazier and Wright 1993).

## 2.5.6 | Deep Western Boundary Current

Since Stommel proposed his abyssal circulation model (Stommel 1958), the existence and importance of the Deep Western Boundary Current (DWBC; also known as the Western Boundary Undercurrent, WBUC) as the major deep limb exporting recently ventilated waters of the AMOC has become well established (Pickart 1992; Dickson and Brown 1994; Smethie Jr. et al. 2000). The DWBC flows around the coast of Greenland ~2000 – 3000 m depth around the “south corner” (Holliday et al. 2009) into the Labrador Sea following bathymetry, then south along the east coast of North America inshore of the 4000 m isobath (Pickart 1992; Schott et al. 2004), transporting LSW, NEADW and DSOW (which combine to form NADW) towards the equator (Stramma et al. 2004). The DWBC follows topography around Orphan Knoll (Xu et al. 2015). However, far from acting simply as a drain for newly ventilated deep waters, CFC budgets indicate that a significant proportion of NADW recirculates from the DWBC into the interior, remaining in the region for several decades (LeBel et al. 2008). Just north of the Flemish Cap, complex topography and interaction with the overlying NAC causes DWBC outflow to split near to Orphan Knoll, ventilating the interior central North Atlantic (Fischer and Schott 2002; Kieke et al. 2009; Xu et al. 2015).

From this point the DWBC does not seem to be one continuous current to the Grand Banks, as shown by profiling float trajectories from the Labrador Sea (Lavender et al. 2000; Fischer and Schott 2002) and tracer distributions with the LSW (Rhein et al. 2002). Computer models suggest that eddy-driven recirculation gyres export deep water along interior pathways from the SPG to the STG (Gary et al. 2011). Thus, the DWBC may not be one continuous current (Lozier 2010), with much southward flow occurring through the ocean basin interior (Bower et al. 2009), potentially within migrating eddies or deep eddy-driven recirculation gyres (Dengler et al. 2004; Gary et al. 2011). Whatever the precise mechanisms, the DWBC forms an important conduit for the removal of cold LSW and DSOW southwards as part of the deep thermohaline circulation (Stramma et al. 2004).

## 2.6 | OCEANOGRAPHY SUMMARY

Ocean circulation within the North Atlantic is complex and variable, and despite being one of the best studied regions in the world, significant uncertainties remain. It is clear from this overview that the concept of thermohaline circulation as a “conveyor belt” shifting water masses smoothly along well-established pathways is a vast simplification. However, physical driving mechanisms and basin shapes will have been largely the same during previous interglacials, so circulation in the North Atlantic is likely to have been broadly similar. From their location to the north and south of the Labrador Sea (Figure 2.1), sediment cores U1305 and U1302 are ideally situated to monitor the subpolar gyre within the Labrador Sea, a pivotal location for the global climate. The next chapter provides an overview of the literature concerning the last interglacial in the Labrador Sea.

*"Eddies," said Ford, "in the space-time continuum."*

*"Ah," nodded Arthur, "is he? Is he?"*

Douglas Adams, *Life, the Universe and Everything*.

# 3 | PALAEOCEANOGRAPHY

The last chapter summarised what is known about the North Atlantic today. This chapter provides a brief summary of Pleistocene glacial cycles (section 3.1), the marine isotope stages (section 3.2), and a discussion of the significance of ice rafted debris (section 3.3). A review of the literature concerning the penultimate deglaciation (section 3.4), the last interglacial itself (section 3.5) and the last glacial inception (section 3.6) is presented, with particular emphasis on the Labrador Sea. Finally, changes in ocean circulation over glacial/interglacial timescales are discussed (section 3.7), with a short summary (section 3.8), which leads into the subsequent three chapters of results.

## 3.1 | PLEISTOCENE GLACIAL CYCLES

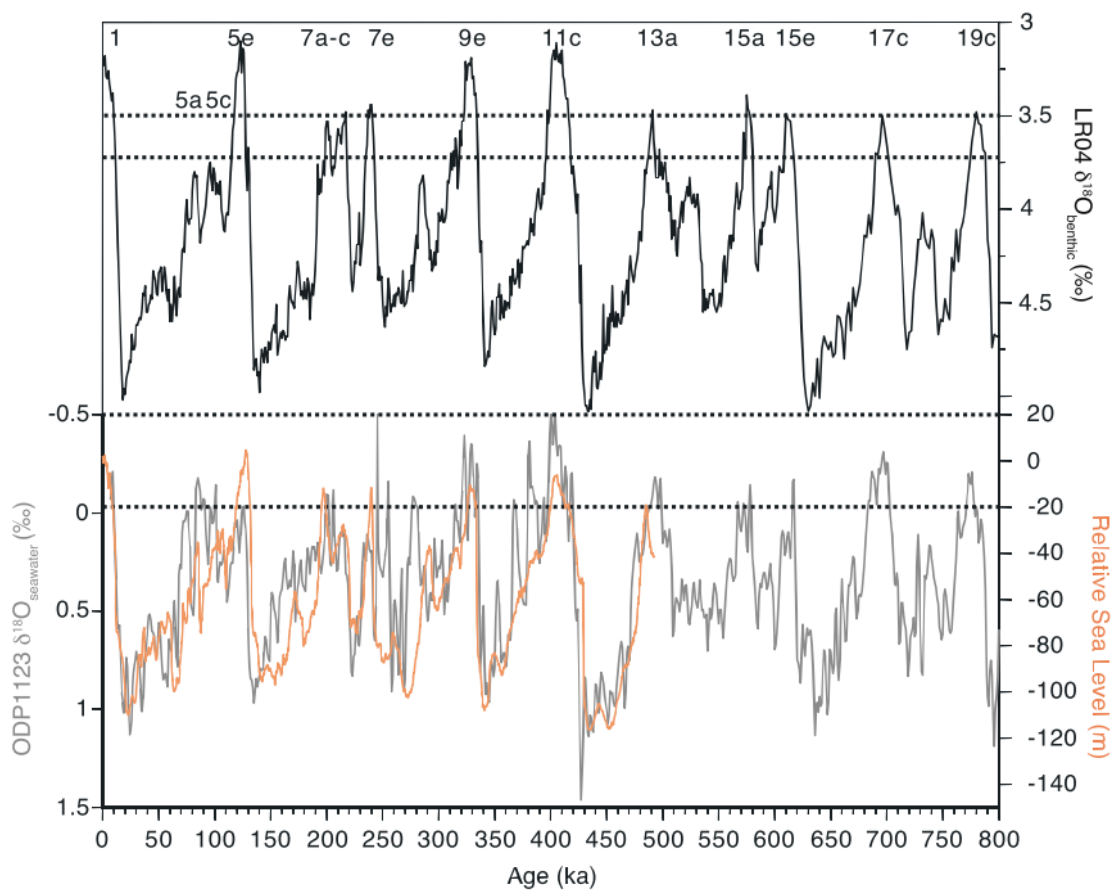


**Figure 3.1** | Interglacials of the last 800 ka, using a sea level definition. Benthic  $\delta^{18}\text{O}$  stack LR04 (black; Lisiecki and Raymo 2005), Red Sea relative sea level (orange; Rohling et al. 2009), and seawater  $\delta^{18}\text{O}$  (grey; Elderfield et al. 2012). This study is concerned with MIS 5e, indicated along the top. Dashed lines indicate threshold values potentially used to define interglacials (Past Interglacials Working Group of PAGES 2016).

The Pleistocene geological epoch (2.58 ma to 11.7 ka) was subject to repeated glaciations, involving the build-up of massive continental ice sheets, as a result of which global sea levels dropped by 100 metres or more (Figure 3.1). These glacial periods were punctuated by warmer interglacials which lasted 10 – 30 ka (Past Interglacials Worked Group of PAGES 2016), during which ice sheets melted and sea level rose, sometimes to higher than present global mean sea level (Kopp et al. 2009; Dutton and Lambeck 2012). Figure 3.1 shows the typical “saw-tooth” pattern of global climate change with the rapid onset of interglacials known as Terminations, followed by slower descent into glacial conditions. It is believed that these dramatic global climate cycles are paced by periodic variations in the pattern and intensity of solar radiation (insolation) received by the Earth due to changing orbital configurations known as Milankovitch cycles (Hays et al. 1976). Figure 3.2 illustrates how insolation differed during the last interglacial as compared to present day, particularly at high northern latitudes. Increasing northern hemisphere insolation seems to initiate Terminations, but this factor alone is insufficient to explain the full range of climate response, which requires feedbacks involving temperature, ice volume and atmospheric composition to amplify the effects (Past Interglacials Working Group of PAGES 2016). Glacial inception seems to happen much more slowly with a global sequence of climate changes and slow continental ice sheet build up.

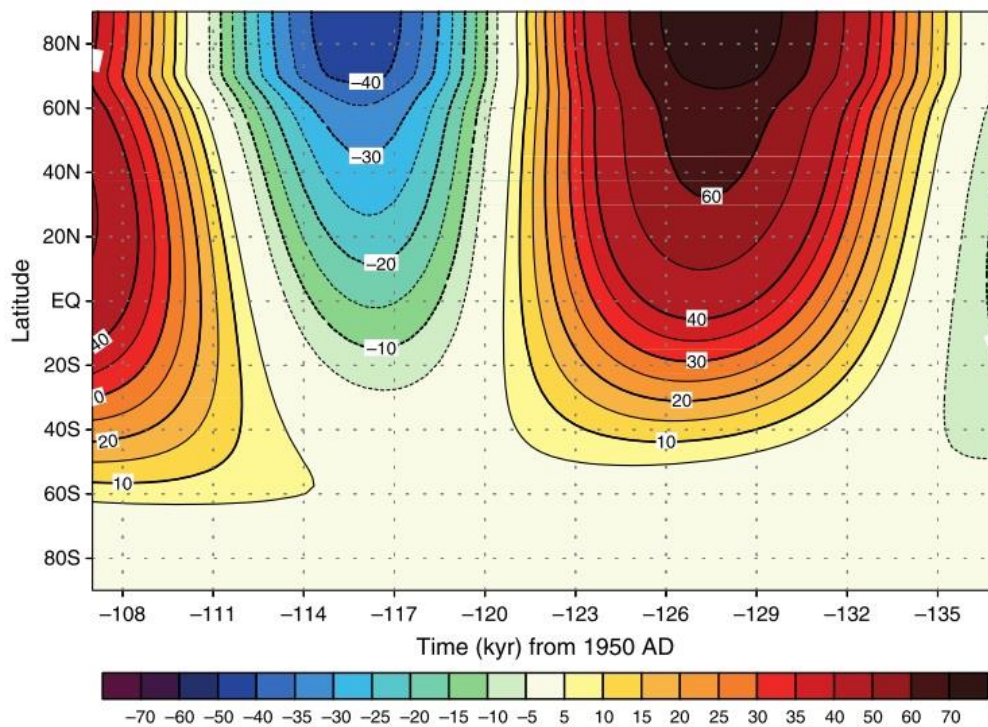


**Figure 3.2** | Distribution of insolation by latitude on 21<sup>st</sup> June (Wm<sup>-2</sup>) during the last interglacial (137 – 107 ka) as a deviation from modern values between 137 and 107 ka BP (Berger et al. 2007).

## 3.2 | MARINE ISOTOPE STAGES

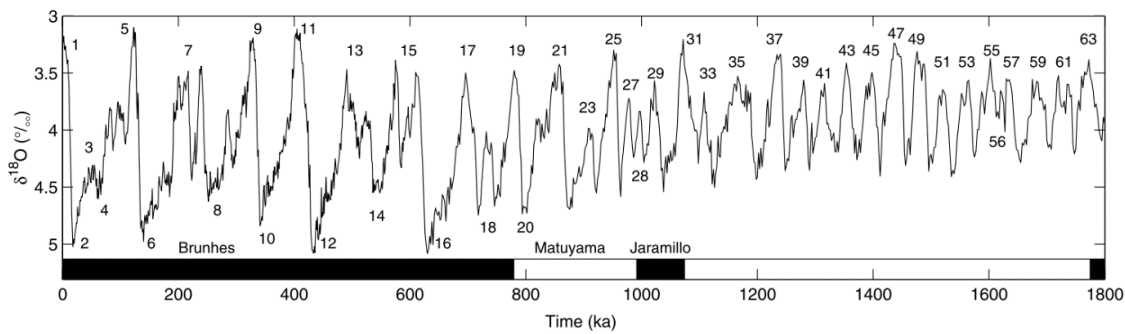


**Figure 3.3** | The LR04 benthic foraminiferal  $\delta^{18}\text{O}$  stack, constructed from 57 globally distributed cores graphically correlated into one stack. Numbers indicate marine isotope stages, odd numbers are interglacials (including the last interglacial, MIS 5) and even numbers indicate glacial stages. Bottom bar shows paleomagnetic reversals (adapted from Lisiecki & Raymo 2005).

It was Emiliani (1955) who first divided the benthic  $\delta^{18}\text{O}$  record of foraminifera (see section 6.3.1) from marine sediment cores into a time sequence of numbered stages (the marine isotope stages) from the coretop downwards, which represent the build-up of terrestrial ice during glacial periods (extracting vast amounts of water from the oceans) and the melting of those ice sheets (and recirculation of that water) during subsequent interglacial periods (Shackleton 1967). Odd numbers represent interglacials and even numbers represent glacial periods (Figure 3.3). Over 100 marine isotope stages (MIS) have been identified spanning the Pliocene (Lisiecki and Raymo 2005). The marine isotope record has since proved to be one of the most complete and regionally uniform systems available, which matches well with the orbital forcing of Milankovitch cycles and has near worldwide validity. The marine isotope system is generally recognised as the basic subdivision in climate stratigraphy.

MIS 5 corresponds to the last warm period in Earth's history, between 130 ka and 80 ka. MIS 5 is divided into five substages (a – e) (Figure 3.4), of which MIS 5e has been associated with the Eemian Interglacial on land as defined by palynologists (e.g. Sánchez Goñi et al. 1999), though the

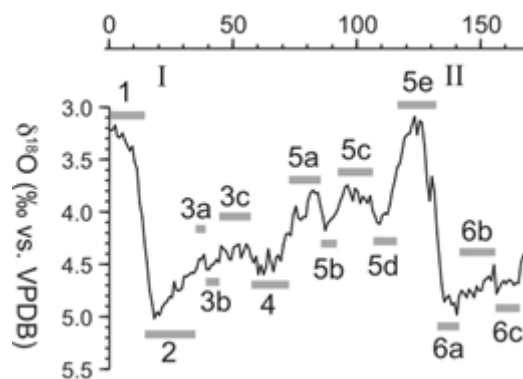


**Figure 3.4** | Recently updated lettering scheme for marine isotope substages used in this study, illustrated using the LR04 benthic  $\delta^{18}\text{O}$  stack (Lisiecki and Raymo 2005), Roman numerals along the top indicate Terminations (Adapted from Railsback et al. 2015).

boundaries between these very different stratigraphic entities are somewhat offset. Confusion surrounding lettered substages, first defined for MIS 5 by Shackleton (1969), has resulted in a recent optimised MIS lettering scheme, coherent for the last 1 million years, illustrated in Figure 3.4 (Railsback et al. 2015). In this thesis, discussion will therefore be structured based on the MIS lettering scheme of Railsback et al. (2015). The term “last interglacial” is used interchangeably with MIS 5e to refer to the last period in Earth’s history when global temperatures were comparable to the present day, and global mean sea level was as high or higher (e.g. Dutton and Lambeck 2012).

### 3.3 | ICE RAFTED DEBRIS

Where glaciers reach the sea, ice calves off and drifts away in ocean currents, carrying frozen within it stones and material plucked from the bedrock. Sediment and volcanic ash can also become entrained within sea ice as it forms. As icebergs are carried into warmer waters they melt, releasing chunks of rock to the sediment much larger than would usually be transported there as wind-blown dust, or via turbidites or ocean currents. Ice rafted debris (IRD) is defined as lithic grains which are sand-sized ( $63\ \mu\text{m}$  –  $2\ \text{mm}$ ) or greater. Typical IRD in the North Atlantic is composed of quartz and feldspar, with occasional inputs of volcanic glass and low levels of detrital carbonate (limestone or dolomite) (Bond et al. 1992). The quantity of IRD in a sediment sample therefore provides information about iceberg calving rates and distribution, mechanisms of transport and the rate of melting (Grobe 1987). The lithology of IRD varies depending on the type of bedrock lying beneath the glacier, and has been used to indicate the source of the icebergs (e.g. Bond and Lotti 1995).

Examination of North Atlantic marine cores has revealed regular IRD layers occurring every 1 – 2 ka during glacial periods (Bond et al. 1993; McManus et al. 1994; Bond and Lotti 1995; Bond et al. 1999; Oppo et al. 2006; Chapman & Shackleton 1999; van Kreveld et al. 2000). These have been associated with the series of stadial and interstadial Dansgaard-Oeschger (D-O) Events first identified in Greenland ice cores (Johnsen et al. 1992; Dansgaard et al. 1993) whose imprint extends to variations in European pollen records (e.g. Guiot et al. 1993; de Beaulieu & Reille 1992), lake cores (e.g. Regattieri et al. 2017) and speleothems (e.g. Demény et al. 2017; Regattieri et al. 2016) and is even seen in Antarctica (Jouzel et al. 2007). The rapid Greenland warming (often only 10 – 100 years) was usually followed by slower cooling (Alley 2007). Millennial-scale

cycles of ice rafting have been attributed to cyclical changes in Atlantic meridional overturning circulation (AMOC) strength (Alley 2007). It should be remembered that IRD input is not regionally uniform, but that the pattern of surface currents (which controls ice drift, and through temperature, melt rate) also presents a control on IRD distribution (Small et al. 2013). Also, the presence of IRD can be diagnostic both of ice sheet decay (i.e. climate warming) and ice sheet advance (i.e. climate cooling) (McCabe and Clark 1998; Clarke et al. 1999). Not all detrital layers are equal however. Though generally IRD layers are considered to be the result of ice sheet instability (i.e. marine calving glaciers), some detrital layers are rich in carbonate, whilst some are not (e.g. Stoner et al. 1995). Also, some are apparently derived from ice rafting, whilst some appear to contain carbonate-rich deposits comprised of much finer (sometimes graded) suspended sediments (Hesse and Khodabakhsh 2017), which have been attributed to turbidity flows from the continental shelf or along the northwest Atlantic mid-ocean channel (NAMOC) (Hillaire-Marcel et al. 1995, Stoner et al. 1995). The most prominent detrital layers across the North Atlantic are associated with Heinrich events.

### 3.3.1 | Heinrich Events

It has long been recognised that IRD input to the North Atlantic was enhanced during glacial periods when large ice sheets were present on land (Ruddiman 1977). Heinrich (1988) identified distinct peaks (“dropstone layers”) every 7 - 10 ka that approached 100% IRD abundance of total entities in the 180 – 300  $\mu\text{m}$  size fraction (most other particles being planktonic foraminifera), and attributed them to periods of intense ice rafting. These Heinrich events were centred along an “IRD belt” between around 40°N and 55°N, associated with the NAC and the polar front (Ruddiman 1977; Grousset et al. 1993) (Figure 3.5). Heinrich events then become the subject of intense study (e.g. Bond et al. 1992, 1993; Broecker et al. 1992; Broecker 1994; Bond and Lotti 1995). Heinrich events occurred during glacial periods, since the existence of large ice sheets is a prerequisite for massive ice rafting episodes. Some were associated with periods of ice sheet breakup during a transition to a warmer climate state, whilst others occurred at the end of warmer interstadials as large ice sheets advanced (Hiscott et al. 2001). The observation of benthic  $\delta^{13}\text{C}$  (see section 6.3.2) depletion of  $\sim 1$  ‰ beginning  $\sim 2$  ka before Heinrich events suggests they may be a consequence of long-term AMOC

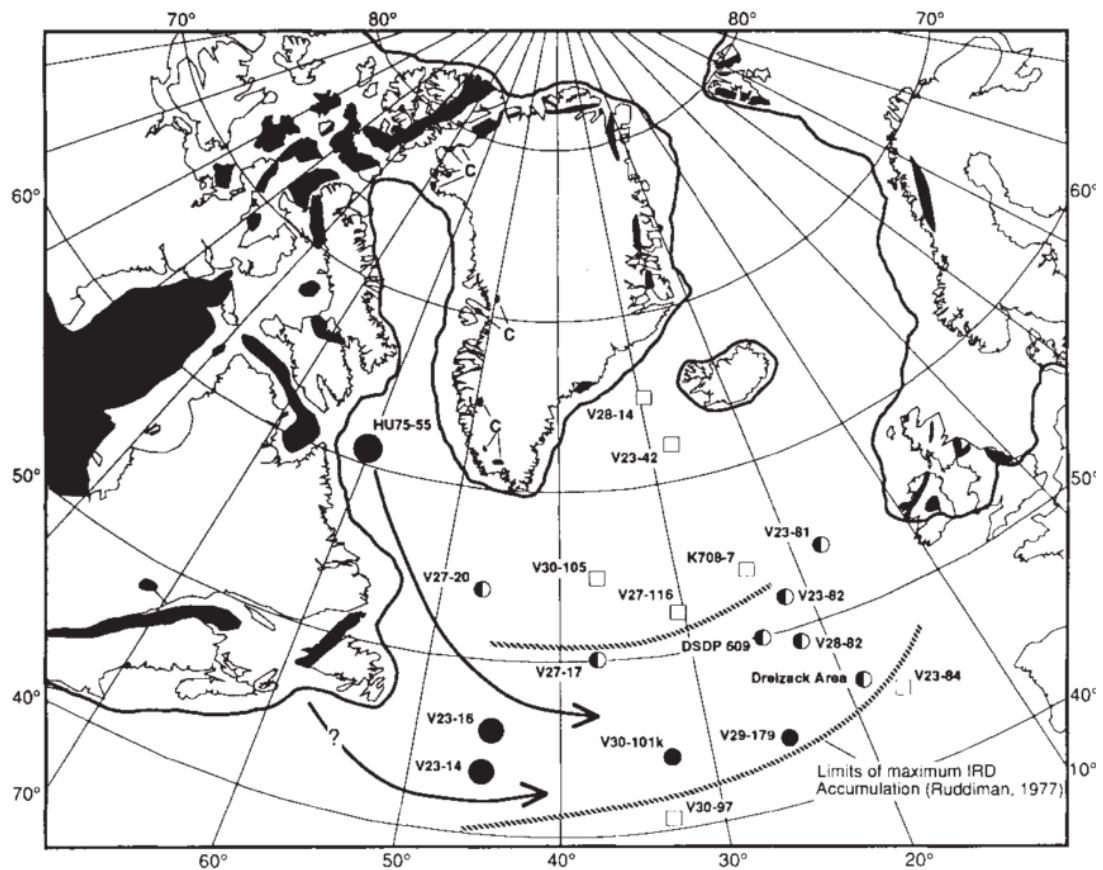


**Figure 3.5** | Location of North Atlantic cores containing Heinrich deposits. Filled circles = carbonate-rich IRD present in all Heinrich deposits; half-filled circles = carbonate-rich IRD absent in some Heinrich deposits; open squares = carbonate-rich IRD absent in all Heinrich deposits. Circle size indicates a westward increase in Heinrich deposit thickness. Solid black areas = limestone and dolomite bedrock. Thick solid line = approximate maximum ice sheet limit during the last glaciation. C = small carbonate rock exposures. Arrows = possible iceberg transport path (Bond et al. 1992).

slowdown rather than a cause (Zahn et al. 1997), though certainly freshwater input during massive ice rafting may have a role to play in feedbacks which prolong and enhance North Atlantic cooling (McManus et al. 2004). The onset of Heinrich events tends to be signalled, at least in the Labrador Sea, by an increase in both coarse lithic material and fine turbidity-driven sediment (Clarke et al. 1999; Hesse and Khodabakhsh 2016). Many (though not all) Heinrich events have been associated with increased detrital carbonate derived from the bedrock underlying the Laurentide ice sheet (LIS) (Andrews & Tedesco 1992). Subsequent decreases in planktonic  $\delta^{18}\text{O}$  values have been taken as indications of reduced salinity caused by isotopically depleted meltwater (Clarke et al. 1999). Although not all Heinrich events are associated with Terminations, Terminations tend to be associated with a Heinrich event, which is then followed by rapid warming and climate reorganisation into an interglacial climate state (Raymo 1997; Cheng et al. 2009). Heinrich events have been associated with changes in Greenland ice

core records (Bond et al. 1993), playing a role in shutting down AMOC during deglacial periods (McManus et al. 2004) with potentially global impacts (Hemming 2004).

Many different mechanisms have been proposed as the cause of Heinrich events. Internal ice sheet fluctuations due to basal freezing of the LIS followed by geothermally-driven basal melt providing enhanced lubrication were implicated in the binge-purge model of MacAyeal (1993). Alternatively, Johnson and Lauritzen (1995) proposed that regular outburst floods (jökulhlaups) were caused by failure of an ice dam at the mouth of Hudson Strait which released huge quantities of fresh glacial meltwater into the North Atlantic, and may have resulted in huge braided sand plains on the abyssal floor east of the NAMOC (Hesse et al. 2001). However, this model would require Hudson Bay to contain a subglacial lake, which is possible but not considered likely during glacial maximum periods (Hemming 2004). Hulbe (1997, 2004) suggested instead the breakup of an ice shelf, due to sea level rise or changes in climate. This model would, however, produce detrital carbonate associated with every Heinrich event, which is not observed, as source regions have been shown to vary. Using Nd-Sr isotopes from core SU-9008 in the central North Atlantic, Grousset et al. (1993) showed that material from H3 was derived from “young crust” (Scandinavia-Arctic-Iceland) whilst H1, H2, H4 and H5 were more “old crust” (Quebec and west Greenland) in origin. The importance of sources around the Labrador Sea for H2, H4 and H5 (Hemming et al. 1998), does not extend to H3, which appears to have had multiple continental sources (Gwiazda et al. 1996). The suggestion that strong AMOC continued throughout H2 – H4 (Stern and Lisiecki 2013) indicates that not all Heinrich events follow the same sequence of events and consequences. Observations such as these which suggest different source regions could be explained by oscillations in atmospheric forcing, capable of affecting multiple ice sheets (Bond and Lotti 1995). Heinrich (1988) proposed that rising insolation injected fresh water into the North Atlantic, which reduced AMOC. This original idea finds support from Cheng et al. (2009), who compared extremely well-dated speleothem  $\delta^{18}\text{O}$  from Sanbao cave, China, with ice core and marine records over the last four Terminations (Figure 3.6). Their persuasive suite of evidence suggests that Terminations are triggered when the rate as well as the magnitude of insolation rise are greatest, causing ice sheet disintegration which suppresses AMOC, resulting in anomalous cold in the North Atlantic (Cheng et al. 2009). As a result, the Intertropical Convergence Zone shifts south, the Asian monsoon is weakened, and temperatures rise in Antarctica (related to rising  $\text{CO}_2$ ,

atmospheric circulation changes and the bipolar seesaw) (Cheng et al. 2009). However, this is not universally agreed upon, as some studies have found little correlation between ice rafting in the Nordic Seas and the North Atlantic through the last glacial period, which argues against a common external forcing mechanism (Dowdeswell et al. 1999).

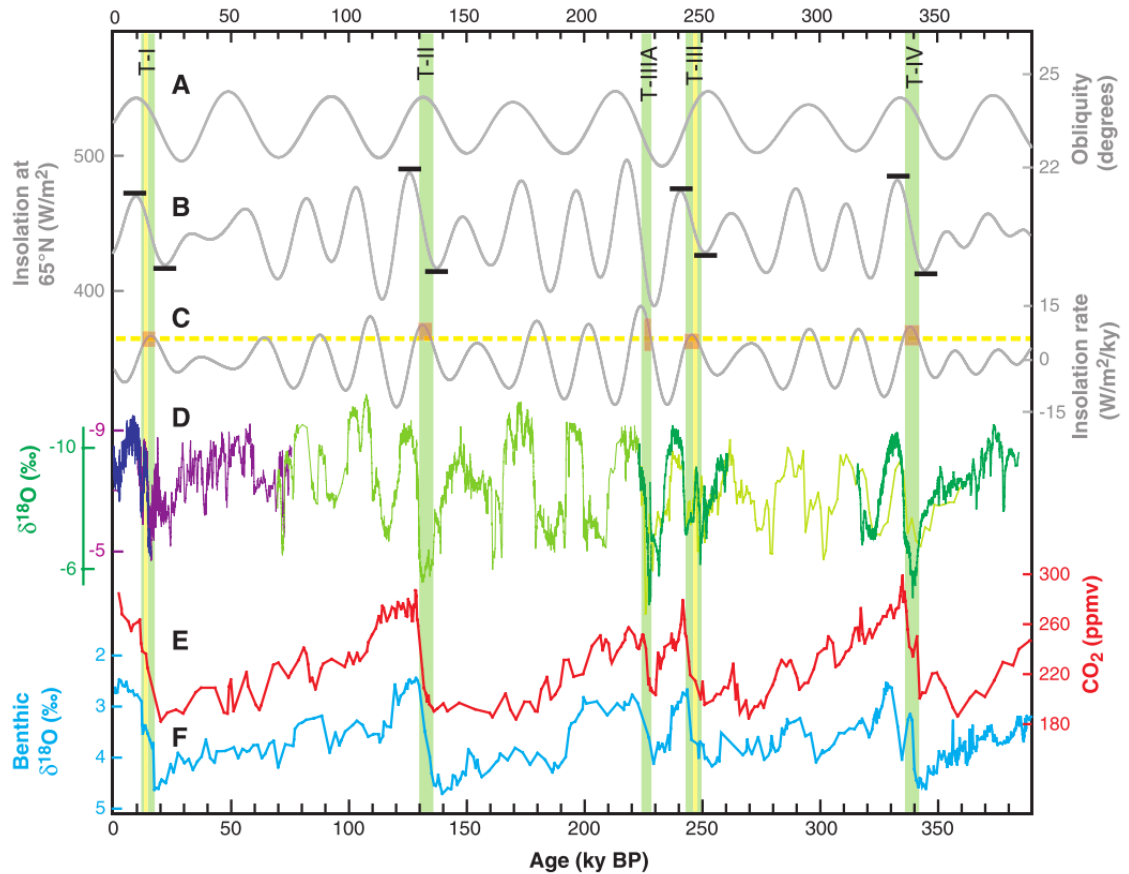


**Figure 3.6** | Comparison of the last four Terminations. (A) Obliquity, (B) insolation (21<sup>st</sup> July 65°N), (C) rates of insolation change, (D) speleothem  $\delta^{18}\text{O}$  from Hulu (purple), Dongge (dark blue), Sanbao (green) and Linzhu (yellow-green) caves, (E) Vostok  $\text{CO}_2$ , (F) benthic  $\delta^{18}\text{O}$  from ODP-980. Terminations I – IV indicated at the top. Green shading indicates weak monsoon intervals, yellow shading indicates warm Bølling-Allerød and a T-III analogue. Figure from Cheng et al. (2009), see their Figure 4 for full list of references.

Based on sedimentary details observed using X-radiographs from a large number of cores from the Labrador Sea, Hesse and Khodabakhsh (2017) conclude that Heinrich event ice rafting is often accompanied by sediment lofting and material from turbidity currents flowing along the NAMOC, as well as turbid surface plumes. They divide Heinrich events into five types (I – V) depending on sedimentary features. Type IV Heinrich Layers were observed in the vicinity of Orphan Knoll and Eirik Ridge during H1, and from where intermittent turbidity overspill from the NAMOC coincides with the drift route of melting icebergs, and therefore contain somewhat bioturbated

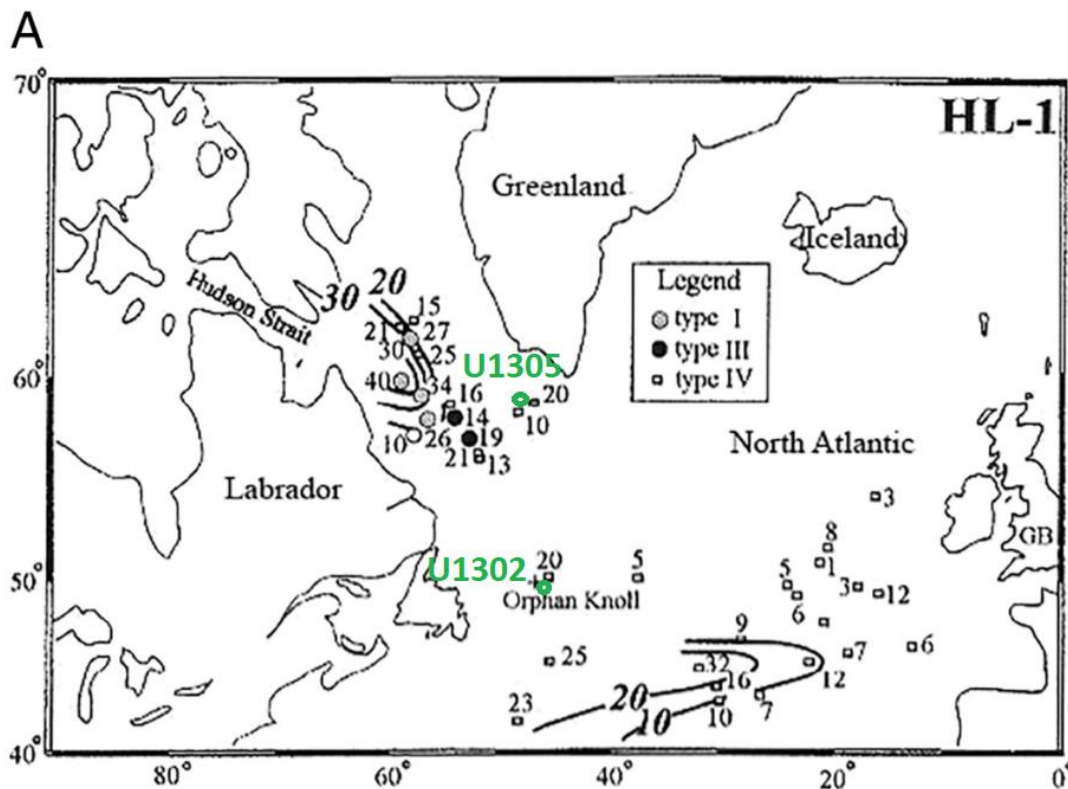


**Figure 3.7** | Distribution of types and thickness of Heinrich Layer 1 in the Labrador Sea. Note type IV layers found around Orphan Knoll and Eirik Ridge (Adapted from Hesse and Khodabakhsh 2017).

alternations of fine and coarse material (Figure 3.7). Depleted *N. pachyderma* (*s*)  $\delta^{18}\text{O}$  values during Heinrich events is attributed to a combination of isotopically depleted meltwater and temperature by Hesse and Khodabakhsh (2017), although the cold temperatures associated with Heinrich events would usually be associated with enriched  $\delta^{18}\text{O}$  values, and is more likely to be due to isotopically depleted brines due to enhanced sea ice production (de Vernal and Hillaire-Marcel 2008).

Determining the number of Heinrich events that have occurred is still an area of active research. Heinrich (1988) initially identified 11 layers using 13 piston cores from the eastern North Atlantic, with the earliest associated with TII at 130 ka (H11). van Kreveld et al. (1996) extended this system back to ~200 ka (h13) using core T88-9P from the northeast Atlantic, and Hiscott et al. (2001) even further using MD95-2025 from Orphan Basin to 340 ka (H13). Using core U1308 in the central North Atlantic, Hodell et al. (2008) found that high carbonate “Hudson Strait” type Heinrich layers began even earlier, appearing after ~640 ka. Recently, Lisiecki and Stern (2016) proposed a peak in their North Atlantic IRD stack at 140 ka be named H12, and associated it with IRD event H6.2 of Channell et al. (2012). It is clear from this brief

summary of the literature that there appears to be no standard method of labelling Heinrich layers. The various overlapping and confusing naming conventions pertinent to the present study are summarised in Table 3.1. To clarify, H7 – H10 are not in common use as they are relatively minor peaks, and are likely synonymous with the widely recognised series of North Atlantic Cold events during the last glacial period, which are used instead in this study. H11 is taken as being the major period of ice rafting during TII (~135.5 – 130 ka). H12 at ~140 ka of Lisiecki and Stern (2016) is also adopted. Estimates for the duration of Heinrich events also vary, between 500 ± 250 years (Hemming 2004) and 4 ka (Stanford et al. 2011) for H1, and ~5 ka for H11 (Oppo et al. 2006).

**Table 3.1** | Comparison of labels (in parentheses) and ages (ka) for Heinrich events within the literature.

Heinrich (1988)	Van Kreveland et al. (1996)	Hiscott et al. (2001)	Rasmussen et al. (2003)	Evans et al. (2007)	Channell et al. (2012)	Lisiecki and Stern (2016)
(H9) 102			(H9) ~90-95			(H9) 104
(H10) 114			(H10) ~105	(5LDC) 111.7		(H10) 109
(H11) 127	(h7) 128-131	(H9) 121-126	(H11) ~130-135	(5DC) 129.3	(H6.1) 128.5	(H11) 135.5 - 129
	(h8) 142	(h8) 143			(H6.2) 135.5	(H12) 140
	(h9) 146-149				(H6.3) 144.3	
	(h10) 164-167	(h10) 159		(6LDC) 152.2	(H6.4) 157	
	(h11) 182-183	(h11) 182				

Records used in the present study date back to ~153.3 ka, well within MIS 6b. In Europe, periods of glacial advance 175 – 160 ka and 150 – 140 ka, associated with enhanced calving of the British ice sheet, bracketed a period of retreat ~157 – 150 ka, during which IRD flux was reduced, presumably due to a lack of marine calving glaciers during this interval (Hibbert et al. 2010). This pattern has been linked to summer insolation increase 155 – 150 ka, associated with a period of European ice sheet disintegration, reflected in enhanced flow of the Fleuve Manche palaeoriver through the English Channel ~155 ka (Penaud et al. 2009; Toucanne et al. 2009). These

observations may relate to strongly depleted  $\delta^{18}\text{O}$  and an increase in coarse fraction documented within the Labrador Sea during MIS 6, but before H11 (Figure 3.8; Hillaire-Marcel et al. 1994).

Using a compilation of cores from the European margin, Eynaud et al. (2007) identified laminated IRD-rich clay layers dating to late MIS 6, related to fresh water pulses from rivers draining the Celtic margin. A piece of coral found stratified 200 cm above the top laminated layer in core MD01-2461 was U-Th dated to  $139.77 \text{ ka} \pm 2500 \text{ years}$ ,

suggesting the laminated layers were deposited long before TII. Mojtahid et al. (2005) also dated a fresh water pulse to between 150 – 145 ka using MD03-2692 from the Celtic margin. This was identified via negative events in a normalised benthic  $\delta^{18}\text{O}$  stack as the “6.3” isotopic event of Prell et al. (1986), initially dated by Imbrie et al. (1984) to 146 ka. This 6.3 event was dated to 142.28 ka by Martinson et al. (1987) using an orbital tuning technique, but more recently to between 150 – 145 ka by Waelbroeck et al. (2002). This fits well with the suggestion of a fresh water pulse due to collapsing ice sheets from the Celtic margin between these dates (Eynaud et al. 2007). This also reflects upon dates from several speleothems which indicated a very early stage of TII melting. Initially the

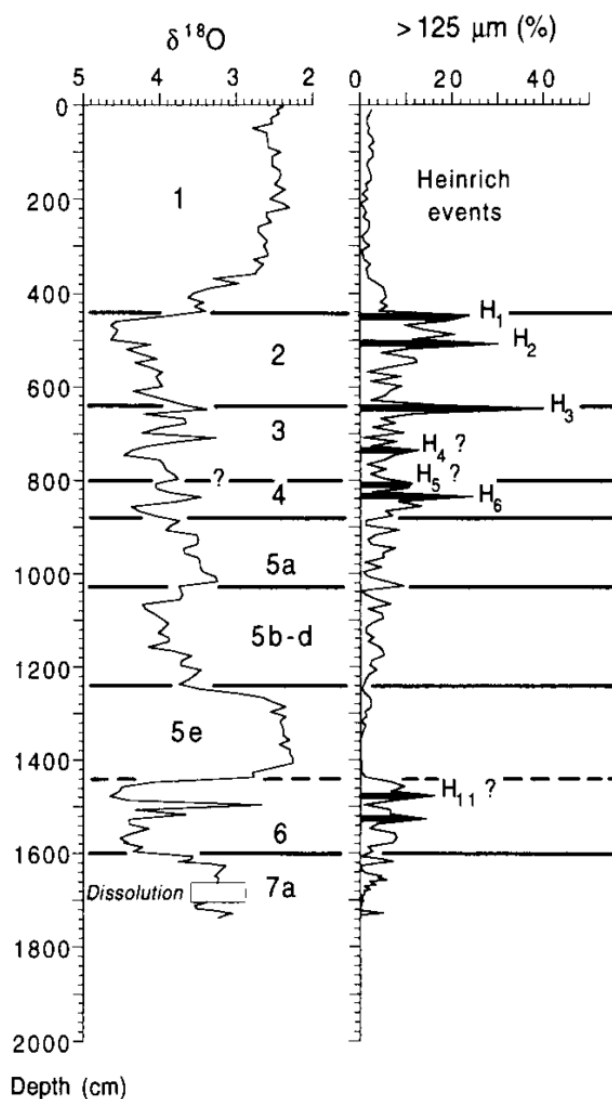


**Figure 3.8** | Planktonic (*N. pachyderma* (*s*))  $\delta^{18}\text{O}$  and coarse fraction from HU90-013-013 on the Eirik Ridge. Depleted  $\delta^{18}\text{O}$  values coincide with an increase in coarse fraction during H11. Note an increase in coarse fraction of comparable magnitude occurred prior to H11, within mid-MIS 6, potentially related to H12 ~140 ka (Lisiecki and Stern 2016) or H13 ~150 ka proposed in this study (Figure from Hillaire-Marcel et al. 1994).

controversial study by Winograd et al. (1988) whose dating of a speleothem from Devil's Hole, US, led to the suggestion that the last interglacial began  $147 \pm 3$  ka, was later revised to the suggestion that TII began  $140 \pm 3$  ka (Winograd et al. 1992) (TII not being synonymous with the last interglacial), with “initiation of warming” from  $\sim 150$  ka. Far from being discounted since then, early dates continue to be identified from U-Th dating of three speleothems within Antro del Corchia, Italy, which suggested TII be placed at  $141 \text{ ka} \pm 2500$  years (Drysdale et al. 2009). Also  $^{230}\text{Th}$  and  $^{231}\text{Pa}$  dated coral terraces suggested sea level was already  $18 \pm 3$  m below present by 135.8 ka (Gallup et al. 2002). These very early dates have led to the suggestion of a double-step structure to the penultimate deglaciation.

### 3.3.2 | Terminations

A Termination represents the rapid suite of deglacial climatic changes associated with a switch from peak glacial conditions (usually associated with the highest benthic  $\delta^{18}\text{O}$  values) (e.g. Imbrie et al. 1984) to interglacial conditions. A Termination usually contains a Heinrich event within it, but not all Heinrich events are associated with a Termination. They are numbered from the present backwards. The most recent, leading into the Holocene, is known as Termination I (TI). The penultimate deglacial, as the beginning of the last interglacial, is known as Termination II (TII). Far more literature exists for TI, plus its suitability for radiocarbon dating makes age constraints far more accurate than for TII. Therefore, a brief description of Termination I will enable comparison between the two.

The Last Glacial Maximum (LGM) was reached  $\sim 26 - 19$  ka, at the end of which insolation induced northern hemisphere ice sheet melt resulting in an abrupt rise in sea levels (Carlson and Clark 2012). Between 19 – 14.5 ka, sea levels rose gradually whilst AMOC weakened (Stanford et al. 2011). It was during this period that Heinrich event 1 occurred ( $\sim 17 - 14.7$  ka) (Figure 3.9), when “huge armadas of icebergs” crossed the North Atlantic (Bond et al. 1992; Broecker 1994), causing surface freshening and a further reduction (Thornalley et al. 2011) or even a complete shutdown of the AMOC (McManus et al. 2004). The first  $\delta^{18}\text{O}$ -enabled climate simulations suggest a different oceanic response during Heinrich events than during cold stadials, with up to 50 %

reduction in AMOC strength during MIS 3 stadials, but a total AMOC shutdown during Heinrich events (Bagniewski et al. 2017).

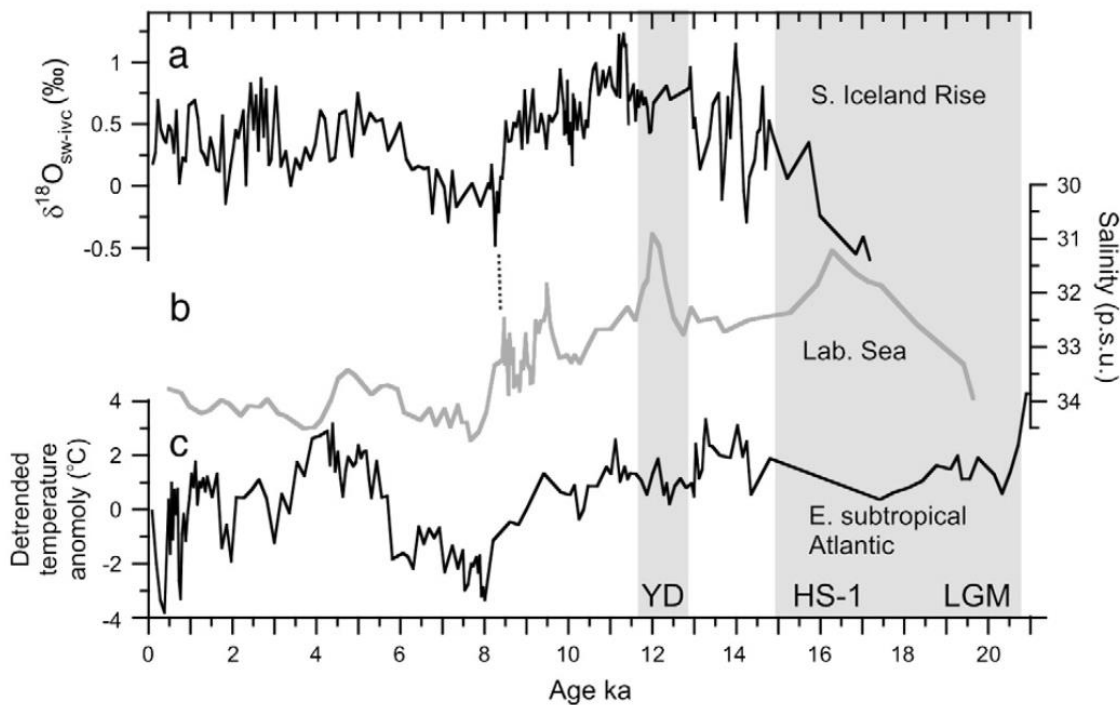


**Figure 3.9** | Sequence of events during the last deglaciation (LGM = last glacial maximum, HS-1 = Heinrich Stadial 1, YD = Younger Dryas) together with proxy records related to the strength of the subpolar gyre, shown with strength increasing downwards. (a) Iceland basin seawater  $\delta^{18}\text{O}$  (b) salinity reconstructed from dinocyst assemblages from core P-013 in the Labrador Sea, (c) temperature anomalies from foraminiferal assemblages in the eastern subtropical Atlantic (Thornalley et al. 2011).

Stanford et al. (2011) used IRD counts, foraminiferal abundance and  $\delta^{18}\text{O}$  to infer that between  $\sim 16.5 - 15$  ka, freshwater pooled within the Nordic Seas, after which the low salinity water drained into the North Atlantic. This changing hydrography may potentially be related to meltwater pulse 1A, which occurred  $\sim 14.6$  ka (Fairbanks 1989; Bard et al. 1990). Increased salinity then allowed deep convection to begin abruptly in the Nordic Seas (Stanford et al. 2011), accounting for the sudden warming into the Bølling-Allerød (B-A) (14.7 – 12.8 ka) during which the AMOC was reinvigorated (Carlson and Clark 2012). A slowing of the AMOC due to freshwater perturbation, potentially via rerouting of Lake Agassiz through the St Lawrence estuary (Broecker et al. 1989), has been implicated in causing the Younger Dryas climate reversal ( $\sim 12.9 - 11.7$  ka) (Waelbroeck et al. 2001; McManus et al. 2004), after which meltwater pulse 1B occurred  $\sim 11.3$  ka (Fairbanks 1989; Bard et al. 1990). Further ice sheet retreat during the early Holocene caused sea levels to continue rising. Thornalley et al. (2011) suggest that sudden warming at the onset of the B-A and the Holocene was due to a

combination of warmer subsurface polar water (i.e. reduced stratification), and enhanced salinity (due to combined brine formation and penetration of saline Atlantic waters further north) may have helped precondition the North Atlantic for deep convection and therefore stronger AMOC flow. It is clear therefore, that H1, in the sense of an IRD event, represents only a subset of the entire deglacial sequence of events lasting ~2.3 ka.

A similar sequence of events to TI has also been inferred for Termination III (~242 – 250 ka), whereby two cold intervals (equivalent to the Younger Dryas and H1) were interrupted by a warm interval (equivalent to the B-A) (Cheng et al. 2009) (Figure 3.6). In contrast, Cheng et al. (2009) found that TII was represented by only one

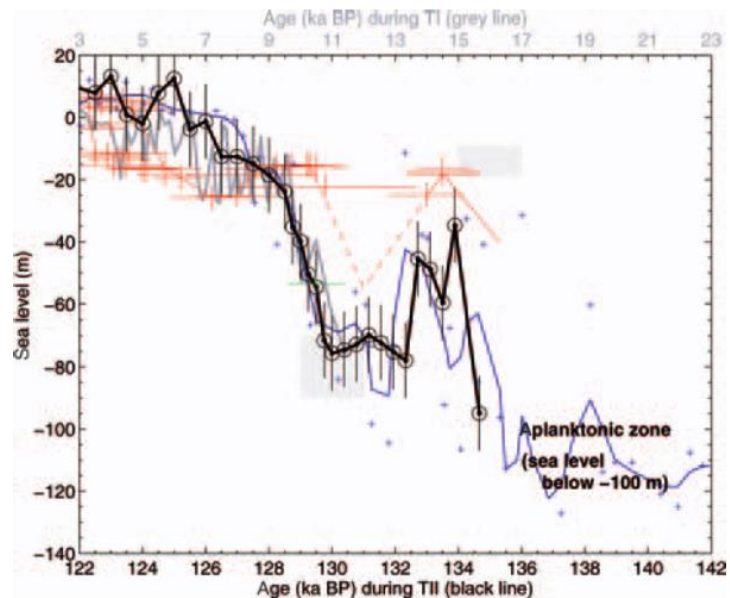


**Figure 3.10** | Estimates of global mean sea level from the Red Sea (thick black line) showing an early highstand ~133 ka followed by a sea level regression during the penultimate deglaciation (Siddall et al. 2006).

cold stadial period, associated with H11, and no climate reversal. Carlson (2008) suggested that ice sheet retreat was faster during TII due to higher boreal insolation, and used this as an explanation for the lack of a Younger Dryas-type climate reversal during the penultimate deglaciation. However, some studies concerned with global mean sea level (GMSL) have found evidence of a “Younger Dryas-Like” climate reversal during TII. Andrews et al. (2007) observed, using uplifted U-Th dated marine carbonates, an early sea level highstand ~136 ka, which was linked to a TII highstand inferred using planktonic (*Globigerinoides ruber*)  $\delta^{18}\text{O}$  from the Red Sea dated to 135.5 ka (Siddall et al. 2006), followed by a sea level regression dated to  $134.8 \pm 2.0$  ka (Figure 3.10). This was linked (within error) to the Aladdin’s Cave event, a regression of 30 - 60 m  $131 \pm 2$  ka (McCulloch and Esat 2000). Similarly, in a study using stable isotopes and foraminifera from two cores from Anholt, Denmark, Seidenkrantz (1993) inferred the existence of a warmer Flakket interstadial ~133 ka, followed by a Kattegat stadial which lasted until ~130 ka, just prior to the Eemian.

### 3.4 | THE PENULTIMATE DEGLACIATION

Obliquity began increasing ~149.4 ka, and northern hemisphere summer insolation (June 21<sup>st</sup> 65°N) began increasing after 139.7 ka (Laskar et al. 2004), both of which provided external forcing to the climate system, initiating early deglacial changes seen before the primary period of ice sheet disintegration, ~135 - ~129 ka, including rapid fluctuations in sea level. Early changes are reflected in U-Th dated speleothem  $\delta^{18}\text{O}$  from Corchia, Italy which suggests deglacial changes began ~141 ka (Drysdale et al. 2009), sea level rising to ~85 m below present by 137 ka (Thomas et al. 2009), and in atmospheric composition and temperature changes from ~136 ka detected in an ice core from EPICA Dome C (Landais et al. 2013). Earlier changes in Antarctica are in line with the concept of a “bipolar seesaw”, first proposed to explain the apparent antiphase during the Younger Dryas when the North Atlantic experienced a cold reversal, at the same time as peak temperatures observed in Antarctic ice (Broecker 1998; Stocker and Johnsen 2003). This appears robust in more recent ice core records (EPICA Community Members 2006) However, as Landais et al. (2013) suggest, it seems likely these early changes are part of a two-step process quite different from Termination I, rather than the start of a continual process of warming, since the ice volume maximum associated with the most strongly enriched benthic  $\delta^{18}\text{O}$  values are typically found ~135 ka, associated with isotope event 6.2 (Imbrie et al. 1984; Martinson et al. 1987), after which a second phase of Termination II was observed between ~130.5 and ~129 ka. This is in agreement with the timing of changes in speleothem  $\delta^{18}\text{O}$  from Sanbao, China indicating intensification of the Asian monsoon (Cheng et al. 2009), and the culmination of massive ice rafting across the North Atlantic (Oppo et al. 2006) associated with Heinrich event 11. There are indications that there was no deep Nordic overflow water into the North Atlantic towards the end of MIS 6, but rather that these overflows began as the same time as warmth is observed in North Atlantic surface waters ~130 ka, though apparently this warmth did not pass into the Nordic Seas until 2 – 3 ka later, at ~127 ka (Rasmussen et al. 2003b). An abrupt shift in Antarctic  $\text{CH}_4$  between 128.9 and  $128.5 \pm 1.7$  ka likely signals the onset of the last interglacial (Loulergue et al. 2008).

In a study comparing TI and TII using MD99-2227 from Eirik Ridge, Winsor et al. (2012) used Mg/Ca ratios from *N. pachyderma* (*s*) to isolate the seawater  $\delta^{18}\text{O}$  component (and hence salinity) of foraminiferal  $\delta^{18}\text{O}$  measurements. In contrast to the

Holocene, they did not observe peak early temperatures during the last interglacial, nor did they observe temperatures warmer than the Holocene (Figure 3.11). They attribute depleted seawater  $\delta^{18}\text{O}$  through the first half of the last interglacial to continued Greenland ice sheet melt, in common with other recent papers (Govin et al. 2012, NEEM Community Members 2013, Zhuravleva et al. 2017). Winsor et al. (2012) use this to infer greater freshwater input enhanced surface stratification and suppressed deep convection. They also observed three prominent phases of IRD deposition at this location between  $\sim 135 - 128$  ka, which will be of relevance to the discussion (section 8.2.3).

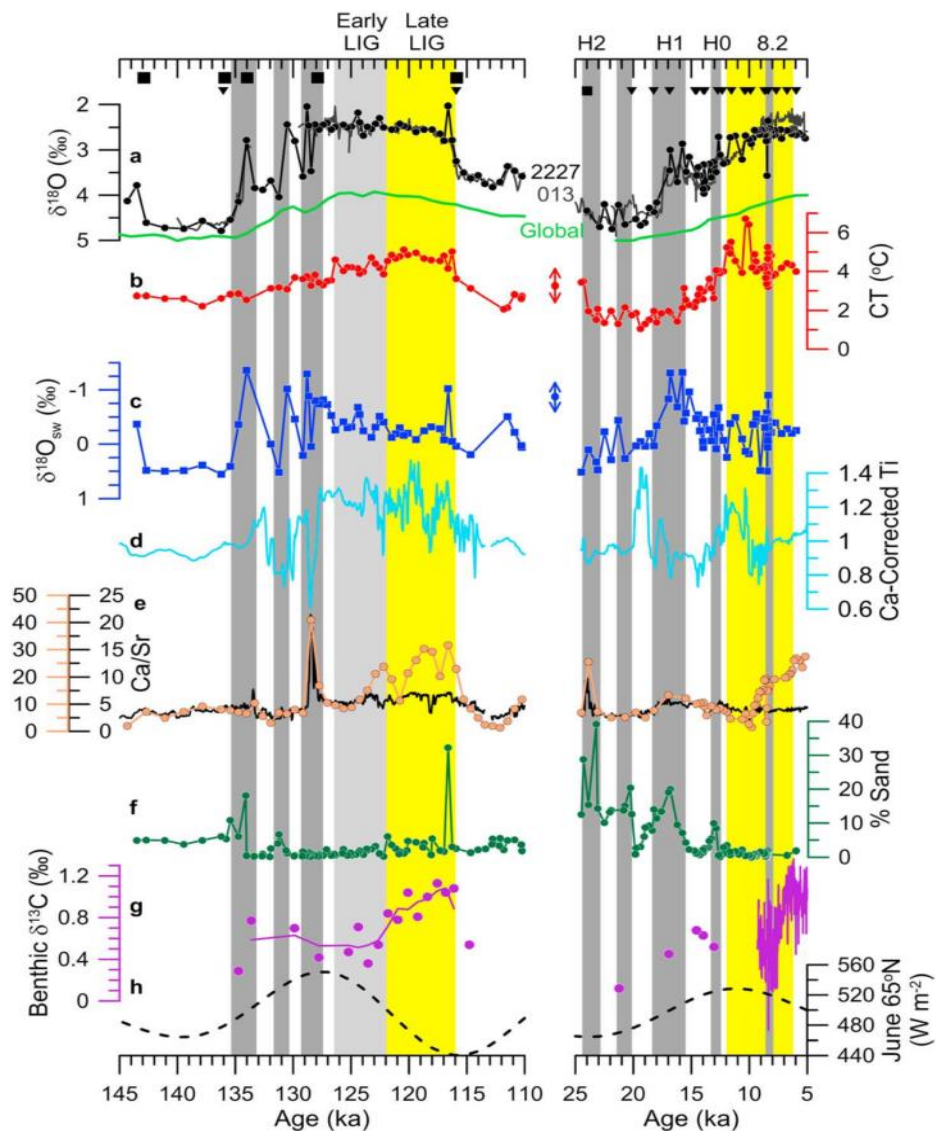


**Figure 3.11** | Comparison between the Termination II (left) and Termination I (right) illustrated using proxy data from MD99-2777. From the top, *N. pachyderma* (*s*)  $\delta^{18}\text{O}$  (black), global seawater  $\delta^{18}\text{O}$  (green), calcification temperature (red), calculated seawater  $\delta^{18}\text{O}$  (blue), Ti concentration corrected for Ca dilution (light blue), weight % of bulk  $\text{CaCO}_3$  (brown) and Ca/Sr (black), coarse fraction ( $>63 \mu\text{m}$ ) (% Sand) (green), HU90-013-013 *C. wuellerstorfi*  $\delta^{13}\text{C}$  (purple), and June insolation at  $60^\circ\text{N}$  (dashed black). Dark grey bands indicate three prominent IRD intervals during TII, and H2, H1, H0 and the 8.2 ka event (Winsor et al. 2012).

### 3.5 | THE LAST INTERGLACIAL

Using a global mean sea-level based definition, the last interglacial period lasted from 129 – 116 ka (Dutton and Lambeck 2012; Past Interglacials Working Group of PAGES 2016), and as discussed above, corresponds to MIS 5e (Shackleton 1969). The length of the last interglacial varies by location, depends on the age model used, and sometimes depends on subjective decisions about what constitutes peak interglacial conditions, but estimates vary between 8 ka (Bauch and Kandiano 2007), 9 ka (Bauch and Erlenkeuser 2008), ~10 ka (Oppo et al. 2006), 11 ka (Shackleton 1969), 12.5 ka (Stolz and Baumann 2010), 14 ka (Kukla et al. 2002a), to 17.7 ka (Allen and Huntley 2009). The last interglacial is generally considered to have been warmer than the present day (Kukla et al. 2002a; Masson-Delmotte et al. 2013). Earth’s orbit at the time had greater eccentricity, which led to more intense northern hemisphere summer insolation (Figure 3.2). Global mean temperatures are estimated to have been ~2°C warmer (Kukla et al. 2002a), pollen data from eastern Canada suggests mean annual temperatures there were 6 – 7°C higher than present (Fréchette and de Vernal 2013), and between 6 – 11°C warmer than preindustrial temperatures over Greenland (Landais et al. 2016). As a result, the Greenland ice sheet (GIS) was likely reduced in extent (North Greenland Ice Core Project

Members 2004). In their reconstruction of a folded ice core, NEEM Community Members (2013) observed a slow increase in ice  $\delta^{18}\text{O}$  between 128.5 – 126 ka, at the same time as a similar reduction in EDML ice from Antarctica, which was taken as evidence of the bipolar see-saw redistributing heat to the Northern

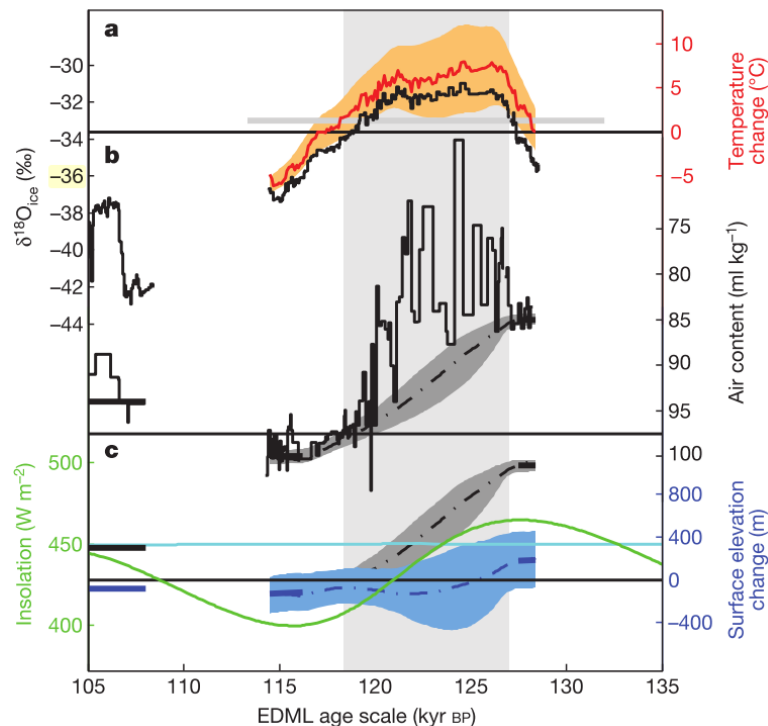


**Figure 3.12** | Reconstructed temperature and elevation history of the NEEM ice core. Temperatures (red) increased until 126 ka, after which a slow cooling began that lasted until the last glacial inception (NEEM Community Members 2013).

Hemisphere (Figure 3.12). They observed warming until 126 ka, when surface temperatures were estimated to be  $8 \pm 4^\circ\text{C}$  (NEEM Community Members 2013), after which, gradual cooling was observed until 110 ka. Pollen evidence also suggests the southern GIS was reduced in extent during the last interglacial (de Vernal and Hillaire-Marcel 2008). It may be that the northeast GIS is the most vulnerable to melting, as it is not compensated by high accumulation rates (Born and Nisancioglu 2012). GIS runoff may have contributed 0.7 to 1.5 m (Quiquet et al. 2013) to global mean sea levels between 6.6 – 9.4 m higher than present during the last interglacial (Kopp et al. 2009; Dutton and Lambeck 2012). Far from being a gradual process, last interglacial sea level rise may have occurred in a “jump” linked to ice sheet instability shortly after ~121 ka (Blanchon et al. 2009). A comprehensive assessment of last interglacial global mean sea level by Kopp et al. (2013) suggested that most likely (98% confidence) there were two highstands, dated to 125 – 123 ka and 122 – 116 ka (Figure 3.13). Interestingly, there also appears to be an increase in GMSL ~131 – 132 ka in Figure 3.13, though their study was not focussed on this period.

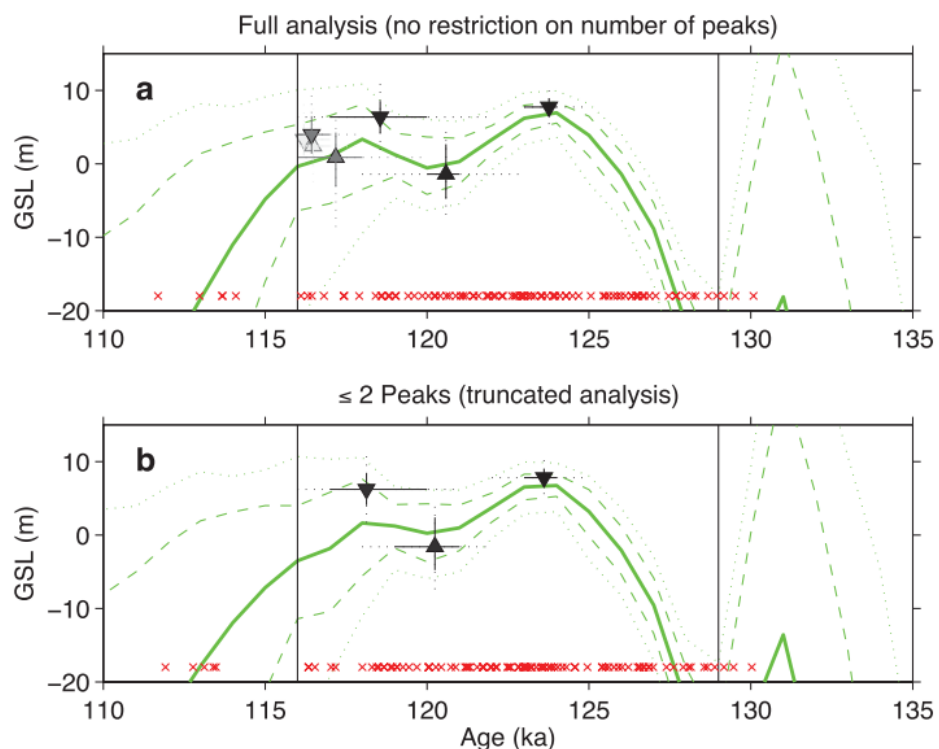


**Figure 3.13** | Peaks (downward triangle) and troughs (upward triangles) in a probabilistic study of last interglacial global sea level (GSL) (solid line = mean, dashed and dotted lines = 95% and 67% confidence intervals, respectively). Colour of triangle fill indicates likelihood of existence (black = 100%, white = 0) (Kopp et al. 2013).

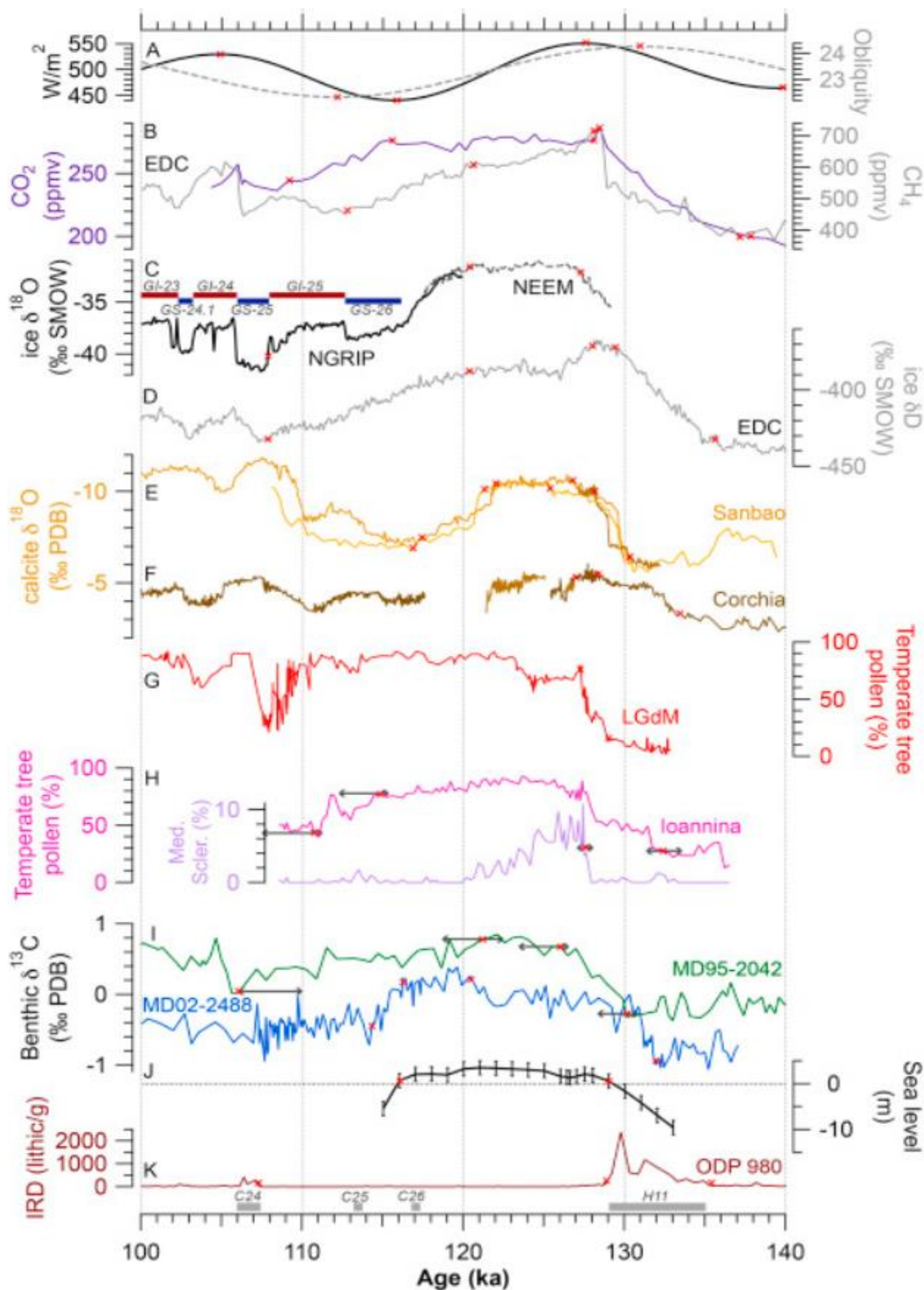


**Figure 3.14** | Selection of palaeoclimate records covering the last interglacial (140 – 100 ka) (A) Obliquity (dashed grey) and insolation (65°N 21<sup>st</sup> June; black), (B) EDC CH<sub>4</sub> (grey) and CO<sub>2</sub> (purple), (C) ice δ<sup>18</sup>O from NGRIP (black) and NEEM (dashed black), (D) EDC δD (grey), speleothem δ<sup>18</sup>O from (E) Sanbao, China (light brown) and (F) Corchia, Italy (dark brown), (G) pollen records from Lago Grande di Monticchio, Italy (red), (H) temperate tree pollen (pink) and Mediterranean Sclerophyll pollen (purple) from Ioannina sequence, Italy, (I) North Atlantic MD95-2042 benthic δ<sup>13</sup>C (green) and Southern Ocean MD02-2488 (blue), (J) global mean sea level (black), (K) IRD from ODP-980, with North Atlantic cold events (C26 – C24) and Heinrich event (H11) (Adapted from Govin et al. 2015, see their Figure 13 for full list of references).

The sequence of events discussed below are based on a thorough review of last interglacial studies by Govin et al. (2015), from which Figure 3.14 is taken. Peak last interglacial temperatures vary in magnitude and by location, but were reached early (~128 ka) in Antarctica (Petit et al. 1999; Landais et al. 2013), in the eastern North Atlantic between ~127.5 ka (Stolz and Baumann 2010) and ~125 ka (Bauch and Kandiano 2007; Lukashina 2013), and in Europe by ~127.2 ka (Allen and Huntley 2009). Peak temperatures appear to have evolved late in the Nordic Seas, between ~127 ka (Rasmussen et al. 2003b) and ~124.5 ka (Bauch and Erlenkeuser 2008). Computer models and proxy data suggest later warmth in the Nordic Seas may be the result of enhanced subtropical inflow (and consequent stable stratification) related to suppression of deep water formation and weaker circulation within the subpolar gyre as a result of freshwater input from melting sea ice 119 – 115 ka (Born et al. 2011). Indeed, steeper temperature gradients between the tropics and cooling northern latitudes late in the last interglacial may have promoted AMOC strength, bringing heat and therefore enhancing precipitation which fed glacier growth into the glacial inception (Guihou et al. 2011).

During the early Holocene, the final draining of Lake Agassiz into the Labrador Sea (Barber et al. 1999) and to the collapse of ice over Hudson Bay ~8.4 – 8.2 ka resulted in the “8.2 ka event” (Alley et al. 1997; Kleiven et al. 2008). This occurred in two phases, associated with carbonate carrying turbidites (Hillaire-Marcel et al. 2007), and has been associated with reduced deep flow speed and associated AMOC strength (Ellison et al. 2006). It was observed that this flood left a layer of red detrital carbonate in its wake (Kerwin 1996, Andrews et al. 1999). Simultaneous changes seen in  $\delta^{18}\text{O}$  within speleothems from Hulu Cave, China and the GISP2 ice core record through this period attest to the global impact of the 8.2 ka event (Wang et al. 2001). There may be a last interglacial equivalent to this event, in the form of a red layer observed in U1302 and U1305 by Nicholl et al. (2012), discussed further in section 4.3.

In the Labrador Sea, there is a mixed picture of the last interglacial. Using multi-proxy data from sediment core MD03-2664 from the Eirik Ridge (close to sediment core U1305), Ircalı et al. (2012) observed peak warmth (3 – 5°C warmer than present) early during the last interglacial (~128.5 - ~126 ka), coincident with the peak in insolation (Figure 3.15), whilst Winsor et al (2012) using core MD99-2227, also recovered nearby on the Eirik Ridge, suggested relatively constant temperatures throughout the last interglacial, with no warmer-than-Holocene peak.

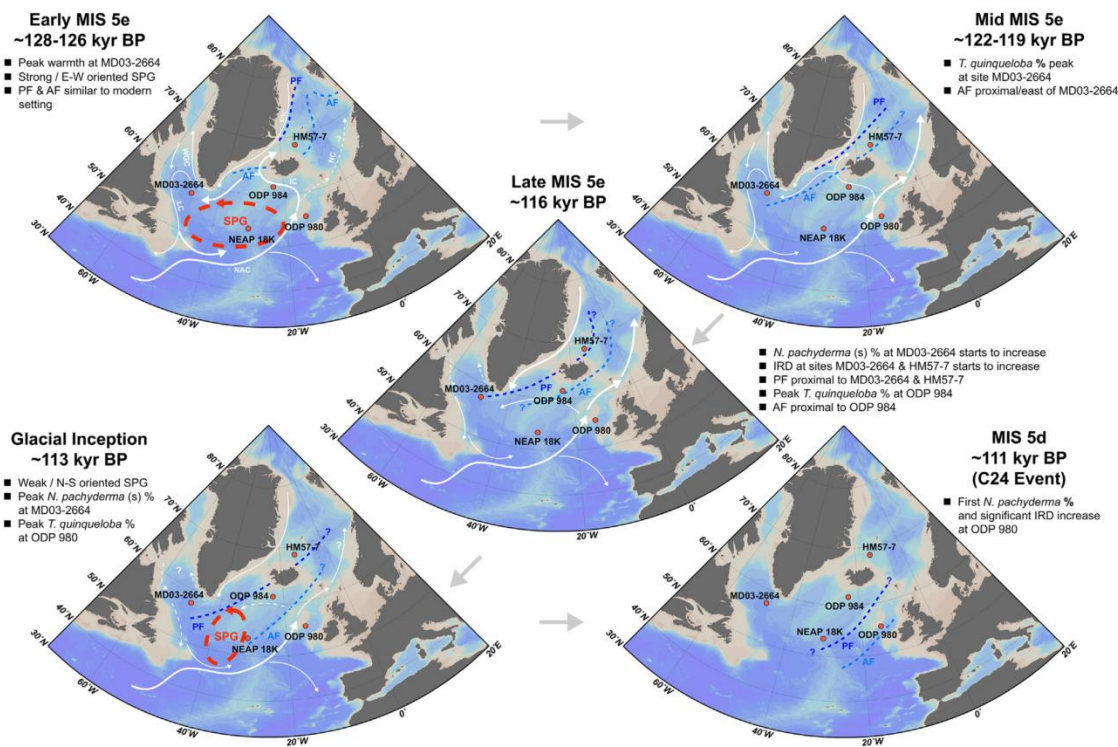


**Figure 3.15** | Schematic suggesting changes to the subpolar gyre (red dashed) and the Arctic (AF) and Polar (PF) fronts during the last interglacial and glacial inception (Irvali et al. 2016).

In a later extended multi-proxy study of MD03-2664, Irvali et al. (2016) observed continued ice melt lasting through the early last interglacial until ~122 ka, coincident with an early climate optimum. They observed indications of cooling starting after ~119 ka, in line with insolation, within which a “117 ka cooling event” was observed, which was also recognised in this study (section 8.3.4). Irvali et al. (2016) also inferred the location of the polar and arctic fronts as the glacial inception progressed, which also has relevance to the discussion (section 8.2.4).

### 3.6 | THE LAST GLACIAL INCEPTION

From long before 116 ka, low northern hemisphere insolation (which started decreasing after 127.5 ka) (Figure 3.2) initiated cooling of high latitudes (Figure 3.14).

Temperatures (reflected in ice  $\delta^{18}\text{O}$ ) decreased over Greenland, after ~121 (North Greenland Ice Core Project Members 2004) to 120.3 ka (NEEM Community Members 2013). At the same time (122-121 ka), Asian speleothem  $\delta^{18}\text{O}$  began increasing (Cheng et al. 2009), alongside decreasing air temperature and greenhouse gasses in Antarctica (Landais et al. 2013). After 116 ka, more enriched benthic  $\delta^{18}\text{O}$  values suggest the

initiation of glacier build-up (Lisiecki and Stern 2016) at the same time as decreasing global mean sea levels (Dutton and Lambeck 2012) and a shift in forest composition towards conifers or more open steppe vegetation across Europe (Kukla et al. 2002a). Glacial advance may counter-intuitively have been fed by intensified late last interglacial AMOC bringing warm tropical waters into the Nordic Seas (Born et al. 2011) and causing a steep high-to-low latitude sea surface temperature gradient resulting in intensified westerly winds (Kukla et al. 2002b), bringing enhanced winter snowfall to high latitudes and feeding glacial advance (Guihou et al. 2011). As the climate evolved towards glacial conditions during MIS 5d, cooling events in the North Atlantic indicated by a series of IRD pulses (Chapman and Shackleton 1999) may have affected the temperature and moisture availability across Europe leading to the decline of temperate forests (Milner et al. 2013). After 115 ka BP, a decline in Nordic Sea temperatures was accompanied by a shift to much cooler conditions in northern Europe as forest cover declined (Tzedakis 2003), cool steppe vegetation established in central Asia (Mackay et al. 2013) and European winter temperatures reduced by  $\sim 5^{\circ}\text{C}$  (Allen and Huntley 2009). One theory is that enhanced freshwater input in the form of Arctic sea ice to the Labrador Sea during the glacial inception may have inhibited convection, reducing the AMOC and the associated heat transport to high latitudes (Born et al. 2010).

### 3.7 | CHANGES IN OCEAN CIRCULATION

Ocean circulation during interglacials, as outlined in the previous chapter, was potentially quite different during glacial epochs. Alley et al. (1999) proposed three modes of North Atlantic thermohaline circulation: modern, glacial and Heinrich (Figure 3.16). During the modern “warm” mode, deepwater formation takes place in the Nordic Seas and North Atlantic. During the glacial “cold” mode, deepwater formation in the Nordic Seas is subdued, and instead high  $\delta^{13}\text{C}$  ( $\sim 1.5$  ‰), low-nutrient glacial North Atlantic intermediate water (GNAIW) is formed above 2000 m north of the polar front within the Iceland Basin (Oppo and Lehman 1993). During the Heinrich “off” mode, production of NADW is greatly reduced or shut down altogether (McManus et al. 2004), allowing low  $\delta^{13}\text{C}$  Antarctic Bottom Water to flow into the deep North Atlantic (Elliot et al. 2002), and triggering high latitude austral warming via the thermal bipolar seesaw (Broecker 1998; Stocker and Johnsen 2003). An alternative source for a low

$\delta^{13}\text{C}$  water mass was suggested by Thornalley et al. (2015). In a study investigating radiocarbon reservoir ages and deep water temperatures, Thornalley et al. (2015) observed that during cold intervals of the glacial period, a warm but very poorly ventilated water mass formed behind the Greenland-Scotland Ridge (Figure 3.17). However, they suggested that overflow of this water mass was weak, and mixing and entrainment on the way to the Labrador Sea would likely attenuate the low  $\delta^{13}\text{C}$  signal. Therefore, low benthic  $\delta^{13}\text{C}$  values in this study are generally attributed to incursions of AABW due to sluggish AMOC (Elliot et al. 2002).

Comparisons between benthic and planktonic isotopes have led to the suggestion that during the last interglacial, Labrador Sea Water was not formed (Hillaire-Marcel et al. 2001), due to thermohaline inhibition of deep winter convection (Hillaire-Marcel and Bilodeau 2000). These observations are supported by climate models which suggest the absence of LSW production during the last interglacial due to freshwater sensitivity in this region, with somewhat reduced convection in the eastern North Atlantic only (Cottet-Puinel et al. 2004).

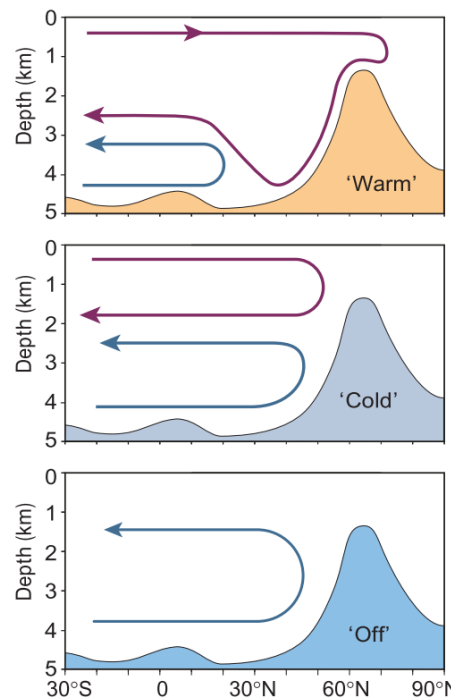


**Figure 3.16** | Section along the North Atlantic including the topographic high of the Greenland-Scotland Ridge showing schematics of three different ocean circulation modes involving North Atlantic overturning (red arrow) and Antarctic bottom water (blue line) (Rahmstorf 2002).

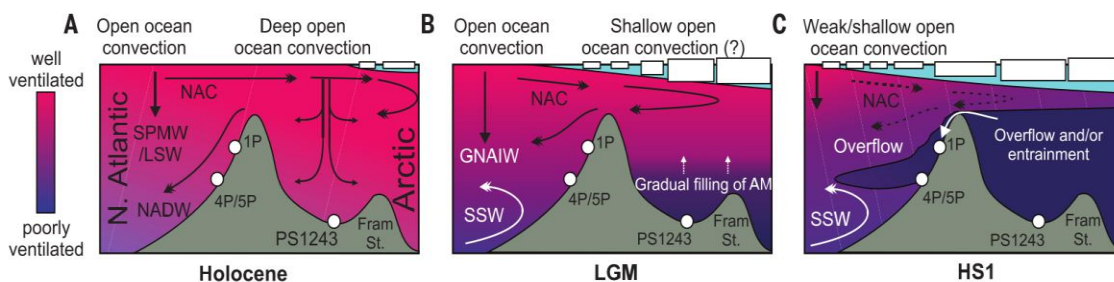


**Figure 3.17** | Proposed circulation and ventilation changes in the North Atlantic, Nordic Seas and Arctic Ocean during the Holocene, Last Glacial Maximum and Heinrich Stadial 1. Shading indicates  $^{14}\text{C}$  ventilation, white rectangles indicate sea ice/icebergs, pale blue indicates fresh surface waters. (A) Vigorous overturning in the Nordic Seas forms NADW during the Holocene. (B) Reduced overturning and formation of GNAIW in the North Atlantic during the last glacial maximum (LGM), whilst subduction of the NAC below surface fresh water creates a fairly warm intermediate water mass. (C) Suppressed deep convection by surface freshwater influence and overflow or entrainment of poorly ventilated deep water during Heinrich Stadial 1 (HS1) (Thornalley et al. 2015).

However, this last interglacial shutdown in LSW production is not universally agreed upon. Other studies suggest deep ventilation was not established in the Labrador Sea until ~122 – 116 ka (Winsor et al. 2012) or in the Iceland Basin until after ~124 ka (Hodell et al. 2009). In a study including cores from the North Atlantic, Labrador and Norwegian Seas, Govin et al. (2012) also detected weaker deep ventilation early during the last interglacial (129 – 125 ka). Another proxy-based reconstruction indicated that meltwater input from the retreating Greenland ice sheet early during the last interglacial may have weakened AMOC through inhibition of deep winter convection in the Labrador Sea, whilst deep convection in the Nordic Seas associated with warm Atlantic inflow continued unabated (Sánchez Goñi et al. 2012), though this is contrary to the interpretation of late last interglacial warming in the Nordic Seas (Born et al. 2011). An investigation using dinoflagellate cyst assemblages in four sediment cores from the Rockall Basin and Nordic Seas suggests early peak warmth higher than today in the North Atlantic, but this warmth was not advected across the Greenland-Scotland Ridge and established in the Nordic Seas until ~118 – 116.5 ka (Van Nieuwenhove et al. 2011). A study of very high-resolution sediment core MD03-2664 from the Eirik Ridge suggested NADW was present from early during the last interglacial, but with several abrupt reductions seen in benthic  $\delta^{13}\text{C}$  records associated with ice rafting events, which suggests sudden shifts in surface buoyancy could affect convection across the region (Galaasen et al. 2014). A study of two sediment cores from the south Labrador Sea near to U1302 indicated rapid changes in ocean circulation and ventilation associated with ice rafting, as a fairly warm, poorly ventilated but nutrient-rich intermediate water mass occupied the southern Labrador Sea during Heinrich events, followed by an early onset of deep convection during the last interglacial, at least down to 1250 m depth (Rasmussen et al. 2003a). There is also some indication using grain size as a proxy for current speed, that the Labrador Current was slower during Heinrich events, but rapidly recovered afterwards, and that the Labrador Current was stronger during MIS 5, 3 and 1 (attributed to enhanced Irminger Current contribution to the SPG), broadly correlated with deep water current speed in the Iceland Basin (Mao et al. 2018). Clearly, the extent and duration of these reorganisations in ocean circulation, and the rapidity of switches between states, remain areas of active research.

### 3.8 | PALAEOCEANOGRAPHY SUMMARY

In summary, much work remains to be done to clarify the regional pattern of climate and ocean circulation during the last interglacial. Warmer than present conditions during the last interglacial were due to enhanced summer insolation, which was around 11% higher between 130 – 127 ka over the Northern high latitudes (CAPE-Last Interglacial Project Members 2006). This was quite different to Holocene conditions (Herold et al. 2012), and caused enhanced seasonality and possibly reduced deep-water formation in the Labrador Sea (Hillaire-Marcel et al. 2001) and changes in AMOC configuration (Rasmussen et al. 2003b; Oppo et al. 2006; Goñi et al. 2012). The sensitivity of the subpolar gyre to freshwater input and heat flux (Toom et al. 2012) means climate change in this region has potentially global significance.

*“Stratigraphy is 90% of Geology”*

John Imbrie

## 4 | SEDIMENTOLOGY

The last chapter summarised the literature related to the last interglacial. This chapter begins with a description of both core locations and the reason for their selection (section 4.1), including a description of sediment core preparation. Following this are three sections of results. The first (section 4.2) details the methods used for IRD counts in this study, and results from both cores. The second (section 4.3) discusses a red layer previously found in U1302 and U1305 (Nicholl et al. 2012), its significance and its implications for the depth scale. The last (section 4.4) describes a diatom mat found in U1305, and its impact upon the age model.

### 4.1 | EXPEDITION 303

Between 25<sup>th</sup> September and 17<sup>th</sup> November 2004, six locations within the North Atlantic were drilled by the research ship *JOIDES Resolution* as part of the Integrated Ocean Drilling Program (IODP) joint science programs Expedition 303/306 (Figure 4.1). The expedition was

designed to provide samples stretching back to the Pliocene from climatically sensitive regions able to provide information about surface conditions, deep water circulation, and layers of lithic material derived from the Laurentian, Inuitian and Greenland ice sheets (Channell et al. 2006). All locations had previously been sampled, during the Ocean Drilling Program, the Deep Sea Drilling Program, or

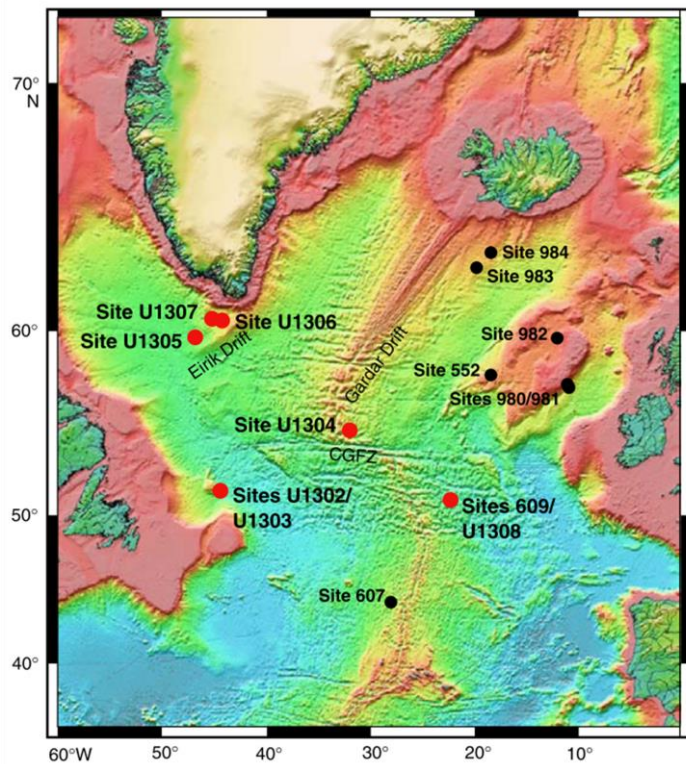


**Figure 4.1** | Site locations for Expedition 303/306 within the North Atlantic with illuminated bathymetry and topography (Channell et al. 2006).

using conventional piston cores, e.g. (Hillaire-Marcel et al. 1994; Stoner et al. 1995; Stoner et al. 1996; Hiscott et al. 2001). Based upon these earlier studies, locations which provided long, high-resolution sediment cores particularly suitable for isotope, microfossil and geomagnetic stratigraphic analysis were revisited. Eirik Ridge and Orphan Knoll were selected because they met these demands, plus their proximity to iceberg export routes via Labrador Sea boundary currents results in particularly good records of ice rafting (Hillaire-Marcel et al. 1994, Stoner et al. 1995, Hiscott et al. 2001), with associated changes in freshwater input to the region (Hillaire-Marcel & Bilodeau 2000), which have been shown to influence deep convection as well as the extent and strength of the subpolar gyre (McManus et al. 2004).

The advanced piston coring (APC) technique was used to provide high quality sediment cores from at least three holes at each site (The “U” in the site names indicates that they are “united” holes). The APC is a hydraulically actuated piston corer, able to recover continuous 9.5 m long core samples with minimal disturbance. Once lowered into position, the inner core barrel strokes into the sediment within 2 – 3 s under ~12,000 kg of force (Graber et al. 2002). The “drillover” strategy was used to extend the depth limit where the core barrel would otherwise become stuck in firm sediments; by advancing the rotary bit, the core barrel could be freed (Channell et al. 2006). The cores were then stratigraphically correlated using shipboard multi-sensor track information to produce a single metres composite depth (mcd) scale for each location, that would account for any gaps or shrinkage that would otherwise accumulate down the core (Shipboard Scientific Party 2005).

Bioturbation can be a problem within marine sediment cores. The sea floor typically has many species of burrowing benthic creatures living within it, and the mixing of sediments that would originally have been in discrete layers is known as bioturbation. This has the effect of averaging out any climate signals, and may affect the perceived absolute time and rapidity of onset of climatic changes (Lövemark et al. 2016). However, examination of the sediments upon collection reported that bioturbation was minimal in both U1305 and U1302 (Channell et al. 2006).

### 4.1.1 | Eirik Ridge

Eirik Ridge is a sediment drift extending to the south west of the southern tip of Greenland (Figure 4.1). It is composed of material deposited from Denmark Straits Overflow Water (DSOW) and the Deep Western Boundary Current (DWBC), as they retroflect around the southern tip of Greenland into the Labrador Sea (Arthur et al. 1989), with some contribution from ice rafting and hemipelagic deposition (Chough and Hesse 1985). This location makes U1305 sensitive to fluctuations in rates of ice calved from east Greenland and swept into the region by the EGC.

At site U1305

(57°29' N, 48°32' W, water depth 3459 m) three holes were drilled 20 – 30 m apart using the APC system down to 287.1 mbsf. Material from holes A and B were used in this study. A total of 211

samples from U1305B (23.03 – 25.93 mcd) and U1305A (25.56 – 33.16 mcd) were used, with a slight overlap between holes where samples alternate on the mcd scale. Each sample was prepared from a slice of mud 2 cm thick, and samples were taken every 5 cm along the core. Average sedimentation rate on the age model produced for

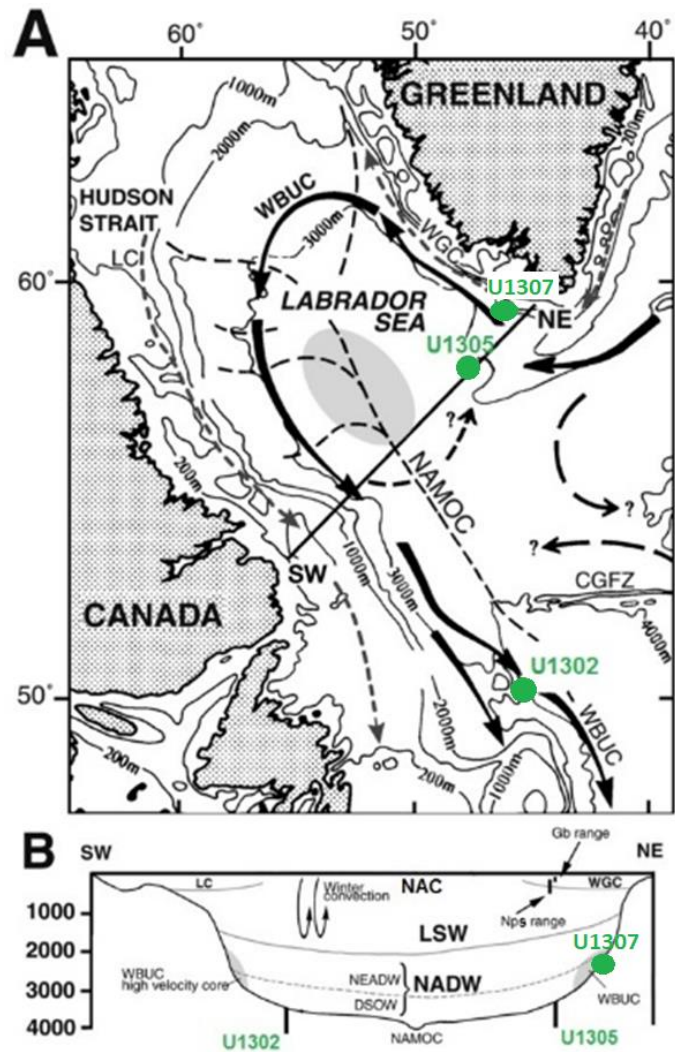


**Figure 4.2 |** (A) Core locations of U1302 and U1305 used in this study, and core U1307 discussed in the text, including the deep western boundary under current (DWBC; black arrows), and surface west Greenland current (WGC) and Labrador Current (LC) (dashed arrows). Grey shading indicates region of deep convection. Bathymetric features include the Charlie-Gibbs Fracture Zone (CGFZ) and Northwest Atlantic Mid-Ocean Channel (NAMOC). (B) Transect across the Labrador Sea (northeast to southwest line in (A)) including depth habitats of planktonic foraminifera species *G. bulloides* (Gb) and *N. pachyderma* (*s*) (Nps). Also shown is the North Atlantic Current (NAC), Labrador Sea Water (LSW), North Atlantic Deep Water (NADW) composed of North East Atlantic Deep Water (NEADW) and Denmark Straits Overflow Water (DSOW) (Adapted from Hillaire-Marcel and Bilodeau 2000).

this study (section 7.4.3) was 38.0 cm/ka, resulting in a resolution of ~280 years. Details of all holes relevant to this study are given in Table 4.1. Sediments at U1305 were dominantly silty clays designated as a single unit containing variable mixtures of gradationally interbedded terrigenous (mostly clay minerals, quartz and detrital carbonate) and biogenic (nannofossil) components, with calcium carbonate varying between 1 – 49 % (Channell et al. 2006). Coretop samples were available for U1305 (but not U1302), which enabled comparison with present day faunal assemblage counts and Mg/Ca temperature estimates.

Sedimentation rate on Eirik Ridge is variable. In U1305 it tends to be low during glacial periods and high during interglacials. There may be two factors behind this observation. One explanation is that sedimentation rate reflects changes in the strength and location of the high-speed core of the DWBC, which tends to cause sediment resuspension (Hillaire-Marcel et al. 1994; Hillaire-Marcel et al. 2011). This is clearly seen when comparing mean sedimentation rates in U1305 (17.5 cm/ka) to the shallower core U1307 (4.8 cm/ka) (Figure 4.2), which presently lies within the scouring influence of the DWBC (Kawamura et al. 2012). Material from the sediment-laden DWBC settles out further offshore down the slope in areas of much lower current speed, around the location of U1305. Piston cores previously taken from the Eirik Ridge also showed sedimentation rate to be strongly determined by proximity to the DWBC (Hillaire-Marcel et al. 1994; Stoner et al. 1998), with expanded glacial periods (> 10 cm/ka) in the shallower HU90-013-012, when the DWBC migrates downslope, but expanded interglacial periods in the deeper HU90-013-013 (> 30 cm/ka during the Holocene), with the DWBC closer to its present-day position (Hillaire-Marcel et al. 1994, Stoner 1998, Hillaire-Marcel & Bilodeau 2000). A second factor may be related to the observation that the main sediment load of the DWBC is supplied by DSOW, which is the main water mass overlying U1305 (Figure 4.2 (B)). Therefore, a high interglacial sedimentation rate in U1305 may reflect either a more vigorous DWBC lying further up-slope from U1305 (Hillaire-Marcel et al. 2001; Channell et al. 2012), or more active production of sediment-rich DSOW (Hunter et al. 2007). Another interpretation is that instead of moving deeper and lying over U1305 during glacial periods, the DWBC shoaled (due to lower salinity), taking its sediment load even further away from U1305 (Channell et al. 2014), though the studies cited above agree that the DWBC slowed or reduced transport during glacial periods. Highly variable sedimentation rates resulting from the age model produced for this study are discussed further in section 7.4.3.

Other important studies based around Eirik Ridge include ODP Leg 105 Site 646, from 82.2 km to the north of U1305, for which planktonic  $\delta^{18}\text{O}$  records have been published (Aksu et al. 1989, Cremer 1989, Arthur et al. 1989) as well as clay-fraction Sm/Nd ratios which indicated fine particle supply to the Labrador Sea from the North American Shield was highly dependent on input from glacial erosion (Fagel and Hillaire-Marcel 2006). Although often considered beyond the influence of the North Atlantic Mid-Ocean Channel (NAMOC) (Figure 4.2), Hiscott et al. (1989) presented sedimentary evidence from Site 646 of

periodic (~100 ka) overspill from NAMOC turbidites, though they also suggest the material may have shed from the Greenland margin. Stoner et al. (1995, 1996, 1998) used piston cores HU90-013-013P (3380 m) and HU90-013-012P (2830 m), amongst others from Eirik Ridge and Orphan Knoll, to distinguish between rapidly-deposited “detrital carbonate” (DC) and “low detrital carbonate” (LDC) layers within the Labrador Sea. A later study by Evans et al. (2007) using four

different piston cores from the Eirik Ridge (JPC15, JPC18, JPC 19 and MD99-2227) observed that DC layers

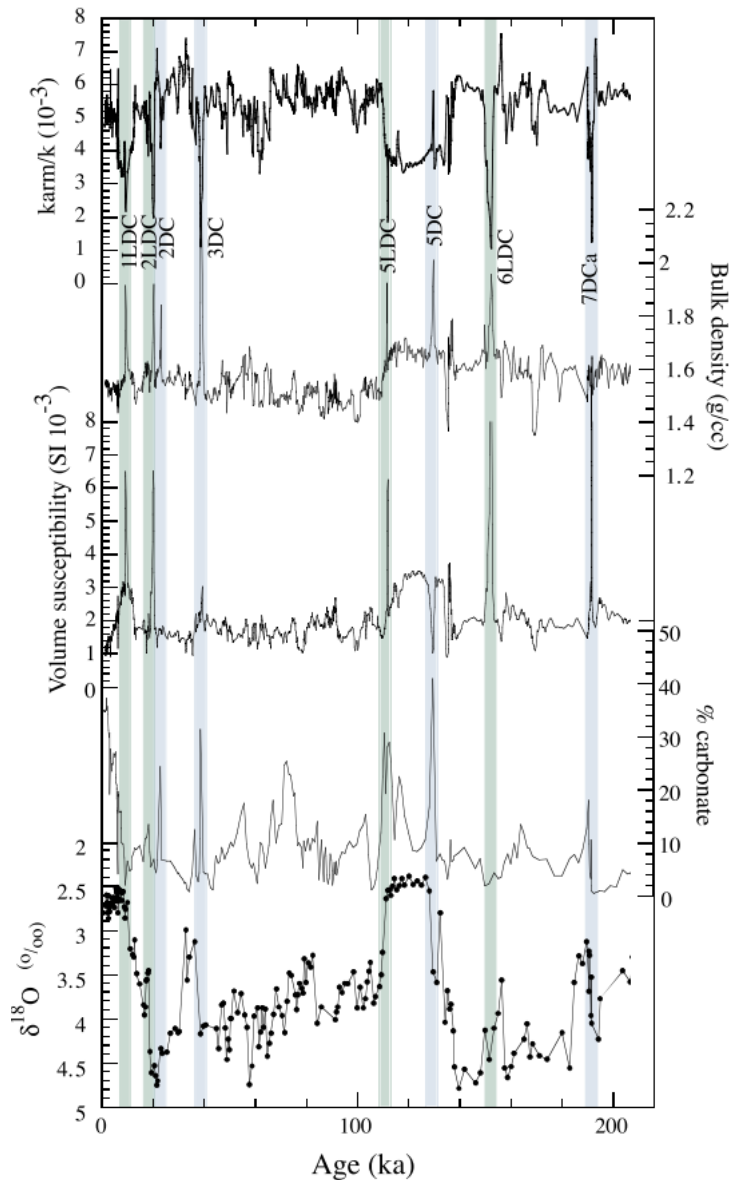


**Figure 4.3** | Evidence from magnetic susceptibility, bulk density (Turon et al. 1999), carbonate content and planktonic oxygen isotopes within Core MD99-2227 of two different types of detrital layers in the Labrador Sea: Detrital carbonate layers (DC; blue shading) and low detrital carbonate layers (LDC; green shading). LDC layers appear associated with melting ~150 ka and during the glacial inception ~110 ka, whilst late during Termination II, a DC layer likely represents H11 ~130 ka. Modified from Evans et al. (2007).

contained abundant IRD. LDC layers did not contain an increase in percentage carbonate, but did feature peaks in bulk (gamma ray attenuation) density and magnetic susceptibility, and lows in a proxy for magnetite grain size ( $k_{arm}/k$ ). These centimetre-scale layers have sharp bases and bioturbated tops, and show some indication of laminae suggestive of rapid deposition from turbidity currents, attributed by the authors to the Greenland slope (Figure 4.3). In a study based upon 25 box and piston cores from 13 locations across the Labrador Sea, Hillaire-Marcel et al. (1994) used stable isotopes to infer the presence of a single homogenous water mass lacking NADW components during glacial periods, and to distinguish between events of fine detrital carbonate deposition (linked to turbidity currents along the NAMOC) and Heinrich events (due to rapid ice calving). Sr-Nd-Pb isotopes from Eirik Ridge core MD99-2227 were used to infer greater retreat of the southern Greenland ice sheet (Colville et al. 2011) especially through the early last interglacial (Hatfield et al. 2016), though combined  $\delta^{18}O$  and Mg/Ca temperatures from the same core did not indicate greater warmth than Holocene conditions (Winsor et al. 2012). Hunter et al. (2007) used modern hydrographic data to investigate the DWBC around Eirik Ridge and observed not only the current's impact upon sedimentation rates discussed above, but changes in the location, structure and water mass ventilation of the DWBC. Faunal assemblages and Mg/Ca-based palaeothermometry from MD95-2664 were used to infer early peak last interglacial warmth interrupted by a sudden cooling event  $\sim 126$  ka (Irvali et al. 2012), rapid changes in deep water  $\delta^{13}C$  indicating unstable NADW production during the last interglacial (Galaasen et al. 2014), and changes associated with last glacial inception beginning earlier during the last half of the last interglacial (Irvali et al. 2016).

**Table 4.1** | Summary of Expedition 303 operations for cores relevant to this study (Channell et al. 2006). Note that information is also provided for holes U1302A and U1305C, which were not used in the present study but are pertinent to the discussion of the red layer discussed below in section 4.3.

Hole	Latitude	Longitude	Water depth (mbsl)	Number of Cores	Interval cored (m)	Core recovered (m)	Recovery (%)
U1302A	50°9.985'N	45°38.271'W	3568.6	13	107.1	91.7	85.6
U1302B	50°9.995'N	45°38.290'W	3563.4	11	104.7	102.8	98.2
U1302C	50°10.007'N	45°38.309'W	3559.2	11	104.5	97.1	92.9
U1305A	57°28.507'N	48°31.842'W	3463.0	30	280.0	294.6	105.2
U1305B	57°28.507'N	48°31.813'W	3459.2	28	264.8	274.3	103.6
U1305C	57°28.509'N	48°31.783'W	3458.8	31	287.1	298.2	103.9

The majority of papers published containing data from U1305 itself were based upon palaeomagnetic studies (Mazaud et al. 2009; Mazaud et al. 2012; Channell et al. 2012; Stoner et al. 2013; Channell 2017a; Channell 2017b; Channell 2017c), and some investigated diagenesis (Kawamura 2010; Kawamura et al. 2012). Planktonic  $\delta^{18}\text{O}$  and  $\delta^{13}\text{C}$  records have been published for U1305 and U1302 that extended through the Pleistocene by Hillaire-Marcel et al. (2011), which indicated that present day circulation with LSW production is unusual, being confined to interglacial periods, and not even present during all interglacials (Hillaire-Marcel et al. 2011). The study of Hillaire-Marcel et al. (2011) also identified similar  $\delta^{18}\text{O}$  values during MIS 5e between *G. bulloides*, *N. pachyderma (s)* and benthic foraminifera (*C. wuellerstorfi*) in core U1305 (and within nearby HU90-013-013P (Hillaire-Marcel et al. 2001)), suggesting homogenised water masses from the surface to sea floor, but very different values within the same species from U1302, which is more akin to Holocene gradients.

#### 4.1.2 | Orphan Knoll

Orphan Knoll is a topographic rise that sits 2 km above the abyssal plain in the southwestern Labrador Sea, 650 km from Newfoundland, eastern Canada (Figure 4.3). It is underlain by an elevated horst of continental crust that detached from the continent of North America during rifting (Tripsanas and Piper 2008). Site U1302 on the south east flank of Orphan Knoll lies beneath the Labrador Current which carries fresh polar waters and icebergs south from the LIS via the Hudson Strait (Channell et al. 2006). This location is sheltered by the presence of Orphan Knoll from sedimentation rate changes associated with high speed deep currents (Figure 4.4) (Hillaire-Marcel et al. 2011), although on the new age model of this study, sedimentation rates increased during H11 due to massive IRD input (section 7.4.3).

At site U1302 (~50°10' N, 45°38' W, water depth ~3560 m, mean sedimentation rate 15.6 cm/ka) five holes were drilled with the APC system, offset by 30 m from each other (Channell et al. 2006). Holes B and C were used in this, comprising a total of 81 samples from U1302C (19.57 – 22.12 mcd) and U1302B (22.15 – 23.60 mcd). Each sample was prepared from a slice of mud 2 cm thick, and samples were taken every 5 cm along the core. Average sedimentation rate on the age model presented in this study (detailed in Chapter 7) was 20.9 cm/ka, resulting in a resolution of ~125 years. Drilling

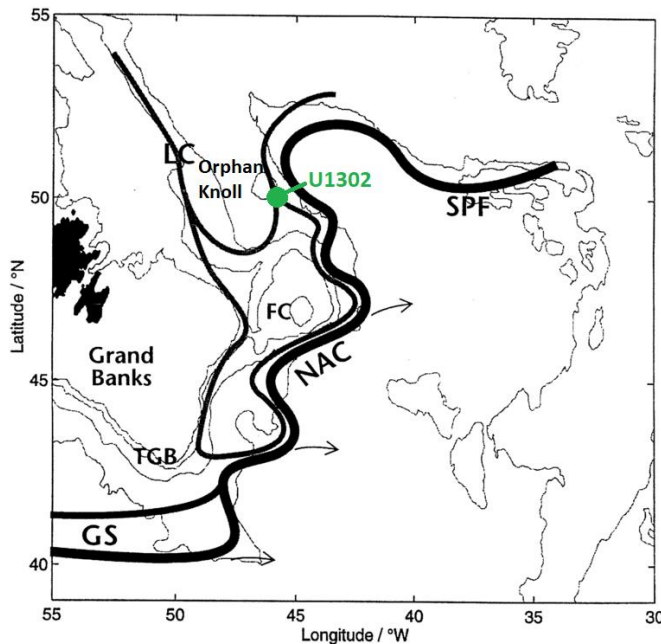


**Figure 4.4** | Schematic showing surface current flow of the North Atlantic Current (NAC; thick line) and Labrador Current (LC; thin lines) past the Flemish Cap (FC) near to Orphan Knoll. The location of U1302 is noted in green. The subpolar front (SPF) lies within the NAC between fresher colder waters to the north and warmer, saline subtropical waters to the south. Arrows indicate water loss from the NAC, bathymetry shows 200, 1000, 2000 and 4000 m isobaths, GS = Gulf Stream, TGB = Tail of the Grand Banks) (Modified after Rossby 1999).

stopped at ~106 mcd after a coarse-grained debris flow was encountered, and moved to nearby site U1303, 5.68 km away. However, the same debris flow was also discovered at U1303, which limited the depth of drilling. Sediments from the last interglacial were found to be between around 19 and 24 mcd, so U1302 proved to be perfectly adequate for purposes of this study. Details of all holes relevant to this study are given in Table 4.1 above.

Sediments at U1302 were also largely silty clays composed of terrigenous and biogenic material designated as a single unit, with calcium carbonate varying between 1 – 47 %, though at this location dropstones (large chunks of rock transported by ice) were found through the entire section (Channell et al. 2006). The single unit was subdivided into undisturbed sediments in subunit IA (0 - ~106 mcd), and the debris flow deposits which stopped drilling, subunit IB (106 – 132 mcd), composed of intraclasts within a sand-silt-clay matrix (Channell et al. 2006).

Orphan Knoll, and the nearby Orphan Basin, have also been sampled previously. Initially, box and piston cores HU91-045-093 and HU91-045-094 revealed low planktonic isotopes associated with detrital layers through the last glacial cycle, indicating the input of isotopically depleted meltwater and low productivity surface waters, and proposed that detrital layers were formed by two mechanisms: fine-grained “glacial flour” derived from turbidity currents along the NAMOC, and ice rafting (Hillaire-Marcel et al. 1994, Hillaire-Marcel & Bilodeau 2000). As discussed above, Stoner et al. (1995, 1996, 1998) also identified detrital carbonate (DC) and low detrital

carbonate (LDC) layers using these cores, attributed to these two different mechanisms. Subsequently, Stoner et al. (1998, 2000) used  $\delta^{18}\text{O}$  and relative palaeointensity geomagnetic records from nearby sediment core MD95-2024 to correlate detrital layers with cold stadials using cosmogenic isotope flux in the GRIP/GISP2 ice core record (Grootes et al. 1993). MD99-2237 was also taken from Orphan Knoll, but nothing has been published from it beyond the shipboard report (Turon et al. 1999). Several piston cores from the Orphan Basin to the south west contained debris-flow wedges, some associated with MIS 6 (Hiscott and Aksu 1996), and MD95-2025 contained IRD layers associated with rapidly decreasing  $\delta^{18}\text{O}$  values, some containing abundant detrital carbonate but some carbonate-poor, stretching back over 340 ka (Hiscott 2001). Two further cores, EW9302-1JPC (1251 m depth) and EW9302-2JPC (2527 m depth) were compared with cores from the Norwegian Sea by Rasmussen et al. (2003) to determine that periods of intense ice rafting were associated with rapid ocean circulation changes. They inferred the presence of a poorly ventilated, nutrient-rich but relatively warm intermediate-depth water mass in the south east Labrador Sea during Heinrich events, followed by rapid resumption of intermediate-depth ventilation (potentially LSW formation) from benthic  $\delta^{13}\text{C}$  values. Rasmussen et al. (2003) also observed conspicuous diatom layers deposited during the last part of TII, a red layer of clay  $^{14}\text{C}$ -dated to the last glacial maximum (21.2 ka), as well as depleted  $\delta^{18}\text{O}$  values associated with IRD deposition during MIS 5. These three features are important to the present study, and will be discussed in sections 4.4, 4.3 and 6.3 respectively.

Fewer studies have been published based on U1302. As discussed above, the isotopic study of Hillaire-Marcel et al (2011) identified depleted  $\delta^{18}\text{O}$  excursions during Heinrich events. Crocket et al. (2012) showed that reduced chemical weathering intensity (deduced from Pb isotopes within FeMn oxyhydroxide phases within U1302/3) corresponded with isotopically enriched surface water  $\delta^{18}\text{O}$  during glacial maximum periods, whilst the most radiogenic values were associated with depleted interglacial  $\delta^{18}\text{O}$  values. Extreme radiogenic excursions during Heinrich events were associated with very high detrital inputs during the collapse of the LIS (Crocket et al. 2012). U1302 has also been used for palaeomagnetic studies (Channell and Hodell 2013; Channell 2017c). Analysis confirms the presence of Heinrich-like detrital layers (analogous to DC layers of Stoner et al. (1995)), and those associated with lofted sediment from debris flow events along the NAMOC (Channell et al. 2012).

### 4.1.3 | Sediment Core Processing

Sediment cores were recovered using the APC technique for U1302 and U1305, as described above. Each 9.5 m core was divided into manageable 1.5 m sections and then split lengthways, one half was archived and the other designated as the “working” half. Each core was uniquely identified using the leg (303) site (1302 or 1305) hole (A, B or C) and core (e.g. 2H) system, and split into seven sections. Each section was analysed using various non-invasive shipboard techniques such as magnetic susceptibility, gamma ray attenuation density measurements and chromatic photography which reveals changes in sediment colour (Channell et al. 2006). Cores were then chilled until processing.

Samples used for this study were prepared at GEOTOP, Université du Québec à Montréal for the stable isotope study conducted by Hillaire-Marcel et al. (2011). Sediment samples were weighed, disaggregated in distilled water on an orbital shaker, wet sieved (106 µm mesh) to separate fine sediment from the coarse size fraction, then dried at 40 – 50°C, weighed using an accurate balance, and finally placed in labelled containers. For the analyses conducted in this study, the coarse fraction of each sample was sieved according to the desired size fraction, scattered onto a clean tray, then examined under a binocular microscope, and manipulated using a fine brush dipped in clean Milli-Q water to avoid contamination (some assemblage slides were later “scavenged” for geochemical analysis). Detailed methods are given in each relevant results section.

## 4.2 | ICE RAFTED DEBRIS

### 4.2.1 | Method

IRD and foraminiferal assemblage counts were performed at the same time. To remove fine material, each sample was dry sieved at 150 µm. This size fraction was used (in preference to 63 µm) as it would contain only coarse grains unlikely to have been reworked (McManus et al. 1996), and only adult foraminifera (smaller juveniles are difficult to identify unambiguously). This coarse fraction was then sprinkled through a splitter which randomly divided the material into two equal portions, one of which was

split again, and so on. The process was repeated until around 300 individual foraminifera remained, which represents a balance between precision and efficiency (Lipps et al. 1979). The coarse fraction was then scattered on a labelled 64-cell slide. IRD grains were counted and separated into categories. Quartz and feldspar (clear or cloudy) were counted separately from red (haematite) stained grains. This red colour indicates an origin from sedimentary “red beds”, likely from Newfoundland or the Canadian Archipelago, though east Greenland could also be a source for U1305 (Figure 4.5). Volcanic material (glass shards, vesicular glass) would most likely be from Iceland or Jan Mayen (Figure 4.5) (Bond et al. 1997). Dark volcanics are likely to be basalt from igneous provinces common around the northwest European margin (Knutz et al. 2001, 2007). For U1302, far less volcanic glass was found, so vesicular glass was included with volcanic glass. Carbonate is discussed below.

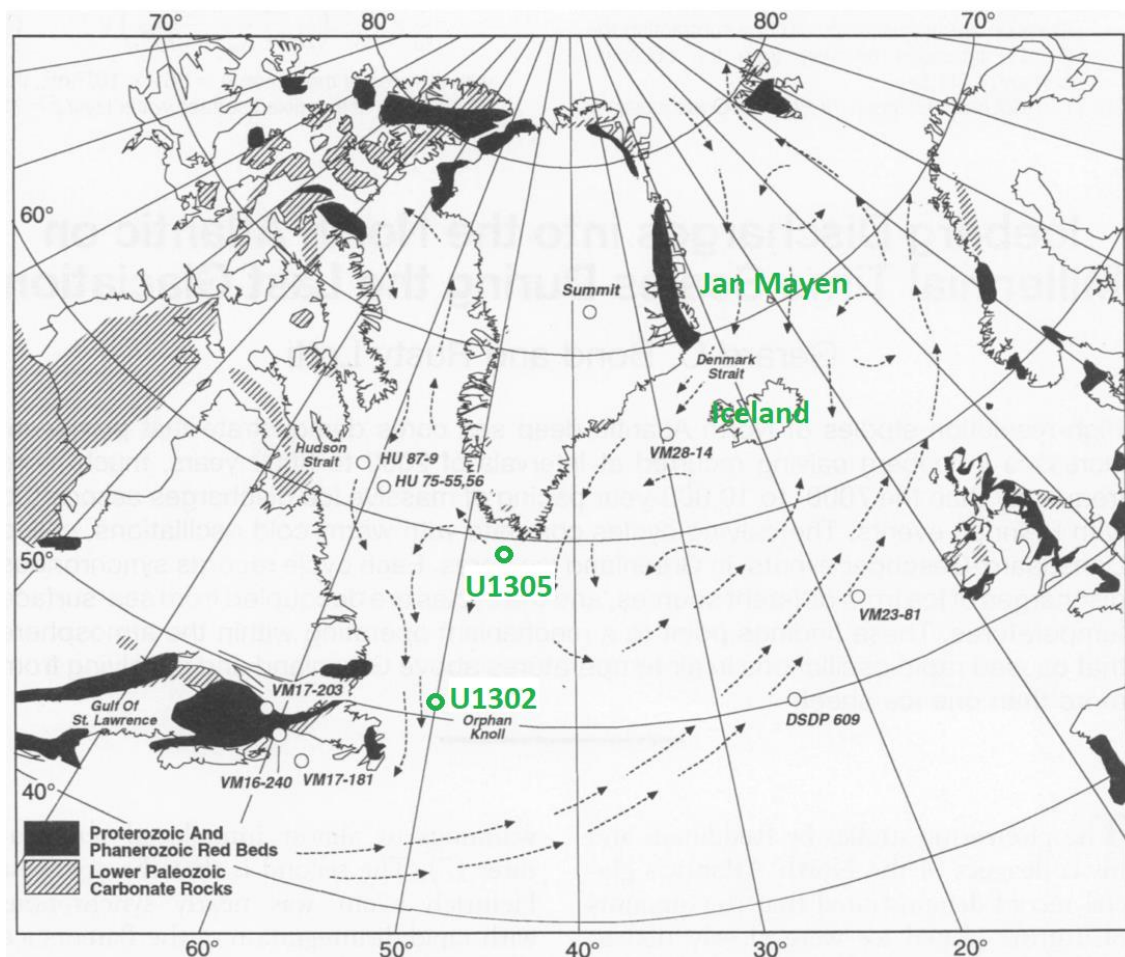


**Figure 4.5** | Map showing potential bedrock sources of ice rafted debris including carbonate via Hudson Strait, red-stained material from beds in Newfoundland, east Greenland or the Canadian Archipelago via Davis Strait, and volcanic material from Iceland or Jan Mayen. Arrows show modern ocean circulation, locations of U1302 and U1305 are also noted. (Adapted from Bond and Lotti 1995).

Planktonic foraminifera were identified by species (details in Chapter 5). Other non-IRD categories include unprocessed mud lumps, siliceous material (diatoms, sponge spicules), mica (a very thin, transparent mineral that can be transported by ocean currents rather than ice), ferro-manganese particles (which form authigenically within the sediment) (Novikov and Murdmaa 2007), benthic organisms (foraminifers, ostracods, burrow casts, agglutinated shells), and foraminifera fragments (broken tests which were too small to be identified at species level).

There are several ways to quantify IRD counts. Some studies use lithic weight percent, either of total dry sample weight or of the coarse fraction, but single large dropstones (some can be several cm) in layers otherwise low in IRD can greatly skew results (Grobe 1987). Therefore, this study uses two methods to present IRD results, firstly as an IRD percentage, i.e. the percentage of lithic grains as a proportion of total entities present (Heinrich 1988). In practice, whatever is not mineral is usually planktonic foraminifera, which can lead to apparent influxes of IRD which are due to a drop in foraminifera abundance instead. Therefore as a second measure, IRD is also presented as a concentration, i.e. number of lithic grains per gram of dry sediment. Sample weights were kindly provided by Claude Hillaire-Marcel (personal communication).

## 4.2.2 | A Question of Carbonate

During IRD counts, fine-grained off-white material was classified as detrital carbonate. However, on later examination it was suspected that carbonate had been mis-identified, and upon inspection such grains were found to be incompletely processed fine-grained mud (usually of a red/brown or grey/green colour) which was incompletely disaggregated during processing. It was easy to crush such grains with a thin wire, and they sometimes incorporated lithic grains or foraminifera shells, which clearly pointed to their origin. As these mud lumps sometimes made up a significant proportion of all IRD grains, it was found to have impacted IRD counts in U1305, particularly during H11. As such, “carbonate” values were removed from the IRD data in order to provide a more accurate result. Figure 4.6 shows that omitting the questionable carbonate values from U1305 does reduce the magnitude of certain peaks, particularly ~28.7 mcd and during the early part of the last interglacial (29 – 32 mcd), but does not change the shape of the data overall, with one major exception. The depth of the last heavy IRD input of

H11 marking Termination II had previously been located by a peak of 75% at 31.41 mcd. Without the spurious carbonate data the last significant input of 15% IRD has moved to 31.76 mcd, and drops to zero thereafter. This brings the IRD as a percentage in line with the IRD concentration (grains per gram) (Figure 4.6) lending support to this measure being justified and leading to an improvement in overall accuracy. Omitting the spurious “carbonate” category makes little observable difference to U1302 (Figure 4.7).

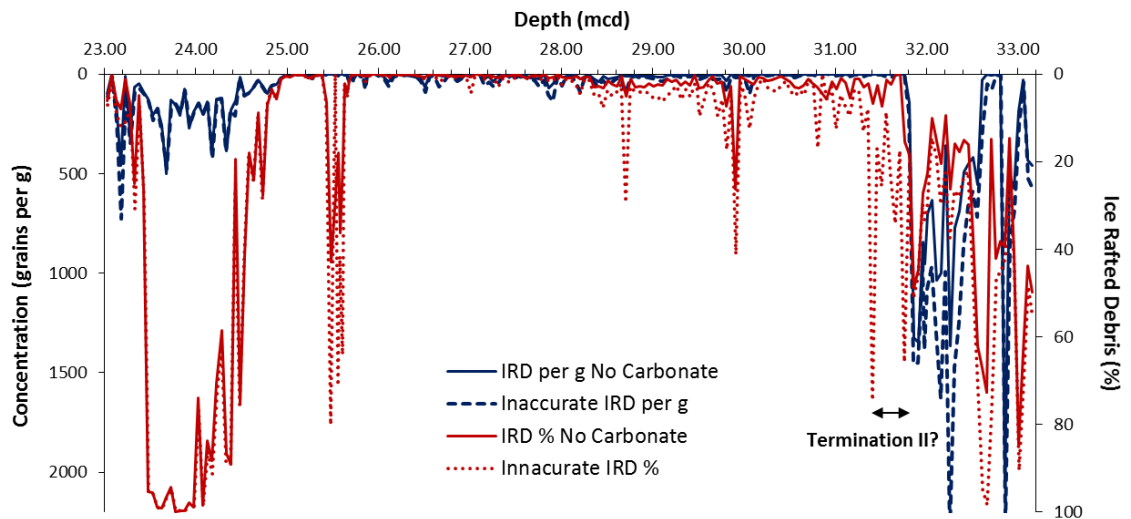


**Figure 4.6** | U1305 IRD percentage abundance (red) and concentration (blue) including spurious carbonate (dashed lines) and omitting spurious carbonate (solid lines). Double-headed arrow indicates the change in position of the last IRD input of Termination II, which brings percentage abundance in line with IRD concentration.

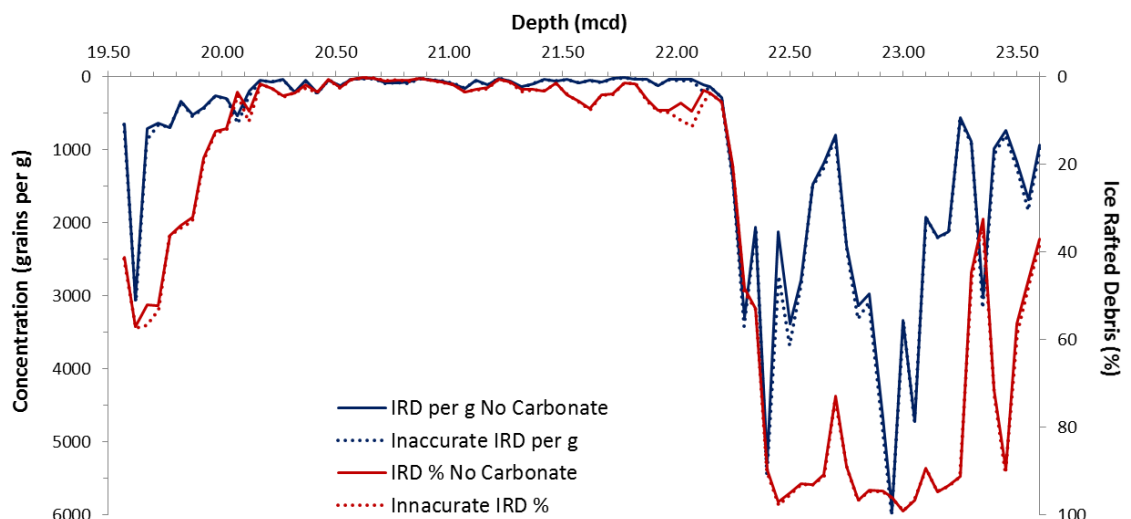


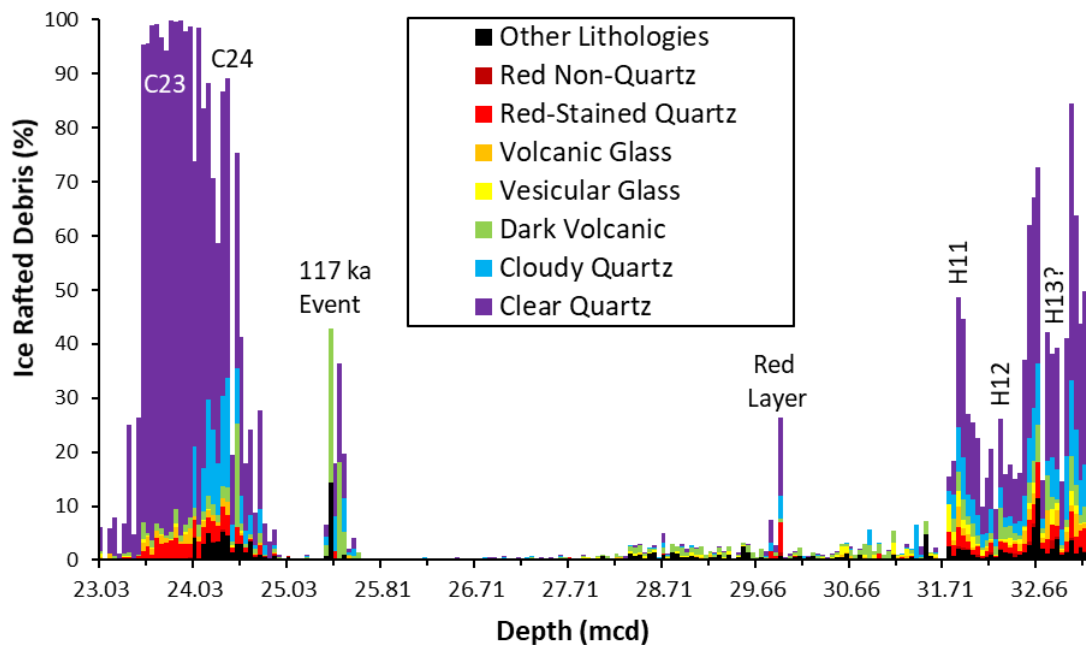
**Figure 4.7** | U1302 IRD percentage abundance (red) and concentration (blue) including spurious carbonate (dashed lines) and omitting spurious carbonate (solid lines). Omitting spurious carbonate data does not significantly alter the results.

This begs the question of the missing carbonate. Heinrich events have long been defined based on an increase in detrital carbonate, and due to their proximity to Hudson Strait, it could be expected that up to 25 % of IRD would be carbonate (Bond et al. 1992). It might be considered that U1305 lies upstream from the major Laurentide iceberg source in Hudson Strait (Figure 4.2), however detrital carbonate (DC) layers have been observed within sediment from Eirik Ridge previously (Stoner et al. 1995, 1996, 1998, Evans et al. 2007). Additionally, this would not explain the lack of carbonate grains in U1302. Although this finding may be due in part to inadequate lithic identification skills, not all IRD layers have been found to contain detrital carbonate (Stoner et al. 1995, 1996, 1998). Although Evans et al. (2007) described a detrital carbonate layer associated with Termination II ~130 ka, their study did not include IRD counts, instead relying on magnetic data to infer grain size. Hodell et al. (2008) examined site U1308 within the North Atlantic IRD belt and despite identifying carbonate layers using bulk Ca/Sr associated with H1, H2, H4 and H5, and during previous glacial periods, they did not find carbonate was associated with Heinrich events during MIS 6 (including H11) (Figure 8.7). They proposed instead that these non-Hudson Strait Heinrich events potentially contained more silicate minerals derived from Greenland or European ice sheets (Grousset et al. 1993; Gwiazda et al. 1996). Another explanation is that the missing carbonate resides within the fine fraction. In type IV Heinrich Layers (those found near Orphan Knoll and Eirik Ridge), over 80 % of the detrital carbonate was found in fine fractions (<63 µm) due to transport of carbonate “glacial flour” by intermittent turbidity overspill, in addition to the ice rafted component (Hesse and Khodabakhsh 2017). Future carbonate analysis of the fine fraction could confirm this. So, given that H11 is well-defined in the results using mainly quartz and volcanics, it was decided to leave the less robust “carbonate” category out of the IRD results presented below.

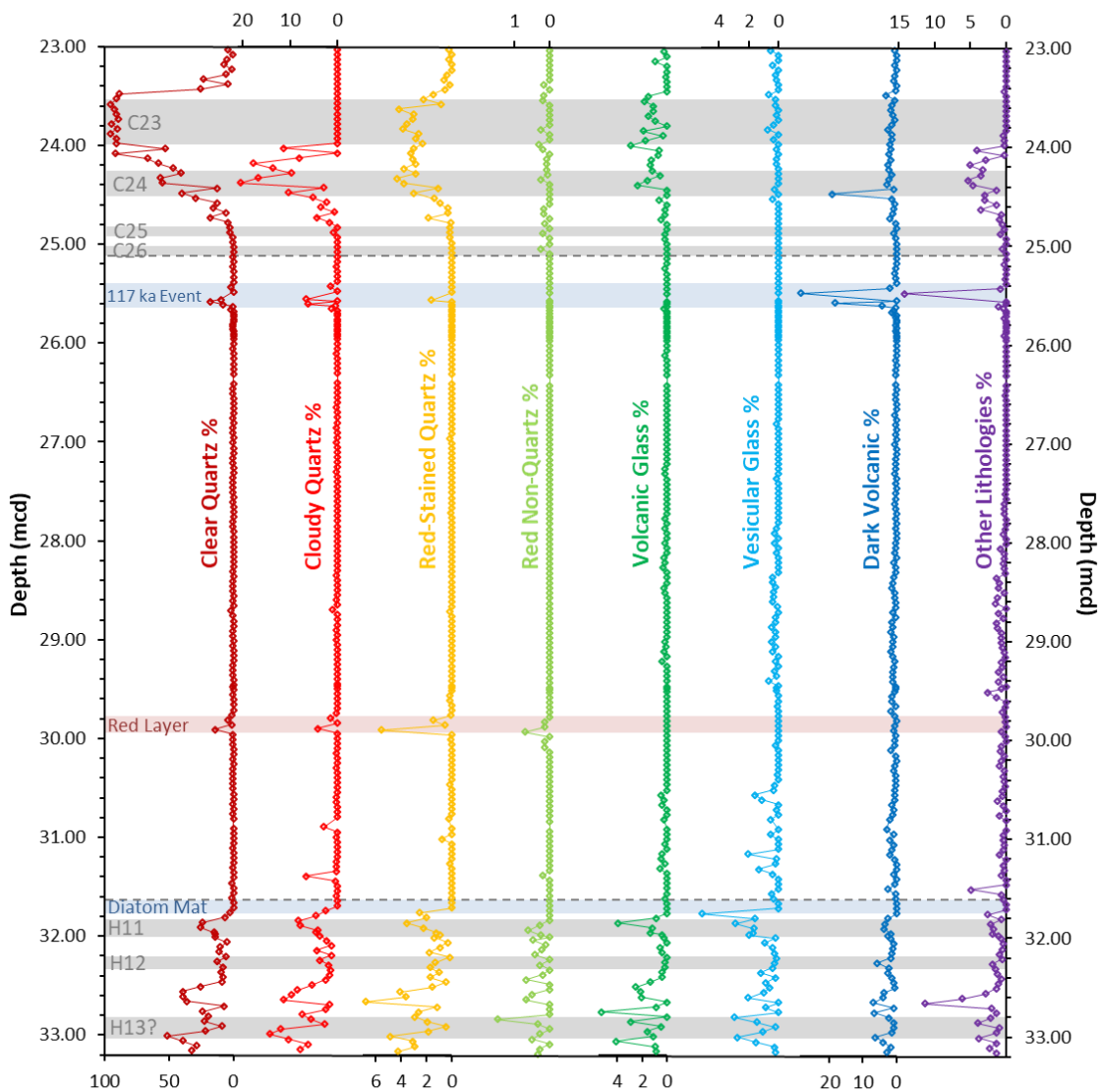
### 4.2.3 | Ice Rafted Debris Count U1305 Results

The graphs in this chapter indicate climate events discussed in the text – Heinrich events (H13 – H11) during the penultimate glacial period, the diatom mat (section 4.4), red layer (Nicholl et al. 2012) and 117 ka event (Irvali et al. 2016), and North Atlantic cold events (C26 – C23) during the glacial inception. Figure 4.8 shows an overview of

the IRD percentage results from U1305 in the form of a stacked bar graph, indicating what proportion of the IRD present is composed of each lithology. High but variable IRD input is noted through MIS 6 (33.16 – 31.66 mcd), with three distinct peaks at 33.01, 32.61 and 31.86 mcd. The dramatic reduction in IRD through the last interglacial is evident between 31.61 – 25.13 mcd (average 2.4 %) (white area in Figure 4.8). Two main periods of ice rafting within MIS 5e are seen centred around 29.91 mcd (associated with the red layer, discussed in section 4.3) and 24.58 – 24.48 mcd (associated with a cooling event ~117 ka, discussed in section 8.3.4). A ramping up of IRD input is then observed during the last glacial inception, which would appear to be much more pronounced than during TII. However, between 23.98 – 23.48 mcd, foraminiferal count is very low (< 50 individuals), making this appear as though a large influx of IRD had occurred, when in fact this IRD dominance is due to the scarcity of foraminifera. There is a clear dominance of quartz (clear and cloudy) over all other lithologies. During high IRD intervals, the proportions of red (haematite) stained material (from Newfoundland, east Greenland and the Canadian Archipelago) increased alongside volcanic material (from the Iceland ice sheet) suggestive of a regional input of ice rafted material, not just from Hudson Strait (see Figure 4.5) (Fronval 1995). Individual percentage abundances are presented in Figure 4.9.



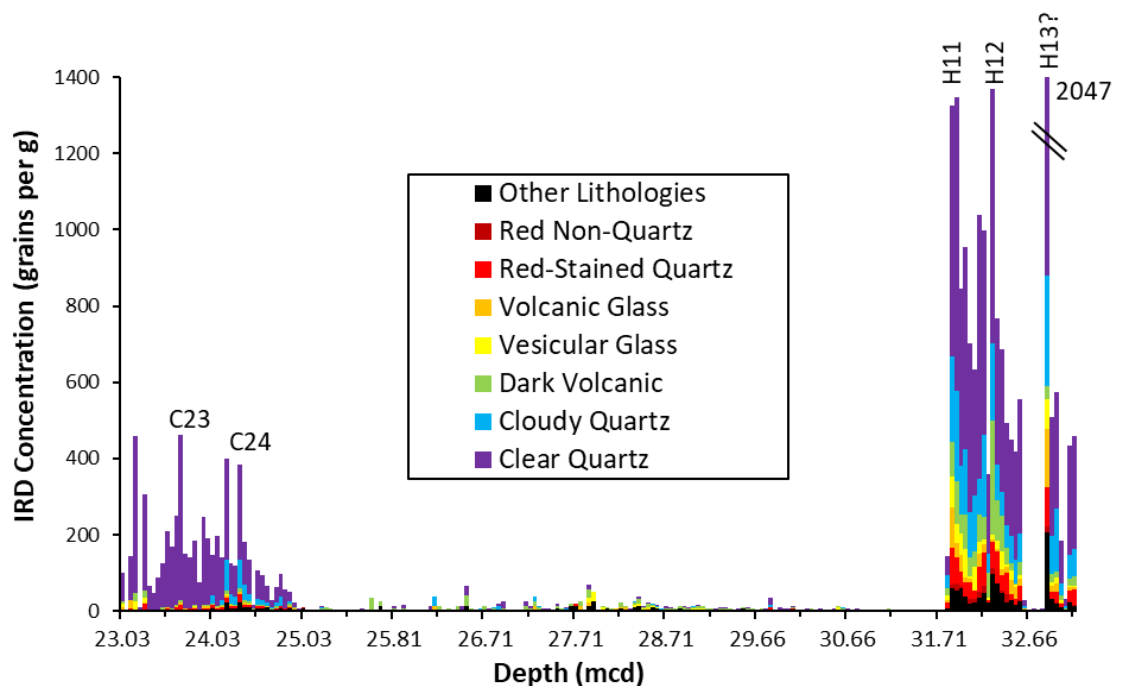
**Figure 4.8** | U1305 IRD percentage composition by lithology. Peaks below 31.71 mcd are related to Heinrich events H11, H12 and potentially H13. IRD peaks during MIS 5e (31.61 – 25.13 mcd) are associated with the red layer and 117 ka event. Increased IRD above 25.03 mcd is associated with C24 and C23.



**Figure 4.9** | U1305 IRD percentage abundance for individual lithologies. Horizontal dashed grey lines indicate the start and end of the last interglacial period (31.61 – 25.13 mcd). Grey shaded areas indicate Heinrich events (H13 – H11) during the penultimate glacial period, and North Atlantic cold events (C26 – C23) during the glacial inception, blue shaded areas indicate the diatom mat and 117 ka event, red shaded area indicates red layer.

Figure 4.9 shows U1305 IRD percentage abundance of each lithology. Clear quartz dominates the IRD composition, being responsible for 50 – 100 % of all IRD through the heavy ice rafting periods associated with TII (below 32.00 mcd) and the MIS 5d inception (above 25 mcd). Cloudy quartz is similar, though during the glacial inception it only increases significantly through 24.48 – 24.03 mcd, being virtually absent through the latter part of this interval. Red stained quartz appears prominent at 32.66, 29.91 and 25.56 mcd, and consistently above 25 mcd, but does not exceed 6.8 %. Although other red material does not exceed 1.5 %, it is of note that the increase at 29.91 %, coincident

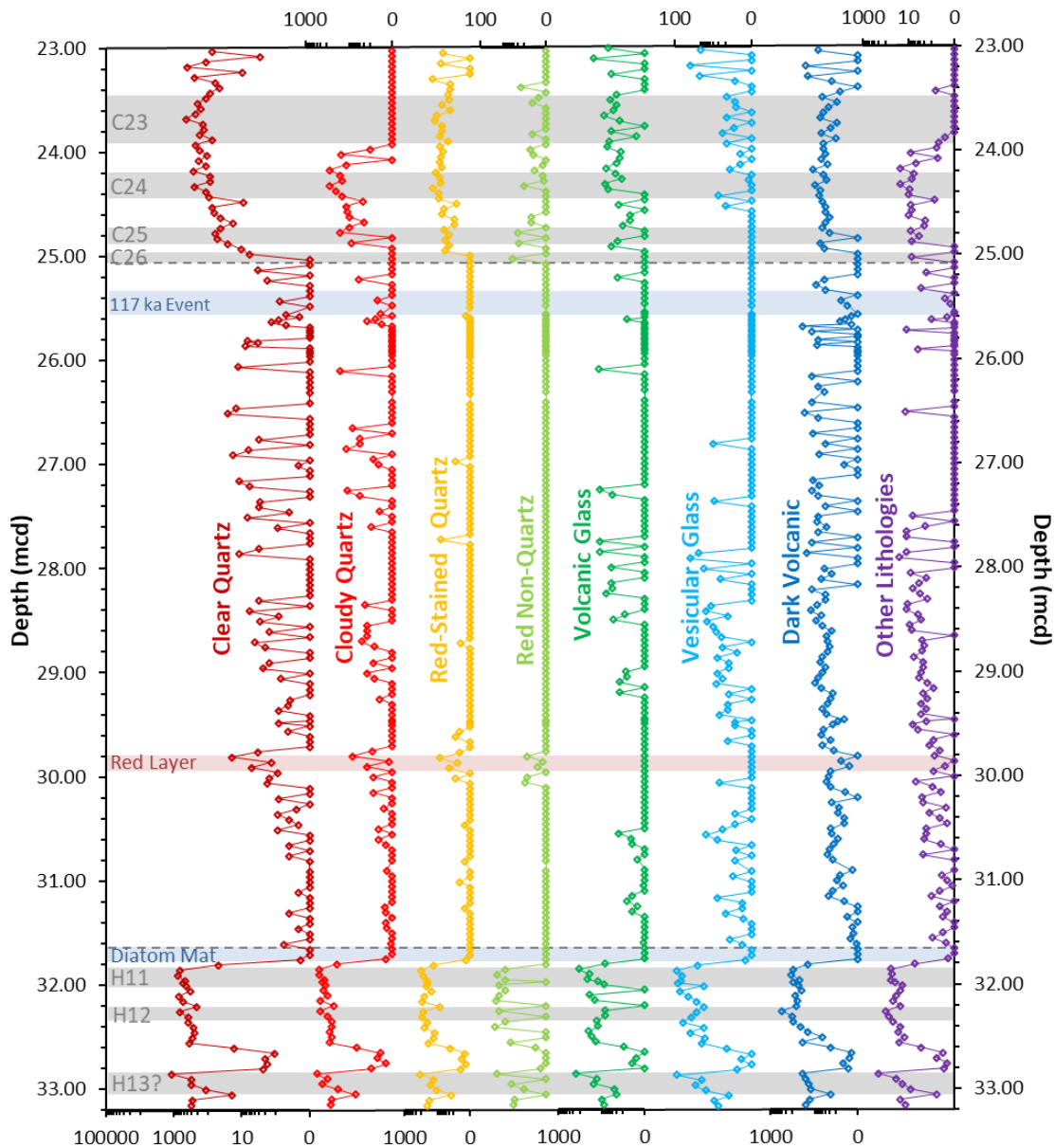
with the increase in red-stained quartz, corresponds with the red clay layer (see section 4.3). Volcanic and vesicular material increase during major inputs of other lithologies, and therefore likely represent material derived from Iceland and Greenland via the EGC, rather than discrete ash layers. Large increases in dark volcanics 25.48 and 24.48 mcd are unusual in light of the lack of this material through H11, but accompany increases in other lithologies generally through these periods, perhaps indicating a contribution from a broad range of sources. To address the shortcomings of artefacts in percentage data due to reductions in foraminiferal abundance, the data is also presented below as a concentration, i.e. number of grains per gram of total dry sediment.



**Figure 4.10** | U1305 IRD composition by lithology as a concentration (number of grains per g). Peaks associated with H11 and H12 are indicated. Double bar at 32.86 mcd indicates a column break due to a single peak of extremely high concentration (2047 grains per g), proposed in this study as a possible H13 event. No intra-interglacial peaks are evident, but C24 and C23 during MIS 5d-c are apparent.

Viewing abundance of lithologies as a proportion of concentration (Figure 4.10) shows that the highest concentration of IRD was in fact found at 32.86 mcd (2047 grains per g), far higher than values associated with H12 (1368 grains per g) and H11 (1348 grains per g). This peak is proposed as a potential ice rafting event, H13, discussed further in section 8.2.1. This is followed by an unusually IRD barren interval 32.81 – 32.61 mcd, comparable to interglacial values (average 8.8 grains per g). This period is also very low in foraminifera indicating that the bulk of material through this layer was composed of

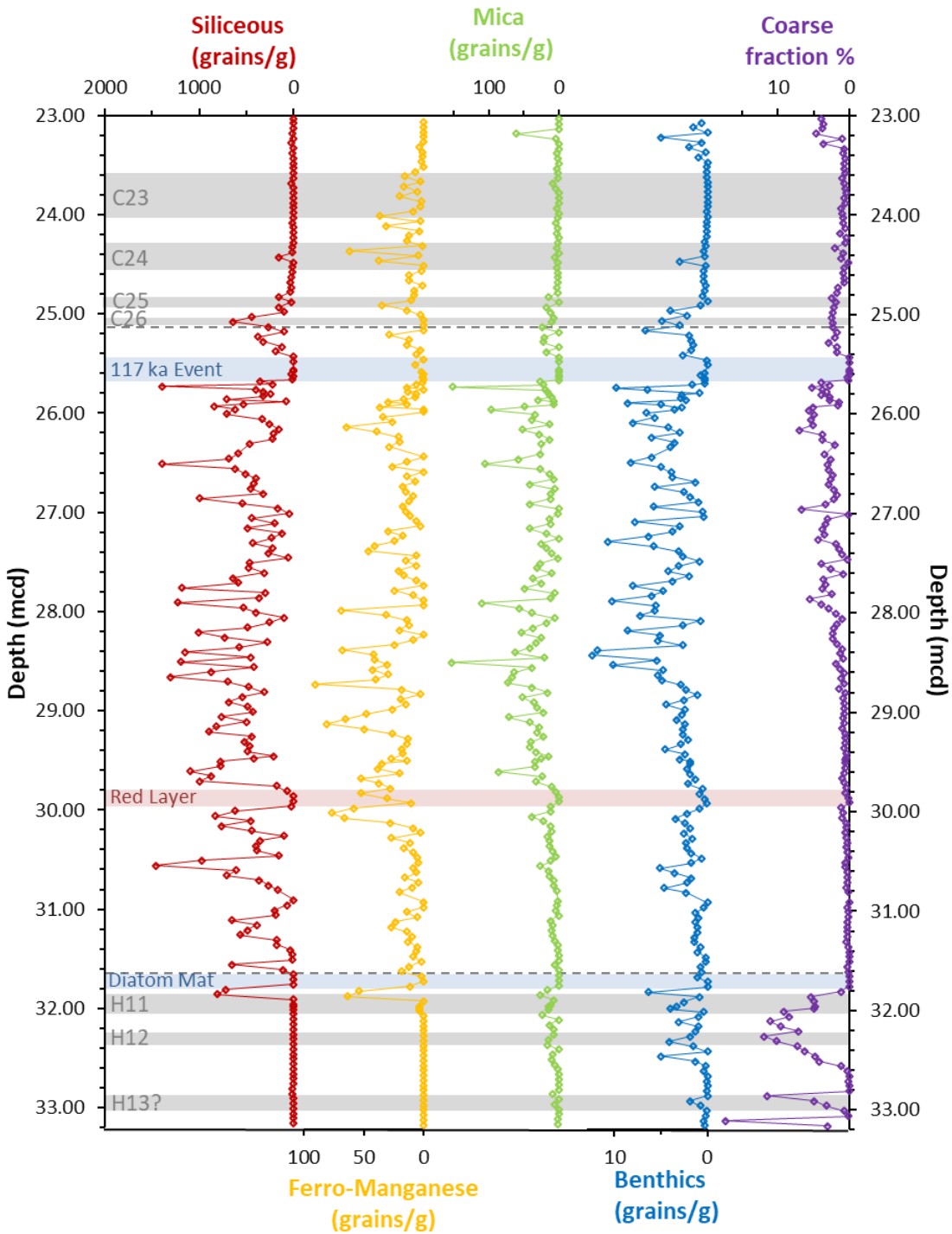
very fine material. Temperature reconstructions estimate warm SSTs through this interval, which is discussed in section 8.2.2. The mid-MIS 5e peaks observed in IRD as a percentage do not stand out in concentration data. Far from being more dominant than H11, Figure 4.10 clearly show that ice rafting during the glacial inception was in fact modest in comparison. In order to bring out detail through the interglacial period itself, this concentration data was plotted on a log scale in Figure 4.11.



**Figure 4.11** | U1305 IRD concentration (grains per g) of individual lithologies, presented on a log scale. Horizontal dashed grey lines indicate the start and end of the last interglacial period (31.61 – 25.13 mcd). Grey shaded areas indicate Heinrich events 11, 12 and 13 during the penultimate glacial period, and North Atlantic cold events (C26 – C23) during the glacial inception, blue shaded areas indicate the diatom mat and 117 ka event, red shaded area indicates red layer.

Figure 4.11 shows high levels of IRD throughout MIS 6, whilst the reduction in all lithologies 32.81 – 32.61 mcd clearly shows the impact of this apparent warm phase. The drop in IRD concentration early during the last interglacial is clearly evident. Clear and cloudy quartz continue to be found steadily through MIS 5e, whilst some red-stained material is associated mainly with the red layer as noted above, with minor increases 27.71 and 26.96 mcd. Quantities of all of these lithologies increase into MIS 5d. Volcanic material and other lithologies are generally higher through the first half of MIS 5e compared with the last half, and also show an increase through MIS 5d, though dark volcanic material continues to be found throughout MIS 5e, showing little change into MIS 5d.

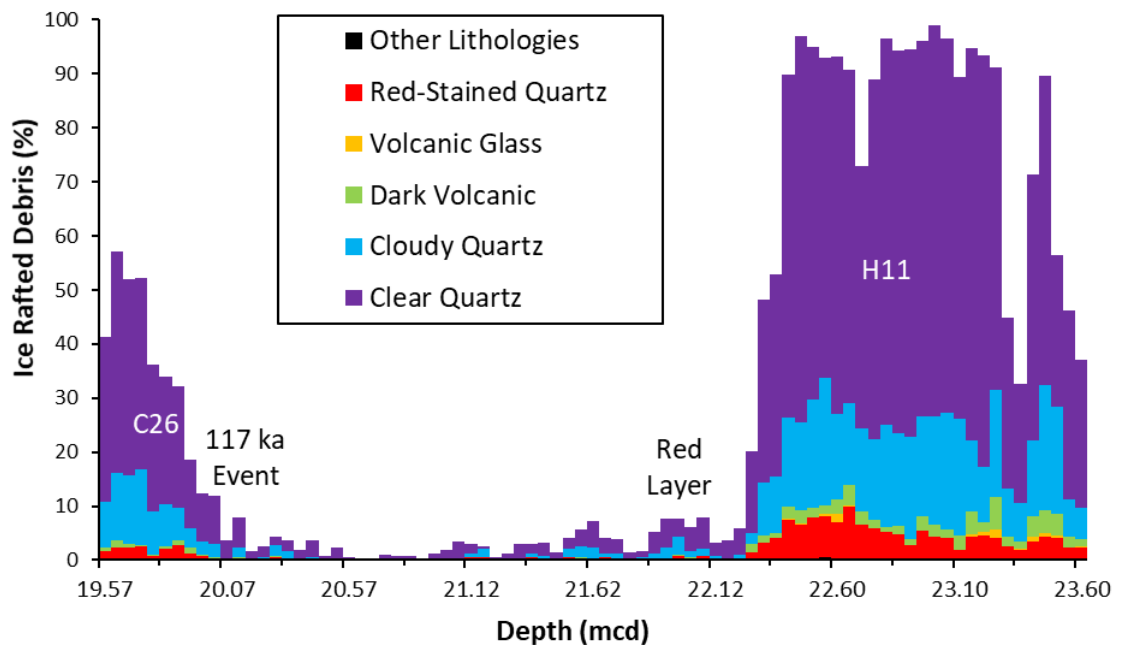
Figure 4.12 shows other categories identified during IRD counts but not classed as ice rafted debris, all are broadly more abundant during the interglacial period. Siliceous material and ferro-manganese grains show similar patterns, with negligible quantities through most of MIS 6, a peak during TII (31.86 – 31.81 mcd), then high but variable values throughout MIS 5e, though siliceous material is virtually absent through MIS 5d, whilst ferro-manganese particles continue to be found. Mica is hardly evident during either MIS 6 or MIS 5d, and doesn't become abundant until the latter part of the last interglacial. Benthic organisms are surprisingly abundant through the latter part of MIS 6, after which their abundance largely mirrors the coarse fraction, with higher values through the last half of MIS 5e, a slight decrease 25.61 – 25.43 mcd, followed by slightly increased values over the beginning of the glacial inception, before reducing to a minimum during MIS 5d. The coarse fraction is comprised mostly of IRD and foraminifera, and therefore shows an IRD-type signal with three peaks through MIS 6, and a foraminifera-type signal through MIS 5e of low values through the first half, but much greater abundance through the second half. Coarse fraction doesn't show much increase during the MIS 5d inception, despite the dominance of IRD as a percentage through this period. This may be because foraminiferal abundance is fairly low through the MIS 5d inception (discussed in Chapter 5).



**Figure 4.12** | U1305 non-IRD categories as a concentration (number per gram of dry sediment), except coarse fraction, which is the weight percent of the > 106  $\mu\text{m}$  size fraction (out of total sample dry weight). Horizontal dashed grey lines indicate the start and end of the last interglacial period (31.61 – 25.13 mcd). Grey shaded areas indicate Heinrich events 11, 12 and 13 during the penultimate glacial period, and North Atlantic cold events (C26 – C23) during the glacial inception, blue shaded areas indicate the diatom mat and 117 ka event, red shaded area indicates red layer.

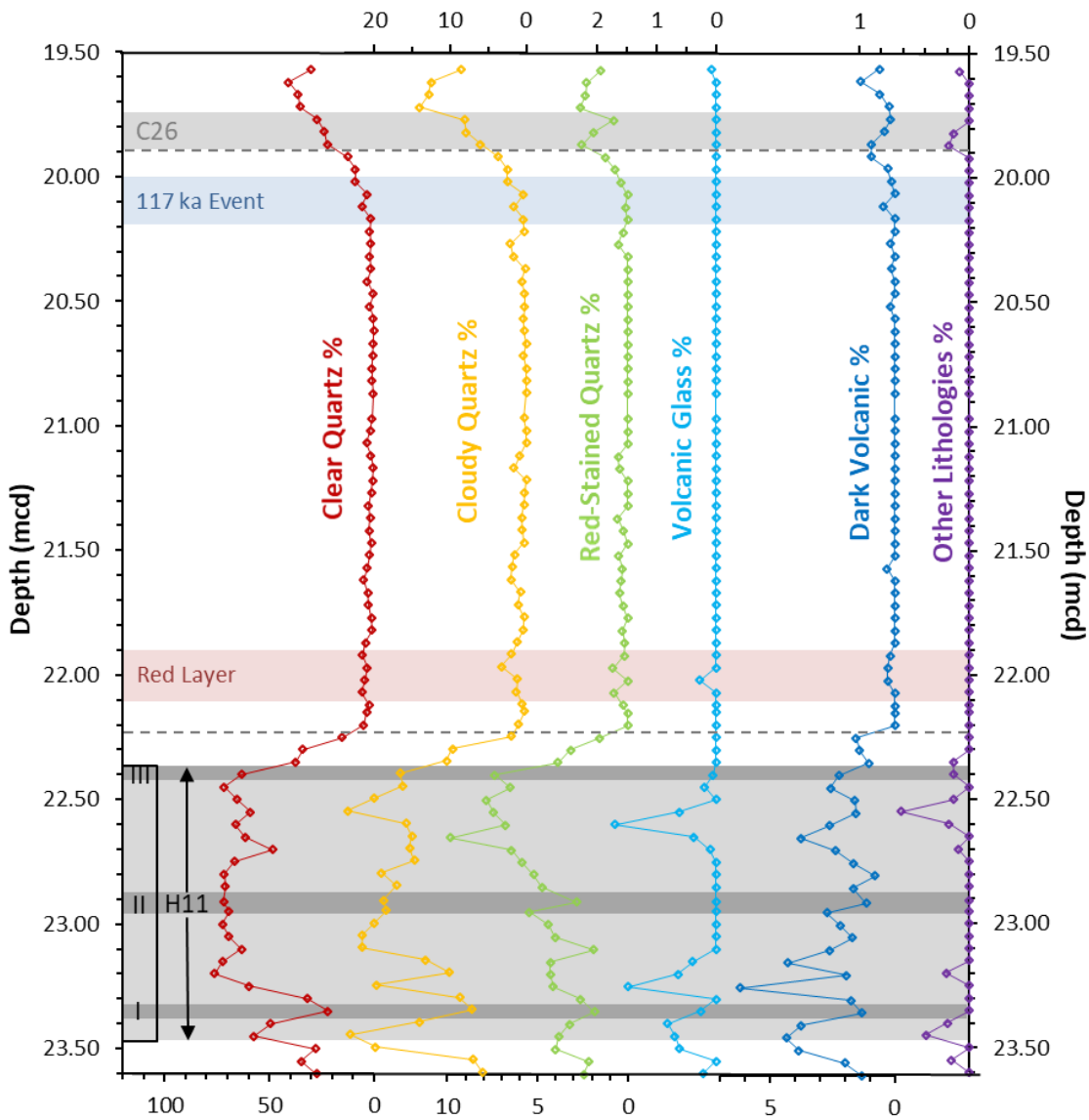
## 4.2.4 | Ice Rafted Debris Count U1302 Results

Figure 4.13 shows percentage abundances for IRD types in sediment core U1302, as stacked bars. Total IRD % approaches 100 % through nearly a metre of core representing TII (below 22.30 mcd). There is some suggestion of three major periods of IRD deposition within TII, centred around 23.45, 23.00 and 22.50 mcd. IRD then reduces to <10 % through MIS 5e, with slightly more through the first half than the second half. IRD as a percentage steadily increases towards MIS 5d (above 20.07 mcd). Quartz (clear and cloudy) is clearly dominant, with a fair proportion of volcanic and red-stained material through MIS 6 and 5d, similar to U1305 results. Again, detailed percentages are presented below.



**Figure 4.13** | U1302 IRD percentage composition by lithology. H11 is strongly represented below 22.12 mcd, the red layer and 117 ka event are indicated, along with C26, the first North Atlantic cold event of the glacial inception.

Figure 4.14 shows that through TII (below 22.30 mcd) there is close mirroring between peaks and troughs in all lithologies, suggesting there was no one particular source of ice rafted material, with increases due to contributions from ice sheets all around the North Atlantic. As in U1305, clear quartz is by far the biggest contribution, remaining at around 75 % through most of TII. Between cloudy quartz contributions at a lower abundance (~20 %), and low but continual amounts of red-stained quartz (<10 %), these three types of quartz dominate the IRD. Volcanic glass input peaks around 23.25 and

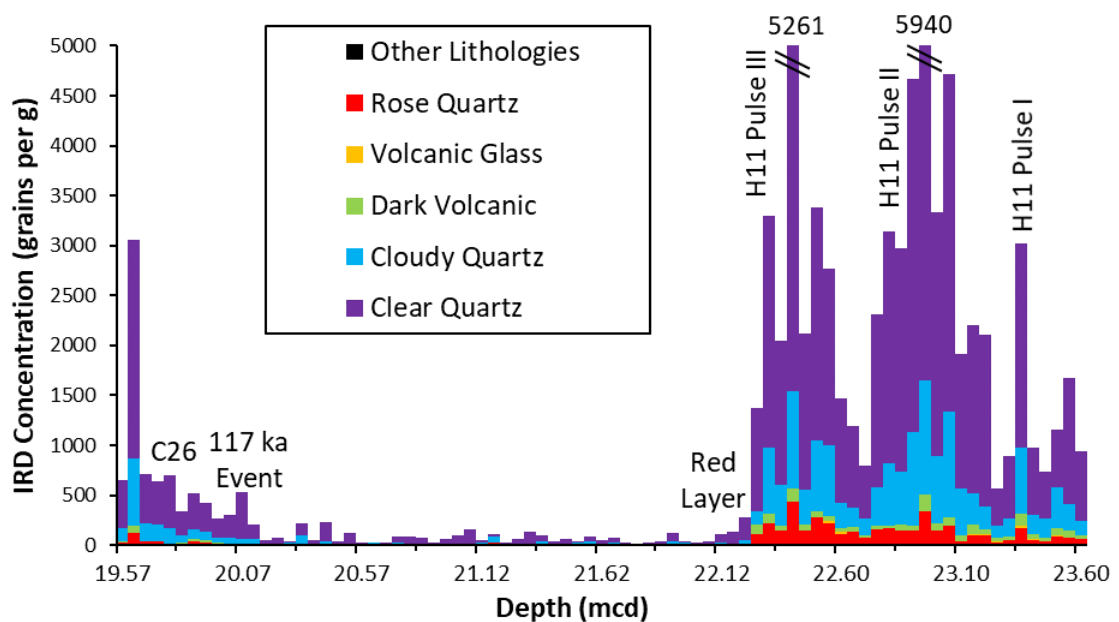


**Figure 4.14** | U1302 IRD percentage abundance for individual lithologies. Horizontal dashed grey lines indicate the start and end of the last interglacial period (22.20 – 19.92 mcd). H11 is indicated in light grey, with the three main pulses in IRD concentration at 23.35, 22.95 and 22.40 mcd indicated with dark grey shading labelled as I, II and III respectively. North Atlantic cold event C26 during the glacial inception is also indicated in grey. Red shading indicates the red layer, blue shading indicates the 117 ka event.

22.60 mcd are echoed in dark volcanics and other lithologies, but at < 2 %, ~6 % and <1 % respectively, these are likely not significant, probably related to general increasing in IRD rates in these layers. IRD input from all lithologies is very low throughout MIS 5e (typically < 5%), but begins increasing from before the MIS 5e/d boundary, starting around 20.07 mcd. Clear and cloudy quartz increase to a peak at 19.62 mcd. Red quartz increases, but decreases slightly at 19.77 mcd. Volcanic glass is not present above 22.02 mcd. Dark volcanics and other lithologies increase slightly towards the MIS 5e/d

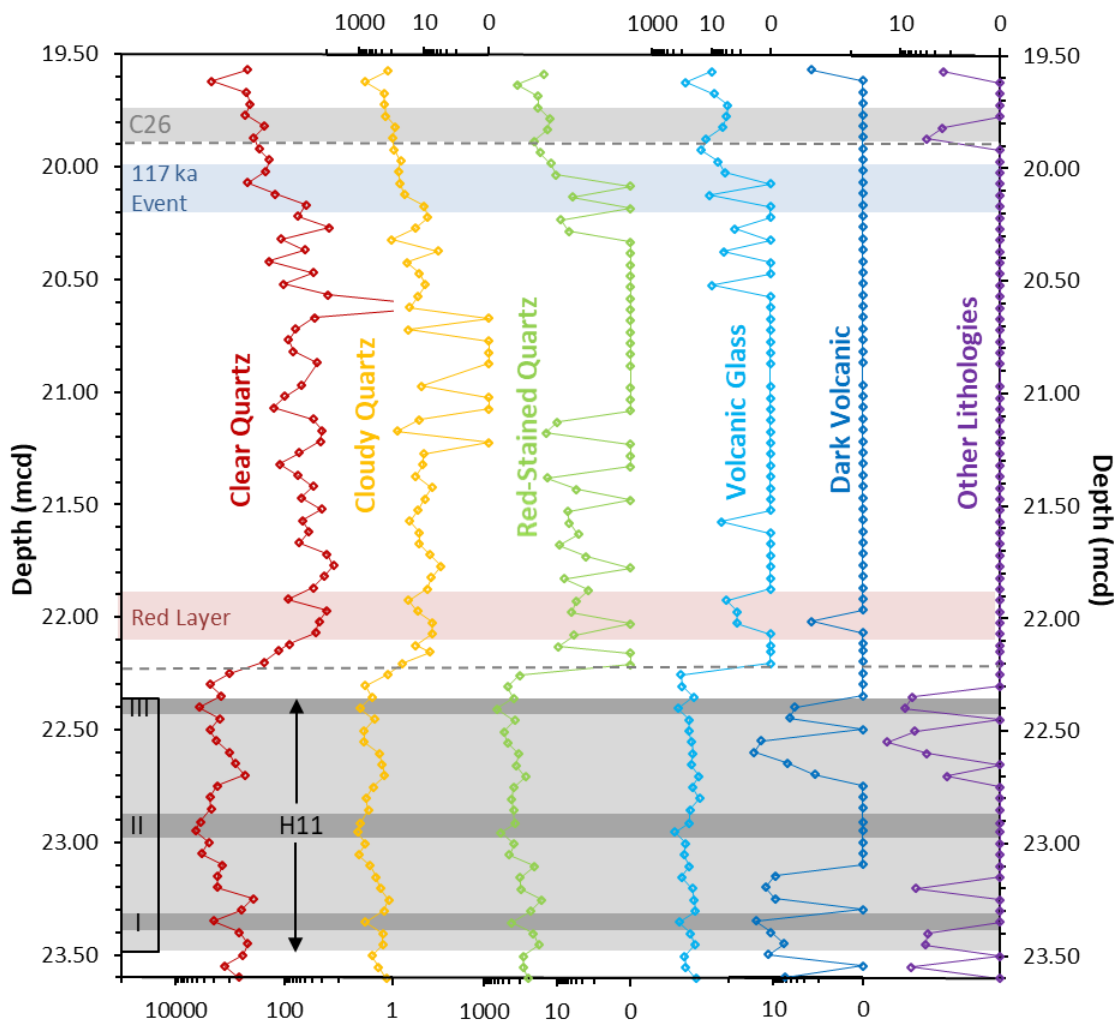
boundary, before decreasing again. Both records show slight increases towards the top of the record. Proportions of IRD as a concentration are presented below.

Figure 4.15 shows abundance of lithologies as a proportion of concentration. The large concentrations of IRD deposited at U1302 through TII are clearly evident, with major peaks at 23.35, 22.95 and 22.40 mcd. Proportions of all lithologies seem to increase during high IRD periods. After very low MIS 5e values, concentration also increases after 20.07 mcd, but not as pronounced as in percentage results (Figure 4.13). A peak in concentration (3056 grains per g) is seen towards the top of the record at 19.62 mcd. Figure 4.16 shows lithology concentrations on a log scale.



**Figure 4.15** | U1302 IRD composition by lithology as a concentration (number of grains per g). The three major pulses of IRD concentration are indicated. Double bars at 22.95 and 22.40 mcd indicate column breaks due to extremely high IRD concentrations (5940 and 5261 grains per g respectively). There is little evidence of the red layer, 117 ka event or C26 in IRD concentrations.

It is evident from Figure 4.16 that the IRD composition through TII is predominantly quartz (all three types) and dark volcanics. Periodic inputs of volcanic glass and other lithologies are seen between 23.60 – 23.15 mcd and again 22.70 – 22.35 mcd. A sharp reduction in all lithologies at the onset of MIS 5e is seen, after which regular varied inputs of clear and cloudy quartz persist throughout MIS 5e. Red-stained quartz is fairly regularly found through the first half of the last interglacial, but not at all between 21.07 – 20.32 mcd. Slight increases in volcanic glass and dark volcanics are seen at 22.02 mcd (associated with the red layer discussed below), with a second rise in volcanic glass



**Figure 4.16** | U1302 IRD concentration (grains per g) of individual lithologies, presented on a log scale. Horizontal dashed grey lines indicate the start and end of the last interglacial period (22.20 – 19.92 mcd). H11 is indicated in light grey, with the three main pulses in IRD concentration at 23.35, 22.95 and 22.40 mcd indicated with dark grey shading labelled I, II and III respectively. North Atlantic cold event C26 during the glacial inception is also indicated in grey. Red shading indicates the red layer, blue shading indicates the 117 ka event.

21.57 mcd, though these increases are small (<5 grains per g). Volcanic glass appears again above 20.52 mcd, red-stained quartz above 20.27 mcd, cloudy and clear quartz begin increasing above 20.27 mcd, and other lithologies above 19.87 mcd. Therefore, a gradual increase in almost all lithologies begins before the end of the last interglacial, though dark volcanics do not increase until the very top of the record.

Figure 4.17 shows other categories identified during IRD counts but not classed as ice rafted debris. Siliceous material is low during TII, with a peak at the onset of MIS 5e

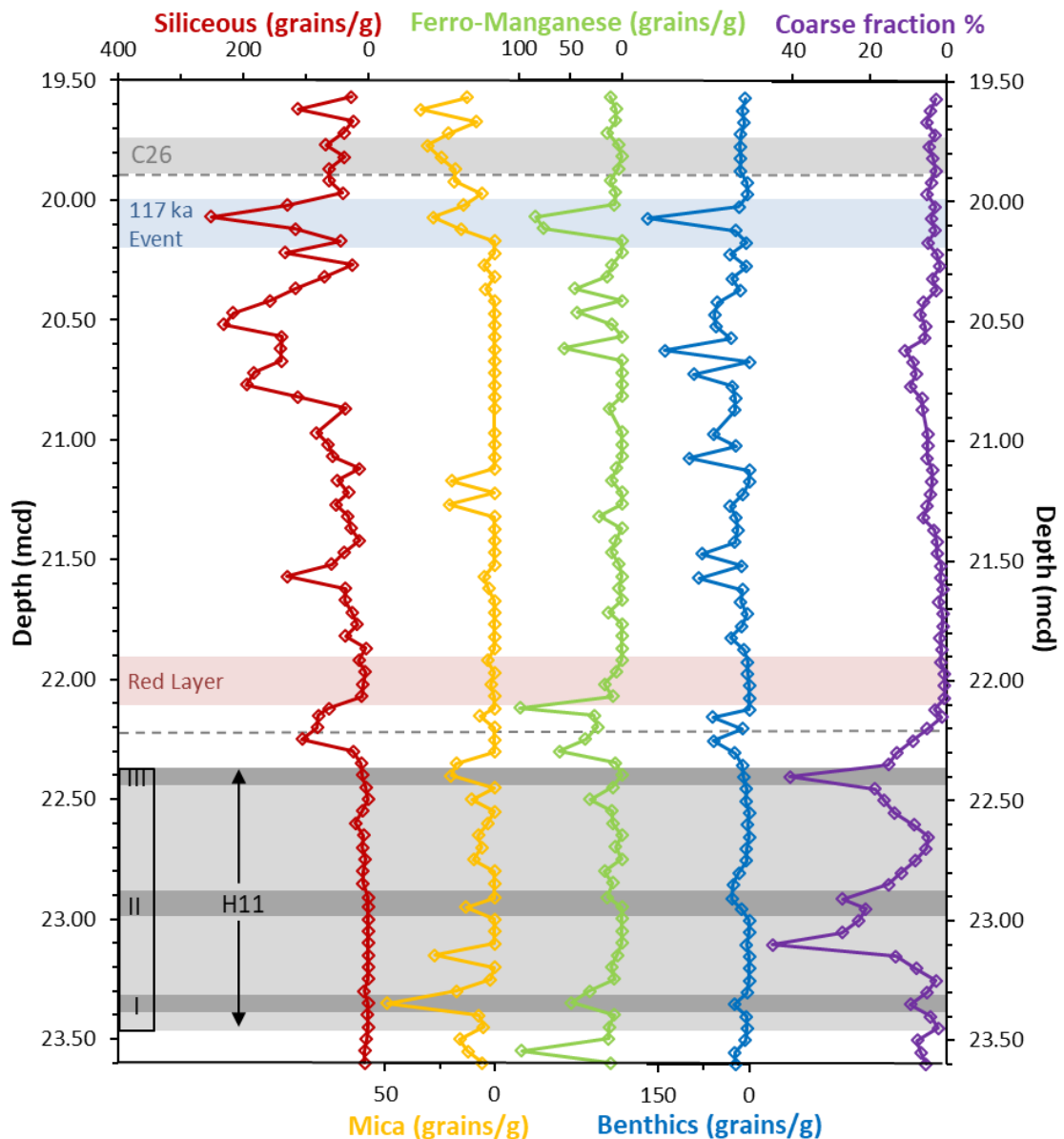


**Figure 4.17** | U1302 non-IRD categories as a concentration (number per gram of dry sediment), except coarse fraction, which is the weight percent of the > 106  $\mu\text{m}$  size fraction (out of total sample dry weight). Horizontal dashed grey lines indicate the start and end of the last interglacial period (22.20 – 19.92 mcd). H11 is indicated in light grey, with the three main pulses in IRD concentration at 23.35, 22.95 and 22.40 mcd indicated with dark grey shading labelled I, II and III respectively. North Atlantic cold event C26 during the glacial inception is also indicated in grey. Red shading indicates the red layer, blue shading indicates the 117 ka event.

and again at 21.57 mcd, before rising to much higher abundance in the last half of MIS 5e. A sharp reduction into 5d is seen. This is similar to U1305, with low glacial and high interglacial concentrations. Mica is found sporadically through TII, but is almost absent during MIS 5e, with the exception of 21.27 – 21.17 mcd, before increasing above 20.12 mcd. This is almost opposite to U1305, where mica was largely absent during glacial periods, but increased through MIS 5e. Similar to U1305, sporadic inputs of

ferro-manganese particles appear through glacial and interglacial alike, with particular peaks at 23.55, 22.12 and 20.07 mcd. Benthic organisms are largely absent during glacial periods, which was also observed in MIS 5d for U1305, though not through TII when they were fairly abundant. An increase in benthics is seen around the onset of MIS 5e, and as in U1305 they appear more regularly through the later part of MIS 5e, particularly at 22.07 mcd. This depth, 22.07 mcd, seems to show an increase in all categories, which may indicate it is an artefact of sample weight, but no anomalies are seen in the coarse fraction percentage at this point. The coarse fraction shows two distinct peaks at 23.10 and 22.40 mcd, likely due to ice rafting during H11.

### 4.3 | RED LAYER IN THE LABRADOR SEA

A paper by Nicholl et al. (2012) discussed a distinctive “red layer” found in both sediment cores U1302 and U1305 after the onset of MIS 5e. This layer was proposed to contain detrital sediment deposited by an outburst flood of a glacial meltwater lake formed by the LIS as it melted, in an event analogous to the Lake Agassiz drainage flood 8.4 ka (Clarke et al. 2004). Using biomarkers, Ca/Sr ratios and bulk carbonate  $\delta^{18}\text{O}$  values, Nicholl et al. (2012) determined that the origin of the red layer was material from the Palaeozoic bedrock in the Hudson Bay area (Figure 4.19). The red layer was ~10 cm thick in U1305 and ~20 cm thick in U1302, apparent as anomalously high values of the red-green colour parameter ( $a^*$ ) (Figure 4.18), and distinctly different to the usual grey sediment observed in the shipboard digital line-scan images (Figure 4.20). The layer had a sharp base at both core sites, indicating fast onset of deposition. The upper unit boundary was more diffuse, particularly in U1302, attributed to bioturbation (Figure 4.18). Nicholl et al. (2012) reported H11 was evident in both cores as a peak in IRD reaching nearly 100%, but the red layer was deposited 40 cm above H11 in U1302, estimated to correspond to ~126 ka, after a period of very low IRD input that probably represents the early last interglacial period. Nicholl et al. (2012) assert that the red layer was not deposited by ice rafting, as there was very little sand-sized ( $>63\ \mu\text{m}$ ) material present in either core. Also the H11 layer did not exhibit a red colour, lending support to the idea that it was deposited by a different mechanism (Nicholl et al. 2012). A red layer was also identified by Galassen et al. (2014) in MD03-2664 from Eirik Ridge lying between 2686-2704 cm depth, which they correlated with that of Nicholl et al. (2012). On the age model of Galassen et al. (2014), based upon correlation

with benthic isotopes in MD99-2042 (Shackleton et al. 2002, 2003), this layer in MD03-2664 was dated to 124.2 – 124.7 ka, somewhat later than the date given by Nicholl et al. (2012) of ~126 ka. The Nicholl et al. (2012) study used different holes at each location (U1302A, U1305C) to those used in the present study (U1302 B and C, U1305 A and B). Nonetheless, the red layer was also identified in the holes used in this study, in digital photographs of the original sediment cores from the IODP website

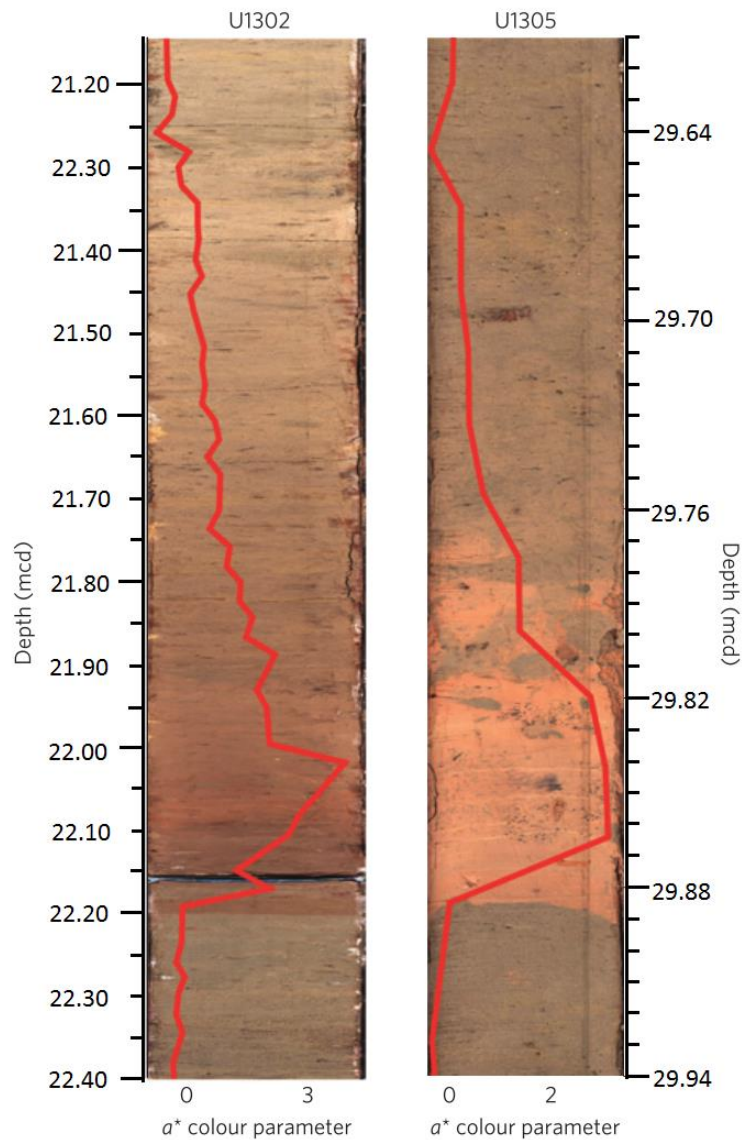


**Figure 4.18** | Digital line-scan images showing a red layer in sediment cores U1302A (left) and U1305C (right). The  $a^*$  colour reflectance parameter (red line) illustrates the degree of increased redness. There is a section break at 22.16 m in core U1302. (Modified from Nicholl et al. (2012) to add tick marks and make the depth scales clearer).

(<http://iodp.tamu.edu/database/coreimages.html>). Nicholl et al. (2012) conclude that Laurentide outburst flood events may have been common during many previous interglacials. Indeed, red layers have been observed in the Labrador Sea during the Holocene.

A distinctive red (haematite-rich) clay layer 5 – 80 cm thick was found in Hudson Bay, and traced for 700 km along the Hudson Strait (Andrews et al. 1995; Kerwin 1996). The source of the red layer has been attributed to Proterozoic bedrock within Hudson Bay (the Dubawnt Formation) (Andrews et al. 1999; Kerwin 1996). Lajeunesse and St-Onge (2008) suggest this red sediment was suspended and transported during the final

catastrophic draining of Lake Agassiz  $\sim 7.7$  ka. This massive proglacial lake was trapped behind the decaying LIS surrounding Hudson Bay. The red layer has been  $^{14}\text{C}$ -dated to 8 – 7.9 ka (Kerwin 1996), and may have led to widespread cooling known as the 8.2 ka event (Barber et al. 1999). Evidence from changes in the seawater  $^{14}\text{C}$  reservoir measured in Hudson Bay sediments (Barber et al. 1999), associated with reductions in planktonic  $\delta^{18}\text{O}$  from two piston cores on the Labrador Shelf (Andrews et al. 1999), suggests a massive freshwater input which reduced surface salinity, enhancing stratification (Teller et al. 2002; Barber et al. 1999), and suppressing winter convection in the Labrador Sea with a consequent reduction in AMOC strength (Kleiven et al. 2008). Rasmussen et al. (2003) also found a “reddish” clay layer within two cores from the Flemish Cap, which they attributed to turbidites. However,  $^{14}\text{C}$ -dating placed one of these layers at 21.2 ka, within the last glacial maximum.

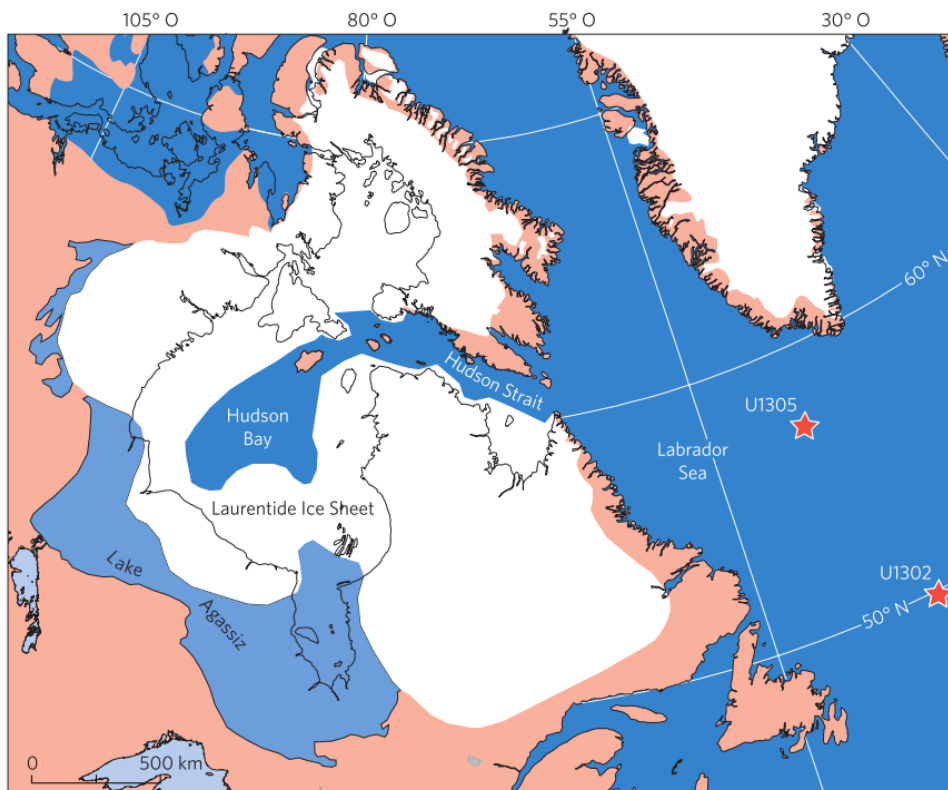


**Figure 4.19** | Map showing glacial lake Agassiz trapped behind the melting Laurentide ice sheet, locations of U1305 and U1302 are indicated (Lajeunesse 2012).

Figure 4.25 contains an expanded graph of IRD % and concentration, coarse fraction percentage and foraminifera concentration within the red layer and the diatom mat (section 4.4). This shows that the apparent increase in IRD observed in U1305 coincides with a marked reduction in concentration of planktonic foraminifera. Since the coarse

fraction is primarily composed of IRD and foraminifera, the apparent increase in IRD may be an artefact instead indicating far fewer foraminifera were present, rather than increased ice rafting. The lack of increase in IRD as a concentration of dry sediment supports this interpretation. The climatic significance of the red layer is reserved until the discussion chapter, in section 8.3.3. However, after examination of the red layer, a discrepancy was discovered between the depth values in metres composite depth (mcd) used by Nichol et al. (2012), and those used in this study, which merits discussion.

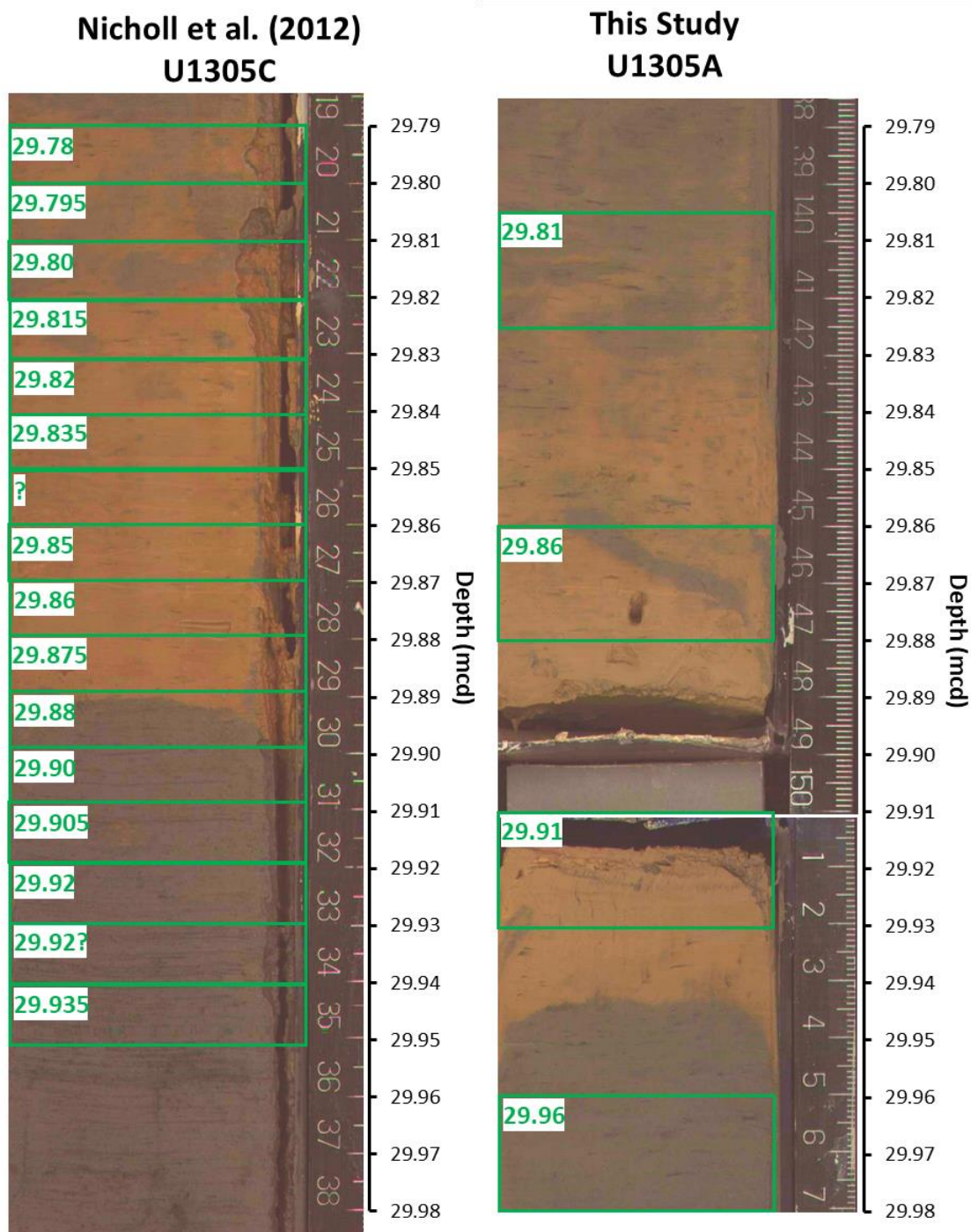
### 4.3.1 | U1305 Depth Measurements

Figure 4.20 clearly shows in the original core photographs the difference in colour between the red layer and the usual grey sediment at this location. These photographs also include the ruler used to measure core depth, which enabled the mapping of the metres composite depth values used throughout this study against the original (metres below sea floor) scale. Figure 4.20 shows close-up photographs of U1305 hole C (left), used by Nicholl et al. (2012) and hole A (right) used in this study. Green rectangles indicate the exact slice of mud used to produce the given samples, with the mcd identifier indicated by the green numbers in the rectangles. (Note that the non-standardised mcd values in the green rectangles of Figure 4.20 (left) by Nicholl et al. (2012) are replicated exactly as they were provided in the supplementary information on [www.pangaea.de](http://www.pangaea.de), despite their inconsistencies; the depth axis was interpolated for convenience to produce a uniform scale consistent with the rest of U1305C). Also notice that above 29.95 mcd, U1305C appears to have been sampled at 1-cm resolution, and at 2-cm resolution below). The red layer in U1305C (Nicholl et al. 2012) begins at ~29.89 mcd and continues to ~ 29.79 mcd. U1305C was sampled at 1 cm intervals, though not all samples were used in their study. As Figure 4.20 (right) shows, the present study used 2cm thick samples taken every 5 cm. The red layer is clearly visible with a sharp base beginning at 29.94 mcd at the top of section 5 and petering out above ~ 29.84 mcd in section 4. This means three samples from the present study contain sediment from the red layer – 29.81, 29.86 and 29.91 mcd. Table 4.2 contains information pertinent to these three samples, indicating the section number, and the top and bottom of each sample – it is these values which are mapped onto the rulers visible in the core photographs (Figure 4.20).

**Table 4.2** | Detailed identification information about samples containing the red layer in U1305A. Depth is given in metres below sea floor (mbsf) and metres composite depth (mcd). A sediment core is split vertically and one half is archived, whilst the other is designated the “working” half (W).

Leg	Site	Hole	Core	Section	Half	Top (cm)	Bottom (cm)	Depth (mbsf)	Depth (mcd)
303	1305	A	3	4	W	135	137	24.25	29.76
303	1305	A	3	4	W	140	142	24.30	29.81
303	1305	A	3	4	W	145	147	24.35	29.86
303	1305	A	3	5	W	0	2	24.40	29.91

Nicholl et al. (2012) assert that the sharp base of the red layer represents the onset of a single outburst event. This seems likely, if the Holocene Laurentide outburst flood was complete within a year (Clarke et al. 2004). The duration of the outburst event is uncertain, but the base of the red layer should be synchronous between all holes at a site, and largely synchronous between cores U1302 and U1305 (within the resolution of the cores). However, a mismatch is clearly visible in Figure 4.20 – the base of the red layer occurs at 29.89 mcd in U1305C (left) but this same base occurs at 29.94 mcd in U1305A (right). The age model constructed for this study (detailed in Chapter 7) yields a sedimentation rate through the red layer of 45.5 cm/ka, with a corresponding resolution of 110 years (per 5 cm interval). In summary then, a 5 cm offset has been discovered between the mcd depth scales of U1305 holes A and C, which could lead to a systematic dating error of ~110 years. A similar offset was discovered in U1302.



**Figure 4.20** | Close-up digital photographs of sediment core U1305 hole C section 2 (left) used by Nicholl et al. (2012) and U1305 hole A sections 4 (top right) and 5 (bottom right) used in the present study. Both photographs include the original ruler depth scale, with the metres composite depth (mcd) scale used to correlate the cores added in green. Green rectangles indicate the slices of mud used to form the samples indicated by the green labels in metres composite depth (mcd). Note the differing sample intervals. Labels in mcd for U1305C (left) are given (despite inconsistencies) exactly as provided in supplementary material provided by Nicholl et al. (2012) on [www.pangaea.de](http://www.pangaea.de), whilst the axis scale has been interpolated to match up with mcd intervals for the rest of U1305C. Images have been lightened, with enhanced contrast and colour saturation (<http://iodp.tamu.edu/database/coreimages.html>).

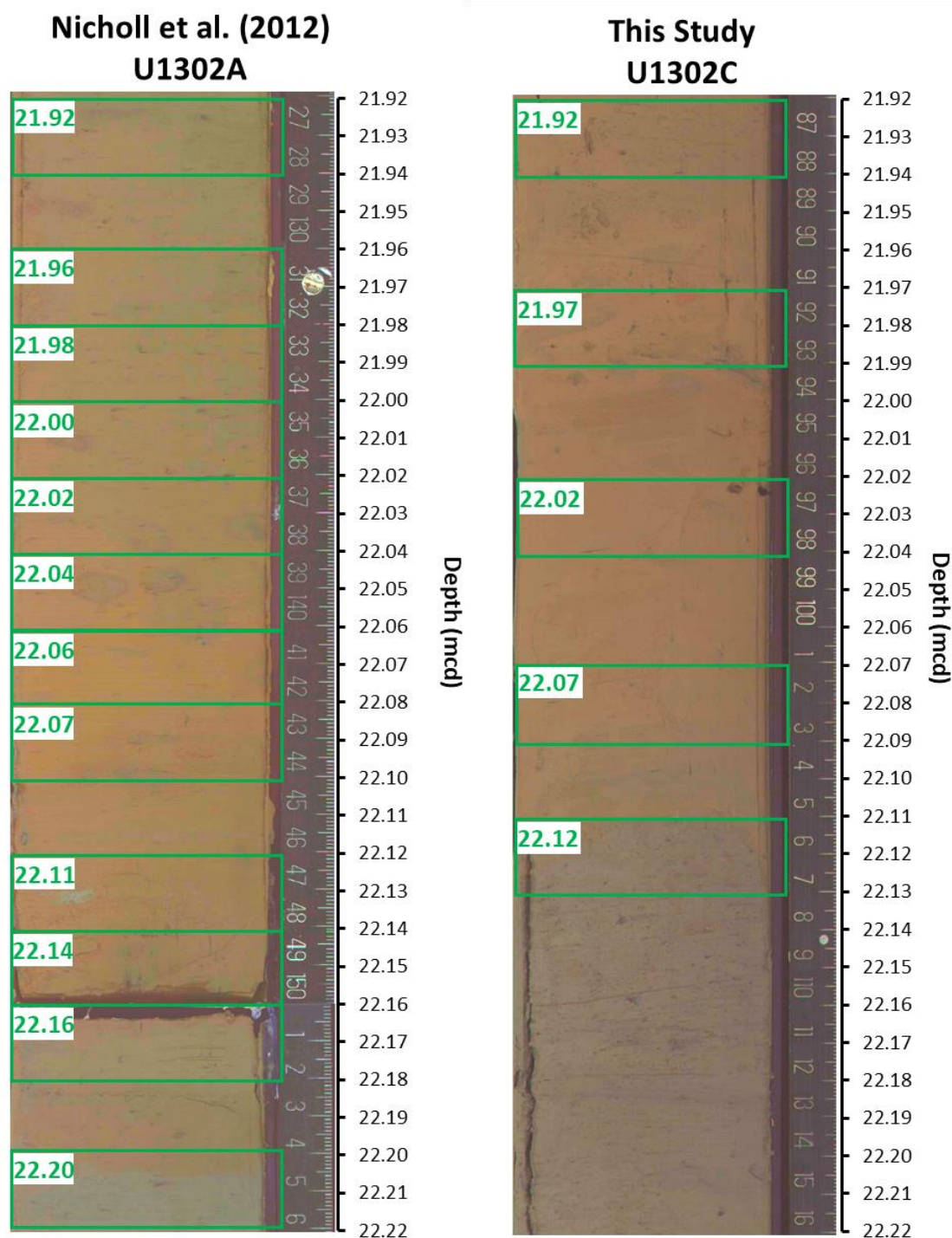
### 4.3.2 | U1302 Depth Measurements

Figure 4.21 shows U1302 hole A used by Nicholl et al. (2012) (left) and U1302C used in this study (right). In U1302A used by Nicholl et al. (2012), sampled at 2 cm resolution this time, the red layer began with a sharp base at 22.20 mcd, and continued upwards for at least 20 cm to 22.00 mcd before slowly fading to grey (Figure 4.21, left). This study used U1302 holes B and C, of which the latter contained the red layer. Figure 4.21 (right) shows that samples were again 2 cm thick and taken every 5 cm (note that samples are not indicated below 22.12 mcd, because this study switched to U1302 hole B below this point) . The red layer began at 22.11 mcd and continued upwards for at least 20 cm to 21.90 mcd. Consequently, at least four samples contain red layer material (22.07, 22.02, 21.97 and 21.92 mcd). Table 4.3 contains the depth information that allowed these samples to be identified in the core photographs.

Again, a mismatch is clearly visible– the base of the red layer occurs at 22.20 mcd in U1302A (Figure 4.21, left) but at 22.11 mcd in U1302C (Figure 4.21, right). U1302 is a lower resolution core than U1305, because it has a lower interglacial sedimentation rate of 20.5 cm/ka on the age model of this study, yielding a resolution of ~240 years per 5 cm interval used in this study. Therefore, a 9 cm offset has been discovered between the mcd depth scales between U1302 holes A and C, which could lead to a systematic dating error of ~500 years.

**Table 4.3** | Detailed identification information about samples containing the red layer in U1302C. Depth is given in metres below sea floor (mbsf) and metres composite depth (mcd). A sediment core is split vertically and one half is archived, whilst the other is designated the “working” half (W).

Leg	Site	Hole	Core	Section	Top (cm)	Bottom (cm)	Depth (mcd)
303	1302	C	2	6	81	83	21.87
303	1302	C	2	6	86	88	21.92
303	1302	C	2	6	91	93	21.97
303	1302	C	2	6	96	98	22.02
303	1302	C	2	6	101	103	22.07
303	1302	C	2	6	106	108	22.12



**Figure 4.21** | Close-up digital photograph of sediment core U1302 hole A (left) sections 6 (top left) and 7 (bottom left) used by Nicholl et al. (2012), and U1302 hole C (right) section 6 used in the present study. Both photographs include the original ruler depth scale, with metres composite depth (mcd) scale used to correlate the cores added in green. Green rectangles indicate the mud slices used to form the samples indicated by the green labels in metres composite depth (mcd). Images have been lightened, with enhanced contrast and colour saturation (<http://iodp.tamu.edu/database/coreimages.html>).

It is worth considering that because the red layer is twice as thick in U1302 than in U1305, roughly twice as much anomalous red sediment must have been delivered to

Orphan Knoll than to Eirik Ridge. This is not unexpected, since the NAMOC runs much closer to Orphan Knoll (Figure 4.2). However, the sedimentation rate at Orphan Knoll is roughly half that at Eirik Ridge. It might be predicted, therefore, that this influx of excess sediment, presumably within a short space of time if it represents a turbidite deposit, also represents a much shorter window of time than the background sedimentation rate might suggest, with potential consequences for the age model. However, with no objective way to estimate the duration of the outburst flood event, the quantity of sediment deposited, or the amount of time settling might take, and with the compounding influence of bioturbation potentially mixing red material upwards in the core, no attempt at accounting for this effect has been made in this study. In future work, this issue could be addressed through calculation of IRD as a flux rather than a concentration or percentage. IRD flux is calculated from bulk mass accumulation rate and linear sedimentation rate, taking the dry bulk density into account, and has been shown to correct for “dilution” of IRD concentration due to fine fraction input (Hibbert et al. 2010).

In conclusion, by comparison with a last interglacial red layer discovered by Nicholl et al. (2012) in different holes but the same locations as this study, a 5 cm offset was discovered between U1305A and C, and a 9 cm offset was discovered between U1302 hole C and A. This suggests an offset in the shipboard multi-track sensor correlations between different holes (Channel et al. 2006). No action was taken to adjust the depth scale used in this study, since it is unclear from data available at the present time which scale is more accurate. However, the depth scale may need to be adjusted for U1305 and U1302 at some point in the future, should it become clear that adjustment is necessary. This would not shift the depth scale more than one or two samples, given the 5 cm resolution. Because the age model is based upon paleoclimatic features of the samples themselves, it can easily be adapted should this prove necessary in the future.

## 4.4 | DIATOM MATS

One constituent of sediment that has not been discussed yet is diatoms, which are siliceous unicellular or chain-forming phytoplankton. Diatoms were generally of minor importance in most samples, however there was a conspicuous and unusual diatom mat within U1305 that merits discussion. After surface waters stratify in the spring, diatoms are usually the first phytoplankton to bloom due to their inherent high growth rate (Egge

and Aksnes 1992). Diatom abundance is generally limited by silicon availability (Allen et al., 2005; Martin-Jézéquel et al., 2000). Once all the silicate has been used up in the euphotic zone, grazing and species competition limit growth and diatom aggregations sink to the bottom (Honjo and Manganini 1993).

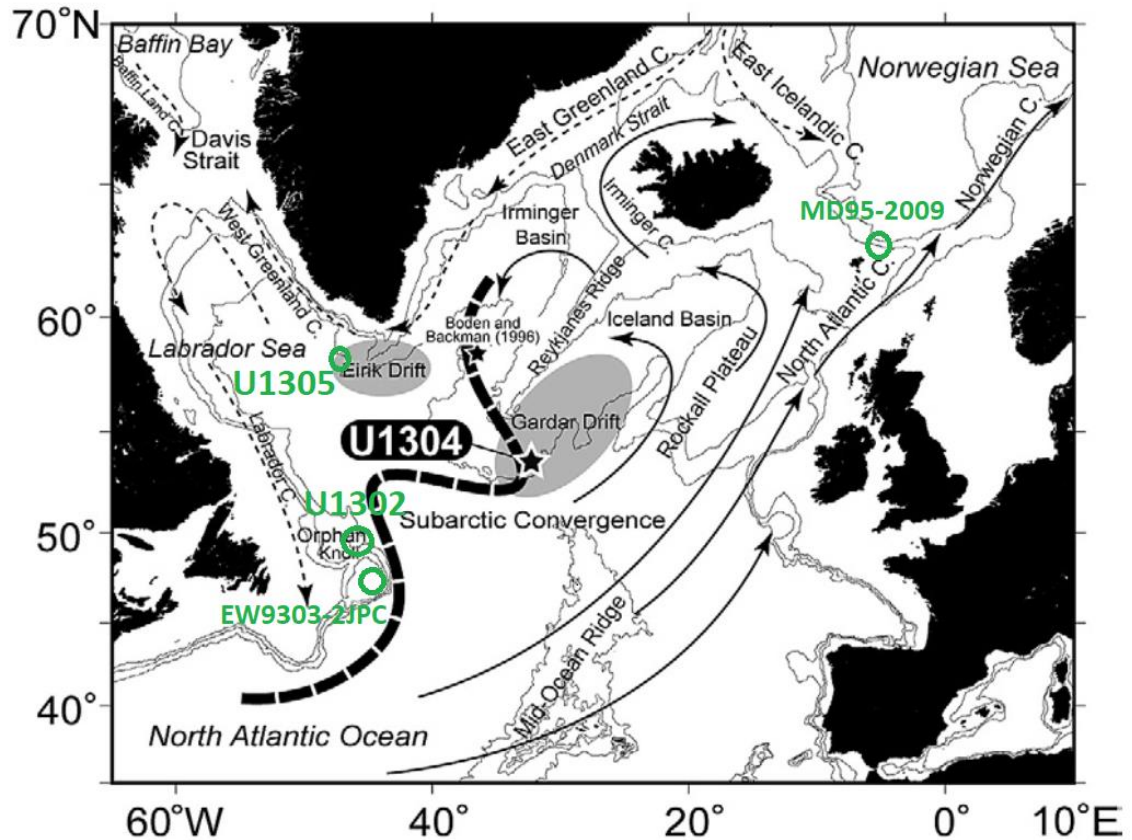


**Figure 4.22** | Location of site U1304 (star), and core EW9303-17 of Boden and Backman (1996), both of which contained thick laminated diatom ooze deposits. Also shown in green are the general locations of the Eirik Drift (core U1305), Orphan Knoll (core U1302) and Flemish Cap (cores EW9302-2JPC), as well as MD95-2009 from the northern slope of the Faeroe continental margin. Solid arrows indicate warm modern surface water currents, dotted arrows indicate cold modern surface currents, and the thick dashed line indicates the subarctic convergence front between warm saline North Atlantic Current/Irminger Current and cold fresher Labrador Sea water (Adapted from Shimada et al. 2008).

Within the North Atlantic, extensive Pleistocene laminated diatom intervals dominated by the fibrous diatom *Thalassiothrix longissima* were found in sediment core U1304, from south of the Gardar Drift, located beneath the subarctic convergence front (Shimada et al. 2008) (Figure 4.22). A thick (3 m) laminated diatom ooze was also discovered on the west flank of the Reykjanes Ridge in sediment core EW9303-17, also composed of *Thalassiothrix longissima* (Boden and Backman 1996) (Figure 4.22). Boden and Backman (1996) suggest that it was deposited by repeated events caused by physical accumulation at the subarctic convergence front during the main part of MIS 5e. Rasmussen et al. (2003) found diatom layers associated with the Terminations I & II

in two cores (EW9302-1JPC and EW9302-2JPC) from the Flemish Cap, south east of Orphan Knoll (Figure 4.22). More specifically, within Termination II they found a diatom mat principally composed of *Coscinodiscus* spp. just after the H11 IRD event (Figure 4.23). Rasmussen et al. (1999) also found a diatom layer

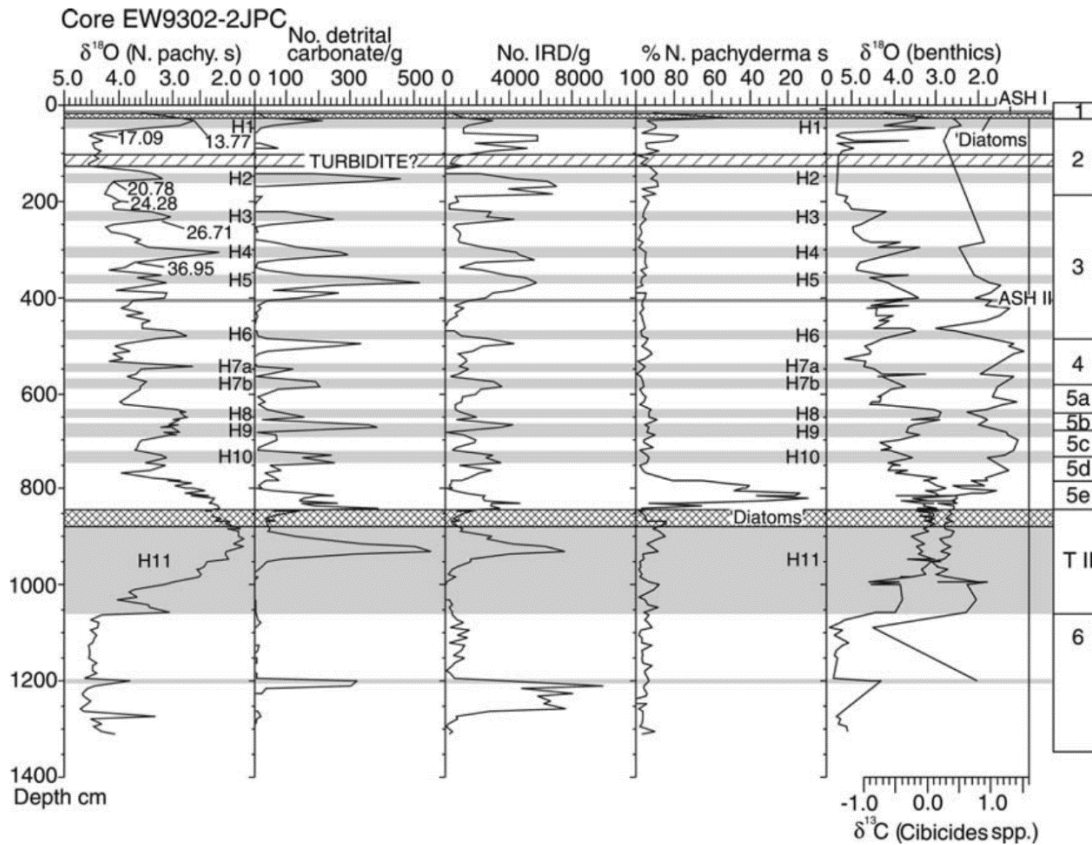


**Figure 4.23** | Climate proxy evidence within core EW9302-2JPC from the Flemish Cap showing the position of a diatom layer. From left: *N. pachyderma* (*s*)  $\delta^{18}\text{O}$ , concentration of carbonate grains and IRD in grains per gram of dry sediment, percentage abundance of *N. pachyderma* (*s*), benthic  $\delta^{18}\text{O}$  and benthic  $\delta^{13}\text{C}$ . Vertical bar at far right indicates marine isotope stages. Grey horizontal bars indicate Heinrich events. Note the position of a diatom mat (hatched horizontal bar) located at the very end of Termination II (T II) and just prior to the onset of MIS 5e (Rasmussen et al. 2003a).

following H11 and within the “warming phase” just before MIS 5e began within sediment core MD95-2009 on the Iceland-Scotland Ridge (Figure 4.22). The formation of diatom oozes is contrary to present day deep-water circulation patterns that favour the silica-poor North Atlantic as a “carbonate” ocean basin (Berger 1970). So what could have caused these diatom accumulations?

## 4.4.1 | Mechanisms of Diatom Mat Deposition

Vast laminated diatom ooze deposits were found in the eastern equatorial Pacific upwelling region by Kemp and Baldauf (1993) composed almost entirely of rapidly deposited *Thalassiothrix* mats throughout much of the Neogene (15 – 4.4 million years ago). In their memorable “Line in the Sea” front cover of *Nature*, Yoder et al. (1994) showed that in the equatorial Pacific the usually buoyant mat-forming diatom genus *Rhizosolenia* can become concentrated into dense aggregations on the warm side of a convergence front. After death, they submerge in large clumps as cold waters subduct (Kemp et al. 2006) (Figure 4.24). A further mechanism has also been discussed by Allen et al. (2005). Where nitrate is available, as is usual in the North Atlantic (Koeve 2001), the diatom bloom can be prolonged in areas where fresh silicate is renewed from deeper waters due to meanders and eddies, which can cause localised nutrient-rich upwelling as a result of baroclinic instability at an unstable ocean front (Strass 1992). Unstable fronts can therefore have a dual effect on diatom sedimentation, enhancing sedimentation rates by

subducting biomass-rich surface waters downwards, whilst enhancing diatom productivity by drawing up nutrient-rich deep water to fuel a continuation of the diatom bloom within the euphotic zone (Allen et al. 2005) (Figure 4.24).

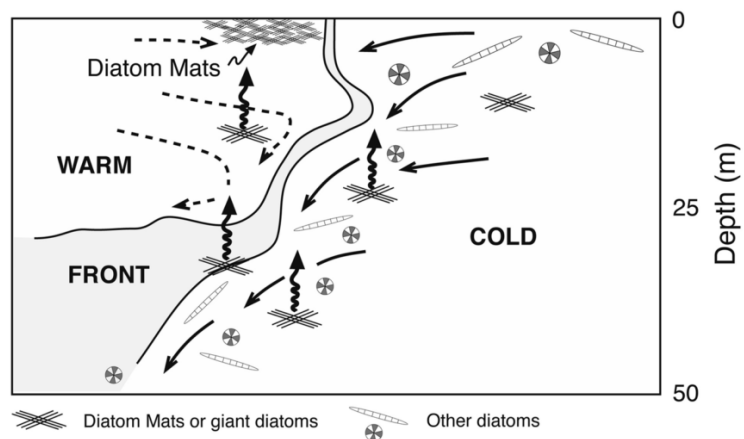


**Figure 4.24** | Schematic of a proposed mechanism which concentrates mat-forming diatoms on the warm side of ocean frontal systems, leading to massive sedimentation events (Kemp et al. 2006).

In a further observation, Kemp et al. (2006) also described how many of the mat-forming diatom species that congregate at ocean fronts, such as *Thalassiothrix* spp. and *Rhizosolenia* spp., are also adapted to stratified surface water conditions, and may flourish within the deep chlorophyll maxima. Mats of *Rhizosolenia* have been found to regulate their own buoyancy to vertically migrate below 100 m to acquire nitrate from deep pools of nutrients, and return to the surface to photosynthesize (Singler and

Villareal 2005). Some diatom species could therefore exploit nutrient-rich deeper waters in the lower euphotic zone, either by adaption to low-light photosynthesis at depth, or by regulating their own buoyancy (Kemp et al. 2006).

These two mechanisms may in fact be manifestations of similar strategies utilised by mat-forming diatoms. Archer et al. (1997) documented, using radiochemical data and nitrate budget calculations, that the *Rhizosolenia* diatoms which had accumulated along the warm North Equatorial Counter Current (NECC) side of the “Line in the Sea” (Yoder et al. 1994) were largely imported from the cold South Equatorial Current (SEC) side of the front. The diatoms within the large surface patch of warm buoyant NECC waters were apparently photosynthesizing without nitrate uptake, suggesting that the diatoms were using previously absorbed nitrate from the colder, nutrient-rich SEC to metabolise (Archer et al. 1997). This observation is similar to the vertical migration documented by Singler and Villareal (2005) and may suggest that the association of diatom mats with both oceanic frontal systems and stratified surface conditions is due to the single strategy of absorbing nitrate from one location and photosynthesizing within another (Kemp et al. 2006). Diatoms may therefore be able to out-compete other plankton within these otherwise difficult conditions and accumulate rapidly within the sediment due to their high inherent growth rate. Diatom layers poor in foraminifera in the north west Labrador Sea have been attributed to strong stratification by a low salinity surface water mass fed by low-nutrient meltwater which suppressed the mixing upwards of nutrient-rich deep waters during the late Quaternary (Aksu and Mudie 1985). If this meltwater also contained abundant silica, it may explain why diatoms were so dominant during these periods (Kemp et al. 2006).

#### 4.4.2 | Diatom Mat in U1305

The diatom mat in U1305 was noted in three consecutive samples (31.76, 31.71 and 31.66 mcd), representing a layer at least 10 cm thick which had extremely low foraminiferal and IRD content (Figure 4.25). These samples were positioned between H11 below and the start of the last interglacial ~128.5 ka above (dashed line in Figure 4.25). A brief description of IRD and foraminiferal data relating to the diatom mat is presented below. The climate significance of the diatom mat is reserved until the discussion chapter (section 8.2.4).

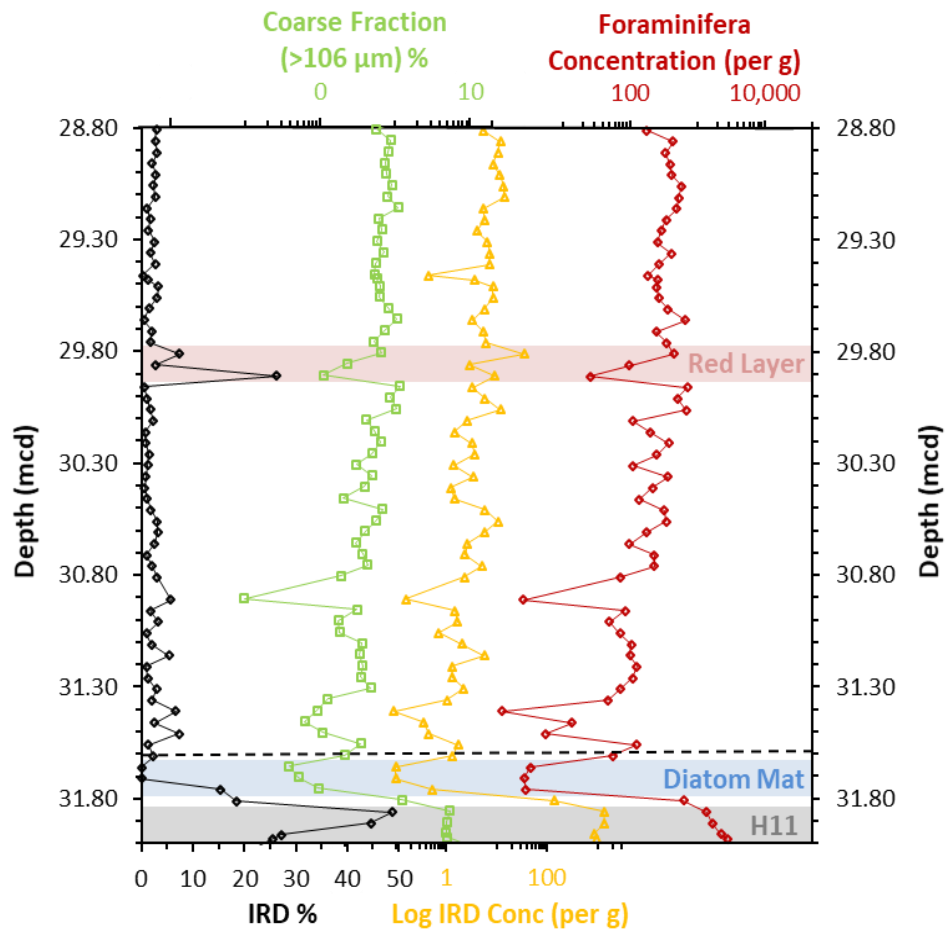


**Figure 4.25** | Selected proxy evidence relating to the red layer and diatom mat found in U1305. All values are on a log scale, except IRD percentage (black). IRD concentration (yellow), coarse fraction as a percentage of dry sediment (green) and foraminifera concentration (red). Red shading indicates red layer, blue shading indicates diatom mat, dashed horizontal line indicates the onset of MIS 5e (128.5 ka), grey shading indicates the end of H11.

Within the diatom mat, IRD was rare (6 grains) or absent, resulting in very low IRD concentrations (<0.5 grains per g), despite the entire sample being counted (Table 4.4).

This is even lower than IRD concentration through the last interglacial, which was on average 9 grains per g. There was also unusually low foraminifera abundance within the diatom mat (Figure 4.24). The average number of foraminifera counted per sample in U1305 was 485, but only 19 – 33 foraminifera were found in the entire

**Table 4.4** | IRD data from the three samples containing a diatom mat in U1305. Split fraction of 1 indicates that the entire sample was examined. Total entities = foraminifera + IRD grains.

Sample depth (mcd)	Split fraction	IRD count	IRD %	IRD per g	Total entities
31.66	1	0	0	0	33
31.71	1	0	0	0	19
31.76	1	6	15	0.5	39

sample count (Table 4.5). The foraminifera concentration, which was typically several hundred and could reach many thousands, was only ~3 per g. Figure 4.24 shows that within the diatom mat the coarse fraction (weight percent of >106 µm fraction out of total dry sediment) was unusually low. This was a consequence of very low IRD and foraminiferal abundance. In contrast, the reduced coarse fraction during the red layer was due almost entirely to a reduction in foraminiferal abundance, since IRD concentration did not reduce, or increased slightly (Figure 4.24).

**Table 4.5** | Individual foraminifera species percentages from the three samples containing a diatom mat in U1305. Also included are foraminifera as a percentage (foram %) of (foraminifera + IRD), concentration (number of foraminifera per g of dry sediment) and total number of foraminifer in the sample (foram count).

Sample depth (mcd)	<i>Gb</i> * %	<i>G. glutinata</i> %	<i>G. inflata</i> %	<i>Ni</i> * %	<i>Nps</i> * %	<i>T. quinqueloba</i> %	<i>G. uvula</i> %	Foram %	Foram per g	Foram count
31.66	63.6	18.2	0	6.1	9.1	3.0	0	100	3.3	33
31.71	15.8	21.1	0	10.5	26.3	21.1	5.26	100	2.7	19
31.76	6.1	3.0	3.0	18.2	24.2	45.5	0	85	2.9	33

\* Abbreviated forms *Gb* = *G. bulloides*, *Ni* = *N. incompta*, *Nps* = *N. pachyderma* (*s*).

The lack of IRD and foraminifera within the diatom mat may be due to unfavourable conditions, perhaps both too warm for ice rafting whilst being strongly stratified with a thick low-nutrient surface layer which inhibited foraminifera blooms. Alternatively, the low abundance of IRD and foraminifera could be attributed to a large increase in sedimentation rate due to an influx of diatoms. If diatom mats are deposited more rapidly than surrounding foraminiferal ooze, then the assumption of uniform sedimentation rates between age control tie points becomes invalid (Kemp and Baldauf 1993). Diatom mats have been shown to accumulate much more rapidly than typical nano-fossil ooze, at rates exceeding 10 cm per thousand years in the equatorial Pacific (Kemp and Baldauf 1993), and up to several millimetres per year beneath the subarctic convergence front in the Atlantic (Boden and Backman 1996). Considering the plausible mechanisms of enhanced deposition and diatom bloom extension connected with a convergent ocean front (Allen et al. 2005), or enhanced diatom export due to stratified surface waters richly supplied in silica (Kemp et al. 2006), it seems likely that the diatom mat was deposited rapidly. Whichever mechanism was responsible it seems

likely that the diatom mat was deposited much more rapidly than the usual sedimentation rate at this location. Therefore, the age model for U1305 was updated to take this into account (section 7.4.3).

## 4.5 | SEDIMENTOLOGY SUMMARY

The first IRD counts for either U1305 or U1302 were presented in section 4.2, and clearly show episodic rather than steady input of marine calving glaciers during glacial periods. Evidence from IRD counts in U1305 extends back to ~153 ka, and indicates episodic bouts of ice rafting during MIS 6b-a, which may have equalled or exceeded H11 during TII, possibly related to H12 ~140 ka (Lisiecki and Stern 2016). A candidate for H13, of greater magnitude than H11 in IRD terms, was identified ~150 ka, and is discussed further in section 8.2.1. GIS deglaciation appears to have progressed smoothly to a peak late during TII (U1305), whilst LIS breakup appears to have occurred in three major pulses (U1302). Evidence of continued IRD input through the early last interglacial supports the suggestion of greater GIS retreat (Winsor et al. 2012; Govin et al. 2012; Zhuravleva et al. 2017), likely as a result of stronger boreal summer insolation (Berger et al. 2007).

A Laurentide outburst flood event analogous to the final draining of Lake Agassiz during the Holocene, leaving evidence in the form of a red layer, has been documented early within MIS 5e in both cores previously (Nicholl et al. 2012). No major input of IRD was found to be associated with this event in either core. An apparent increase in U1305 IRD is attributed instead to a reduction in foraminifera concentration due to dilution by an influx of fine fraction material. In U1305, the onset of the last interglacial appears to have been heralded by unusual hydrographic conditions which led to the deposition of a thick (10 cm) diatom mat, a phenomenon which has also been documented elsewhere in the Labrador Sea (Rasmussen et al. 2003). Glacial expansion does not appear synchronous at a local or regional scale, with the presence of Laurentide marine calving glaciers documented well within the last interglacial period (from ~119 ka) at U1302, but not at the site of U1305 until after the end of the last interglacial (~114 ka). The next chapter presents background information about planktonic foraminifera, followed by results from faunal assemblage counts.

*“He had long ago decided, since he was a serious scholar, that the caves of ocean bear no gems, but only soggy glub and great gobs of mucky gump.”*

**James Thurber, *Further Fables for Our Time***

## 5 | PLANKTONIC FORAMINIFERA

Besides the ice rafted debris data presented in the previous chapter, the rest of the proxy evidence used in this study is based upon the shells of prolific marine organisms called planktonic foraminifera, which are abundant in the open ocean and play a significant role in the marine ecosystem. This chapter introduces planktonic foraminifera (section 5.1), describes the ecology and environmental preferences of the main species found within the subpolar North Atlantic (section 5.2), which underpins how species census counts can be used as a proxy for past sea water temperatures, and explains why particular species were chosen for geochemical analyses in the following chapter. The transfer function chosen to derive quantitative climate reconstructions from planktonic foraminiferal assemblages is outlined (section 5.3). This is followed by the method and results of the faunal assemblage counts (section 5.4), including cluster analyses and detailed individual species abundances for both sediment cores, with a brief summary (section 5.5), which leads into the following chapter concerning geochemistry.

### 5.1 | PLANKTONIC FORAMINIFERA

Foraminifera (sometimes called “forams”) are single-celled amoeboid protists, which are abundant in both the benthos (bottom-dwelling organisms) and plankton (floating organisms). There are an estimated fifty extant morphospecies (i.e. characterised by physical structure alone) of planktonic foraminifera today (Darling and Wade 2008). Adult planktonic foraminifera are typically 100 – 500  $\mu\text{m}$ , though some tropical species are much larger. Abundance patterns of planktonic foraminifera reflect primary organic productivity. The oligotrophic “deserts” of the central subtropical gyres have saline surface waters and weak circulation, resulting in low foraminiferal abundance (<1000 per  $\text{m}^3$ ). Far greater concentrations (up to 30,000 per 1000  $\text{m}^3$ ) are associated with regions of upwelling and with major frontal systems ((Bé and Tolderlund 1971). Most live within the photic zone, with the highest concentration generally between 25 – 50 m where optimum light, temperature and nutrients can be found, but different species reach peak abundance at different depths, and some inhabit waters at depths of 1000 m or more (Bé and Tolderlund 1971). This vertical stratification means different species can be studied within the same samples to gain information about past water column structure (e.g. Hillaire-Marcel et al. 2011).

Foraminifera secrete a protective calcium carbonate shell called a “test” (an internal shell), which usually has one main aperture or opening, and either one or several chambers that coil around as they are added during growth. The word “foraminifera” (d’Orbigny, 1826) is Latin and means “that which carries an opening or hole”, in reference to the aperture. Biologically, they are composed protoplasm that can emerge through this aperture, or in some species through pores in the test, as thin pseudopodia, which are used for feeding or locomotion (Boltovskoy and Wright 1976 p.13). Planktonic foraminifera are omnivorous and feed upon the spring and autumn blooms of phytoplankton (diatoms, bacteria, algae or small zooplankton), which are fuelled by convective mixing of nutrient-rich deep waters into the photic zone by storms. Some species harbour symbiotic algae within their cytoplasm (Lee and Anderson 1991). Although they are very abundant in the warmer months, foraminifera density is patchy, and numbers reduce during winter (Jonkers et al. 2010).

After a lifespan of several weeks, their skeletal remains settle to the sea floor and accumulate within the sediment, where they are abundantly preserved in sediment over 47 percent of the sea floor (Sverdrup, Johnson and Fleming 1942). Foraminifera tests fossilise well, as long as they reside in sediment above the calcium compensation depth, below which they can dissolve (Hemleben 1989). Their abundance, and the fact that fossilised foraminifera have been found in rocks as old as 500 million years (NHM website, accessed 2017), makes foraminifera eminently suitable for palaeoceanographic studies. The calcite test is composed of elements drawn from the ancient seas in which the foraminifera lived, the chemistry of which can be influenced by physical conditions such as temperature and salinity. This makes foraminifera extremely useful for geochemical analysis. The present chapter is confined to what examination of the species themselves can reveal.

## 5.2 | MAJOR SUBPOLAR PLANKTONIC FORAMINIFERAL SPECIES

Planktonic foraminifera lack self-locomotion and are passively transported by global ocean currents, but are restricted in their geographic (horizontal) and bathymetric (vertical) distribution because each species has specific environmental and ecological preferences and tolerances (Boltovskoy and Wright 1976 p.166). Therefore, each species of planktonic foraminifera thrives and becomes abundant only in particular

temperatures and at preferred depths (Figure 5.1), generally due to hydrography and food availability (Schiebel et al. 1997). Schott (1934) was the first to make quantitative analyses of modern species distributions in the equatorial Atlantic. Since then many similar regional investigations have taken place. Of these, one of the most commonly cited papers relevant to the present study was by Bé and Tolderlund (1971), who divided twenty-seven common species of foraminifera collected from 703 plankton tows from the Atlantic and Indian Oceans into five general latitudinal provinces – polar (0 – 5°C), subpolar (5 – 10°C), transitional (10 – 18°C), subtropical (18 – 24°C) and tropical (24 – 30°C). The greatest species diversity lies in tropical and subtropical waters (Figure 5.2). Because of this, only seven main species with a relative abundance of over 2 % of the total assemblage were identified in the North Atlantic cores used for this study.

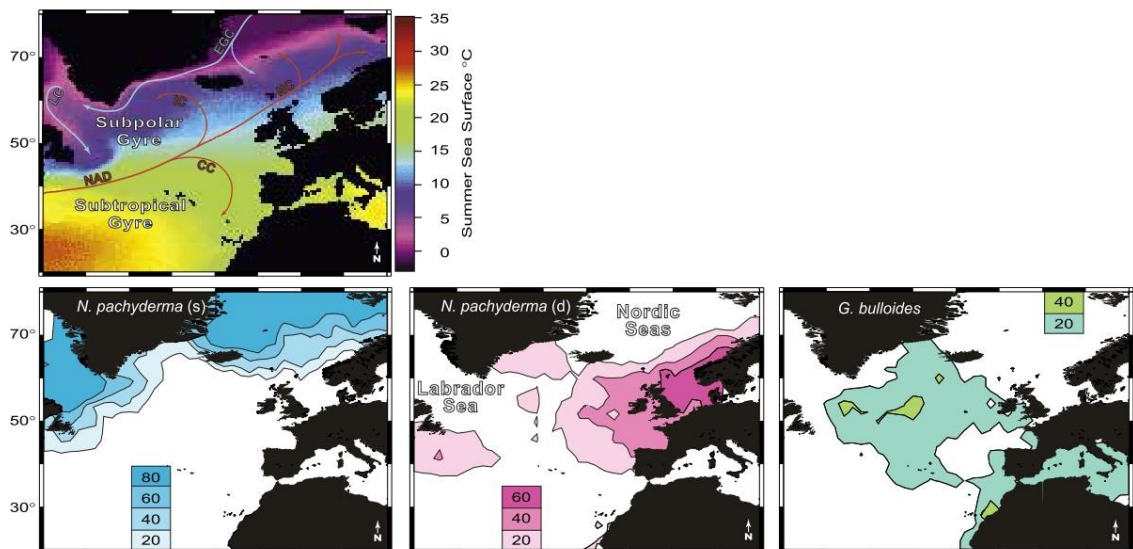


**Figure 5.1** | Biogeographical abundance of three dominant modern polar-subpolar-transitional planktonic foraminifera. Note: *N.pachyderma (d)* is equivalent to *N. incompta* in this work following Darling et al. (2006). Top: North Atlantic mid-June (1985 – 1997) sea surface temperatures, major gyres, and warm (red) and cold (blue) surface currents. EGC = East Greenland Current, LC = Labrador Current, NC = Norwegian Current, IC = Irminger Current, CC = Canary Current, NAD = North Atlantic Drift (Adapted from Bauch and Kandiano 2007).

Foraminifera are primarily identified and classified based upon the shape and characteristics of the test: whether living specimens are spinose (have many tiny spines extending from the test, which are generally present in species which inhabit surface waters) (Bé and Tolderlund 1971); the number, shape and arrangement of chambers; coiling direction; the shape and position of any apertures; wall structure and surface texture; other morphological features such as calcite overgrowth. Recently, molecular

information has proved useful in clarifying taxonomic relationships between species (e.g. Darling et al. 2006). The ecology and characteristics used to identify each one is discussed below.

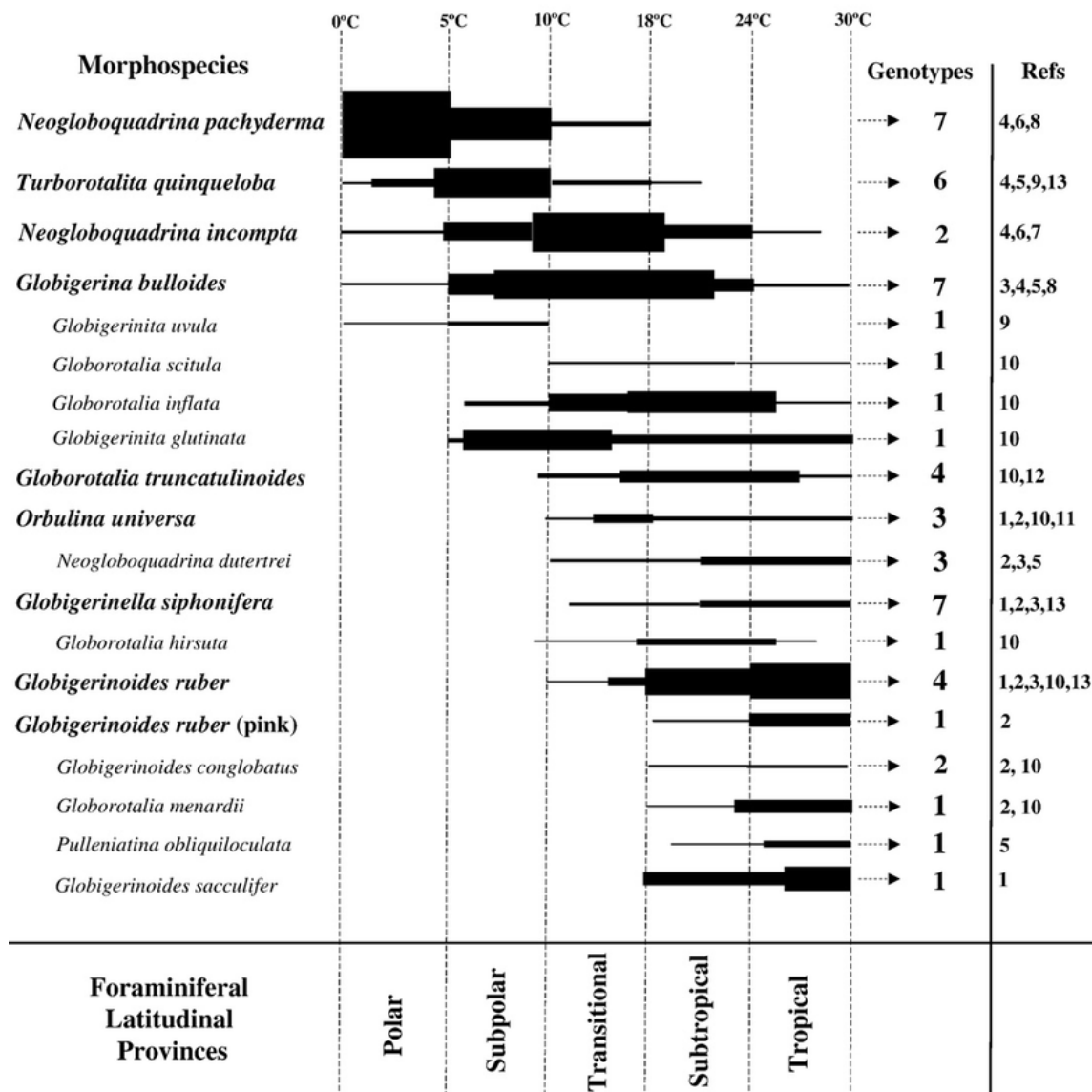


**Figure 5.2** | Summary of species distribution, assemblage and abundance across the five major latitudinal provinces (see Darling et al. 2008 and their Figure 2 for the full list of references).

## 5.2.1 | *Neogloboquadrina pachyderma (sinistral)*

### Ecology

*N. pachyderma (s)* (Ehrenberg 1861) (Figure 5.3) is a non-spinose asymbiotic mesopelagic foraminifer which is the dominant species in the Labrador Sea. It is considered to be the sole index species of polar waters, and although it is also found in subpolar and transitional waters, *N. pachyderma (s)* is most abundant at temperatures below 4°C, often reaching 100 % abundance (Bé and Tolderlund 1971). Like many deep dwelling species, *N. pachyderma (s)* live in the euphotic zone during early ontogeny between 50 – 100 m, and migrate beneath the pycnocline at the base of the thermocline on maturation (100 - 200 m depth) (Bauch et al. 1997; Simstich et al. 2003). Also, when meltwater reduces salinity, the modern Arctic Type I genotype has been observed to descend below surface freshwater layers (Schiebel et al. 2017). Therefore, *N. pachyderma (s)* geochemistry is usually interpreted as reflecting conditions just under the base of the seasonal mixed layer (Jonkers et al. 2010). Figure 5.10 shows this depth preference in comparison with monthly mean temperatures at the locations of U1302 and U1305. They are most abundant below 80 m (Figure 5.1) (Bauch and Kandiano 2007). At depth, they are prone to secondary calcification which can increase shell density by 3 or 4 times (Kohfeld et al. 1996; Simstich et al. 2003). This secondary layer may be added to increase the weight of the individual and therefore be a method of buoyancy regulation (Boltovskoy and Wright 1976 p.192). *N. pachyderma (s)* are most abundant during early spring and autumn blooms (Jonkers et al. 2010).

### Description

Test has four to four-and-a-half spherical-to-ovate chambers in the final whorl in a low trochospiral (each new chamber develops in a helical pattern) arrangement that increases rapidly in size, with radial depressed sutures; the overall shape is trapezoidal; coiling direction is sinistral (< 3 % aberrant coiling rate) (Darling et al. 2006); final chamber can be small or irregular with a laterally-directed interio-marginal aperture with a low arch having a thick apertural rim; macroperforate surface texture with

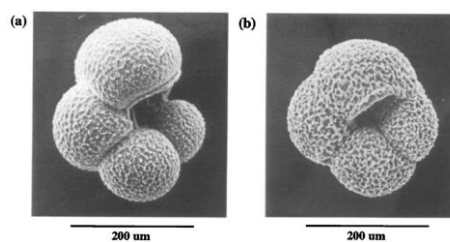


**Figure 5.3** | Scanning electron microscope image of *N. pachyderma (s)* showing (a) non-encrusted and (b) highly encrusted form affected by secondary calcification. Adapted from Kohfeld et al. (1996).

distinct pore pits that usually appears reticulate or “sugar-like” due to heavy overgrowth by secondary calcification; sutures between chambers can become so reduced by crustal thickening that they become flush with the surface, and individual chambers become difficult to recognise (Bandy 1972, Kennett and Srinivasan 1983).

## 5.2.2 | *Neogloboquadrina incompta*

### Ecology

*N. incompta* (Cifelli 1961) (Figure 5.4) is a non-spinose asymbiotic subpolar to transitional species.

Typical of less well-mixed (low productivity)

surface waters and locations experiencing low

seasonality (Staines-Urías et al. 2013), they are found within the upper 100 m without

showing a significant depth preference (Schiebel et al. 2001). In the Labrador Sea, *N.*

*incompta* are most abundant in the upper 20 m, but can migrate deeper in warmer waters

(Figure 5.2) (Bauch and Kandiano 2007). Figure 5.10 shows this depth preference in

comparison with monthly mean temperatures at the locations of U1302 and U1305. *N.*

*incompta* is most abundant during late spring and summer (Darling et al. 2006), when

summer surface temperatures are  $>8^{\circ}\text{C}$  (Staines-Urías et al. 2013)

Also known as *N. pachyderma (dextral)*. When identification was based only upon

morphology, it used to be believed that *N. pachyderma* was one species and that coiling

direction was environmentally determined, with left-coiling (sinistral) variant on the

cooler side of a  $7.2^{\circ}\text{C}$  (April) surface isotherm, and right-coiling (dextral) variant on the

warmer side, intergrading into *G. dutertrei* in subtropical waters, with all three variants

linked as a genetic cline (Bé and Tolderlund 1971). Recently, genotyping techniques

have determined that coiling direction is a heritable genetic trait, and that *N.*

*pachyderma (sinistral)* and *N. pachyderma (dextral)* are in fact separate species

(Darling et al. 2006). Here we adopt the convention suggested by Darling et al. (2006)

of using *N. incompta* to denote the right-coiling morphotype of *N. pachyderma*.

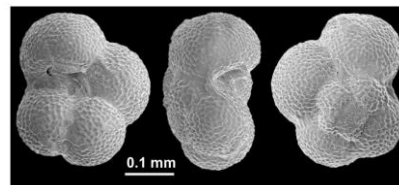


**Figure 5.4** | Scanning electron microscope image of *N. incompta* showing ventral, edge and dorsal views. Scale bar is 100  $\mu\text{m}$ . Adapted from Darling et al. (2006).

## Description

*N. incompta* is fairly small, with four spherical to ovate chambers in the final whorl in a low trochospiral arrangement, overall shape is trapezoidal; coiling direction is dextral (< 3 % aberrant coiling rate) (Darling et al. 2006); final chamber has a laterally-directed interio-marginal aperture with a low arch; macroperforate reticulate pitted wall texture that appears “sugar-like” or crystalline in appearance (Kennett and Srinivasan 1983).

### 5.2.3 | *Globigerina bulloides*

#### Ecology

*G. bulloides* (d’Orbigny 1826) (Figure 5.5) is a spinose asymbiotic foraminifer common in subpolar to temperate regions (Bé and Tolderlund 1971) and associated with high-productivity surface waters (Schiebel et al. 2001). Most commonly found in the shallow

surface mixed layer above 60 m (Schiebel et al. 1997) and in the North Atlantic, above 40 m (Figure 5.2) (Bauch and Kandiano 2007). Figure 5.10 shows this shallow depth preference in comparison with monthly mean temperatures at the locations of U1302 and U1305. Coretop analysis has also indicated that *G. bulloides* also records carbon isotopic variability correlated with phosphate levels, which may therefore be taken as productivity indicator (Ganssen and Kroon 2000). At lower latitudes *G. bulloides* is typical of the spring bloom, but at higher latitudes in the North Atlantic, *G. bulloides* blooms during late spring and summer (Schiebel et al. 1997). Most abundant between 4 – 14°C (Staines-Urías et al. 2013).

#### Description

Fairly large foraminifera (most common in 300 – 355 µm size fraction), with typically four spherical to sub-spherical chambers in the final whorl that increase regularly in size with distinct sutures between them, growth is low trochospiral, the final chamber is large with a high symmetrical aperture leading to an umbilicus (internal space

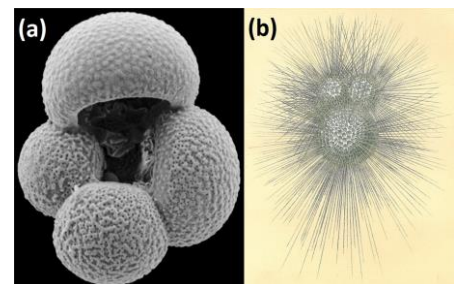


**Figure 5.5** | (a) Scanning electron microscope image of *G. bulloides* showing its open aperture and distinct final chamber (Hayward et al. 2015); (b) sketch of the living form showing spines (Brady 1884, Pl. 77).

communicating between chambers) (Kennett and Srinivasan 1983). Densely perforate calcite walls with a rough texture due to many spine bases which are visible when the calcite is wet (Schiebel et al. 1997).

#### 5.2.4 | *Globigerinita glutinata*

##### Ecology

*G. glutinata* (Egger 1893) (Figure 5.6) is non-spinose and asymbiotic, and is very unusual in being a cosmopolitan species with a global distribution in all water types, albeit at low abundance (< 5 %) (Bé and Tolderlund 1971). More abundant at low latitudes where nutrient mixing at the depth of the seasonal thermocline stimulates primary production, but also present in large numbers (up to 50 %) in the Labrador Sea during summer months where the thermocline is shallow (< 50 m) (Schiebel et al. 2017). *G. glutinata* has been associated with the autumn bloom (Schiebel et al. 2017).

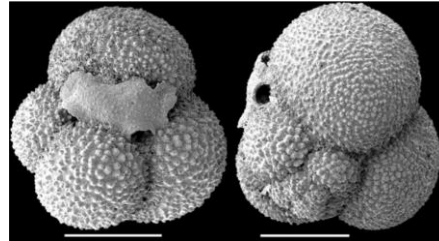


**Figure 5.6** | Scanning electron microscope image of *G. glutinata* with bulla covering aperture (Hayward et al. 2015).

##### Description

Small, with three to four globulose chambers in the final whorl in a trochospiral arrangement, overall shape largely spherical; aperture is interiomarginal, umbilical, with a low arch and a thin lip, which is sometimes covered by an irregular bulla (a blister-like covering); surface texture is smooth and shiny, microperforate, and covered with small pustules; related to *G. uvula* but bigger and less trochospiral (Kennett and Srinivasan 1983).

#### 5.2.5 | *Globigerinita uvula*

##### Ecology

*G. uvula* (Ehrenberg 1861) (Figure 5.7) is a non-spinose asymbiotic subpolar species also found in polar and transitional waters, formerly known as *Globigerinita bradyi* (Bé and

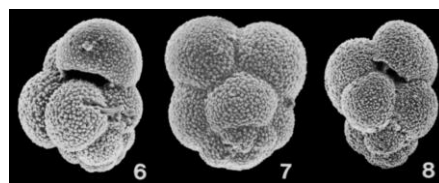


**Figure 5.7** | Scanning electron microscope image of *G. uvula* (Kennett and Srinivasan 1983).

Tolderlund 1971). Its behaviour is opportunistic, and it is generally associated with the spring bloom (Schiebel et al. 2017). Often associated with oceanic fronts or areas with a strong thermocline, *G. uvula* can vertically migrate where competition or temperature create unfavourable conditions, and inhabits the deep chlorophyll maximum (40 – 100 m), (Staines-Urías et al. 2013).

## Description

Very small and with a very high trochospiral test that resembles a cluster of grapes; spherical chambers increase in size as they are added, with three to four chambers in the final whorl; aperture is interiomarginal, umbilical, with a low arch and thin lip; surface texture is smooth, covered in small crystallites, and microperforate (Kennett and Srinivasan 1983).

### 5.2.6 | *Turborotalita quinqueloba*

#### Ecology

*T. quinqueloba* (Natland 1938) (Figure 5.8) is a spinose subpolar species that is also found in polar and transitional waters, and can contain

dinoflagellate symbionts (Bé and Tolderlund 1971). In warmer Atlantic-source waters it is abundant at the surface, in the open ocean it is most abundant in subsurface waters (50 – 100 m) (Carstens et al. 1997), but is found at 100 – 150 m depth near the sea-ice margin depending on salinity and prey availability, and as deep as 150 – 200 m beneath sea ice (Schiebel et al. 2017). Often associated with *G. bulloides*, it is rarely found within warm waters south of the transition zone (Bé and Tolderlund 1971). Most abundant between 4 – 18°C, where high abundance has been associated with a deep mixed layer and high productivity surface waters (Staines-Urías et al. 2013).



**Figure 5.8** | Scanning electron microscope image of *T. quinqueloba* (Kennett and Srinivasan 1983).

## Description

Small and low trochospiral with a largely circular outline, resembles a small flower; five chambers in the final whorl, the final chamber is slightly elongate with a diagnostic

flap-like feature with a lip that covers the umbilicus and low aperture; surface texture finely perforate and smooth (Bé and Tolderlund 1971, Kennett and Srinivasan 1983).

## 5.2.7 | *Globorotalia inflata*

### Ecology

*G. inflata* (d'Orbigny 1839) (Figure 5.9) is a non-spinose asymbiotic foraminifera and the only indigenous indicator species of transitional waters

(Bé and Tolderlund 1971). It is a deep-dwelling species with a wide vertical range, which is abundant in the euphotic zone during early ontogeny, but prefers sub-surface waters below 50 m and reflect conditions between 100 – 400 m depth (Ganssen and Kroon 2000). *G. inflata* is often associated with frontal systems and eddies (Schiebel et al. 2017) such as the boundary between the Labrador Current and the Gulf Stream (Bé and Tolderlund 1971). Common where surface waters are 4 – 11°C, although it typically lives at depth (Staines-Urías et al. 2013).

### Description

Fairly large foraminifer (most common in 300 – 355 µm size fraction), having three to three and a half sub-globular chambers in the final whorl that increase regularly in size and are more inflated on the umbilical side, overall shape rounded; wide, high-arched interiomarginal aperture; thick-walled, imperforate microstructure with a smooth texture (Kennett and Srinivasan 1983). It is dorso-ventrally flattened, with a large horizontal surface which increases buoyancy (Bé and Tolderlund 1971). *G. inflata* have been observed to secrete secondary calcite as they mature and migrate deeper, similar to *N. pachyderma* (s) (Boltovskoy and Wright 1976, p. 243).

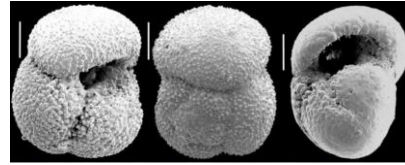


**Figure 5.9** | Scanning electron microscope image of *Globorotalia inflata* showing ventral, dorsal and edge views. Scale bar is 100 µm. (Hayward et al. 2015).

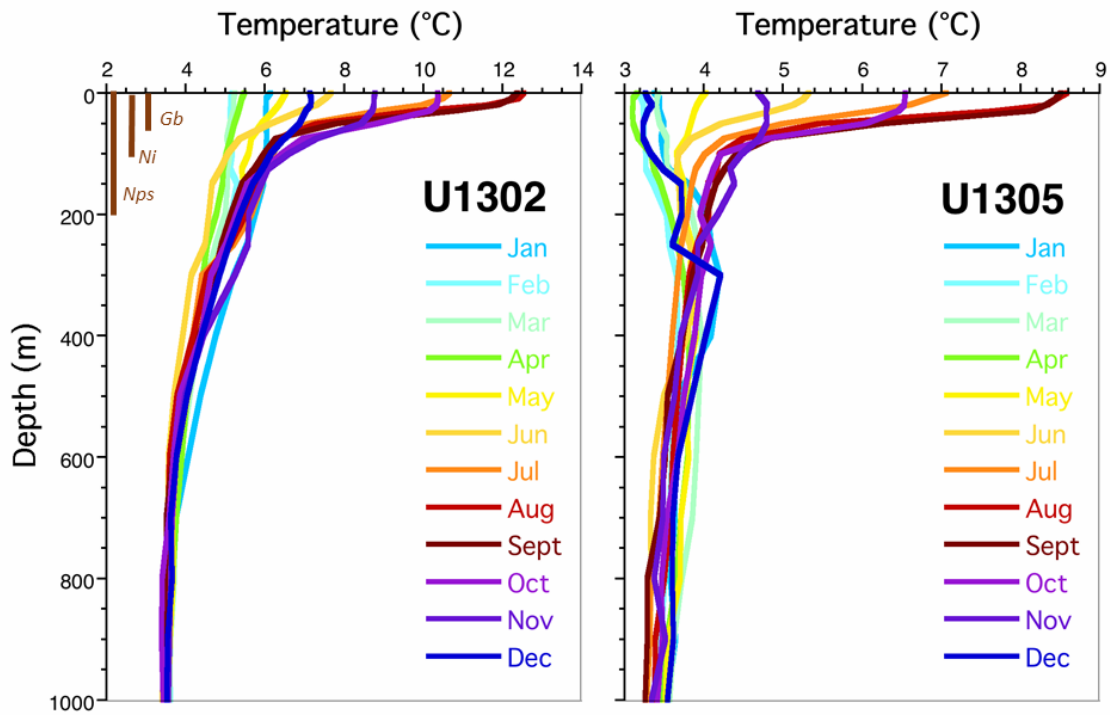


**Figure 5.10** | Monthly modern seawater temperature profiles at the locations of U1302 (left) and U1305 (right) from the surface to 1 km depth (World Ocean Atlas 1998). Surface waters (the top 100 m) become stratified during warmer months (May - October) with sea surface temperatures 6°C or 7°C higher than during winter, when surface cooling and turbulent mixing by winter storms breaks down stratification and the entire water column becomes well mixed. Also indicated in brown (top left) are the typical depth preferences of *G. bulloides* (Gb), *N. incompta* (Ni) and *N. pachyderma* (*s*) (Nps).

## 5.2.8 | Complications with Foraminifera

The ecology and depth preferences outlined above can be observed in the present day. However, ocean conditions were very different during glacial periods and during periods of rapid climate change. Foraminifera have been observed to adapt their behaviour, vertically migrating to track their optimum temperature range (Tolderlund and Bé 1971; Schiebel et al. 2001). Also, sub-surface dwellers (i.e. below 50 m) such as *N. pachyderma* (*s*) can be distributed over a considerable vertical range, usually inhabiting the euphotic zone during early development and settling deeper in late ontogeny (Bé and Tolderlund 1971). Secondary calcite encrustation added at depth can induce more enriched  $\delta^{18}\text{O}$  values (Schiebel et al. 2017). This biological flexibility makes using different foraminiferal species as indicators of past vertical water mass structure imprecise.

These problems can be compounded by differing seasonal preferences, such as the observation from sediment trap time series (Figure 5.11) that in the North Atlantic *N.*

*pachyderma* (*s*) usually blooms twice, once during early spring and late summer, whilst *G. bulloides* blooms broadly across midsummer and continues later into autumn (Jonkers et al. 2010). Also, because at high latitudes shell flux approaches zero during winter when low light conditions inhibit phytoplankton growth (Schiebel et al. 2001; Jonkers et al. 2010), foraminifera test geochemistry usually reflects spring to autumn conditions.

As such, peak summer surface temperatures and the coldest winter extremes are unlikely to be represented.

Alternatively, foraminifera may shift the season of their peak bloom to suit the most favourable conditions. Therefore, species adapted to warmer conditions may shift development from early spring to the warmest late summer months during colder periods (Hillaire-Marcel and Bilodeau 2000). These combined factors mean that geochemical analyses are likely to represent smoothed temperature records, due to their natural adaptability as living organisms.

Other factors than temperature may also impact upon both vertical and horizontal foraminifera distribution such as pH, light levels, sea ice distribution, dissolved oxygen, nutrient availability, calcium carbonate concentration and water turbidity (Boltovskoy and Wright 1976 p. 224), but these are outside the scope of the present study.

### 5.3 | TRANSFER FUNCTIONS

A transfer function is usually a multivariate calibration function which provides a quantitative estimate of an unknown (unmeasurable) parameter given a (measurable)

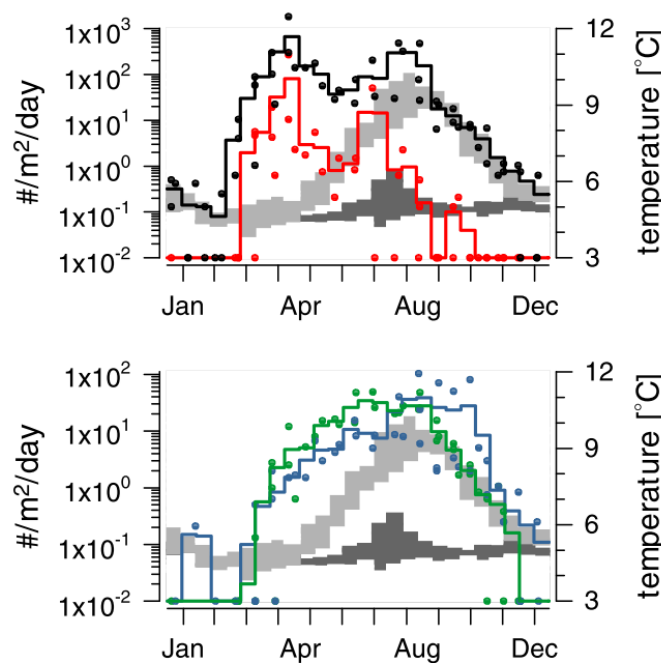


**Figure 5.11** | Annually stacked (circles) and biweekly averages (thick lines) from a sediment trap time-series of *N. pachyderma* (*s*) (top) and *G. bulloides* (bottom) shell flux. Grey shading indicates biweekly temperatures ( $\pm 1 \sigma$ ) (Jonkers et al. 2010)

input value of some proxy, due to an established ecological relationship between the two. In palaeoceanography, transfer functions can be used to estimate a vast array of past environmental parameters (such as temperature, chlorophyll *a* or salinity) given an observable species assemblage from the fossil record (such as planktonic foraminifera, diatoms or ostracods) (e.g. Jones and Juggins 1995; Kucera et al. 2005; Ramón Mercau and Laprida 2016).

Palaeoceanographic reconstructions may fail if underlying principles, requirements or assumptions are violated (Birks et al. 2010). There are three main assumptions upon which transfer function theory rests (Birks 1995). The first is related to Lyell's uniformitarian principle, and assumes that the ecology of species has not changed since the time period of the climate reconstruction (Scott 1963). This is difficult to prove, especially since populations can differentiate and ecologically adapt without speciating (Magurran 1998). Different strains of the same species can react differently to the same habitat (Weisse et al. 2011), and similar habitats can show variable modern assemblages (Birks et al. 1990). Without a direct method of testing this assumption on fossil assemblages, it must stand as a source of uncertainty. The second assumption is ecological causality, that there is a systematic relationship between faunal composition and the environmental parameter in question (in this case, temperature). Generally, the most important water mass properties are considered to be temperature, salinity and nutrient availability. Morey et al. (2005) examined the relationship between Atlantic and Pacific core-top samples and 35 different properties of preservation and of the water column, and concluded that mean annual sea surface temperature was the dominant control on planktonic foraminiferal abundance (30.4% of faunal variance). Nonetheless, census counts may contain taxa which respond to different environmental parameters (Birks et al. 2010). The third assumption is that there exists within the calibration data set a recent analogue assemblage similar enough to allow interpretation of the fossil assemblage. This problem differs depending on the numerical approach used and the quality (geographic coverage and representativeness), of the calibration data set. Most transfer functions include mathematical methods of calculating the similarity between the recent calibration data set and the fossil census count. If a novel or non-equilibrium fossil ecosystem has no modern analogue and lies outside calibration data set, or has multiple modern analogues with conflicting associated climate variables, the "no-analogue" problem is encountered, although this can be countered by finding the least

dissimilar taxa combinations and/or the past variability of species to determine more robust assemblage parameters (Mix et al. 1999; Birks et al. 2010).

If the above assumptions are met, then a transfer function can be developed based upon an internally consistent multi-species training or calibration dataset, which often contains counts of taxa (usually expressed as a percentage of the total census count) from several hundred recent coretop samples representing a wide range of environmental parameters (Birks et al. 2010). A mathematical equation is derived based upon the link between the environmental parameter in question and the biogeographical distributions of the calibration dataset. The first step involves a regression to establish the responses of recent taxa to present day climate variables (Birks et al. 2010). The second step is where the modern ecological responses are used to quantitatively infer past climates from the fossil assemblage composition. How robust the output is depends upon the mathematical technique used (Birks et al. 2010). Confidence intervals for faunal census counts can be used along with a minimal abundance threshold to improve transfer function accuracy. In the future, climate reconstruction methods may become incorporated into a Bayesian framework, which has the potential to improve handling of uncertainties in the data (Haslett and Challenor 2010). Imbrie and Kipp (1971) were the first to derive a paleoceanographic transfer function that was based upon planktonic foraminifera using a principal components regression of faunal counts (22 species) from sixty-one coretops from the Atlantic and Indian Oceans. Since then, several different methods have been devised, each with different strengths and weaknesses.

For this study, the Modern Analogue Technique (MAT) developed by Hutson and Prell (1980) was chosen. This multivariate assemblage approach uses an index of faunal similarity to find which subset of 'nearest neighbours' (usually between 6 and 10) from the calibration data set is most similar to the fossil assemblage. The average of the environmental properties from this subset is the output, weighted by the inverse of dissimilarity so that the most similar modern analogues carry the greatest weight (Birks et al. 2010). Similarity is usually calculated using squared chord distance after a comparative study by Prell (1985). The number of analogues to include is usually derived by cross-validation, excluding a different portion of the data set each time as a test sample in many iterations for 1, 2, ...  $k$  modern samples from the calibration data set; the difference between predicted and observed values is calculated for each test sample, and the value of  $k$  associated with the lowest root mean squared error of

prediction is used (Birks 1995; Barrows and Juggins 2005). MAT can produce the most robust results if based upon a well-populated quality calibration data set with wide spatial coverage and representing as broad a range of environmental conditions as possible (Birks et al. 2010). Pflaumann et al. (2003, 1996) developed a modern analogue technique using a similarity index (SIMMAX) in which the most similar samples are weighted by inverse geographical distance. The large SIMMAX data set of 947 modern analogues included many high latitude examples. However, at the “cold end” below 3°C SSTs SIMMAX tends to over-estimate temperatures (up to 3°C for summer and up to 1.5°C for winter), because during glacial periods faunal maximums may migrate away from their present locations, violating the assumption of “geographic stability”, and the assemblage becomes almost monospecific for *N. pachyderma* (*s*). Therefore, to provide the most accurate results even during very cold glacial periods, the MAT technique was used without geographic weighting, but populated by the large SIMMAX database.

## 5.4 | ASSEMBLAGE COUNTS

### 5.4.1 | Methods

Faunal assemblage counts were performed at the same time as IRD counts, so the method was the same. Species were identified under a binocular light microscope. Individuals were identified at species level where possible. Some specimens were ambiguous, malformed or damaged, which made identification difficult. If identification was not certain, they were classed as “other”, and not included in the transfer function. This category had little

**Table 5.1** | Summary statistics for faunal assemblage data from U1305 and U1302 used in generating a MAT SST estimate.

	U1305	U1302
Number of samples	211	81
Average number of foraminifera	494	332
Minimum number of foraminifera	50	50
Maximum number of foraminifera	1231	704
Population Standard Deviation	178	120
Number of small samples (<50 foraminifera)	23	15
Number of small samples monospecific for <i>N. pachyderma</i> ( <i>s</i> )	15	15
Average relative abundance of <i>N. pachyderma</i> ( <i>s</i> ) in small samples	96	96

effect on the total assemblage, accounting for 0.04 % abundance in U1305 and 0.2 % abundance in U1302.

To convert census counts to temperatures the Modern Analogue Technique was used (configured with the squared chord distance metric and the 8 best analogues) and down core samples were matched to the 947 coretops in the SIMMAX data base. Sample counts of less than 50 forams in total are not considered statistically reliable, however SST estimates from small samples have been shown in the results below (indicated by open circles) only where samples were approaching monospecific (> 75 %) for polar species *N. pachyderma* (*s*), because an increased count size would not likely change the temperature estimate very much. Standard deviation of the residuals is 1.2°C. Summary statistics for faunal counts are included in Table 5.1.

## Cluster Analysis

In order to objectively identify different stratigraphic foraminiferal zones, cluster analysis of the faunal assemblage was carried out using the R package Rioja (Juggins 2009, 2013), which was designed for analysis of Quaternary ecological data. The function `chclust` implements hierarchical clustering, constrained so that clusters only contain adjacent samples, of a dissimilarity matrix (the chord distance between core samples) using the multivariate CONISS (stratigraphically Constrained Incremental Sums of Squares) algorithm (Grimm 1987). The assumption is that the zones have a minimum of within-zone dispersion (identified by incremental sum of squares), and therefore represent periods containing the most homogenous fossil assemblages, though some may be transitional periods between two different states (Grimm 1987). Zones are identified by drawing a line across the dendrogram (see Figures 5.12 and 5.13). The choice of dispersion level at which to separate clusters is somewhat subjective. A balance between detail and random noise was struck (total dispersion 20 in U1305, and 5 in U1302), which produced zones containing palaeoceanographically relevant information and facilitated discussion of the results. A further subdivision in U1305 at total dispersion 19 was added to separate zones Ca and Cb. Table 5.2 lists the specific depths and ages (see Chapter 7 for details of the age model) of the stratigraphic zones identified by the cluster analysis, discussed in the results below.

**Table 5.2** | Depths in metres composite depth and ages in thousands of years (see 7.4.4 for age model construction) of stratigraphic zonation of the planktonic assemblage identified by cluster analysis.

Zone	U1305 depth (mcd)	U1305 Age (ka)	Zone	U1302 depth (mcd)	U1302 Age (ka)
A	33.16 - 31.86	153.3 – 130.0	A	23.60 - 22.40	135.3 – 130.0
B	31.81 - 30.61	129.3 – 127.3	B	22.35 - 21.92	129.6 – 125.8
Ca	30.56 - 29.86	127.3 – 126.4			
Cb	29.81 - 29.21	126.3 – 125.0	C	21.87 - 21.57	125.5 – 124.1
D	29.16 - 28.11	124.9 – 122.5	D	21.52 - 21.32	123.8 – 122.8
E	28.06 - 26.16	122.4 – 118.3	Ea	21.27 - 20.97	122.6 – 121.1
			Eb	20.87 - 20.32	120.6 – 118.0
Fa	26.11 - 25.66	118.2 – 117.2			
Fb	25.63 - 25.13	117.1 – 116.0	F	20.27 - 19.92	117.7 – 116.0
G	25.08 - 23.03	115.5 – 100.9	G	19.87 - 19.57	115.8 – 114.7

## 5.4.2 | U1305 Faunal Assemblage Results

Figure 5.12 shows the faunal assemblage results from sediment core U1305, including percentage abundance (out of total planktonic foraminifera) of the seven major species (> 2 % relative abundance). Other species (purple) present but at low abundance are shown in Table 5.3. Small samples within the MAT SST record (pink open circles) are included because they are almost monospecific for *N. pachyderma* (*s*). Almost all fall within zone G (aside from 32.76 mcd in zone A, which is a similar temperature to reliable SST estimates either side), and fill in what would otherwise be a fairly large gap in results. They all show cold SSTs (mean ~2°C) in keeping with SST estimates either side (Figure 5.12). A coretop (0 – 2 cm) sample was available for U1305, from which arrows on the left axis of Figure 5.12 show modern species abundances, and MAT summer SST estimated from this sample using the same transfer function was  $8.5 \pm 1.4^\circ\text{C}$ . This is in close agreement with summer (JJA) surface ocean atlas temperatures for this location (8°C) (World Ocean Atlas 1998).

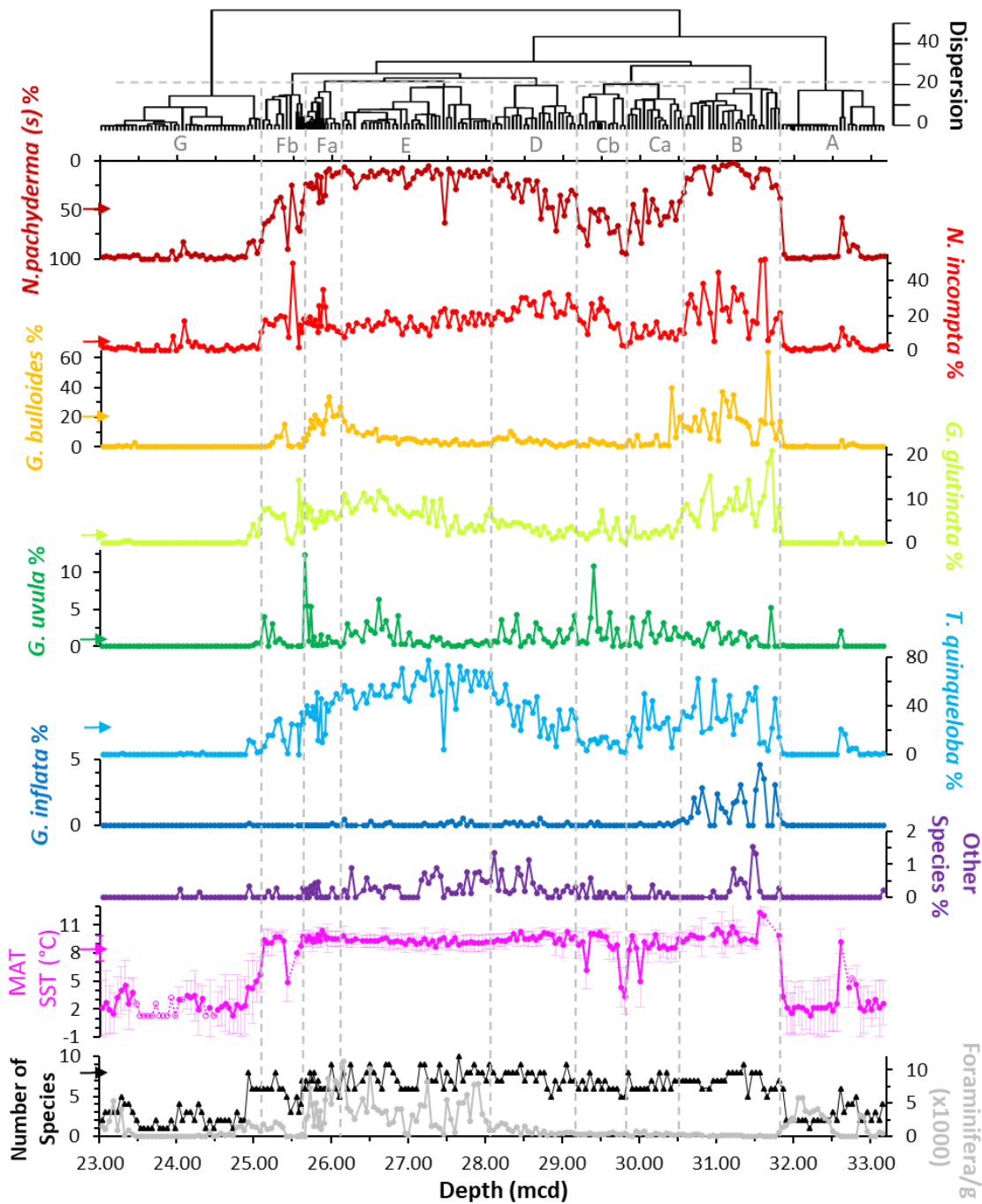


**Figure 5.12** | U1305 planktonic foraminiferal percentage abundance results. Cluster analysis dendrogram (top) with assemblage zones A – G (vertical grey dashed lines) identified at a dispersion measure of 20, further subdivided at 19 to separate zone Ca and Cb (see Table 5.2 for specific depths). Major species over 2 % relative abundance are shown; arrows on the axes indicate coretop values. Other minor species (purple) are listed in Table 5.3, none of which exceeded 1.3 % abundance. MAT SST estimate (pink) with standard deviation (pink error bars); pink arrow on the axis indicates coretop MAT SST estimate of  $8.5 \pm 1.4^{\circ}\text{C}$ ; dotted lines indicate missing data; open circles indicate small samples containing < 50 foraminifera (mean 17), which were included where they were almost monospecific for *N. pachyderma* (*s*) (mean 96 %). Bottom graph shows number of species (black) as a measure of community diversity, and foraminifera concentration per gram of dry sediment (grey). Coloured arrows on left axis indicate modern coretop values.

The top panel in Figure 5.12 shows the cluster analysis dendrogram, an illustration of the hierarchical relationships between clusters. Unsurprisingly, there are three major divisions at a level containing a broad measure of dispersion within clusters (40), which likely correlate with MIS 6b-a (A), MIS 5e (B – F) and MIS 5d-c (G). At a lower measure of dispersion (25), the last interglacial period becomes broadly divided into early (B – C) and late (D – F) clusters.

A total dispersion of 20 (horizontal dashed grey line in Figure 5.12) was chosen to separate clusters for discussion in this study. In addition, a further subdivision at dispersion of 19 was added which separated zone Ca from Cb, because the division between these two clusters (29.86 – 29.81 mcd) lay within the red layer identified by Nicholl et al. (2012), which has some climatological implications, and resulted in more meaningful comparison between clusters identified in U1302 which also contained a division within the red layer.

Zone A is almost totally dominated by polar foraminifera *N. pachyderma* (*s*), with a brief period of diversity between 32.81 – 32.61 mcd, which MAT SSTs indicate was warm (up to ~9°C), though foraminiferal concentration was low. Outside this warm phase, the MAT SST estimate is ~1 – 2°C through zone A. The increase in foraminiferal concentration towards the top of zone A is due almost entirely to *N. pachyderma* (*s*).

Zone B is defined by a sharp increase in SST to ~10°C at 31.81 mcd, high species diversity, low *N. pachyderma* (*s*) abundance, and contains the warmest SST of the entire interglacial (~12°C at 31.56 mcd). Zone B is also the only period where *G. inflata* was abundant (> 0.5 %), reaching a maximum of 5 % relative abundance. This may indicate that the SAC front lay close to this location through zone B (see Figure 3.15).

Zones Ca and Cb are similar and likely transitional in nature, marking as they do a steady increase in *N. pachyderma* (*s*) abundance from 32 – 72 % (zone Ca) at the expense of warmer water species, to a period of climate instability including the lowest MAT SST of the entire interglacial period (~3°C), followed by a steady decrease in *N. pachyderma* (*s*) abundance from 95 – 67 % (zone Cb). Zone Ca is more abundant in *T. quinqueloba*, whilst zone Cb is more abundant in *N. incompta* and *G. uvula*. Zone D shows a continuation of the decrease in *N. pachyderma* (*s*) (from 34 – 19 %), fairly abundant *N. incompta*, and increasing *T. quinqueloba*.

**Table 5.3** | Maximum relative abundance (as a percentage of total foraminifera present) of low abundance species (< 2 %) in sediment cores U1305 and U1302, including number of samples (out of 211 for U1305, out of 81 for U1302) which contained the stated species. “Others” include specimens of uncertain identification, which may be due to abnormal or deformed growth, or physical or chemical damage. None of these species were included in the transfer function calculation.

Species	U1305		U1302	
	Maximum Relative Abundance (%)	Number of Samples	Maximum Relative Abundance (%)	Number of Samples
<i>G. aequilateralis</i>			0.7	2
<i>G. calida</i>	0.2	1		
<i>G. conglobatus</i>			0.3	2
<i>B. digitata</i>			0.3	1
<i>G. falconensis</i>			0.8	2
<i>G. hirsuta</i>	0.6	1	0.7	22
<i>G. ruber (pink)</i>			0.2	2
<i>G. ruber (white)</i>	0.5	10	1.7	38
<i>G. sacculifer (no sac)</i>			0.3	2
<i>G. sacculifer (with sac)</i>	1.0	18	0.6	7
<i>G. scitula</i>	1.3	49	1.4	23
<i>G. truncatulinoides (dextral)</i>	0.2	1	0.6	11
<i>G. truncatulinoides (sinistral)</i>	0.2	1	0.6	12
<i>O. universa</i>	0.2	7	1.4	41
<i>Others</i>	0.9	28	1.0	37

The first half of the last interglacial (zones B – D) shows low foraminiferal concentration (mean = 394 per g), but this concentration increases dramatically in zone E (mean = 3860 per g), which is a fairly homogenous zone with consistent MAT SST estimates, and high *G. glutinata* and *T. quinqueloba* abundance, typically associated with high productivity surface waters (Staines-Urías et al. 2013).

Cluster analysis shows zones Fa and Fb are statistically not that similar, but both appear to be transitional periods, showing across both zones increasing *N. pachyderma (s)* from 11 – 65 %, and decreasing *T. quinqueloba* from 45 – 6 %, although both contain fairly high *N. incompta* abundance. In contrast, zone Fa has higher *G. bulloides* abundance

(18 %) than zone Fb (4 %), higher foraminifera concentration (4232 per g) than zone Fb (802 per g), and although generally warm (~ 10°C), zone Fb contains some climate instability, with a low SST value of ~5°C, associated with generally lower species diversity.

Zone G is almost monospecific for *N. pachyderma* (*s*) (90 – 100 %), with low foraminiferal diversity and concentration, and low (mean = 3°C) if variable (1 – 5°C) SST estimates. There are two periods of faunal diversity which may represent warmer periods, 24.23 – 23.93 mcd within which there is an increase in *N. incompta* but at low overall foraminiferal concentration (mean = 28 per g), and above 23.43 mcd which coincided with a much higher concentration of foraminifera (mean = 1851 per g).

### 5.4.3 | U1302 Faunal Assemblage Results

Figure 5.13 shows the faunal assemblage results from sediment core U1302, again showing percentage abundance of the same seven major species (> 2 % relative abundance). Other low abundance species (purple) are also shown in Table 5.3. The cluster analysis dendrogram (top panel) again reveals three major divisions at a broader measure of dispersion (10) likely representing MIS 6b-a (A), MIS 5e (B – F) and the glacial inception and MIS 5d-c (G - H). A lower total dispersion (5) was chosen for this study, which divided the last interglacial period into meaningful periods for discussion. The early phase (zone B) ended within the red layer (21.92 mcd), and likely corresponds to both zones B and Ca in U1305, the latter of which also ended within the red layer. This is a useful point of reference, because it is assumed that the red layer was deposited synchronously within both cores. This difference between cores probably results from the much lower interglacial sedimentation rate in U1302, which results in a much lower resolution record. The ensuing zones C – Eb cluster fairly closely with zone B, whilst zone F is statistically somewhat different, and likely corresponds with both zones Fa and Fb in U1305. Interestingly, in contrast to U1305, the last part of the last interglacial (zone F) clusters more closely with MIS 5d (zone G) than with the rest of the last interglacial (zones B – Eb), likely representing a transitional period and perhaps indicates that climate deterioration during the penultimate glacial inception was more pronounced near Orphan Knoll than Eirik Ridge.

Zones A is again almost totally dominated by polar foraminifera *N. pachyderma* (*s*) (mean relative abundance 96 %), with brief periods of diversity resulting in slightly

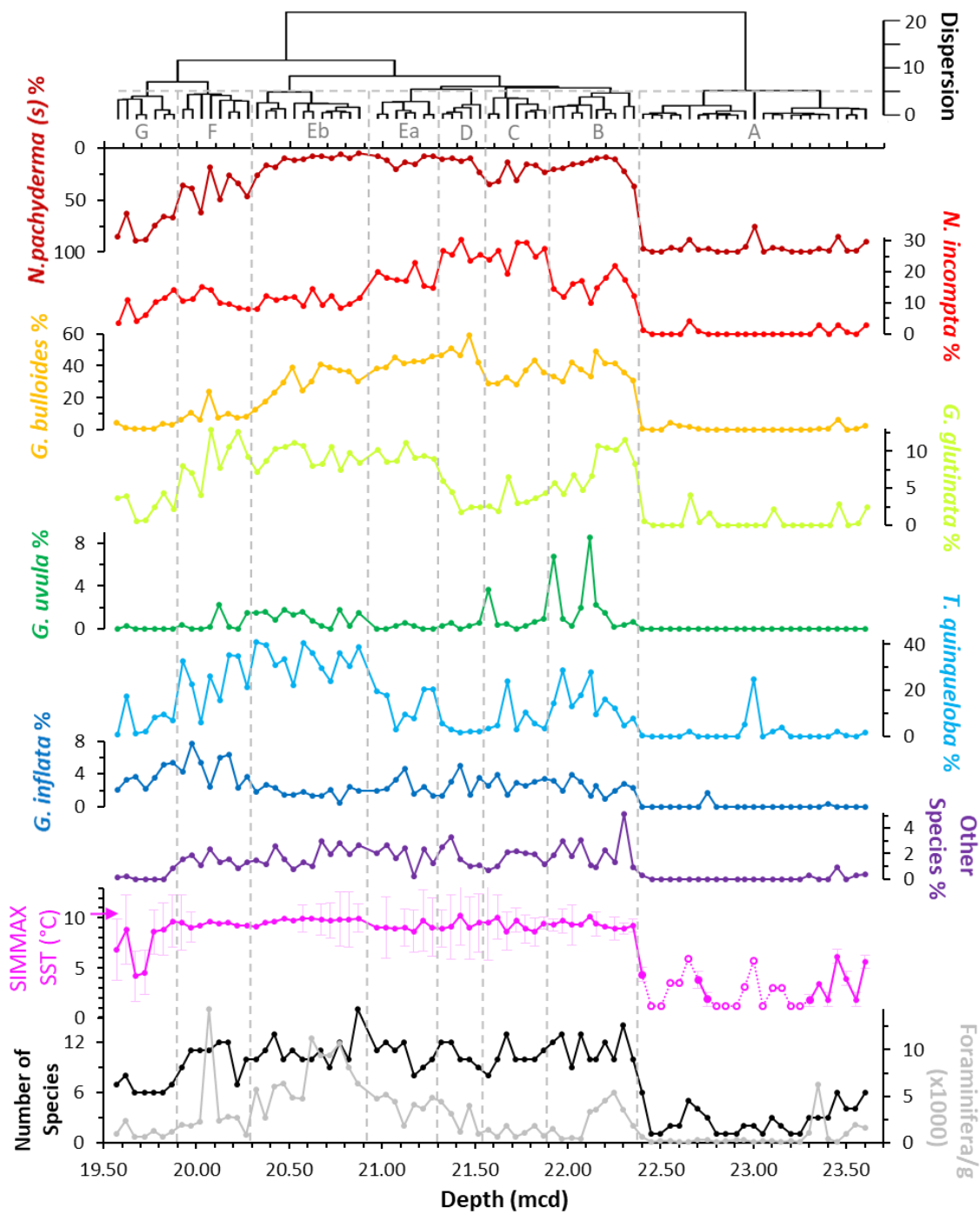


**Figure 5.13** | U1302 planktonic foraminiferal percentage abundance results. Cluster analysis dendrogram (top) with assemblage zones A – G (vertical grey dashed lines) identified at a dispersion measure of 5 (see Table 5.2 for specific depths). Major species over 2 % relative abundance are shown. Other minor species (purple) are listed in Table 5.3, none of which exceeded 1.7 % abundance. MAT SST estimate (pink) with standard deviation (pink error bars); pink arrow on axis indicates modern ocean atlas summer (JJA) surface (0 – 10 m) temperature at the location of U1302 of 10.3°C (World Ocean Atlas 1998); open circles indicate small samples containing < 50 foraminifera (mean 25), which were included where they were almost monospecific for *N. pachyderma* (s) (mean 96 %). Bottom graph shows number of species (black) as a measure of community diversity, and foraminifera concentration per gram of dry sediment (grey).

warmer MAT SSTs around 23.45, 23.00 and 22.65 mcd (Figure 5.13). Foraminiferal concentration (mean 628 per g) is low through zone A, apart from a peak at 23.35 mcd of 6254 per g composed almost entirely of *N. pachyderma* (*s*). Low foraminiferal abundance is often associated with Heinrich events (e.g. Bond et al. 1992), which is indicated by IRD results from the previous chapter (mean IRD abundance 82 %, mean IRD concentration 2412 grains per g). The 15 small samples (pink open circles) containing < 50 individuals (almost exclusively *N. pachyderma* (*s*)) were all found within zone A, and generally show very cold MAT SSTs (~1°C), though with two distinct peaks (~6°C) at 23.00 and 22.65 mcd. This might be attributed to unreliable SSTs due to small sample sizes, except that they compare very closely with two more reliable warm MAT SST estimates at 23.60 and 23.45 mcd.

The onset of zone B is defined by a sharp increase in SST estimate to ~9°C at 22.35 mcd. Zone B is a period of high foraminiferal diversity and low *N. pachyderma* (*s*) abundance (mean 17 %), again indicating an early climate optimum within the last interglacial. There is an early peak in foraminifera concentration from 22.35 – 22.12 mcd (mean 3696 per g), due to increases in *N. incompta* and *G. bulloides*, and an early peak in *G. glutinata* and other species. *G. uvula* abundance peaks somewhat later in zone B, and *T. quinqueloba* increases throughout zone B. *G. inflata* reaches an early peak abundance (5 %) in zone B at 22.30 mcd, but in contrast to U1305, *G. inflata* continues to be present through the rest of the interglacial, albeit at low abundance (mean 3 %). This may indicate the presence of a nearby frontal system, likely between the Labrador Current and North Atlantic Current (Bé and Tolderlund 1971). The last sample within zone B, 21.92 mcd, is the top of the red layer identified by Nicholl et al. (2012), and was likely deposited synchronously with the end of zone Ca in U1305. This means zone B in U1302 is equivalent to zones B and Ca in U1305.

Located just above the red layer in U1302, zone C contains the highest *N. pachyderma* (*s*) abundance within the last interglacial period (mean 24 %). *N. incompta* remain abundant, but there are reductions in *G. bulloides*, *G. glutinata*, *G. uvula*, *T. quinqueloba* abundances, compared to zone B.

Zone D would appear to be similar to zone D in U1305, in that it appears to be transitional between the less faunally diverse zone C, and more diverse last half of the last interglacial. *N. pachyderma* (*s*) abundance decreases (mean 13 %), whilst *N. incompta* abundance reaches its peak (30 %), along with *G. bulloides* (59 %), and there

is an increase in *G. glutinata*, other species, diversity in general and foraminiferal concentration across zone D.

Although not statistically clustered very closely, zones Ea and Eb have been identified with zone E in U1305 based upon dating derived from the age model constructed for this study (detailed in Chapter 7). Zone Ea had variable *N. pachyderma* (*s*) abundance (7 – 20 %), slightly lower *N. incompta* and reducing *G. bulloides* but higher *G. glutinata* than zone D. *T. quinqueloba* abundance increased, and species diversity and concentration was high overall. Through zone Eb, *N. pachyderma* (*s*) abundance is low, *G. bulloides* reduced, and *G. glutinata* and *T. quinqueloba* abundances were high. The first sample in zone Eb (20.87 mcd) contained the most diverse fauna of the entire record (16 different species), though there is a reduction in *N. incompta* compared to zones B – Ea, and an overall fall in foraminiferal concentration. Zones Ea and Eb appear to represent fairly stable warm conditions through the last part of the last interglacial, in common with zone E of U1305.

As stated above, although zone F is considered to pertain to the last part of the last interglacial, in U1302 it clusters more closely with zone G than with the rest of the interglacial period. Through zone F there is an increase in *N. pachyderma* (*s*) and a decrease in *G. bulloides*, *G. glutinata*, and *T. quinqueloba*, although strangely there appears to be an increase in *G. inflata* throughout zone F to a peak of 8 % relative abundance. This may indicate increasing proximity to the migrating SAC front at this time. Zone F is the last to contain “other” species as well as fairly high diversity overall, and although there is a peak in foraminiferal concentration (14,363 per g) at 20.07 mcd, concentration generally decreases.

Zone G is likely synonymous with zone G in U1305 in representing MIS 5d with a reduction in all other warmer-water species resulting in low species diversity and a return to *N. pachyderma* (*s*) dominance (mean 76 %). Despite this, SSTs generally remain warm (mean ~7°C), but with a cold period 19.72 – 19.67 mcd of ~4°C.

Like U1305, the highest foraminiferal concentration is to be found in the latter half of the last interglacial (zones E – F), with high early diversity (zone B) and indications of mid-last interglacial climate instability in zones C and D (reduced diversity, increase in *N. pachyderma* (*s*)), though without showing much decrease in SST estimates.

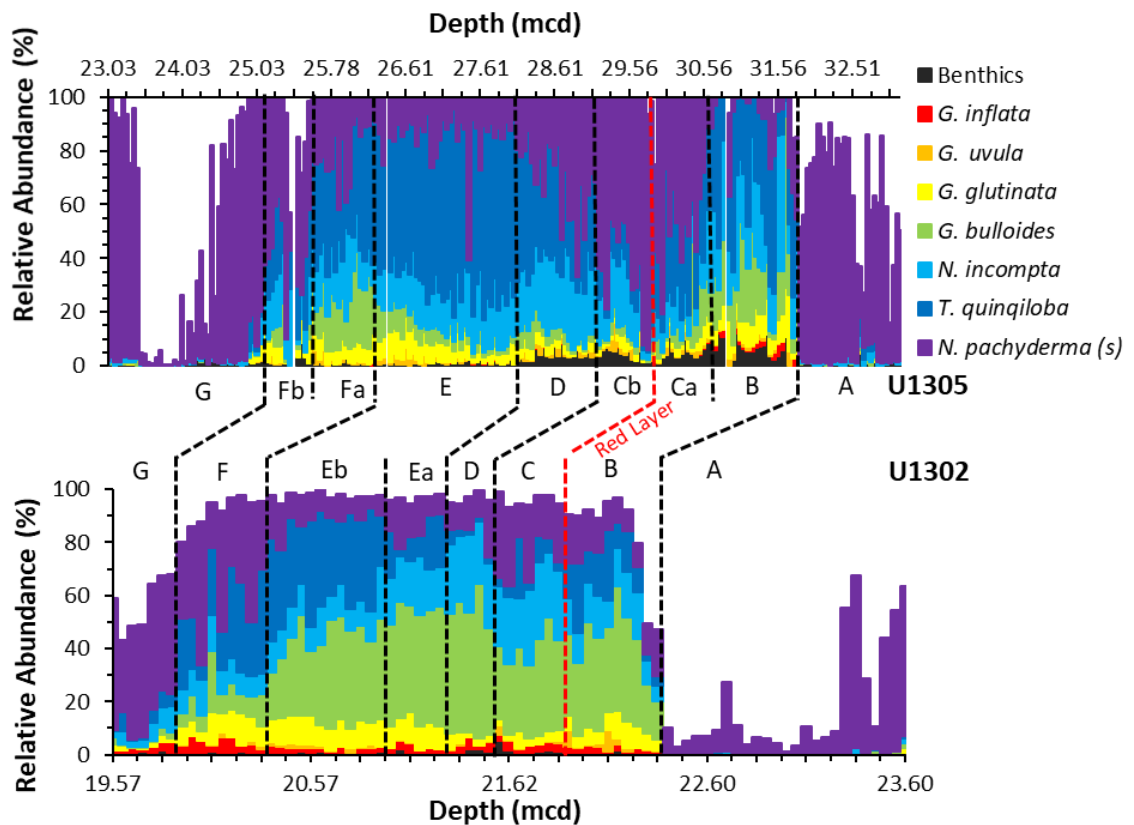


**Figure 5.14** | Proportion of major (i.e. > 2%) foraminifera species percentage abundance in sediment cores U1305 (top) and U1302 (bottom). Also included were benthic species, as a proportion of (planktonic + benthic + IRD). Foraminiferal assemblage zones identified by cluster analysis are indicated, dashed black lines indicate likely correlation of these zones between cores, red dashed line indicates the red layer. Note that, based on the age model of this study, U1302 zones B and F likely correspond with both U1305 zones B and Ca, and zone Fa and Fb, and that U1305 zone E likely corresponds to zones Ea and Eb in U1302.

Finally, an overview of results from both cores are presented in Figure 5.14 showing the relative proportions of major foraminifera species (> 2% relative abundance) as a percentage of entities in the >150 $\mu$ m fraction (planktonic foraminifera) and IRD (area in white). Note that the depth scales and sedimentation rates are very different, therefore foraminiferal assemblage zones have been only roughly correlated between cores, based on the dates obtained from the age model constructed for this study (Table 5.2). Figure 5.13 shows clearly the dominance of *N. pachyderma* (s) through MIS 6b-a (zone A) and 5d-c (zone G), and the dramatic increase in species diversity through the last interglacial. Benthic organisms are also shown in black in Figure 5.14, which are not abundant in U1302, but are most abundant during zone B-D in U1305, with a reduction evident around the position of the red layer, between zones Ca and Cb. The red layer appears to fall within a period of climate deterioration, seen most clearly by the increase to >90% in *N. pachyderma* (s) in U1305. It is also clear from Figure 5.14, however,

that the trend towards cooler temperatures began well above the red layer, from the onset of zone Ca in U1305 at 30.56 mcd.

In both cores, faunal assemblage results indicate extremely cold glacial conditions during zone A, which pertains to the penultimate glacial peak and H11 as indicated by lithological results in the previous chapter. There are indications (increased species diversity leading to warm MAT SSTs) of a warm phase within zone A between 32.81 and 32.61 mcd in U1305, which is discussed in section 8.2.1. Indications from MAT SSTs, peak species diversity in U1302 and peak abundance of *G. inflata* in U1305 are that zone B represents a climate optimum during the very first phase of the last interglacial. The climate deterioration evident throughout zone Ca in U1305, culminating with the red layer, suggests that this outburst flood event was a response to a deterioration in climate rather than a cause, though it seems likely that massive freshwater input could have enhanced and prolonged this cold climate event through impacts on AMOC throughout zone C in U1302 and Cb in U1305. Zone D appears to represent the recovery period from this climate perturbation, and culminates in a long and stable zone E of U1305 (Ea and Eb in U1302), during which indication from faunal abundances are that this represented a second climate optimum during the last interglacial. Unlike zone B, zone E was not associated with high *G. inflata* or benthic organisms in U1305, instead being dominated by *T. quinqueloba* in both cores, suggesting this later climate optimum was of a different character to zone B. A progressively cooler climate during zone F is evident, suggesting changes associated with the glacial inception began within the latter part of MIS 5e. In U1305, because climate deterioration began during zone Fa, well above the enhanced IRD (white space in Figure 5.13) and *N. pachyderma* (*s*) dominance 25.61 – 25.43 mcd indicating the 117 ka event, this suggests the ice rafting event was a consequence of changes in climate rather than a cause. The increase in *G. inflata* towards the top of zone F in U1302 may indicate that the subpolar front was located closer to Orphan Knoll during this time, or potentially that enhanced turbulence was driving more warm-core eddies across the Labrador Sea from the NAC, carrying hapless *G. inflata* within them.

It is interesting to note from Table 5.3 that some examples of tropical and sub-tropical species (e.g. *G. sacculifer*, *G. truncatulinoides*, *G. ruber*, *O. universa*) were found in low abundance in both cores during the last interglacial. These warm-water species can be transported to mid-latitudes by the Gulf Stream. Figure 5.1 shows that summer sea

surface temperatures in the present day range from 0 – 10°C in the Labrador Sea, which is too cold for tropical species. Their low abundance but steady presence suggests they may have reached these cold areas within random currents or warm-core eddies peeling away from the North Atlantic Current. There is often mixing along boundary currents and displacement by eddies that can expatriate species beyond their usual habitat, as discussed in Chapter 2.

## 5.5 | FORAMINIFERA SUMMARY

The first planktonic foraminiferal assemblage data for U1302 and U1305 are presented in this chapter, and are used to derive robust records of summer sea surface temperature variability in both cores. Cluster analysis of these results indicates that the broad pattern of climate evolution is similar across both cores (deglacial, interglacial and glacial inception), though with subtle differences in expression to the north and south of the Labrador Sea, and identifies the red layer as representing a statistically visible division between transitional climate states. The onset of the last interglacial appears to have been very rapid in both cores (within a few hundred years), with the sudden appearance of multiple warm-water species occurring between one sample and the next. In U1305 to the north, the warmest temperatures (~12.3°C) appear to have occurred very early during the last interglacial (~128.4 ka), whilst in U1302 to the south, maximum temperatures were not as high (~10.3°C). The climate would appear to have been more stable in U1302, without the cooling events evident during zones Ca and Cb associated with the red layer (~126.5 ka) (Nicholl et al. 2012) or during zone Fb towards the end of the last interglacial in U1305, perhaps associated with the 117 ka event (Ircalı et al. 2016). The red layer itself would appear to be the culmination of a period of climate deterioration following the early peak warm temperatures in U1305, which was followed by a slow recovery. This suggests the outburst flood event may have been a consequence of wider changes in climate rather than a cause. A series of warm and cold fluctuations during the glacial inception in U1305 are likely related to the series of millennial-scale North Atlantic cold events (e.g. Chapman and Shackleton 1999, Bond et al. 1999, McManus et al. 1994), and possibly to the series of Greenland stadial and interstadial events (North Greenland Ice Core Project Members 2004). The next chapter examines what can be discovered from geochemical analysis of foraminiferal calcite.

*“The first accounts of the discovery of foraminifera are found in the works of Strabo (63 BC - 20 AD) who described specimens of Nummulites from the pyramids of Egypt. Strabo considered them as fossilized lentils which had been used as food by the slaves who constructed the pyramids.”*

**Boltovskoy and Wright (1976, p. 205)**

## 6 | GEOCHEMISTRY

The last chapter presented results from faunal assemblage counts of planktonic foraminifera. The present chapter turns to what can be learned from geochemical analysis of their calcite test. Section 6.1 concerns magnesium-to-calcium ratios (Mg/Ca), which are a proxy for calcification temperature. Methods used to clean and analyse samples are detailed. There follow results from a series of tests performed to assess the reliability and reproducibility of Mg/Ca ratios, along with details of the species-specific transfer functions used to produce the palaeotemperature estimates. Results from multiple foraminifera species are then given. Mg/Ca analyses had not been performed in U1302 or U1305 before and present a useful geochemical estimate of palaeotemperatures, which supplements the faunal assemblage MAT estimates from the previous chapter. Section 6.2 introduces barium-to-calcium ratio (Ba/Ca), which were not a major focus of this study but provide supplementary information on rates of meltwater runoff in the absence of direct ice rafting (i.e. glacier melting inland). Finally, section 6.3 introduces stable carbon and oxygen isotopes. Additional samples were analysed for this study to infill gaps in the original planktonic isotope stratigraphy of Hillaire-Marcel et al. (2011). Also, an entirely new benthic  $\delta^{18}\text{O}$  record was produced for U1305. These geochemical data are invaluable for the age model, which forms the focus of the following chapter.

### 6.1 | Mg/Ca RATIOS

Since the ratio between seawater magnesium and calcium are nearly constant, Chave (1954) showed that the varying magnesium-to-calcium ratio (Mg/Ca) of foraminiferal tests was dependent upon ambient water temperature during calcification. Foraminifera form their skeletons out of calcite, a trigonal polymorph of calcium carbonate ( $\text{CaCO}_3$ ). Within the flexible corner-sharing molecular structure of the calcite lattice, calcium ions (ionic radius: 1.00 Å) can be substituted by divalent cations of a similar radius, including magnesium (0.72 Å) and barium (1.35 Å) (Katz 1973). Katz (1973) showed that Mg incorporation during inorganic calcite precipitation is temperature dependent. However, the concentration of Mg during inorganic precipitation of calcite is an order of magnitude higher than that found in biogenic calcite, due to vital effects (physiological processes that alter the expected chemistry of the test).

Over the last 30 years, scores of sediment trap (e.g. Anand et al. 2003; McConnell and Thunell 2005; Gibson et al. 2016; Gray et al. 2018), coretop (e.g. Brown and Elderfield 1996; Elderfield and Ganssen 2000; Anand and Elderfield 2005; Kozdon et al. 2009; Farmer et al. 2010), plankton tow (e.g. Sadekov et al. 2008; Martínez-Botí et al. 2011; van Raden et al. 2011; Friedrich et al. 2012; Marr et al. 2013), and laboratory culture experiments (e.g. Nürnberg et al. 1996; Lea et al. 1999; Bemis et al. 2000; Anand et al. 2003; Russell et al. 2004; Hönisch et al. 2011; Allen et al. 2016) and combinations thereof (e.g. Delaney et al. 1985), have established an empirical (usually exponential) relationship between foraminiferal Mg/Ca and calcification temperature. This term is used rather than inferring sea surface temperatures, to remove uncertainties concerning depth habitat and differing seasonality. Temperature estimates are typically quoted with an uncertainty of  $\pm 1^\circ\text{C}$  (Lea et al. 1999; Anand et al. 2003; McConnell and Thunell 2005; Von Langen et al. 2005). Mg/Ca ratios were obtained from three species in U1305, usually associated with surface (*G. bulloides*) and mid-depth (*N. incompta*) waters, and the pycnocline (*N. pachyderma (s)*). In U1302, only *G. bulloides* and *N. pachyderma (s)* were used due to a lack of material.

### 6.1.1 | Picking

Samples were dry sieved for specific size fractions, scattered onto a tray and picked under a binocular light microscope. Table 6.1 shows the preferred size fraction and number of individuals picked for Mg/Ca analysis, which varied by species depending on test size and thickness to ensure sufficient calcite would remain after the cleaning process. Size fractions are discussed further in section 6.1.6. Only complete shells without holes, yellow/orange staining or black particles were chosen, to minimise

Table 6.1 | Preferred size fractions and number of each foraminifera species picked for Mg/Ca analysis. Where insufficient individuals were found, smaller size fractions and/or numbers were used instead.

Species	Size Fraction ( $\mu\text{m}$ )	Number of Individuals
<i>G. bulloides</i>	300-355	40
<i>N. incompta</i>	250-300	50
<i>N. pachyderma (s)</i>	250-300	40

diagenetic or sedimentary contamination. Further tests were performed to ascertain what effect picking “dirty” foraminifera from samples with insufficient clean whole individuals would have on Mg/Ca ratios (section 6.1.6.4).

The procedure is based on the method of Barker et al. (2003), derived from methods originally developed for Cd/Ca and Ba/Ca analysis (Boyle 1981; Boyle and Keigwin 1985; Lea and Boyle 1991). Samples were cleaned in batches of 16 using reagents made up from Aristar concentrated stock and Milli-Q H<sub>2</sub>O for dilution. Procedural blanks were included in some batches to ensure no contamination was introduced. Samples were first gently crushed in excess water between two clean glass microscope slides to open chambers and facilitate cleaning whilst avoiding over-crushing into fine particles, which would result in the excessive loss of carbonate during cleaning. Samples were then viewed over white paper and obvious contaminants removed, before being transferred to an acid cleaned vial. There are four sequential steps to the cleaning process: (1) clay removal, (2) oxidation of organic matter, (3) removal of coarse silicates, (4) dilute acid “polish” to remove adsorbed contaminants. A corrosive reductive step sometimes used in the cleaning process was not employed in this study, as it was found to cause partial dissolution the fragile calcite tests, with a consequent reduction in Mg/Ca ratios of around 10 – 15% (Barker et al. 2003).

## 6.1.2 | Cleaning

### 6.1.2.1 | Clay Removal

Much marine sediment is composed of clay minerals containing around 1 – 10% Mg by weight, which must be removed to obtain a reliable foraminiferal Mg/Ca ratio (Barker et al. 2003). A minimum of 5 Milli-Q water washes were performed (or more, if clay was still visible in suspension). 500 µl of Milli-Q was added to a sample and “minimal settling” allowed, whereby large carbonate particles were allowed to settle out (~30 seconds), then the overlying fluid was quickly removed leaving 10 – 20 µl containing the carbonate particles at the bottom of the vial. Clays and fine silicate material were separated from test surfaces and brought into suspension by 1 – 2 minutes in an ultrasonic bath between washes. Then two 250 µl washes of low-viscosity methanol were performed in the same manner to dislodge any remaining clays. This was followed by two water washes to remove the methanol.

### 6.1.2.2 | Organic Matter Oxidation

Organic material may contain Mg or clays trapped within the organic matrix. This was removed by oxidation in 250 µl alkali-buffered (NaOH) solution of 1% H<sub>2</sub>O<sub>2</sub> at 100°C for 10 minutes. At 2.5 and 7.5 minutes, samples were tapped on the bench to dislodge CO<sub>2</sub> bubbles, and at 5 minutes samples were placed in an ultrasonic bath for a few seconds, to maintain contact between the carbonate particles and the reagent. The reagent was then removed and the process repeated, followed by two water washes.

### 6.1.2.3 | Coarse Silicate Removal

Silicate grains can leach during acid dissolution or enter the plasma during analysis, with the potential to influence Mg/Ca ratios. This can be a particular issue in samples which contain a large proportion of ice rafted debris which can get inside the test chambers. To remove large grains which settle too quickly to be removed during clay cleaning, samples were viewed under a light microscope over both light and dark backgrounds and any non-carbonate particulates, as well as discoloured carbonate, were removed with a fine hair brush.

### 6.1.2.4 | Dilute Acid Leach

A weak acid “polish” was used to dislodge any contaminants which had adsorbed to the carbonate fragments during the cleaning process. 250 µl of 0.001 M HNO<sub>3</sub> was added, samples were then placed in the ultrasonic bath for 30 seconds. The acid was removed, followed as quickly as possible by two water washes in order to prevent excess dissolution. Any remaining liquid was then carefully removed using a small pipette tip. Samples were then stored until analysis.

## 6.1.3 | ICP-OES Analysis

Samples were analysed using a Varian Vista Inductively Coupled Plasma Optical Emission Spectrographer (ICP-OES) at the University of East Anglia. Analytical error of a laboratory standard solution (mean Mg/Ca = 2.073 mmol/mol, mean Ca concentration = 110 ppm) run at least six times in parallel with each batch was 0.056 mmol/mol (1  $\sigma$ ).

### 6.1.3.1 | Dissolution

On the day of analysis samples were dissolved in 500 µl of 0.075M HNO<sub>3</sub>, using an ultrasonic bath to enhance the reaction. Samples were agitated to remove CO<sub>2</sub> build-up until dissolution was complete. Samples were then centrifuged at 5000 rpm for 5 minutes to separate any solid contaminants, and the dissolved samples transferred to clean vials. A five-fold dilution of each sample was then prepared (50 µl of sample in 200 µl of Milli-Q H<sub>2</sub>O) for initial analysis of Ca concentration on the ICP-OES.

### 6.1.3.2 | ICP-OES Analysis

The ICP-OES was run for an hour to stabilise using the same 0.075M HNO<sub>3</sub> as for dissolution, before calibration with a series of standards of precise Ca and Mg concentrations, and contaminant standards. Vial blanks were analysed before sample dissolution to ensure no contaminants were present. The five-fold dilutions were analysed to determine the initial Ca concentration in each sample. Using this, a dilution factor (i.e. the exact quantity of both sample and acid) was calculated to achieve a solution of known carbonate concentration. Standards were available for 100 ppm, 60 ppm, 40ppm and 20 ppm (with 60 ppm being the preferred concentration as this was found to be the most accurate). Ratios were calculated directly from the intensity ratios to correct for any matrix effect using the method of de Villiers et al. (2002).

### 6.1.3.3 | Contaminants

The presence of contaminants was monitored using Fe and Al values (Barker et al. 2003). Table 6.2 summarises the screening criteria. Out of all 416 samples, 22 were omitted due to Al or Fe contamination. Additionally, any samples having Ca concentrations of < 15 ppm or fewer than 20 foraminifera per sample were omitted, as insufficient calcium was found to be present.

**Table 6.2** | Criteria used to screen samples for contaminant phases of clay or silicate which could compromise Mg/Ca ratios (Barker et al. 2003).

Elemental ratio	Threshold for contamination (mmol/mol)	Mean sample ratio (mmol/mol)
Al/Ca	0.4	0.074
Fe/Ca	0.4	0.139
Fe/Mg	0.2	0.085

## 6.1.4 | Temperature Calibration

A transfer function is a mathematical equation which defines the relationship between the measurable (foraminiferal Mg/Ca) and the unmeasurable (past seawater temperature). This is a thermodynamic relationship, but vital effects cause substantial differences between species due to physiological factors. Figure 6.1 illustrates a range of different transfer functions obtained through different approaches. Although multi-species transfer functions exist (e.g. Anand et al. 2003), differences in depth habitat and seasonality mean species-specific calibration is preferable. Uncertainty is usually quoted as  $\pm 1^\circ\text{C}$  (Lea et al. 1999; Anand et al. 2003; McConnell and Thunell 2005; Von Langen et al. 2005).

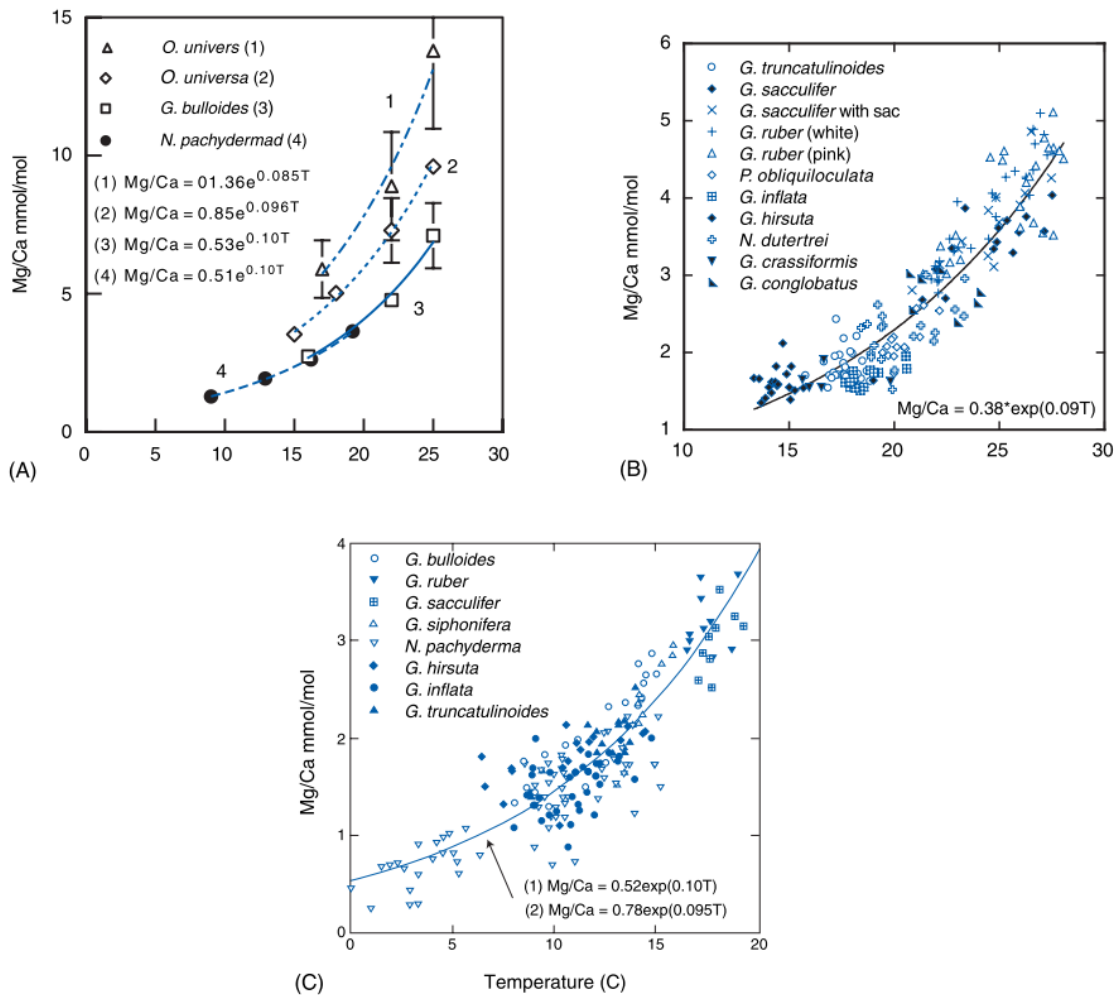


**Figure 6.1** | Illustration of Mg/Ca calibrations from (A) laboratory culture including *G. bulloides* (Lea et al. 1999) and *N. incompta* (Von Langen et al. 2005), (B) Sargasso Sea sediment traps, (C) coretops including *G. bulloides* and *N. incompta* (shown as *N. pachyderma d*) (Elderfield and Ganssen 2000) (Rosenthal and Linsley 2007).

#### 6.1.4.1 | *G. bulloides*

Several transfer functions have been published for *G. bulloides* (Lea et al. 1999; Mashiotta et al. 1999; Elderfield and Ganssen 2000; Barker and Elderfield 2002; McConnell and Thunell 2005). To determine the most appropriate, coretop samples from U1305 were analysed for Mg/Ca and compared to average ocean atlas values at the typical depth of *G. bulloides* (0 – 30 m depth) (Bauch and Kandiano 2007) between June – September when they typically bloom (Schiebel et al. 1997) which was 7.8°C (World Ocean Atlas 1998). The closest value (8.5°C) was obtained using the transfer function of Barker and Elderfield (2002), which was therefore used in this study:

$$\text{Mg/Ca (mmol/mol)} = 0.72 \exp(0.10T)$$

#### 6.1.4.2 | *N. incompta*

The majority of early studies considered *N. incompta* to be the dextral form of *N. pachyderma (s)*, which genetic studies have since shown to be a different species (Darling et al. 2006). Due to difficulties in laboratory culturing, only one species-specific transfer function (derived from culture experiments) was found for *N. incompta*, therefore the transfer equation of von Langen et al. (2005) was used:

$$\text{Mg/Ca (mmol/mol)} = 0.51 \exp(0.10T)$$

#### 6.1.4.3 | *N. pachyderma (sinistral)*

Several calibrations are available for *N. pachyderma (s)* (e.g. Elderfield and Ganssen 2000; Nürnberg et al. 2000; Kozdon et al. 2009). Most Mg/Ca transfer functions are exponential (Figure 6.1) and tend to be derived from much warmer waters than are typical in the Labrador Sea (e.g. Nürnberg et al. 1996). Since at low temperatures this relationship approaches a straight line, Kozdon et al. (2009) derived a linear equation for *N. pachyderma (s)* using coretops from the Nordic Seas, which is more accurate for high latitudes. Figure 6.2 shows that using the independently-derived temperature estimate from  $\delta^{44/40}$  (rather than ocean atlas data or  $\delta^{18}\text{O}$  temperatures), a more accurate

calibration can be obtained for the temperature range  $\sim 3 - 6^\circ\text{C}$  by a linear equation, which was adopted for this study:

$$\text{Mg/Ca (mmol/mol)} = 0.13T + 0.35$$

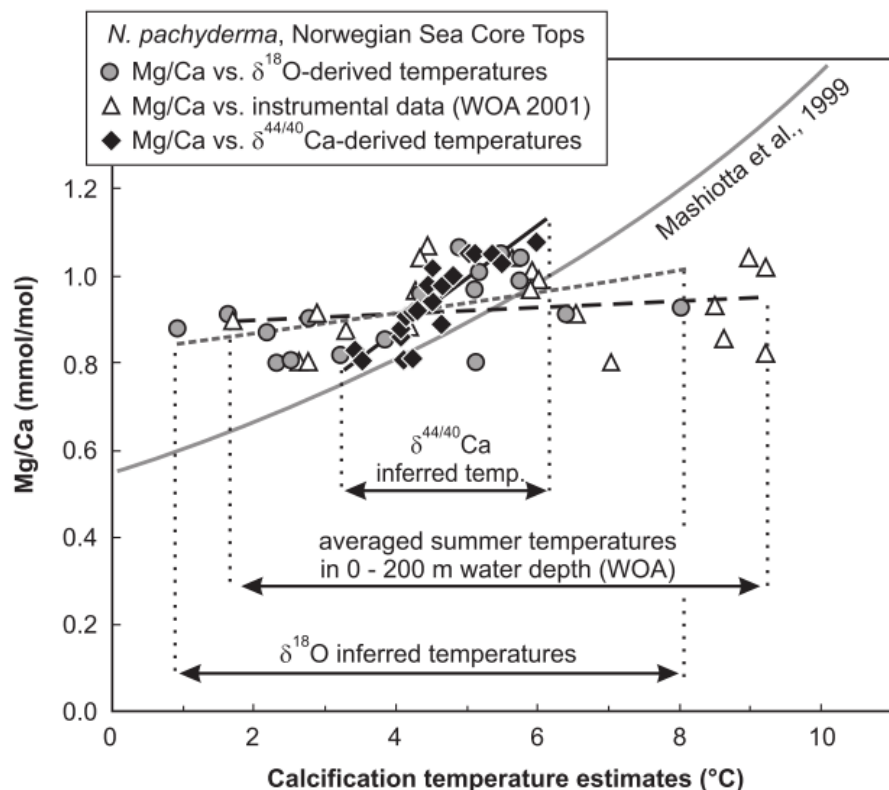


**Figure 6.2** | Comparison between Mg/Ca ratios in *N. pachyderma* (*s*) and estimates of calcification temperature from (A)  $\delta^{18}\text{O}$  temperatures (circles) (B) modern July – Sept 0 – 200 m SST (triangles) and (C)  $\delta^{44/40}\text{Ca}$  (diamonds) (Kozdon et al. 2009).

#### 6.1.4.4 | Other Controls on Mg/Ca Ratios

Several field and laboratory studies have examined whether other environmental criterion to temperature, such as pH and seawater carbonate ion concentration ( $[\text{CO}_3^{2-}]$ ), dissolved inorganic carbon (DIC) or salinity (Nürnberg et al. 1996; Ferguson et al. 2008), may cause variations in foraminiferal Mg/Ca ratios (e.g. Lea et al. 1999; Anand and Elderfield 2003; Russell et al. 2004). Although Gibson et al. (2016) concluded from a sediment trap study that low pH and  $[\text{CO}_3^{2-}]$  values can cause higher Mg/Ca ratios due to a high-Mg secondary coating of inorganic carbonate, particularly in high-productivity low-oxygen environments, their data was taken from the eastern tropical North Pacific where conditions are quite different to the North Atlantic. In their recent study of trace element inclusions in planktonic foraminifera, Allen et al. (2016)

confirmed in culture experiments that temperature was the major factor controlling foraminiferal Mg/Ca. They conclude that since there is a relatively small potential effect from changes in salinity and  $[\text{CO}_3^{2-}]$ , corrections to Mg/Ca ratios are not recommended, at least in the tropical species covered, which included *G. bulloides*.

Another complication is the observation from core-top samples that foraminiferal Mg/Ca ratios can be lowered by dissolution below the lysocline (Russell et al. 1994; Brown and Elderfield 1996; Rosenthal et al. 2000). This preservation bias can result in underestimation of palaeotemperatures (Mekik et al. 2007). A ranking of the susceptibility of planktonic foraminifera species in the high latitude South Atlantic Ocean using a dissolution index found *N. pachyderma (s)* to be the most resistant, *G. bulloides* was average with *N. incompta* slightly more susceptible, although not the most susceptible in the study (Malmgren 1983). However, both U1305 and U1302 cores were recovered from above the lysocline, also dissolved strontium values within both core sediments were at or below seawater values, which indicates very little carbonate dissolution in either core (Channell et al. 2006).

### 6.1.5 | Vial Blanks

Samples were stored, cleaned, dissolved and analysed within acid cleaned 500  $\mu\text{l}$  thin-walled vials. The cleaning process involved soaking for >24 hours in 10%  $\text{HNO}_3$ , then five Milli-Q rinses. Vials were then dried within a fume hood, closed, and stored in sealed bottles in a covered container within the clean lab. Six vial blanks were analysed per ICP-OES run in order to check that the vials and reagents used were clean.

However, prior to running the first batch of samples, unusually high vial blank Ca concentrations (>1 ppm) were observed (typical values were ~0.05 ppm Ca). The clean lab was thoroughly cleaned, after which an experiment was designed to investigate the vial cleaning and drying procedure. Vials were acid cleaned and dried horizontally to minimise dust contamination. Five drying locations were tested:

1. In the open upon the central bench
2. Within a lidded container upon the central bench
3. Within a fume cupboard
4. Within a laminar flow cupboard
5. Within a laminar flow cupboard under an infrared lamp

Drying times at each location were checked hourly (Figure 6.3). Vials were then analysed on the ICP-OES using 250 µl of clean 0.075 M HNO<sub>3</sub> alongside freshly washed vials that were not dried. Results show that vials dried within the laminar flow hood had the lowest mean Ca content (Table 6.3). This is attributed to the fact that vials in the laminar flow cupboard dried the quickest (90% dry within 1 hour, all within 3 hours) (Figure 6.3).

**Table 6.3** | Results from the vial blank cleaning test, showing Ca concentration under five different test drying conditions, and freshly washed vials that were not dried.

Drying conditions	Mean Ca (ppm)	Standard Deviation
On open bench	0.029	0.011
In lidded container	0.019	0.016
Fume cupboard	0.024	0.043
Laminar flow cupboard	0.016	0.005
Laminar flow under infrared	0.027	0.015
Freshly washed vials	0.024	0.026

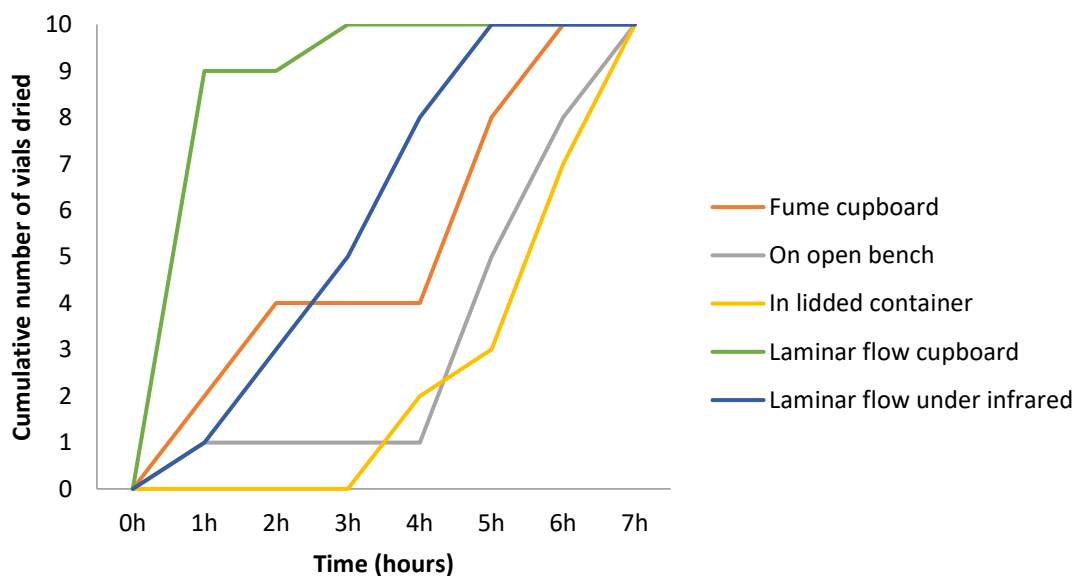


**Figure 6.3** | The effect of drying location upon the drying time of 10 acid cleaned vials.

To test whether reagents were contaminated, 18 procedural blanks were analysed. Mean Ca concentration was 0.011 ppm (0.01 1σ), with a maximum value of 0.036 ppm. This is well within acceptable Ca levels (0.05 ppm), therefore reagents were found to be clean. As a result of these tests, vials were subsequently all dried in the laminar flow cupboard, closed and stored as soon as possible. Additionally, vial blanks were run before sample dissolution on the day of analysis, to ensure they were clean.

## 6.1.6 | U1305 Size Fraction Tests

Mg/Ca ratio can be affected by differing depth preferences during ontogeny, whereby early in their lifespan many species of foraminifera live (and calcify) near the surface, but as they mature some species (notably *N. pachyderma (s)*) descend in the water column, putting on a covering of gametogenic calcite (Darling et al. 2006). Whole-test ICP-OES analysis would therefore reflect differing temperatures depending on whether juveniles (reflecting warm surface temperatures) or adults (reflecting deep cold temperatures) were used. Several studies have shown a size-dependent fractionation can impact Mg/Ca ratios (e.g. Anand et al. 2003; Cléroux et al. 2008; Elderfield et al. 2002). Therefore, specific size fractions were picked for Mg/Ca analysis (Table 6.1). However, insufficient individuals were found within some samples, even after scavenging from faunal assemblage slides, particularly though the critical early last interglacial section. To address this problem, and to determine whether smaller size fractions could be used to fill gaps in the data, a series of tests were performed using coretop samples. A comparison was made between size fractions within typical glacial and typical interglacial conditions (section 6.1.6.1). To test for reproducibility of results, multiple samples from different size fractions within two coretop samples (0 – 2 cm and 5 – 7 cm) from U1305 were analysed for *G. bulloides* (section 6.1.6.2) and *N. pachyderma (s)* (section 6.1.6.3). Coretop Mg/Ca values were also used to help choose the most appropriate transfer function (section 6.1.4), though insufficient *N. incompta* were found for analysis. An investigation of “clean” vs “dirty” foraminifera was made (section 6.1.6.4). Downcore results are presented separated by size fraction (section 6.1.6.5) and the results are summarised (section 6.1.6.6).

### 6.1.6.1 | Glacial vs Interglacial samples

Different size fractions of *N. pachyderma (s)* from samples representing typical glacial (32.36 mcd) and interglacial (26.01 mcd) periods in U1305 were analysed for Mg/Ca. Three replicate samples from small (150 – 250 µm, 60 individuals), medium (212 – 250 µm, 50 individuals) and large (250 – 300 µm, 40 individuals) size fractions were used. Results are summarised in Figure 6.4, which shows that for interglacial conditions, the larger size fraction produced a higher Mg/Ca ratio. The large group was statistically different from the medium group ( $t(3) = 3.205$ ,  $p = 0.0491$ ), and whilst not statistically

different from the small group ( $t(3) = 3.1656, p = 0.0507$ ) this effect could still influence palaeotemperature estimates by up to  $3^{\circ}\text{C}$ . The differences were lower during glacial conditions, with similar mean temperature estimates ( $\sim 2^{\circ}\text{C}$ ) that are not statistically different from each other. Full details are presented in Table 6.4. This result was unexpected, since larger adults were expected to descend to the colder pycnocline upon maturation, and therefore represent colder temperatures.

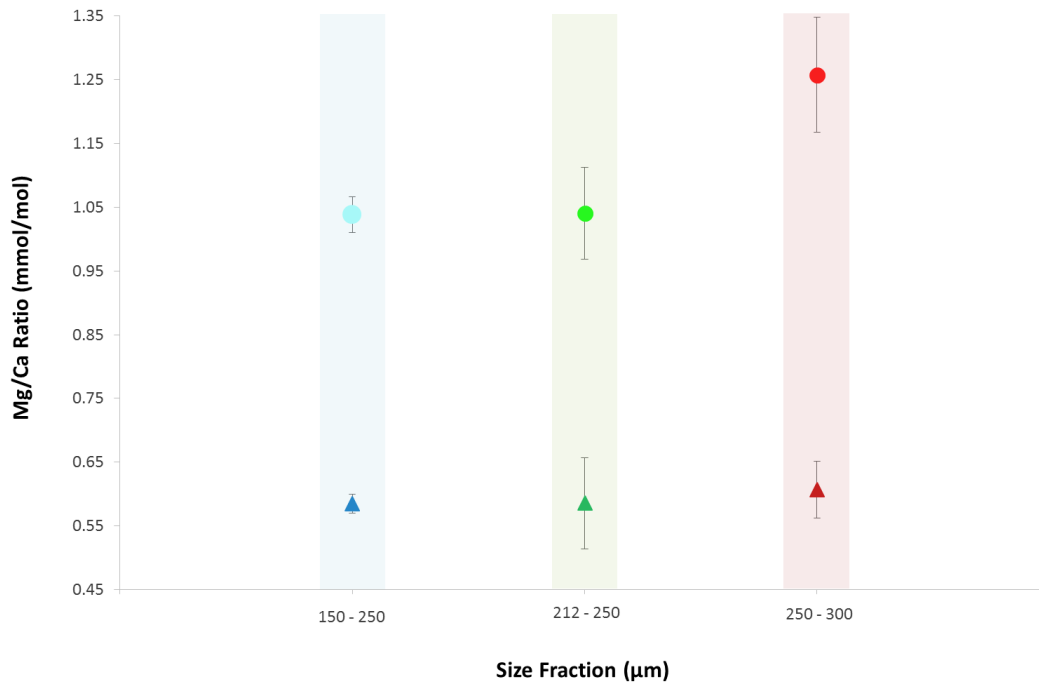


**Figure 6.4** | Size fraction tests for typical interglacial (circles) and glacial (triangles) conditions using *N. pachyderma* (*s*) from sediment core U1305. Three replicates were picked for each sample,  $1\sigma$  error bars are shown.

**Table 6.4** | Summary statistics for size fraction tests representing typical interglacial (26.01 mcd) and glacial (32.36 mcd) samples using *N. pachyderma* (*s*) from sediment core U1305.

Depth (mcd)	Size fraction (µm)	Number of replicates	Mean Mg/Ca (mmol/mol)	Mg/Ca Standard deviation	Standard Error	Mean temperature ( $^{\circ}\text{C}$ )	Temperature standard deviation ( $^{\circ}\text{C}$ )
26.01	250-300	3	1.258	0.091	0.052	7	0.7
26.01	212-250	3	1.041	0.072	0.042	5	0.6
26.01	150-250	3	1.038	0.028	0.016	5	0.2
32.36	250-300	3	0.607	0.044	0.025	2	0.3
32.36	212-250	3	0.586	0.072	0.041	2	0.6
32.36	150-250	3	0.585	0.015	0.009	2	0.1

### 6.1.6.2 | *G. bulloides* Coretop Samples

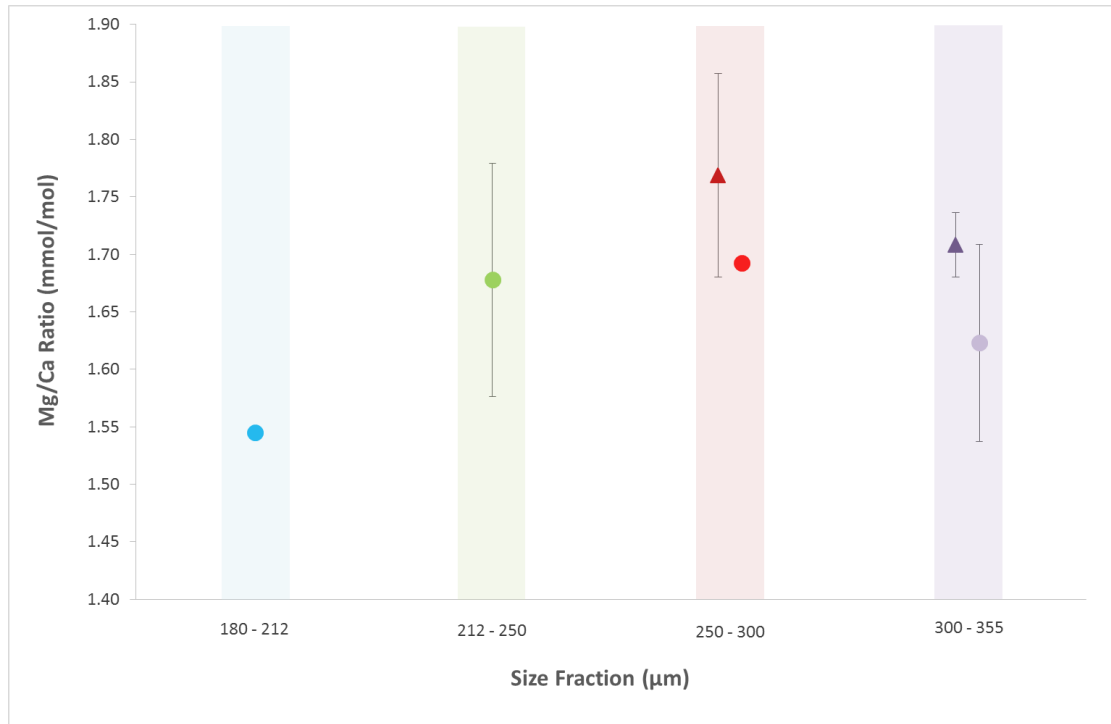


**Figure 6.5** | Replicate analyses for four *G. bulloides* size fractions from U1305 coretop samples. Triangles represent 0 – 2 cm depth, and circles represent 5 – 7 cm depth; the two depths are slightly offset along the x-axis for clarity. Error bars show 1σ where applicable.

The smallest size fraction produced a low Mg/Ca ratio, although in this case the largest size fraction (300 – 355 µm) was slightly lower than the next size down (250 – 300 µm), which was unexpected. However, none of the size fractions were found to be statistically different from any other (Table 6.5). The mean coretop (0 – 2 cm) calcification temperature of all 6 *G. bulloides* test samples in all size fractions was  $8.9 \pm 0.4^\circ\text{C}$ . This was the same (within  $\pm 1^\circ\text{C}$  error) as ocean atlas summer (July – Sept) surface (0 – 30 m) temperatures of  $8^\circ\text{C}$  (World Ocean Atlas 1998), and the MAT coretop SST estimate of  $8.5 \pm 1.4^\circ\text{C}$  (section 5.4.2). The similarity between results from these two very different proxy techniques and the measured ocean atlas value provides strong support for both techniques, and strengthens confidence in the interpretations based upon the data produced for this study.

**Table 6.5** | Summary statistics for size fraction tests using *G. bulloides* from U1305 coretop samples

Dept h (cm)	Size fraction ( $\mu\text{m}$ )	Number of replicates	Mean Mg/Ca (mmol/mol)	Mg/Ca Standard deviation	Standard Error	Mean temperature ( $^{\circ}\text{C}$ )	Temperature standard deviation ( $^{\circ}\text{C}$ )
0 - 2	300-355	2	1.708	0.028	0.020	8.6	0.2
0 - 2	250-300	2	1.769	0.089	0.063	9.0	0.5
0 - 2	212-250	1	1.854	-	-	9.5	-
0 - 2	180-212	1	1.676	-	-	8.5	-
5 - 7	300-355	3	1.623	0.085	0.049	8.1	0.5
5 - 7	250-300	2	1.693	0.004	0.003	8.5	0.1
5 - 7	212-250	2	1.678	0.101	0.072	8.5	0.6
5 - 7	180-212	1	1.545	-	-	7.6	-

### 6.1.6.3 | *N. pachyderma* (s) Coretop Samples

For *N. pachyderma* (s), in addition to investigating size fractions, a distinction was made between normal “clean” individual tests, and “dirty” individuals that would usually be rejected during picking, to see if this approach influenced results (Figure 6.6). There were no statistically significant differences between different size fractions for 0 - 2 cm samples, as determined by one-way ANOVA ( $F(2,35) = 2.277$ ,  $p = 0.118$ ). However, the 180 – 212  $\mu\text{m}$  size fraction from the 5 – 7 cm depth was statistically different from both the 212 – 250  $\mu\text{m}$  ( $t(24) = 4.280$ ,  $p = 0.001$ ), and the 250 – 300  $\mu\text{m}$  ( $t(17) = 4.551$ ,  $p = 0.001$ ) size fractions. When results from both depths were pooled, there was also a significant difference between size fractions, as determined by one-way ANOVA ( $F(2,74) = 7.615$ ,  $p = 0.001$ ). Again, it appears that the larger size fraction produced the highest Mg/Ca results, which was contrary to expectations, although in this case the “dirty” foraminifera from the smallest size fraction did produce high Mg/Ca results also (discussed below). The results from this size fraction test show that for the 0 – 2 cm sample, no difference in calcification temperature was observed between size fractions. For the 5 – 7 cm sample, temperature differences were seen (250 – 300  $\mu\text{m} = 6^{\circ}\text{C}$  vs 180 – 212  $\mu\text{m} = 4^{\circ}\text{C}$ ), however these values are still within the typical uncertainty envelopes surrounding Mg/Ca palaeothermometry of  $\pm 1^{\circ}\text{C}$  (Table 6.6). Therefore, although a size fraction effect was observed, it was unlikely to influence results beyond the usual uncertainty range. Mean calcification temperature of

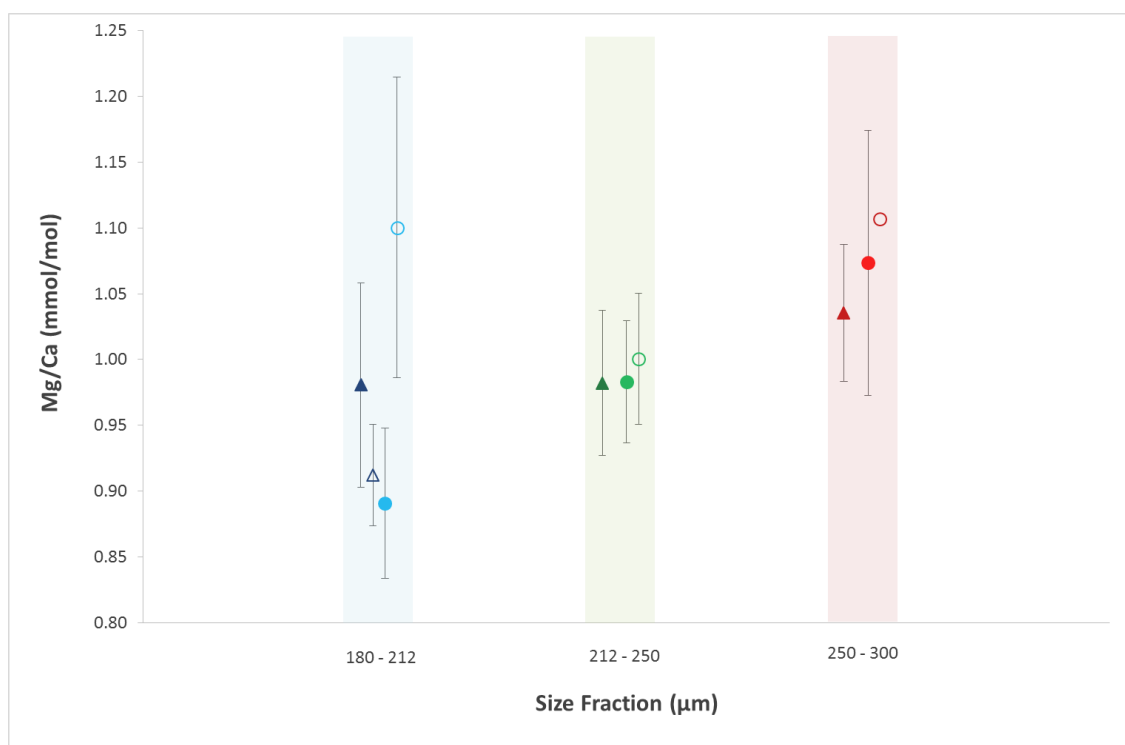


**Figure 6.6** | Replicate analyses for three different size fractions using *N. pachyderma* (*s*) from the coretop of sediment core U1305. Triangles represent 0 – 2 cm depth, and circles represent 5 – 7 cm depth; the two depths are slightly offset along the x-axis for clarity. Filled markers represent “clean” foraminifera without obvious staining or chamber fill that would typically be preferentially picked, whilst open symbols show “dirty” foraminifera with black infill or stained carbonate that would usually be avoided; both were cleaned according to the usual protocol. Error bars show 1σ where applicable.

**Table 6.6** | Summary statistics for surface replicate Mg/Ca analyses using different size fractions of *N. pachyderma* (*s*) from the coretop of sediment core U1305. Temperature calibration used is that of Kozdon et al. (2009).

Depth (cm)	Size fraction (µm)	Number of replicates	Mean Mg/Ca (mmol mol <sup>-1</sup> )	Standard deviation	% RSD	Standard Error	Mean temperature (°C)	Temperature standard deviation (°C)
0 – 2	250 - 300	4	1.036	0.05	5.0	0.03	5	0.4
0 – 2	212 - 250	13	0.982	0.06	5.6	0.02	5	0.4
0 – 2	180 - 212	15	0.981	0.08	7.9	0.02	5	0.6
5 – 7	250 - 300	3	1.073	0.10	9.4	0.06	6	0.8
5 – 7	212 - 250	10	0.983	0.05	4.8	0.02	5	0.4
5 – 7	180 - 212	16	0.891	0.06	6.4	0.01	4	0.4
Pooled Results		61	0.991	0.08	7.9	0.01	5	0.5

32 clean coretop (0 – 2 cm) samples across all size fractions was  $4.9 \pm 0.5^\circ\text{C}$ . This was the same (within  $\pm 1^\circ\text{C}$  error) as ocean atlas spring to early summer (March - July) mid-depth (0 – 200 m) temperature of  $4^\circ\text{C}$  (World Ocean Atlas 1998) typically associated with peak *N. pachyderma* abundance (Jonkers et al. 2010).

#### 6.1.6.4 | “Clean” versus “Dirty” Foraminifera

To investigate whether Mg/Ca ratios would differ from the usual “clean” foraminifera analysed above (whole white individuals with little or no chamber fill or staining), the most “dirty” individuals were analysed from the coretop samples. This would determine whether, for samples where only dirty individuals were available, analyses could still be made. Table 6.7 contains a summary results from “dirty” foraminifera. It is worth noting that of the “dirty” foraminifera, none were rejected due to contaminant phases. The thresholds used to indicate clay or ferro-manganese contamination were Al/Ca  $0.4 \text{ mmol/mol}^{-1}$ , Fe/Ca  $0.4 \text{ mmol/mol}^{-1}$  and Fe/Mg  $0.2 \text{ mmol/mol}^{-1}$  (Barker et al. 2003). It can be seen in Table 6.7 that mean Al/Ca was  $0.057 \text{ mmol/mol}^{-1}$ , mean Fe/Ca was  $0.077 \text{ mmol/mol}^{-1}$  and mean Fe/Mg was  $0.070 \text{ mmol/mol}^{-1}$ , all well below the thresholds for contamination.

**Table 6.7** | Summary statistics for surface replicate Mg/Ca analyses of “dirty” specimens of *N. pachyderma* (*s*) subject to the usual cleaning protocol from the coretop of sediment core U1305. Temperature calibration used is that of Kozdon et al. (2009).

Depth (cm)	Size fraction ( $\mu\text{m}$ )	Number of replicates	Mean Mg/Ca ( $\text{mmol mol}^{-1}$ )	Standard deviation	Mean Al/Ca ( $\text{mmol mol}^{-1}$ )	Mean Fe/Ca ( $\text{mmol mol}^{-1}$ )	Mean Fe/Mg ( $\text{mmol mol}^{-1}$ )	Mean temperature ( $^\circ\text{C}$ )	Temperature standard deviation ( $^\circ\text{C}$ )
0 – 2	180 - 212	7	0.912	0.04	0.029	0.042	0.044	4	0.3
5 – 7	250 - 300	1	1.107	N/A	0.069	0.101	0.088	6	N/A
5 – 7	212 - 250	4	1.001	0.05	-0.002	0.032	0.031	5	0.4
5 – 7	180 - 212	4	1.100	0.11	0.133	0.132	0.115	6	0.9
Pooled Results		16	1.030	0.10	0.057	0.077	0.070	5	0.8

Results show that across all size fractions, mean Mg/Ca was  $1.030 \pm 0.1$  mmol mol<sup>-1</sup> for dirty foraminifera, and  $0.991 \pm 0.08$  mmol mol<sup>-1</sup> for clean foraminifera. These results are identical within error. This suggests the cleaning procedure was sufficient to remove contamination, even in individuals that were observed to contain detritus or staining. The smallest (180 – 212 μm) dirty size fraction from the 5 – 7 cm depth produced a calcification temperature 2°C higher than the clean foraminifera, indicating that contamination is more of an issue for smaller individuals. This would be logical since they have thinner test walls and contain less carbonate, and suggests that avoiding “dirty” foraminifera is best practice to avoid contamination, particularly for small size fractions, but may not produce significantly different results providing the usual cleaning procedure is employed.

#### 6.1.6.5 | Mg/Ca Results by Size Fraction

Given the caveats about size fraction effects discussed above, down-core Mg/Ca values were plotted to show where smaller size fractions had been used. Results show that particularly for *G. bulloides* (Figure 6.7) and *N. incompta* (Figure 6.8) values from the smaller size fractions generally produce Mg/Ca ratios in keeping with the larger size fraction. Even the cluster of very low values above 23.50 mcd are not as low as a large size fraction sample from the same interval, suggesting these values are not unreliable, but instead reflect a cold environment. *N. incompta* small samples are very much in line with the larger size fraction (Figure 6.8). Although in the *N. pachyderma* (*s*) results (Figure 6.9) the smaller size fractions were responsible for some of the lower Mg/Ca ratios, they also produced some of the higher ones and were generally in keeping with the range of variability of the larger size fractions, suggesting this is not a systematic offset.

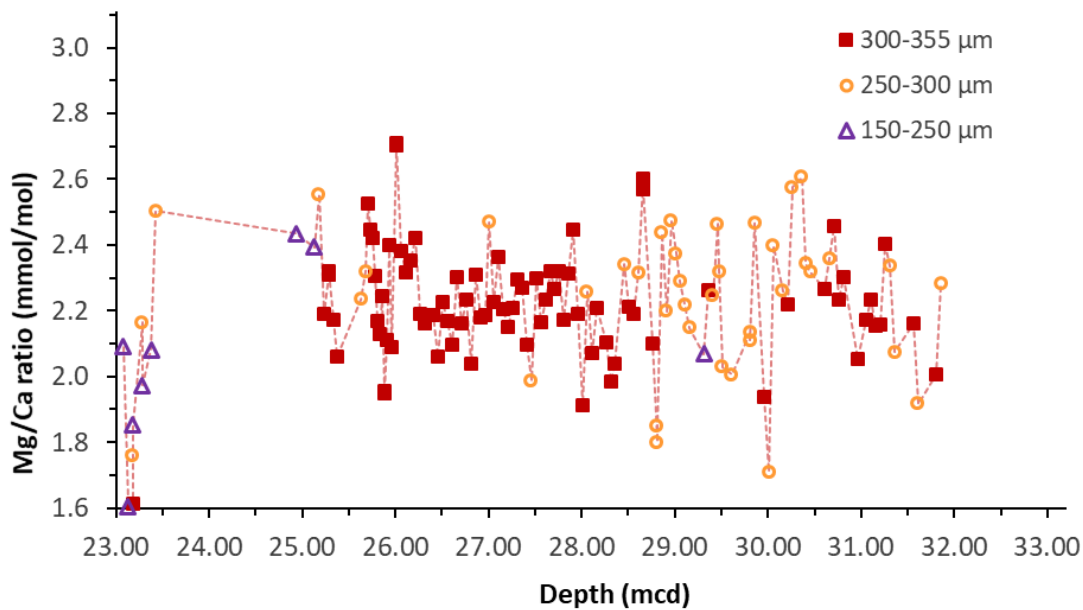


**Figure 6.7** | Size fractions used to produce Mg/Ca ratios from U1305 *G. bulloides*. The preferred larger size fraction (300 – 355  $\mu\text{m}$ ; red squares) was supplemented by other size fractions (250 – 300  $\mu\text{m}$ , orange circles; 150 – 250  $\mu\text{m}$ , purple triangles) where necessary.

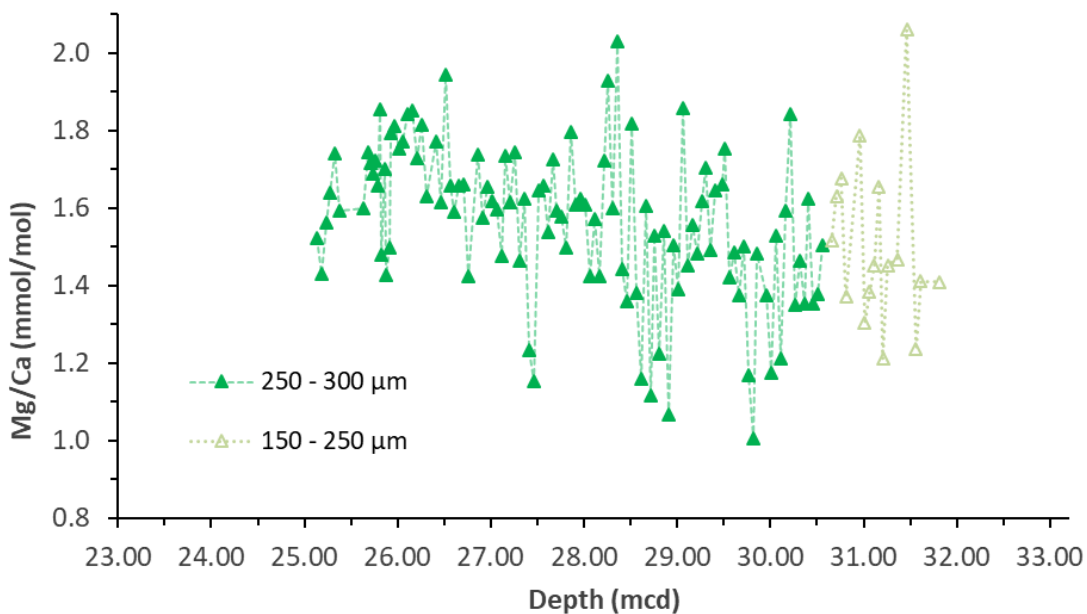


**Figure 6.8** | Size fractions used to produce Mg/Ca ratios from U1305 *N. incompta*. The preferred larger size fraction (250 – 300  $\mu\text{m}$ ; filled triangles) was supplemented by a smaller size fraction (150 – 250  $\mu\text{m}$ , open triangles) where necessary.

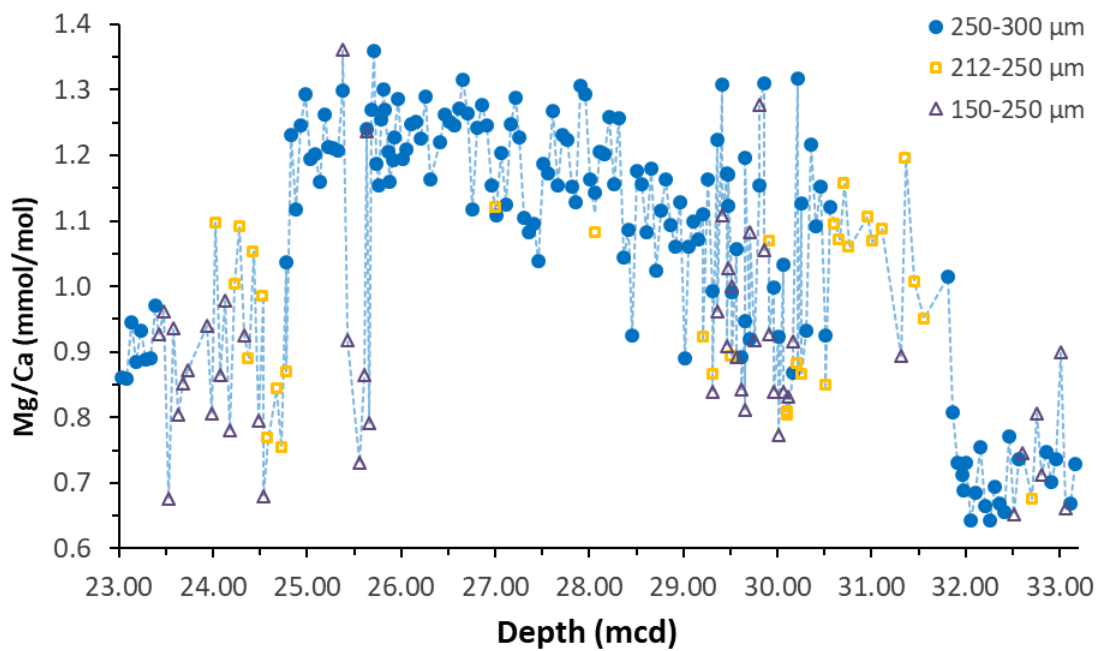


**Figure 6.9** | Size fractions used to produce Mg/Ca ratios from U1305 *N. pachyderma* (*s*). The preferred larger size fraction (250 – 300  $\mu\text{m}$ ; blue circles) was supplemented by a smaller size fractions (212 – 250  $\mu\text{m}$ , orange squares; 150 – 250  $\mu\text{m}$ , purple triangles) where necessary.

### 6.1.6.6 | Size Fraction Tests Summary

Investigation of the size fraction effect suggests that, in line with other studies (Elderfield et al. 2002; Anand et al. 2003; Cl  roux et al. 2008), where possible, the preferred size fraction should be used to provide the most reliable and self-consistent results (Table 6.1). However, although a statistically significant difference was observed between typical interglacial period size fractions, no significant difference was observed between typical glacial period size fractions for *N. pachyderma* (*s*) (Figure 6.4). This difference may be because surface waters in the Labrador Sea experienced reduced seasonality (a smaller range of temperatures across the year) during glacial periods. In replicate coretop analyses of *G. bulloides*, no significant difference was observed between size fractions, and calcification temperatures were found to be the very similar ( $8.5 \pm 0.5^\circ\text{C}$ ) to ocean atlas values ( $8^\circ\text{C}$ ) (Figure 6.5). In replicate coretop analyses of *N. pachyderma* (*s*), the 0 – 2 cm sample did not show a statistically significant difference between size fractions, and where different calcification temperatures were reconstructed in the 5 – 7 cm sample, the difference between the two values (4 and  $6^\circ\text{C}$ ) means the results were still within the typical bounds of uncertainty of each other ( $\pm 1^\circ\text{C}$ ). No significant difference was found between “clean” and “dirty” foraminifera

either, which suggests that the cleaning procedure is sufficient to remove contaminants even when they are obviously present (Table 6.7). Downcore Mg/Ca results when plotted by size fraction did not display significant offsets between size fractions.

Therefore, where insufficient foraminifera were present, smaller size fractions were used to fill gaps in the record, with the caveat that small size fraction Mg/Ca calcification temperature errors should be considered higher ( $\pm 2^\circ\text{C}$ ) than for the preferred size fraction ( $\pm 1^\circ\text{C}$ ). It is also worth noting that smaller size fractions were typically used through foraminifera-poor intervals, usually associated with climate deterioration (such as the 25.66 – 25.43 mcd “117 ka event”, discussed in section 8.3.4), during which MAT SSTs and IRD counts also indicate cold temperatures, which makes it more likely these low calcification temperatures reflect a real climate signal. Therefore, Mg/Ca results should be referenced against other proxies to ensure the climate interpretation is robust.

## 6.1.7 | Mg/Ca Ratio Results

### 6.1.7.1 | U1305

U1305 Mg/Ca calcification temperature results are shown in Figure 6.10 alongside species diversity and MAT SSTs. The *N. pachyderma* (*s*) Mg/Ca results show rapid warming after 31.86 mcd, echoing MAT results. In all three Mg/Ca records, variability seems highest during the first half of the last interglacial. Initial warmth appears to have been interrupted at around 30.01 mcd, when all three Mg/Ca records show lower values. This climate instability may be associated with the red layer (29.91 mcd), interpreted as a deposit laid down during a Laurentide outburst event (Nicholl et al. 2012). This layer is discussed in section (8.3.2). There are indications in all species, but most pronounced in *N. pachyderma* (*s*), of a trend towards warmer temperatures towards the end of the last interglacial, which given the differing species depth preferences would indicate a less strongly stratified upper water column. During this latter period of the last interglacial, an abrupt cooling at the pycnocline is evident between 25.43 and 25.66 mcd in the *N. pachyderma* (*s*) results, which will be discussed in relation to the 117 ka event in section 8.3.4. A fairly abrupt transition into the last glacial period appears to have occurred at 24.73 mcd.

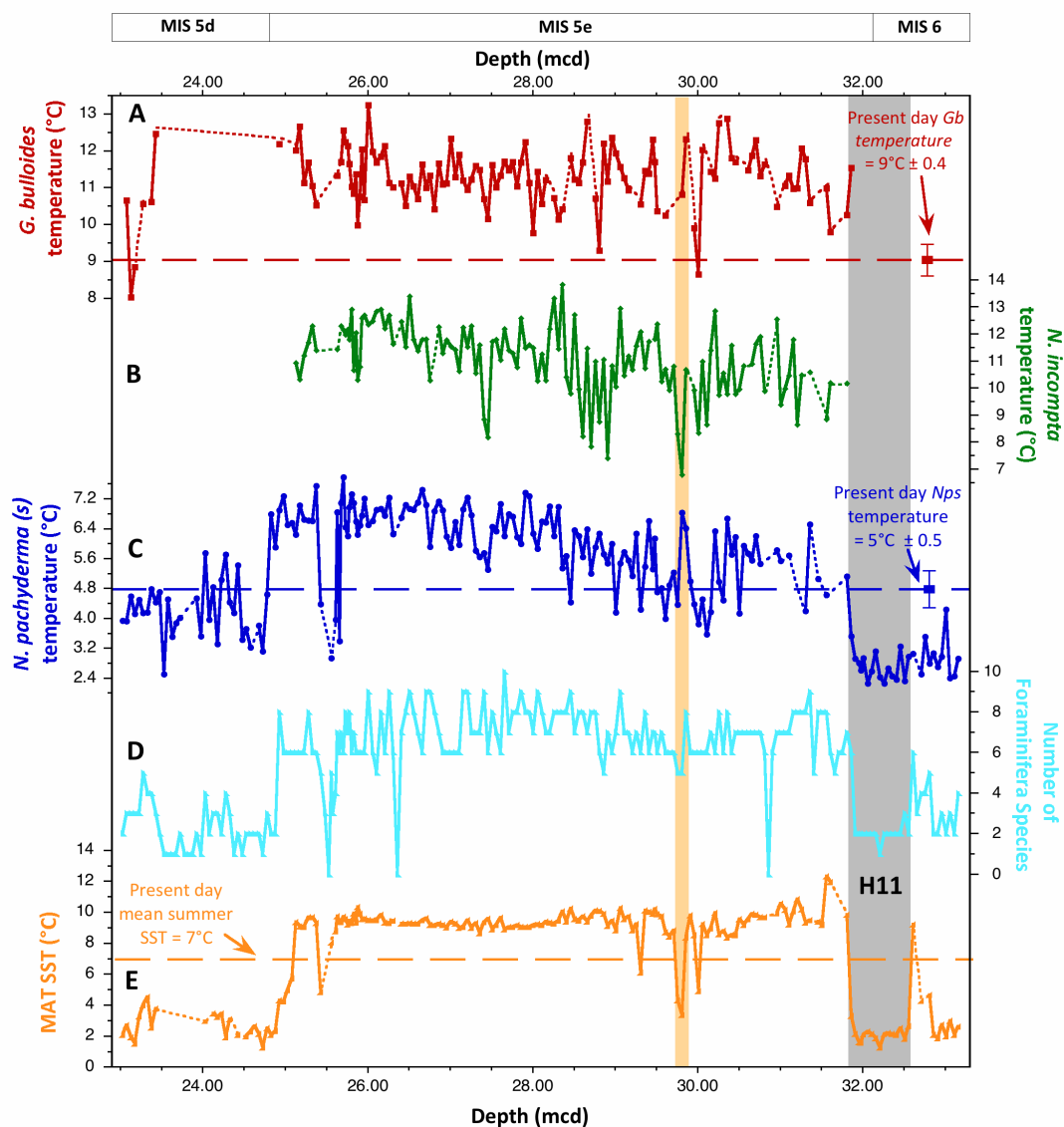


**Figure 6.10** | U1305 Mg/Ca temperatures for (A) *G. bulloides*, (B) *N. incompta* and (C) *N. pachyderma* (*s*) MAT-derived temperatures. Dotted sections indicate missing data. Coretop Mg/Ca calcification temperatures are shown as horizontal dashed lines for *G. bulloides* and *N. pachyderma* (*s*) with  $1\sigma$  error bars. Present day mean summer (JJA) SST of  $7.0^{\circ}\text{C}$  is shown as a horizontal dashed line in comparison with MAT SSTs (World Ocean Atlas 1998). The yellow shading indicates a red layer present in the sediment core between 29.91–29.81 mcd associated with a Laurentide outburst event (Nicholl et al. 2012). Grey shading indicates the H11 ice rafting event.

### 6.1.7.2 | U1302

U1302 Mg/Ca calcification temperature results are shown in Figure 6.11 alongside MAT SSTs, species diversity, IRD % and *N. pachyderma* (*s*) abundance. Prior to the abrupt warming into the last interglacial at 22.35 mcd, a surprising amount of variability in *N. pachyderma* (*s*) Mg/Ca calcification temperatures and MAT SST estimates is observed during H11. In contrast to U1305, both *G. bulloides* and *N. pachyderma* (*s*)

calcification temperatures appear similar to the present day, or slightly cooler. A colder sub-surface layer could indicate stronger surface stratification. In common with U1305, there appears to be a trend towards increasing Mg/Ca temperatures towards the end of the last interglacial. Cooling appears to arrive just above the red layer in U1302, rather than just below as in U1305, but low resolution hampers detailed investigation.

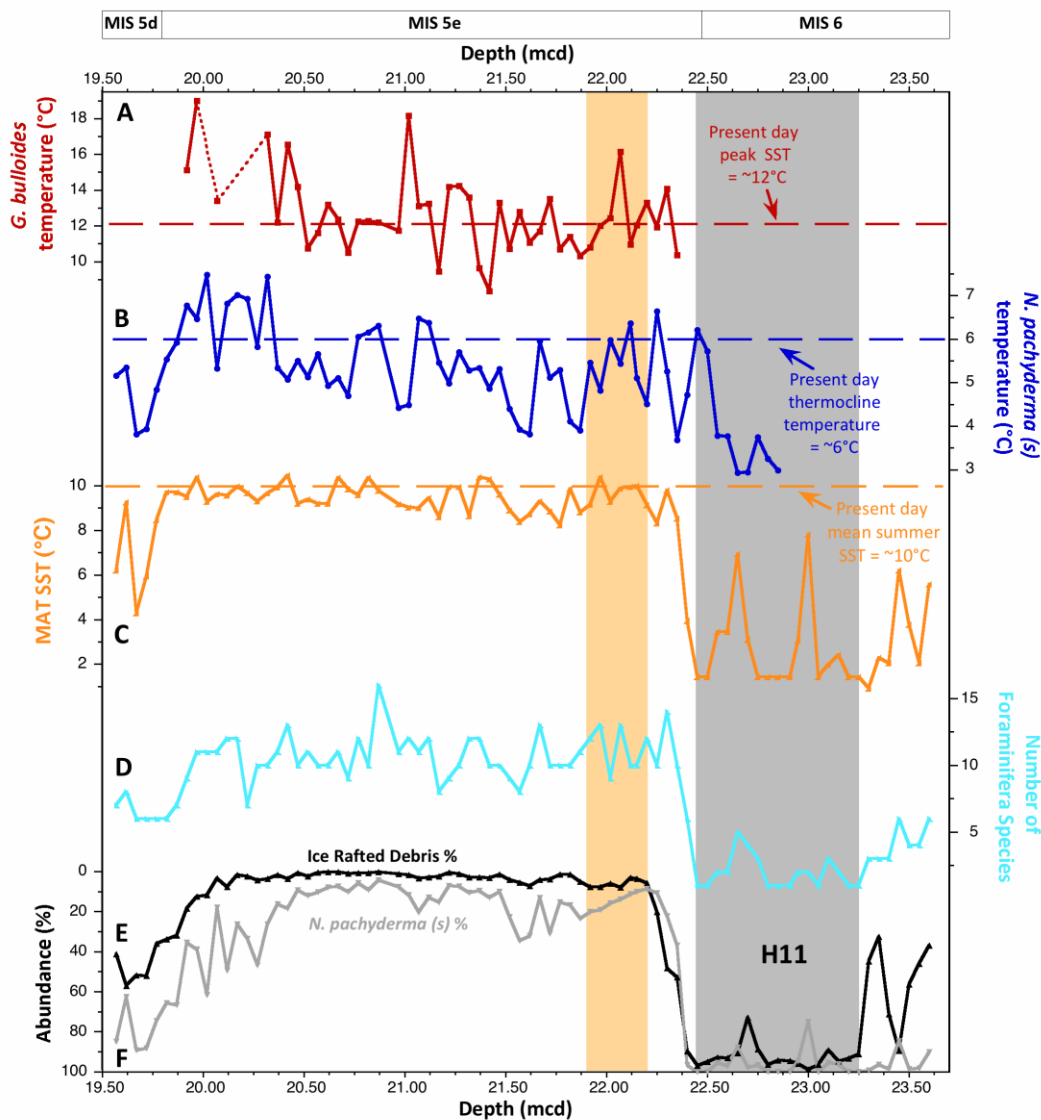


**Figure 6.11** | Temperature proxies and abundance data from sediment Core U1302 plotted by depth. Mg/Ca temperature estimates from (A) *G. bulloides* and (B) *N. pachyderma* (*s*), (C) species assemblage MAT-derived temperatures, (D) planktonic foraminiferal species diversity, and percentage abundances of (E) ice rafted debris and (F) *N. pachyderma* (*s*). Dotted sections indicate missing data. Horizontal dashed lines indicate modern peak summer SSTs (red), thermocline temperatures (dark blue) and mean SURFACE summer (JJA) temperatures of 10.3°C (World Ocean Atlas 1998). The yellow shading indicates a red layer present in the sediment core between 22.07 – 21.92 mcd suggestive of a Laurentide outburst event (Nicholl et al. 2012). The grey shading indicates the H11 ice rafting event.

## 6.2 | BA/CA AS A PROXY FOR MELTWATER RUNOFF

The alkaline earth metal barium (Ba) is a divalent cation ( $2^+$ ) that can substitute into the calcite lattice during foraminiferal test secretion in much the same way that magnesium can. Ba incorporation is proportional to seawater barium concentrations (Lea and Boyle 1989; Lea and Spero 1994). Seawater Ba concentrations are variable, with extremely low, relatively uniform values in the surface ocean, but much higher nearshore values (Broecker and Peng 1982). The vertical distribution of Ba is generally similar to alkalinity and silica in showing surface water depletion and regeneration at depth (Lea and Boyle 1989). Ba is primarily transported into surface waters by river runoff as dissolved ion complexes, or is desorbed from suspended particles (Hanor and Chan 1977) with a smaller deep water input from ocean ridge hydrothermal effluent (Edmond et al. 1979). Enhanced weathering and erosion during glaciation is believed to enrich river runoff in barium during deglaciation (Hall and Chan 2004). Additionally, barium that had previously been adsorbed onto clays in freshwater coastal sediments may have desorbed via ion exchange in saline waters as sea levels rose during Termination II (Hall and Chan 2004). In combining culture experiments with a review of published studies, Hönisch et al. (2011) showed that Ba/Ca ratios in planktonic foraminiferal species including *Neogloboquadrina* are unaffected by pH, temperature, salinity or symbiont photosynthesis. Ba/Ca ratios can therefore be used as a proxy for barium-rich glacial meltwater discharge into the oceans (Hall and Chan 2004).

As part of the Mg/Ca analysis undertaken for the present study, the ICP-OES was calibrated for contaminants phases aluminium, barium, iron, manganese, sodium, potassium, silicon, titanium and zinc. The calibrations are not as precise as for Mg/Ca, but are sufficient to screen out samples which may contain contaminants of various types. As a consequence, Ba/Ca ratios for *N. pachyderma* (*s*) were available.

Figure 6.12 displays the Ba/Ca ratios from sediment core U1305. A strong ( $< 40$   $\mu\text{mol/mol}$ ) meltwater signal is associated with H11 which ends abruptly after 31.81 mcd, after which values drop to 5 – 10  $\mu\text{mol/mol}$  for most of the last interglacial. There are slight peaks above the red layer at 30.51 mcd (15.5  $\mu\text{mol/mol}$ ) and 30.21 mcd (16.5  $\mu\text{mol/mol}$ ). Elevated values at the base of the red layer (9.6  $\mu\text{mol/mol}$ ) appear to reduce to a minimum (4.1  $\mu\text{mol/mol}$ ), before increasing again (8.2  $\mu\text{mol/mol}$ ), though values are not conspicuously high, and much lower than the preceding peaks. Values remain low, but rise abruptly at 27.31 mcd (13.2  $\mu\text{mol/mol}$ ), remaining high if variable for the red

of the record. Unexpectedly low values appear associated with the “117 ka cooling event” 25.61 – 25.43 mcd, though these values depended on small size fractions and therefore may be less robust. Peaks in Ba/Ca 23.98 (21.6  $\mu\text{mol/mol}$ ) and 23.58  $\mu\text{mol/mol}$ ) appear linked to heavy IRD input through this interval.

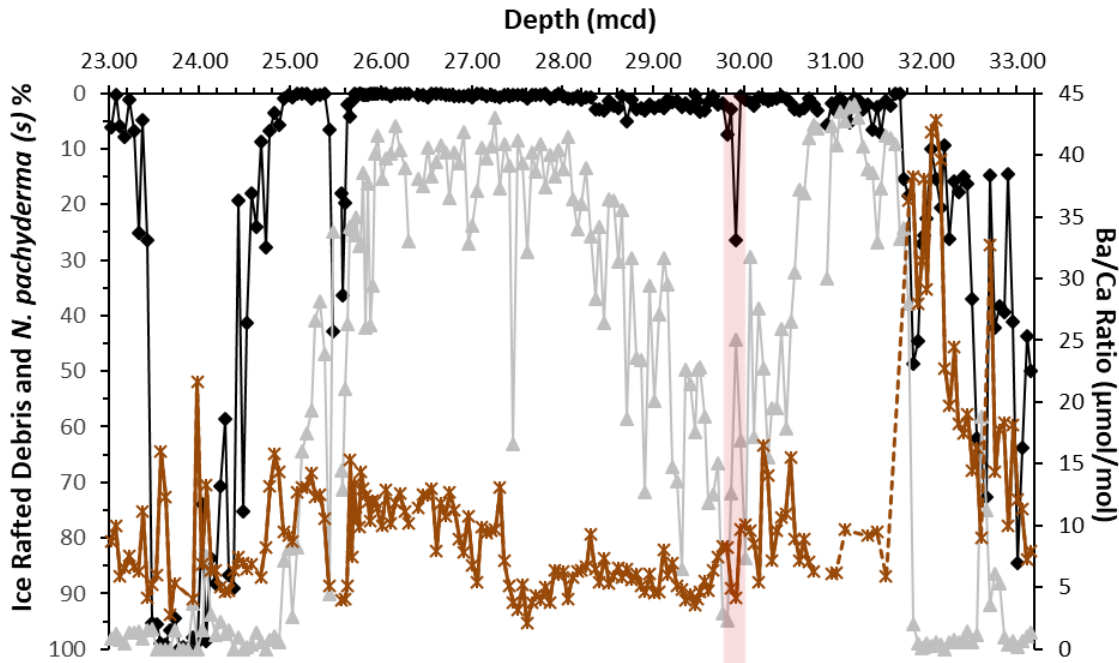


**Figure 6.12** | U1305 Ba/Ca ratios in *N. pachyderma* (*s*) (brown stars) together with ice rafted debris percentage (black diamonds) and *N. pachyderma* (*s*) abundance (grey triangles). Dashed lines indicate gaps in the data. Pink shading indicates the red layer of Nicholl et al. (2012).

Figure 6.13 shows similar results in sediment core U1302, though with lower overall values. High but fluctuating values associated with H11 build to an obvious peak of  $>10$   $\mu\text{mol/mol}$  between 22.25 – 22.35 mcd through Termination II, followed by consistently lower interglacial values ( $\sim 2 - 3$   $\mu\text{mol/mol}$ ), although there does seem to be some continuing intermittent meltwater influence through the first half of the last interglacial between 21.92 and 21.32 mcd with values of 4 – 6  $\mu\text{mol/mol}$ . A slight rise to 3.9  $\mu\text{mol/mol}$  is seen towards the top of the red layer. Slightly elevated values are seen at 20.17 mcd (3  $\mu\text{mol/mol}$ ) and 20.02 mcd (3.4  $\mu\text{mol/mol}$ ), but values are not especially high in relation to the increase in IRD towards the top of the record.

These results do suggest in both cores elevated Ba/Ca ratios are associated with H11. Slightly elevated values were associated with the red layer, though more at the base in U1305 and towards the top in U1302, suggesting some local variation in timing of this event.

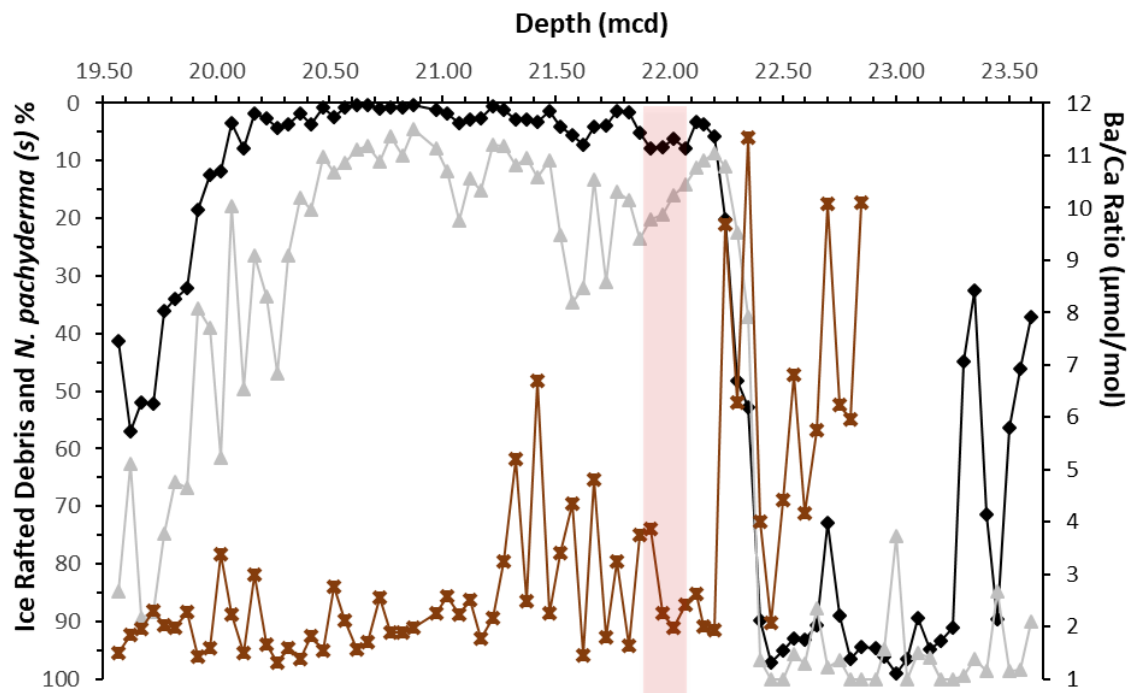


**Figure 6.13** | U1302 Ba/Ca ratios in *N. pachyderma (s)* (brown stars) together with ice rafted debris percentage (black diamonds) and *N. pachyderma (s)* abundance (grey triangles). Pink box indicates red layer of Nicholl et al. (2012).

## 6.3 | STABLE ISOTOPES

Stable isotope geochemistry is a standard tool of palaeoclimatology. Relative isotopic abundance is measured by mass spectrometry and provides a ratio of the heavy isotope to the lighter isotope relative to a standard sample, typically Vienna-PeeDee Belemnite (V-PDB), given in per mil (‰).

### 6.3.1 | Oxygen

The classic paper of Urey (1947) proposed that the temperature dependence of oxygen isotope fractionation due to the thermodynamic properties of the  $\text{CO}_2\text{-H}_2\text{O-CaCO}_3$  system may provide the basis for deriving temperatures at the time of carbonate precipitation. Emiliani (1955) first applied this method to foraminifera. The empirical relationship between  $\delta^{18}\text{O}$  and palaeotemperature is (Erez and Luz 1982):

$$T = 16.98 - 4.52 (\delta^{18}\text{O}_c - \delta^{18}\text{O}_w) + 0.028 (\delta^{18}\text{O}_c - \delta^{18}\text{O}_w)^2$$

Where  $T$  = isotopic temperature,  $\delta^{18}\text{O}_c$  = solid carbonate isotopic composition, and  $\delta^{18}\text{O}_w$  = isotopic composition of the seawater in which the carbonate precipitated. A change of 1 ‰ corresponds with an apparent temperature change of  $\sim 5^\circ\text{C}$ .

It was later realised that this  $\delta^{18}\text{O}$  signal is not purely a function of temperature, but also of seawater  $\delta^{18}\text{O}$ , which is related to global ice volume (Shackleton 1967; Shackleton 1987). Significant isotopic fractionation occurs during evaporation and condensation. Differing vapour pressures cause lighter  $^{16}\text{O}$  to be preferentially evaporated, and during glacial periods it falls as snow over high latitudes and gets “locked” within large continental ice sheets. As a result, seawater becomes enriched in  $^{18}\text{O}$ , a process that is largely globally synchronous due to the shorter mixing time of the ocean ( $\sim 1$  ka) compared with the slower response times of ice sheets (several thousand years). One final factor is that local hydrographic variability such as the precipitation-evaporation balance or sea ice formation can affect  $\delta^{18}\text{O}$  values (Thunell and Williams 1989; Duplessy et al. 1992). These factors result in fairly stable patterns of seawater  $\delta^{18}\text{O}$  which allow water masses to be traced (Figure 2.8). As a result, a relationship between salinity and  $\delta^{18}\text{O}$  of sea water has been derived empirically (Zahn and Mix 1991):

$$\delta^{18}\text{O}_w = 1.53S - 53.18$$

where  $\delta^{18}\text{O}_w$  is seawater isotopic composition and  $S$  is salinity.

By itself, it is impossible to distinguish the temperature signal from the global ice volume (salinity) signal with  $\delta^{18}\text{O}$  measurements, so an independent means of palaeotemperature measurement or global ice volume estimation must be used to untangle these signals. This will be possible due to the Mg/Ca data produced for this study, and it is intended this will be included in a future publication.

Since the deep ocean has more uniform temperatures and salinities, benthic (bottom-dwelling) foraminifera are often preferred in palaeoceanographic proxies over planktonic (surface-dwelling) species, to minimise local and regional climate variability. The most commonly used benthic species are *Uvigerina peregrine* and *Cibicides wuellerstorfi*, which requires a species-specific offset correction (+0.64 ‰) to enable stacking (Shackleton and Hall 1984).

## 6.3.2 | Carbon

Lower atmospheric CO<sub>2</sub> concentrations during glacial periods observed in ice cores (e.g. Landais et al. 2013), at the same time that large areas of land were arid or covered in ice sheets, indicate that large amounts of isotopically depleted terrestrial carbon must have been stored within the ocean (Peterson et al. 2014). Sinking of organic matter generated by surface productivity can sequester carbon to depth, in a process known as the “biological pump” (Sigman and Boyle 2000). This organic material is oxidised (decays) through respiration, releasing <sup>12</sup>C into deep water masses. A resulting increase in dissolved inorganic carbon (DIC) would have the effect of lowering pH and affecting the equilibration between dissolved carbon species (Sanyal et al. 1995). This carbon sink may have resulted in a whole-ocean depletion in δ<sup>13</sup>C, estimated for the last glacial maximum as 0.38 ± 0.08 ‰ (for 0.5 – 5 km depth), observed in a large-scale study using 480 core sites (Peterson et al. 2014).

In addition to these global changes in carbon storage, δ<sup>13</sup>C varies between water masses. Surface water δ<sup>13</sup>C is highly variable, depending on the biologically mediated balance between isotopic fractionation during photosynthesis, rates of oxidation, air-sea CO<sub>2</sub> exchange, and mixing between contrasting water masses (Curry et al. 1988, Duplessy et al. 1988). As primary producers preferentially utilise <sup>12</sup>C, surface waters become enriched in <sup>13</sup>C (i.e. more positive δ<sup>13</sup>C values). There is therefore a relationship between δ<sup>13</sup>C and nutrient availability (Broecker and Peng 1982), whereby if surface nutrients were completely used up, the δ<sup>13</sup>C of seawaters would be ~2.0 ‰ (Curry et al. 1988). In practice (due to respiration and incomplete nutrient consumption), freshly formed (recently ventilated) NADW has typical high dissolved oxygen content, due to recent contact with the atmosphere, and positive δ<sup>13</sup>C values of 1.0 – 1.5 ‰, and (Curry et al. 1988). As a result of this relationship to nutrients, planktonic δ<sup>13</sup>C has been interpreted as an indicator of palaeoproductivity (Hillaire-Marcel and Bilodeau 2000), though due to changes in atmospheric CO<sub>2</sub> over glacial-interglacial cycles (Peterson et al. 2014) and overprinting by changes in [CO<sub>3</sub><sup>2-</sup>] (Spero et al. 1997) this interpretation is not unequivocal (Peterson et al. 2014). At depth, δ<sup>13</sup>C is not a conservative tracer due to the aging effect of organic matter remineralisation, but this process is slow and δ<sup>13</sup>C gradients can still be used to trace deep water masses (Duplessy et al. 1984; Duplessy et al. 1988). In the North Atlantic, the signature of poorly-ventilated (low oxygen) high-nutrient (aged) AABW is very negative δ<sup>13</sup>C values of less than –0.2 ‰ (Curry and

Oppo 2005). Benthic  $\delta^{13}\text{C}$  can therefore be used as an indication of AMOC intensity, whereby during periods of vigorous AMOC the deep North Atlantic is bathed in positive  $\delta^{13}\text{C}$  NADW components, readily distinguished from the strongly negative benthic  $\delta^{13}\text{C}$  signature of AABW during periods when Nordic Seas overflow water is reduced, allowing AABW to flood into the region at the lowest levels (Kroopnick 1985; Lehman and Keigwin 1992). At intermediate levels too, the rate of Labrador Sea Water production is reflected in  $\delta^{13}\text{C}$  values, with minimal differences during interglacial periods between surface-dwelling *G. bulloides* and pycnocline-dwelling *N. pachyderma* (*s*) when the pycnocline is weak, allowing winter convection, but a large offset between *N. pachyderma* (*s*) and benthic  $\delta^{13}\text{C}$  indicating the presence of NADW at the deepest layers (Hillaire-Marcel and Bilodeau 2000). A larger offset during glacial periods and Heinrich events, is seen between *G. bulloides* and *N. pachyderma* (*s*) when deep convection is inhibited by a low-salinity surface layer, but a much lower difference between *N. pachyderma* (*s*) and benthic  $\delta^{13}\text{C}$ , either due to the presence of a poorly-ventilated single water mass, as suggested by Hillaire-Marcel and Bilodeau (2000), or the incursion of more negative  $\delta^{13}\text{C}$  AABW at the lowest layers (Zahn et al. 1997; Curry and Oppo 2005).

However, plankton tow studies indicate that vital effects may obscure environmental correlation (Spero 1992; Spero and Lea 1996). In the North Atlantic, *N. pachyderma* (*s*) is typically 1 ‰ enriched (more positive) than *G. bulloides*, attributed to differing temperatures and photosynthesis-respiration balance at different depth preferences, vital effects, and differing rates of convection (de Vernal and Hillaire-Marcel 2006). Also, a fall in glacial  $\text{CO}_2$  partial pressure implies increased surface water carbonate ion concentration ( $[\text{CO}_3^{2-}]$ ), which has been shown to decrease  $\delta^{13}\text{C}$  values in planktonic foraminifera (Spero et al. 1997). During glacial periods, the pH and  $[\text{CO}_3^{2-}]$  of seawater was higher (Sanyal et al. 1995) leading to generally depleted surface  $\delta^{13}\text{C}$  values, typically -0.5 ‰ in *N. pachyderma* (*s*), in contrast to interglacial values of nearly +1 ‰ (e.g. Hillaire-Marcel et al. 2011). Covariance between  $\delta^{18}\text{O}$  and  $\delta^{13}\text{C}$  has therefore been attributed to changes in ocean alkalinity, with increased alkalinity resulting in decreased  $\delta^{13}\text{C}$  and  $\delta^{18}\text{O}$  (Spero et al. 1996, 1997). In benthic species, *U. peregrina*  $\delta^{13}\text{C}$  values are usually adjusted by + 0.9 ‰ to enable stacking with *C. wuellerstorfi* records (Shackleton and Hall 1984).

### 6.3.3 | Stable Isotope Methods

For both U1305 and U1302, previously published planktonic stable isotope ratios from *N. pachyderma (s)* were available (Hillaire-Marcel et al. 2011). However, gaps in the U1305 record through the critical early last interglacial and glacial inception periods hindered age model construction and palaeoceanographic interpretation, therefore new data was produced for this study to fill in the gaps. In addition, new stable isotope data from *G. bulloides* and *N. incompta* were also produced for U1305. For planktonic foraminifera, 20 individuals were picked from the 150 – 250  $\mu\text{m}$  size fraction where available.

No benthic isotope stratigraphy has been published for either core, however an unpublished multi-species benthic record (adjusted to enable stacking) has been prepared for U1302 by S. Kaboth (manuscript in preparation), who kindly allowed this data to be displayed in this thesis. To address the lack of benthic isotope stratigraphy in U1305, *C. wuellerstorfi* were picked where possible from the  $>150 \mu\text{m}$  size fraction to produce the first last interglacial benthic record for this core. The typical procedure was to heat benthic foraminifera at 250°C under vacuum for an hour before analysis, then all samples were reacted at 90°C with 100% orthophosphoric acid prior to mass spectrometer analysis (Hillaire-Marcel et al. 2011), which was done at the Stable Isotope Facility, Cambridge by Dr Mark Chapman. Figure 6.14 compares these new U1305 planktonic data with the previously published *N. pachyderma (s)* record (Hillaire-Marcel et al. 2011) to highlight not only where the new data infills gaps in the published record, but shows that values were comparable. Benthic data also included in Figure 6.14 show generally similar trends.

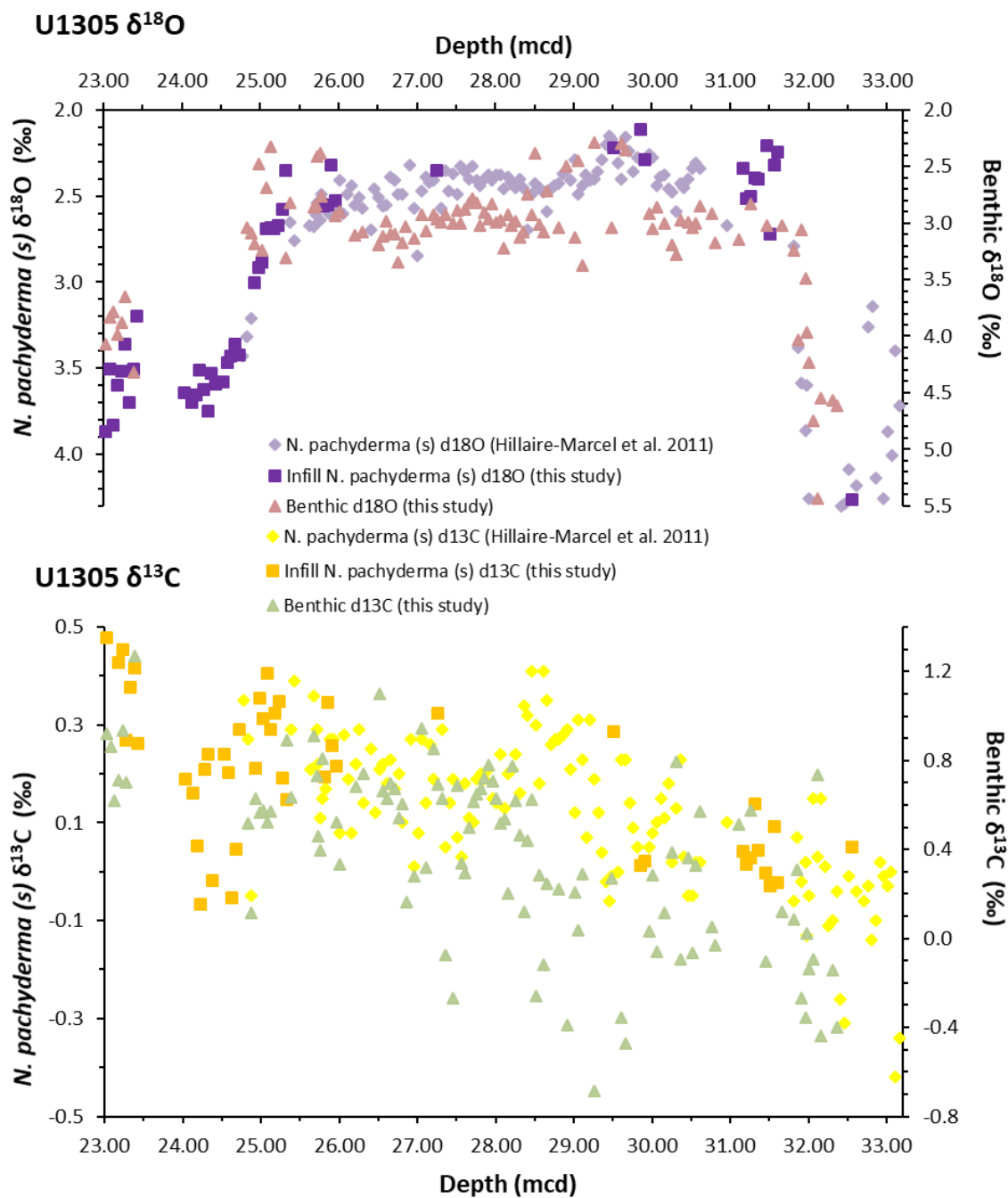


**Figure 6.14** | Comparison between new and previously published U1305 stable oxygen (top) and carbon (bottom) data. New benthic (*C. wuellerstorfi*)  $\delta^{18}\text{O}$  (pink triangles) and  $\delta^{13}\text{C}$  (green triangles) are shown alongside new infill planktonic (*N. pachyderma (s)*)  $\delta^{18}\text{O}$  (dark purple squares) and  $\delta^{13}\text{C}$  (orange squares) produced for this study, to fill gaps in the previously published  $\delta^{18}\text{O}$  (light purple diamonds) and  $\delta^{13}\text{C}$  (yellow diamonds) records of Hillaire-Marcel et al. (2011).

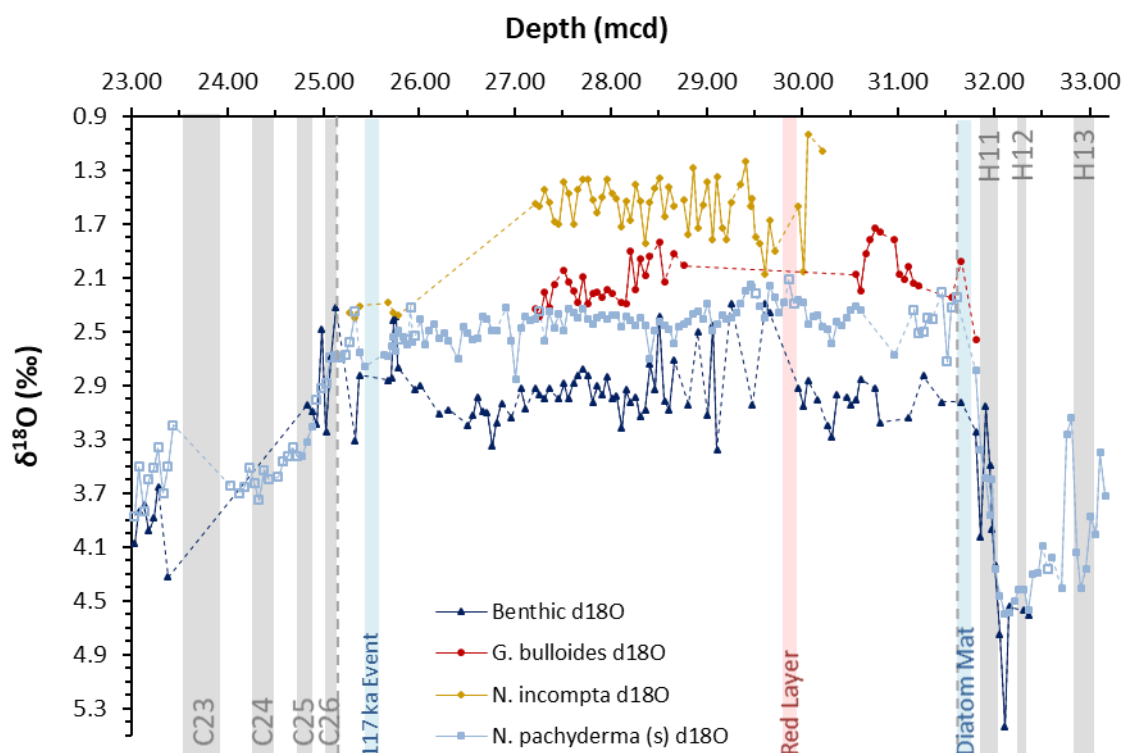


**Figure 6.15** | U1305 multi-species  $\delta^{18}\text{O}$  data. Benthic (*C. wuellerstorfi*)  $\delta^{18}\text{O}$  (dark blue triangles). Planktonic *G. bulloides* (red circles), *N. incompta* (brown diamonds) and *N. pachyderma* (*s*) (light blue squares), open squares indicate infill data produced for this study, filled squares indicate the planktonic record of Hillaire-Marcel et al. (2011). Dotted lines indicate gaps in the records. Vertical dashed grey lines indicate the start and end of the last interglacial (31.61 – 25.13 mcd). Grey shading indicates Heinrich events (H13 – H11), and North Atlantic cold events (C26 – C23). Blue shading indicates diatom mat and 117 ka event, and red shading indicates red layer.

### 6.3.4 | Stable Isotope Results

Figure 6.15 shows the new U1305 multi-species planktonic and *C. wuellerstorfi* benthic  $\delta^{18}\text{O}$  data produced for this study along with previously published *N. pachyderma* (*s*) isotopes from Hillaire-Marcel et al. (2011). Offsets may be due to a combination of different depth habitats and differing vital effects between species. The peak in enriched benthic and planktonic  $\delta^{18}\text{O}$  at 32.11 mcd is striking, and was linked with isotope event 6.2 identified elsewhere in the North Atlantic (Imbrie et al. 1984). There is close agreement between benthic and planktonic values through H11 and Termination II. The infill *N. pachyderma* (*s*) values and the new benthic record through the early last interglacial period (31.61 – 31.16 mcd) indicate that strongly depleted “interglacial type”  $\delta^{18}\text{O}$  values were reached very early, toward the top of the diatom mat, which had not been clear previously, though the data do not appear uniformly stable. Fluctuations reflected in *G. bulloides* may be due to periodic freshwater input associated with continued Greenland ice sheet melt inferred through this period (Govin et al. 2012).

Variable  $\delta^{18}\text{O}$  values just below the red layer are likely related to declining temperatures during foraminiferal assemblage zone Ca inferred from MAT SST and increasing *N. pachyderma* (*s*) abundances (Figure 5.12). The most depleted *N. pachyderma* (*s*)  $\delta^{18}\text{O}$  values within and just above the red layer may be related to the influx of isotopically depleted flood water (Hillaire-Marcel et al. 2000), amidst a series of highly variable  $\delta^{18}\text{O}$  in all species during the transitional foraminiferal assemblage zone Cb. A period of more stable values appears between 28.06 – 26.01 mcd, reinforcing the inference that there was a long period of stable conditions during foraminiferal assemblage zone E in the latter part of the last interglacial.

There is a puzzling series of strongly enriched U1305 *N. incompta* values 25.78 – 25.28 mcd which are very similar to *N. pachyderma* (*s*) values, and appear to echo a convergence with *N. pachyderma* (*s*) values also seen in U1305 *G. bulloides* towards 27.21 mcd (Figure 6.15). A large preceding gap in the data set makes it difficult to judge whether this represents a rapid shift or part of a longer-term trend. Nonetheless, these unusual data points may be linked to the 117 ka event around which they cluster, and coincide with some strongly fluctuating benthic  $\delta^{18}\text{O}$  values, although there is a lack of data points through the 117 ka event itself. The possible significance of these data points are discussed in section 8.3.4.

The end of the last interglacial in U1305 marks the point from which planktonic (*N. pachyderma* (*s*))  $\delta^{18}\text{O}$  grows steadily more enriched into MIS 5d, whilst benthic  $\delta^{18}\text{O}$  shows a series of strongly depleted values bracketing C26. A gap in the benthic data series makes it difficult to tell where and how rapidly benthic  $\delta^{18}\text{O}$  returned to glacial values, but the new data produced for this study indicate steady planktonic enrichment through C25 and C24. Although a gap in the planktonic  $\delta^{18}\text{O}$  record occurred during C23, the strong IRD evidence suggests this was a significant climate event at this location, followed by a period of more depleted values in both planktonic and benthic  $\delta^{18}\text{O}$  assumed to represent climate amelioration during MIS 5c.

Figure 6.16 shows the new U1305 multi-species planktonic and *C. wuellerstorfi* benthic  $\delta^{13}\text{C}$  data produced for this study, along with previously published *N. pachyderma* (*s*) isotopes from Hillaire-Marcel et al. (2011). Note that *G. bulloides*  $\delta^{13}\text{C}$  has been plotted on a separate axis, due to strongly depleted values in comparison to other records. In the North Atlantic, de Vernal and Hillaire-Marcel (2006) have previously observed that  $\delta^{13}\text{C}$  in *G. bulloides* tends to be ~1 ‰ more negative than *N. pachyderma* (*s*). The

authors attributed this observation to differences in ambient temperatures, vital effects, the balance between productivity and respiration near the surface and base of the mixed layer, and different ventilation rates at depth. Figure 6.16 shows that both planktonic and benthic records have an overall trend towards more enriched values, likely related to wider long-term changes in the Nordic Seas (Fronval et al. 1998; Bauch 2013).

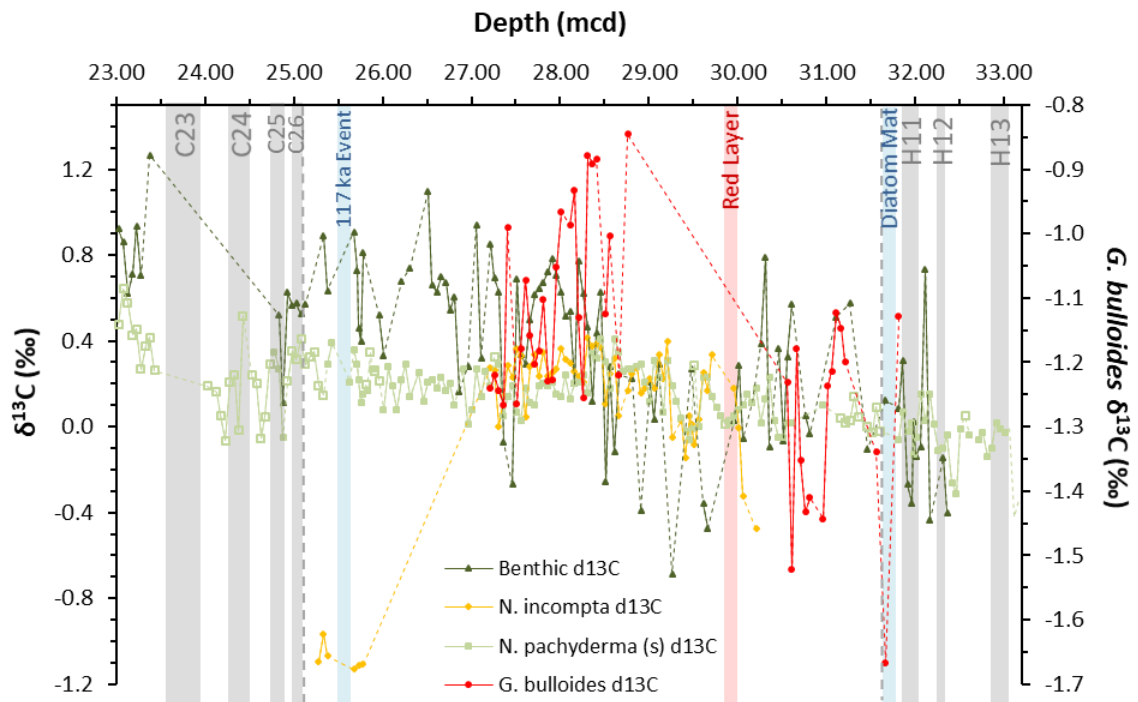


**Figure 6.16** | U1305 multi-species  $\delta^{13}\text{C}$  data. Benthic (*C. wuellerstorfi*)  $\delta^{13}\text{C}$  (dark green triangles). Planktonic *G. bulloides* (red circles) plotted on a separate axis due to more negative values than other records, *N. incompta* (orange diamonds) and *N. pachyderma* (*s*) (light green squares), open squares indicate infill data produced for this study, filled squares indicate the planktonic record of Hillaire-Marcel et al. (2011). Dotted lines indicate gaps in the records. Vertical dashed grey lines indicate the start and end of the last interglacial (31.61 – 25.13 mcd). Grey shading indicates Heinrich events (H13 – H11), and North Atlantic cold events (C26 – C23). Blue shading indicates diatom mat and 117 ka event, and red shading indicates red layer.

Benthic and planktonic values are generally similar below the diatom mat, suggesting the typical lack of deep ventilation associated with glacial periods (e.g. Figure 3.17). The conspicuous positive benthic  $\delta^{13}\text{C}$  at 32.11 mcd is coincident with the strongly enriched  $\delta^{18}\text{O}$  peak seen in Figure 6.15, though it is not clear why benthic  $\delta^{13}\text{C}$  should be so much more positive than planktonic values. The strongly negative *G. bulloides*  $\delta^{13}\text{C}$  value 31.66 mcd may be related to suppressed surface productivity associated with the conditions that led to the deposition of the diatom mat (see section 4.4). Generally positive benthic  $\delta^{13}\text{C}$  through the early last interglacial suggests AMOC may have been established by this point. A shift to more negative benthic  $\delta^{13}\text{C}$  above the red layer

suggests that perhaps the event that led to its deposition caused or coincided with some interruption to AMOC. The brief but fairly regular appearance of negative benthic  $\delta^{13}\text{C}$  values above the red layer suggest the brief but recurrent appearance of AABW in the deep Labrador Sea within the last interglacial, supporting similar observations by Galaasen et al. (2014).

Above 27.31 mcd benthic  $\delta^{13}\text{C}$  became more positive than planktonic values, suggesting strong AMOC with abundant well-ventilated NADW production through this period. Although *N. incompta*  $\delta^{13}\text{C}$  had been very similar to *N. pachyderma* (*s*) through most of the record, there is a cluster of strongly negative values 25.78 – 25.28 mcd around the 117 ka event. These negative values accompany the enriched  $\delta^{18}\text{O}$  values noted above (Figure 6.15), and do suggest some unusual conditions surrounded the 117 ka event, although continued positive benthic  $\delta^{13}\text{C}$  indicates that whatever occurred did not involve a reduction in AMOC strength.

Somewhat more negative planktonic and benthic values are associated with the series of North Atlantic cold events during the early part of the glacial inception. More positive values at the top of the record may indicate overturning was well established during the warmer interstadial conditions of MIS 5c.

Previously published U1302 planktonic (Hillaire-Marcel et al. 2011) and as yet unpublished benthic (Kaboth et al. unpublished) isotopes are shown in Figure 6.17. The most striking feature of U1302 planktonic  $\delta^{18}\text{O}$  record is the coincidence of depleted  $\delta^{18}\text{O}$  values with Heinrich events. There is also some suggestion of depleted values associated with the red layer, 117 ka event, and the onset of some of the North Atlantic cold events. This observation is in striking contrast to U1305 planktonic  $\delta^{18}\text{O}$  (Figure 6.15), in which these events are generally associated with a shift to enriched values (with the exception of the red layer). Therefore, different mechanisms must be at play to account for these different patterns of isotopic response in the north and south of the Labrador Sea to the same climate events. Although, as in U1305 (Figure 6.15), the most enriched benthic and planktonic  $\delta^{18}\text{O}$  values associated with isotope event 6.2 are in close agreement at 23.65 mcd, there is particularly striking series of depleted planktonic  $\delta^{18}\text{O}$  values set within H11, which from the IRD (Figure 4.13) and faunal assemblage MAT SST data (Figure 5.13) produced for this study, is clearly a period of extreme cold and heavy ice rafting. This issue of depleted U1302  $\delta^{18}\text{O}$  excursions during periods of cold and ice rafting is discussed further in section 8.2.3. Planktonic  $\delta^{18}\text{O}$  remains

somewhat enriched through the early last interglacial, with a shift to the most depleted values within the red layer. In contrast, the most depleted benthic  $\delta^{18}\text{O}$  values occur through the early part of the last interglacial, whilst above the red layer, values become slowly more enriched as the interglacial progresses. The onset of the 117 ka event, C26 and C25 all see a shift to depleted planktonic  $\delta^{18}\text{O}$  values, though C24 and C23 appear linked with more enriched values.

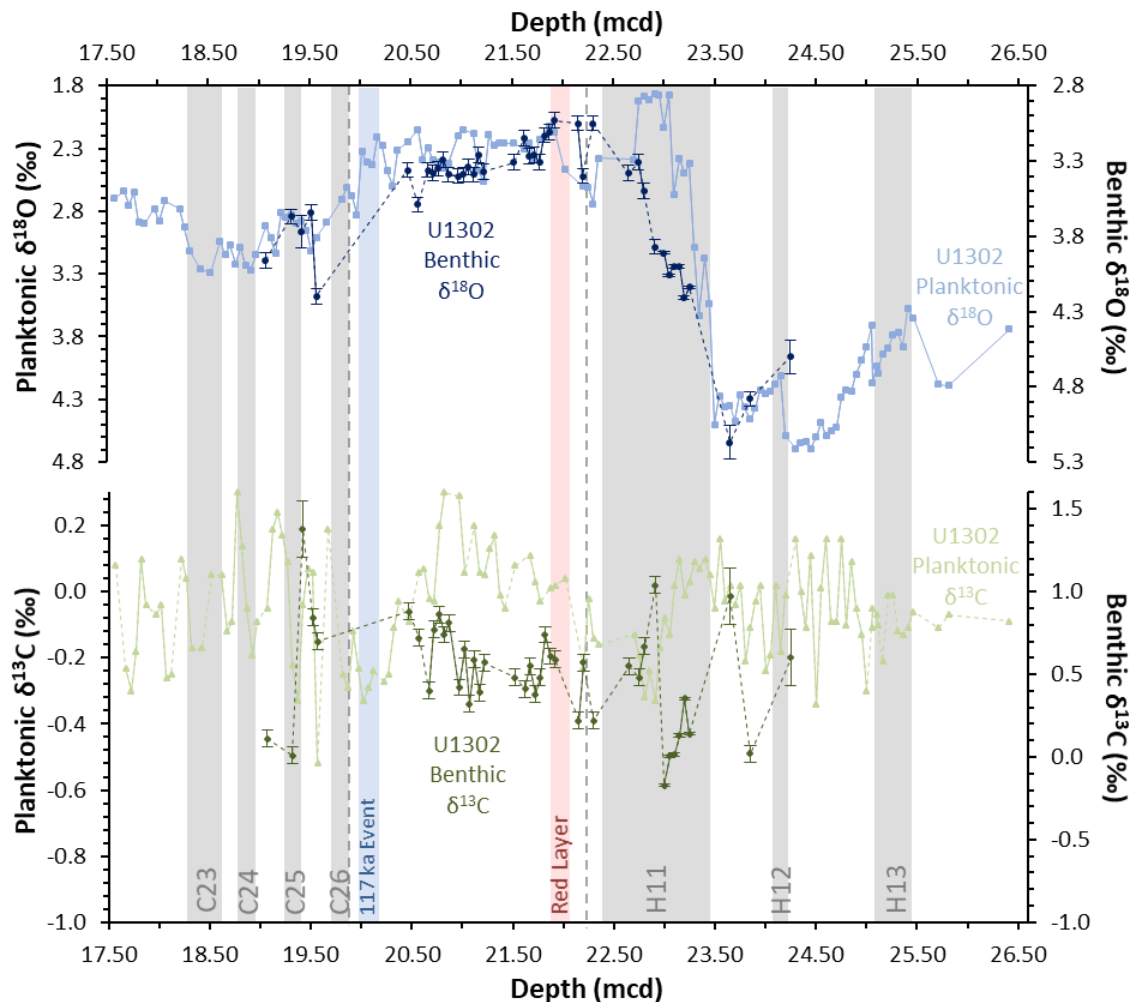


**Figure 6.17** | Comparison between U1302 oxygen (top) and carbon (bottom) isotopes. Planktonic (*N. pachyderma (s)*)  $\delta^{18}\text{O}$  (light blue squares) and  $\delta^{13}\text{C}$  (light green triangles) from Hillaire-Marcel et al. (2011). Multi-species benthic (*C. wuellerstorfi* and *Uvigerina spp.*)  $\delta^{18}\text{O}$  (dark blue circles) and  $\delta^{13}\text{C}$  (dark green diamonds) corrected to allow stacking (Kaboth et al. unpublished). Dotted lines indicate gaps in the records. Vertical dashed grey lines indicate the start and end of the last interglacial (31.61 – 25.13 mcd). Grey shading indicates Heinrich events (H13 – H11), and North Atlantic cold events (C26 – C23). Blue shading indicates diatom mat and 117 ka event, and red shading indicates the red layer.

In general, Figure 6.17 shows that U1302 planktonic  $\delta^{13}\text{C}$  ( $\sim 0.0$  ‰) appears more negative than benthic values ( $\sim 0.5$  ‰), and slightly more negative than the U1305 planktonic record ( $\sim 0.2$  ‰). This offset may be due to local hydrography affecting

nutrient utilisation at the depth of *N. pachyderma* (*s*) peak abundance, producing a  $\delta^{13}\text{C}$  gradient across the Labrador Sea (Curry et al. 1988). The long-term increase observed for U1305 is apparent in U1302 benthic  $\delta^{13}\text{C}$ , but not planktonic values, which begin to decrease above 20.82 mcd and remain more negative than U1305 for the rest of the record, perhaps suggesting a gradient in pycnocline depth developed across the Labrador Sea.

Shortly before H11, a reduction in both planktonic and benthic  $\delta^{13}\text{C}$  is evident 23.85 – 23.80 mcd (Figure 6.17). Similar reductions have been observed for later Heinrich events, and have been interpreted as the slowing of AMOC due to climate deterioration (Zahn et al. 1997). During H11, a rapid fluctuation in benthic and planktonic  $\delta^{13}\text{C}$  23.00 – 22.91 mcd may be related to IRD pulse II (Figure 4.15) discussed in section 8.2.3. Planktonic and benthic  $\delta^{13}\text{C}$  follow the trend towards more positive values up until 20.82 mcd, after which planktonic  $\delta^{13}\text{C}$  instead become progressively more negative toward the end of the last interglacial. These negative values are more akin to glacial conditions and may indicate climate deterioration at Orphan Knoll beginning long before the end of the last interglacial, which is not observed in U1305 (Figure 6.16). C26, C25 and C24 appear to be marked by rapid fluctuations in both planktonic and benthic  $\delta^{13}\text{C}$ , suggesting a role for AMOC perturbation during these events.

## 6.4 | GEOCHEMISTRY SUMMARY

This chapter presents the first multi-species foraminiferal Mg/Ca measurements available for U1305 and U1302. These centennial-scale Mg/Ca records appear to show an increase in temperatures at the onset of MIS 5e and ongoing warming towards the end of the last interglacial. This suggests there was a second, late climate optimum long after peak MAT temperatures ~128.5 - ~126.5 ka (section 5.4), at a time when insolation was low and falling (Berger et al. 2007). Increasing IRD input in U1302 suggests this period was associated with a reconfiguration of the LIS. There is some evidence of fluctuating temperatures associated with the red layer in U1305 (Nicholl et al. 2012), and pronounced sub-surface cooling related to the 117 ka event (Irvalı et al. 2016) in U1305 *N. pachyderma* (*s*) results. Ba/Ca results in section 6.2 highlight the very high rates of runoff during TII in both cores, with comparable values only during MIS 6 (~145.3 ka), possibly related to the H13 event discussed in section 8.2.1. Existing

U1305 *N. pachyderma* (s) planktonic isotope records (Hillaire-Marcel et al. 2011) were supplemented with new data which suggest that MIS 5e was established early (~128.5 ka). New *G. bulloides*, *N. incompta* and benthic *C. wuellerstorfi* isotopes for U1305 provide a fuller and more detailed picture than was previously available the Labrador Sea, particularly during sensitive transitional periods through early and late MIS 5e. These new data were all used in the process of forming an age model for both cores, detailed in the following chapter.

*“There was a young man from Cornell  
Who pronounced every “delta” as “del”  
But the spirit of Urey  
Returned in a fury  
And transferred that fellow to Hell!”*

Professor Harmon Craig, Scripps Institution of  
Oceanography (Hayes 1983)

## 7 | AGE MODEL

The previous three chapters presented multi proxy results from U1302 and U1305 by depth. In order to compare these results to other climate archives, it is essential to place the sediment cores on an absolute timescale as accurately and precisely as possible. For marine cores which lack absolute age markers such as magnetic anomalies (e.g. Channell et al. 2009) or dated tephra layers (e.g. Davies et al. 2014), chronologies are typically derived by matching relative stratigraphic climate indicators (such as  $\delta^{18}\text{O}$ , IRD or *N. pachyderma* (*s*) percentages) to corresponding events in other records which have independent chronologies. To assess the reliability of any dating strategy, and to therefore present a realistic assessment of the uncertainties involved, it is important to understand the underlying climate hypotheses (Govin et al. 2015). Therefore, this chapter provides a brief discussion of benthic  $\delta^{18}\text{O}$  (section 7.1), radiometric dating (section 7.2) and ice core chronologies (section 7.3), and then moves on to describe the age models constructed for this study (section 7.4). These age models are central to the discussion in the final chapter.

### 7.1 | BENTHIC FORAMINIFERAL OXYGEN ISOTOPES

Stratigraphy provides the geological backbone for understanding the history of the Earth. The many characteristics of marine sediment change over time and are often separated into relative stratigraphic units, which can be correlated with similar sequences in other records. This process is called stratigraphic correlation, whereby proxy climate signals are aligned based upon features of the signals themselves, such as peaks or transitions from one state to another (Prell et al. 1986). Relative dating therefore describes the order of events. Calibrating this onto an absolute time scale is usually achieved by aligning a record with a dated reference which already has an absolute chronology, with the assumption that changes within both proxies are synchronous (Govin et al. 2015). Probably the “gold standard” for dating and correlating marine sediment cores is benthic foraminiferal  $\delta^{18}\text{O}$  stratigraphy, which represents a compound signal of both temperature and global ice volume. Marine isotope stages were introduced in section 3.2. A discussion of what  $\delta^{18}\text{O}$  is, how it is measured and what it represents is included in section 6.3. In the present chapter, discussion is limited to the application of  $\delta^{18}\text{O}$  to climatostratigraphy.

The correlation between global ice volume and benthic  $\delta^{18}\text{O}$  has enabled the creation of sediment “stacks”, which contain averaged time series of foraminiferal  $\delta^{18}\text{O}$  from multiple locations to provide a useful standard chronological reference as a template for comparison (Lisiecki and Raymo 2005). To do this, several individual records are normalised and then averaged together to produce a single generalised isotopic curve through time in which extraneous localised influences upon  $\delta^{18}\text{O}$  should cancel each other out, boosting the global ice-volume signal against background noise. Producing a stack in this way does improve the signal-to-noise ratio, though it has the disadvantage of reducing resolution compared with the initial records used (Channell et al. 2009). Lisiecki & Raymo (2005) constructed a 5.3 million-year-long global sediment stack based on 57 different cores known as LR04, a type section that has for many years set the benchmark in providing a common time scale for foraminiferal  $\delta^{18}\text{O}$  studies. The age model for LR04 was determined by aligning the  $\delta^{18}\text{O}$  stack to an ice model based on summer (21<sup>st</sup> June) insolation at 65°N (Lisiecki and Raymo 2005). Due to uncompacted sediments towards the top of sediment cores distorting sedimentation rates, a different strategy was adopted from 0 – 135 ka. The first 22 ka of the  $\delta^{18}\text{O}$  stack were dated by correlation with benthic foraminiferal  $\delta^{18}\text{O}$  in sediment core NA 87-22 (55° 29' N, 14° 41' W, 2,161 m water depth), which were <sup>14</sup>C-dated (Waelbroeck et al. 2001); from 22 – 120 ka LR04 was aligned with the benthic  $\delta^{18}\text{O}$  record of site MD95-2042 from the Iberian Margin (37° 48'N, 10° 10'W, 3146 m water depth) (Shackleton et al. 2002), which was dated by matching planktonic  $\delta^{18}\text{O}$  features to the  $\delta^{18}\text{O}$  from the GRIP ice core (Johnsen et al. 1992). Termination II was dated to 130 ka using U-Th dating of uplifted coral terraces (Bard et al. 1990; Stein et al. 1993). However, these age control methods are now outdated, and it has been recognised that globally asynchronous climate responses mean a more regional approach is preferable (Lisiecki and Raymo 2016).

LR04 has therefore been superseded for the last glacial cycle by LS15 (Lisiecki and Stern 2016). Although it only stretches back over the last 150 ka, LS15 provides eight regional intermediate and deep water benthic isotope stacks, as well as a volume-weighted global benthic stack drawing upon 263 marine cores (Lisiecki and Stern 2016). Another advantage over LR04 is that LS15 contains records from the Labrador Sea (Irvalı et al. 2012; Winsor et al. 2012). A far more precise age model was constructed as well. For 0 – 40 ka Lisiecki and Stern (2016) used regional radiocarbon dating, for 40 – 56 ka the layer-counted NGRIP Greenland ice core was used (North

Greenland Ice Core Project Members 2004, Wolff et al. 2010), and for 56 – 150 ka radiometric speleothem records were used from both Sanbao and Hulu in China (Cheng et al. 2009) and the northern Alps in Europe (Boch et al. 2011). These methods produce a consistent timescale, despite being completely independent from each other, and avoid the 1 – 2 ka bias found in the LR04 stack, though uncertainty through the last interglacial remains at  $\pm 4$  ka (Lisiecki and Stern 2016). Lisiecki and Stern (2016) also used 15 North Atlantic records to produce an IRD stack with a 500 year resolution scaled using arbitrary units (maximum = 1), by extending the work of Stern and Lisiecki (2013). The major drawback is that the IRD stack cannot account for different timings due to IRD deposition from different ice sheets across the region, but the idea is an interesting one and due to the strong regional nature of Heinrich events in the North Atlantic, has produced a valuable reference. Therefore, LS15 was chosen as the reference used in the creation of the age model for this study.

One of the drawbacks of stack production is that it tends to “smooth out” local variation. Visual “wiggle matching” of features to isotopic stacks can be arbitrary and rather subjective, though software has been developed to automatically correlate records by comparing all possible alignments and choosing the optimal fit (Lisiecki and Lisiecki 2002). Different methodology is employed in different studies, with some using the mid-point of a transition between extreme values (e.g. Hillaire-Marcel et al. 2011), whilst others look for the beginning and end of sustained values (e.g. Shackleton et al. 2002, 2003) and others identify minima and maxima (e.g. Prell et al. 1986) or threshold values (e.g. McManus et al. 1999). Also, some  $\delta^{18}\text{O}$  events such as Terminations are rapid and clear cut, but where the climate changes gradually it is more difficult to assign a single tie point. The climate hypothesis assumes that benthic  $\delta^{18}\text{O}$  values change synchronously around the world primarily due to changes in global ice volume (Shackleton 1967) and therefore global mean sea level. However, Pacific benthic  $\delta^{18}\text{O}$  values have been shown to lag Atlantic changes by 1.6 ka during Terminations, a lag which increased to  $\sim 4$  ka at 128 ka (Lisiecki and Raymo 2009). Changes in local seawater temperature or  $\delta^{18}\text{O}$  can also influence benthic  $\delta^{18}\text{O}$  values (Skinner and Shackleton 2005). One way to improve or assess the validity of an age model is to compare it with other independently dated climate archives, such as radiometrically dated material or ice core records.

## 7.2 | RADIOMETRIC DATING

Age models can be improved using absolute dates from radiometrically dated material. Uranium-Thorium disequilibrium dating can be applied to calcium carbonate samples such as corals or speleothems. Whilst U is soluble in natural waters Th is not, so carbonate precipitated from fresh or sea water typically initially contains no Th at all, leading to a large U-Th ratio (Hellstrom 2003). U-Th dating can be used on samples up to around 500 ka, so it is particularly useful for late Quaternary materials. Another method exploiting the complex Uranium-series decay chain,  $^{234}\text{U}$ - $^{238}\text{U}$  dating can be used to date samples between 10 ka and 2 million years ago, and is therefore also applicable to last interglacial samples

Uranium-series dating can be successfully used to date calcite and aragonite samples, so it might be thought that foraminifera could be dated directly using these techniques. However, this has not proved to be the case. Despite other trace elements within foraminiferal calcite being largely robust to diagenesis, addition of U via a diagenetic coating and U exchange with surrounding pore water contaminates foraminiferal U measurements and precludes the use of U-series dating on foraminifera (Henderson and Keith O'nions 1995). This may be either because U resides interstitially rather than directly within the calcite structure, or is incorporated into the organic material inside the calcite test and is therefore vulnerable to diagenetic processes (Henderson and Keith O'nions 1995). Radiometric dating of bulk sediment, as used by Emiliani (1955) has not proved to be suitably precise or accurate either (Shackleton et al. 2002).

Whilst radiometric methods can provide independent and extremely precise results with errors of  $\pm 100$  years or less (e.g. Cheng et al. 2009), linking marine sediment core records with the isotopic composition of terrestrial radiometrically dated material is not unequivocal. Complications arise because of the assumption that shifts in marine foraminiferal  $\delta^{18}\text{O}$  must be synchronous with shifts in speleothem  $\delta^{18}\text{O}$ , which may not always hold true (Govin et al. 2015) and can be difficult to interpret. For example, the speleothem record from the Italian Corchia cave suggested that the warming of Termination II began 141 ka (Drysdale et al. 2009), which is  $\sim 6$  ka older than typical  $\delta^{18}\text{O}$  records suggest (e.g. Shackleton 2002, Lisiecki and Stern 2016). Differences between marine records and absolute speleothem-derived ages may occur because speleothem  $\delta^{18}\text{O}$  is a product of the local or regional hydrological cycle, which varies in intensity, especially in locations subject to annual monsoons such as China (Cheng et al.

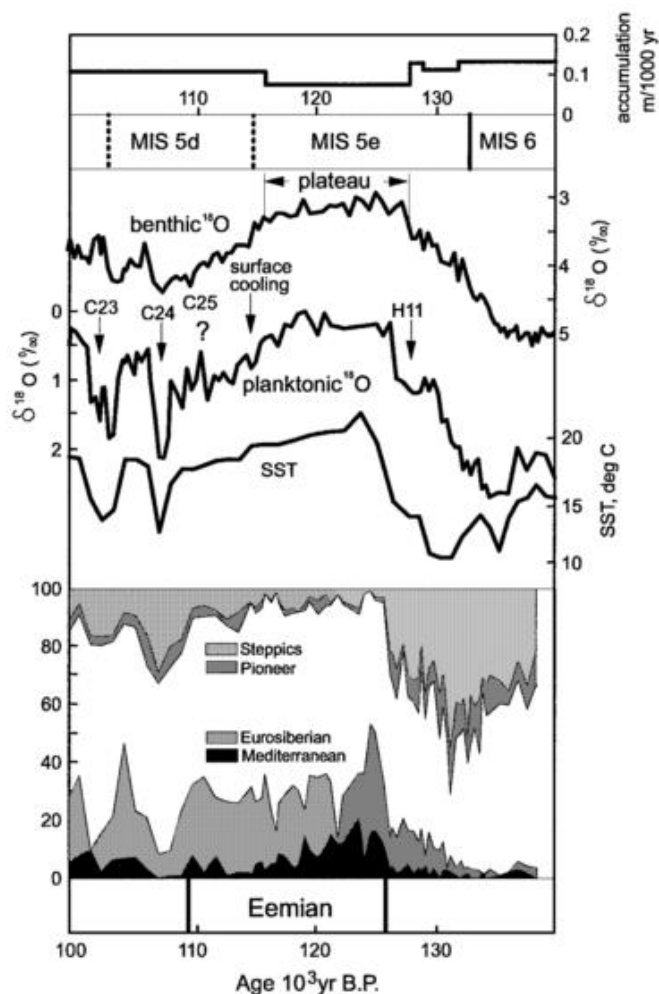


**Figure 7.1** | Last interglacial records from sediment core MD95-2042 using radiometric dating of fossil corals. From the top: sedimentation rate (steps indicate age control points); marine isotope substage divisions; benthic  $\delta^{18}\text{O}$  values; planktonic  $\delta^{18}\text{O}$  values with North Atlantic cold events as per Chapman & Shackleton (1999); alkenone sea surface temperature; major pollen taxa and the identification of the Eemian Interglacial (Adapted from Shackleton et al., 2002)

### 7.3 | ICE CORE CHRONOLOGIES

Many different chronologies have been developed for ice cores using different strategies. For example, the North Greenland Ice Core Project and GRIP have been dated by layer-counting where annual accumulation rate is sufficiently high (Rasmussen et al. 2006; Svensson et al. 2011). A timescale was developed for the ice core from Epica Dome C (ECD) in Antarctica using a parameterised ice-flow model (EPICA Community Members 2004; Parrenin et al. 2007). More recently, a coherent global ice core chronology known as the AICC2012 has extended the previous Bayesian Datic inverse dating method, to produce a consistent Greenland and Antarctic gas and ice

2009). In Europe, local temperatures influence meteoric water which goes on to form speleothems (Drysdale et al. 2009). Under these circumstances, it is important to examine the climatic assumptions underlying any stratigraphic alignment (Govin et al. 2015). For cores such as MD95-2042 which are from near the Iberian Peninsula, they may well be dated using nearby continental speleothem records.

timescale by combining glaciological modelling with stratigraphic and absolute tie points (Lemieux-Dudon et al. 2010), without using radiometrically-dated speleothems (thus avoiding the associated assumptions of climatological synchronicity) (Bazin et al. 2013; Veres et al. 2013). However, due to a scarcity of age control points, AICC2012 is imprecise during the glacial inception period, with differences of several millennia from the GICC05modelext, which remains the most accurate age model for Greenland ice cores (Govin et al. 2015).

Linking ice core records to marine records is not without its own pitfalls. Marine proxy records can be influenced by local stochastic processes such as mesoscale eddies and rings, upwelling or downwelling due to unusual weather events, and episodic nutrient input due to terrestrial flooding or sediment flows, which produce noise in high-resolution records (Crowley 1999). This can mean surface water proxy records in particular are not necessarily representative of the mean state of the regional climate over longer timescales. However, by making the assumption that proximal marine and terrestrial records respond to climate change synchronously (Rousseau et al. 2006), marine sediment cores have been convincingly dated by correlation with  $\delta^{18}\text{O}$  in ice core records (e.g. Shackleton 2000; Capron et al. 2014; Govin et al. 2014). The next section describes methods used to produce the age models for this study.

## 7.4 | AGE MODELS FOR U1305 AND U1302

Age models within the Labrador Sea are notoriously awkward to devise, due to regional difficulties with two of the major proxies used in palaeoceanography: percentage of planktonic foraminifera *N. pachyderma* (*s*), and foraminiferal  $\delta^{18}\text{O}$  (Govin et al. 2012). Firstly, in cold waters (below 6.5°C) the faunal assemblage is dominated almost entirely by *N. pachyderma* (*s*) even though regional surface temperatures during glacial periods can get as low as 3°C (Govin et al. 2012) (Figure 7.2). This means MAT SST estimates become insensitive through very cold periods as the proxy signal becomes saturated (McManus et al. 1996), which makes defining the start of Termination II and the degree of warming difficult using *N. pachyderma* (*s*) percentages alone. Secondly,  $\delta^{18}\text{O}$  values in this location may be sensitive to the influx of glacial meltwater during Termination events. This can be attributed directly to the input of  $^{18}\text{O}$ -depleted meltwater (Rasmussen et al. 2003; Hillaire-Marcel et al. 2011), or may be due to increased sea ice

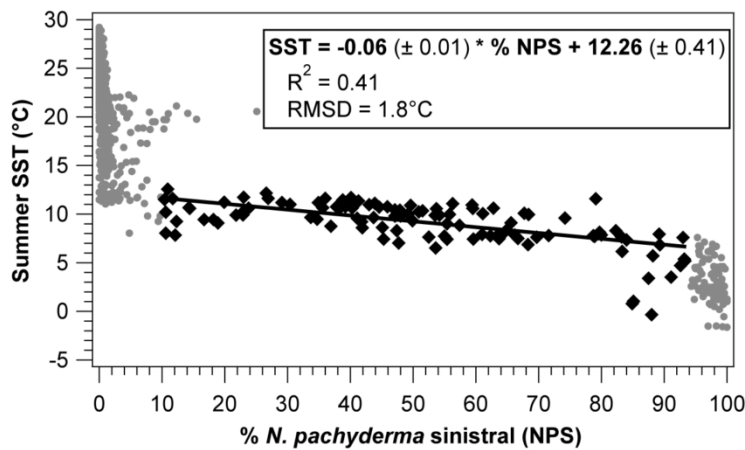


**Figure 7.2** | The relationship between percentage of *N. pachyderma* (*s*) and summer SST in the North Atlantic. Black diamonds indicate *N. pachyderma* (*s*) abundance between 10% - 94% and SST below 15°C, which determine the linear relationship shown. Grey circles show database sites having SST over 15°C or *N. pachyderma* (*s*) abundance over 94% or under 10%. Figure from Govin et al. (2012), using data from the MARGO database of Kucera et al. (2005).

formation caused by surface cooling and freshening, which results in the formation of isotopically depleted brines, and can carry depleted  $\delta^{18}\text{O}$  values into mesopelagic and deep waters if they become dense enough to sink (Risebrobakken et al. 2006; Hillaire-Marcel and de Vernal 2008). To combat these

drawbacks, this study used a multi-proxy approach rooted in the data generated for this study to create more comprehensive age models than were available for U1302 or U1305 before.

### 7.4.1 | Previously Published Chronologies

Age models for both U1305 and U1302 have been published based upon planktonic  $\delta^{18}\text{O}$  by Hillaire-Marcel et al. (2011), which was correlated with the LR04 benthic  $\delta^{18}\text{O}$  isotope stack (Lisiecki and Raymo 2005) back to 1.1 million years ago (MIS 32) in U1305. Chronostratigraphy was determined for the most part using tie points at isotopic transitions, whereby a depth was assigned as the mid-point of an isotopic shift between marine isotope stages (e.g. MIS 6/5e transition), with identification of the depth representing some stadial and interstadial peaks and troughs of MIS 5 in U1302 (e.g. 5e peak, 5d peak, 5c peak). Age control points of Hillaire-Marcel et al. (2011) pertinent to the present study are fairly sparse (Table 7.1). Sedimentation rate at U1305 varies nearly 10-fold between glacial and interglacial conditions due to sediment focusing beneath a stronger WBUC (Hillaire-Marcel et al. 1994; Hillaire-Marcel et al. 2001), but is more consistent in U1302, as illustrated in Figure 7.3, which shows the sedimentation rates of these age models. Ages between tie points were obtained by linear interpolation assuming constant sedimentation rate. However, given the wide variation in

**Table 7.1** | Age control points pertinent to the present study together with depth in metres composite depth (mcd), items left blank were not defined by Hillaire-Marcel et al. (2011).

U1305 depth (mcd)	U1305 sedimentation rate (cm/ka)	U1302 depth (mcd)	U1302 sedimentation rate (cm/ka)	Description	Age (ka)
18.50	15	11.20	25	4/5	71
		17.40	13	5c peak	96
				5d peak	109
24.90	47	19.80	15	5d/5e	115
		21.00	34	5e peak	123
32.00	5	23.40	11	6/5e	130
35.09	5	30.00	11	6/7	191

sedimentation rate (particularly in U1305), and that gaps between tie points are as much as 61 ka apart through this period, it is clear this age model is very simple and coarse in resolution. Multi-proxy data from U1305 and U1302 on the chronology of Hillaire-Marcel et al. (2011) are shown in comparison with LS15 in Figure 7.4.

It is apparent that the scarcity of age control points produces some inaccuracy with this age model. Figure 7.4 shows good agreement with the mid-point of the MIS 6/5e transition between benthic and planktonic  $\delta^{18}\text{O}$  and references, as is to be expected since this was utilised as the age control point at 130 ka. However, the peak glacial

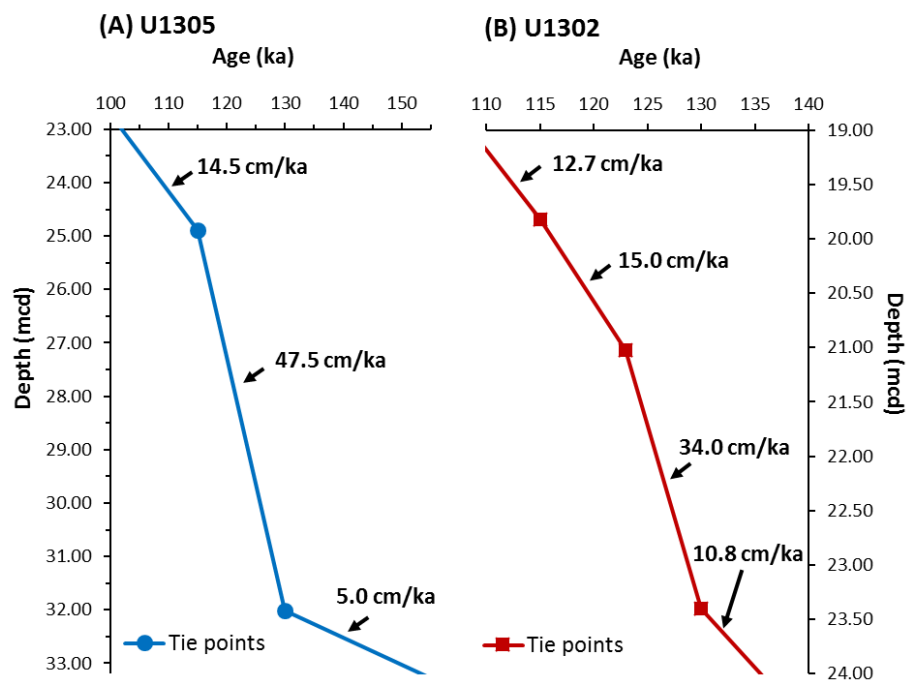


**Figure 7.3** | Sedimentation rates from the age model of Hillaire-Marcel et al. (2011) for (A) U1305 and (B) U1302.

benthic  $\delta^{18}\text{O}$  values denoting the penultimate glacial peak (isotope event 6.2 of Imbrie et al. 1984) occur 3.5 ka later than the LS15 stacks, and would result in an extremely rapid Termination II (TII). There is a large discrepancy between the last “interglacial” type benthic  $\delta^{18}\text{O}$  values between U1302 (~119 ka) and U1305 (114 ka), neither of which agree well with LS15, though it is likely this difference may be an artefact of

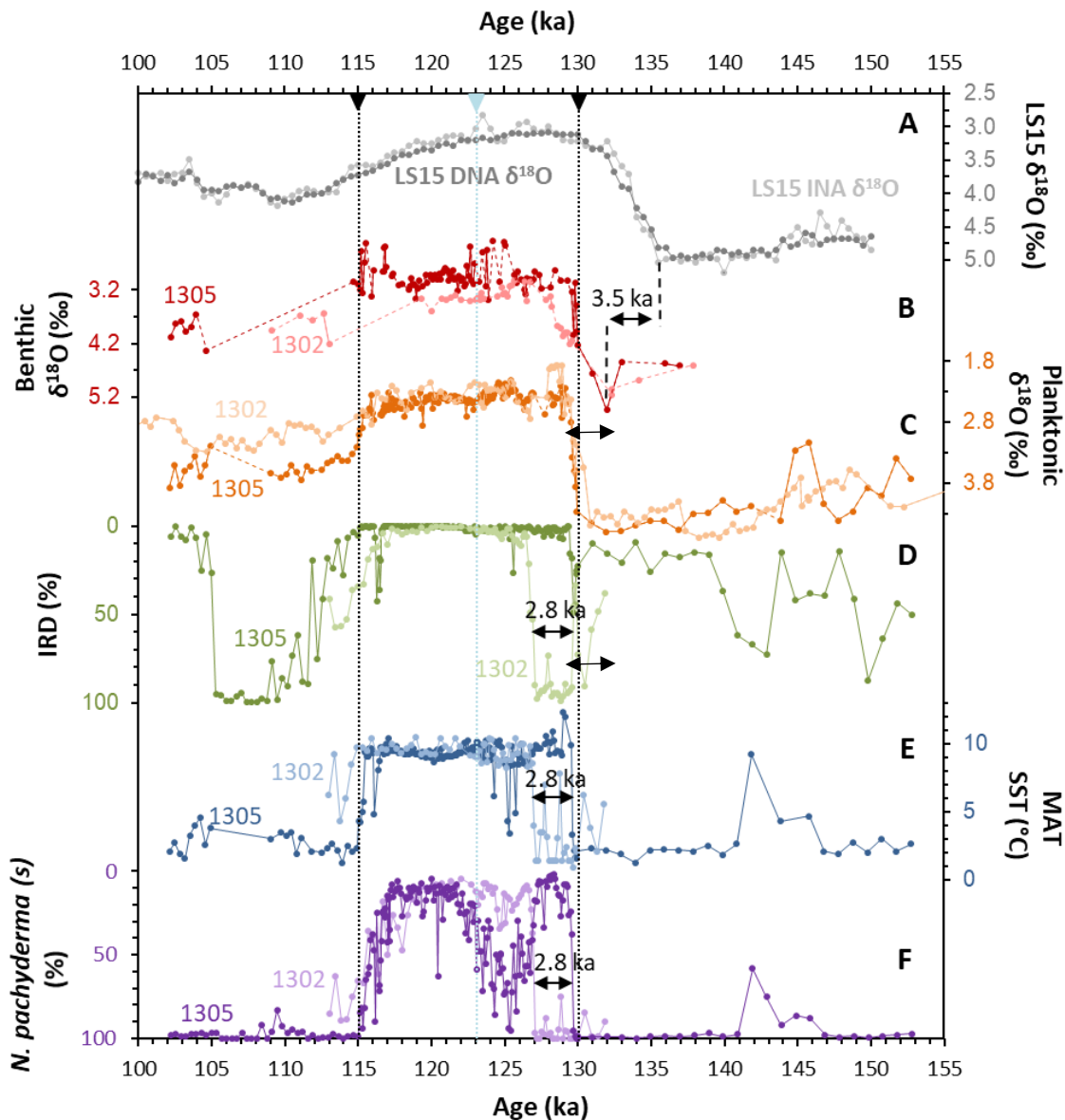


**Figure 7.4** | U1305 and U1302 data plotted on the timescale of Hillare-Marcel et al. (2011). (A) LS15 Intermediate North Atlantic (INA; light grey) and Deep North Atlantic (DNA; dark grey) benthic  $\delta^{18}\text{O}$  stacks (Lisiecki and Stern 2016). (B) U1305 benthic  $\delta^{18}\text{O}$  (red; this study) and U1302 multi-species benthic  $\delta^{18}\text{O}$  (Kaboth et al. unpublished). (C) U1305 (dark orange) and U1302 (light orange)  $N. pachyderma$  ( $s$ )  $\delta^{18}\text{O}$  from Hillaire-Marcel et al. (2011). (D) U1305 (dark green) and U1302 (light green) IRD percentage (this study). (E) U1305 (dark blue) and U1302 (light blue) MAT SST estimates (this study). (F) U1305 (dark purple) and U1302 (light purple) percentage of  $N. pachyderma$  ( $s$ ) (this study). Dotted lines indicate gaps in the records. Vertical dotted lines indicate age control points for both cores (black) and for U1302 only (light blue) of Hillaire-Marcel et al. (2011). Black double-headed arrows indicate discrepancies of 3.5 ka between peak enriched benthic  $\delta^{18}\text{O}$  and the LS15 stacks, and 2.8 ka between data produced for U1302 and U1305 in this study.

gaps in both benthic isotopic records through the glacial inception. It is also apparent from Figure 7.4 that despite the agreement between  $\delta^{18}\text{O}$  records of U1305 and U1302 through TII, there is a large discrepancy when comparing the IRD, MAT SST and *N. pachyderma* (*s*) abundance data produced in this study. All three proxies would indicate a gap between the onset of interglacial conditions of around 2.8 ka between U1305 and U1302, which seems unlikely since these cores lie within the same ocean basin. These issues suggest that there are some higher frequency sedimentation rate changes present in the cores that are not accounted for by this simple model based solely upon planktonic isotopes.

A second age model was published by Channell et al. (2012) for U1302 and the nearby site U1303 also from the south-east flank of Orphan Knoll. In an attempt to avoid isotopic perturbation of age models by meltwater events, ice surging and/or brine production by sea-ice growth recognised as an issue in the Hillaire-Marcel et al. (2011) age model, Channell et al. (2012) derived their age model using tandem correlation between planktonic *N. pachyderma* (*s*)  $\delta^{18}\text{O}$  (due to a paucity of benthic foraminifera through crucial periods) and relative geomagnetic palaeointensity, with the intention of improving on the resolution of the Hillaire-Marcel et al. (2011) age model. Also, the latest (unpublished) working age model for U1305 was kindly obtained from Claude

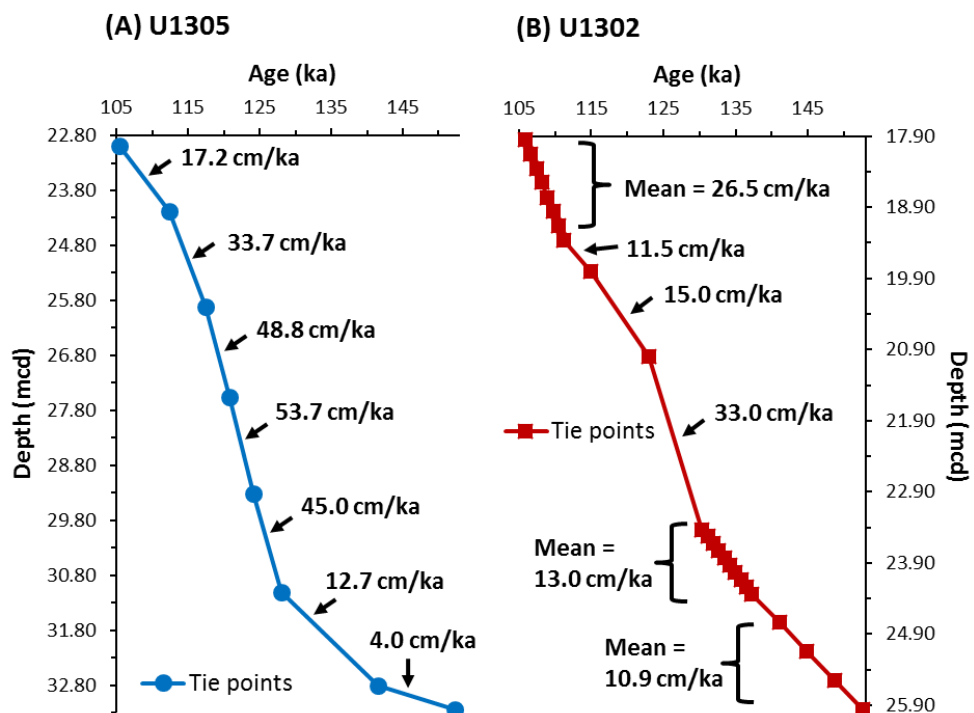


**Figure 7.5** | Sedimentation rates for (A) the latest working U1305 age model of Hillaire-Marcel (personal communication), and (B) the published age model for U1302 of Channell et al. (2012). Tie points are estimated based upon changes in sedimentation rate for U1305.

**Table 7.2** | Estimated tie points with ages in thousand years (ka) and depths in metres composite depth (mcd) derived from sedimentation rate changes from the latest working age model for U1305 (Claude Hillaire-Marcel, personal communication), and the published age model of Channell et al. (2012) for U1302.

U1305 <sup>a</sup>			U1302 (Channell et al. 2012)		
Depth (mcd)	Age (ka)	Average subsequent sedimentation rate (cm/ka)	Depth (mcd)	Age (ka)	Average subsequent sedimentation rate (cm/ka)
22.98	105.36	17.2	17.95	105.9	26.0
24.18	112.33	33.7	18.15	106.67	26.3
25.91	117.46	48.8	18.35	107.43	26.3
27.56	120.84	53.7	18.55	108.19	27.3
29.31	124.1	45.0	18.76	108.96	26.3
31.11	128.1	12.7	18.96	109.72	26.0
32.81	141.53	4.0	19.16	110.49	27.6
33.24	152.2	4.0	19.37	111.25	11.5
			19.80	115	15.0
			21.00	123	33.0
			23.43	130.36	13.0
			23.53	131.13	13.2
			23.63	131.89	13.2
			23.73	132.65	13.0
			23.83	133.42	13.2
			23.93	134.18	13.0
			24.03	134.95	14.5
			24.14	135.71	13.0
			24.24	136.48	13.2
			24.34	137.24	10.5
			24.74	141.06	10.7
			25.15	144.88	10.7
			25.56	148.71	10.5
			25.96	152.53	11.9

<sup>a</sup> Critical tie points for this unpublished working age model were estimated based upon changes in sedimentation rate.

Hillaire-Marcel (personal communication). Tie points for both of these age models are estimated in Table 7.2, sedimentation rates are shown in Figure 7.5 and data from this study is again is plotted on these age models plotted in Figure 7.6.

Figure 7.6 shows that these latest age models present even larger discrepancies. The difference between U1302 and U1305 peak glacial benthic and planktonic  $\delta^{18}\text{O}$  values is 3.8 ka and 4.3 ka respectively. This gap is even more apparent between IRD % (6.4

ka), MAT SSTs (7.8 ka) and *N. pachyderma* (*s*) abundance (7.7 ka). These differences are well beyond the uncertainty associated with LS15 through this period ( $\pm 4$  ka), and clearly indicate the need for new age models for these cores.

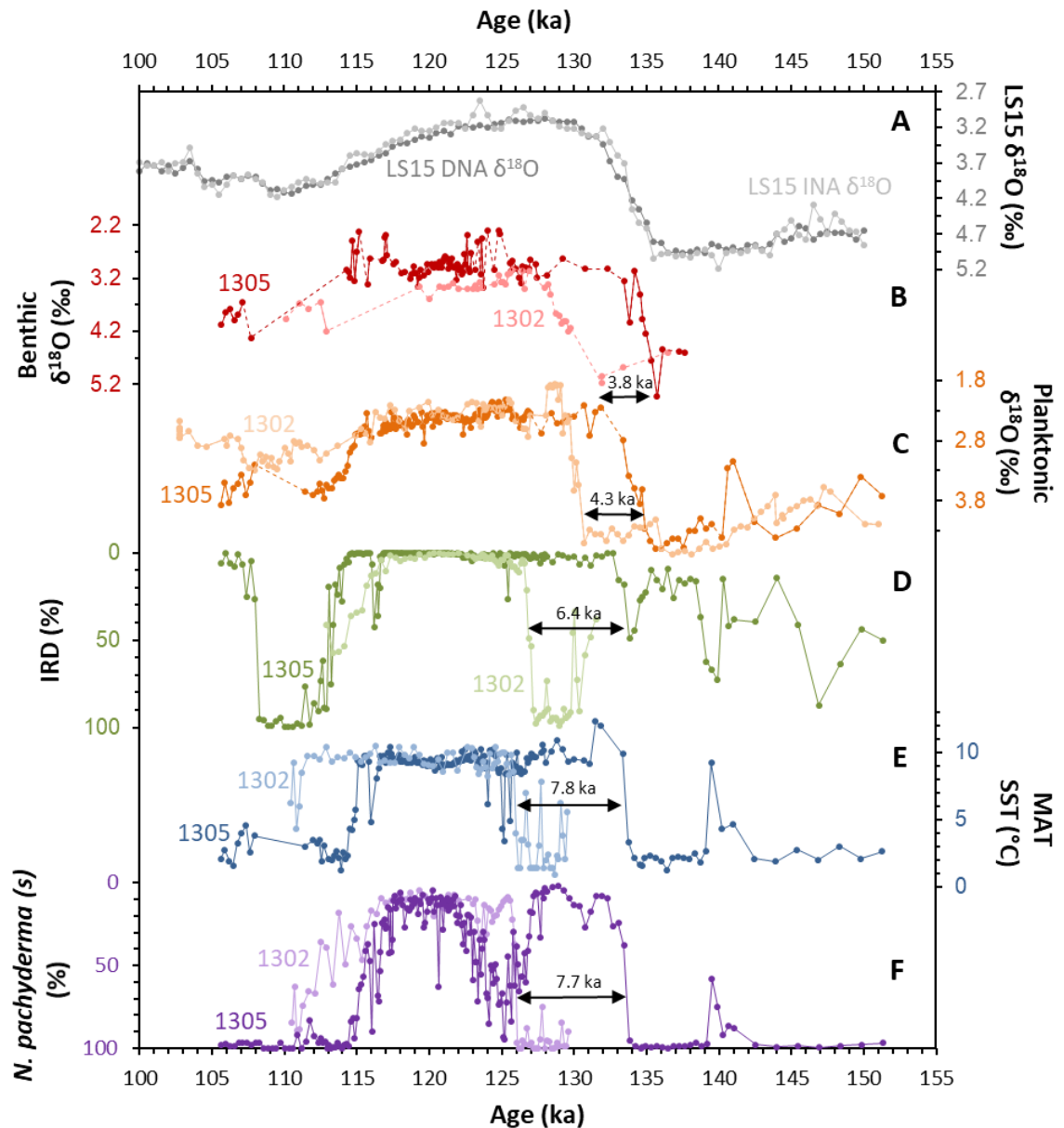


**Figure 7.6** | U1305 data on the latest working age model of Hillaire-Marcel (personal communication) and U1302 data on the timescale of Channell et al. (2012). (A) LS15 Intermediate North Atlantic (INA; light grey) and Deep North Atlantic (DNA; dark grey) benthic  $\delta^{18}\text{O}$  stacks (Lisiecki and Stern 2016). (B) U1305 benthic  $\delta^{18}\text{O}$  (red; this study) and U1302 multi-species benthic  $\delta^{18}\text{O}$  (Kaboth et al. unpublished). (C) U1305 (dark orange) and U1302 (light orange) *N. pachyderma* (*s*)  $\delta^{18}\text{O}$  from Hillaire-Marcel et al. (2011). (D) U1305 (dark green) and U1302 (light green) IRD percentage (this study). (E) U1305 (dark blue) and U1302 (light blue) MAT SST estimates (this study). (F) U1305 (dark purple) and U1302 (light purple) percentage of *N. pachyderma* (*s*) (this study). Dotted lines indicate gaps in the records. Age control points are listed in Table 7.2. Black double-headed arrows indicate discrepancies in timing between glacial indicators in data produced from U1302 and U1305 in this study.

**Table 7.3** | Isotopic range of mean  $\delta^{18}\text{O}$  values for the penultimate glacial (132 – 142 ka) and last interglacial (128 – 116 ka) periods from planktonic foraminifera *N. pachyderma* (s) using the latest available working age model for U1305 (Hillaire-Marcel, personal communication) and Channell et al. (2012) for U1302.

Site	Mean glacial $\delta^{18}\text{O}$ (‰)	Mean interglacial $\delta^{18}\text{O}$ (‰)	Peak Interglacial $\delta^{18}\text{O}$ (‰)
U1305	4.05	2.44	2.11
U1302	4.41	2.36	2.12

Upon investigation, it was noted that between 23.05 and 22.75 mcd, the planktonic  $\delta^{18}\text{O}$  values from U1302 had “exceptionally” depleted values (mean

= 1.92 ‰). However, these samples lie within nearly a metre of core (23.25 – 22.40 mcd) characterised by very heavy IRD input (mean 93 %) and *N. pachyderma* (s) dominance (mean 96.3 %), both strong indications of extremely cold conditions with abundant icebergs, presumably corresponding with Heinrich event 11. For comparison, average subsequent planktonic  $\delta^{18}\text{O}$  values through the last interglacial period on the chronology of Channell et al. (2012) (128 – 116 ka) were 2.36 ‰ (Table 7.3). In their careful and thorough planktonic isotope study of U1302 and U1305, Hillaire-Marcel et

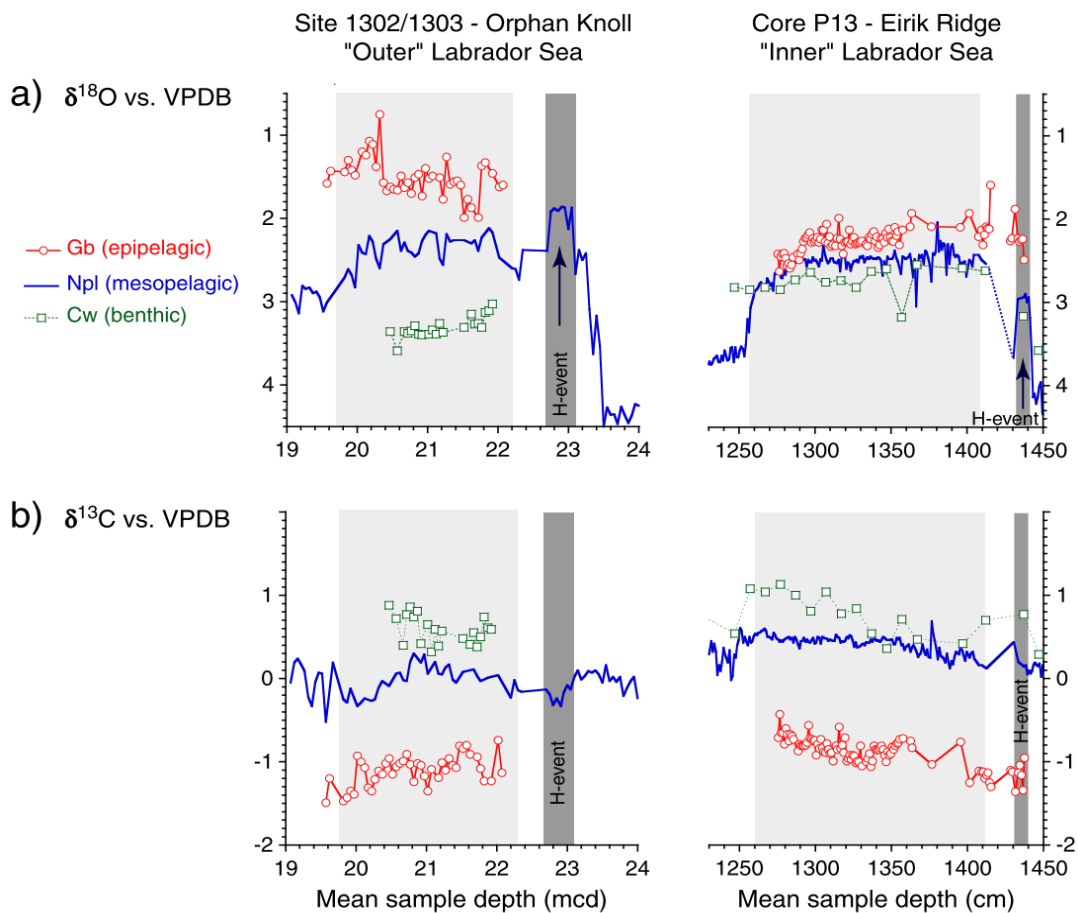


**Figure 7.7** | Multi-species oxygen (a) and carbon (b) isotopes from U1302 (left) and Eirik Ridge core HU90-013-013 (right), highlighting the highly depleted oxygen isotopic values during H11 (dark grey shading). Light grey indicates the last interglacial interval (Hillaire-Marcel et al. 2011).

al. (2011) also noted such observations, and associated “large amplitude isotopic excursions during glacial stages” with Heinrich events in particular. Figure 7.7 illustrates the phenomenon by comparing planktonic  $\delta^{18}\text{O}$  (a) and  $\delta^{13}\text{C}$  (b) from U1302 (left) and HU90-013-013P (right), a core from Eirik Ridge close to U1305, which highlights a period of very depleted  $\delta^{18}\text{O}$  values through H11 (dark grey shading in Figure 7.7). It is clear that this excursion is much more pronounced in U1302, with more depleted values than during MIS 5e (light grey shading in Figure 7.7).

This was not the first study to make such observations in the Labrador Sea. Depleted  $\delta^{18}\text{O}$  values have long been associated with Heinrich events, typically within but towards the end of ice rafted layers (e.g. Clarke et al. 1999, Hiscott et al. 2001). Rasmussen et al. (2003) attributed this association of depleted  $\delta^{18}\text{O}$  excursions during periods of heavy IRD input directly to the influx of isotopically depleted meltwater. In light of this observation, their age model took IRD abundance into consideration, and instead assigned the onset of MIS 5e based on decrease in *N. pachyderma* (*s*) abundance, taking it as an indication of warm SSTs. An alternative explanation, favoured by Hillaire-Marcel et al. (2011), is that these depleted  $\delta^{18}\text{O}$  excursions were due to the “production and sinking of isotopically light brines” during sea ice formation, promoted by fresh cold surface waters from iceberg melt, rather than to the isotopic dilution of the meltwater itself (Hillaire-Marcel and de Vernal 2008). The mechanism behind these depleted  $\delta^{18}\text{O}$  values is discussed in section 8.2.3. In order to account for this effect, a new method of producing consistent age models for marine cores in the Labrador Sea using a range of proxy data is outlined below.

## 7.4.2 | Age Model Construction

Age models for this study were based upon correlation with the LS15 regional intermediate and deep North Atlantic  $\delta^{18}\text{O}$  stacks of Lisiecki and Stern (2016), together with their North Atlantic IRD stack. Tie points were chosen based upon multiple proxy evidence where possible, including planktonic  $\delta^{18}\text{O}$ , for which much longer and more complete records were available than for benthic isotopes, and temperature reconstructions from faunal assemblages and Mg/Ca ratios. Other tie points were based on sedimentological features (the red layer and U1305 diatom mat introduced in Chapter 4). Depending on the climate hypothesis behind each tie point, some were

single events in time (e.g. peaks in IRD input), whilst some represent the start and end of a “plateau” in values (e.g. a period of sustained low benthic or planktonic  $\delta^{18}\text{O}$  values). Tie points were also chosen with an eye to minimise sudden changes in sedimentation rates where possible, but it was deemed more important to produce chronologies that made climatic sense and were coherent with each other, since the underlying assumption that sedimentation rate is consistent and smoothly varying through glacial-interglacial cycles may not necessarily be true at these locations. Ages were derived using linear interpolation assuming a constant sedimentation rate between tie points. The rationale behind each tie point is explained below.

Planktonic isotopes for both cores were from Hillaire-Marcel et al. (2011). However, gaps in the record for U1305 hindered the accuracy of any age model based upon them. Therefore, as outlined in section 6.3, monospecific *N. pachyderma (s)* samples were picked to extend the isotopic record for U1305 where sufficient foraminifera could be found, particularly through the early last interglacial (31.61 – 31.16 mcd) and the glacial inception (25.33 – 23.33 mcd). Whilst some gaps remain, this study has greatly improved the resolution of planktonic isotopic values available for U1305, and it is to be hoped, improved the age models of this study. In addition, insufficient benthic foraminifera had been found from U1305 for isotopic analysis previously. To address this lack of data, benthic foraminifera *C. wuellerstorfi* was picked for U1305 wherever possible and analysed for  $\delta^{18}\text{O}$  and  $\delta^{13}\text{C}$ . Though the record is patchy and gaps remain, most notably through MIS 5d, this new benthic  $\delta^{18}\text{O}$  record has significantly contributed to the development of the age model in this study.

### 7.4.3 | Tie Points

Tie points for the age models created for this study are listed in Table 7.4, and the rationale behind each point is detailed in the following section. Tie points are illustrated graphically on a depth scale for U1305 (Figure 7.8) and U1302 (Figure 7.9). Figure 7.10 illustrates proxy data using these new age models for both cores.

It was decided to frame the age model within published tie points to LR04 by Hillaire-Marcel et al. (2011) of 71 ka (U1305), 96 ka (U1302) and 191 ka (both), which determined the dates at the beginning and end of each section of core. Although there

**Table 7.4** | Tie points used to construct age models for U1302 and U1305 in this study. Depth is given in metres composite depth (mcd) and ages in thousands of years (ka).

U1305 Depth (mcd)	U1302 Depth (mcd)	Age (ka)	Reason(s)	Proxy used	Dating Reference
18.50		71	MIS 5/4 transition	Planktonic $\delta^{18}\text{O}$	LR04 <sup>a</sup>
	17.40	96	MIS 5c peak	Planktonic $\delta^{18}\text{O}$	LR04 <sup>a</sup>
23.43	18.22	103.5	Depleted planktonic $\delta^{18}\text{O}$ , first warm temperatures	Planktonic $\delta^{18}\text{O}$ , MAT and Mg/Ca SSTs	LS15 <sup>b</sup>
24.03	18.62	106	Depleted planktonic $\delta^{18}\text{O}$ last warm temperatures	Planktonic $\delta^{18}\text{O}$ , MAT and Mg/Ca SSTs	LS15 <sup>b</sup>
24.23	18.82	108	Depleted planktonic $\delta^{18}\text{O}$ first warm temperatures	Planktonic $\delta^{18}\text{O}$ , MAT and Mg/Ca SSTs	LS15 <sup>b</sup>
24.68	19.07	111.5	Depleted planktonic $\delta^{18}\text{O}$ warm temperatures	Planktonic $\delta^{18}\text{O}$ , MAT and Mg/Ca SSTs	LS15 <sup>b</sup>
24.98	19.62	114.5	Depleted planktonic $\delta^{18}\text{O}$ , last warm temperatures	Planktonic $\delta^{18}\text{O}$ , MAT and Mg/Ca SSTs,	LS15 <sup>b</sup>
25.13	19.92	116	End of the last interglacial	<i>N. pachyderma</i> (s) %, MAT SSTs, IRD, planktonic and benthic $\delta^{18}\text{O}$ , cluster analysis	LS15 <sup>b</sup>
29.91	22.07	126.5	Red layer onset assumed to be synchronous	Visible in core	This study
31.61	22.20	128.5	Start of the last interglacial	<i>N. pachyderma</i> (s) %, MAT SSTs, IRD, planktonic $\delta^{18}\text{O}$	LS15 <sup>b</sup>
31.76		128.677	First sample containing the diatom mat	Diatom mat	This study
31.86	22.40	130	Heinrich event 11 peak	IRD % Cluster analysis	LS15 <sup>b</sup>
32.11	23.65	135.5	Enriched benthic $\delta^{18}\text{O}$	Planktonic and/or benthic $\delta^{18}\text{O}$	LS15 <sup>b</sup>
32.26	24.15	140	H12	IRD, planktonic $\delta^{18}\text{O}$	LS15 <sup>b</sup>
32.81		146.5	Depleted planktonic $\delta^{18}\text{O}$	Planktonic $\delta^{18}\text{O}$	LS15 <sup>b</sup>
	25.05	147.48	Tied to U1305 IRD peak	Planktonic $\delta^{18}\text{O}$ , IRD	This study
35.09	30.00	191	MIS 7/6 transition	Planktonic $\delta^{18}\text{O}$	LR04 <sup>a</sup>

<sup>a</sup> (Lisiecki and Raymo 2005; Hillaire-Marcel et al. 2011)

<sup>b</sup> (Lisiecki and Stern 2016)

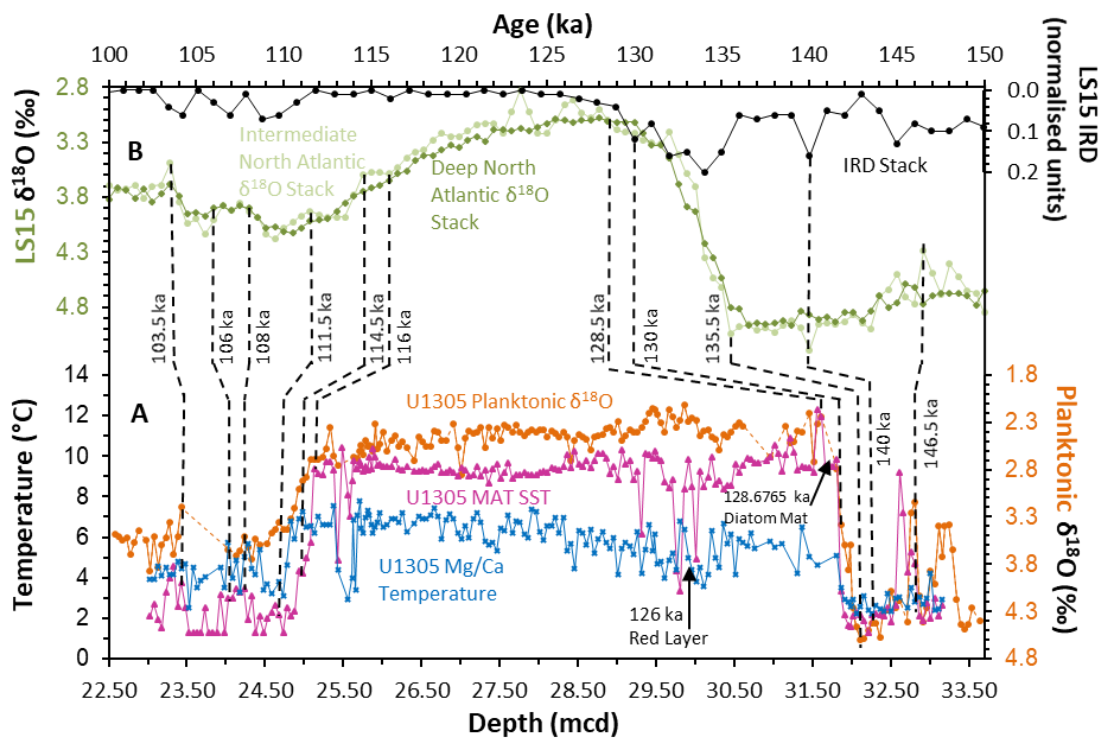


**Figure 7.8** | Age control points used to tie (A) U1305 to (B) LS15 North Atlantic intermediate (light green) and deep (dark green)  $\delta^{18}\text{O}$  stacks, and IRD stack (black) (Lisiecki and Stern 2016). Planktonic  $\delta^{18}\text{O}$  (orange), MAT SSTs (pink) and Mg/Ca temperatures (blue) for U1305 are included. Black arrows indicate two additional age control points along with the reason for their selection. Each tie point is discussed in the text.

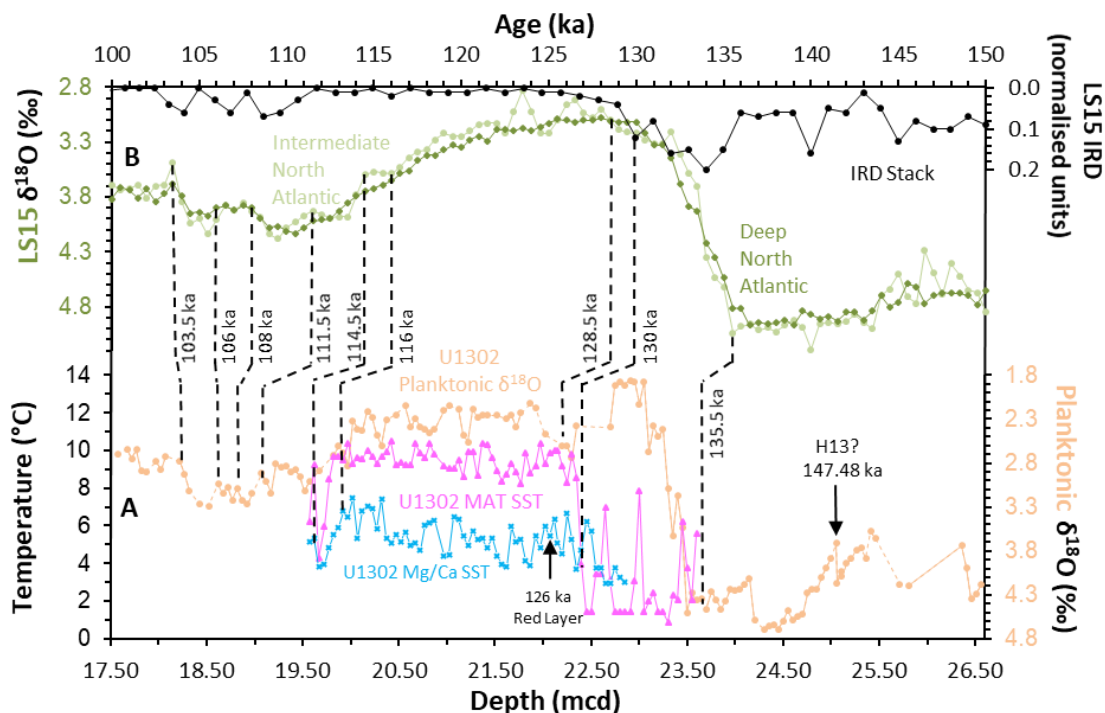


**Figure 7.9** | Age control points used to tie (A) U1302 to (B) LS15 North Atlantic intermediate (light green) and deep (dark green)  $\delta^{18}\text{O}$  stacks, and IRD stack (black) (Lisiecki and Stern 2016). Planktonic  $\delta^{18}\text{O}$  (orange), MAT SSTs (pink) and Mg/Ca temperatures (blue) for U1302 are included. Black arrows indicate two additional age control points along with the reason for their selection. Each tie point is discussed in the text.

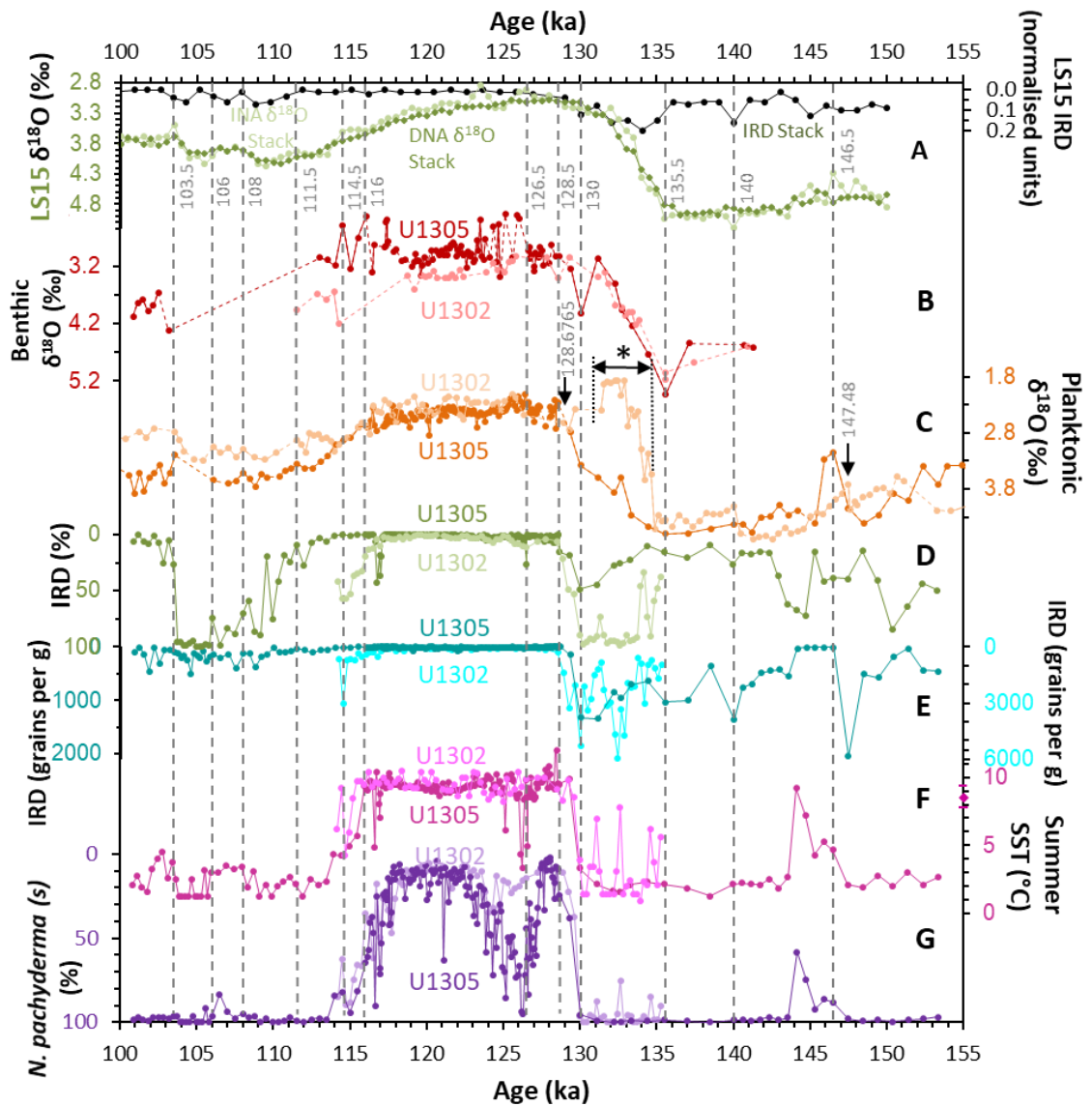


**Figure 7.11** | Multi-proxy U1305 and U1302 data illustrating tie points used in the construction of the age model for this study. Vertical figures in grey associated with vertical dashed grey lines are tie points in ka. Black arrows in (C) indicate tie points adopted for U1302 only at 147.48 ka, and for U1305 only at 128.6765 ka, discussed in the text. All records present data produced for this study, unless otherwise indicated. Dotted lines in all records indicate gaps in the records. (A) LS15 Intermediate North Atlantic (INA; light green) and Deep North Atlantic (DNA; dark green)  $\delta^{18}\text{O}$  stacks, together with the North Atlantic IRD stack (black). (B) U1305 benthic  $\delta^{18}\text{O}$  (dark red) and U1302 multi-species benthic  $\delta^{18}\text{O}$  (pale red; Kaboth et al., unpublished). (C) *N. pachyderma* (*s*) planktonic  $\delta^{18}\text{O}$  for U1305 (dark orange) and U1302 (pale orange) (Hillaire-Marcel et al. 2011), asterisk with double-headed arrow indicates U1302 planktonic depleted isotope excursion discussed in the text. (D) IRD percentage for U1305 (dark green) and U1302 (light green). (E) IRD concentration for U1305 (dark turquoise) and U1302 (light turquoise). (F) MAT SSTs for U1302 (light pink) and U1305 (dark pink), pink diamond on the y-axis indicates U1305 MAT modern SST. (G) *N. pachyderma* (*s*) percentage for U1305 (dark purple) and U1302 (light purple).

was a mis-match between peak U1305 and U1302 benthic  $\delta^{18}\text{O}$  and the LS15 stack of 3.5 ka (Figure 7.4), it is more accurate than the more recent age models, which increased discrepancies between the cores to up to 7.8 ka (Figure 7.6). These tie points

also have the advantage of setting long-term average sedimentation rates at each location.

A tie point for U1305 was adopted at 32.81 mcd to 146.5 ka, by correlating the most depleted MIS 6 planktonic  $\delta^{18}\text{O}$  value to LS15. A tie point for U1302 was adopted at 25.05 mcd, with the age of 147.48 ka taken from the date of a large peak in IRD concentration observed in U1305 (Figure 7.11). IRD counts were not available for U1302 back to this period, but this event is identified based on a shift to depleted planktonic  $\delta^{18}\text{O}$  values (Figure 7.10), that corresponded with a peak in Ca/Sr and GRAPE density documented by Channel et al. (2012) (Figure 8.6), and taken as evidence of a layer pertaining to a potential H13 ice rafting event (see section 8.2.1). The adoption of this tie point for U1302 brought planktonic  $\delta^{18}\text{O}$  and  $\delta^{13}\text{C}$  records into much closer agreement with U1305. H12 at 140 ka in LS15 was assigned to 32.26 mcd in U1305, to align with a large increase in IRD concentration (1368 grains per g), and with a shift to depleted planktonic  $\delta^{18}\text{O}$  in U1302 at 24.15 mcd.

The most enriched benthic  $\delta^{18}\text{O}$  values of U1305 (32.11 mcd) and U1302 (23.65 mcd) were assumed to be regionally synchronous, and tied to 135.5 ka in LS15, presumably related to isotopic event 6.2 (Imbrie et al. 1984). The peak of ice rafting in both U1305 and U1302 appeared within the upper part of H11, and was therefore tied to the last high IRD value in LS15 (130 ka). In U1305, this was assigned to 31.86 mcd based upon an IRD percentage value of 48 %, which coincided with a peak in IRD concentration (1326 grains per g). In U1302, IRD percentages approached 100% through around a metre of core, therefore a conspicuous peak in IRD concentration at 22.40 mcd was used for this tie point (5261 grains per g) following Bond and Lotti (1995). The inclusion of these tie points is strengthened by cluster analysis of faunal assemblages, which identified this same point as the top of zone A in both cores (Figure 5.13).

The onset of the last interglacial at 128.5 ka was associated in U1302 with the simultaneous reduction in *N. pachyderma* (*s*) abundance and IRD to <10% (and IRD concentration to <300 grains per g) at 22.20 mcd. Similar values were observed in U1305 at 31.61 mcd, which coincided with a shift to very warm MAT SSTs (~12°C) and depleted planktonic  $\delta^{18}\text{O}$  values (2.25 ‰). This was also the first sample lying above the diatom mat (section 4.4). The use of this first sample above a diatom mat as the onset of the last interglacial follows the work of Rasmussen et al. (2003) who made similar observations in two cores from the Flemish Cap. It is generally considered that

diatom mats were deposited rapidly (e.g. Kemp and Baldauf 1993; Yoder et al. 1994; Boden and Backman 1996; Archer et al. 1997; Kemp et al. 2006; Allen et al. 2005). The sedimentation rate during the early last interglacial period (~128.5 – 126.5 ka) according to the age model of this study was also extremely high (85 cm/ka), particularly in comparison with the sedimentation rate during H11 (4.5 – 7.6 cm/ka). This very high sedimentation rate is in line with observations of similarly very high postglacial sedimentation rate during the Holocene in U1305 of over 90 cm/ka (Stoner et al. 2013). Therefore, a further age control tie point was adopted for the lowest sample containing the diatom mat in U1305 (31.76 mcd) of 128.6765 ka. This (highly specific) date was used to extend the extremely high early last interglacial sedimentation rate of 85 cm/ka to include the diatom mat. Without any objective way of estimating the duration of the diatom mat formation, this was deemed an appropriate way of accounting for any offset caused by the diatom mat on the age model.

Following the observation by Nicholl et al. (2012) of a turbidite-driven red layer associated with a Laurentide glacial outburst flood event through the Hudson Strait in both U1302 and U1305, the sharp base of this layer (22.07 and 29.91 mcd respectively) was assumed to be synchronous across the Labrador Sea within the resolution of the cores. This seems likely, if the last interglacial flood event was similar to the catastrophic drainage of Lake Agassiz during the Holocene, which is estimated to have occurred in less than a year (Clarke et al. 2004). Initially, the base of the red layer on the age model of this study was dated to ~125.2 ka in U1305 and ~127.8 ka in U1302. Therefore, to account for the synchronous deposition of this layer, the average of these two dates (126.5 ka) was assigned to the base of the red layer in both cores. This value is in good agreement, within uncertainty, with the date of ~126 ka given by Nicholl et al. (2012), and provides a rare and valuable age control point within the last interglacial period itself.

The end of the last interglacial at 116 ka was tied to 25.13 mcd in U1305, identified as the last sample containing low *N. pachyderma* (*s*) abundance (<80 %), warm MAT temperatures (> 9°C), and depleted *N. pachyderma* (*s*) planktonic (2.69 ‰) and benthic (2.32 ‰)  $\delta^{18}\text{O}$  values. This tie point is further strengthened by cluster analysis, which identified 25.13 mcd as the last sample in zone Fb, the upper zone pertaining to last interglacial-type faunal assemblages. In U1302 this age point was assigned to 19.92 mcd as the last sample containing low *N. pachyderma* (*s*) abundance (< 60 %), low IRD

input (<30 %) and fairly depleted planktonic  $\delta^{18}\text{O}$  values (2.68 ‰). The MAT SST estimate remained high for the ensuing three samples (> 9°C), but those same samples also contained quite a lot of IRD (33 – 36 %) and far more *N. pachyderma* (s) (66 – 75 %). Also, the tie point at 19.92 mcd was identified by cluster analysis of the faunal assemblage as the end of zone F, further justifying its selection.

A tie point at 114.5 ka representing the last sample before a series of enriched  $\delta^{18}\text{O}$  values in LS15 was introduced in U1305 at 24.98 mcd, as the last sample containing depleted planktonic (2.92 ‰) and benthic (2.48 ‰)  $\delta^{18}\text{O}$  values, which coincided with the last warm Mg/Ca temperatures (~7°C) and MAT SSTs (~4°C) just before all these proxies indicate a period of cooling, likely associated with the onset of MIS 5d. In U1302, 114.5 ka was tied to 19.62 mcd, associated with warm MAT (~9°C) and Mg/Ca (~5°C) temperature estimates, also located just below a period of enriched planktonic and benthic  $\delta^{18}\text{O}$  values. Detailed multi-proxy data did not extend above this point for U1302, so all subsequent tie points were based on links to planktonic  $\delta^{18}\text{O}$ .

A depleted  $\delta^{18}\text{O}$  value in the LS15 Intermediate North Atlantic  $\delta^{18}\text{O}$  stack at 111.5 ka was linked with a depleted peak in U1302 at 19.07 mcd. In U1305, this point was assigned to 24.68 mcd based on simultaneous depleted planktonic  $\delta^{18}\text{O}$  (3.36 ‰) and slight increases in Mg/Ca and MAT SSTs. The tie point at 108 ka was introduced at the onset of a period of depleted  $\delta^{18}\text{O}$  values in LS15, based on planktonic  $\delta^{18}\text{O}$  for U1302 and U1305, though in the latter this also coincided with the onset of slightly warmer MAT and Mg/Ca and SSTs (~4 and 5°C respectively). The tie point at 106 ka represents the end of this period of depleted  $\delta^{18}\text{O}$  values, again assigned based on planktonic  $\delta^{18}\text{O}$  in U1302, and the coincidence of depleted planktonic  $\delta^{18}\text{O}$  with the last indications of warmth in MAT and Mg/Ca SSTs (~3 and 6°C respectively). The tie point at 103.5 ka, indicating a depleted  $\delta^{18}\text{O}$  value in LS15, was placed at the start of a period of depleted planktonic  $\delta^{18}\text{O}$  values in U1302, and the most depleted planktonic  $\delta^{18}\text{O}$  value since the last interglacial in U1305, which coincided with the onset of slightly warmer conditions indicated by MAT and Mg/Ca temperature (~4°C for both). Interestingly, this depth in U1305 is the first point since the last interglacial that *G. bulloides* Mg/Ca temperature estimates are available, and they suggest very warm surface conditions (~12°C). As with the earliest tie points above, the final tie points for both cores were provided by Hillaire-Marcel et al. (2011), with 71 ka at 18.50 mcd in U1305 and 96 ka at 17.40 mcd in U1302. Despite the lack of multi-proxy data through the glacial inception in U1302,

the close agreement between planktonic  $\delta^{18}\text{O}$  and temperature proxies (both MAT and Mg/Ca) in U1305 suggests this age model is robust.

As Figure 7.11 shows, this age model greatly improves coherence between both U1302 and U1305. Benthic  $\delta^{18}\text{O}$  values (Figure 7.11 B) are much more synchronous, though there is still some discrepancy towards the glacial inception, where both records seem to diverge from each other, but there are large gaps through this interval in both records so this may be an artefact of resolution. The depleted  $\delta^{18}\text{O}$  excursion in U1302 is very apparent during Termination II (Figure 7.11 C), but outside of this event the records align much more closely. This may be because during periods not prone to meltwater incursions such as the glacial inception,  $\delta^{18}\text{O}$  may be a more reliable stratigraphic tool. General coherence between both cores in IRD, MAT temperatures and *N. pachyderma* (*s*) abundance is very good. There is some difference during the glacial inception between IRD input, which begins increasing even before 116 ka in U1302 but not until after 112.5 ka in U1305. But to bring these IRD records into alignment with each other would put planktonic isotopes, MAT temperatures and *N. pachyderma* (*s*) out of synchrony. Instead, it is assumed that the differing depositional environments cause the difference in this climate proxy. U1302 is located beneath the Labrador Current, which forms the major Hudson Strait iceberg discharge route, but U1302 is also close to where the NAC turns the “northwest corner”, potentially supplying warm surface waters to make Orphan Knoll a hotspot for iceberg melting. The sustained warmth observed in U1302 MAT SSTs into the glacial inception period supports this interpretation. The greater impact of IRD input at U1302 can also be observed by the differing sedimentation during H11 (~135 - 130 ka), which is only 0.25 m thick in U1305 but 1.25 m thick in U1302.

Figure 7.12 shows sedimentation rate changes for U1305 and U1302 on the new age models. Average sedimentation rates are 13.8 cm/ka for U1302 and 23.4 cm/ka for U1305. As observed previously (Hillaire-Marcel et al. 2011, Channel et al. 2006), sedimentation rate is more continuous at U1302, but higher during periods of high IRD deposition. The opposite pattern is observed in U1305, in which sedimentation rates vary from as low as 3.3 cm/ka during peak glacial conditions, and as high as 85.0 cm/ka during the early last interglacial. This variability in sedimentation rate on Eirik Ridge has been observed previously (e.g. Hillaire-Marcel et al. 1994, 2011, Stoner et al. 1995, 1996, 1998, Hunter et al. 2007, Kawamura et al. 2012) and discussed in section 4.1.1.

Support for this age model can be found in palaeomagnetic investigation of U1305 during the Holocene, whereby radiocarbon dating has determined postglacial sedimentation rates varied from ~35 to > 90 cm/ka (Stoner et al. 2013).

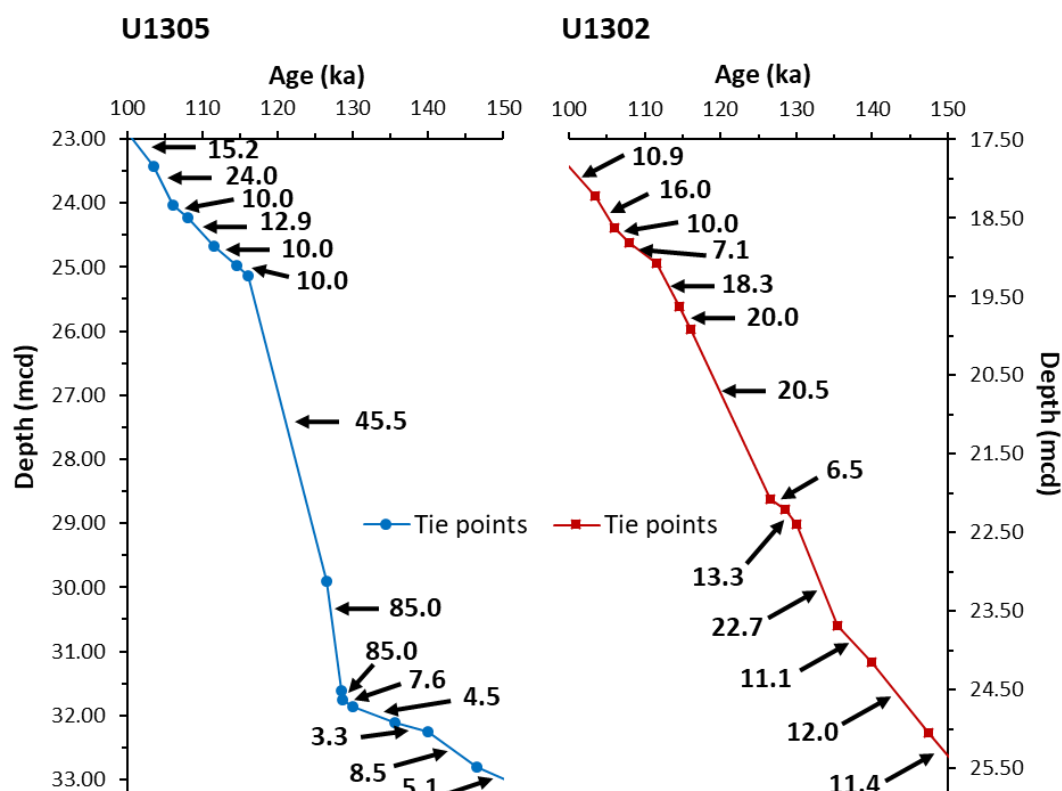


**Figure 7.12** | Tie points for the age model constructed for this study showing sedimentation rates (all figures are in cm/ka) for U1305 (blue) and U1302 (red).

#### 7.4.4 | Age Models for Reference Records

In order to enable more meaningful comparison with U1305 and U1302, three reference records were also tuned to LS15 (Lisiecki and Stern 2016), for display in the graphs of the discussion chapter. MD03-2664 (Figure 7.13) was retrieved from Eirik Ridge close to U1305. MD95-2042 from the Iberian Margin (Figure 7.14) and ODP-980 from the Feni Drift (Figure 7.15) provide excellent resolution records from the wider North Atlantic region. Further details about these cores are given in section 8.1.3 and Table 8.2.

The published age model for MD03-2664 (Irvali et al. 2012; Galaasen et al. 2014; Irvali et al. 2016) was based upon correlating benthic  $\delta^{18}\text{O}$  to MD95-2042, which was itself dated by correlation to the radiometric timescale of Stirling et al. (1998) (Shackleton et

al. 2002, 2003). ODP-980 was originally dated by correlation to orbital chronology of Martinson et al. (1987). For the present study, the same tie points identified by Galassen et al. (2014) were assigned dates based instead on LS15 (Figure 7.13). The red layer of Nicholl et al. (2012) was also recognised in MD03-2664, on their original timescale the base of this layer was dated to 124.7 ka. Given the close proximity to U1305 and the likely rapid onset of any turbidity-driven layer such as this, a tie point at 126.5 ka was added at 27.04 m depth, to synchronise the base of the red layer with the age models for U1302 and U1305. This tie point had the effect of changing the mean interglacial sedimentation rate from 32.4 cm/ka to 49.5 cm/ka below (and reducing it to 29.1 cm/ka above the red layer), but this pattern (higher sedimentation rate during the early last interglacial) is comparable with U1305, and compares favourably with  $^{14}\text{C}$ -dated postglacial Holocene sedimentation rates in U1305 (Stoner et al. 2013).

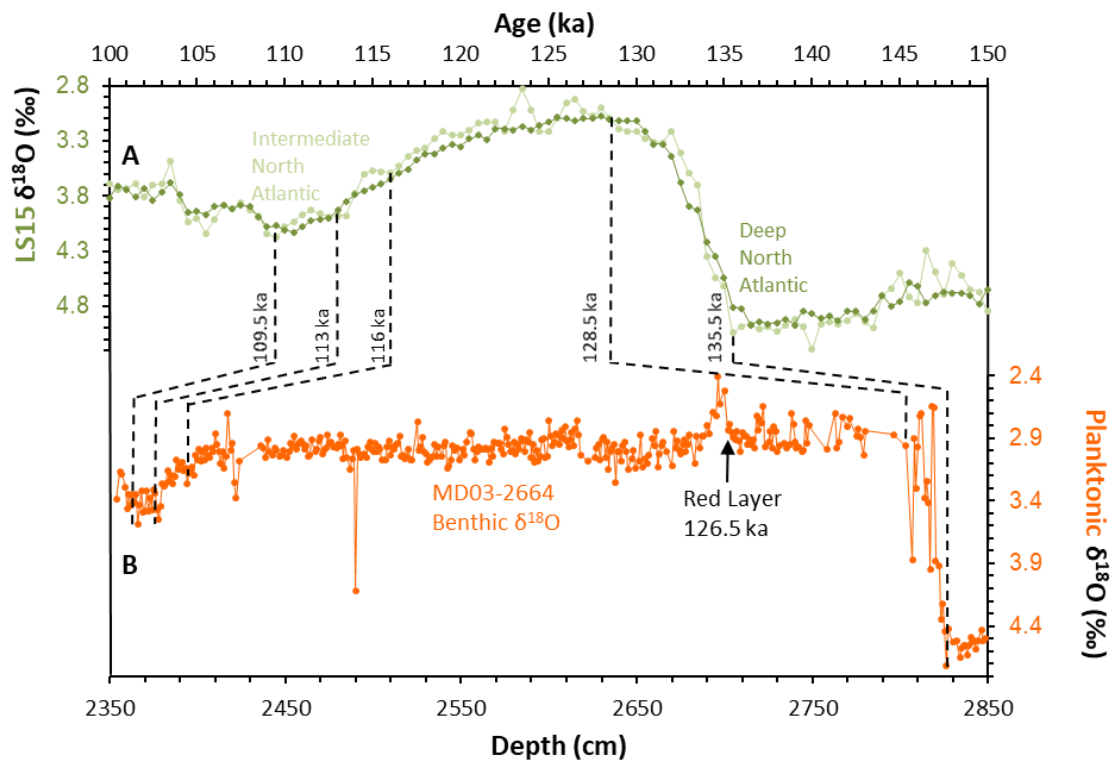


**Figure 7.13** | Age model adjusting MD03-2664 to LS15 (Lisiecki and Stern 2016). Arrow indicates tie point related to the base of the red layer. Benthic isotopes from Galassen et al. (2014).

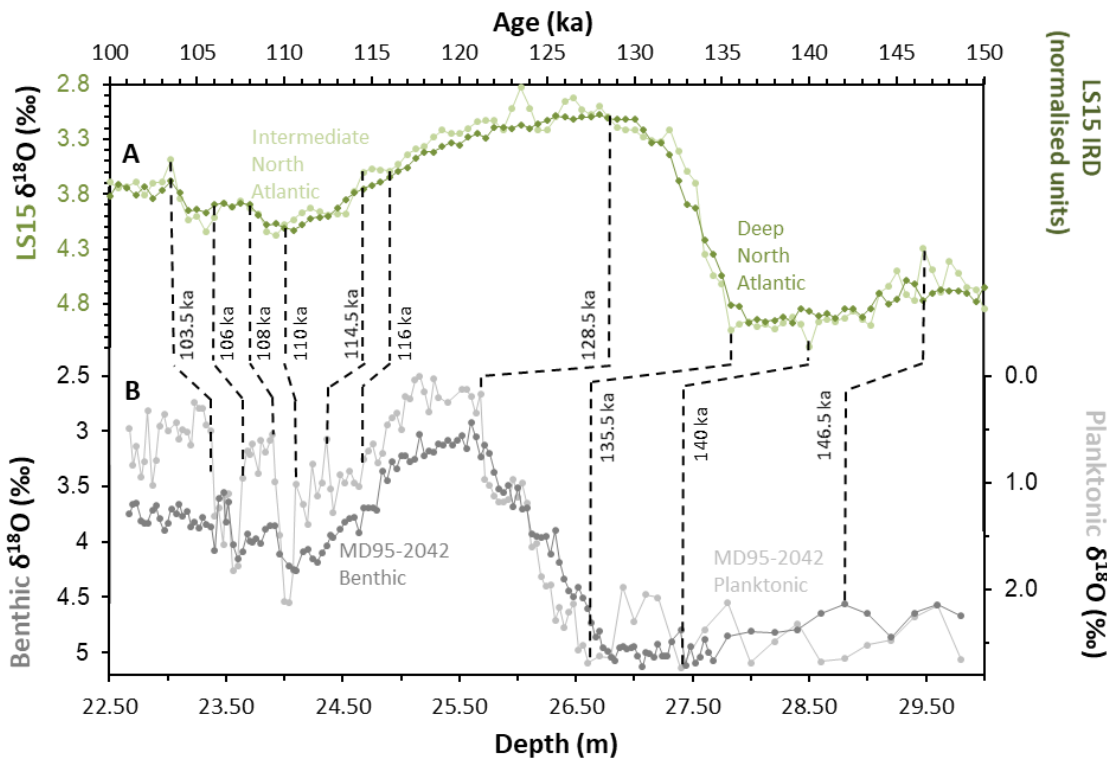


**Figure 7.14** | Age model adjusting MD95-2042 (Shackleton et al. 2002, 2003) to LS15 (Lisiecki and Stern 2016). Benthic (dark grey) and planktonic (light grey) oxygen isotope records are shown.

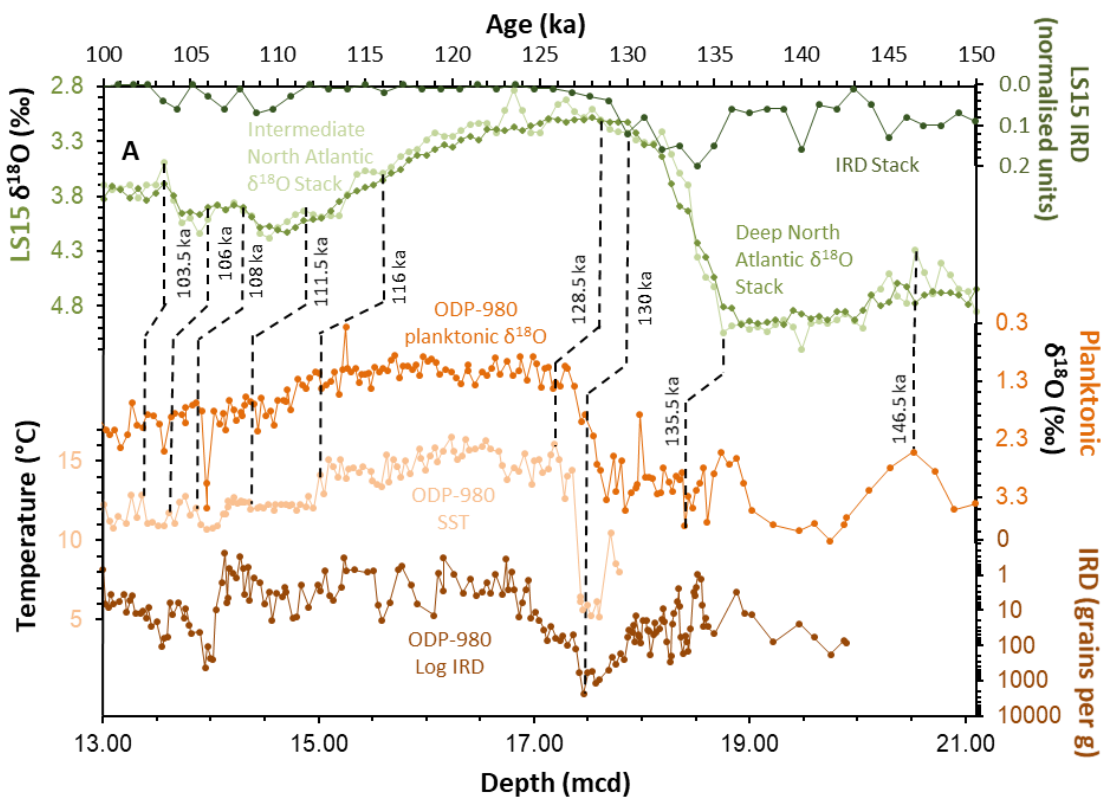


**Figure 7.15** | Age model adjusting ODP-980 (Oppo et al. 2006) to LS15 (Lisiecki and Stern 2016). Planktonic isotopes derived from *N. incompta* (orange), MAT SSTs (light orange) and IRD concentration on a log scale (brown).

**Table 7.5** | Tie points used to construct age models for MD03-2664, MD95-2042 and ODP-980 based on LS15. Depth is given in metres (m) for every core and ages in thousands of years (ka).

MD03-2664 <sup>a</sup>		MD95-2042 <sup>b</sup>		ODP-980 <sup>c</sup>	
Depth (m)	Age (ka)	Depth (m)	Age (ka)	Depth (m)	Age (ka)
23.54	106	21.84	87.2	10.37	60
23.66	109.5	23.37	103.5	13.42	103.5
23.78	113	23.64	106	13.62	106
23.98	116	23.90	108	13.87	108
27.04	126.5	24.10	110	14.36	111.5
28.03	128.5	24.36	114.5	15.02	116
28.26	135.5	24.68	116	17.2	128.5
28.48	142.9	25.76	128.5	17.46	130
		26.83	135.5	18.4	135.5
		27.44	140	20.52	146.5
		28.8	146.5		

<sup>a</sup> Original data from (Irvali et al. 2012; Galaasen et al. 2014; Irvali et al. 2016)

<sup>b</sup> Original data from (Shackleton et al. 2002; 2003)

<sup>c</sup> Original data from (Oppo et al. 2006)

## 7.5 | AGE MODEL SUMMARY

An important element of this research was the production of robust age models spanning the onset and demise of the last interglacial, accounting for the notoriously complicated conditions within the Labrador Sea. The following protocol was developed in this study:

1. The LS15 deep and intermediate North Atlantic benthic  $\delta^{18}\text{O}$  and IRD stacks are recommended as dating references (Lisiecki and Stern 2016).
2. IRD counts (both percentage of coarse fraction and concentration per g of dry sediment), percentage abundance of *N. pachyderma* (*s*), planktonic foraminifera assemblage derived MAT summer SST estimates, Mg/Ca calcification temperatures (from both *G. bulloides* and *N. pachyderma* (*s*) where possible), and both planktonic and benthic stable isotope data should be combined wherever possible, to enable cross-checking between proxies of the interpreted palaeoclimate events.

3. Cluster analysis of foraminiferal assemblage counts can help to identify major climate transitions. This should avoid misinterpreting climate signals by identifying features such as depleted planktonic  $\delta^{18}\text{O}$  excursions during Heinrich events, or apparent increases in IRD % which are in fact due to decreases in planktonic foraminifera abundance.
4. A series of palaeoclimatic events, summarised in Table 7.6, can be recognised, and used as a reference when constructing new chronologies. The application of this approach is represented graphically in Figures 7.8 and 7.9.

The age models produced for U1305 and U1302 in this study are consistent with each other, and the approach used helps to resolve many of the difficulties encountered in this region. It is proposed that these age models improve on previously published chronologies, and the identification of a red layer as a rare and valuable age control tie point within the last interglacial period can help to synchronise chronologies in this region.

**Table 7.6** | Protocol for age model construction in the Labrador Sea, based on the methods outlined in this study. INA = Intermediate North Atlantic benthic  $\delta^{18}\text{O}$  stack (Lisiecki and Stern 2016).

Date (ka)	Climate Event	Proxy Evidence	Dating Reference
103.5	MIS 5c	First depleted planktonic $\delta^{18}\text{O}$ , warm temperatures	LS15 <sup>b</sup>
106	Start of C23	Last depleted planktonic $\delta^{18}\text{O}$ , warm temperatures	LS15 <sup>b</sup>
108	End of C24	First depleted planktonic $\delta^{18}\text{O}$ , warm temperatures	LS15 <sup>b</sup>
111.5	Depleted INA $\delta^{18}\text{O}$	Depleted planktonic $\delta^{18}\text{O}$ , warm temperatures	LS15 <sup>b</sup>
114.5	Last depleted INA $\delta^{18}\text{O}$	Last sample containing depleted planktonic and benthic $\delta^{18}\text{O}$ , warm temperatures	LS15 <sup>b</sup>
116	End of the last interglacial	Last sample containing low <i>N. pachyderma</i> ( <i>s</i> ) % abundance, low IRD, warm temperatures, depleted planktonic and benthic $\delta^{18}\text{O}$ , cluster analysis zone break	LS15 <sup>b</sup>
126.5	Red layer sharp base	Visible in sediments or core photographs, or <i>a</i> * colour reflectance parameter	This study
128.5	Start of the last interglacial	First sample containing low <i>N. pachyderma</i> ( <i>s</i> ) % abundance, reduced IRD, warm temperatures, depleted planktonic $\delta^{18}\text{O}$ plateau.	LS15 <sup>b</sup>
128.7	Diatom mat	Visible in sediments or coarse fraction as thickly matted siliceous strands	This study
135 - 130	Heinrich event 11	Peak in IRD, transition from enriched to depleted $\delta^{18}\text{O}$ , last cold temperatures, cluster analysis zone break	LS15 <sup>b</sup>
135.5	Isotope event 6.2	Peak enriched benthic and/or planktonic $\delta^{18}\text{O}$	LS15 <sup>b</sup>
140	Heinrich event 12	Peak in IRD, depleted planktonic $\delta^{18}\text{O}$	LS15 <sup>b</sup>
146.5	Possible interstadial (peak depleted INA $\delta^{18}\text{O}$ )	Low IRD concentrations, depleted planktonic $\delta^{18}\text{O}$ , warm temperatures	LS15 <sup>b</sup>
150.4 – 147.5	Heinrich event 13	Peak in IRD, depleted planktonic $\delta^{18}\text{O}$	This study

*“The moving hand once having writ moves on. Nor all thy piety nor wit can lure it back to cancel half a line.”*

Omar Khayyám, *Rubáiyát of Omar Khayyám*

## 8 | DISCUSSION

The development of new age models for U1305 and U1302 in the previous chapter allows them to be directly compared to each other, and with published records. Initially, the framework of climate events that structures the following discussion is laid out (section 8.1), which progresses chronologically and with reference to regional and global implications. Section 8.2 concerns the penultimate glacial period (MIS 6b-a), for which separate graphs are presented due to the long timescale involved. Discussion of last interglacial (MIS 5e) in section 8.3 and the glacial inception (MIS 5d-c) in section 8.4, precede the conclusion (section 8.5) which integrates the threads to form a comprehensive picture of climate change through the last interglacial within the Labrador Sea, summarising the most important findings and the contribution this work has made to the palaeoceanography of the last interglacial in the Labrador Sea, together with suggestions for improvement that will help to clarify the shortcomings and uncertainties that remain.

### 8.1 | CAUSE FOR CONTROVERSY

This section addresses the difficulty in identifying and dating climate events through the last interglacial, to clarify the basis around which the discussion is centred. Boundaries between marine isotope substages are after Railsback et al. (2015), except for the addition of Termination II (TII), defined as the period within which  $\delta^{18}\text{O}$  measurements change from their peak maximum glacial values, to the onset of MIS 5e, ~135 – 128.5 ka. Often, the MIS 6a/5e boundary is assigned to the mid-point of the transition in climate proxies (usually benthic  $\delta^{18}\text{O}$ ), but this makes the last part of MIS 6a very warm, and the first part of MIS 5e very cold. The use of TII reserves the use of the term MIS 5e for the warmest interval of the last interglacial. TII is therefore not quite synonymous with Heinrich event 11 (H11), which was an event within this period that pertains to the major ice sheet collapse (~134.6 – 129.8 ka). The discussion below quotes ages in both cores to 1 decimal place, for ease of identification and reference on the graphs. However, it should be remembered that age uncertainty of the LS15 stack is around  $\pm 4$  ka through this period (Lisiecki and Stern 2016), so all dates given are provisional and would best be considered rounded to the nearest 1000 years.

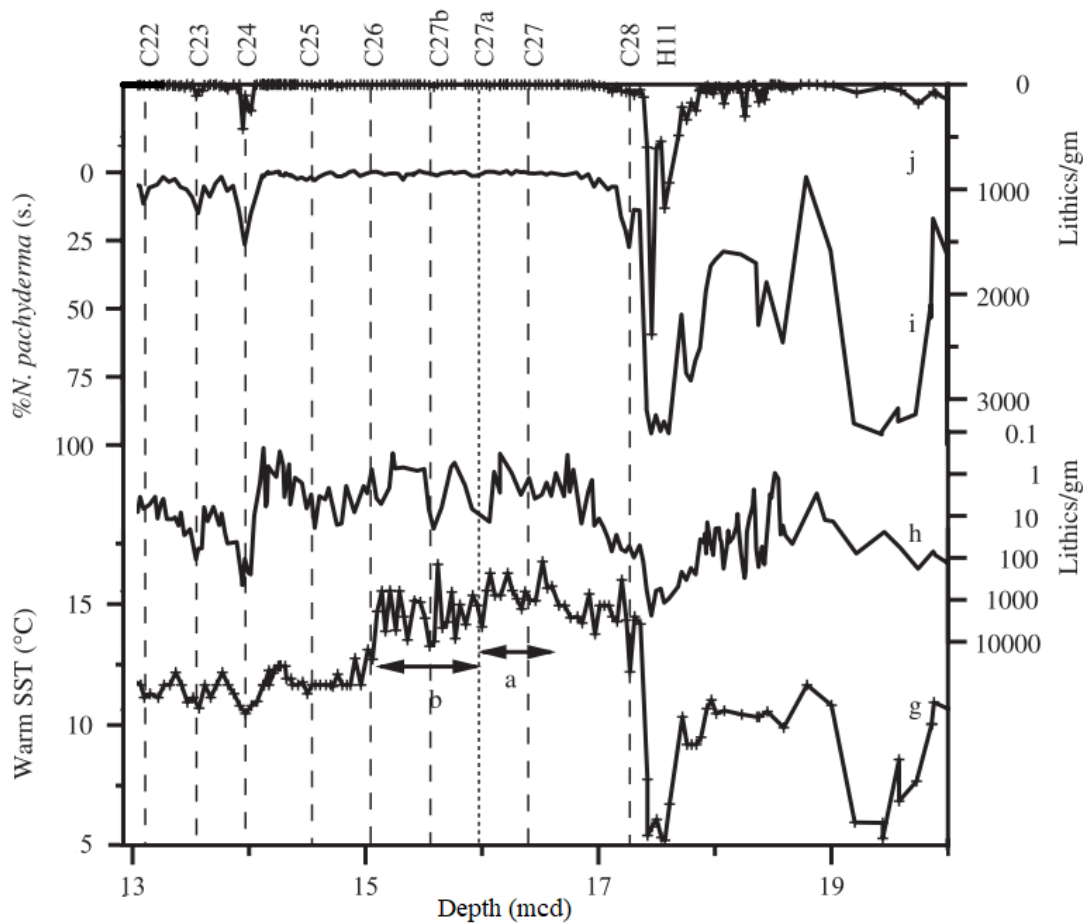
## 8.1.1 | Heinrich Events

Table 8.1 lists climate events discussed in this chapter, together with their approximate duration. The most prominent climate event in both cores was Heinrich event 11 (H11), which was assigned to the longest, heaviest period of IRD input. In U1305, IRD reached 49% in a layer 25 cm thick. H11 was particularly intense in U1302, where a layer 1.25 m thick was dominated by heavy IRD deposition (average 82%) that reached huge concentrations (5940 grains per g). Although the duration of Heinrich events varies (e.g. Hemming 2004, Stanford et al. 2011), in these cores from the Labrador Sea, so close to the collapsing Laurentide and Greenland ice sheets, a longer H11 fits the data, as well as matching with recent well-dated studies (Govin et al. 2015; Lisiecki and Stern 2016). Following Lisiecki & Stern (2016), this study also identifies H12 (~140 ka), based upon a simultaneous increase in IRD percentage and concentration in U1305. Additionally, this study also uses the new data from U1305 presented in this study to propose a further ice rafting event, H13, between ~150.4 - 147.5 ka (section 8.2.1).

## 8.1.2 | North Atlantic Cold Events

Millennial-scale climate events within the North Atlantic during the last glacial stage are well established (e.g. Bond et al. 1999, Bond and Lotti 1995, Chapman & Shackleton 1999, McManus et al. 1994). C26 was first identified by Chapman and Shackleton (1999) using NEAP 18K from the North Atlantic, as a rapid ~0.6 ‰ increase in *G. bulloides*  $\delta^{18}\text{O}$ , though it was not associated with significant ice rafting at that location. C25 and C24, however, were associated with widespread ice rafting and strong surface cooling during MIS 5d. Oppo et al. (2006) extended this sequence back through the last interglacial using sediment core ODP-980 from the Feni Drift in the eastern subpolar North Atlantic. They added the C27 events along with C28 to the roster of climate instability (Figure 8.1). Of relevance to this study are C23 – C28 (Oppo et al. 2006). However, there is plenty of local variation in expression, dating and duration. Each cold event tends to be several centuries to millennia long, and these events occur every few millennia. Given that in some locations individual events are not well represented, and the age uncertainty (especially for marine cores) can be up to 6 ka, it is entirely possible to mistake one cold event for another, or in low resolution records to alias two cold events together with the warm period between, and conclude that no

climate oscillations had occurred. This can result in identification of climate events becoming a bit of a duck shoot. For example, C23, also labelled as H9 in some studies (Chapman and Shackleton 1998; Lisiecki and Stern 2016), is sometimes denoted as falling within MIS 5c (Chapman and Shackleton 1999; Incarbona et al. 2010), and sometimes within MIS 5d (Kandiano et al. 2014). Absolute ages vary from ~102 ka (Oppo et al. 2001), ~103 ka (Chapman and Shackleton 1999), ~105 – ~103 (Drysdale et al. 2007), ~105 – 104 ka (Kandiano et al. 2014), ~105 ka (Gorbarenko et al. 2017), ~106 ka (Incarbona et al. 2010) to nearly 107 ka (Mokeddem et al. 2014). It is beyond the scope of this study to determine which is most accurate, but for clarity within this study, the use of a single reference would be preference.



**Figure 8.1** | IRD, abundance of *N. pachyderma* (*s.*) and MAT summer SSTs from sediment core ODP-980, illustrating the series of North Atlantic cold (“C”) events. The cold events during the last interglacial were new to the study, but later ones had been documented from a range of North Atlantic sites (Adapted from Oppo et al. 2006).

Table 8.1 | Sequence of climate events indicated in the graphs of this chapter including dates, proxies used and references.

Climate Event	Approximate Age (ka)	Rationale/Proxy Used	Reference Core	Reference
C23	106 - 104	IRD	ODP-980	(Oppo et al. 2006)
C24	110 – 108	IRD	ODP-980	(Oppo et al. 2006)
C25	113.5 – 112.7	IRD	ODP-980	(Oppo et al. 2006; Govin et al. 2012)
C26	116 – 115	IRD, MAT and Mg/Ca SSTs	ODP-980	(Oppo et al. 2006)
Last interglacial end	116	IRD, MAT and Mg/Ca SSTs, cluster analysis	LS15	(Lisiecki and Stern 2016)
117 ka cooling event	117.2 – 116.7	IRD, MAT and Mg/Ca SSTs	MD95-2664	(Irvah et al. 2016)
C27b	119.7 – 119	IRD	ODP-980	(Oppo et al. 2006)
C27a	122 – 121.4	IRD	ODP-980	(Oppo et al. 2006)
C27	124.3 – 123.6	IRD	ODP-980	(Oppo et al. 2006)
Red Layer	126.5 – 125.8	Visible in core	U1305 U1302	(Nicholl et al. 2012)
Last interglacial beginning	128.5	IRD, planktonic and benthic $\delta^{18}\text{O}$ , Mg/Ca and MAT SSTs	U1302 U1302	(Lisiecki and Stern 2016)
Diatom mat	128.7 – 128.5	Visible in sediment	U1305	This study
U1302 Isotopic excursion	134.6 – 130.2	Planktonic $\delta^{18}\text{O}$	U1302	(Hillaire-Marcel et al. 2011)
H11	134.6 – 129.8	IRD	ODP-980	(Oppo et al. 2006)
H12	~140	IRD	LS15	(Lisiecki and Stern 2016)
Warm Phase?	146.5 - 144	MAT and Mg/Ca SSTs, IRD, planktonic $\delta^{18}\text{O}$	U1305	This study
H13?	150.4 – 147.5	IRD	U1302 and U1305	This study

The reference chosen to identify and name these cold events was the work of Oppo et al. (2006) (Figure 8.1). To facilitate comparison with the cores used in this study, ODP-980 was placed on the same LS15 timescale (section 7.4.4). Each event was identified based upon ODP-980 IRD and SST records, and the duration was selected with reference to all records presented. Timings and durations therefore represent the local expression of these events within the Labrador Sea on the timescale of this study, and

should not be applied to other regions and chronologies, with which they will likely conflict. The exception is C28, which was not labelled on the graphs in this chapter. C28 was a late deglacial cold reversal, identified based upon MAT SST estimates and an increase in *N. pachyderma* (s) % (Oppo et al. 2006). There is no conspicuous cold reversal during this period in the palaeotemperature estimates from this study, instead the late deglacial period is characterised by a diatom mat in U1305, and in cores from the Flemish Cap near to U1302 (Rasmussen et al. 2003; section 8.2.4). Therefore, C28 was not labelled on the graphs in this chapter, and is assumed to be related to the diatom mat, which is labelled instead.

### 8.1.3 | Cores for Comparison

In order to interpret results from U1305 and U1302 in the context of the wider region, their relation to records from nearby and outside the Labrador Sea is desirable. For this purpose, published data from three other high-resolution sediment cores were chosen. The first was MD95-2664 from Eirik Ridge, to the south west of U1305, and in slightly shallower water (+20 m), which has been studied recently (Irvalı et al. 2012; Galaasen et al. 2014; Irvalı et al. 2016). The second was ODP-980 in the eastern North Atlantic (Oppo et al. 2006), and finally MD95-2042 from the Iberian Margin (Shackleton et al. 2002) (Figure 8.2). Table 8.2 contains locations, water depths and references for these cores. To enable a more meaningful comparison between records, the age models of these three cores have been updated with reference to LS15 (section 7.4.4). Because of its proximity, excellent resolution and the importance of its climate record, particularly through the last glacial inception NGRIP  $\delta^{18}\text{O}$  (a proxy for surface air temperature) is also displayed on relevant graphs below (North Greenland Ice Core Project Members 2004) on the latest GICC05modelext age model (Wolff et al. 2010), which is considered

to be the most accurate age model for Greenland ice cores (Govin et al. 2015).

**Table 8.2** | Details of North Atlantic sediment cores discussed in the text. After Irvalı et al. (2016).

Core Name	Latitude	Longitude	Water Depth	Reference
MD03-2664	57°26'N	48°36'W	3440 m	(Galaasen et al. 2014; Irvalı et al. 2016)
ODP-980	55°29'N	14°42'W	2179 m	(Oppo et al. 2006)
MD95-2042	37°48'N	10°10'W	3146 m	(Shackleton et al. 2002)

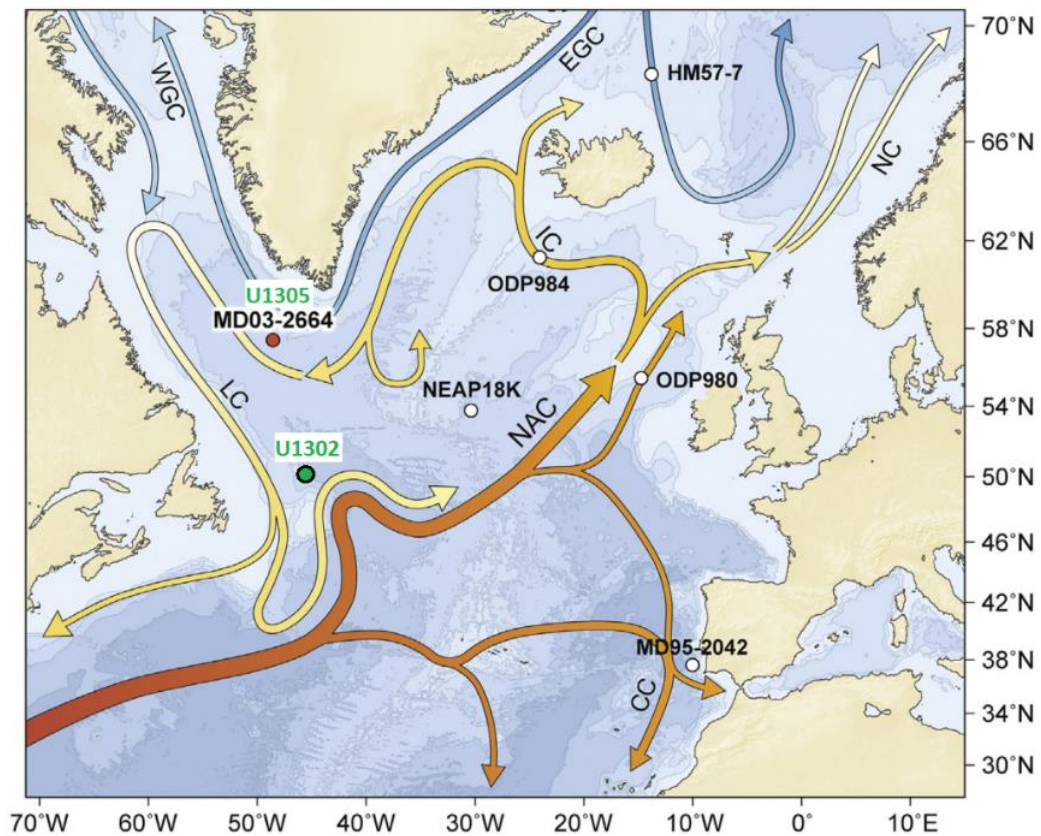


**Figure 8.2** | Map showing location of sediment cores MD03-2664, ODP-980 and MD95-2042 used as references for data from the cores in this study, together with U1305 and U1302 (green). Warm (red) and cold (blue) surface currents are also shown (arrows) (modified after Irvall et al. 2016).

## 8.2 | PENULTIMATE GLACIAL PERIOD

Figure 8.3 shows multi-proxy data from this study, together with the chosen reference records, through the penultimate glacial period (MIS 6b - a) and Termination II (TII). A longer record was available for U1305, which extended back to ~153 ka, than for U1302, for which detailed multi-proxy data only extended back to ~135 ka. Therefore, the majority of records from the latter were plotted separately (Figure 8.4) for clarity, together with benthic isotopes from U1305 (this study) and U1302 (Kaboth et al. unpublished), which were only available from ~140 ka. The last graph of this section (Figure 8.5) shows an expanded section of TII to bring out detail. In the graphs below, where foraminifera count was <50, IRD % results are presented with open circles. This is because anomalously high IRD % values can result where foraminifera are scarce, so these values should be compared against IRD concentrations. Similarly, MAT SSTs from small samples (<50 individuals) are also shown with open circles, only where they were nearly monospecific for *N. pachyderma* (*s*) (>75 %).

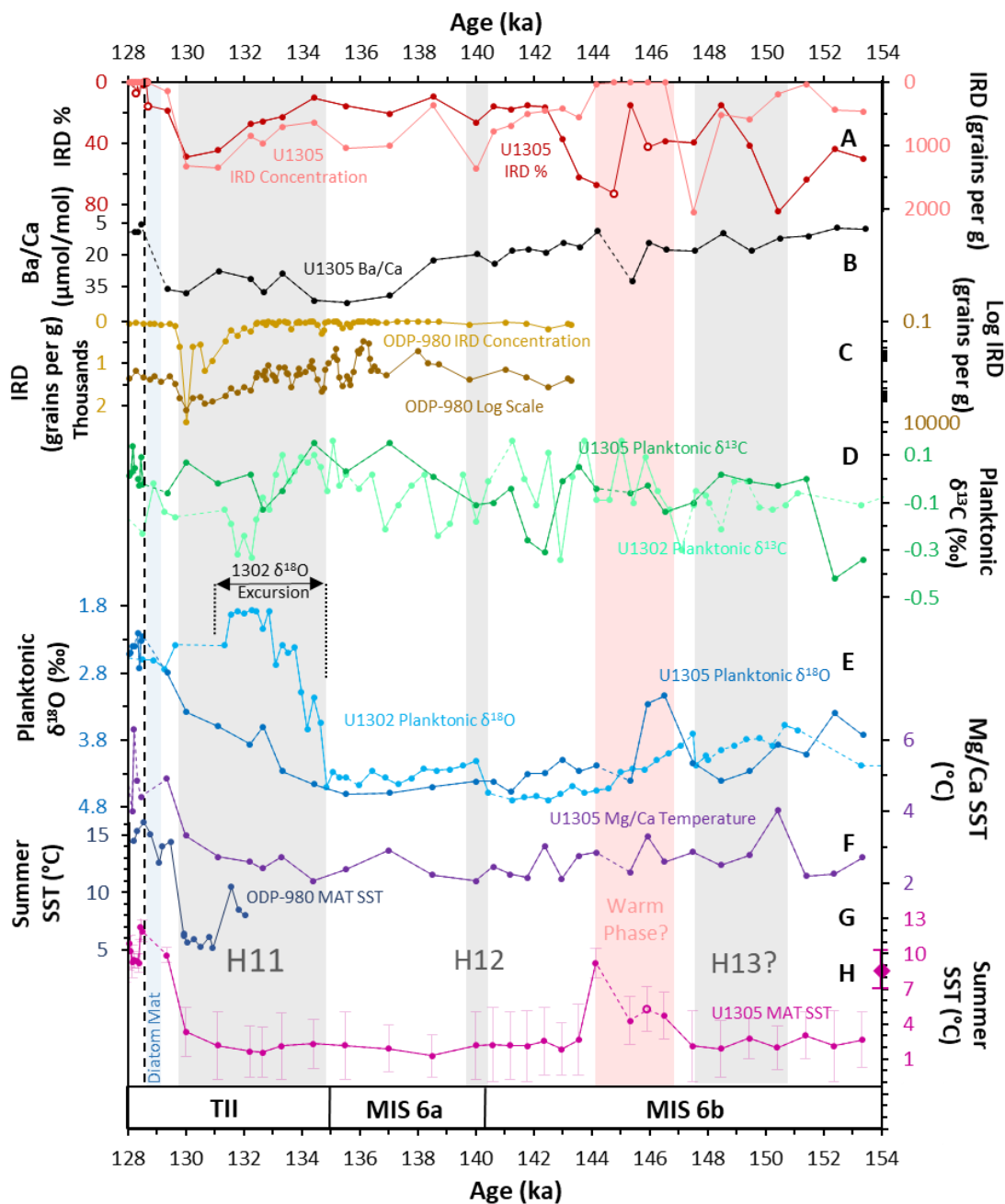


**Figure 8.3** | U1305 multi-proxy results and planktonic isotopes from U1302 through 128 – 154 ka, including Termination II (TII) and late MIS 6. (A) U1305 IRD percentage (dark red), open circles indicate low foraminifera samples (<50), and IRD concentration (light red) (this study). (B) Ba/Ca from *N. pachyderma* (*s*) (black), a proxy for meltwater runoff (this study). (C) IRD concentration (light brown) from ODP-980 (Oppo et al. 2006), also plotted on a log scale (dark brown). (D) planktonic  $\delta^{13}\text{C}$  from *N. pachyderma* (*s*) for U1305 (dark green) and U1302 (light green) (Hillaire-Marcel et al. 2011). (E) Planktonic  $\delta^{18}\text{O}$  from *N. pachyderma* (*s*) for U1305 (dark blue) and U1302 (light blue) (Hillaire-Marcel et al. 2011), indicating the U1302 depleted  $\delta^{18}\text{O}$  excursion. (F) *N. pachyderma* (*s*) Mg/Ca temperatures from U1305 (purple; this study), (G) MAT SSTs from ODP-980 (navy) (Oppo et al. 2006). (H) U1305 faunal assemblage MAT SSTs (pink; this study), error bars are standard deviation of the 6 closest modern analogues, open circles indicate small samples, pink diamond with error bars on the axis indicates present day temperature (8.5°C,  $1\sigma$  error = 1.4°C). Pink shading indicates a warm interstadial, grey shading indicates Heinrich events H11 and H12, and the proposed H13. Blue shading indicates late TII diatom mat in U1305, vertical dashed line indicates the start of the last interglacial (128.5 ka). Dotted lines indicate gaps in the records.

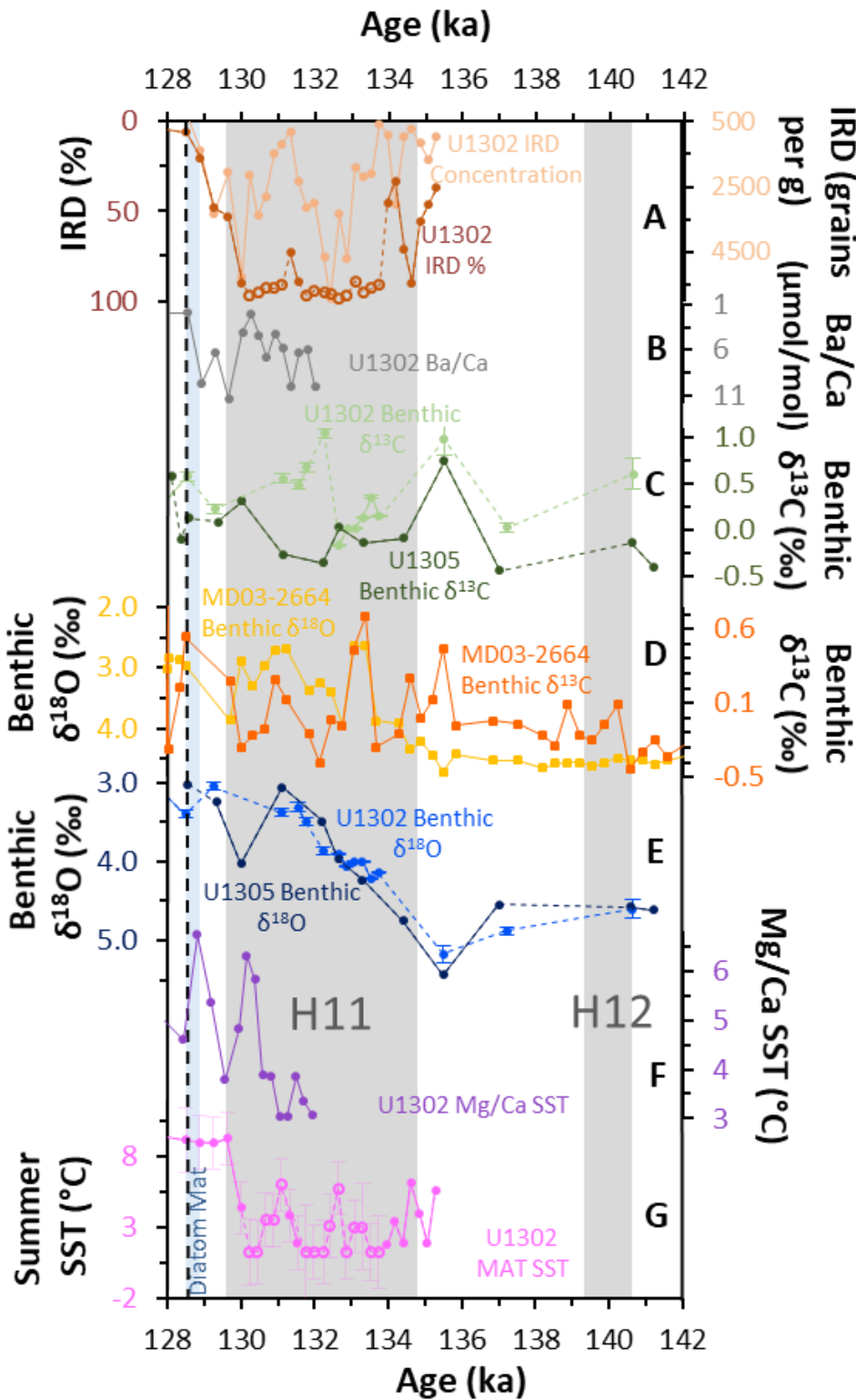


**Figure 8.4** | U1302 multi-proxy results, and benthic isotopes from U1305 and MD03-2664 through 128 – 142 ka, including TII and late MIS 6. (A) U1302 IRD percentage (dark brown), open circles indicate low foraminifera samples (<50), and concentration (light brown) (this study). (B) Ba/Ca from *N. pachyderma* (*s*) (grey), a proxy for meltwater runoff (this study). (C) Benthic  $\delta^{13}\text{C}$  for U1305 (dark green; this study) and U1302 (light green; Kaboth et al., unpublished), (D) Benthic  $\delta^{18}\text{O}$  (orange) and  $\delta^{13}\text{C}$  (yellow) from MD03-2664 (Galaasen et al. 2014). (E) benthic  $\delta^{18}\text{O}$  from U1305 (navy; this study) and U1302 (royal blue; Kaboth et al. unpublished). (F) *N. pachyderma* (*s*) Mg/Ca temperatures from U1302 (purple; this study), (G) U1302 faunal assemblage MAT SSTs (pink; this study), error bars are standard deviation of the 6 closest modern analogues, open circles indicate small samples. Grey shading indicates Heinrich events H11 and H12, and blue shading indicates late TII diatom mat in U1305, vertical dashed black line indicates the start of the last interglacial (128.5 ka). Dotted lines indicate gaps in the records.

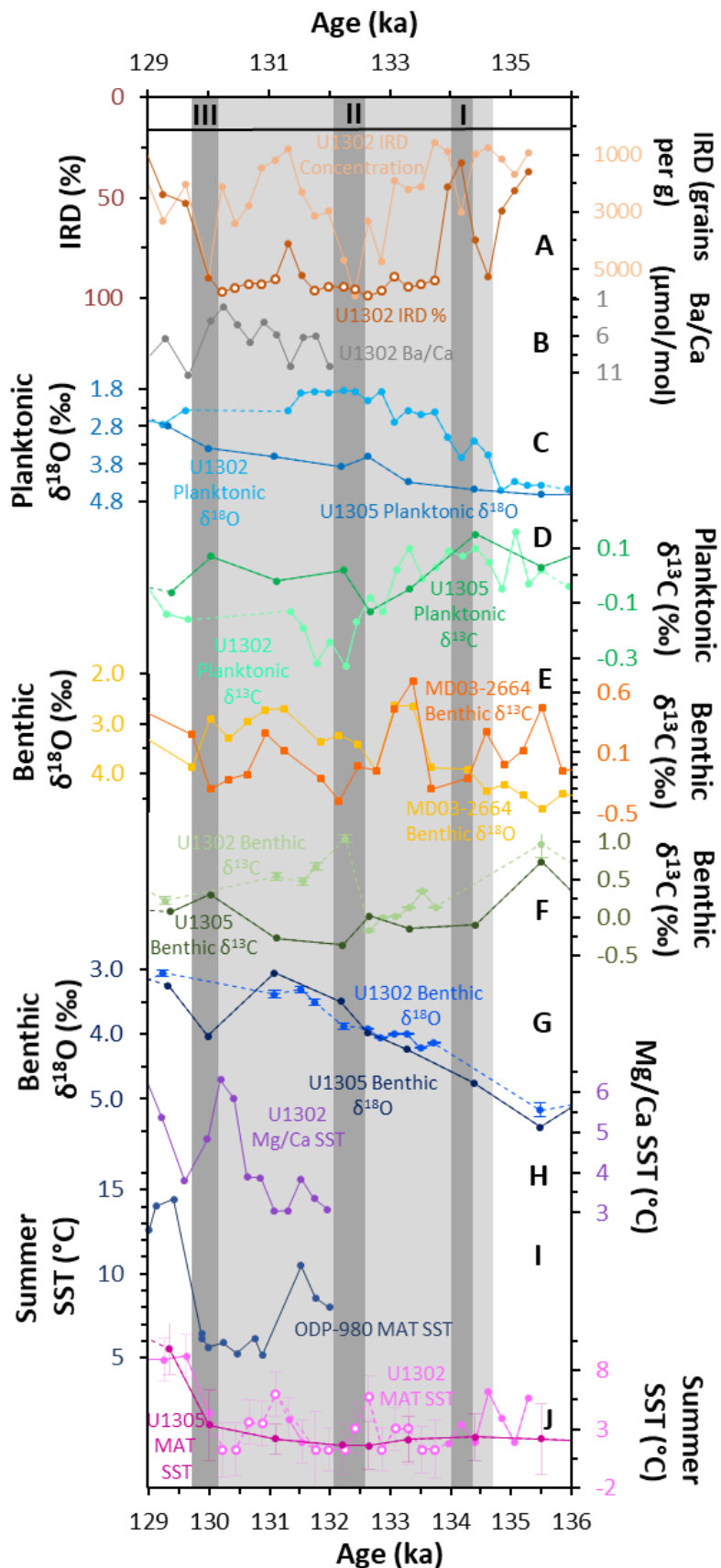


**Figure 8.5** | Expanded section showing Heinrich Event 11 in detail. Dark grey shading (I, II and III) indicate periodic pulses of intense IRD concentration in U1302. (A) U1302 IRD percentage (dark brown), open circles indicate low foraminifera samples (<50), and concentration (light brown) (this study). (B) Ba/Ca from *N. pachyderma* (*s*) (grey), a proxy for meltwater runoff (this study). (C) planktonic  $\delta^{13}\text{C}$  from U1305 (dark blue) and U1302 (light blue) (Hillaire-Marcel et al. 2011). (D) planktonic  $\delta^{13}\text{C}$  for U1305 (dark green) and U1302 (light green) (Hillaire-Marcel et al. 2011). (E) Benthic  $\delta^{18}\text{O}$  (orange) and  $\delta^{13}\text{C}$  (yellow) from MD03-2664 (Galaasen et al. 2014). (F) benthic  $\delta^{13}\text{C}$  for U1305 (dark green; this study) and U1302 (light green; Kaboth et al., unpublished). (G) Benthic  $\delta^{18}\text{O}$  from U1305 (navy; this study) and U1302 (royal blue; Kaboth et al. unpublished), (H) *N. pachyderma* (*s*) Mg/Ca temperatures from U1302 (purple; this study). (I) MAT SSTs from ODP-980 (Oppo et al. 2006). (J) U1302 faunal assemblage MAT SSTs (pink; this study), error bars are standard deviation of the 6 closest modern analogues, open circles indicate small samples. Dotted lines indicate gaps in the records.

Figures 8.3 – 8.5 indicate there was fair amount of variability through MIS 6b-a, with typically ~20 % of the coarse fraction in U1305 composed of IRD and some rapid swings in both planktonic isotopes and temperature reconstructions. H11 is well represented in all proxies between ~135 – 130 ka, with further IRD peaks attributed to H12 ~140 ka, and potentially H13 ~150.4 – 147.5 ka, with a warm interstadial phase between them ~144 - 146.5 ka.

## 8.2.1 | Heinrich Event 13

The very earliest period (before 152 ka) shows steady IRD input (~45%) which indicates the presence of marine calving glaciers, and is marked by strongly negative U1305 mesopelagic *N. pachyderma* (*s*)  $\delta^{13}\text{C}$  values (-0.42 ‰), comparable in magnitude to similar values observed in U1302 during H11. This is accompanied by depleted planktonic  $\delta^{18}\text{O}$  (3.4 ‰), which cannot be attributed to warm temperatures since MAT and Mg/Ca temperature estimates are low (~2 – 3°C). Instead, these depleted  $\delta^{18}\text{O}$  values are likely due to low salinity meltwater, or abundant sea ice formation which can spread isotopically depleted brines into the mesopelagic layer (Hillaire-Marcel and de Vernal 2008). Shortly after, at ~151.4 ka, U1305 planktonic  $\delta^{13}\text{C}$  abruptly becomes ~0.4 ‰ more positive and  $\delta^{18}\text{O}$  becomes ~0.6 ‰ more enriched, suggesting perhaps the increased influence of high-  $\delta^{13}\text{C}$  Glacial North Atlantic Intermediate Water (GNAIW), a change in temperature and/or surface productivity over Eirik Ridge at this time.

IRD % in U1305 then begins an increase that culminates ~150.4 ka at 85 %, that appears to have been of greater intensity than during H11 (49 %). This can be attributed to a marked reduction in planktonic foraminiferal abundance, from typical glacial values of several hundred to many thousands, down to ~30 per gram (Figure 5.12). This may be an indication of reduced productivity due to low-salinity low-nutrient meltwater (Aksu and Mudie 1985), or due to sediment dilution from the sudden influx of IRD. This IRD pulse coincides with a transient increase in Mg/Ca temperature of ~2°C, though summer SST (MAT) temperatures remain very low (~1°C). This may be attributed to warming of thermocline temperatures due to reduced deep convection, as observed in the Nordic Seas (Thornalley et al. 2015), or a vertical change in the *N. pachyderma* (*s*) habitat (perhaps due to a shallower surface mixed layer). Planktonic

$\delta^{18}\text{O}$  values then become progressively more enriched towards ~148.5 ka (4.41 ‰) whilst IRD concentration peaks later at ~147.5 ka (2047 grains per g) through a period of low temperatures (~2 – 3°C). Both IRD peaks appear to coincide with more depleted  $\delta^{18}\text{O}$  values in U1302 (~3.6 – 3.7 ‰). Shortly after this interval, U1302 planktonic  $\delta^{13}\text{C}$  reduced to -30 ‰, comparable to H11, before steadily increasing in tandem with a shift to strongly depleted U1305 planktonic  $\delta^{18}\text{O}$ . Similar shifts in planktonic isotopes in the Labrador Sea have previously been linked with Heinrich events (Hillaire-Marcel and Bilodeau 2000), and observed to coincide with increases in the coarse fraction of HU-90-013-133 during MIS 6b (Figure 3.8; Hillaire-Marcel et al. 1994). This is interesting, because periods of ice rafting, strongly negative  $\delta^{13}\text{C}$  values accompanied by depleted planktonic  $\delta^{18}\text{O}$  and generally very cold temperatures share many similarities with later Heinrich events, and may present a candidate for Heinrich event 13.

This potential Heinrich event coincides with a low detrital carbonate (LDC) layer dated to ~150 ka by Evans et al. (2007) in their palaeomagnetic and  $\delta^{18}\text{O}$ -based examination of marine core MD99-2227, also from the Eirik Ridge near U1305 (Figure 4.3). These LDC layers had been observed previously (Stoner et al. 1995, 1996) and were attributed by Evans et al. (2007) to turbidite activity from the Greenland Slope. However, in their recent detailed sedimentological study of Heinrich layers within the Labrador Sea, Hesse and Khodabakhsh (2017) identified type IV Heinrich layers associated with H1 on Eirik Ridge (Figure 3.7). The authors suggest type IV layers were formed by alternating periods of IRD deposition interspersed with turbidites from the northwest Atlantic mid ocean channel (NAMOC) that runs along the axis of the Labrador Sea. The LDC turbidite layers on Eirik Ridge could therefore be due to deposition from turbidites associated with ice surging from Hudson Strait overspilling the NAMOC. In a palaeomagnetic study spanning 750 ka, Channell et al. (2012) identified a strong peak in Ca/Sr and gamma-ray attenuation porosity evaluator (GRAPE) bulk density, but not associated with an increase in coarse fraction, indicated as event 6.3, ~137 ka (Figure 8.6). The age model from Channell et al. (2012), illustrated using proxy data from this study in Figure 7.6, was discussed in section 7.4.1 and found to place peak ice rafting in U1302 at 126 – 130 ka. The new age model of the present study would instead place this event 6.3 at ~147.5 ka. These observations suggest that far from being a localised turbidite event from the Greenland slope, 6LDC of Evans et al. (2007) was a wider turbidite event, likely associated with material moving down the NAMOC from Hudson

Strait. Large peaks in Ca/Sr and GRAPE density in U1302 suggest this event was of similar magnitude to H11 and H12 (events 6.1 and 6.2 on Figure 8.6). Evidence presented above leads to the suggestion that these observations may be related to a Heinrich event (H13), centred ~150.4 – 147.5 ka, based on massive ice rafting discovered in U1305 (Figure 8.3). That both IRD percentage and concentration are found to have much larger peaks than H12 or even H11 supports this

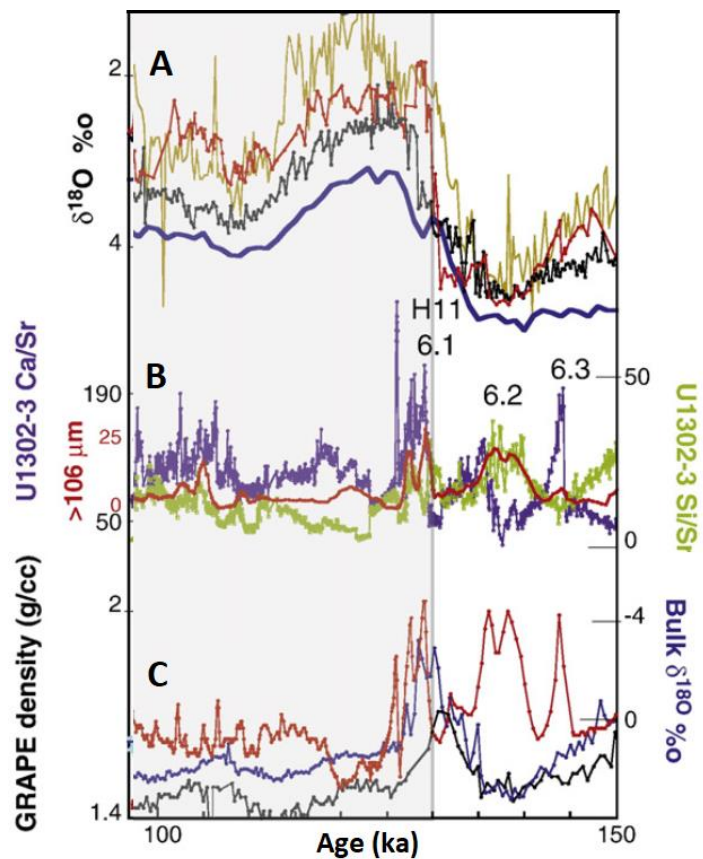


**Figure 8.6** | U1302 multi-proxy data showing (A) U1302 planktonic  $\delta^{18}\text{O}$  (red) with U1308 benthic (black) and planktonic (brown)  $\delta^{18}\text{O}$  and LR04 (blue). (B) U1302 XRF scanning Ca/Sr (blue) and Si/Sr (green), coarse fraction (>106  $\mu\text{m}$ ) weight % (red). (C) GRAPE density from U1302 (red) and U1308 (black), with U1308 bulk carbonate  $\delta^{18}\text{O}$  (blue) (Adapted from Channel et al. 2012).

assertion. The lack of ice rafting in MD99-2227 may be related to a methodological difference, in that Evans et al. (2007) did not undertake bulk IRD counts. Likewise, the lack of an increase in coarse fraction observed by Channel et al. (2012) for event 6.3 may be due to a synchronous decrease in foraminiferal abundance, potentially linked to an influx of fresh surface water inhibiting productivity (Aksu and Mudie 1985), as observed in relation to the red layer of Nicholl et al. (2012) (Figure 4.24). If this were a Heinrich event, and not just a local event, it could be expected to have wider regional or even global effects, which may indeed be the case.

There are two important points to note about the study by Hodell et al. (2008) based on U1308 from the eastern North Atlantic. Firstly, they observed two periods of increased ice rafting during MIS 6 (shown by peaks in bulk  $\delta^{18}\text{O}$ , increased influx of silicate minerals (Si/Sr) and sediment density (Figure 8.7). Their observation of a peak in ice rafting preceding H11, centred around 150 ka, supports the interpretation of this event

as H13, since it appears to have spread across the North Atlantic. Secondly, these events were not associated with an increase in carbonate (Ca/Sr). This supports the finding from IRD counts in the present study of few detrital carbonate grains in this region.

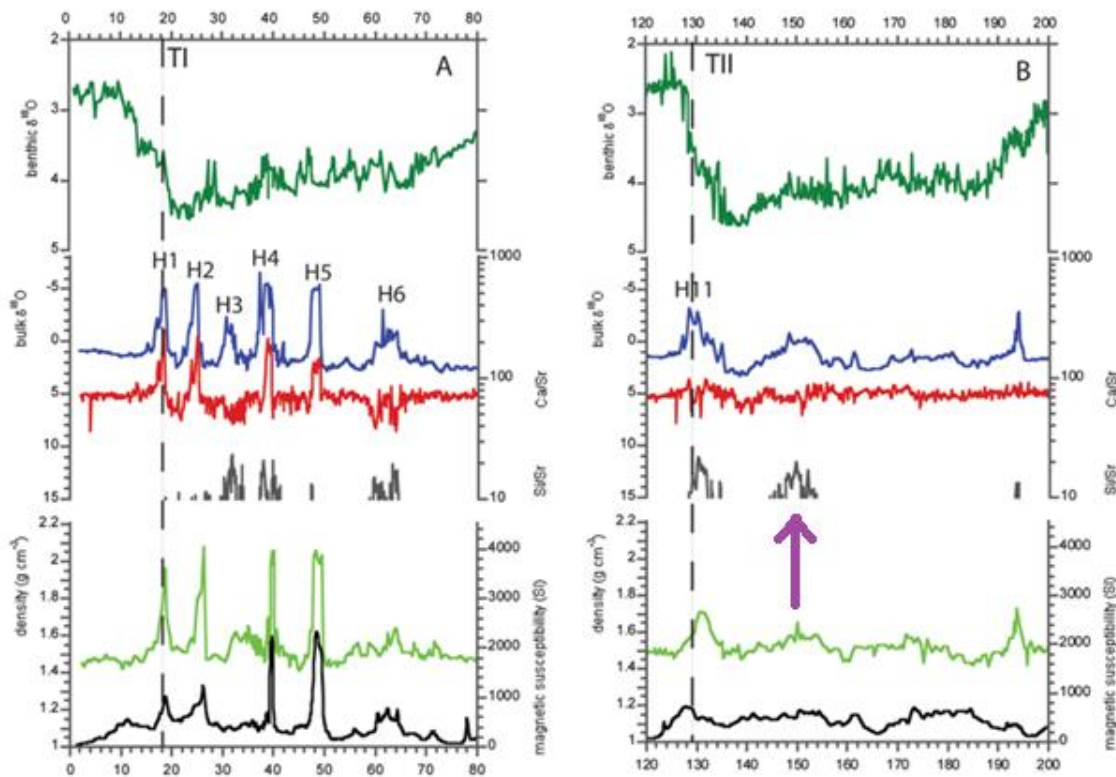


**Figure 8.7** | Proxy data from U1308 (eastern North Atlantic) comparing TI (left) with TII (right). From the top: Benthic (dark green) and bulk carbonate (blue)  $\delta^{18}\text{O}$ , Ca/Sr (red), Si/Sr (grey), sediment density (light green), magnetic susceptibility (black). Purple arrow indicates the potential H13 event (Adapted from Hodell et al. 2008).

The proposed H13 (~150.4 – 147.5 ka) may coincide with the collapse of European ice sheets attributed to a rise in insolation (particularly at  $15^\circ\text{N}$ ) during MIS 6b 155 - 150 ka (Penaud et al. 2009; Toucanne et al. 2009). Palynological records from northeast North Atlantic core MD03-2692 indicate a cold interval in the eastern North Atlantic (“Phase 2” on Figure 8.8), deduced from high *N. pachyderma* (*s*) % (unusual at this location), increased IRD concentrations, far more reworked (pre-Quaternary) dinocysts indicative of river runoff, accompanied by very low Quaternary dinocyst concentrations (indicating low productivity) (Penaud et al. 2009). These are taken as indications of massive discharges of the Fleuve Manche palaeoriver (Toucanne et al. 2009, Penaud et al. 2009), also associated with a period of reduced IRD flux to the Rockall Trough due to a retreat of the British ice sheet (Hibbert et al. 2010). A period of enhanced IRD flux from the British ice sheet was found in MD04-2822 from the Rockall Trough, dated to

~147 – 141 ka by Hibbert et al. (2010), though their age model, based on linking benthic  $\delta^{18}\text{O}$  to LR04 and the orbitally-tuned SPECMAP, which has an uncertainty of  $\pm 5000$  years (Lisiecki and Raymo 2005; Martinson et al. 1987), does not rule out the placement of this event somewhat earlier.

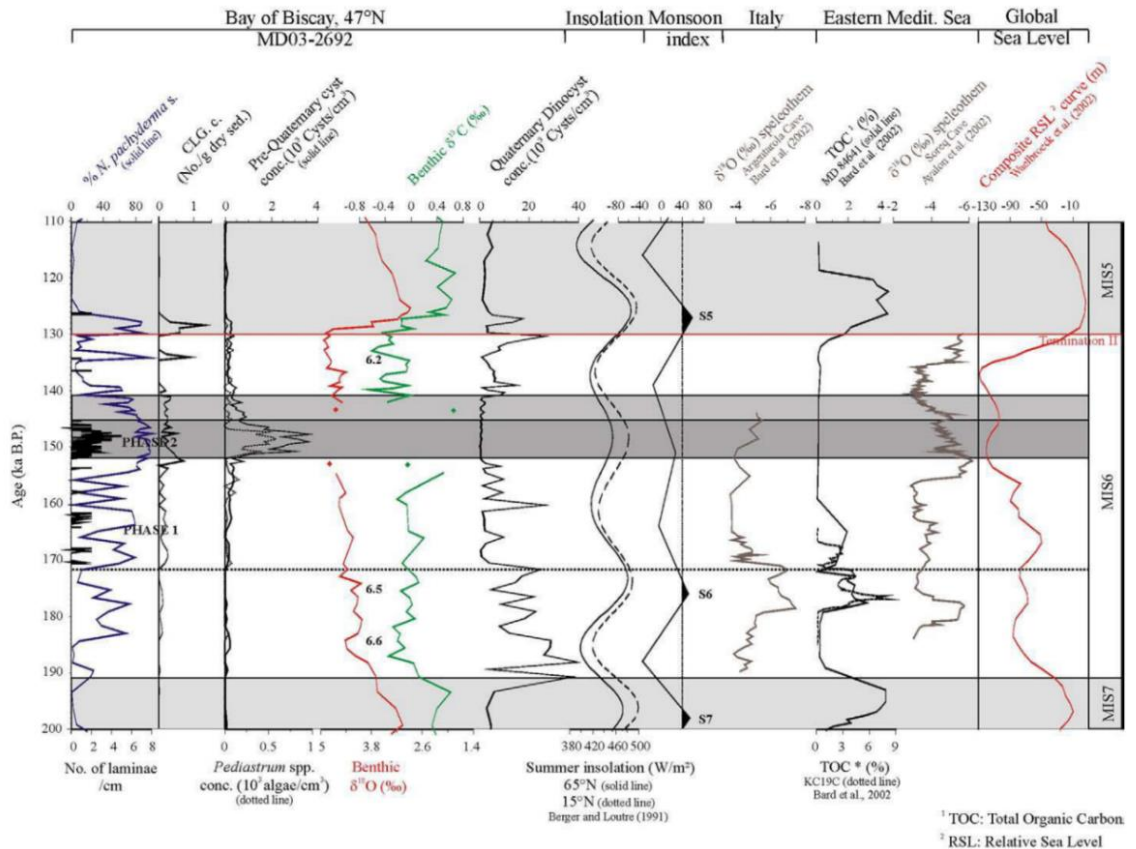


**Figure 8.8** | Evidence for a period of cold surface waters related to European ice sheet collapse at ~150 ka (dark grey band marked “Phase 2”). *N. pachyderma* (*s*) %, coarse lithic grain concentration (CLG. c.) and reworked (Pre-Quaternary) dinoflagellate cyst assemblages indicating continental river runoff, from core MD03-2692 in the Bay of Biscay. Benthic  $\delta^{18}\text{O}$  (red) and  $\delta^{13}\text{C}$  (green), Quaternary dinocysts (a proxy for primary productivity) are shown, alongside summer insolation at  $15^\circ\text{N}$  (dashed line) and  $65^\circ\text{N}$  (solid line), and a suite of other global and regional indicators (Penaud et al. 2009).

There are also indications of a rise in GMSL shortly after 150 ka. By using Mg/Ca palaeothermometry to isolate the temperature effect, Lea et al. (2002) calculated the residual  $\delta^{18}\text{O}$  of seawater from a core on Cocos Ridge in the Pacific. They observed large decreases in seawater  $\delta^{18}\text{O}$  associated with Terminations, but of more relevance to the present discussion, they identified a “period of intermediate sea level ( $\sim -30$  m)” during MIS 6b, beginning ~150 ka (Figure 8.9).

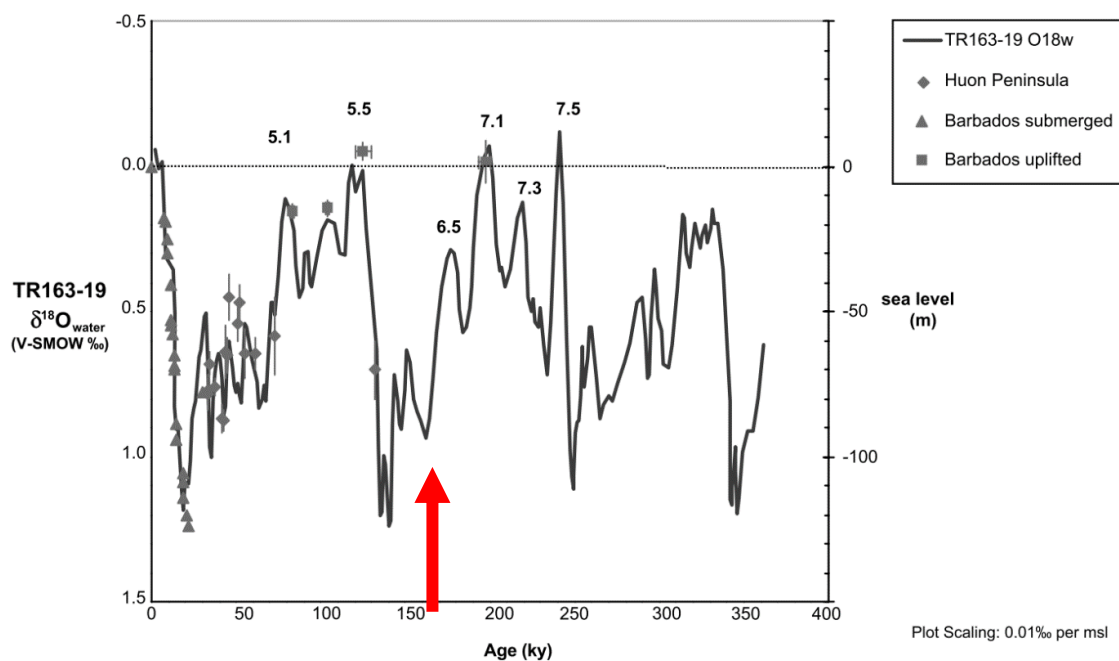


**Figure 8.9** | Detrended seawater  $\delta^{18}\text{O}$  (scaled to sea level at 0.01 ‰ per msl) from Pacific core TR163-19 compared with uplifted and submerged coral reefs corrected for island uplift (adapted from Lea et al. (2002), see their Figure 7 for reef references). MIS numbers are after Imbrie et al. (1984). Red arrow indicates a period of sea level rise ~150 ka, potentially related to H13 (Adapted from Lea et al. 2002).

Following the proposed H13 event, comes a period of interstadial warmth. Typical MAT SSTs throughout MIS 6b-a are  $\sim 1 - 2^\circ\text{C}$ , however between  $\sim 146.5 - 144$  ka this rises to between  $\sim 5$  and  $9^\circ\text{C}$ , which is comparable to the present day ( $8.5^\circ\text{C} \pm 1.4$ ). A slight increase in Mg/Ca temperature is also seen at  $\sim 146$  ka to  $\sim 4^\circ\text{C}$ , but temperatures reduce again after this point, and the later peak in MAT temperatures is not represented. This may be due to differences between the proxies, whereby MAT results reconstruct summer surface temperatures, but *N. pachyderma* (s) Mg/Ca represents early spring subsurface temperatures at the base of the mixed layer, which are likely determined during winter convection (Bauch et al. 1997; Simstich et al. 2003; Jonkers et al. 2010). The abrupt 1.0 ‰ shift to depleted planktonic  $\delta^{18}\text{O}$  in U1305 follows a similar (though smaller) change in U1302, which may be attributed either to warming temperatures, or isotopic dilution following isotopically depleted meltwater after H13 (Curry et al. 1999). Planktonic  $\delta^{13}\text{C}$  values are fairly positive in both cores, suggesting basin-wide productivity and/or overturning. IRD concentrations are extremely low through this period ( $< 5$  grains per g), but foraminifera are also rare ( $< 24$  per g). The fairly high IRD percentages (38 and 67 %) indicated by open circles in Figure 8.3 are likely therefore to be an artefact of low foraminiferal abundance, though a peak in Ba/Ca  $\sim 145$  ka that approaches values seen through H11 would support the suggestion of meltwater input,

potentially responsible for the depleted  $\delta^{18}\text{O}$  values. There is some indication of cooling in the midst of this warm phase, in that U1305 planktonic  $\delta^{18}\text{O}$  abruptly returns to typical glacial values, as do Mg/Ca temperatures,  $\sim 145.5$  ka. MAT temperatures then reach a peak of  $\sim 9^\circ\text{C}$   $\sim 144.1$  ka, accompanied and slightly followed by an increase in IRD to ( $\sim 65\%$ ), which appears to mark the end of this warm phase, after which MAT SSTs drop dramatically by  $\sim 6^\circ\text{C}$ . Possibly a northward shift in the polar front, a reinvigoration of AMOC following H13, or enhanced advection by the Irminger Current, brought warm surface waters to the Labrador Sea through this period, which enhanced iceberg melt, resulting in the high subsequent IRD input, which in turn suppressed AMOC circulation.

Early warming beginning around 150 ka was also suggested by Lea et al. (2002) using information from an eastern equatorial Pacific sediment core TR163-9. They reconstructed sea water  $\delta^{18}\text{O}$  by subtracting Mg/Ca temperature estimates from the  $\delta^{18}\text{O}$  of the foraminifera shells themselves, and identified a potential warming phase beginning at 150 ka (Figure 8.10). However, it is evident from these records that early ( $\sim 150$  ka) warming does not represent the start of a continual trend towards interglacial conditions, as temperatures indicate a subsequent intense cold phase prior to TII itself, and  $\delta^{18}\text{O}$  records show a progression towards the most enriched values of MIS 6 (isotope event 6.2 of Imbrie et al. 1984).

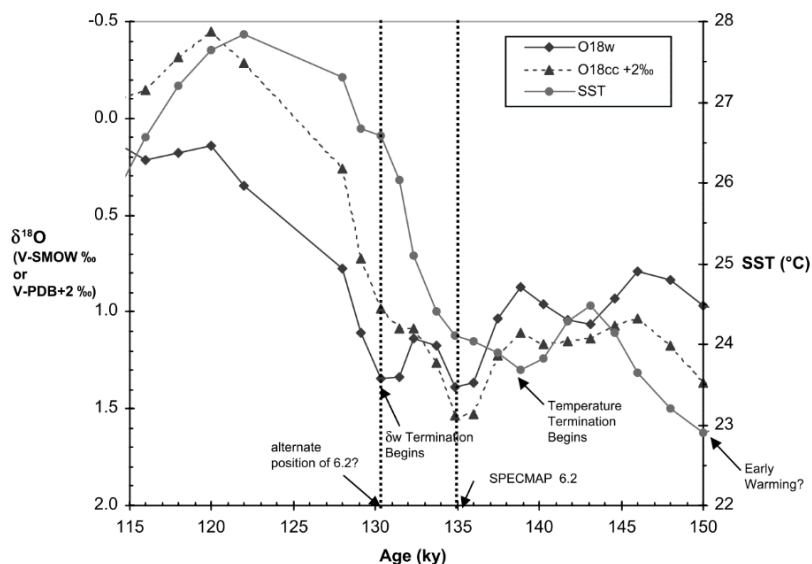


**Figure 8.10** | The timing of Mg/Ca SST,  $\delta^{18}\text{O}$  of calcite (cc), which is offset by  $+2\text{‰}$  to enable comparison with and seawater  $\delta^{18}\text{O}$  (w) from eastern equatorial Pacific sediment core TR163-19 over the last interglacial. Early warming is seen from  $\sim 150 - \sim 143$  ka, with a subsequent cold period before the start of Termination 2, which shows a clear progression, beginning  $\sim 139$  ka in temperatures,  $\sim 135$  ka in calcite  $\delta^{18}\text{O}$ , and  $\sim 130$  ka in seawater  $\delta^{18}\text{O}$ . SPECMAP MIS 6.2 is shown based on calcite  $\delta^{18}\text{O}$ , but if based on seawater  $\delta^{18}\text{O}$  would occur  $\sim 5$  ka later (Lea et al. 2002).

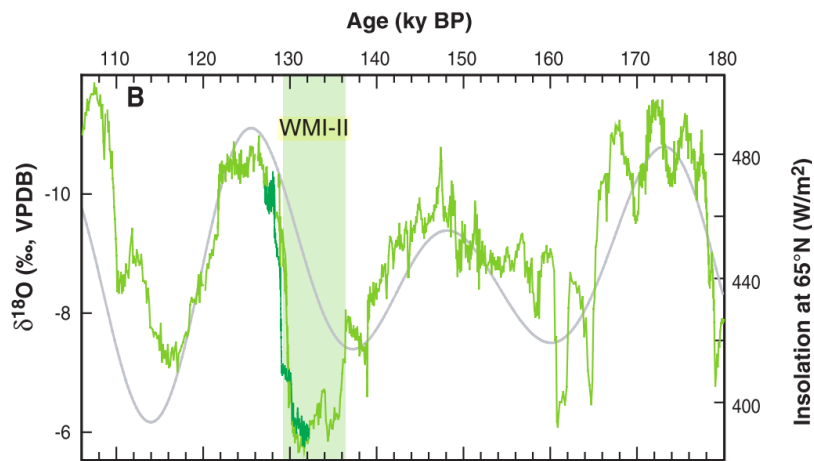


**Figure 8.11** | Speleothem  $\delta^{18}\text{O}$  (green) from Sanbao Cave, China (Wang et al. 2008; Cheng et al. 2009) together with summer insolation (grey curve) showing depleted values coinciding with an increase in insolation centred around 150 ka (Wang et al. 2009).

Figure 8.11 shows speleothem  $\delta^{18}\text{O}$  from Sanbao Cave, China, compared with summer insolation. A potential warming phase ~150 ka indicated by depleted speleothem  $\delta^{18}\text{O}$  values is associated with rising

insolation. Speleothem  $\delta^{18}\text{O}$  then becomes more enriched as insolation falls, though there is a slight reversal ~136 ka, potentially related to indications of high global mean sea levels around this time (e.g. Andrews et al. 2007). However, it is clear from Figure 8.11 that between ~136 – 130 ka, despite rising insolation during the weak monsoon interval (WMI-II) speleothem  $\delta^{18}\text{O}$  became very strongly enriched, in line with benthic  $\delta^{18}\text{O}$  event 6.2 (Imbrie et al. 1984) ~135.5 ka (Lisiecki and Stern 2016).

## 8.2.2 | The Penultimate Glacial Maximum

After the warm interstadial phase, temperature estimates become uniformly cold (~1 – 3°C) until TII (Figure 8.3). Very negative planktonic  $\delta^{13}\text{C}$  values in both cores appear ~142.9 – 142.4 ka, suggest wider fluctuations in the carbon cycle and/or hydrography across the Labrador Sea through this last part of MIS 6b. IRD concentration mirrors percentages after ~144 ka, and steady IRD input alongside increasing Ba/Ca and increasingly enriched planktonic  $\delta^{18}\text{O}$  through this interval indicate glacial build-up. An IRD peak in U1305 at ~140 ka, slightly higher in concentration (1368 grains per g) than H11 (1326 grains per g), along with a ~0.3 ‰ shift to depleted U1302 planktonic  $\delta^{18}\text{O}$  is identified with H12 in LS15 (Lisiecki and Stern 2016). There is little evidence of H12 in ODP-980, so this event may not have reached the eastern North Atlantic. These observations should be compared with the proposed H13, which had a higher IRD % and concentration than H12, was followed by a much larger depleted  $\delta^{18}\text{O}$  shift at least

in U1305, and a more pronounced negative  $\delta^{13}\text{C}$  excursion in U1302, and was observed across the North Atlantic, at least as far as U1308 (Hodell et al. 2008). In U1302, Channel et al. (2012) observed increased coarse fraction and Si/Sr ratios, along with a spike in GRAPE density, attributed to event 6.2 in Figure 8.6. As discussed above, their age model places this event between 135 – 140 ka, but on the present age model these observations would occur ~140 – 143 ka, and are likely associated with H12. Though it was clearly of a different nature to H13, which was not linked to coarse fraction or Si/Sr increases but instead to a large Ca/Sr peak (which during H12 was in fact very low) (Figure 8.6). Following H12, aside from some fairly small-amplitude fluctuations in U1302 planktonic  $\delta^{13}\text{C}$ , all proxies appear consistent with peak penultimate glacial maximum conditions, with very cold temperatures, strongly enriched planktonic  $\delta^{18}\text{O}$ , and increasing IRD and Ba/Ca suggesting continual ice calving.

From ~141 ka, benthic isotopes become available (Figure 8.4), and show enriched  $\delta^{18}\text{O}$  values (4.6 ‰) in all records, consistent with full glacial conditions. Fluctuations in MD03-2664 benthic  $\delta^{13}\text{C}$  from -0.4 to 0.0 ‰ are associated with H12. This suggests an influx and rapid retreat of  $\delta^{13}\text{C}$ -depleted deep waters, usually attributed to incursions of AABW into the North Atlantic due to a slowdown in AMOC during H12 (Galaasen et al. 2014; Curry and Oppo 2005). At ~135.5 ka, the most enriched U1305 and U1302 benthic  $\delta^{18}\text{O}$  values of either core are observed (5.44 ‰ and 5.17 ‰ respectively), presumably related to isotope event 6.2 (Imbrie et al. 1984). At the same time, benthic  $\delta^{13}\text{C}$  becomes more positive in both U1305 and U1302 (0.74 ‰ and 0.97 ‰ respectively), a pattern mirrored in MD03-2664 ( $\delta^{18}\text{O} = 4.72$  ‰,  $\delta^{13}\text{C} = 0.42$  ‰). This suggests that recently ventilated deep waters reached the Labrador Sea at this time, likely Nordic Seas overflow water, suggesting a vigorous AMOC. Shortly after, negative benthic  $\delta^{13}\text{C}$  values associated with the onset of H11 are attributed to the suppression of AMOC during Heinrich event 11 (McManus et al. 2004).

From this point on, detailed multi-proxy records from U1302 are available (Figure 8.5), and show a complex series of subtle changes, whilst U1305 shows only steady cold temperatures and IRD input with steadily decreasing planktonic  $\delta^{18}\text{O}$  (Figure 8.3). These differences might be an issue of resolution. The highly expanded section of U1302 through TII (1.25 m) due to a high sedimentation rate (22.7 cm/ka) resulted in a sample-to-sample resolution of ~220 years. The same period (135.5 – 130 ka) covered only 0.25 m in U1305, associated with a lower sedimentation rate (4.5 cm/ka) resulted

in a lower resolution of ~440 – 1,100 years (due to slightly different sample intervals). Therefore, the sub-millennial events apparent in U1302 may be below the resolution of U1305. In light of this, Figure 8.5 shows an expanded section over TII (136 – 129 ka) containing mostly proxy data from U1302, around which discussion of this period will largely revolve, due to its much higher resolution than U1305.

### 8.2.3 | Termination II

H11 signals the heaviest period of IRD deposition across the North Atlantic of the penultimate glacial cycle. In U1305 IRD increased steadily through the ~5 ka interval to peak between ~131 – 130 ka (Figure 8.3), but a much more complex pattern was seen in U1302. IRD percentages were almost 100 % through around a metre of core, at least in part due to low foraminifera numbers, which were almost entirely *N. pachyderma* (*s*) (<50 individuals, indicated by open circles in Figure 8.5). However, IRD as a concentration reveals three distinct peaks, indicated by dark grey shading in Figure 8.5 as pulses I (~134 ka), II (~132 ka) and III (~130 ka). Accepting large dating uncertainties, the duration of each appears short (~440, 620 and 520 years respectively), but the IRD concentrations were enormous, containing 3018, 5940 and 5261 grains per g respectively. Pulse III coincides with the largest peak in ODP-980 IRD also at ~130 ka (Figure 8.3), as this heaviest point of IRD inundation was used as a tie point for the age models. Multiple peaks in coarse fraction, with the most prominent IRD peak towards the top of the Heinrich layers, have been observed during Heinrich event records from Orphan Knoll previously (Stoner et al. 1996; Clarke et al. 1999). Winsor et al. (2012) observed three IRD peaks during TII in their study of MD99-2227 from Eirik Ridge (Figure 3.11). Sequential peaks in SSTs, ice rafting and depleted  $\delta^{18}\text{O}$  values have been observed during H3 – H5 in MD95-2025 from Orphan Basin, and attributed to differential response times to insolation or incursions of warm NAC waters (Hiscott et al. 2001). A “step like” prolonged deglacial was also proposed by Zhuravleva et al. (2017). Although some studies have concluded that SST is independent of IRD (Bond and Lotti 1995), this may be regionally variable. These IRD pulses may be linked to millennial-scale fluctuations in GMSL through TII (Thomas et al. 2009).

In U1305 it is not easy to pinpoint using IRD alone when H11 begins (Figure 8.3). The highest Ba/Ca values begin ~137 ka, and a case could be made for ice sheet

disintegration starting after ~138.5 ka, though the resolution of U1305 is fairly low. Periodic inputs of IRD are also seen in ODP-980 from ~137 ka. However, neither  $\delta^{18}\text{O}$  nor MAT or Mg/Ca temperatures produced for this study indicate anything other than extreme cold until ~135.5 ka, suggesting these early IRD inputs are due to abundant marine calving glaciers in a cold climate, rather than ice sheet disintegration. The indications of an early highstand in GMSL (Andrews et al. 2007) are difficult to reconcile with the widespread observation that the most enriched benthic  $\delta^{18}\text{O}$  values occurred at ~135.5 ka (e.g. Lisiecki and Stern 2016). It is possible the benthic  $\delta^{18}\text{O}$  signal is instead one of cold bottom waters rather than enriched seawater isotopic composition due to peak global ice volume ~135.5 ka (and therefore minimum GMSL), though this would require some mechanism of simultaneously cooling deep water masses globally.

H11 marks the most elevated period of Ba/Ca ratios in both cores, with higher absolute values in U1305 (30 – 40  $\mu\text{mol/mol}$ ) (Figure 8.3) than U1302 (5 – 10  $\mu\text{mol/mol}$ ) (Figure 8.5). This was despite the lower IRD percentage and concentration in U1305, possibly due to the close proximity of Eirik Ridge to the major source of meltwater from Greenland, compared with the distance between Orphan Knoll and Hudson Strait, which would result in dilution. This may also indicate that more ice was melting inland on Greenland, causing meltwater influx at U1305 without a great amount of marine-calving icebergs bringing IRD. Variable U1302 Ba/Ca (Figure 8.5) supports the theory of pulsed glacial collapse, though the record does not extend back beyond this to see if the earlier peak at ~134 ka is also represented.

Both Mg/Ca and MAT SSTs remain very low (~2 – 3°C) throughout H11 in U1305 (Figure 8.3), though this may be a smoothed record due to low resolution. However, it would appear that each of the three IRD peaks was preceded by a period of summer surface warmth in U1302, evidenced by three oscillations seen in MAT temperatures between ~1°C and ~6°C (Figure 8.5). Large temperature oscillations were also seen in U1302 Mg/Ca, of similar magnitude to that seen in MAT SSTs (between ~3°C and ~6°C), but apparently in antiphase, though the short record makes it difficult to be certain. MAT temperatures reflect summer surface SSTs, whilst this Mg/Ca temperature record was obtained from thermocline-dwelling *N. pachyderma* (*s*), which blooms during early spring. The peak in sub-surface Mg/Ca temperatures of ~6°C at ~130 ka, whilst MAT SSTs from the same sample suggest surface temperatures ~1°C is

unexpected, and one would not expect this temperature gradient to be stable. Possibly cold but extremely fresh surface waters with abundant sea ice overlay warmer, but extremely saline intermediate waters, which inhibited convection during winter storms. This water mass could have originated in the Nordic Seas, where a warm, saline and poorly ventilated deep water mass was observed to have formed during the last glacial period (Figure 3.17) (Thornalley et al. 2015). Regular incursions of warm water from the North Atlantic Current have been observed previously in the south of the Labrador Sea during glacial ice rafting events (Hiscott et al. 2001). A warm peak in ODP-980 MAT SSTs of nearly 11°C at 131.5 ka suggests that periodic warmth between IRD pulses could extend across the North Atlantic. Whether warm surface (or sub-surface) waters promoted subsequent iceberg melting, or whether subsequent iceberg melting suppressed surface water temperature, is impossible to say, but these temperature and IRD oscillations are striking. They also support the suggestion of “oscillatory behaviour of thermohaline circulation”, deduced from fluctuations in benthic  $\delta^{13}\text{C}$  during more recent Heinrich events (Zahn et al. 1997).

U1302 planktonic  $\delta^{13}\text{C}$  is highly variable through H11, with fairly positive values similar to U1305, followed by a shift to more negative values ~132.2 ka, which may be associated with IRD pulse II (Figure 8.3). Negative planktonic  $\delta^{13}\text{C}$  excursions have been observed during Heinrich events previously (Spero and Lea 2002), perhaps due to the suppression of open ocean convection by fresh surface meltwater (Marshall and Schott 1999), or a change in the balance between surface productivity and oxidation at depth (Hillaire-Marcel et al. Bilodeau 2000).

A striking feature of H11, clearly identified by the multi-proxy approach used in the present study, is the large-amplitude depleted planktonic  $\delta^{18}\text{O}$  excursion seen in U1302 (Figure 8.3) originally identified by Hillaire-Marcel et al. (2011) (Figure 7.7). U1302 planktonic  $\delta^{18}\text{O}$  decreased to a minimum at ~132.9 ka in three major steps. The depleted values continued for over 1000 years, during which U1302 planktonic  $\delta^{18}\text{O}$  was an average of 1.92 ‰. Values became more enriched ~131.3 ka, coincident with warmer MAT SSTs and reduced IRD input in both U1302 and ODP-980 (Figure 8.3 & Figure 8.5), which suggests this signal was due to a change in seawater  $\delta^{18}\text{O}$  rather than lower temperatures, potentially signalling an influx of high-salinity NAC water to the region, which would also account for the warming between IRD pulses. If the NAC influence were localised to the south of the Labrador Sea (i.e. a strong NAC but a weak SPG

associated with a weak or diluted Irminger Current), this interpretation would also explain why more enriched  $\delta^{18}\text{O}$  values were not represented in U1305.

Though often attributed to surface water freshening (due to a depleted meltwater  $\delta^{18}\text{O}$  signature) (Dokken and Jansen 1999), no depleted  $\delta^{18}\text{O}$  excursion is evident in U1305, despite strong IRD and Ba/Ca evidence of ice melting in the area (Figure 8.3). This observation supports the interpretation that depleted  $\delta^{18}\text{O}$  excursions during Heinrich events are the result of isotopically depleted brine production, rather than the direct effect of meltwater input

(Hillaire-Marcel and de Vernal 2008). When sea ice is formed,  $\text{H}_2\text{O}^{18}$  is preferentially incorporated into sea ice, leaving behind isotopically depleted brine (Toyota et al. 2013). In the present day, sea ice is formed in the Labrador Sea during winter, but at much higher concentrations near U1302 than U1305 (Figure 8.12).

If this pattern were similar during glacial periods, it could explain the lack of a depleted  $\delta^{18}\text{O}$  excursion in U1305.

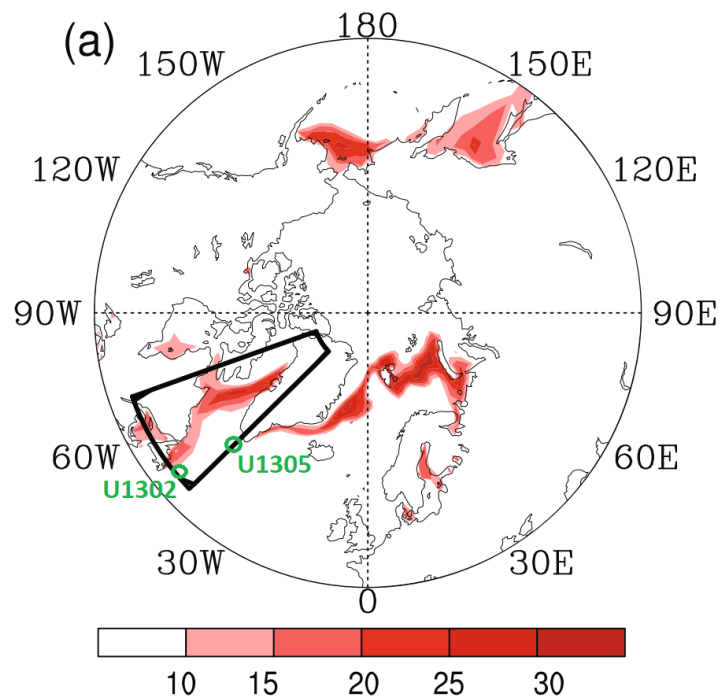


**Figure 8.12** | Sea ice cover in the Labrador Sea. Shading indicates winter average (December, January, February) of the present day monthly standard deviation of sea-ice concentration (%) (Han and Li 2018).

It is interesting that U1305 planktonic isotopes show none of this variability, with  $\delta^{18}\text{O}$  increasing smoothly from enriched to depleted, although this may be a smoothed record due to low resolution. In this, U1305 planktonic  $\delta^{18}\text{O}$  is much more similar to benthic  $\delta^{18}\text{O}$  from both cores (Figure 8.4), which increase smoothly towards the last interglacial, with only one perturbation. After  $\sim 131.1$  ka, there is an increase in U1305 benthic  $\delta^{18}\text{O}$  of  $0.97$  ‰ at  $\sim 130$  ka, also observed in MD03-2664 benthic  $\delta^{18}\text{O}$ , and coincident with an increase in U1302 planktonic  $\delta^{18}\text{O}$ , perhaps suggesting a climate deterioration associated with the final IRD peak of phase III. This may be related to the

probabilistic indications of highstand in GMSL  $\sim$ 132 ka followed by a sea level regression of  $\sim$ 15 m (Figure 3.13). The low resolution of benthic isotopes in this study may be a hinderance, because in the higher-resolution MD03-2664 (Galaasen et al. 2014), benthic isotopes and the three IRD pulses identified in this study correlate fairly closely (Figure 8.5). Enriched MD03-2664 benthic  $\delta^{18}\text{O}$  and negative  $\delta^{13}\text{C}$  values appear to coincide with each IRD pulse, suggesting perhaps the incursion of very cold and poorly ventilated AABW due to AMOC slackening associated with each IRD pulse, with warmer, more recently ventilated water present between the pulses. In contrast, in U1305 and U1302, benthic  $\delta^{18}\text{O}$  and  $\delta^{13}\text{C}$  appear to have varied in almost complete antiphase throughout H11, though the low resolution of the records through this period makes it difficult to be certain (Figure 8.5).

A positive benthic  $\delta^{13}\text{C}$  value in U1302  $\sim$ 132.2 ka conflicts with negative benthic  $\delta^{13}\text{C}$  in U1305 and MD03-2664, and is much more positive than planktonic  $\delta^{13}\text{C}$  during IRD pulse II, though it is difficult to see where this well-ventilated water could have come from if it was not observed to be present either above (i.e. planktonic) or across the Labrador Sea (i.e. U1305). If it were due to the localised sinking of brines, not only would these have to be sufficiently dense to sink to the sea floor, which seems unlikely, but benthic  $\delta^{18}\text{O}$  should record some fluctuation, which is not observed. This value remains unexplained.

During Termination I, if freshwater perturbation of the AMOC caused the Younger Dryas (e.g. Broecker et al. 1989), then a similar climate reversal might be expected to have occurred during TII. Supporting evidence comes mostly from studies of palaeo-sea level, though these tend to place the Bølling-Allerød analogue very early, at  $\sim$ 134.8 - 137 ka (e.g. Andrews et al. 2007; Siddall et al. 2006; McCulloch and Esat 2000; Thomas et al. 2009), during the period associated with the penultimate glacial maximum in the present study (Figure 8.3). In common with many other studies (e.g. Hibbert et al. 2010, Cheng et al. 2009), this study did not find evidence of a single dramatic Younger Dryas-like Kattégat climate reversal during TII (Seidenkrantz 1993). Instead, there were indications of oscillatory behaviour during H11, with a sequence of warm SSTs preceding three major IRD pulses, potentially due to oscillations in AMOC strength evidenced by tight coupling with benthic  $\delta^{18}\text{O}$  and  $\delta^{13}\text{C}$ , particularly in MD03-2664 (Figure 8.5). If anything, then, this study provides evidence in the form of MAT SSTs and IRD counts of up to three “Bølling-Allerød” analogues centred  $\sim$ 134.6, 133.3

and (the most pronounced) at ~131.1 ka (Figure 8.5). This last would be the most likely candidate to associated with the indication of a rise in GMSL ~131 ka observed in the data from Kopp et al. (2013; Figure 3.13). There are certainly indications of climate deterioration associated with IRD pulse III in the form of reduced MAT (just below) and Mg/Ca (just above) temperature estimates accompanied by low temperatures across the North Atlantic in ODP-980, and a shift to enriched benthic  $\delta^{18}\text{O}$  in U1305 and MD03-2664 (Figure 8.5). However, these indications ended abruptly with the melting ice, and so are not taken as indications of a prolonged period of cold, but rather as transient indications of the local effect of massive ice rafting, after which the climate quickly reorganised into interglacial conditions.

## 8.2.4 | Diatom Mat

In U1305, an unusual 10-cm layer (31.66 – 31.76 mcd) was observed just above detrital layers attributed to H11, which contained thickly matted diatom frustules but very little IRD or foraminifera. Although foraminifera were not abundant enough for a reliable MAT SST within the layer, in common with Rasmussen et al. (2003) who observed a diatom mat in a core from the Flemish Cap, a major change in foraminiferal assemblage at the top of the diatom mat was reflected in the warmest MAT SSTs of the entire last interglacial (~12°C), and the varied species present within the diatom mat were typical of the warm North Atlantic assemblage (section 4.4). This together with low IRD and depleted  $\delta^{18}\text{O}$  values suggests the diatom mat was deposited in warm surface waters. In the North Atlantic, diatom mats have been associated with transitions from cold to warm isotope stages (Aksu and Mudie 1985; Jennings et al. 1996), and with downwelling along the subarctic convergence front (Figure 4.22) (Boden and Backman 1996). Firstly, Kemp et al. (2006) suggest a dual mechanism during meltwater events whereby huge quantities of cold, low-salinity water cause surface stratification which suppresses usual surface productivity whilst bringing in dissolved silica that may stimulate huge blooms of diatom species able to vertically migrate to access nutrients. If this were the case, it might be expected to have the effect of suppressing deep convection, and thereby inhibiting AMOC strength (McManus et al 2004). However, fairly positive benthic  $\delta^{13}\text{C}$  values within and surrounding the diatom mat do not support this theory (Figure 8.5). Alternatively, the diatom mat may an indicator of

proximity to the subarctic convergence front (Boden and Backman 1996), which can enhance deposition and prolong the bloom (Allen et al. 2005). Reorganisation of surface currents during this period may have brought the northern arm of the subarctic convergence front to reside above the Eirik Drift for a time (Shimada et al. 2008). This may represent a transitional period when the polar and arctic fronts were migrating from their glacial southerly extreme, but had not yet reached their peak interglacial locations further to the north along the eastern Greenland coast (Figure 3.15). Perhaps, if as benthic  $\delta^{13}\text{C}$  suggests, AMOC was active, a stronger Irminger Current brought the warmer surface waters into the Labrador Sea, also accounting for the peak MAT SSTs observed just above the diatom mat. Either way, its anomalous climatological significance (no other diatom mat was discovered in the sections of core studied here) suggest hydrographic conditions changed abruptly across the Labrador Sea, and may have resulted in unusual surface water properties or surface current patterns.

Cluster analysis identified a shift between polar foraminiferal assemblage zone A and early last interglacial zone B just above the final IRD layer (Figure 5.13), suggesting that surface hydrography reorganised rapidly across the Labrador Sea after the ice melted. The rapidity of interglacial onset was ascribed by Thornalley et al. (2011) to reduced stratification (due to warmer subsurface water) and enhanced salinity (due to brine production). Evidence for both these processes is found in this study, with *N. pachyderma* (s) Mg/Ca temperatures between IRD pulses II and III indicating subsurface waters may have been up to  $\sim 5^\circ\text{C}$  warmer than surface temperatures (Figure 8.5), and evidence from a depleted planktonic  $\delta^{18}\text{O}$  excursion observed within U1302 of enhanced sea ice production through H11 (Figure 8.3).

### 8.3 | THE LAST INTERGLACIAL

Due to the large amount of data involved, graphs are split to combine surface temperature proxies (Figure 8.13), ice rafting and meltwater proxies (Figure 8.14), benthic and planktonic  $\delta^{18}\text{O}$  (Figure 8.15) and benthic and planktonic  $\delta^{13}\text{C}$  (Figure 8.16). It should be noted that there is a large difference in sedimentation rates between the two cores. In contrast to the situation during H11 where U1302 was much higher resolution, in U1302 only 3 samples (13 cm) separate the onset of the last interglacial ( $\sim 128.5$  ka) from the red layer ( $\sim 126.5$  ka), discussed below, resulting in a resolution of

580 – 960 years (due to varying sample depth intervals). In U1305 however, this same interval is spread across 1.7 m due to the highest sedimentation rate of either core (85.0 cm/ka), resulting in an impressive potential resolution of 59 years (not including mixing by bioturbation). This means the evidence from U1302 represents only the broadest scale impression, whilst U1305 can be looked to for detail and structure. This resulted in correlation between the broader category of faunal assemblage zone B in U1302 appearing to split into B and Ca in U1305 (Figure 5.13). Above the red layer, sedimentation rates were more comparable at 45.5 cm/ka (110 year resolution) in U1305 and 20.5 cm/ka (244 year resolution) in U1302.

In general terms, U1302 proxy records follow the shape and pattern of MD95-2042 much more closely than they do Eirik Ridge records, likely indicating the strong influence of the NAC and associated “Atlantic signature” at Orphan Knoll. In contrast, indications from Eirik Ridge of close coupling between surface and deep water masses suggests the northern Labrador Sea climate is much more closely linked to that of the Nordic Seas.

Figure 8.13 shows that overall U1302 and U1305 MAT SSTs were similar to each other through the last interglacial ( $\sim 9 - 10^{\circ}\text{C}$ ). Present day ocean atlas summer (JJA) surface water temperatures are  $10.3^{\circ}\text{C}$  at the location of U1302, but only  $7.0^{\circ}\text{C}$  above U1305 (World Ocean Atlas 1998) (Figure 5.10). Coretops were not available for U1302, but although U1305 coretop MAT SSTs ( $8.5 \pm 1.4^{\circ}\text{C}$ ) were warmer than ocean atlas values, they were in close agreement with coretop Mg/Ca calcification temperatures from *G. bulloides* ( $8.5 \pm 0.4^{\circ}\text{C}$ ). Therefore, the last interglacial appears no warmer than present at Orphan Knoll, which supports the findings of Winsor et al. (2012) using MD99-2227 from Eirik Ridge (Figure 3.11). But this finding is at odds with results from U1305 (also from Eirik Ridge), which saw peak last interglacial temperatures of  $\sim 12.3^{\circ}\text{C}$   $\sim 128.4$  ka ( $\sim 3^{\circ}\text{C}$  warmer than coretop values, and  $\sim 5^{\circ}\text{C}$  warmer than ocean atlas values), and MAT temperatures were consistently  $1 - 2^{\circ}\text{C}$  warmer than coretop values through the last interglacial (Figure 8.13). These differences may be partially explained by location. U1305 is to the south east of MD99-2777, and may therefore have been more directly influenced by warmer Irminger Current water. These temperatures may therefore indicate that the SPG was more vigorous during the last interglacial, with a stronger Irminger current bringing warmer waters to the location of U1305. On the other hand, these may be taken as indications that higher last interglacial temperatures were more

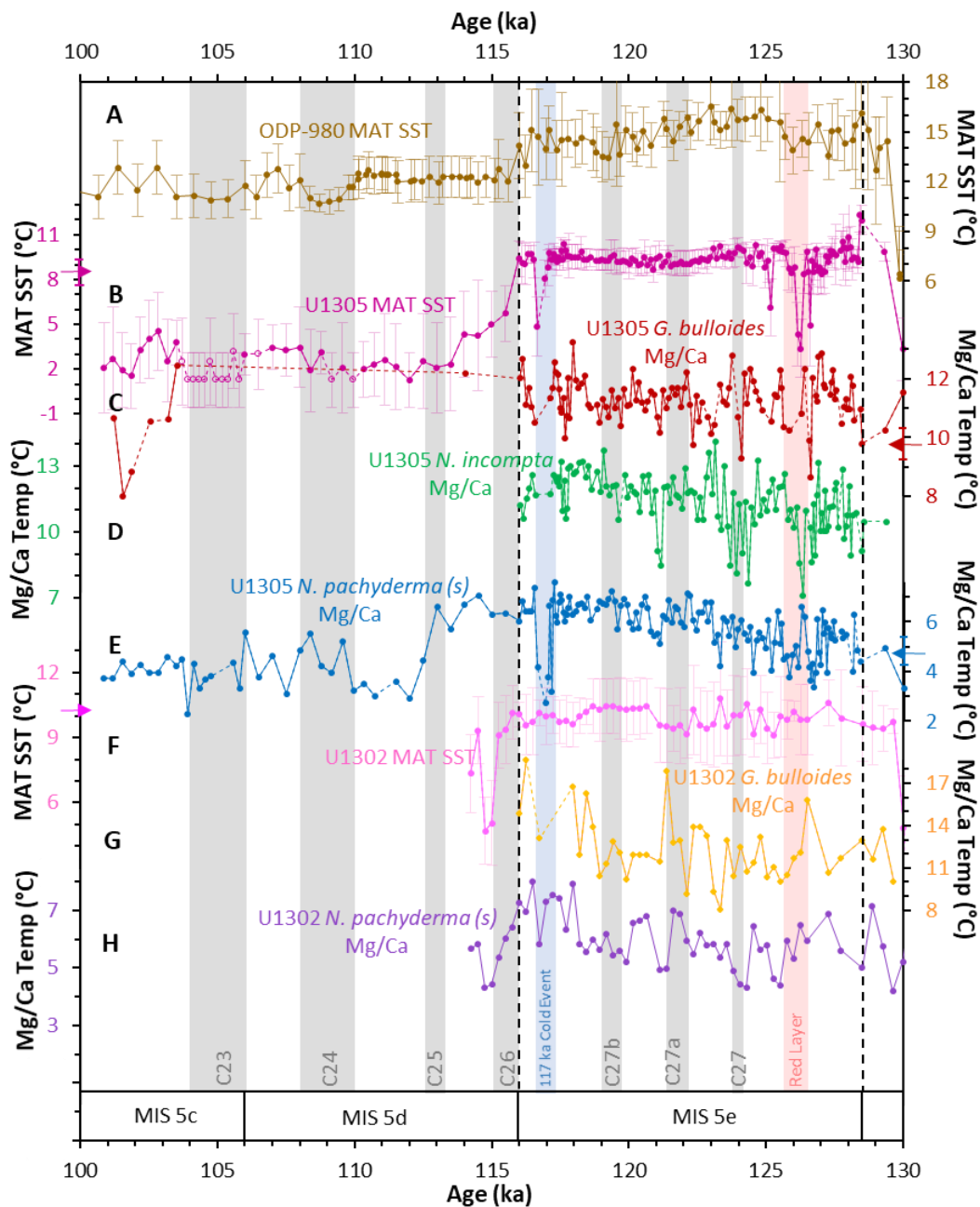


**Figure 8.13** | Last interglacial palaeotemperature estimates. (A) ODP-980 MAT SSTs (brown) including  $1\sigma$  error bars (Oppo et al. 2006). (B) U1305 MAT SSTs (dark pink; this study) including  $1\sigma$  error bars, open circles indicate small samples, dark pink arrow on axis indicates coretop temperature estimate ( $8.5^{\circ}\text{C} \pm 1.4$ ). (C) U1305 *G. bulloides* Mg/Ca temperatures (red; this study), red arrow on axis indicates coretop temperature ( $8.9^{\circ}\text{C} \pm 0.4$ ). (D) U1305 *N. incompta* Mg/Ca temperatures (green; this study). (E) U1305 *N. pachyderma* (s) Mg/Ca temperatures (dark blue; this study), blue arrow on axis indicates coretop temperatures ( $4.9^{\circ}\text{C} \pm 0.5$ ), (F) U1302 MAT SSTs (light pink; this study) including  $1\sigma$  error bars, open circles indicate small samples, light pink arrow on axis indicates summer (JJA) surface (0 – 10 m) temperatures at the location of U1302 (World Ocean Atlas 1998). (G) U1302 *G. bulloides* Mg/Ca temperatures (orange; this study). (H) U1302 *N. pachyderma* (s) Mg/Ca temperatures (purple; this study). Dotted lines indicate gaps in the records. Along the bottom are marine isotope substages (MIS). Grey shading indicates North Atlantic cold events (C23 – C27). Blue shading indicates the U1305 diatom mat and 117 ka cold event. Pink shading indicates the red layer. Dashed vertical lines indicate the boundaries of the last interglacial 128.5 – 116 ka.

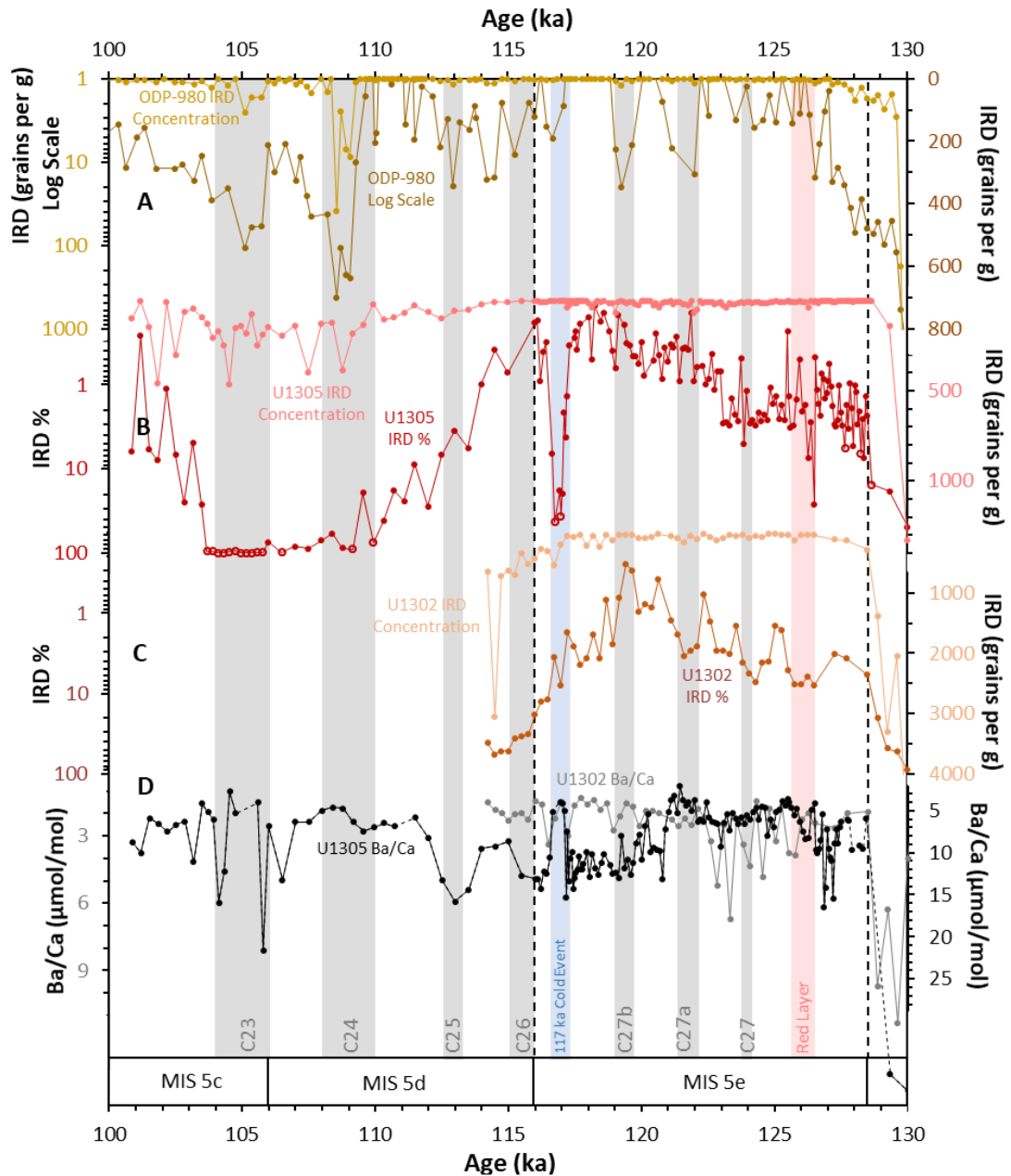


**Figure 8.14** | Last interglacial IRD and Ba/Ca results. (A) ODP-980 IRD concentration (light brown) also shown on a log scale (dark brown) (Oppo et al. 2006). (B) U1305 IRD concentrations (pink) and percentage (red) on a log scale, open circles indicate samples containing <50 foraminifera (this study). (C) U1302 IRD concentration (peach) and percentage (dark peach) on a log scale (this study). (D) U1305 (black) and U1302 (grey) Ba/Ca ratios from *N. pachyderma* (*s*), a proxy for meltwater runoff (this study). Dotted lines indicate gaps in the records. Along the bottom are marine isotope substages (MIS). Grey shading indicates North Atlantic cold events (C23 – C27). Blue shading indicates the U1305 diatom mat and 117 ka cold event. Pink shading indicates the red layer. Dashed vertical lines indicate the boundaries of the last interglacial 128.5 – 116 ka.

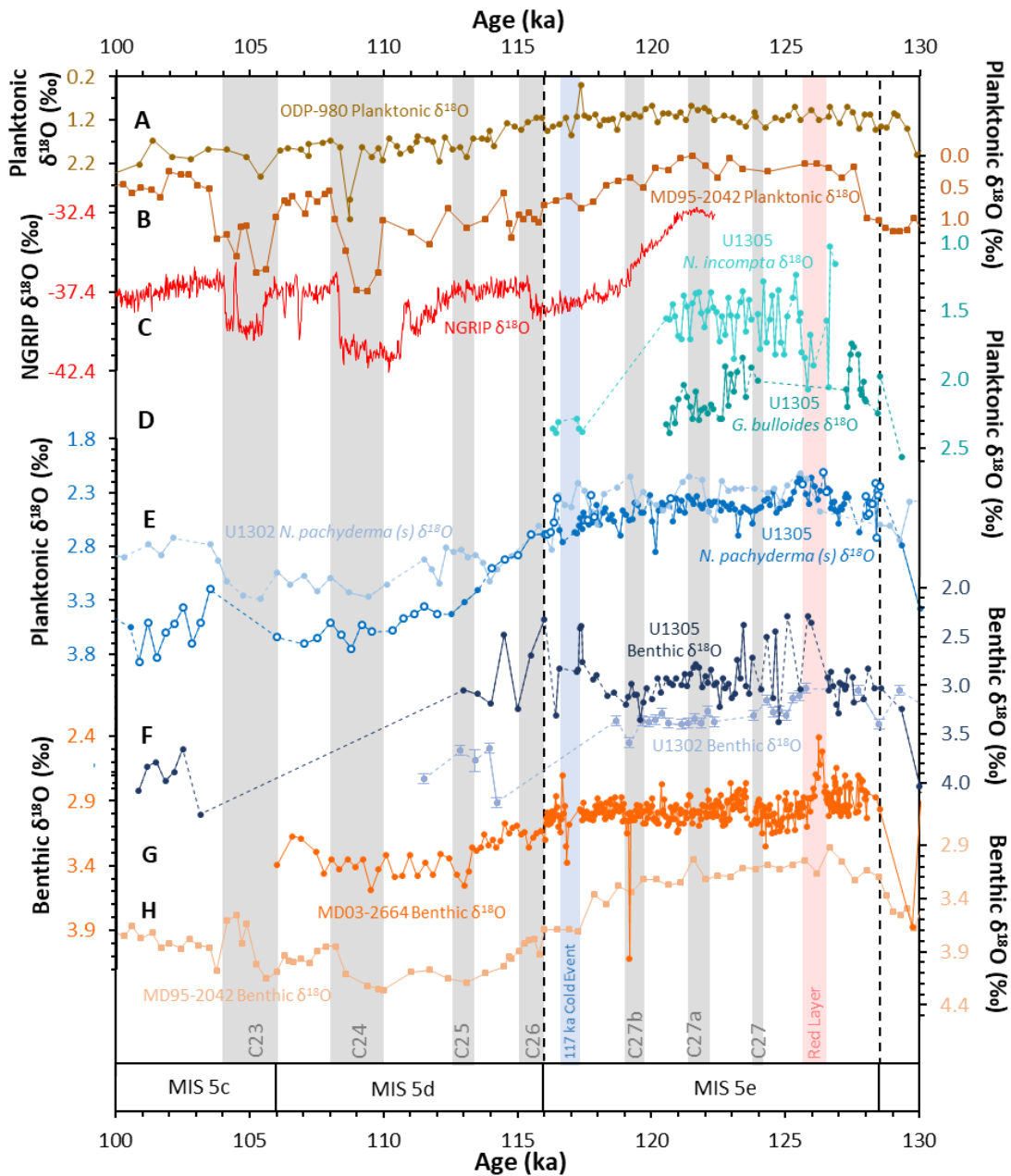


**Figure 8.15** | Last interglacial ice core (C), planktonic (A, B, D, E) and benthic (F – H)  $\delta^{18}\text{O}$ . (A) ODP-980 *N. incompta*  $\delta^{18}\text{O}$  (Oppo et al. 2006). (B) MD95-2042 *G. bulloides*  $\delta^{18}\text{O}$  (Shackleton 2002). (C) NGRIP  $\delta^{18}\text{O}$  (North Greenland Ice Core Project Members 2004). (D) U1305  $\delta^{18}\text{O}$  from *G. bulloides* (dark turquoise) and *N. incompta* (light turquoise) (this study). (E) *N. pachyderma* (*s*)  $\delta^{18}\text{O}$  from U1305 (royal blue) and U1302 (light blue), solid circles are from Hillaire-Marcel et al. (2011), open circles indicate data from this study. (F) Benthic  $\delta^{18}\text{O}$  from U1305 (navy; this study) and U1302 (pale blue; Kaboth et al. unpublished). (G) MD03-2664 benthic  $\delta^{18}\text{O}$  (Galaasen et al. 2014). (H) MD95-2042 benthic  $\delta^{18}\text{O}$  (peach) (Shackleton et al. 2002). Dotted lines indicate gaps in the records. Along the bottom are marine isotope substages (MIS). Grey shading indicates North Atlantic cold events (C23 – C27). Blue shading indicates the U1305 diatom mat and 117 ka cold event. Pink shading indicates the red layer. Dashed vertical lines indicate the boundaries of the last interglacial 128.5 – 116 ka.

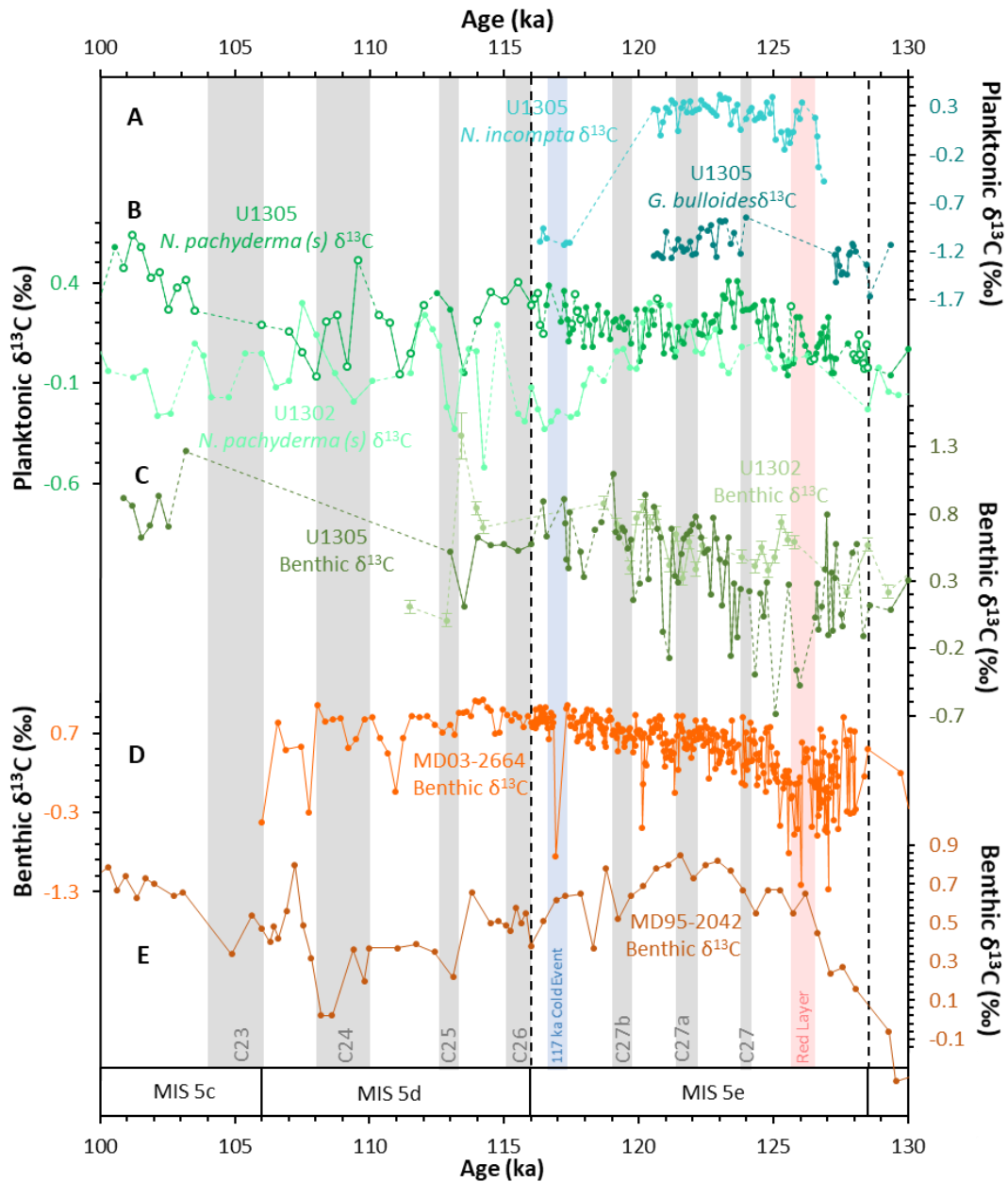


**Figure 8.16** | Last interglacial planktonic (A, B) and benthic (C – E)  $\delta^{13}\text{C}$ . (A) U1305  $\delta^{13}\text{C}$  from *G. bulloides* (dark turquoise) and *N. incompta* (light turquoise) (this study). (B) *N. pachyderma* (*s*)  $\delta^{13}\text{C}$  from U1302 (light green) and U1305 (dark green), solid circles are from Hillaire-Marcel et al. (2011), open circles indicate data from this study. (C) Benthic  $\delta^{13}\text{C}$  from U1305 (dark green; this study) and U1302 (pale green; Kaboth et al. unpublished). (D) MD03-2664 benthic  $\delta^{13}\text{C}$  (Galaasen et al. 2014). (E) MD95-2042 benthic  $\delta^{13}\text{C}$  (brown; Shackleton et al. 2002). Dotted lines indicate gaps in the records. Along the bottom are marine isotope substages (MIS). Grey shading indicates North Atlantic cold events (C23 – C27). Blue shading indicates the U1305 diatom mat and 117 ka cold event. Pink shading indicates the red layer. Dashed vertical lines indicate the boundaries of the last interglacial 128.5 – 116 ka.

strongly felt further north, and may be related to indications of greater GIS retreat during the last interglacial (Hillaire-Marcel et al. 2001; Otto-Bliesner 2006; Stone et al. 2013).

All Mg/Ca results show a trend towards warmer calcification temperatures with less variability through the last part of the last interglacial (Figure 8.13), which is in striking similarity to U1305 and U1302 benthic  $\delta^{13}\text{C}$  records, and to the excellently high resolution benthic  $\delta^{13}\text{C}$  record of MD03-2664 (Figure 8.16) (Galaasen et al. 2014). This suggests there may be some link between nutrient cycling and calcification temperatures in the surface waters of the Labrador Sea and the Nordic Seas, where deep NADW constituents acquire their  $\delta^{13}\text{C}$  signature. If so it might be expected that planktonic  $\delta^{13}\text{C}$  would echo this trend (more positive values with less variability towards end of the last interglacial) which appears to be the case for U1305, but not however U1302. U1302 planktonic  $\delta^{13}\text{C}$  reaches a peak at ~120.4 ka, after which values become increasingly negative, and appear to reach glacial-type values ~117.7 ka (Hillaire-Marcel et al. 2011). Although it may appear that U1305 *G. bulloides*  $\delta^{13}\text{C}$  echoes this trend, examination of the longer HU90-013-013 *G. bulloides* isotope record from Eirik Ridge close to U1305 (Hillaire-Marcel et al. 2011) on the right in Figure 7.7 shows that *G. bulloides* follows *N. pachyderma* (*s*) in increasingly positive values over time. This divergence in values between U1305 and U1302 is not reflected in planktonic  $\delta^{18}\text{O}$ , however.

IRD input in both cores decreased sharply after H11 (Figure 8.14). The log scale used for IRD percentages in Figure 8.14 brings out detail in the interglacial record, which suggests ice sheet melting continued in U1305 until ~122.8 ka, and until even later in U1302 (~121.1 ka). This is reflected in planktonic  $\delta^{18}\text{O}$  values, which all show the most depleted values early in the last interglacial (Figure 8.15), likely indicating decreased surface salinity since sustained surface warmth is not indicated in MAT SSTs (Figure 8.13). These observations are in keeping with indications from the NEEM ice core of continued warming and ice sheet melting up until ~126 ka (Figure 3.12) (NEEM Community Members 2013), likely responsible for indications of continued ice sheet melting in the Labrador Sea during the first part of the last interglacial (Govin et al. 2012, Winsor et al. 2012, Irválı et al. 2016) (Figure 3.11).

### 8.3.1 | The Early Last Interglacial

Despite fairly constant long-term MAT SSTs, Figure 8.13 shows there are indications in all proxies of transient warmth, particularly through the very earliest part of the last

interglacial (~128.5 – 126.5 ka), as observed by Zhuravleva et al. (2017) in a core from the Iceland Sea. This period coincided with faunal assemblage zone B in both cores (and zone Ca in U1305), which ended within the red layer (Figure 5.14), indicating that the event or events leading to its deposition had a powerful effect on surface plankton communities that interrupted the early warm climate. Figure 8.13 shows that peak temperatures (~12°C) in U1305 MAT SSTs were coincident with the onset of the last interglacial ~128.5 ka, and is ~3°C warmer than coretop MAT SSTs ( $8.5 \pm 1.4^\circ\text{C}$ ). This anomalous warmth is likely due to the reorganisation of surface currents (particularly the warm Irminger Current) following the end of H11. This interpretation is supported by the location of these warm values directly above the diatom mat in U1305, which was itself taken as an indication of an unusual position of the subarctic convergence front as it migrated north from its glacial location somewhat nearer the latitude of the UK (Figure 3.15). This initial warmth is reflected in the eastern North Atlantic in ODP-980 (~16°C) suggesting it was regional in extent. In U1305, temperatures appear to have declined slightly after ~127.3 ka (~2°C), corresponding with foraminiferal assemblage zone Ca which appears to mark the transition towards the climate deterioration centred on the red layer. U1302 MAT SSTs show a sharp temperature rise of ~7°C somewhat earlier at ~129.6 ka, and instead peak slightly later at ~127.3 ka, supporting the interpretation of climate deterioration after this date.

Mg/Ca temperatures in all species also show early warmth between ~130 – 129 ka. In contrast to faunal assemblages however, all Mg/Ca temperature records show some indications of cooling during or just after the period of the diatom mat deposition, likely related to the C28 event observed in ODP-980 by Oppo et al (2006). However, all species show warm calcification temperatures through the early last interglacial, generally 10 – 13°C at the surface (*G. bulloides* and *N. incompta*), and 4 – 7°C at the thermocline (*N. pachyderma (s)*), with if anything a warming trend towards the red layer. Mg/Ca temperatures are highly variable through this first period however, much more so than later in the last interglacial, perhaps reflecting unstable hydrography disrupting the depth or seasonality of foraminifera peak blooms. All U1305 Mg/Ca results appear to show the greatest warmth ~127 - 126.5 ka.

After ~128.5 ka, Figure 8.14 shows IRD input in both cores continue to reduce towards the red layer, mirroring similar reductions in ODP-980, with slightly more at Orphan Knoll (mean IRD concentration in U1305 = 2.9 grains per g, U1302 = 174 grains per g).

Elevated Ba/Ca ratios in U1305 ~127.2 – 126.8 ka suggests sustained meltwater runoff, increasing in the millennium prior to the red layer. This also supports palaeomagnetic evidence from Eirik Ridge Core MD99-2227 of a broad period of coarse grain size during the early last interglacial, interpreted as detrital input from the continued melting on land of the Greenland Ice Sheet during this period (Evans et al. 2007). This low salinity is reflected in the early onset of depleted U1305 planktonic  $\delta^{18}\text{O}$ , clearly shown by the new data produced for this study (open circles in Figure 8.15 E), though values become slightly more enriched ~127.7 ka, before progressing towards more depleted values associated with the onset of the red layer. Simultaneous shifts are seen through this period in in *G. bulloides*  $\delta^{18}\text{O}$  and  $\delta^{13}\text{C}$  (Figure 8.16), perhaps due to changes in productivity response to fluctuations in surface salinity or climate-mediated alterations in the balance between precipitation and evaporation that are not so pronounced at the base of the surface mixed layer inhabited by *N. pachyderma* (*s*).

The climate deterioration after ~127.3 ka observed in U1305 faunal assemblages (Figure 8.13) is also apparent in benthic  $\delta^{13}\text{C}$  values (Figure 8.16), which both decrease towards the red layer, with very negative MD03-2664 benthic  $\delta^{13}\text{C}$  ~127 ka interpreted as abrupt shoaling of NADW and incursion of AABW (Galassen et al. 2014). This suggests changes in deepwater formation rates or AMOC vigour occurring in the millennium leading up to the red layer, which is interesting, as it implies that the red layer may be a consequence of a longer-term trend, rather than a cause. The trend towards warmer Mg/Ca calcification temperatures suggests this may be linked to peak surface warmth over Greenland ~126 ka (Figure 3.12), which may have induced the final melting of an ice dam in Hudson Bay, leading to catastrophic draining of a Laurentide glacial lake, potentially responsible for the many indications of climate deterioration at around this time.

### 8.3.2 | The Red Layer

The red layer (~126.5 ka) documented by Nicholl et al. (2012) within U1302 and U1305 was attributed to a Laurentide outburst flood event analogous to the final draining of Lake Agassiz 8.4 ka (Kerwin 1996; Lajeunesse & St-Onge 2008). The authors suggest this may have had similar effects on ocean circulation (Kleiven et al. 2008) through a massive freshwater flux (Barber et al. 1999; Teller et al. 2002) causing suppression of

deep convection (Andrews et al. 1999). Carlson (2008) also discussed these red layers, deposited after both TI and TII, and suggested they are evidence of considerable retreat of the Laurentide ice sheet. Carlson (2008) argues that an analogous influx of meltwater that suppressed AMOC during TI causing the Younger Dryas, and that this occurred earlier during the last interglacial, before a vigorous AMOC had become established (and therefore had less impact on the climate). The date given by Carlson (2008) for the timing of a red clay layer (129 – 130 ka) was based on orbital tuning of foraminifera  $\delta^{18}\text{O}$ , however this method of dating is associated with large uncertainties (which are not quoted), nor is precise information given about the method used. Therefore, a date of ~126.5 ka may be realistic given typical uncertainty of  $\pm 4$  ka through this period (e.g. Lisiecki and Stern 2016). Also, the inference that the Laurentide ice sheet was already “greatly diminished prior to peak boreal summer insolation”, is at odds with more recent observations that ice sheet disintegration continued well into the first half of the last interglacial (Govin et al. 2012; Winsor et al. 2012).

Figure 8.14 indicates slightly enhanced IRD input through the red layer in both cores. However, the increase at U1302 is not outside general variability at this site (8%), and the increase in U1305 (26%) can instead be attributed to a marked reduction in planktonic foraminifera, against which IRD % is calculated (Figure 4.25). Indeed, the coarse fraction of U1305 actually decreased (Figure 4.25), suggesting instead an influx of fine material may have swamped the usual rate of foraminiferal settling through the water column. No increase in IRD concentration was observed at either location.

Nicholl et al. (2012) did not consider the red layer to be associated with IRD either, although examination of their IRD percentage U1302 (Figure 8.17) does show a slight increase to ~10%, with a much larger increase to ~30% at the top of the red layer. The authors suggest this latter peak is “unlikely to share a source with the red layer” because it did not contain detrital carbonate grains. The percentage of bulk carbonate in Figure 8.17 shows a large increase to ~40 %, suggestive of fine fraction carbonates likely to have been mobilised in the outburst flood. U1305 Ba/Ca declined across the red layer, whilst U1302 increases (Figure 8.14), suggesting reduced Greenland melt influence coincident with increased Laurentide meltwater input. There is a peak in red-stained lithics within the U1305 red layer (Figures 4.8 and 4.9), further reinforcing the Hudson Bay origin of this material. Taken together, IRD and foraminiferal assemblage data generated for this study show that the reduction in coarse fraction (>63  $\mu\text{m}$  size

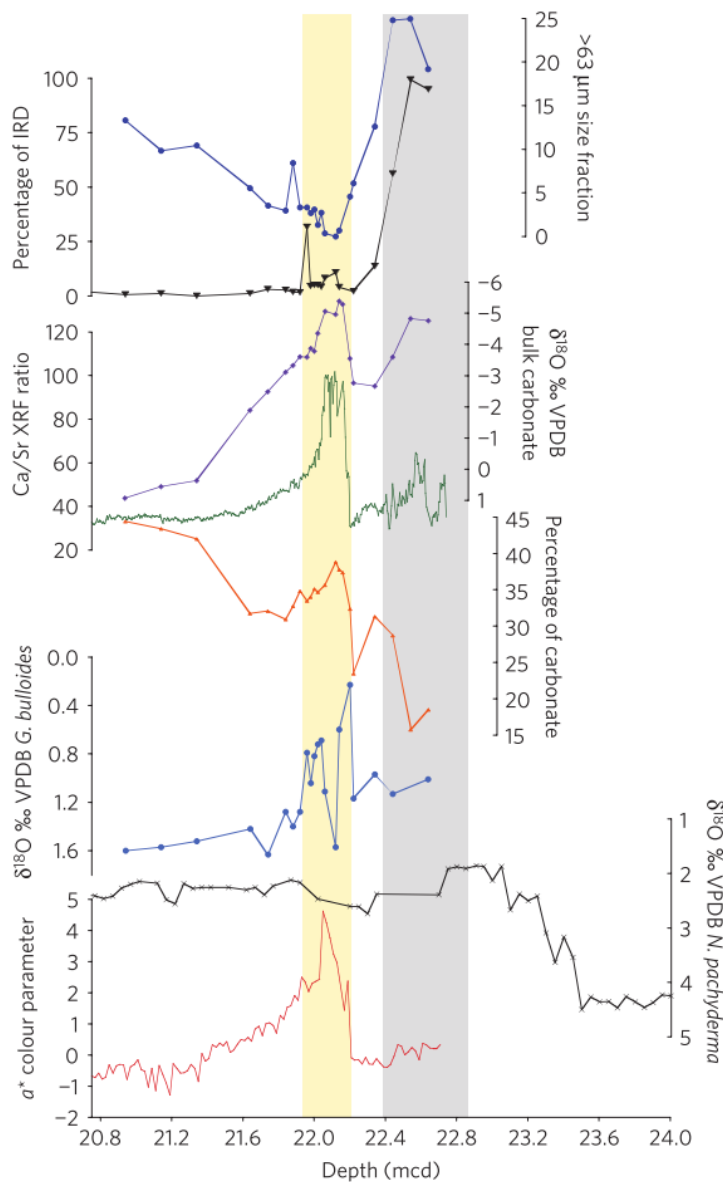


**Figure 8.17** | Data concerning the red layer from U1302 by Nicholl et al. (2012), including from the top coarse fraction weight % (dark blue), IRD % (black triangles), bulk carbonate  $\delta^{18}\text{O}$  (purple), Core-scanning XRF Ca/Sr (green), bulk sediment carbonate weight % (orange), *G. bulloides*  $\delta^{18}\text{O}$  (blue), *N. pachyderma* (*s*)  $\delta^{18}\text{O}$  (black crosses) and  $a^*$  colour reflectance parameter (red). Yellow shading indicates the red layer, grey shading indicates H11 (Nicholl et al. 2012).

fraction) associated with the onset of the red layer observed by Nicholl et al. (2012) (Figure 8.17) is due to a sharp reduction in foraminifera abundance (Figure 4.25) as a result of the influx of fine-grained carbonate material (Figure 8.17).

Figure 8.13 shows the red layer is certainly one of the coldest events during the last interglacial within U1305, comparable with the 117 ka event discussed below. In U1305 this cooling appears at the base of the red layer or just below, whilst in U1302 both Mg/Ca records instead show initial warmth, with cooling through the layer reaching minimum temperatures just above it. Similarly, faunal

assemblage cluster analysis identified the division between zones Ca and Cb halfway through the red layer in U1305 (Figure 5.12), but in U1302 the similar division (between B and C in this case) lay at the very top of the red layer (Figure 5.13).

In all records, *N. pachyderma* (*s*) and benthic  $\delta^{18}\text{O}$  records generally reach the most depleted values of the last interglacial within the red layer. However, U1305 *N. incompta*  $\delta^{18}\text{O}$  (Figure 8.15) and *G. bulloides* (Figure 7.7a) both show a rapid shift to

enriched values bracketing the red layer, perhaps related to cold temperatures observed in U1305 MAT SSTs and Mg/Ca calcification temperatures. The lack of cooling in U1302 MAT SSTs cannot be explained by this mechanism, but is perhaps due to low resolution, however the division between zone B and A in U302 certainly indicates a statistical change in faunal assemblage associated with the red layer (Figure 5.13).

Figure 8.16 shows that in U1305 there are large amplitude changes in *N. incompta*  $\delta^{13}\text{C}$ , suggesting large carbon cycle perturbations in surface waters. Extremely negative U1305 and MD03-2665 benthic  $\delta^{13}\text{C}$  values around this period have been interpreted as periodic AABW incursions due to abrupt but transitory reductions in AMOC strength (Galaasen et al. 2014). This may indicate that freshwater input from an outburst flood weakened subpolar gyre circulation, suppressed deep convection and reduced AMOC vigour at this time, cooling the Labrador Sea. These variations are not reflected in U1302 however, which instead are more similar to MD95-2042, with a more gradual trend towards more positive values.

The large fluctuations in temperature estimates and planktonic isotopes, particularly towards the base and top of the red layer, may indicate two or more episodes of flooding, which models (Clarke et al. 2004) and multi-core studies from the Labrador Sea (Lewis et al. 2012) suggest occurred during the 8.2 ka event, though this is difficult to confirm without detailed sedimentological examination and more precise dating methods. Also, if type IV Heinrich layers are attributed to intermittent turbidity currents from Hudson Strait combined with more constant IRD deposition (Hesse and Khodabakhsh 2017), it is not clear why H11 sediments were not also a distinctive red colour. If, as seems likely, the red layer was due to an outburst flood from Hudson Bay, it is unclear how this observation fits with other outburst floods from the same location (such as the jökulhlaups theory of Heinrich events) which did not leave a distinctive red layer. Perhaps the location or extent of lake buildup or routing has an effect (Lewis et al. 2012; Hesse and Khodabakhsh 2016). Using multi-proxy data from MD03-2664, Irvali et al. (2012) documented cooling ~126 ka BP, possibly indicating a “rapid switch” to a different mode of SPG circulation, coincident with a large decrease in planktonic  $\delta^{18}\text{O}$  values of ~0.8‰, perhaps due to enhanced Greenland ice sheet melting (de Vernal and Hillaire-Marcel 2008), supported by model data (Govin et al. 2012). A brief, abrupt shift is observed in  $\delta^{13}\text{C}$  from lake sediments in central Italy ~126 ka (Regattieri et al. 2017), and as far away as Lake Baikal, a notable perturbation of diatom silica  $\delta^{18}\text{O}$  was

observed ~126.5 – 126 ka, attributed by Mackay et al. (2013) to the final stages of H11, though given the improved Labrador Sea age model of this study, would fit better with a response to the outburst flood event. Support for the date derived in this study for the red layer at ~126.5 ka is found in the observation of enhanced freshwater input followed by cooler temperatures in a core from the Iceland Basin at this time (Zhuravleva et al. 2017).

Finally, it should be noted that Rasmussen et al. (2003) found a “reddish” clay layer in a core from the Flemish Cap, which was  $^{14}\text{C}$ -dated to 21.2 ka, within the last glacial maximum. This suggests that whatever causes the distinctive red layers, they are not restricted to interglacial periods.

### 8.3.3 | The C27 Last Interglacial Climate Events

The only indications of cooling associated with C27 (~124 ka) are U1305 *G. bulloides* and *N. incompta* (~3°C) and U1302 *N. pachyderma* (s) Mg/Ca (~2°C) (Figure 8.13). This echoes the pattern seen in planktonic isotopes through the red layer (surface cooling at Eirik Ridge not reflected at the pycnocline, instead reflected at the Orphan Knoll pycnocline but not the surface). There were slight increases in IRD at both locations, and enhanced 1302 Ba/Ca.

C27a (~122 ka) falls just after the start of foraminiferal zone E (Figure 5.14), and appears between fluctuations of ~2 - 4°C in U1305 *G. bulloides* and *N. incompta* Mg/Ca (Figure 8.13). In U1302 however, C27a is marked by extreme fluctuations in *G. bulloides* calcification temperature, with an abrupt cooling of ~5°C followed by abrupt warming of ~9°C, which coincides with a drop in *N. pachyderma* (s) Mg/Ca of ~2°C. This results in a potential surface to pycnocline temperature gradient of ~14°C, however none of this variability is reflected in U1302 MAT SSTs, except that just after C27a a step-change of ~1°C occurs. A slight increase in U1302 IRD (Figure 8.14) accompanied ~0.4 ‰ shift to depleted *N. pachyderma* (s)  $\delta^{18}\text{O}$  (Figure 8.15), but these changes are not dramatic. In fact, all benthic  $\delta^{13}\text{C}$  records show a narrow range of positive values (Figure 8.16), suggesting stable vigorous deep convection. Therefore, these apparently large surface Mg/Ca fluctuations are not considered to be representative of the larger climate, instead perhaps due to noise in the record or stochastic local processes during peak *G. bulloides* bloom.

C27b shows  $\sim 2^{\circ}\text{C}$  reductions in most Mg/Ca records (Figure 8.13), and  $\sim 0.2\text{‰}$  depleted  $\delta^{18}\text{O}$  shift in U1302 *N. pachyderma* (*s*) (Figure 8.15). At depth however, fluctuations were seen in benthic  $\delta^{18}\text{O}$  and  $\delta^{13}\text{C}$  records (Figures 8.15 and 8.16). The lack of local ice rafting (Figure 8.14) suggests instead this may have been related to hydrographic changes rather than iceberg melting. The shift from negative benthic  $\delta^{13}\text{C}$  to positive in U1305 suggests C27b was related to instability in AMOC circulation.

### 8.3.4 | The 117 ka Cold Event

After  $\sim 119$  ka, U1302 IRD deposition began to progressively increase towards MIS 5d (Figure 8.14), paralleled remarkably closely by a negative trend in U1302 *N. pachyderma*  $\delta^{13}\text{C}$  (Figure 8.16). This trend is not observed in U1305 (which had very low IRD and instead a positive trend in *N. pachyderma*  $\delta^{13}\text{C}$ ), implying asynchronous LIS and GIS buildup, and an increasing gradient in pycnocline  $\delta^{13}\text{C}$  across the Labrador Sea through the last part of the last interglacial (Figure 8.14). Increasing gradients in temperature and salinity towards the latter part of the last interglacial were previously observed by Cortijo et al. (1999). This period contained some of the warmest Mg/Ca calcification temperatures in both cores (Figure 8.18), and a slight increase in U1305 MAT SSTs to  $\sim 10^{\circ}\text{C}$  at  $\sim 117.7$  ka (Figure 8.13). This late warm period may be related to the late MIS 5e sea level highstand (122 – 116 ka) suggested by Kopp et al. (2013) (Figure 3.13).

These indications of warmth bracket and perhaps highlight a pronounced cold event, linked in this study to the 117 ka cold event of Iralı et al. (2016), first observed within MD03-2664. In U1305, MAT SSTs reduced by  $\sim 5^{\circ}\text{C}$  (Figure 8.13), and all Mg/Ca calcification temperatures also indicated cooling (although very few foraminifera were available through the interval itself, leading to a gap in the data). What foraminifera were present, mostly small *N. pachyderma* (*s*), suggest very low Mg/Ca calcification temperatures ( $\sim 3^{\circ}\text{C}$ ), although the uncertainty on this value is probably  $\pm 2^{\circ}\text{C}$  due to potential size fraction effects (see section 6.1.6.6). However, some cooling was also observed in U1302 (Figure 8.18) and associated with pronounced but abrupt increase in U1305 and U1302 IRD (Figure 8.14; the very low Ba/Ca values through this interval may be an artefact of the small size fraction).

This cold event within a warm climate optimum coincides with the strange interval of strongly negative U1305 *N. incompta*  $\delta^{13}\text{C}$  values 117.4 – 116.3 ka (Figure 8.16). Up until ~120 ka, *N. incompta*  $\delta^{13}\text{C}$  was similar to *N. pachyderma* (*s*) values, but the cluster of negative *N. incompta*  $\delta^{13}\text{C}$  values ~117 ka are far more similar to *G. bulloides* (typically -1.2 ‰) (Figure 6.17). This suggests a shift to a shallower habitat by *N. incompta*, or a change in seasonality of peak bloom, which might be due to changing hydrographic parameters such as surface water alkalinity or salinity. There are indications of increased salinity at U1305 at this time, in the form of more enriched *N. incompta* and *N. pachyderma* (*s*)  $\delta^{18}\text{O}$  values (Figure 6.15).

The strongly depleted  $\delta^{13}\text{C}$  values in U1305 *N. incompta* and U1302 *N. pachyderma* (*s*) through this interval (Figure 8.16), combined with rapid benthic  $\delta^{13}\text{C}$  and  $\delta^{18}\text{O}$  fluctuations (Figure 8.15), suggest a role for AMOC perturbation. The evidence suggests a dramatic cold event lasting just a few centuries, after which temperature proxies indicate the climate recovered again before the last interglacial drew to a close. Evidence for this 117 ka event was also found by Zhuravleva et al. (2017) in the Iceland Basin (though dated by them to ~118 ka), though not reflected in ODP-980 or MD95-2025 (Figure 8.13). It is clear that although some climate instability was observed to parallel the C27 series of last interglacial cold events of Oppo et al. (2006), their impact was muted in comparison with more localised events surrounding the red layer and the 117 ka cold event.

### 8.3.5 | Normalised Last Interglacial Temperature Estimates

Temperature estimates generated for this study have been further explored by normalising them against their interglacial mean values (128.5 – 116 ka) in order to highlight longer term trends and deviation from the average value for each record (black bar). This method allows direct comparison between each SST proxy (Figure 8.18).

MAT and *G. bulloides* Mg/Ca produce the most variable temperature estimates, as might be expected from a surface-dwelling species. Overall, in U1305 more variability is evident through the first half of the last interglacial. In contrast, in U1302 early temperatures are more consistently warm prior to the red layer, with greater variability coming afterwards. The temperature asymmetry is apparent, whereby cooling appears in

U1305 at the base of the red layer, but in U1302 cooling appears towards the top and just afterwards. Dating uncertainties are reduced surrounding the red layer, as although the duration is uncertain, at least the base is assumed to be synchronous between cores, justifying this interpretation. Although fluctuations are apparent during the C27 series of events, these changes are not pronounced, and not especially different from background variability. Increased warmth in all records appears during the late last interglacial, after ~121 ka. This “Indian Summer” from ~119 ka – 116 ka, although locally punctuated by the 117 ka cold event, is similar to climate records from the Norwegian Sea, where peak warmth was also indicated late during the last interglacial (~118.5 – 116 ka) (Bauch and Erlenkeuser 2008). Cooling during the 117 ka event is apparent in all records, even U1302 MAT SSTs.

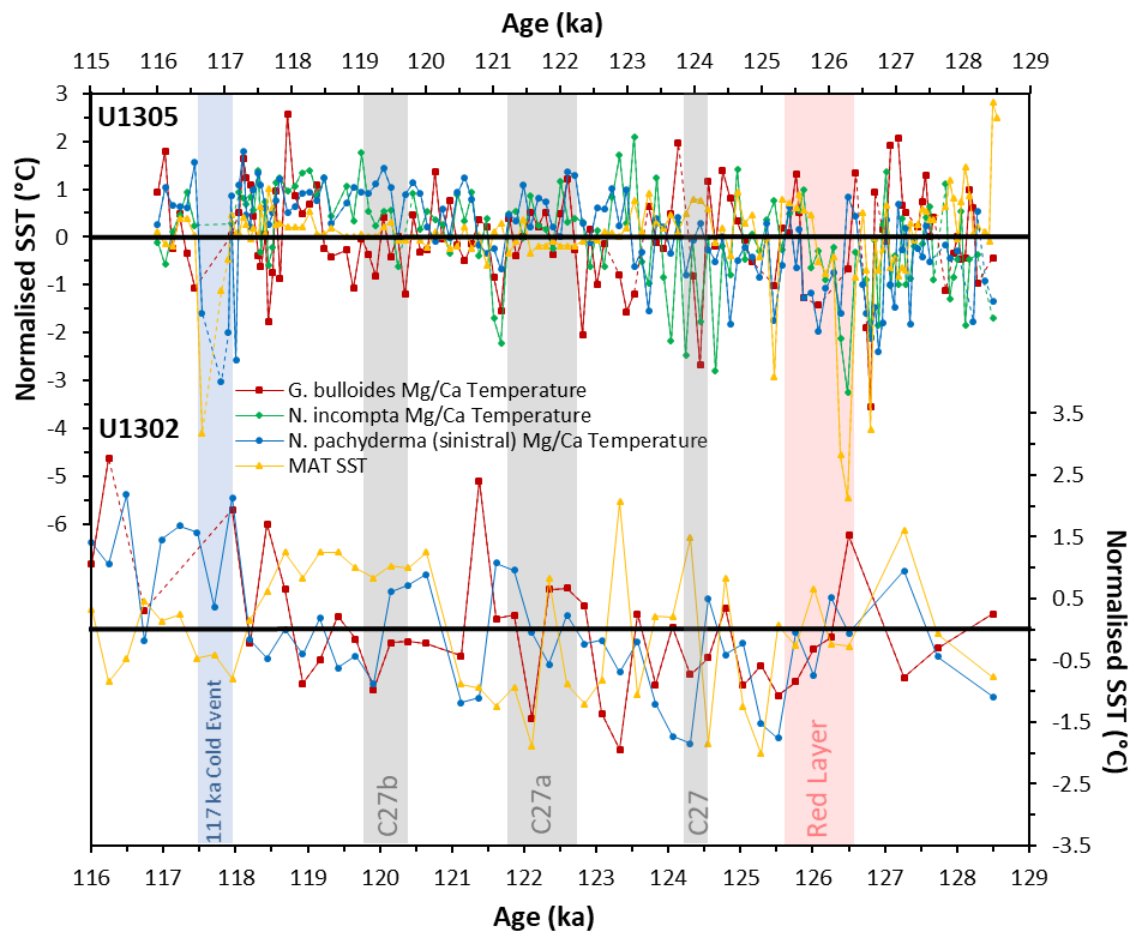


**Figure 8.18** | Normalised temperature reconstructions using MAT (orange), and Mg/Ca from *G. bulloides* (red), *N. incompta* (green) and *N. pachyderma* (*s*) (blue) for U1305 (top) and U1302 (bottom). Records have been normalised to the interglacial mean of each record (black horizontal lines). Pink shading indicates red layer of Nicholl et al. (2012), grey shading indicates last interglacial cold events (Oppo et al. 2006), blue shading indicates 117 ka cold event.

## 8.4 | THE LAST GLACIAL INCEPTION

The end of the last interglacial is synonymous with the end of the MIS 5e  $\delta^{18}\text{O}$  plateau in most records, the U1305 and U1302 *N. pachyderma (s)* records being no exception (Figure 8.15). However, during C26 which immediately followed (and perhaps defined) the end of the last interglacial, the similarities between U1302 and U1305 end there. There is no clear pattern in benthic isotopes, U1302 being marked by a large gap in the data and U1305 by large amplitude rapid  $\delta^{18}\text{O}$  fluctuations. There is a large difference between U1305 (0.4 ‰) and U1302 (-0.3 ‰) *N. pachyderma (s)*  $\delta^{13}\text{C}$  values during C26, but the lack of large-amplitude benthic  $\delta^{13}\text{C}$  fluctuations indicates that deep water formation was not impeded during C26 (Figure 8.16). U1302 IRD, which began increasing ~119 ka, reached >30% (~500 grains per g), and >50% after C26, whilst U1305 IRD remained <1% (~5 grains per g) until ~114 ka, suggesting negligible calving from the GIS until C24, well into MIS 5d (Figure 8.14). Unexpectedly, this is in contrast to the Ba/Ca values, which are much higher at U1305 than U1302. The picture in temperature estimates is even more confusing, with a rapid drop of ~3°C in U1305 MAT SSTs during C26, whilst U1305 *N. pachyderma (s)* Mg/Ca calcifications remain similar to interglacial values until ~113 ka, when they finally decrease during C25 (Figure 8.13). In contrast, U1302 MAT SSTs remain similar to interglacial values until ~115.3 ka, before rapidly shifting between ~9°C and ~4°C and back again within several centuries, whilst at the same time U1302 *N. pachyderma (s)* Mg/Ca calcification temperatures decrease more slowly across C26 (Figure 8.13). Therefore both U1305 and U1302 show evidence of drop in temperatures similar to the 2 – 3°C associated with C26 (Figure 8.19) initially described by Chapman and Shackleton (1999) using NEAP18K from the central North Atlantic, but both cores also contain evidence to suggest even more cooling occurred later. This supports the interpretation of C26 as being characterised by a cooling in surface temperatures which was unusual in not being associated with an increase in IRD to the wider North Atlantic region, or to Eirik Ridge. One interpretation is that the persistent warm surface temperatures at Orphan Knoll (U1302) during the first part of MIS 5d caused icebergs to melt at this location, before they could be released into the wider North Atlantic, and that the greater extent of MIS 5e GIS retreat hampered iceberg delivery to Eirik Ridge (U1305) until much later, during C25.

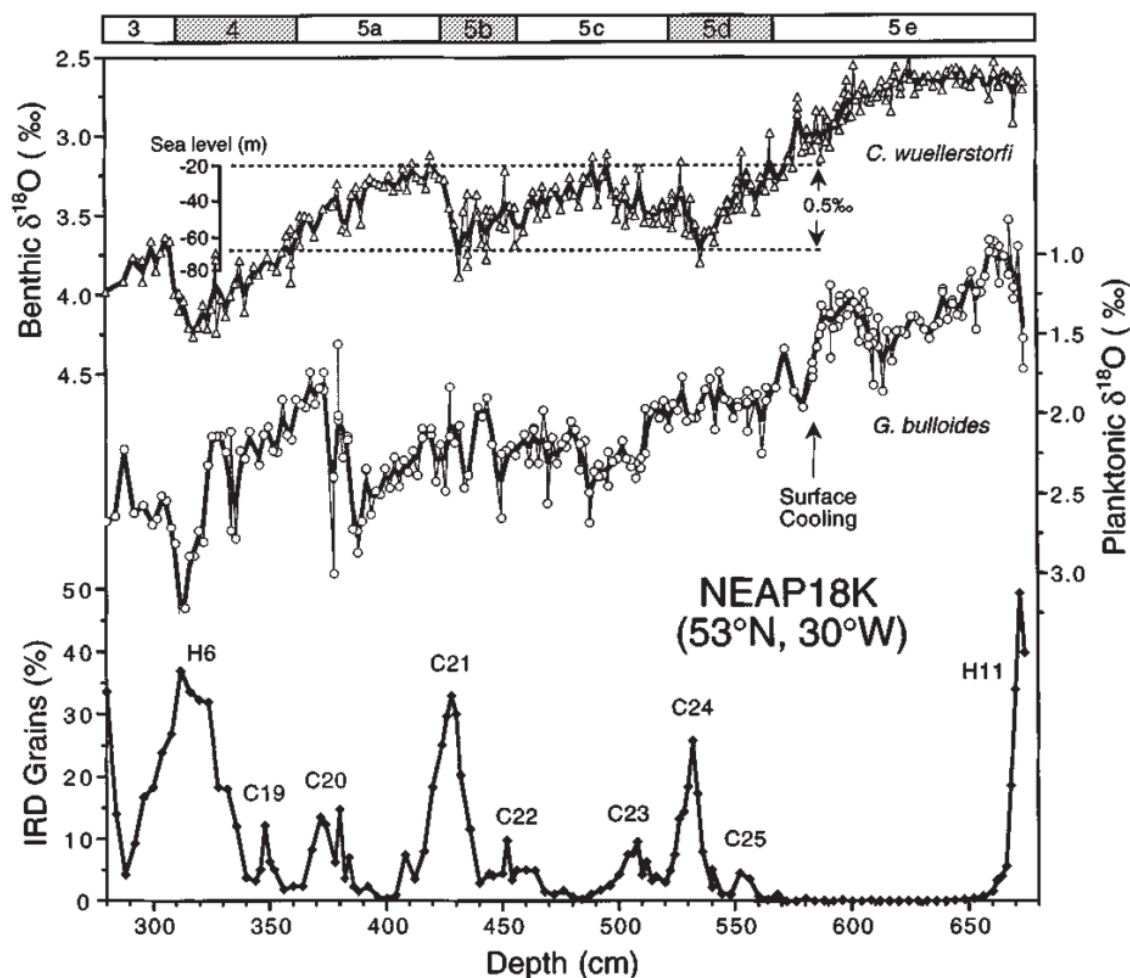


**Figure 8.19** | Proxy records from NEAP18K in the North Atlantic, showing benthic  $\delta^{18}\text{O}$ , planktonic  $\delta^{18}\text{O}$  and IRD counts. The surface cooling noted at the end of the MIS 5e plateau was identified as C26 by the authors, it was not associated with a peak in ice rafting, but rather  $\sim 2 - 3^\circ\text{C}$  surface cooling, suggesting climate and hydrographic reorganisation which was not associated with an increase in marine calving glaciers (Adapted from Chapman and Shackleton 1999).

In contrast, C25 was well represented in data produced for this study, with cold temperatures, increased IRD and Ba/Ca, and enriched benthic  $\delta^{18}\text{O}$  and negative  $\delta^{13}\text{C}$  values indicative of perturbations to the AMOC (Figures 8.13 – 8.16). This is consistent with C25 as the first regional-scale cooling event after MIS 5e, with the drop in MAT SSTs of  $\sim 7^\circ\text{C}$  compared to MIS 5e values remarkably similar to the estimate from NEAP 18K of  $\sim 6 - 7^\circ\text{C}$  cooling (Chapman and Shackleton 1999). The ensuing period ( $\sim 112 - 110$  ka) shows indications of warm U1305 and ODP-980 MAT SSTs, coincident with warm interstadial 25 in the NGRIP record (North Greenland Ice Core Project Members 2004) (Figure 8.13). Simultaneous cold subsurface *N. pachyderma* (*s*) Mg/Ca temperatures indicates strong surface stratification, which may have suppressed local overturning. This may be an explanation for the similarity between the pattern of

U1302 and U1305 planktonic and MD03-2664 benthic  $\delta^{13}\text{C}$  (Figure 8.16), which suggests simultaneous surface and deep water changes in ventilation rates.

During C24 large amounts of IRD are seen in both U1305 and ODP-980 (Figure 8.14) in concert with cold MAT surface temperatures (Figure 8.13), consistent with NGRIP stadial 25 (Figure 8.15). Strongly enriched planktonic and benthic  $\delta^{18}\text{O}$  values in all records through C24 likely reflect glacial build-up combined with low temperatures (Figure 8.15). A warmer subsurface in the Labrador Sea observed in U1305 *N. pachyderma* (*s*) Mg/Ca records (Figure 8.13) combined with negative  $\delta^{13}\text{C}$  values (Figure 8.16) suggests reduced AMOC strength, possibly related to a warm, poorly ventilated water mass originating in the Nordic Seas (Thornalley et al. 2015). The ensuing  $\sim 2^\circ\text{C}$  rise in MAT SSTs  $\sim 108$  ka, at the same time as cooling at the pycnocline, is similar to the situation  $\sim 113 - 110$  ka and suggests strong surface stratification during these warmer periods. C23 is also represented by cold temperatures, with abundant ice rafting reflected in high Ba/Ca values. At the end of C23, a clear amelioration of conditions occurred within MIS 5c, with MAT SSTs up to  $\sim 5^\circ\text{C}$ , and *G. bulloides* reappeared within the record (itself an indication of a warmer climate), which produced an early very high calcification temperature of  $\sim 12^\circ\text{C}$ , though this species has been observed in this study to fluctuate more widely than most proxies (Figure 8.13). A dramatic drop in U1305 and ODP-980 IRD % is observed, and a shift to more positive  $\delta^{13}\text{C}$  values suggests vigorous AMOC activity during MIS 5c. The relatively enriched U1305 planktonic and benthic  $\delta^{18}\text{O}$  suggests this warmth and vigorous overtuning occurred at a time when large ice sheets persisted on land.

Overall, it is interesting that U1302  $\delta^{18}\text{O}$  values become consistently more depleted than U1305 values after  $\sim 114$  ka (Figure 8.15). This cannot be attributed solely to increased sea ice production at this location, because this offset is not observed during the penultimate glacial period before  $\sim 135$  ka, when the two records were remarkably similar (Figure 8.3). Similarly, comparable  $\delta^{13}\text{C}$  values between the two cores prior to  $\sim 135$  ka and during MIS 5e begin to diverge after  $\sim 112$  ka. The associated gradient in  $\delta^{18}\text{O}$  and  $\delta^{13}\text{C}$  appears to have been stable over a long period of time during MIS 5d – c, perhaps indicating a different circulation regime, the influence of perennial ice cover, or a difference in peak seasonal *N. pachyderma* (*s*) bloom between the north and the south of the Labrador Sea during the early glacial inception.

## 8.5 | SUMMARY AND CONCLUSIONS

The multi-proxy approach adopted in this study has yielded many benefits. This study presents the first detailed centennially-resolved ice rafted debris (IRD), faunal assemblage modern analogue technique (MAT) and multi-species Mg/Ca palaeothermometry record for both U1305 and U1302. These results, combined with the first benthic stable isotope series from U1305 covering MIS 5e and supplementary planktonic isotope measurements that build upon previously published records (Hillaire-Marcel et al. 2011) constitute a major contribution to the literature. In addition, this study integrates these new records to derive an entirely new coherent and detailed chronology for the Labrador Sea based upon benthic isotope stack LS15 (Lisiecki and Stern 2016) which fits well with published data from the region.

Data presented in this study have been used to address and answer, at least in part, the inter-linked research questions posed in section 1.1. For example, a new protocol for dating marine sediment cores in the Labrador Sea based upon multiple lines of evidence is presented in this study (section 7.5). It is hoped that this approach will produce more cohesive age models that account for the regional peculiarities such as depleted  $\delta^{18}\text{O}$  excursions during Heinrich events in this notoriously awkward region.

Episodic increases in rates of marine calving glacier breakup were recorded in the IRD record through the entire interval. A proposed H13 event was identified using U1305 IRD data 150.4 – 147.5 ka. This assertion is supported by observation of mid-MIS 6 detrital layers across the Labrador Sea (Hillaire-Marcel et al. 1994; Stoner et al. 1995, 1996; Evans et al. 2007; Channel et al. 2012) and within the North Atlantic (Hodell et al. 2008, Hibbert et al. 2010) potentially associated with a collapse of European ice sheets (Mojtahid et al. 2005; Eynaud et al. 2007; Toucanne et al. 2009, Penaud et al. 2009), with ramifications for global mean sea level (Lea et al. 2002). However, this work is the first to categorise this as a Heinrich event. Strongly negative U1305 planktonic  $\delta^{13}\text{C}$  values (-0.42 ‰) just before H13 (~152.3 ka) (Figure 8.3) are similar to those observed before other Heinrich events, interpreted as the “breakdown of surface water stratification” (Spero and Lea 2002).

The interpretation of interstadial conditions ~146.5 – 144 ka within the Labrador Sea may be linked with the very early indications of deglaciation observed in speleothems from Devil’s Hole from ~147 ka (Winograd 1988, 1992), and possibly (given dating

errors) with the very early changes seen in speleothems from Corchia, Italy  $141 \pm 2.5$  ka (Drysdale et al. 2009). Heinrich event 12 was detected  $\sim 140$  ka, but appears different in nature to H13 or H11, being marked by only modest ice rafting and potentially including more fine fraction carbonate material from Hudson Strait (Hodell et al. 2008; Channell et al. 2012).

Cooling episodes in the Labrador Sea during periods of increased ice rafting identified in this study, including Heinrich events, the red layer, the 117 ka event, and the series of North Atlantic cold events (Chapman and Shackleton 1999), were typically clearly developed, though the relationship with foraminiferal  $\delta^{18}\text{O}$  is more complicated. These cold periods were associated with depleted  $\delta^{18}\text{O}$  values in U1302, particularly during Heinrich event 11 (Figure 8.3). This observation is considered most likely due to the production of isotopically depleted brines due to enhanced sea ice production near Orphan Knoll (Hillaire-Marcel and de Vernal 2008), rather than the impact of meltwater itself, since U1305 planktonic  $\delta^{18}\text{O}$  values were not affected. Variations in IRD,  $\delta^{18}\text{O}$  and Ba/Ca ratios presented in this study support the suggestion (e.g. Winsor et al. 2012, Govin et al. 2012) of continued Greenland ice sheet (GIS) melt through the first part of the last interglacial, in response to increased summer boreal insolation (Berger et al. 2007), supporting studies which suggest that during MIS5e the GIS was reduced in comparison with the Holocene (Hillaire-Marcel et al. 2001; Otto-Bliesner 2006; Stone et al. 2013).

Laurentide glacial build-up appears to have begun during the last interglacial period itself (after 119 ka), as shown by increased IRD input, and planktonic foraminiferal changes (increased *N. pachyderma* (*s*) abundance) in U1302. This is much earlier than evidence for GIS advance shown by IRD in U1305, which did not begin rising until after 114 ka. Perhaps the further retreat of the GIS during the last interglacial hampered the process of glacial build-up to the coastal margins of Greenland.

Penultimate deglacial ice sheet collapse recorded in the Labrador Sea does not appear to have been a single event restricted to Termination II (TII), in that episodes of minor ice sheet collapse had occurred  $\sim 140$  ka (H12) and  $\sim 150$  ka (H13), long before the major deglacial events during TII. However, the period of extreme cold and enriched benthic and planktonic  $\delta^{18}\text{O}$  centred  $\sim 135.5$  ka identified in this work does not support a very early TII (i.e. before  $\sim 135$  ka). In common with several other studies (e.g. Hibbert et al. 2010, Cheng et al. 2009), this investigation did not find evidence for a sustained

Younger Dryas-type climate reversal during TII. Instead, evidence from U1302 suggests H11 comprised a series of climate oscillations between warm surface temperatures followed by cold phases of massive ice rafting. These results therefore support the broad pattern recognised by Winsor et al. (2012) of three major pulses of ice sheet collapse in the Labrador Sea during the last interglacial, comparable in magnitude and timing to H2 and H1, and other IRD events during TI (Figure 3.11), and linked to changes in Atlantic meridional overturning circulation (AMOC) strength on the basis of coupled changes in benthic  $\delta^{18}\text{O}$  and  $\delta^{13}\text{C}$ . Rapid large-scale deglacial changes occurred within a few centuries (the resolution of the cores) or even faster, lending support to the suggestion that climate reorganisation can occur very rapidly where forcing is sufficiently strong, even in close proximity to the ice sheets.

In some records (such as U1305), the start of the last interglacial in the Labrador Sea can be recognised as immediately following a rapidly-deposited diatom mat, caused either by the migrating subarctic convergence (SAC) front (e.g. Boden and Backman 1996) or a thick layer of low-nutrient low-productivity surface meltwater (e.g. Kemp et al. 2006). The lack of a diatom mat in U1302 may be due to low resolution, but does suggest the diatom mat was instead due to the SAC front being positioned above Eirik Ridge. In locations where this diatom mat was not observed (such as U1302), the onset of the last interglacial in the Labrador Sea is most reliably defined by the combination of abrupt surface warming, cessation of IRD deposition, depleted benthic and planktonic  $\delta^{18}\text{O}$ , and the first appearance of diverse warmer-water planktonic foraminifera species. The new planktonic  $\delta^{18}\text{O}$  data produced for this study suggest that the MIS 5e  $\delta^{18}\text{O}$  plateau was reached very early, ~128.5 ka in U1305, an observation that was not previously clear.

The evidence for how warm the last interglacial was appears to be location dependent. In U1302, temperatures appear no warmer than the present (Figure 8.13), an observation which has been made elsewhere in the Labrador Sea (Winsor et al. 2012). However, in U1305 peak temperatures (~12.3°C) were reached very early (~128.4 ka), when MAT SSTs were ~3°C warmer than coretop estimates and ~5°C warmer than ocean atlas values above Eirik Ridge (World Ocean Atlas 1998). Subsequently, all U1305 proxies show that temperatures were ~1 – 2°C warmer than modern values throughout the last interglacial, aside from transient climate events (Figure 8.13). These warmer than present last interglacial temperatures in the northeast Labrador Sea may be related to the

reduced GIS extent discussed above. A progression towards the end of the last interglacial of warmer Mg/Ca calcification temperatures in all species with less variability (Figure 8.18), suggests that there may have been two periods of “optimum climate”. One very early shorter period (~128.5 – 126.5 ka) associated with the most diverse foraminiferal zone B (and Ca in U1305), and a later, longer (~123 – 117 ka) period of stable warm climate associated with foraminiferal zones D and E (and Fa in U1305) (Figure 5.14). The early climate optimum is likely due to stronger boreal insolation (e.g. Berger et al. 2007), but the later climate optimum occurred at a time when insolation was decreasing (Figure 3.2), and escalating IRD input in U1302 suggests the Laurentide ice sheet had already begun to build up (Figure 8.14). The Mg/Ca trends seem strikingly similar to benthic (and U1305 planktonic)  $\delta^{13}\text{C}$  records (Figure 8.16) suggesting a link with AMOC strength and a role for favourable nutrient cycling linked with the later climate optimum. This interpretation of two climate optima fits well with the probabilistic sea level curve of Kopp et al. (2013) who determined that most likely there were two GMSL highstands, 125 – 123 ka and 122 – 116 ka (Figure 3.13). The later dates of the sea level curve compared to the temperature estimates in this study may represent the lag between atmospheric climate forcing and the slower cumulative effect of subsequent ice sheet melting and surface ocean warming, together with dating and age model uncertainties.

There is clear evidence of a MIS 5e Laurentide glacial lake outburst flood event analogous to a similar event 8.4 ka during during the Holocene (Alley et al. 1997; Kleiven et al. 2008). The resulting red layer was clearly visible in shipboard core photographs (Figures 4.20 and 4.21), and was associated with a break between foraminiferal assemblage zones identified by cluster analysis (Figure 5.14). In the higher resolution core U1305, it is apparent that the red layer marks the culmination of a period of climate deterioration, which cluster analysis suggests began ~127.3 ka, and so appears to be a consequence of wider changes in climate, rather than a cause. That said, some rapid shifts were associated with the red layer in both planktonic and benthic  $\delta^{18}\text{O}$  and  $\delta^{13}\text{C}$  (Figures 8.15 and 8.16). These, coupled with the series of strongly negative subsequent benthic  $\delta^{13}\text{C}$  episodes in U1305 suggest that the influx of meltwater may have caused instability in AMOC strength, leading to periodic slackening in deep northern overturning rates which allowed high-nutrient AABW to flow into the deep North Atlantic, perhaps four times between 126 – 123.4 ka (Figure 8.16). It is likely this

outburst flood may have been responsible for the observation of a “major freshwater event” ~126.5 ka off the East Greenland margin (Zhuravleva et al. 2017).

Evidence for the C27 series of intra-interglacial climate events (Oppo et al. 2006) is limited, with no clear deepwater impacts, and no surface water evidence in U1305. There is some suggestion of depleted U1302  $\delta^{18}\text{O}$  (Figure 8.15) and U1302 IRD increases during C27 and C27a (Figure 8.14), but these are not as pronounced as the red layer or the 117 ka event, so it appears that these events were not strongly represented in the Labrador Sea. In contrast, strong evidence is presented in this work for a 117 ka event, observed as an abrupt shift to a colder climate, which the MD03-2664 negative  $\delta^{13}\text{C}$  excursions suggest was linked to a perturbation of AMOC (Irvalı et al. 2016) perhaps related to a late MIS 5e meltwater event from the east Greenland margin (Zhuravleva et al. 2017), although reduced U1305 Ba/Ca values argue against a Greenland source (Figure 8.14). The North Atlantic series of cold events (e.g. Chapman and Shackleton 1999, Bond et al. 1999, McManus et al. 1994) appear well represented in temperature, IRD and isotope records, and link with changes in Greenland ice core records (North Greenland Ice Core Project Members 2004). At least in U1305, C26 is not associated with an increase in IRD or changes in benthic  $\delta^{13}\text{C}$ , but instead with rapid surface cooling, suggesting a change in surface circulation followed the end of the last interglacial. A change in the extent of the SPG or a weaker Irminger current could account for these observations. C25 – C23 were well developed cold periods of heavy ice rafting which negative MD95-2042 benthic  $\delta^{13}\text{C}$  values indicate involved wide-scale suppression of AMOC strength. These periodic climate oscillations were therefore regional events which involved greater or lesser amounts of ice rafting, interspersed with warmer periods. Divergence between U1302 and U1305 planktonic  $\delta^{18}\text{O}$  after ~114 ka is interesting (Figure 8.15), and was not observed during the penultimate glacial (Figure 8.3). This gradient of ~0.6 ‰ across the Labrador Sea may represent different surface circulation patterns during the last glacial inception.

## 8.6 | SUGGESTIONS FOR FUTURE IMPROVEMENTS

- The use of surface water proxies presented in this study (Mg/Ca and/or MAT) to isolate the temperature effect using the palaeotemperature equation to determine seawater  $\delta^{18}\text{O}$  may help clarify issues concerning surface salinity, the depleted

$\delta^{18}\text{O}$  excursion, and may help to resolve the nature of some of the unusual patterns of  $\delta^{13}\text{C}$  gradients across the Labrador Sea.

- Calculation of IRD flux rather than concentration (using bulk mass accumulation rate) (Hibbert et al. 2010) to account for sedimentation rate changes associated with influxes of fine material due to turbidity current activity along the NAMOC could be helpful in constraining the duration of H11 and H12, and particularly of the red layer, within which fine sediment is likely to be high.
- Extended U1302 Mg/Ca and Ba/Ca data through the entirety of H11 may help to clarify the nature of TII.
- To help address the noted lack of intra-MIS 5e age control points (Govin et al. 2015), correlation of the red layer (Nicholl et al. 2012), dated in this study to ~126.5 ka, within affected proximal records may prove useful.
- Future recounts of IRD, in addition to including bulk carbonate analysis of the fine fraction, may help clarify the case of the “missing” carbonate.
- To address the confusion in naming systems, more detailed and widespread investigations into the timing and duration of possible Heinrich events during earlier glacial cycles may lead to a standardised system.
- Clarification of the relationship between the different holes used to produce the common mcd scale in U1305 and U1302 could enable more precise correlation between records. Shipboard results often can be fine-tuned following the acquisition of high resolution multi-proxy records.

*“O’Time, what a master art thou,  
what slaves to thee, are we, O’Time.  
With grappling hand you grasp a life and crush  
Whilst with other hand in fairy godmother-like touch  
Bestow such charms and happiness that fill with love  
As false security dotes upon us defying stars above  
And whilst we may win temporary respite,  
Beating you; O’Time, ‘tis only for a night,  
Or little more indeed, as you in laughter and in greed  
Take all in no uncertain speed, O’Time.  
One hundred years is not indeed so long  
Yet those who lived here, in that time ago are gone.  
Great men and small, no matter what performance played,  
Unequaled again perhaps, but not able to be stayed.  
Your gifts you give to us, O’Time, are great,  
but stay that other hand  
For, few more years, and we will be but bones, o’er fresh,  
inhabited land.*

*But enduring human pain as we may bear,  
Sometimes we shout and cry for time to tear  
But tick by tick, in steady, even tread  
No speeding up, no halts, no turn of heads  
No heart to rule, no conscience pricked  
No loves, no cares, no trust is tricked.  
Mysteriously, O’Time, you slip away  
Gone tomorrow, what we live today.  
And how long will memories alone remain?  
It rests with you, O’Time. We humans cannot claim.”*

W. R. Batchelor, *Time* (Ramm, 1994)

# REFERENCES

- Allen JRM, Huntley B (2009) Last Interglacial palaeovegetation, palaeoenvironments and chronology: a new record from Lago Grande di Monticchio, southern Italy. *Quat Sci Rev* 28:1521–1538. doi: 10.1016/j.quascirev.2009.02.013
- Allen JT, Brown L, Sanders R, et al (2005) Diatom carbon export enhanced by silicate upwelling in the northeast Atlantic. *Nature* 437:728–732. doi: 10.1038/nature03948
- Allen KA, Hönisch B, Eggins SM, et al (2016) Trace element proxies for surface ocean conditions: A synthesis of culture calibrations with planktic foraminifera. *Geochim Cosmochim Acta* 193:197–221. doi: 10.1016/j.gca.2016.08.015
- Alley RB (2007) Wally Was Right: Predictive Ability of the North Atlantic “Conveyor Belt” Hypothesis for Abrupt Climate Change. *Annu Rev Earth Planet Sci* 35:241–272. doi: 10.1146/annurev.earth.35.081006.131524
- Anand P, Elderfield H (2005) Variability of Mg/Ca and Sr/Ca between and within the planktonic foraminifers *Globigerina bulloides* and *Globorotalia truncatulinoides*. *Geochemistry, Geophys Geosystems* 6:1–15. doi: 10.1029/2004GC000811
- Anand P, Elderfield H, Conte MH (2003) Calibration of Mg/Ca thermometry in planktonic foraminifera from a sediment trap time series. *Paleoceanography* 18:n/a-n/a. doi: 10.1029/2002PA000846
- Andrews JE, Portman C, Rowe PJ, et al (2007) Sub-orbital sea-level change in early MIS 5e: New evidence from the Gulf of Corinth, Greece. *Earth Planet Sci Lett* 259:457–468. doi: 10.1016/j.epsl.2007.05.005
- Andrews JT, Keigwin L, Hall F, Jennings AE (1999) Abrupt deglaciation events and Holocene palaeoceanography from high-resolution cores, Cartwright Saddle, Labrador Shelf, Canada. *J Quat Sci* 14:383–397. doi: 10.1002/(SICI)1099-1417(199908)14:5<383::AID-JQS464>3.0.CO;2-J
- Andrews JT, Maclean B, Kerwin M, et al (1995) Final stages in the collapse of the Laurentide ice sheet, Hudson Strait, Canada, NWT:14C AMS dates, seismic stratigraphy, and magnetic susceptibility logs. *Quat Sci Rev* 14:983–1004. doi: 10.1016/0277-3791(95)00059-3
- Andrews JT, Tedesco K (1992) Detrital carbonate rich sediments, northwest Labrador Sea: Implications for ice-sheet dynamics and iceberg rafting Heinrich events in the North Atlantic. *Geology* 20:1087–1090. doi: 10.1130/0091-7613(1992)020<1087:DCRSNL>2.3.CO;2
- Archer D, Aiken J, Balch W, et al (1997) A meeting place of great ocean currents: Shipboard observations of a convergent front at 2°N in the Pacific. *Deep Res Part II Top Stud Oceanogr* 44:1827–1849. doi: 10.1016/S0967-0645(97)00031-3
- Arthur MA, Srivastava SP, Kaminski M, et al (1989) Seismic Stratigraphy and History of Deep Circulation and Sediment Drift Development in Baffin Bay and the Labrador Sea. *Proc Ocean Drill Program, 105 Sci Results*. doi: 10.2973/odp.proc.sr.105.118.1989
- Avsic T, Karstensen J, Send U, Fischer J (2006) Interannual variability of newly formed Labrador Sea water from 1994 to 2005. *Geophys Res Lett* 33:1–6. doi: 10.1029/2006GL026913
- Bagniewski W, Meissner KJ, Menviel L (2017) Exploring the oxygen isotope fingerprint of Dansgaard-Oeschger variability and Heinrich events. *Quat Sci Rev* 159:1–14. doi: 10.1016/j.quascirev.2017.01.007
- Barber DC, Dyke A, Hillaire-Marcel C, et al (1999) Forcing of the cold event of 8,200 years ago by catastrophic drainage of Laurentide lakes. *Nature* 400:344–348. doi: 10.1038/22504
- Bard E, Hamelin B, Fairbanks RG (1990) U-Th ages obtained by mass spectrometry in corals from Barbados: sea level during the past 130,000 years. *Nature* 346:456–458.
- Barker S, Elderfield H (2002a) Foraminiferal Calcification Response to Glacial-Interglacial Changes in Atmospheric CO<sub>2</sub>. *Science* (80- ) 297:833–836. doi: 10.1126/science.1072815
- Barker S, Elderfield H (2002b) Foraminiferal calcification response to glacial-interglacial changes in atmospheric CO<sub>2</sub>. *Science* (80- ) 297:833–836. doi: 10.1126/science.1072815
- Barker S, Greaves M, Elderfield H (2003) A study of cleaning procedures used for foraminiferal Mg/Ca paleothermometry. *Geochemistry Geophys Geosystems* 4:1–20. doi: 10.1029/2003GC000559
- Barrows TT, Juggins S (2005) Sea-surface temperatures around the Australian margin and Indian Ocean during the Last Glacial Maximum.
- Bauch D, Carstens J, Wefer G (1997) Oxygen isotope composition of living *Neogloboquadrina pachyderma* (sin.) in the Arctic Ocean. *Earth Planet Sci Lett* 146:47–58. doi: 10.1016/S0012-821X(96)00211-7

- Bauch HA (2013) Interglacial climates and the Atlantic meridional overturning circulation: Is there an Arctic controversy? *Quat Sci Rev* 63:1–22. doi: 10.1016/j.quascirev.2012.11.023
- Bauch HA, Erlenkeuser H (2008) A “critical” climatic evaluation of last interglacial (MIS 5e) records from the Norwegian Sea. *Polar Res* 27:135–151. doi: 10.1111/j.1751-8369.2008.00059.x
- Bauch HA, Kandiano ES (2007) Evidence for early warming and cooling in North Atlantic surface waters during the last interglacial. *Paleoceanography* 22:1–11. doi: 10.1029/2005PA001252
- Bazin L, Landais A, Lemieux-Dudon B, et al (2013) An optimized multi-proxy, multi-site Antarctic ice and gas orbital chronology (AICC2012): 120–800 ka. *Clim Past* 9:1715–1731. doi: 10.5194/cp-9-1715-2013
- Bemis BE, Spero HJ, Lea DW, Bijma J (2000) Temperature influence on the carbon isotopic composition of *Globigerina bulloides* and *Orbulina universa* (planktonic foraminifera). *Mar Micropaleontol* 38:213–228.
- Berger A, Loutre MF, Kaspar F, Lorenz SJ (2007) 2. Insolation during interglacial. *Dev Quat Sci* 7:13–27. doi: 10.1016/S1571-0866(07)80027-3
- Bersch M (2002) North Atlantic Oscillation–induced changes of the upper layer circulation in the northern North Atlantic Ocean. *J Geophys Res* 107:3156. doi: 10.1029/2001JC000901
- Bigg GR, Rohling EJ (2000) An oxygen isotope data set for marine waters. *J Geophys Res* 105:8527–8535.
- Birks HJB (1995) Quantitative palaeoenvironmental reconstructions. In: Maddy D, Brew JS (eds) *Statistical Modelling of Quaternary Science Data. Technical Guide 5*, Quaternary Research Association, Cambridge. 271 pp., pp 161–254
- Birks HJB, Heiri O, Seppa H, Bjune AE (2010) Strengths and Weaknesses of Quantitative Climate Reconstructions Based on Late-Quaternary Biological Proxies. *Open Ecol J* 3:68–110. doi: 10.2174/1874213001003020068
- Blanchon P, Eisenhauer A, Fietzke J, Liebetrau V (2009) Rapid sea-level rise and reef back-stepping at the close of the last interglacial highstand. *Nature* 458:881–4. doi: 10.1038/nature07933
- Boch R, Cheng H, Spötl C, et al (2011) NALPS: A precisely dated European climate record 120–60 ka. *Clim Past* 7:1247–1259. doi: 10.5194/cp-7-1247-2011
- Boden P, Backman J (1996) A laminated sediment sequence from the northern North Atlantic Ocean and its climatic record. *Geology* 24:507–510.
- Bond G, Broecker W, Johnsen S, et al (1993) Correlations between climate records from North Atlantic sediments and Greenland Ice. *Nature* 365:143–147.
- Bond G, Heinrich H, Broecker W, et al (1992) Evidence for massive discharges of iceberg into the North Atlantic ocean during the last glacial period. *Nature* 360:245–249. doi: 10.1038/355242a0
- Bond G, Showers W, Cheseby M, et al (1997) A Pervasive Millennial-Scale Cycle in North Atlantic Holocene and Glacial Climates. *Science* (80- ) 278:1257–1266. doi: 10.1126/science.278.5341.1257
- Bond GC, Lotti R (1995) Iceberg Discharges into the North Atlantic on Millennial Time Scales During the Last Glaciation. *Science* (80- ) 267:1005–1010. doi: 10.1126/science.267.5200.1005
- Bond GC, Showers W, Elliot M, et al (1999) The North Atlantic’s 1–2 kyr climate rhythm: Relation to Heinrich events, Dansgaard/Oeschger cycles and the Little Ice Age. In: Clark PU, Webb RS, Keigwin LD (eds) *Mechanisms of Global Climate Change at Millennial Time Scales. Geophysical Monograph, AGU.*, pp 35–58
- Born A, Nisancioglu KH (2012) Melting of Northern Greenland during the last interglaciation. *Cryosphere* 6:1239–1250. doi: 10.5194/tc-6-1239-2012
- Born A, Nisancioglu KH, Braconnot P (2010) Sea ice induced changes in ocean circulation during the Eemian. *Clim Dyn* 35:1361–1371.
- Born A, Nisancioglu KH, Risebrobakken B (2011) Late Eemian warming in the Nordic Seas as seen in proxy data and climate models. *Paleoceanography* 26:1–10. doi: 10.1029/2010PA002027
- Bower AS, Hendry RM, Amrhein DE, Lilly JM (2013) Direct observations of formation and propagation of subpolar eddies into the Subtropical North Atlantic. *Deep Res Part II Top Stud Oceanogr* 85:15–41. doi: 10.1016/j.dsr2.2012.07.029
- Bower AS, Le Cann B, Rossby T, et al (2002) Directly measured mid-depth circulation in the northeastern North Atlantic Ocean. *Nature* 419:603–607. doi: 10.1038/nature01078
- Bower AS, Lozier MS, Gary SF, Böning CW (2009) Interior pathways of the North Atlantic meridional overturning circulation. *Nature* 459:243–247. doi: 10.1038/nature07979
- Boyle EA (1981) Cadmium, zinc, copper, and barium in foraminifera tests. *Earth Planet Sci Lett* 53:11–35. doi: 10.1016/0012-821X(81)90022-4

- Boyle EA, Keigwin LD (1985) Comparison of Atlantic and Pacific paleochemical records for the last 215,000 years: changes in deep ocean circulation and chemical inventories. *Earth Planet Sci Lett* 76:135–150. doi: 10.1016/0012-821X(85)90154-2
- Broecker W, Bond G, Klas M, et al (1992) Origin of the northern Atlantic's Heinrich events. *Clim Dyn* 6:265–273. doi: 10.1007/BF00193540
- Broecker WS (1998) Paleocean circulation during the 1st deglaciation: A bipolar seasaw? *Paleoceanography* 13:119–121.
- Broecker WS (1991) The Great Ocean Conveyor. *Oceanography* 4:79–89. doi: 10.5670/oceanog.1991.07
- Broecker WS (1994) Massive iceberg discharges as triggers for global climate change. *Nature* 372:421–424.
- Broecker WS, Kennett JP, Flower BP, et al (1989) Routing of meltwater from the Laurentide Ice Sheet during the Younger Dryas cold episode. *Nature* 341:318–321. doi: 10.1038/341318a0
- Brown SJ, Elderfield H (1996) Variations in Mg/Ca and Sr/Ca ratios of planktonic foraminifera caused by postdepositional dissolution: Evidence of shallow Mg-dependent dissolution. *Paleoceanography* 11:543–551. doi: 10.1029/96PA01491
- Capron E, Govin A, Stone EJ, et al (2014) Temporal and spatial structure of multi-millennial temperature changes at high latitudes during the Last interglacial. *Quat Sci Rev* 103:116–133. doi: 10.1016/j.quascirev.2014.08.018
- Carlson AE (2008) Why there was not a Younger Dryas-like event during the Penultimate Deglaciation. *Quat Sci Rev* 27:882–887. doi: 10.1016/j.quascirev.2008.02.004
- Carlson AE, Clark PU (2012) Ice sheet sources of sea level rise and freshwater discharge during the last deglaciation. *Rev Geophys* RG4007. doi: 10.1029/2011RG000371.1.INTRODUCTION
- Carstens J, Hebbeln D, Wefer G (1997) Distribution of planktic foraminifera at the ice margin in the Arctic (Fram Strait). *Mar Micropaleontol* 29:257–269. doi: 10.1016/S0377-8398(96)00014-X
- Channell JET (2017a) Magnetic excursions in the late Matuyama Chron (Olduvai to Matuyama-Brunhes boundary) from North Atlantic IODP sites. *J Geophys Res Solid Earth* 122:773–789. doi: 10.1002/2016JB013616
- Channell JET (2017b) Complexity in Matuyama–Brunhes polarity transitions from North Atlantic IODP/ODP deep-sea sites. *Earth Planet Sci Lett* 467:43–56. doi: 10.1016/j.epsl.2017.03.019
- Channell JET (2017c) Mid-Brunhes magnetic excursions in marine isotope stages 9, 13, 14, and 15 (286, 495, 540, and 590 ka) at North Atlantic IODP Sites U1302/3, U1305, and U1306. *Geochemistry, Geophys Geosystems* 18:473–487. doi: 10.1002/2016GC006626
- Channell JET, Hodell D a., Romero O, et al (2012) A 750-kyr detrital-layer stratigraphy for the North Atlantic (IODP Sites U1302–U1303, Orphan Knoll, Labrador Sea). *Earth Planet Sci Lett* 317–318:218–230. doi: 10.1016/j.epsl.2011.11.029
- Channell JET, Hodell DA (2013) Magnetic signatures of Heinrich-like detrital layers in the Quaternary of the North Atlantic. *Earth Planet Sci Lett* 369–370:260–270. doi: 10.1016/j.epsl.2013.03.034
- Channell JET, Kanamatsu T, Sato T, et al (2006) Expedition 303 summary. *Proc IODP*. doi: 10.2204/iodp.proc.303306.101.2006
- Channell JET, Xuan C, Hodell DA (2009) Stacking paleointensity and oxygen isotope data for the last 1.5 Myr (PISO-1500). *Earth Planet Sci Lett* 283:14–23.
- Chapman MR, Shackleton NJ (1999) Global ice-volume fluctuations, North Atlantic ice-rafting events, and deep-ocean circulation changes between 130 and 70 ka. *Geology* 27:795–798.
- Chapman MR, Shackleton NJ (1998) Millennial-scale fluctuations in North Atlantic heat flux during the last 150 000 years. *Earth Planet Sci Lett* 159:57–70. doi: 10.1016/S0012-821X(98)00068-5
- Cheng H, Edwards RL, Broecker WS, et al (2009) Ice Age Terminations. *Science* (80- ) 326:248–252. doi: 10.1126/science.1177840
- Chough SK, Hesse R (1985) Contourites from Eirik Ridge, south of Greenland. *Sediment Geol* 41:185–199. doi: 10.1016/0037-0738(84)90061-7
- Clark PU, Pisias NG, Stocker TF, Weaver AJ (2002a) The role of the thermohaline circulation in abrupt climate change. *Nature* 415:863–869.
- Clark PU, Pisias NG, Stocker TF, Weaver AJ (2002b) The role of the thermohaline circulation in abrupt climate change. *Nature* 415:863–869.
- Clarke GKC, Leverington DW, Teller JT, Dyke AS (2004) Paleohydraulics of the last outburst flood from glacial Lake Agassiz and the 8200 BP cold event. *Quat Sci Rev* 23:389–407. doi: 10.1016/j.quascirev.2003.06.004

- Clarke GKC, Marshall SJ, Hillfire-marcel C, et al (1999) A Glaciological Perspective on Heinrich Events from the Laurentide Ice Sheet to the North Atlantic Ocean, are a puzzling instability of the Ice-Age climate system. Although there is broad agreement on the defining characteristics of the Laurentide issue f.
- Cléroux C, Cortijo E, Anand P, et al (2008) Mg/Ca and Sr/Ca ratios in planktonic foraminifera: Proxies for upper water column temperature reconstruction. *Paleoceanography* 23:1–16. doi: 10.1029/2007PA001505
- Colville EJ, Carlson AE, Beard BL, et al (2011) Sr-Nd-Pb Isotope Evidence for Ice-Sheet Presence on Southern Greenland During the Last Interglacial. *Science* (80- ) 333:620–623. doi: 10.1126/science.1204673
- Cortijo E, Lehman S, Keigwin L, et al (1999) Changes in meridional temperature and salinity gradients in the North Atlantic Ocean ( 30°-72°N ) during the last interglacial period. *Paleoceanography* 14:23–33.
- Cottet-Puinel M, Weaver AJ, Hillaire-Marcel C, et al (2004) Variation of Labrador Sea Water formation over the Last Glacial cycle in a climate model of intermediate complexity. *Quat Sci Rev* 23:449–465. doi: 10.1016/S0277-3791(03)00123-9
- Crockett KC, Vance D, Foster GL, et al (2012) Continental weathering fluxes during the last glacial/interglacial cycle: Insights from the marine sedimentary Pb isotope record at Orphan Knoll, NW Atlantic. *Quat Sci Rev* 38:89–99. doi: 10.1016/j.quascirev.2012.02.004
- Crowley TJ (1999) Correlating high-frequency climate variations. *Paleoceanography* 14:271–272. doi: 10.1029/1999PA900003
- Cuny J, Rhines PB, Niiler PP, Bacon S (2002) Labrador Sea Boundary Currents and the Fate of the Irminger Sea Water. *J Phys Oceanogr* 32:627–647. doi: 10.1175/1520-0485(2002)032%3C0627:lsbc%3E2.0.co;2
- Curry WB, Oppo DW (2005) Glacial water mass geometry and the distribution of  $\delta^{13}\text{C}$  of  $\Sigma\text{CO}_2$  in the western Atlantic Ocean. *Paleoceanography* 20:1–12. doi: 10.1029/2004PA001021
- Dansgaard W, Johnsen SJ, Clausen HB, et al (1993) Evidence for general instability of past climate from a 250-kyr ice-core record. *Nature* 364:218–220. doi: 10.1038/364218a0
- Darling KF, Kucera M, Kroon D, Wade CM (2006) A resolution for the coiling direction paradox in *Neoglobobulimina papyroderma*. *Paleoceanography* 21:1–14. doi: 10.1029/2005PA001189
- Darling KF, Wade CM (2008) The genetic diversity of planktic foraminifera and the global distribution of ribosomal RNA genotypes. *Mar Micropaleontol* 67:216–238. doi: 10.1016/j.marmicro.2008.01.009
- de Beaulieu JL, Reille M (1992) The last climatic cycle at La Grande Pile (Vosges, France) a new pollen profile. *Quat Sci Rev* 11:431–438. doi: 10.1016/0277-3791(92)90025-4
- de Boissésou E, Thierry V, Mercier H, et al (2012) Origin, formation and variability of the Subpolar Mode Water located over the Reykjanes Ridge. *J Geophys Res Ocean* 117:n/a-n/a. doi: 10.1029/2011JC007519
- De Jong MF, Van Aken HM, Våge K, Pickart RS (2012) Convective mixing in the central Irminger Sea: 2002–2010. *Deep Res Part I Oceanogr Res Pap* 63:36–51. doi: 10.1016/j.dsr.2012.01.003
- de Vernal A, Hillaire-Marcel C (2008) Natural variability of Greenland climate, vegetation and ice volume during the past million years. *Science* (80- ) 320:1622–1625.
- de Vernal A, Hillaire-Marcel C (2006) Provincialism in trends and high frequency changes in the northwest North Atlantic during the Holocene. *Glob Planet Change* 54:263–290. doi: 10.1016/j.gloplacha.2006.06.023
- de Villiers S, Greaves M, Elderfield H (2002) An intensity ratio calibration method for the accurate determination of Mg/Ca and Sr/Ca of marine carbonates by ICP-AES. *Geochemistry, Geophys Geosystems* 3:n/a-n/a. doi: 10.1029/2001GC000169
- Delaney ML, W.H.Bé A, Boyle EA (1985) Li, Sr, Mg, and Na in foraminiferal calcite shells from laboratory culture, sediment traps, and sediment cores. *Geochim Cosmochim Acta* 49:1327–1341. doi: 10.1016/0016-7037(85)90284-4
- Demény A, Kern Z, Czuppon G, et al (2017) Stable isotope compositions of speleothems from the last interglacial – Spatial patterns of climate fluctuations in Europe. *Quat Sci Rev* 161:68–80. doi: 10.1016/j.quascirev.2017.02.012
- Dengler M, Schott FA, Eden C, et al (2004) Break-up of the Atlantic deep western boundary current into eddies at 8°S. *Nature* 432:1018–1020. doi: 10.1038/nature03134
- Dickson R, Lazier J, Meincke J, et al (1996) Long-term coordinated changes in the convective activity of the North Atlantic. *Prog Oceanogr* 38:241–295. doi: 10.1016/S0079-6611(97)00002-5
- Dickson RR, Brown J (1994) The production of North Atlantic Deep Water: Sources, rates, and pathways. *J Geophys Res Ocean* 99:12319–12341. doi: 10.1029/94JC00530
- Dokken TM, Jansen E (1999) Rapid changes in the mechanism of ocean convection during the last glacial period.

Nature 401:458–461. doi: 10.1038/46753

- Drysdale RN, Hellstrom JC, Zanchetta G, et al (2009) Evidence for obliquity forcing of glacial Termination II. *Science* (80- ) 325:1527–1531. doi: 10.1126/science.1170371
- Drysdale RN, Zanchetta G, Hellstrom JC, et al (2007) Stalagmite evidence for the precise timing of North Atlantic cold events during the early last glacial. *Geology* 35:77–80. doi: 10.1130/G23161A.1
- Duplessy JC, Labeyrie L, Arnold M, et al (1992) Changes in surface salinity of the North Atlantic Ocean during the last deglaciation. *Nature* 358:485–488.
- Duplessy JC, Shackleton NJ, Fairbanks RG, et al (1988) Deepwater source variations during the last climatic cycle and their impact on the global deepwater circulation. *Paleoceanography* 3:343–360. doi: 10.1029/PA003i003p00343
- Duplessy JC, Shackleton NJ, Matthews RK, et al (1984) 13C Record of benthic foraminifera in the last interglacial ocean: Implications for the carbon cycle and the global deep water circulation. *Quat Res* 21:225–243. doi: 10.1016/0033-5894(84)90099-1
- Dutton A, Lambeck K (2012) Ice volume and sea level during the last interglacial. *Science* (80- ) 337:216–219. doi: 10.1126/science.1205749
- Edmond JM, Measures C, McDuff RE, et al (1979) Ridge crest hydrothermal activity and the balances of the major and minor elements in the ocean: The Galapagos data. *Earth Planet Sci Lett* 46:1–18. doi: 10.1016/0012-821X(79)90061-X
- Egge JK, Aksnes DL (1992) Silicate as regulating nutrient in phytoplankton competition. *Mar Ecol Prog Ser* 83:281–289. doi: 10.3354/meps083281
- Elderfield H, Ferretti P, Greaves M, et al (2012) Evolution of ocean temperature and ice volume through the mid-Pleistocene climate transition. *Science* (80- ) 337:704–709. doi: 10.1594/PANGAEA.786205
- Elderfield H, Ganssen G (2000) Past temperatures and  $\delta^{18}\text{O}$  of surface ocean waters inferred from foraminiferal Mg/Ca ratios. *Nature* 405:442–445.
- Elderfield H, Vautravers M, Cooper M (2002) The relationship between shell size and Mg/Ca, Sr/Ca,  $\delta^{18}\text{O}$ , and  $\delta^{13}\text{C}$  of species of planktonic foraminifera. *Geochemistry, Geophys Geosystems* 3:1–13. doi: 10.1029/2001GC000194
- Elliot M, Labeyrie L, Duplessy JC (2002) Changes in North Atlantic deep-water formation associated with the Dansgaard - Oeschger temperature oscillations (60-10 ka). *Quat Sci Rev* 21:1153–1165. doi: 10.1016/S0277-3791(01)00137-8
- Ellison CRW, Chapman MR, Hall IR (2006) Surface and Deep Ocean Interactions During the Cold Climate Event 8200 Years Ago. *Science* (80- ) 312:1929–1932. doi: 10.1126/science.1127213
- EPICA Community Members (2006) One-to-one coupling of glacial climate variability in Greenland and Antarctica. *Nature* 444:195–198. doi: 10.1038/nature05301
- EPICA Community Members (2004) Eight glacial cycles from an Antarctic ice core. *Nature* 429:623–628. doi: [http://www.nature.com/nature/journal/v429/n6992/supinfo/nature02599\\_S1.html](http://www.nature.com/nature/journal/v429/n6992/supinfo/nature02599_S1.html)
- Erez J, Luz B (1982) Temperature control of oxygen-isotope fractionation of cultured planktonic foraminifera. *Nature* 297:220–222.
- Evans HF, Channell JET, Stoner JS, et al (2007) Paleointensity-assisted chronostratigraphy of detrital layers on the Eirik Drift (North Atlantic) since marine isotope stage 11. *Geochemistry, Geophys Geosystems*. doi: 10.1029/2007GC001720
- Eynaud F, Zaragosi S, Scourse JD, et al (2007) Deglacial laminated facies on the NW European continental margin: The hydrographic significance of British-Irish Ice Sheet deglaciation and Fleuve Manche paleoriver discharges. *Geochemistry, Geophys Geosystems*. doi: 10.1029/2006GC001496
- Fagel N, Hillaire-Marcel C (2006) Glacial/interglacial instabilities of the Western Boundary Under Current during the last 365 kyr from Sm/Nd ratios of the sedimentary clay-size fractions at ODP site 646 (Labrador Sea). *Mar Geol* 232:87–99. doi: 10.1016/j.margeo.2006.08.006
- Fairbanks RG (1989) A 17,000-year glacio-eustatic sea level record: influence of glacial melting rates on the Younger Dryas event and deep-ocean circulation. *Nature* 342:637–642. doi: 10.1038/342637a0
- Farmer EJ, Chapman MR, Andrews JE (2010) North Atlantic Globorotalia inflata coretop Mg/Ca calibrations and temperature reconstructions over Termination I. *IOP Conf Ser Earth Environ Sci* 9:012019. doi: 10.1088/1755-1315/9/1/012019
- Ferguson JE, Henderson GM, Kucera M, Rickaby REM (2008) Systematic change of foraminiferal Mg/Ca ratios

- across a strong salinity gradient. *Earth Planet Sci Lett* 265:153–166. doi: 10.1016/j.epsl.2007.10.011
- Fischer J, Schott F a. (2002) Labrador Sea Water Tracked by Profiling Floats—From the Boundary Current into the Open North Atlantic. *J Phys Oceanogr* 32:573–584. doi: 10.1175/1520-0485(2002)032<0573:LSWTBP>2.0.CO;2
- Flatau MK, Talley L, Niiler PP (2003) The North Atlantic Oscillation, Surface Current Velocities, and SST Changes in the Subpolar North Atlantic. *J Clim* 16:2355–2370.
- Fratantoni DM (2001) North Atlantic surface circulation during the 1990's observed with satellite-tracked drifters. *J Geophys Res* 106:22067–22093.
- Fratantoni PS, Pickart RS (2007) The Western North Atlantic Shelfbreak Current System in Summer. *J Phys Oceanogr* 37:2509–2533. doi: 10.1175/JPO3123.1
- Fréchette B, de Vernal A (2013) Evidence for large-amplitude biome and climate changes in Atlantic Canada during the last interglacial and mid-Wisconsinan periods. *Quat Res (United States)* 79:242–255. doi: 10.1016/j.yqres.2012.11.011
- Friedrich O, Schiebel R, Wilson PA, et al (2012) Influence of test size, water depth, and ecology on Mg/Ca, Sr/Ca,  $\delta^{18}\text{O}$  and  $\delta^{13}\text{C}$  in nine modern species of planktic foraminifers. *Earth Planet Sci Lett* 319–320:133–145. doi: 10.1016/j.epsl.2011.12.002
- Fronval T, Jansen E, Haflidason H, Sejrup HP (1998) Variability in surface and deep water conditions in the nordic seas during the last interglacial period. *Quat Sci Rev* 17:963–985. doi: 10.1016/S0277-3791(98)00038-9
- Galaasen E V., Ninnemann US, Irval N, et al (2014) Rapid Reductions in North Atlantic Deep Water During the Peak of the Last Interglacial Period. *Science (80- )* 343:1129–1132. doi: 10.1126/science.1248667
- Ganachaud A, Wunsch C (2000) Improved estimates of global ocean circulation, heat transport and mixing from hydrographic data. *Nature* 408:453–457. doi: 10.1038/35044048
- Ganssen GM, Kroon D (2000) The isotopic signature of planktonic foraminifera from NE Atlantic surface sediments: implications for the reconstruction of past oceanic conditions. *J Geol Soc London* 157:693–699. doi: 10.1144/jgs.157.3.693
- Gary SF, Susan Lozier M, Böning CW, Biastoch A (2011) Deciphering the pathways for the deep limb of the Meridional Overturning Circulation. *Deep Res Part II Top Stud Oceanogr* 58:1781–1797. doi: 10.1016/j.dsr2.2010.10.059
- Gascard JC, Watson AJ, Messias MJ, et al (2002) Long-lived vortices as a mode of deep ventilation in the Greenland Sea. *Nature* 416:525–527. doi: 10.1038/416525a
- Gibson KA, Thunell RC, Machain-Castillo ML, et al (2016) Evaluating controls on planktonic foraminiferal geochemistry in the Eastern Tropical North Pacific. *Earth Planet Sci Lett* 452:90–103. doi: 10.1016/j.epsl.2016.07.039
- Goñi MFS, Bakker P, Desprat S, et al (2012) European climate optimum and enhanced Greenland melt during the last interglacial. *Geology* 40:627–630. doi: 10.1130/G32908.1
- Gorbarenko S, Velivetskaya T, Malakhov M, Bosin A (2017) Glacial terminations and the Last Interglacial in the Okhotsk Sea; Their implication to global climatic changes. *Glob Planet Change* 152:51–63. doi: 10.1016/j.gloplacha.2017.02.006
- Govin A, Braconnot P, Capron E, et al (2012) Persistent influence of ice sheet melting on high northern latitude climate during the early Last Interglacial. *Clim Past* 8:483–507. doi: 10.5194/cp-8-483-2012
- Govin A, Capron E, Tzedakis PC, et al (2015) Sequence of events from the onset to the demise of the Last Interglacial: Evaluating strengths and limitations of chronologies used in climatic archives. *Quat Sci Rev* 129:1–36. doi: 10.1016/j.quascirev.2015.09.018
- Govin A, Chiessi CM, Zabel M, et al (2014) Terrigenous input off northern South America driven by changes in Amazonian climate and the North Brazil Current retroflection during the last 250 ka. *Clim Past* 10:843–862. doi: 10.5194/cp-10-843-2014
- Gray WR, Weldeab S, Lea DW, et al (2018) The effects of temperature, salinity, and the carbonate system on Mg/Ca in *Globigerinoides ruber* (white): A global sediment trap calibration. *Earth Planet Sci Lett* 482:607–620. doi: 10.1016/j.epsl.2017.11.026
- Grimm EC (1987) Constrained Cluster Analysis By the Method of Incremental Sum of Squares. *Comput Geosci* 13:13–35. doi: 10.1016/0098-3004(87)90022-7
- Grobe H (1987) A Simple Method for the Determination of Ice-Rafted Debris in Sediment Cores. *Polarforschung* 57:123–126.

- Grootes PM, Stuiver M, White JWC, et al (1993) Comparison of oxygen isotope records from the GISP2 and GRIP Greenland ice cores. *Nature* 366:552–554. doi: 10.1038/366552a0
- Group TLS (1998) The Labrador Sea Deep Convection Experiment. *Bull Am Meteorol Soc* 79:2033–2058. doi: 10.1175/1520-0477(1998)079<2033:TLSDCE>2.0.CO;2
- Grousset FE, Labeyrie L, Sinko JA, et al (1993) Patterns of ice-rafted detritus in the glacial North Atlantic (40–55°N). *Paleoceanography* 8:175–192. doi: 10.1029/92PA02923
- Guihou A, Pichat S, Govin A, et al (2011) Enhanced Atlantic Meridional Overturning Circulation supports the Last Glacial Inception. *Quat Sci Rev* 30:1576–1582. doi: 10.1016/j.quascirev.2011.03.017
- Guiot J, de Beaulieu JL, Cheddadi R, et al (1993) The climate in Western Europe during the last Glacial/Interglacial cycle derived from pollen and insect remains. *Palaeogeogr Palaeoclimatol Palaeoecol* 103:73–93. doi: 10.1016/0031-0182(93)90053-L
- Gwiazda RH, Hemming SR, Broecker WS (1996) Provenance of icebergs during Heinrich event 3 and the contrast to their sources during other Heinrich episodes. *Paleoceanography* 11:371–378.
- Hakkinen S, Rhines PB (2004) Decline of Subpolar North Atlantic Circulation During the 1990s. *Science* (80- ) 304:555–559. doi: 10.1126/science.1094917
- Hall JM, Chan L-H (2004) Ba/Ca in *Neogloboquadrina pachyderma* as an indicator of deglacial meltwater discharge into the western Arctic Ocean. *Paleoceanography* 19:PA1017. doi: 10.1029/2003PA000910
- Han Z, Li S (2018) Precursor role of winter sea-ice in the Labrador Sea for following-spring precipitation over southeastern North America and western Europe. *Adv Atmos Sci* 35:65–74. doi: 10.1007/s00376-017-6291-3
- Hanor JS, Chan LH (1977) Non-conservative behavior of barium during mixing of Mississippi River and Gulf of Mexico waters. *Earth Planet Sci Lett* 37:242–250. doi: 10.1016/0012-821X(77)90169-8
- Hansen B, Østerhus S (2000) North Atlantic–Nordic Seas exchanges. *Prog Oceanogr* 45:109–208. doi: 10.1016/S0079-6611(99)00052-X
- Hatfield RG, Reyes A V., Stoner JS, et al (2016) Interglacial responses of the southern Greenland ice sheet over the last 430,000 years determined using particle-size specific magnetic and isotopic tracers. *Earth Planet Sci Lett* 454:225–236. doi: 10.1016/j.epsl.2016.09.014
- Hatun H (2005) Influence of the Atlantic Subpolar Gyre on the Thermohaline Circulation. *Science* (80- ) 309:1841–1844. doi: 10.1126/science.1114777
- Hayes JM (1983) Practice and principles of isotopic measurements in organic geochemistry. *Org geochemistry Contemp Anc sediments* 5:e5. doi: 10.2307/1938584
- Hays JD, Imbrie J, Shackleton NJ (1976) Variations in the Earth's Orbit: Pacemaker of the Ice Ages. *Science* (80- ) 194:1121–1132. doi: 10.1126/science.194.4270.1121
- Heinrich H (1988) Origin and consequences of cyclic ice rafting in the Northeast Atlantic Ocean during the past 130,000 years. *Quat Res* 29:142–152. doi: 10.1016/0033-5894(88)90057-9
- Hellstrom J (2003) Rapid and accurate U/Th dating using parallel ion-counting multi-collector ICP-MS. *J Anal At Spectrom* 18:1346. doi: 10.1039/b308781f
- Hemming SR (2004) Heinrich events: Massive late Pleistocene detritus layers of the North Atlantic and their global climate imprint. *Rev Geophys* 42:RG1005. doi: 10.1029/2003RG000128.1.INTRODUCTION
- Hemming SR, Broecker WS, Sharp WD, et al (1998) Provenance of Heinrich layers in core V28-82, northeastern Atlantic: <sup>40</sup>Ar/<sup>39</sup>Ar ages of ice-rafted hornblende, Pb isotopes in feldspar grains, and Nd-Sr-Pb isotopes in the fine sediment fraction. *Earth Planet Sci Lett* 164:317–333. doi: 10.1016/S0012-821X(98)00224-6
- Henderson GM, Keith O'Nions R (1995) <sup>234</sup>U/<sup>238</sup>U ratios in quaternary planktonic foraminifera. *Geochim Cosmochim Acta* 59:4685–4694. doi: 10.1016/0016-7037(95)00327-4
- Herold N, Yin QZ, Karami MP, Berger a. (2012) Modelling the climatic diversity of the warm interglacials. *Quat Sci Rev* 56:126–141. doi: 10.1016/j.quascirev.2012.08.020
- Hesse R, Khodabakhsh S (2016) Anatomy of Labrador Sea Heinrich layers. *Mar Geol* 380:44–66. doi: 10.1016/j.margeo.2016.05.019
- Hesse R, Khodabakhsh S (2017) Anatomy of Labrador Sea Heinrich layers. *Mar Geol* 393:67–92. doi: 10.1016/j.margeo.2016.05.019
- Hibbert FD, Austin WEN, Leng MJ, Gatliff RW (2010) British ice sheet dynamics inferred from North Atlantic ice-rafted debris records spanning the last 175 000 years. *J Quat Sci* 25:461–482. doi: 10.1002/jqs.1331
- Hillaire-Marcel C, Bilodeau G (2000) Instabilities in the Labrador Sea water mass structure during the last climatic

- cycle. *Can J Earth Sci* 37:795–809. doi: 10.1139/e99-108
- Hillaire-Marcel C, de Vernal A (2008) Stable isotope clue to episodic sea ice formation in the glacial North Atlantic. *Earth Planet Sci Lett* 268:143–150. doi: 10.1016/j.epsl.2008.01.012
- Hillaire-Marcel C, de Vernal A, Bilodeau G, Weaver A J (2001) Absence of deep-water formation in the Labrador Sea during the last interglacial period. *Nature* 410:1073–7. doi: 10.1038/35074059
- Hillaire-Marcel C, de Vernal A, Bilodeau G, Wu G (1994) Isotope stratigraphy, sedimentation rates, deep circulation, and carbonate events in the Labrador Sea during the last ~200 ka. *Can J Earth Sci* 31:63–89.
- Hillaire-Marcel C, de Vernal A, McKay J (2011) Foraminifer isotope study of the Pleistocene Labrador Sea, northwest North Atlantic (IODP Sites 1302/03 and 1305), with emphasis on paleoceanographical differences between its “inner” and “outer” basins. *Mar Geol* 279:188–198.
- Hillaire-Marcel C, de Vernal A, Piper DJW (2007) Lake Agassiz Final drainage event in the northwest North Atlantic. *Geophys Res Lett* 34:1–5. doi: 10.1029/2007GL030396
- Hiscott RN, Aksu AE (1996) Quaternary Sedimentary Processes and Budgets in Orphan Basin, Southwestern Labrador Sea. *Quat Res* 45:160–175. doi: 10.1006/qres.1996.0017
- Hiscott RN, Aksu AE, Mudie PJ, Parsons DF (2001) A 340,000 year record of ice rafting, palaeoclimatic fluctuations, and shelf-crossing glacial advances in the southwestern Labrador Sea. *Glob Planet Change* 28:227–240. doi: 10.1016/S0921-8181(00)00075-8
- Hiscott RN, Cremer M, Aksu AE (1989) Evidence from sedimentary structures for processes of sediment transport and deposition during post-Miocene time at sites 645, 646, and 647, Baffin Bay and the Labrador Sea. *Proc Ocean Drill Program, Sci Results* 105:53–63.
- Hodell D a., Minth EK, Curtis JH, et al (2009) Surface and deep-water hydrography on Gardar Drift (Iceland Basin) during the last interglacial period. *Earth Planet Sci Lett* 288:10–19. doi: 10.1016/j.epsl.2009.08.040
- Hodell DA, Channeil JET, Curtis JH, et al (2008) Onset of “Hudson Strait” Heinrich events in the eastern North Atlantic at the end of the middle Pleistocene transition (~640 ka)? *Paleoceanography* 23:1–16. doi: 10.1029/2008PA001591
- Holliday NP, Bacon S, Allen J, McDonagh EL (2009) Circulation and Transport in the Western Boundary Currents at Cape Farewell, Greenland. *J Phys Oceanogr* 39:1854–1870. doi: 10.1175/2009JPO4160.1
- Holliday NP, Meyer A, Bacon S, et al (2007) Retroflexion of part of the east Greenland current at Cape Farewell. *Geophys Res Lett* 34:1–5. doi: 10.1029/2006GL029085
- Hönisch B, Allen KA, Russell AD, et al (2011) Planktic foraminifers as recorders of seawater Ba/Ca. *Mar Micropaleontol* 79:52–57. doi: 10.1016/j.marmicro.2011.01.003
- Honjo S, Manganini SJ (1993) Annual biogenic particle fluxes to the interior of the North Atlantic Ocean; studied at 34°N 21°W and 48°N 21°W. *Deep Res Part II* 40:587–607. doi: 10.1016/0967-0645(93)90034-K
- Hulbe CL (1997) An ice shelf mechanism for Heinrich layer production. *Paleoceanography* 12:711–717. doi: 10.1029/97PA02014
- Hulbe CL, MacAyeal DR, Denton GH, et al (2004) Catastrophic ice shelf breakup as the source of Heinrich event icebergs. *Paleoceanography* 19:n/a-n/a. doi: 10.1029/2003PA000890
- Hunter S, Wilkinson D, Louarn E, et al (2007) Deep western boundary current dynamics and associated sedimentation on the Eirik Drift, Southern Greenland Margin. *Deep Res Part I Oceanogr Res Pap* 54:2036–2066. doi: 10.1016/j.dsr.2007.09.007
- Hurrell JW (1995) Decadal Trends in the North Atlantic Oscillation: Regional Temperatures and Precipitation. *Science* (80- ) 269:676–679. doi: 10.1126/science.269.5224.676
- Imbrie J, Hays JD, Martinson DG, et al (1984) The orbital theory of Pleistocene climate: Support from a revised chronology of the marine  $\delta^{18}\text{O}$  record. *Milankovitch Clim Underst Response to Astron Forcing* 269–305. doi: -
- Incarbona A, Di Stefano E, Sprovieri R, et al (2010) Millennial-scale paleoenvironmental changes in the central Mediterranean during the last interglacial: Comparison with European and North Atlantic records. *Geobios* 43:111–122. doi: 10.1016/j.geobios.2009.06.008
- IPCC (2013) *Climate Change 2013: The Physical Science Basis*.
- Irvali N, Ninnemann US, Galaasen E V., et al (2012) Rapid switches in subpolar North Atlantic hydrography and climate during the Last Interglacial (MIS 5e). *Paleoceanography* 27:1–16. doi: 10.1029/2011PA002244
- Irvali N, Ninnemann US, Kleiven HKF, et al (2016) Evidence for regional cooling, frontal advances, and East

- Greenland Ice Sheet changes during the demise of the last interglacial. *Quat Sci Rev* 150:184–199. doi: 10.1016/j.quascirev.2016.08.029
- Jennings AE, Tedesco KA, Andrews JT, Kirby ME (1996) Shelf erosion and glacial ice proximity in the Labrador Sea during and after Heinrich events (H-3 or 4 to H-0) as shown by foraminifera. *Geol Soc London, Spec Publ* 111:29–49. doi: 10.1144/GSL.SP.1996.111.01.04
- Johnsen SJ, Clausen HB, Dansgaard W, et al (1992) Irregular glacial interstadials recorded in a new Greenland ice core. *Nature* 359:311–313.
- Johnson RG, Lauritzen SE (1995) Hudson Bay-Hudson Strait jökulhlaups and Heinrich events: a hypothesis. *Palaeogeogr Palaeoclimatol Palaeoecol* 117:123–137. doi: 10.1016/0031-0182(94)00120-W
- Jones VJ, Juggins S (1995) The construction of a diatom-based chlorophyll a transfer function and its application at three lakes on Signy Island (maritime Antarctic) subject to differing degrees of nutrient enrichment. *Freshw Biol* 34:433–445. doi: 10.1111/j.1365-2427.1995.tb00901.x
- Jonkers L, Brummer GJA, Peeters FJC, et al (2010) Seasonal stratification, shell flux, and oxygen isotope dynamics of leftcoiling *N. pachyderma* and *T. quinqueloba* in the western subpolar North Atlantic. *Paleoceanography* 25:1–13. doi: 10.1029/2009PA001849
- Jouzel J, Masson-Delmotte V, Cattani O, et al (2007) Orbital and millennial antarctic climate variability over the past 800,000 years. *Science* (80- ) 317:793.
- Kandiano ES, Bauch HA, Fahl K (2014) Last interglacial surface water structure in the western Mediterranean (Balearic) Sea: Climatic variability and link between low and high latitudes. *Glob Planet Change* 123:67–76. doi: 10.1016/j.gloplacha.2014.10.004
- Katz A (1973) The interaction of magnesium with calcite during crystal growth at 25–90°C and one atmosphere. *Geochim Cosmochim Acta*. doi: 10.1016/0016-7037(73)90091-4
- Kawamura K (2010) Burial Consolidation Processes of Deep-Sea Sediments: an Example of Core Sediments Collected From the Labrador Sea in the Northwest Atlantic. *Soils Found* 50:623–632. doi: 10.3208/sandf.50.623
- Kawamura N, Ishikawa N, Torii M (2012) Diagenetic alteration of magnetic minerals in Labrador sea sediments (IODP sites U1305, U1306, and U1307). *Geochemistry, Geophys Geosystems* 13:Q08013. doi: 10.1029/2012GC004213
- Kemp AES, Baldauf JG (1993) Vast Neogene laminated diatom mat deposits from the eastern Pacific Ocean. *Nature* 362:141–144.
- Kemp AES, Pearce RB, Grigorov I, et al (2006) Production of giant marine diatoms and their export at oceanic frontal zones: Implications for Si and C flux from stratified oceans. *Global Biogeochem Cycles* 20:1–13. doi: 10.1029/2006GB002698
- Kieke D, Klein B, Stramma L, et al (2009) Variability and propagation of Labrador Sea Water in the southern subpolar North Atlantic. *Deep Res Part I Oceanogr Res Pap* 56:1656–1674. doi: 10.1016/j.dsr.2009.05.010
- Kieke D, Rhein M, Stramma L, et al (2006) Changes in the CFC Inventories and Formation Rates of Upper Labrador Sea Water, 1997–2001. *J Phys Oceanogr* 36:64–86. doi: 10.1175/JPO2814.1
- Kleiven HF, Kissel C, Laj C, et al (2008) Reduced North Atlantic Deep Water Coeval with the Glacial Lake Agassiz Freshwater Outburst. *Science* (80- ) 319:60–64. doi: 10.1126/science.1148924
- Koenigk T, Mikolajewicz U, Haak H, Jungclaus J (2007) Arctic freshwater export in the 20th and 21st centuries. *J Geophys Res Biogeosciences* 112:1–11. doi: 10.1029/2006JG000274
- Koeve W (2001) Wintertime nutrients in the north atlantic - New approaches and implications for new production estimates. *Mar Chem* 74:245–260. doi: 10.1016/S0304-4203(01)00016-0
- Kohfeld KE, Fairbanks RG, Smith SL, Walsh ID (1996) *Neogloboquadrina pachyderma* (sinistral coiling) as paleoceanographic tracers in polar oceans: Evidence from Northeast Water Polynya plankton tows, sediment traps, and surface sediments. *Paleoceanography* 11:679–699. doi: 10.1029/96PA02617
- Kopp RE, Simons FJ, Mitrovica JX, et al (2009) Probabilistic assessment of sea level during the last interglacial stage. *Nature* 462:863–867. doi: 10.1038/nature08686
- Kopp RE, Simons FJ, Mitrovica JX, et al (2013) A probabilistic assessment of sea level variations within the last interglacial stage. *Geophys J Int* 193:711–716. doi: 10.1093/gji/ggt029
- Kozdon R, Eisenhauer A, Weinelt M, et al (2009) Reassessing Mg/Ca temperature calibrations of *Neogloboquadrina pachyderma* (sinistral) using paired  $\delta^{44/40}\text{Ca}$  and Mg/Ca measurements. *Geochemistry Geophys Geosystems*. doi: 10.1029/2008GC002169

- Kroopnick PM (1985) The distribution of  $^{13}\text{C}$  of  $^{14}\text{CO}_2$  in the world oceans. *Deep Sea Res Part A, Oceanogr Res Pap* 32:57–84. doi: 10.1016/0198-0149(85)90017-2
- Kucera M, Weinelt M, Kiefer T, et al (2005) Reconstruction of sea-surface temperatures from assemblages of planktonic foraminifera: Multi-technique approach based on geographically constrained calibration data sets and its application to glacial Atlantic and Pacific Oceans. *Quat Sci Rev* 24:951–998. doi: 10.1016/j.quascirev.2004.07.014
- Kuhlbrodt T, Griesel A, Montoya M, et al (2007) On the driving processes of the Atlantic meridional overturning circulation. *Rev Geophys* 45:RG2001. doi: 10.1029/2004RG000166
- Kukla GJ, Bender ML, de Beaulieu J-L, et al (2002a) Last Interglacial Climates. *Quat Res* 58:2–13. doi: 10.1006/qres.2001.2316
- Kukla GJ, Clement AC, Cane MA, et al (2002b) Last Interglacial and Early Glacial ENSO. *Quat Res* 58:27–31. doi: 10.1006/qres.2002.2327
- Lajeunesse P (2012) Palaeoclimate: A history of outbursts. *Nat Geosci* 5:846–847. doi: 10.1038/ngeo1651
- Lajeunesse P, St-Onge G (2008) The subglacial origin of the Lake Agassiz–Ojibway final outburst flood. *Nat Geosci* 1:184–188. doi: 10.1038/ngeo130
- Landais A, Dreyfus G, Capron E, et al (2013) Two-phase change in  $\text{CO}_2$ , Antarctic temperature and global climate during Termination II. *Nat Geosci* 6:1062–1065. doi: 10.1038/ngeo1985
- Landais A, Masson-Delmotte V, Capron E, et al (2016) How warm was Greenland during the last interglacial period? *Clim Past* 12:1933–1948. doi: 10.5194/cp-12-1933-2016
- Laskar J, Robutel P, Joutel F, et al (2004) A long-term numerical solution for the insolation quantities of the Earth. *Astron Astrophys* 428:261–285. doi: 10.1051/0004-6361:20041335
- Lavender KL, Davis RE, Owens WB (2000) Mid-depth recirculation observed in the interior Labrador and Irminger seas by direct velocity measurements. *Nature* 407:66–69. doi: 10.1038/35024048
- Lazier J, Hendry R, Clarke A, et al (2002) Convection and restratification in the Labrador Sea, 1990–2000. *Deep Res Part I Oceanogr Res Pap* 49:1819–1835. doi: 10.1016/S0967-0637(02)00064-X
- Lazier JRN (1973) The renewal of Labrador Sea Water. *Deep Res* 20:341–353. doi: 10.1016/0011-7471(73)90058-2
- Lazier JRN, Wright DG (1993) Annual Velocity Variations in the Labrador Current. *J. Phys. Oceanogr.* 23:659–678.
- Lea D, Boyle E (1989) Barium content of benthic foraminifera controlled by bottom-water composition. *Nature* 338:751–753. doi: 10.1038/338751a0
- Lea DW, Boyle EA (1991) Barium in planktonic foraminifera. *Geochim Cosmochim Acta* 55:3321–3331. doi: 10.1016/0016-7037(91)90491-M
- Lea DW, Martin PA, Pak DK, Spero HJ (2002) Reconstructing a 350 ky history of sea level using planktonic Mg/Ca and oxygen isotope records from a Cocos Ridge core. *Quat Sci Rev* 21:283–293. doi: 10.1016/S0277-3791(01)00081-6
- Lea DW, Mashiotto TA, Spero HJ (1999) Controls on magnesium and strontium uptake in planktonic foraminifera determined by live culturing. *Geochim Cosmochim Acta* 63:2369–2379. doi: 10.1016/S0016-7037(99)00197-0
- Lea DW, Spero HJ (1994) Assessing the reliability of paleochemical tracers: Barium uptake in the shells of planktonic foraminifera. *Paleoceanography* 9:445–452. doi: 10.1029/94PA00151
- LeBel DA, Smethie WM, Rhein M, et al (2008) The formation rate of North Atlantic Deep Water and Eighteen Degree Water calculated from CFC-11 inventories observed during WOCE. *Deep Res Part I Oceanogr Res Pap* 55:891–910. doi: 10.1016/j.dsr.2008.03.009
- LeGrande AN, Schmidt GA (2006) Global gridded data set of the oxygen isotopic composition in seawater. *Geophys Res Lett* 33:1–5. doi: 10.1029/2006GL026011
- Lehman SJ, Keigwin LD (1992) Sudden changes in North Atlantic circulation during the last deglaciation. *Nature* 356:757–762. doi: 10.1038/356757a0
- Lemieux-Dudon B, Blayo E, Petit JR, et al (2010) Consistent dating for Antarctic and Greenland ice cores. *Quat Sci Rev* 29:8–20. doi: 10.1016/j.quascirev.2009.11.010
- Lewis CFM, Miller AAL, Levac E, et al (2012) Lake Agassiz outburst age and routing by Labrador Current and the 8.2 cal ka cold event. *Quat Int* 260:83–97. doi: 10.1016/j.quaint.2011.08.023
- Lilly JM, Rhines PB (2002) Coherent Eddies in the Labrador Sea Observed from a Mooring. *J Phys Oceanogr* 32:585–598. doi: 10.1175/1520-0485(2002)032<0585:CEITLS>2.0.CO;2

- Lisiecki LE, Lisiecki PA (2002) Application of dynamic programming to the correlation of paleoclimate records. *Paleoceanography* 17:1-1-1-12. doi: 10.1029/2001PA000733
- Lisiecki LE, Raymo ME (2005) A Pliocene-Pleistocene stack of 57 globally distributed benthic  $\delta^{18}\text{O}$  records. *Paleoceanography* 20:PA1003. doi: 10.1029/2004PA001071
- Lisiecki LE, Raymo ME (2009) Diachronous benthic  $\delta^{18}\text{O}$  responses during late Pleistocene terminations. *Paleoceanography* 24:1-14. doi: 10.1029/2009PA001732
- Lisiecki LE, Stern J V (2016) Regional and global benthic  $\delta^{18}\text{O}$  stacks for the last glacial cycle. *Paleoceanography* 31:1368-1394. doi: 10.1002/2016PA003002.Received
- Loulergue L, Schilt A, Spahni R, et al (2008) Orbital and millennial-scale features of atmospheric  $\text{CH}_4$  over the past 800,000 years. *Nature* 453:383-386. doi: 10.1038/nature06950
- L wemark L, Chao WS, Gyllencreutz R, et al (2016) Variations in glacial and interglacial marine conditions over the last two glacial cycles off northern Greenland. *Quat Sci Rev* 147:164-177. doi: 10.1016/j.quascirev.2015.10.035
- Lozier MS (2010) Deconstructing the Conveyor Belt. *Science* (80- ) 328:1507-1511. doi: 10.1126/science.1189250
- Lozier MS (2012) Overturning in the North Atlantic. *Ann Rev Mar Sci* 4:291-315. doi: 10.1146/annurev-marine-120710-100740
- Lukashina NP (2013) Water masses of the northern part of the Iceland Basin in the late Pleistocene. *Oceanology* 53:99-109. doi: 10.1134/S0001437013010128
- MacAyeal DR (1993) Binge/purge oscillations of the Laurentide Ice Sheet as a cause of the North Atlantic's Heinrich events. *Paleoceanography* 8:775-784. doi: 10.1029/93PA02200
- Mackay AW, Swann GEA, Fagel N, et al (2013) Hydrological instability during the Last Interglacial in central Asia: A new diatom oxygen isotope record from Lake Baikal. *Quat Sci Rev* 66:45-54. doi: 10.1016/j.quascirev.2012.09.025
- Magurran AE (1998) Population differentiation without speciation. *Philos Trans R Soc London, Ser B* 353:275-286. doi: 10.1098/rstb.1998.0209
- Malmgren BA (1983) Ranking of dissolution susceptibility of planktonic foraminifera at high latitudes of the South Atlantic Ocean. *Mar Micropaleontol* 8:183-191. doi: 10.1016/0377-8398(83)90023-3
- Manabe S, Stouffer RJ (1988) Two Stable Equilibria of a Coupled Ocean-Atmosphere Model. *J. Clim.* 1:841-866.
- Mao L, Piper DJW, Saint-Ange F, Andrews JT (2018) Labrador Current fluctuation during the last glacial cycle. *Mar Geol* 395:234-246. doi: 10.1016/j.margeo.2017.10.012
- Marr JP, Carter L, Bostock HC, et al (2013) Southwest Pacific Ocean response to a warming world: Using Mg/Ca, Zn/Ca, and Mn/Ca in foraminifera to track surface ocean water masses during the last deglaciation. *Paleoceanography* 28:347-362. doi: 10.1002/palo.20032
- Marshall J, Schott F (1999) Open-Ocean Convection: Observations, theory, and Models. *Rev Geophys* 37:1-64. doi: 10.1029/98RG02739
- Martin-Jezequel V, Hildebrand M, Brzezinski MA (2000) Silicon Metabolism in Diatoms: Implications for Growth. *J Phycol* 36:821-840. doi: 10.1046/j.1529-8817.2000.00019.x
- Mart nez-Bot  MA, Mortyn PG, Schmidt DN, et al (2011) Mg/Ca in foraminifera from plankton tows: Evaluation of proxy controls and comparison with core tops. *Earth Planet Sci Lett* 307:113-125. doi: 10.1016/j.epsl.2011.04.019
- Martinson DG, Pisias NG, Hays JD, et al (1987) Age dating and the orbital theory of the ice ages: Development of a high resolution 0 to 300 000 year chronostratigraphy. *Quat Res* 27:1-29. doi: 10.1016/0033-5894(87)90046-9
- Mashiotta TA, Lea DW, Spero HJ (1999) Glacial-interglacial changes in Subantarctic sea surface temperature and  $\delta^{18}\text{O}$ -water using foraminiferal Mg. *Earth Planet Sci Lett* 170:417-432. doi: 10.1016/S0012-821X(99)00116-8
- Masson-Delmotte V, Schulz M, Abe-Ouchi A, et al (2013) Information from Paleoclimate Archives. In: *Climate Change 2013: The Physical Science Basis. Contribution of Working Group I to the Fifth Assessment Report of the Intergovernmental Panel on Climate Change.* Cambridge University Press, Cambridge, United Kingdom and New York, NY, USA
- Mazaud A, Channell JET, Stoner JS (2012) Relative paleointensity and environmental magnetism since 1.2Ma at IODP site U1305 (Eirik Drift, NW Atlantic). *Earth Planet Sci Lett* 357-358:137-144. doi: 10.1016/j.epsl.2012.09.037
- Mazaud A, Channell JET, Xuan C, Stoner JS (2009) Upper and lower Jaramillo polarity transitions recorded in IODP

- Expedition 303 North Atlantic sediments: Implications for transitional field geometry. *Phys Earth Planet Inter* 172:131–140. doi: 10.1016/j.pepi.2008.08.012
- McCartney MS, Talley LD (1982) The Subpolar Mode Water of the North Atlantic Ocean. *J. Phys. Oceanogr.* 12:1169–1188.
- McConnell MC, Thunell RC (2005) Calibration of the planktonic foraminiferal Mg/Ca paleothermometer: Sediment trap results from the Guaymas Basin, Gulf of California. *Paleoceanography* 20:1–18. doi: 10.1029/2004PA001077
- McCulloch MT, Esat T (2000) The coral record of last interglacial sea levels and sea surface temperatures. *Chem Geol* 169:107–129. doi: 10.1016/S0009-2541(00)00260-6
- McManus JF, Bond GC, Broecker WS, et al (1994) High-resolution Climate Records from the North Atlantic During the Last Interglacial. *Nature* 371:326–329.
- McManus JF, Francois R, Gherardl JM, et al (2004) Collapse and rapid resumption of Atlantic meridional circulation linked to deglacial climate changes. *Nature* 428:834–837. doi: 10.1038/nature02494
- McManus JF, Major CO, Flower B, Fronval T (1996) Variability in sea-surface conditions in the North Atlantic-Arctic gateways during the last 140,000 years. *Proc Ocean Drill Program Sci Results* 151:437–444.
- Mekik F, François R, Soon M (2007) A novel approach to dissolution correction of Mg/Ca-based paleothermometry in the tropical Pacific. *Paleoceanography* 22:1–12. doi: 10.1029/2007PA001504
- Members CLIP (2006) Last Interglacial Arctic warmth confirms polar amplification of climate change. *Quat Sci Rev* 25:1383–1400. doi: 10.1016/j.quascirev.2006.01.033
- Members N community (2013) Eemian interglacial reconstructed from a Greenland folded ice core. *Nature* 493:489–494. doi: 10.1038/nature11789
- Members NGICP (2004) High-resolution record of Northern Hemisphere climate extending into the last interglacial period. *Nature* 431:147–151. doi: 10.1038/nature02805
- Milner AM, Müller UC, Roucoux KH, et al (2013) Environmental variability during the Last Interglacial: A new high-resolution pollen record from Tenaghi Philippon, Greece. *J Quat Sci* 28:113–117. doi: 10.1002/jqs.2617
- Mix AC, Morey AE, Pisias NG (1999) Foraminiferal faunal estimates of paleotemperature: Circumventing the no-analog problem yields cool ice age tropics. *Paleoceanography* 14:350–359.
- Mokeddem Z, McManus JF, Oppo DW (2014) Oceanographic dynamics and the end of the last interglacial in the subpolar North Atlantic. *Proc Natl Acad Sci* 111:11263–11268. doi: 10.1073/pnas.1322103111
- Morey AE, Mix AC, Pisias NG (2005) Planktonic foraminiferal assemblages preserved in surface sediments correspond to multiple environment variables. *Quat Sci Rev* 24:925–950. doi: 10.1016/j.quascirev.2003.09.011
- Myers PG, Donnelly C, Ribergaard MH (2009) Structure and variability of the West Greenland Current in Summer derived from 6 repeat standard sections. *Prog Oceanogr* 80:93–112. doi: 10.1016/j.pocean.2008.12.003
- Myers PG, Kulan N, Ribergaard MH (2007) Irminger water variability in the West Greenland Current. *Geophys Res Lett* 34:2–7. doi: 10.1029/2007GL030419
- Nicholl JAL, Hodell DA, Naafs BDA, et al (2012) A Laurentide outburst flooding event during the last interglacial period. *Nat Geosci* 5:901–904. doi: 10.1038/ngeo1622
- Novikov G V, Murdmaa IO (2007) Ion exchange properties of oceanic ferromanganese nodules and enclosing pelagic sediments. *Lithol Miner Resour* 42:137–167. doi: 10.1134/S0024490207020034
- Nürnberg D, Bijma J, Hemleben C (1996) Assessing the reliability of magnesium in foraminiferal calcite as a proxy for water mass temperatures. *Geochim Cosmochim Acta* 60:803–814. doi: 10.1016/0016-7037(95)00446-7
- Nürnberg D, Müller a., Schneider RR (2000) Paleo-sea surface temperature calculations in the equatorial east Atlantic from Mg/Ca ratios in planktic foraminifera: A comparison to sea surface temperature estimates from UK37, oxygen isotopes, and foraminiferal transfer function. *Paleoceanography* 15:124–134. doi: 10.1029/1999pa000370
- Oppo DW, Keigwin LD, McManus JF, Cullen JL (2001) Persistent suborbital climate variability in marine isotope stage 5 and Termination II. *Paleoceanography* 16:280–292.
- Oppo DW, Lehman SJ (1993) Mid-Depth Circulation of the Subpolar North Atlantic During the Last Glacial Maximum. *Science* (80-) 259:1148–1152. doi: 10.1126/science.259.5098.1148
- Oppo DW, McManus JF, Cullen JL (2006) Evolution and demise of the Last Interglacial warmth in the subpolar North Atlantic. *Quat Sci Rev* 25:3268–3277. doi: 10.1016/j.quascirev.2006.07.006
- Otto-Bliesner BL (2006) Simulating Arctic Climate Warmth and Icefield Retreat in the Last Interglaciation. *Science*

(80-) 311:1751–1753. doi: 10.1126/science.1120808

- PAGES PIWG of (2016) Interglacials of the last 800,000 years. *Rev Geophys* 54:162–219. doi: 10.1002/2015RG000482. Received
- Parrenin F, Barnola JM, Beer J, et al (2007) The EDC3 chronology for the EPICA Dome C ice core. *Clim Past* 3:485–497. doi: 10.5194/cp-3-485-2007
- Penaud A, Eynaud F, Turon JL, et al (2009) What forced the collapse of European ice sheets during the last two glacial periods (150 ka B.P. and 18 ka cal B.P.)? Palynological evidence. *Palaeogeogr Palaeoclimatol Palaeoecol* 281:66–78. doi: 10.1016/j.palaeo.2009.07.012
- Peterson CD, Lisiecki LE, Stern J V. (2014) Deglacial whole-ocean  $\delta^{13}\text{C}$  change estimated from 480 benthic foraminiferal records. *Paleoceanography* 29:549–563. doi: 10.1002/2013PA002552
- Petit JR, Jouzel J, Raynaud D, et al (1999) Climate and atmospheric history of the past 420,000 years from the Vostok ice core, Antarctica. *Nature* 399:429–436. doi: 10.1038/20859
- Pflaumann U, Duprat J, Pujol C, Labeyrie LD (1996) SIMMAX: A modern analog technique to deduce Atlantic sea surface temperatures from planktonic foraminifera in deep-sea sediments. *Paleoceanography* 11:15–35. doi: 10.1029/95PA01743
- Pflaumann U, Sarnthein M, Chapman M, et al (2003) Glacial North Atlantic: Sea-surface conditions reconstructed by GLAMAP 2000. *Paleoceanography* 18:n/a-n/a. doi: 10.1029/2002PA000774
- Pickart RS (1992) Water mass components of the North Atlantic deep western boundary current. *Deep Sea Res Part I Ocean Res P* 39:1553–1572. doi: 10.1016/0198-0149(92)90047-W
- Pickart RS, Smethie WM (1993) How Does the Deep Western Boundary Current Cross the Gulf Stream? *J Phys Oceanogr* 23:2602–2616. doi: 10.1175/1520-0485(1993)023<2602:HDTDWB>2.0.CO;2
- Pickart RS, Smethie WM, Lazier JRN, et al (1996) Eddies of newly formed upper Labrador Sea water. *J Geophys Res Ocean* 101:20711–20726. doi: 10.1029/96JC01453
- Pickart RS, Straneo F, Moore GWK (2003) Is Labrador Sea Water formed in the Irminger basin? *Deep Res Part I Oceanogr Res Pap* 50:23–52. doi: 10.1016/S0967-0637(02)00134-6
- Prater MD (2002) Eddies in the Labrador Sea as Observed by Profiling RAFOS Floats and Remote Sensing. *J Phys Oceanogr* 32:411–427. doi: 10.1175/1520-0485(2002)032<0411:EITLSA>2.0.CO;2
- Prell WL, Imbrie J, Martinson DG, et al (1986) Graphic correlation of oxygen isotope stratigraphy application to the late Quaternary. *Paleoceanography* 1:137–162.
- Quiquet A, Ritz C, Punge HJ, Salas Y Méliá D (2013) Greenland ice sheet contribution to sea level rise during the last interglacial period: A modelling study driven and constrained by ice core data. *Clim Past* 9:353–366. doi: 10.5194/cp-9-353-2013
- Rahmstorf S (1995) Bifurcations of the Atlantic thermohaline circulation in response to changes in the hydrological cycle.
- Rahmstorf S (2002) Ocean circulation and climate during the past 120,000 years. *Nature* 419:207–214. doi: 10.1038/nature01090
- Rahmstorf S, Ganopolski A (1999) Long-Term Global Warming Scenarios Computed With an Efficient Coupled Climate Model. *Clim Chang* 43:353–367.
- Railsback LB, Gibbard PL, Head MJ, et al (2015) An optimized scheme of lettered marine isotope substages for the last 1.0 million years, and the climatostratigraphic nature of isotope stages and substages. *Quat Sci Rev* 111:94–106. doi: 10.1016/j.quascirev.2015.01.012
- Ramm, T (ed) (1994) *1994 Anthology*. Arrival Press, Woodston, Peterborough.
- Ramón Mercou J, Laprida C (2016) An ostracod-based calibration function for electrical conductivity reconstruction in lacustrine environments in Patagonia, Southern South America. *Ecol Indic* 69:522–532. doi: 10.1016/j.ecolind.2016.05.026
- Rasmussen SO, Andersen KK, Svensson AM, et al (2006) A new Greenland ice core chronology for the last glacial termination. *J Geophys Res* 111:D06102. doi: 10.1029/2005JD006079
- Rasmussen TL, Balbon E, Thomsen E, et al (1999) Climate records and changes in deep outflow from the Norwegian Sea ~ 150–55 ka. *Terra Nov* 11:61–66. doi: 10.1046/j.1365-3121.1999.00226.x
- Rasmussen TL, Oppo DW, Thomsen E, Lehman SJ (2003a) Deep sea records from the southeast Labrador Sea: Ocean circulation changes and ice-rafting events during the last 160,000 years. *Paleoceanography* 18:1018. doi: 10.1029/2001PA000736

- Rasmussen TL, Thomsen E, Kuijpers A, Wastegård S (2003b) Late warming and early cooling of the sea surface in the Nordic seas during MIS 5e (Eemian Interglacial). *Quat Sci Rev* 22:809–821. doi: 10.1016/S0277-3791(02)00254-8
- Raymo ME (1997) The timing of major climate terminations. *Paleoceanography* 12:577–585. doi: 10.1029/97PA01169
- Regattieri E, Giaccio B, Nomade S, et al (2017) A Last Interglacial record of environmental changes from the Sulmona Basin (central Italy). *Palaeogeogr Palaeoclimatol Palaeoecol* 472:51–66. doi: 10.1016/j.palaeo.2017.02.013
- Regattieri E, Zanchetta G, Drysdale RN, et al (2016) Environmental variability between the penultimate deglaciation and the mid Eemian: Insights from Tana che Urla (central Italy) speleothem trace element record. *Quat Sci Rev* 152:80–92. doi: 10.1016/j.quascirev.2016.09.027
- Reverdin G (2003) North Atlantic Ocean surface currents. *J Geophys Res* 108:3002. doi: 10.1029/2001JC001020
- Rhein M, Fischer J, Smethie WM, et al (2002) Labrador Sea Water: Pathways, CFC Inventory, and Formation Rates. *J Phys Oceanogr* 32:648–665. doi: 10.1175/1520-0485(2002)032<0648:LSWPCI>2.0.CO;2
- Risebrobakken B, Balbon E, Dokken T, et al (2006) The penultimate deglaciation: High-resolution paleoceanographic evidence from a north-south transect along the eastern Nordic Seas. *Earth Planet Sci Lett* 241:505–516. doi: 10.1016/j.epsl.2005.11.032
- Roach AT, Aagaard K, Carsey F (1993) Coupled ice-ocean variability in the Greenland sea. *Atmos - Ocean* 31:319–337. doi: 10.1080/07055900.1993.9649474
- Rohling EJ, Grant K, Bolshaw M, et al (2009) Antarctic temperature and global sea level closely coupled over the past five glacial cycles. *Nat Geosci* 2:500–504. doi: 10.1038/ngeo557
- Rosenthal Y, Linsley B (2007) Mg/Ca and Sr/Ca Paleothermometry. *Encycl Quat Sci* 1723–1731. doi: 10.1016/B0-44-452747-8/00306-9
- Rosenthal Y, Lohmann GP, Lohmann KC, Sherrell RM (2000) Incorporation and Preservation of Mg in *Globigerinoides sacculifer*: Implications for Reconstructing the Temperature and  $18\text{O}/16\text{O}$  of Seawater. *Paleoceanography* 15:135–145. doi: 10.1029/1999pa000415
- Rosby T (1999) On gyre interactions. *Deep Res Part II Top Stud Oceanogr* 46:139–164. doi: 10.1016/S0967-0645(98)00095-2
- Rosby T (1996) The North Atlantic Current and Surrounding Waters: At the Crossroads. *Rev Geophys* 34:463–481.
- Rousseau DD, Kukla G, McManus J (2006) What is what in the ice and the ocean? *Quat Sci Rev* 25:2025–2030. doi: 10.1016/j.quascirev.2006.03.009
- Ruddiman WF (1977) Late Quaternary deposition of ice-rafted sand in the subpolar North Atlantic (lat  $40^\circ$  to  $65^\circ\text{N}$ ). *Bull Geol Soc Am* 88:1813–1827. doi: 10.1130/0016-7606(1977)88<1813:LQDOIS>2.0.CO;2
- Russell AD, Emerson S, Nelson BK, et al (1994) Uranium in foraminiferal calcite as a recorder of seawater uranium concentrations. *Geochim Cosmochim Acta* 58:671–681. doi: 10.1016/0016-7037(94)90497-9
- Russell AD, Hönisch B, Spero HJ, Lea DW (2004) Effects of seawater carbonate ion concentration and temperature on shell U, Mg, and Sr in cultured planktonic foraminifera. *Geochim Cosmochim Acta* 68:4347–4361. doi: 10.1016/j.gca.2004.03.013
- Sadekov A, Eggins SM, De Deckker P, Kroon D (2008) Uncertainties in seawater thermometry deriving from intratest and intertest Mg/Ca variability in *Globigerinoides ruber*. *Paleoceanography* 23:1–12. doi: 10.1029/2007PA001452
- Sánchez Goñi MF, Eynaud F, Turon JL, Shackleton NJ (1999) High resolution palynological record off the Iberian margin: Direct land-sea correlation for the Last Interglacial complex. *Earth Planet Sci Lett* 171:123–137. doi: 10.1016/S0012-821X(99)00141-7
- Sanyal A, Hemming NG, Broecker WS, Hansont GN (1995) Evidence for a higher pH in the glacial ocean from boron isotopes in foraminifera. *Nature* 373:234–236.
- Sarafanov A (2009) On the effect of the North Atlantic Oscillation on temperature and salinity of the subpolar North Atlantic intermediate and deep waters. *Oxford Journals* 1448–1454.
- Schiebel R, Bijma J, Hemleben C (1997) Population dynamics of the planktic foraminifer *Globigerina bulloides* from the eastern North Atlantic. *Deep Sea Res Part I Oceanogr Res Pap* 44:1701–1713. doi: 10.1016/S0967-0637(97)00036-8
- Schiebel R, Spielhagen RF, Garnier J, et al (2017) Modern planktic foraminifers in the high-latitude ocean. *Mar Micropaleontol* 136:1–13. doi: 10.1016/j.marmicro.2017.08.004

- Schiebel R, Waniek J, Bork M, Hemleben C (2001) Planktic foraminiferal production stimulated by chlorophyll redistribution and entrainment of nutrients. *Deep Res Part I Oceanogr Res Pap* 48:721–740. doi: 10.1016/S0967-0637(00)00065-0
- Schmidt GA (1999) Forward Modeling of Carbonate Proxy Data from Planktonic Foraminifera using Oxygen Isotope Tracers in a Global Ocean Model. *14:482–497*. doi: 10.1029/1999PA900025
- Schmitz WJ, McCartney MS (1993) On the North Atlantic Circulation. *Rev Geophys* 31:29–49. doi: 10.1029/92RG02583
- Schott F a., Zantopp R, Stramma L, et al (2004) Circulation and Deep-Water Export at the Western Exit of the Subpolar North Atlantic. *J Phys Oceanogr* 34:817–843. doi: 10.1175/1520-0485(2004)034<0817:CADEAT>2.0.CO;2
- Schott F, Visbeck M, Fischer J (1993) Observations of vertical currents and convection in the central Greenland Sea during the winter of 1988 - 1989. *J Geophys Res* 98:14401–14421.
- Schott FA, Fischer J, Dengler M, Zantopp R (2006) Variability of the deep western boundary current east of the grand banks. *Geophys Res Lett* 33:3–7. doi: 10.1029/2006GL026563
- Scott GH (1963) Uniformitarianism, the uniformity of nature, and paleoecology. *New Zeal J Geol Geophys* 6:510–527. doi: 10.1080/00288306.1963.10420063
- Seidenkrantz MS (1993) Benthic foraminiferal and stable isotope evidence for a “Younger Dryas-style” cold spell at the Saalian-Eemian transition, Denmark. *Palaeogeogr Palaeoclimatol Palaeoecol* 102:103–120. doi: 10.1016/0031-0182(93)90008-7
- Shackleton N (1967) Oxygen isotope analyses and pleistocene temperatures re-assessed. *Nature* 215:15–17. doi: 10.1038/215015a0
- Shackleton NJ (1969) The Last Interglacial in the Marine and Terrestrial Records. *Proc R Soc B Biol Sci* 174:135–154. doi: 10.1098/rspb.1969.0085
- Shackleton NJ (1987) Oxygen isotopes, ice volume and sea level. *Quat Sci Rev* 6:183–190. doi: 10.1016/0277-3791(87)90003-5
- Shackleton NJ, Chapman M, Sánchez-Goñi MF, et al (2002) The Classic Marine Isotope Substage 5e. *Quat Res* 58:14–16. doi: 10.1006/qres.2001.2312
- Shackleton NJ, Hall M a, Vincent E (2000) Phase relationships between millennial-scale events 64,000- 24,000 years ago. *Paleoceanography* 15:565–569. doi: 10.1029/2000pa000513
- Shackleton NJ, Hall MA (1984) 16 . Oxygen and Carbon Isotope Stratigraphy of Deep Sea Drilling Project Hole 552a: Plio-Pleistocene Glacial History. *Initial Reports DSDP* 81:599–609. doi: 10.2973/dsdp.proc.81.116.1984
- Shackleton NJ, Sánchez-Goñi MF, Pailler D, Lancelot Y (2003) Marine Isotope Substage 5e and the Eemian Interglacial. *Glob Planet Change* 36:151–155. doi: 10.1016/S0921-8181(02)00181-9
- Shimada C, Sato T, Toyoshima S, et al (2008) Paleocological significance of laminated diatomaceous oozes during the middle-to-late Pleistocene, North Atlantic Ocean (IODP Site U1304). *Mar Micropaleontol* 69:139–150. doi: 10.1016/j.marmicro.2008.07.004
- Siddall M, Bard E, Rohling EJ, Hemleben C (2006) Sea-level reversal during termination II. *Geology* 34:817–820. doi: 10.1130/G22705.1
- Sigman DM, Boyle EA (2000) Glacial/Interglacial Variations In Atmospheric Carbon Dioxide. *Nature* 407:859–869. doi: 10.1038/35038000
- Simstich J, Sarnthein M, Erlenkeuser H (2003) Paired  $\delta^{18}O$  signals of *Neogloboquadrina pachyderma* (s) and *Turborotalita quinqueloba* show thermal stratification structure in Nordic Seas. *Mar Micropaleontol* 48:107–125. doi: 10.1016/S0377-8398(02)00165-2
- Singler HR, Villareal TA (2005) Nitrogen inputs into the euphotic zone by vertically migrating *Rhizosolenia* mats. *J Plankton Res* 27:545–556. doi: 10.1093/plankt/fbi030
- Skinner LC, Shackleton NJ (2005) An Atlantic lead over Pacific deep-water change across Termination I: Implications for the application of the marine isotope stage stratigraphy. *Quat Sci Rev* 24:571–580. doi: 10.1016/j.quascirev.2004.11.008
- Small D, Austin W, Rinterknecht V (2013) Freshwater influx, hydrographic reorganization and the dispersal of ice-rafted detritus in the sub-polar North Atlantic Ocean during the last deglaciation. *J Quat Sci* 28:527–535. doi: 10.1002/jqs.2644
- Smethie Jr. WM, Fine R a., Putzka A, Jones EP (2000) Tracing the flow of the North Atlantic Deep Water using chlorofluorocarbons. *J Geophys Res* 105:14297–14323. doi: 10.1029/1999JC900274

- Spero HJ (1992) Do planktic foraminifera accurately record shifts in the carbon isotopic composition of seawater ZCO<sub>2</sub>? *Mar Micropaleontol* 19:275–285. doi: 10.1016/0377-8398(92)90033-G
- Spero HJ, Bijma J, Lea DW, Bemis BE (1997) Effect of seawater carbonate concentrations on foraminiferal carbon and oxygen isotopes. *Nature* 390:497–500--.
- Spero HJ, Lea DW (1996) Experimental determination of stable isotope variability in *Globigerina bulloides*: Implications for paleoceanographic reconstructions. *Mar Micropaleontol* 28:231–246. doi: 10.1016/0377-8398(96)00003-5
- Spero HJ, Lea DW (2002) The cause of carbon isotope minimum events on glacial terminations. *Science* (80- ) 296:522–525. doi: 10.1126/science.1069401
- Staines-Urfas F, Kuijpers A, Korte C (2013) Evolution of subpolar North Atlantic surface circulation since the early Holocene inferred from planktic foraminifera faunal and stable isotope records. *Quat Sci Rev* 76:66–81. doi: 10.1016/j.quascirev.2013.06.016
- Stanford JD, Rohling EJ, Bacon S, et al (2011) A new concept for the paleoceanographic evolution of Heinrich event 1 in the North Atlantic. *Quat Sci Rev* 30:1047–1066. doi: 10.1016/j.quascirev.2011.02.003
- Stein M, Wasserburg GJ, Aharon P, et al (1993) TIMS U-series dating and stable isotopes of the last interglacial event in Papua New Guinea. *Geochim Cosmochim Acta* 57:2541–2554. doi: 10.1016/0016-7037(93)90416-T
- Stern J V., Lisiecki LE (2013) North Atlantic circulation and reservoir age changes over the past 41,000 years. *Geophys Res Lett* 40:3693–3697. doi: 10.1002/grl.50679
- Stirling CH, Esat TM, Lambeck K, McCulloch MT (1998) Timing and duration of the Last Interglacial: Evidence for a restricted interval of widespread coral reef growth. *Earth Planet Sci Lett* 160:745–762. doi: 10.1016/S0012-821X(98)00125-3
- Stocker TF, Johnsen SJ (2003) A minimum thermodynamic model for the bipolar seesaw. *Paleoceanography* 18:1–9. doi: 10.1029/2003PA000920
- Stolz K, Baumann K-H (2010) Changes in palaeoceanography and palaeoecology during Marine Isotope Stage (MIS) 5 in the eastern North Atlantic (ODP Site 980) deduced from calcareous nannoplankton observations. *Palaeogeogr Palaeoclimatol Palaeoecol* 292:295–305. doi: 10.1016/j.palaeo.2010.04.002
- Stommel H (1958) The Abyssal Circulation. *Nature* 180:733–734. doi: 10.1038/180733a0
- Stone EJ, Lunt DJ, Annan JD, Hargreaves JC (2013) Quantification of the Greenland ice sheet contribution to Last Interglacial sea level rise. *Clim Past* 9:621–639. doi: 10.5194/cp-9-621-2013
- Stoner JS, Channell JET, Hillaire-Marcel C (1995) Late Pleistocene relative geomagnetic paleointensity from the deep Labrador Sea: Regional and global correlations. *Earth Planet Sci Lett* 134:237–252. doi: 10.1016/0012-821X(95)00134-X
- Stoner JS, Channell JET, Hillaire-Marcel C (1998) A 200 ka geomagnetic chronostratigraphy for the Labrador Sea: indirect correlation of the sediment record to SPECMAP. *Earth Planet Sci Lett* 159:165–181. doi: 10.1016/S0012-821X(98)00069-7
- Stoner JS, Channell JET, Hillaire-Marcel C (1996) The magnetic signature of rapidly deposited detrital layers from the Deep Labrador Sea: Relationship to North Atlantic Heinrich layers. *Paleoceanography* 11:309. doi: 10.1029/96PA00583
- Stoner JS, Channell JET, Mazaud A, et al (2013) The influence of high-latitude flux lobes on the Holocene paleomagnetic record of IODP Site U1305 and the northern North Atlantic. *Geochemistry, Geophys Geosystems* 14:4623–4646. doi: 10.1002/ggge.20272
- Stouffer RJ, Yin J, Gregory JM, et al (2006) Investigating the causes of the response of the thermohaline circulation to past and future climate changes. *J Clim* 19:1365–1387. doi: 10.1175/JCLI3689.1
- Stramma L, Kieke D, Rhein M, et al (2004) Deep water changes at the western boundary of the subpolar North Atlantic during 1996 to 2001. *Deep Res Part I Oceanogr Res Pap* 51:1033–1056. doi: 10.1016/j.dsr.2004.04.001
- Straneo F (2006) Heat and Freshwater Transport through the Central Labrador Sea. *J Phys Oceanogr* 36:606–628. doi: 10.1175/JPO2875.1
- Strass VH (1992) Chlorophyll patchiness caused by mesoscale upwelling at fronts. *Deep Sea Res Part A, Oceanogr Res Pap* 39:75–96. doi: 10.1016/0198-0149(92)90021-K
- Svensson a., Bigler M, Kettner E, et al (2011) Annual layering in the NGRIP ice core during the Eemian. *Clim Past* 7:1427–1437. doi: 10.5194/cp-7-1427-2011
- Sy A, Rhein M, Lazier JRN, et al (1997) Surprisingly rapid spreading of newly formed intermediate waters across the

North Atlantic Ocean. *Nature* 386:675–679.

- Talley LD, McCartney MS (1982) Distribution and Circulation of Labrador Sea Water. *J. Phys. Oceanogr.* 12:1189–1205.
- Tanhua T, Olsson KA, Jeansson E (2005) Formation of Denmark Strait overflow water and its hydro-chemical composition. *J Mar Syst* 57:264–288. doi: 10.1016/j.jmarsys.2005.05.003
- Teller JT, Leverington DW, Mann JD (2002) Freshwater outbursts to the oceans from glacial Lake Agassiz and their role in climate change during the last deglaciation. *Quat Sci Rev* 21:879–887. doi: 10.1016/S0277-3791(01)00145-7
- Thomas AL, Henderson GM, Deschamps P, et al (2009) Penultimate Deglacial Sea-Level Timing from Uranium/Thorium Dating of Tahitian Corals. *Science* (80- ) 324:1186–1189. doi: 10.1126/science.1168754
- Thornalley DJR, Bauch HA, Gebbie G, et al (2015) A warm and poorly ventilated deep Arctic Mediterranean during the last glacial period. *Science* (80- ) 349:706–710. doi: 10.1126/science.aaa9554
- Thornalley DJR, Elderfield H, McCave IN (2011) Reconstructing North Atlantic deglacial surface hydrography and its link to the Atlantic overturning circulation. *Glob Planet Change* 79:163–175. doi: 10.1016/j.gloplacha.2010.06.003
- Thunell RC, Williams DF (1989) Glacial-Holocene salinity changes in the Mediterranean Sea: hydrographic and depositional effects. *Nature* 338:493–496. doi: 10.1038/340301a0
- Toom M Den, Dijkstra HA, Cimadoribus AA, Drijfhout SS (2012) Effect of atmospheric feedbacks on the stability of the Atlantic meridional overturning circulation. *J Clim* 25:4081–4096. doi: 10.1175/JCLI-D-11-00467.1
- Toucanne S, Zaragosi S, Bourillet JF, et al (2009) Timing of massive “Fleuve Manche” discharges over the last 350 kyr: insights into the European ice-sheet oscillations and the European drainage network from MIS 10 to 2. *Quat Sci Rev* 28:1238–1256. doi: 10.1016/j.quascirev.2009.01.006
- Toyota T, Smith IJ, Gough AJ, et al (2013) Oxygen isotope fractionation during the freezing of sea water. *J Glaciol* 59:697–710. doi: 10.3189/2013JoG12J163
- Tripanas EK, Piper DJW (2008) Late Quaternary stratigraphy and sedimentology of Orphan Basin: Implications for meltwater dispersal in the southern Labrador Sea. *Palaeogeogr Palaeoclimatol Palaeoecol* 260:521–539. doi: 10.1016/j.palaeo.2007.12.016
- Tzedakis C (2003) Timing and duration of Last Interglacial conditions in Europe: A chronicle of a changing chronology. *Quat Sci Rev* 22:763–768. doi: 10.1016/S0277-3791(03)00004-0
- Urey HC (1947) The thermodynamic properties of isotopic substances. *J Chem Soc* 562–581.
- Våge K, Pickart RS, Sarafanov A, et al (2011) The Irminger Gyre: Circulation, convection, and interannual variability. *Deep Res Part I Oceanogr Res Pap* 58:590–614. doi: 10.1016/j.dsr.2011.03.001
- van Krevelend S a., Knappertsbusch M, Ottens J, et al (1996) Biogenic carbonate and ice-rafted debris (Heinrich layer) accumulation in deep-sea sediments from a Northeast Atlantic piston core. *Mar Geol* 131:21–46. doi: 10.1016/0025-3227(95)00143-3
- Van Nieuwenhove N, Bauch H a., Eynaud F, et al (2011) Evidence for delayed poleward expansion of North Atlantic surface waters during the last interglacial (MIS 5e). *Quat Sci Rev* 30:934–946. doi: 10.1016/j.quascirev.2011.01.013
- van Raden UJ, Groeneveld J, Raitzsch M, Kucera M (2011) Mg/Ca in the planktonic foraminifera *Globorotalia inflata* and *Globigerinoides bulloides* from Western Mediterranean plankton tow and core top samples. *Mar Micropaleontol* 78:101–112. doi: 10.1016/j.marmicro.2010.11.002
- Veres D, Bazin L, Landais A, et al (2013) The Antarctic ice core chronology (AICC2012): An optimized multi-parameter and multi-site dating approach for the last 120 thousand years. *Clim Past* 9:1733–1748. doi: 10.5194/cp-9-1733-2013
- Visbeck M (2007) Power of pull. *Nature* 447:383. doi: 10.1038/447383a
- Von Langen PJ, Pak DK, Spero HJ, Lea DW (2005) Effects of temperature on Mg/Ca in neogloboquadrinid shells determined by live culturing. *Geochemistry, Geophys Geosystems*. doi: 10.1029/2005GC000989
- Wadhams P, Comiso JC, Prussen E, et al (1996) The development of the Odden ice tongue in the Greenland Sea during winter 1993 from remote sensing and field observations. *J Geophys Res Ocean* 101:18213–18235. doi: 10.1029/96JC01440
- Waelbroeck C, Duplessy JC, Michel E, et al (2001) The timing of the last deglaciation in North Atlantic climate records. *Nature* 412:724–727. doi: 10.1038/35106623
- Wang Y, Cheng H, Edwards RL, et al (2008) Millennial- and orbital-scale changes in the East Asian monsoon over

- the past 224,000 years. *Nature* 451:1090–1093. doi: 10.1038/nature06692
- Wang YJ, Cheng H, Edwards RL, et al (2001) A High-Resolution Absolute-Dated Late Pleistocene Monsoon Record from Hulu Cave, China. *Science* (80- ) 294:2345–2349. doi: 10.1126/science.1064618
- Weisse T, Berendonk T, Kamjunke N, et al (2011) Significant habitat effects influence protist fitness: evidence for local adaptation from acidic mining lakes. *Ecosphere* 2:art134. doi: 10.1890/ES11-00157.1
- Willis JK (2010) Can in situ floats and satellite altimeters detect long-term changes in Atlantic Ocean overturning? *Geophys Res Lett* 37:n/a-n/a. doi: 10.1029/2010GL042372
- Winograd IJ, Coplen TB, Landwehr JM, et al (1992) Continuous 500,000-Year Climate Record from Vein Calcite in Devils Hole, Nevada. *Science* (80- ) 258:255–260. doi: 10.1126/science.258.5080.255
- Winograd IJ, Coplen TB, Szabo BJ, Riggs AC (1988) A 250,000-year climatic record from great basin vein calcite: implications for milankovitch theory. *Science* 242:1275–1280. doi: 10.1126/science.242.4883.1275
- Winsor K, Carlson AE, Klinkhammer GP, et al (2012) Evolution of the northeast Labrador Sea during the last interglaciation. *Geochemistry Geophys Geosystems* 13:Q11006. doi: 10.1029/2012GC004263
- Wolff EW, Chappellaz J, Blunier T, et al (2010) Millennial-scale variability during the last glacial: The ice core record. *Quat Sci Rev* 29:2828–2838. doi: 10.1016/j.quascirev.2009.10.013
- Wunsch C (2002) What Is the Thermohaline Circulation? *Science* (80- ) 298:1179–1181. doi: 10.1126/science.1079329
- Xu X, Rhines PB, Chassignet EP, Schmitz WJ (2015) Spreading of Denmark Strait Overflow Water in the Western Subpolar North Atlantic: Insights from Eddy-Resolving Simulations with a Passive Tracer. *J Phys Oceanogr* 45:2913–2932. doi: 10.1175/JPO-D-14-0179.1
- Yashayaev I (2007) Hydrographic changes in the Labrador Sea, 1960–2005. *Progress in Oceanography*, 73(3–4), 242–276. <http://doi.org/10.1016/j.pocean.2007.04.015>
- Yashayaev, I., Bersch, M., & van Aken, H. M. (2007). Spreading of the Labrador Sea Water to the Irminger and Iceland basins. *Geophysical Research Letters*, 34(10), 1–8. <http://doi.org/10.1029/2006GL028999>
- Yoder, J. A., Ackleson, S. G., Barber, R. T., Flament, P., & Balch, W. M. (1994). A line in the sea. *Nature*, 371, 689–692.
- Zahn, R., & Mix, A. C. (1991). Benthic foraminiferal  $\delta^{18}O$  in the ocean's temperature-salinity-density field: constraints on ice age thermohaline circulation. *Paleoceanography*, 6(1), 1–20.
- Zahn, R., Schönfeld, J., Kudrass, H. R., Park, M. H., Erlenkeuser, H., & Grootes, P. (1997). Thermohaline instability in the North Atlantic during melt water events: Stable isotope and ice-rafted detritus records from core SO75-26KL, Portuguese margin. *Paleoceanography*, 12(5), 696–710. <http://doi.org/10.1029/97PA00581>
- Zhuravleva, A., Bauch, H. A., & Van Nieuwenhove, N. (2017). Last Interglacial (MIS5e) hydrographic shifts linked to meltwater discharges from the East Greenland margin. *Quaternary Science Reviews*, 164, 95–109. <http://doi.org/10.1016/j.quascirev.2017.03.026>